I N A U G U R A L – D I S S E R T A T I O N

zur

Erlangung der Doktorwürde

der

Gesamtfakultät für
Mathematik, Ingenieur- und Naturwissenschaften

der

Ruprecht - Karls - Universität
Heidelberg

vorgelegt von

M.Sc. Lennart Singer

aus Aglasterhausen

Tag der mündlichen Prüfung: 28.06.2023

Untersuchung von lithiumreichen Antiperowskiten und nanostrukturierten Übergangsmetallverbindungen für Lithium-Ionen-Batterien

Gutachter: Prof. Dr. Rüdiger Klingeler

PD Dr. Loredana Gastaldo

Untersuchung von lithiumreichen Antiperowskiten und nanostrukturierten Übergangsmetallverbindungen für Lithium-Ionen-Batterien

Die vorliegende Arbeit befasst sich mit der Untersuchung der physikalischen und elektrochemischen Eigenschaften von potenziellen Anoden- und Kathodenmaterialien für die nächste Generation an Lithium-Ionen-Batterien. Als potenzielle Anodenmaterialien werden aufgrund ihrer Konversionsreaktionen multielektronenspeicherfähige Fe_3O_4-, MoO_2- sowie MoS_2-Nano-Kohlenstoffkomposite untersucht. Auf der Kathodenmaterialseite wird die Klasse der lithiumreichen Antiperowskite, welche sowohl kationische als auch anionische Redoxaktivität aufweisen, beispielhaft anhand von $(Li_2Fe)SeO$ studiert. Die physikalische Charakterisierung erfolgt mittels Röntgendiffraktometrie, Röntgenphotoelektronenspektroskopie, Rasterelektronenmikroskopie und Magnetisierungsmessungen. Zyklische Voltammetrie, galvanostatische Zyklierung und potentiostatische elektrochemische Impedanzspektroskopie geben Aufschluss über die elektrochemischen Eigenschaften. Die vorgestellten Ergebnisse zeigen für Fe_3O_4@HCS in Zyklus 250 eine Kapazität von 1050 mAh g^{-1}, welche deutlich über der theoretischen Kapazität von 694 mAh g^{-1} liegt. Der Ursprung der zusätzlichen Kapazität der Fe_3O_4-Nanopartikel konnte auf eine während des Zyklierens sich auf- und abbauende kapazitäre Oberflächenschicht zurückgeführt werden. Die vorgestellten MoO_2-Kohlenstoffkomposite zeigen, dass auch mit preisgünstigen Kohlenstoffquellen eine kompetitive elektrochemische Performance erreicht werden kann und dass sowohl die Partikelgröße als auch der Kohlenstoffgehalt einen entscheidenden Einfluss auf die elektrochemische Performance besitzen. Studien an blumenartigen Graphen-MoS_2 offenbaren die intrinsischen physikalischen und elektrochemischen Eigenschaften des Materials. Die durchgeführten Untersuchungen am lithiumreichen Antiperowskit $(Li_2Fe)SeO$ belegen dessen vielversprechende elektrochemische Eigenschaften. Das festkörpersynthetisierte $(Li_2Fe)SeO$ erreicht eine Kapazität von 225 mAh g^{-1} bei einer Stromdichte von 0,1C. Des Weiteren wurde die Ursache für die schlechte Zyklenstabilität der lithiumreichen Antiperowskite gefunden und ein Verfahren zur Verbesserung der Zyklenstabilität vorgestellt.

Investigation of lithium-rich antiperovskites and nanostructured transition metal compounds for lithium-ion-batteries

This thesis studies the physical and electrochemical properties of potential anode and cathode materials for the next generation of lithium-ion-batteries. In this context, the conversion-based multielectron storage materials Fe_3O_4-, MoO_2- as well as MoS_2 nano carbon composites are investigated as potential anode materials. On the cathode material side, the class of lithium-rich antiperovskites, which exhibit both cationic and anionic redox activity, is studied using $(Li_2Fe)SeO$ as an example. The physical characterization is performed by means of X-ray diffraction, X-ray photoelectron spectroscopy, scanning electron microscopy and magnetization measurements. Cyclic voltammetry, galvanostatic cycling, and potentiostatic electrochemical impedance spectroscopy provide information on the electrochemical properties. The results presented show for Fe_3O_4@HCS a capacity of 1050 mAh g^{-1} in cycle 250, which is significantly higher than the theoretical capacity of 694 mAh g^{-1}. The origin of the additional capacity could be attributed to a build-up and down capacitative surface layer. In the case of the presented MoO_2/carbon composite, competitive electrochemical performance is achieved with low-cost carbon sources. Moreover, the results demonstrate that both particle size and carbon content have a crucial impact on the electrochemical performance. Studies on flower-like graphene MoS_2 reveal the materials intrinsic physical and electrochemical properties. Investigations on the lithium-rich antiperovskite $(Li_2Fe)SeO$ displays promising electrochemical properties of 225 mAh g^{-1} at 0.1C. Furthermore, the underlying cause behind the poor cycling stability was determined and a way to improve cycling stability presented.

Inhaltsverzeichnis

Kapitel 1 Einleitung

Eine der größten Herausforderungen des 21. Jahrhunderts besteht in der Bewältigung des Klimawandels. Um diese Herausforderung zu meistern, ist eine umfassende Transformation des Energiebereichs von fossilen Brennstoffen hin zu erneuerbaren Energiequellen zwingend erforderlich. Ein zentraler Aspekt dieser Transformation ist die Elektrifizierung von Prozessen sowie der simultane massive Ausbau in der Gewinnung erneuerbaren Energien und deren Speicherung [1]. Im Bereich der kurzzeitigen und auch portablen Energiespeicherung sind besonders Batterien von großer Bedeutung, da sie eine sehr hohe Effizienz in der reversiblen Speicherung von elektrischer Energie in Form von elektrochemischer Energie aufweisen. Das etablierte Batteriekonzept, das bereits heute in nahezu allen Bereichen unseres modernen Lebens allgegenwärtig ist, wird daher weiter an Bedeutung gewinnen und in immer mehr Anwendungen eingesetzt werden [2]. Um dies gewährleisten zu können, bedarf es der Weiterentwicklung hin zu immer effektiveren, preisgünstigeren Batterien mit hohen gravimetrischen und volumetrischen Energiedichten. In diesem Zusammenhang sind Lithium-Ionen-Batterien (LIBs) aufgrund des geringen ionischen Radius von Lithium und seiner hohen Elektronegativität einzigartig [3, 4]. Diese intrinsischen Eigenschaften von Lithium führen dazu, dass Lithium-Ionen-Batterien in Bereichen, in denen möglichst viel Energie in einem möglichst geringen Gewicht oder Volumen gespeichert werden muss (Mobiltelefone, Fahrzeuge), nicht nur heute, sondern auch in naher Zukunft unangefochten sind [3, 4] (siehe Abbildung 1.1a).

Lithium-Ionen-Batterien (LIB), siehe Abbildung 1.1b, bestehen aus einer Anode (Minuspol), einer Kathode (Pluspol) und einem ionendurchlässigen Separator, der die Elektroden voneinander trennt. Dieser Separator ist mit einem Elektrolyten getränkt, der die Bewegung von Lithium-Ionen ermöglicht. Die Menge an elektrischer Energie, die in einem Batteriematerial gespeichert werden kann, ist hauptsächlich von zwei Faktoren abhängig. Erstens von der Menge der gespeicherten Ladung, welche der Kapazität entspricht und zweitens der Differenz der elektrochemischen Potenziale der Redoxpaare [6]. Die Möglichkeit der

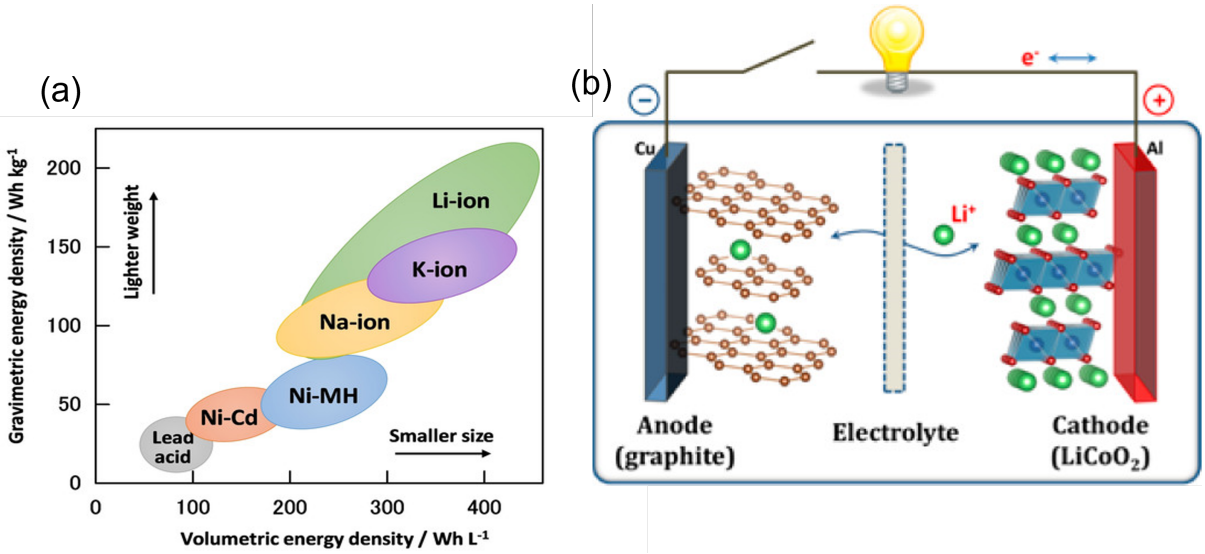

Abbildung 1.1: (a) Vergleich verschiedener Batterietypen in Bezug zu erreichbaren gravimetrischen und volumetrischen Energiedichten, entnommen aus [5]. (b) Schematische Darstellung einer Lithium-Ionen-Batterie, entnommen aus [6].

Energiespeicherung einer Batterie ist daher determiniert durch die Menge des vorhandenen Aktivmaterials und der Zellchemie. Die Verbesserungen der letzten Jahre lassen sich vor allem auf die Erhöhung des Aktivmaterialanteils in der Batterie durch Optimierungen in der Herstellung zurückführen [7, 8]. Auch in der Zukunft sind weitere Verbesserungen aus diesem Bereich der Batterieforschung zu erwarten, allerdings existiert hier auch ein festes Limit. Die maximal erreichbare Energiedichte ist durch die intrinsischen Eigenschaften der verwendeten Aktivmaterialien festgelegt. Weitere, bahnbrechende Verbesserungen können somit nur aus der Verwendung anderer, neuer Batteriematerialien entspringen. Die Erforschung neuartiger Materialien mit anderer, neuer Zellchemie zur Speicherung von Lithium-Ionen ist daher von zentraler Bedeutung für weitere wegweisende Verbesserungen. Speziell werden Materialien gesucht, die folgende inhärente positive Eigenschaften aufweisen: Hohe Energiedichten (1), hohe Leistung (2), lange Lebensdauer (3), hohe Sicherheit (4), bestehend aus umweltfreundlichen, nicht kritischen Rohstoffen (5) und final noch möglichst preisgünstig (6) [4].

Der enorme Bedarf an immer höheren Energiedichten ließ vor allem Elektrodenmaterialien, die eine höhere theoretische Kapazität aufweisen, in den Fokus der Forschung rücken. Bisher basieren alle kommerzialisierten Materialien auf dem Speichermechanismus der Interkalation, bei dem Li^+-Ionen in freie Plätze im Kristallgitter eingelagert werden. Der Vorteil eines Interkalationsmaterials ist dabei, dass es im Normalfall nur zu einer kleinen

kristallografischen Änderung der Wirtsstruktur aufgrund der Lithiumaufnahme/-abgabe kommt. Aufgrund dieses Wirkungsprinzips besitzen Interkalationsmaterialien in aller Regel weitere positive Eigenschaften, wie eine hohe Zyklenstabilität und Leistung [9–11]. Die Kristallstruktur begrenzt die maximale Kapazität aber auch auf ein oder weniger als ein Elektronentransfer pro Formeleinheit [10]. Die Art der reversiblen Speicherung von Lithium bestimmt daher maßgeblich die erreichbare Kapazität und damit direkt auch die speicherbare Energie [12]. Es wird daher aktiv nach Materialien gesucht, die Lithium mittels eines anderen Speichermechanismus einlagern [10, 13].

Auf der Anodenseite, mit den derzeit kommerzialisierten Anodenmaterialien Graphit und $Li_4Ti_5O_{12}$ [14], liegt ein klarer Fokus auf dem Erforschen und Verwenden der zwei Multielektronenspeichermechanismen Legierung und Konversion (siehe Abbildung 1.2 b,c).

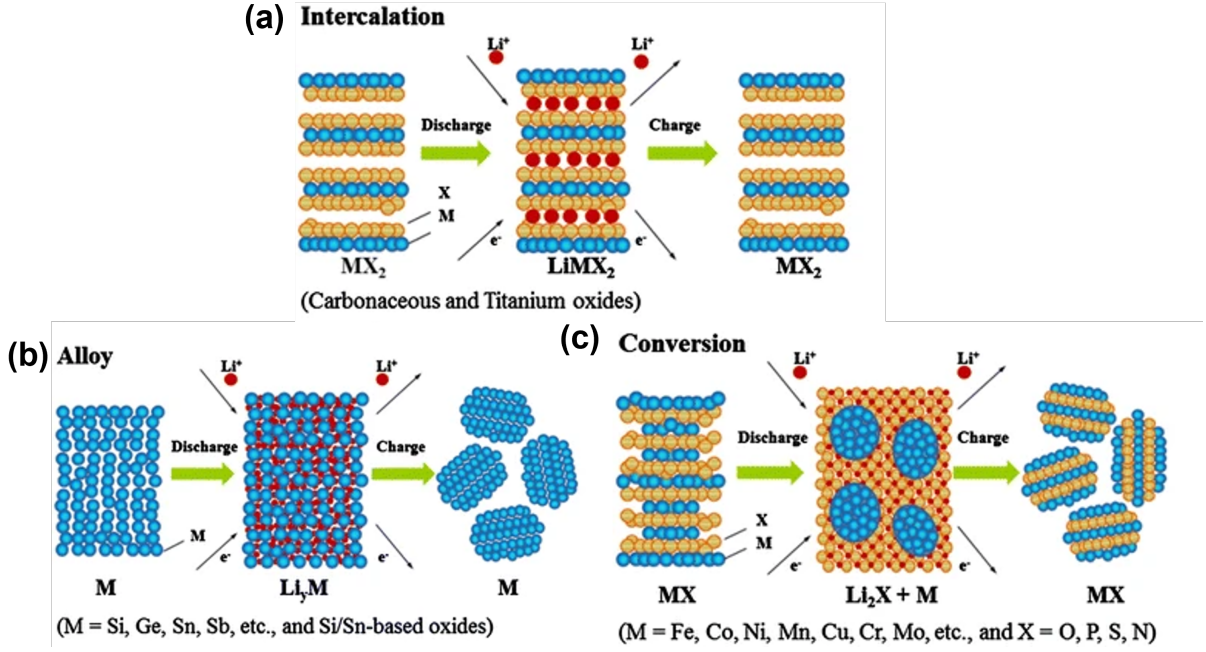

Abbildung 1.2: Schematische Darstellung der unterschiedlichen Li^+-Ionen-Speichermechanismen: (a) Interkalation, (b) Legierung und (c) Konversion. Adaptiert von [15].

Die Speicherung von Lithium mittels Legierungsbildung mit Metallen/Halbmetallen kann sehr hohe Kapazitäten liefern, wie z. B. im Falle von Silizium (4200 mAh g^{-1} für $Li_{4.4}Si$ und damit 10-mal so hoch wie bei Graphit) [16]. Die praktische Nutzung ist durch die auftretenden großen Volumenänderungen allerdings nicht einfach. Aufgrund der intensiven Forschung in den letzten Jahren steht der Einsatz von legierungsbildenden Materialien am Rande der Kommerzialisierung [17].

Eine interessante und vielfach erforschte Gruppe an Materialien sind Übergangsmetallverbindungen M_nX_y (M = Fe, Co, Ni etc., X = O, N, F, S, P,). Diese Materialklasse nimmt Lithium über sogenannte Konversionsreaktionen auf. Bei der Konversionsreaktion ($M_nO_y + 2yLi^+ + 2ye^- \rightarrow yLi_2O + nM$), hier beispielhaft für Übergangsmetalloxide, wird das Übergangsmetall vollständig reduziert und Li_2O gebildet. Diese Art der Speicherung erlaubt es, ein Vielfaches der Kapazität von Interkalationsmaterialien zu erreichen. Konversionsmaterialien besitzen allerdings auch eine Vielzahl an inhärenten Nachteilen, die ihre Kommerzialisierung bisher verhindert haben [10, 13].

Um die Energiedichte auf der Kathodenseite zu verbessern, werden Materialien erforscht die neben der bisher verwendeten kationischen Redoxreaktion von Übergangsmetallionen auch eine reversible anionische Redoxreaktion besitzen. Dieser Ansatz in der Entwicklung von Kathodenmaterialien kann im Idealfall zu einer Verdopplung der Kapazität führen [2]. Die kürzlich entdeckte Materialklasse der lithiumreichen Antiperowskite $(Li_2\,TM)\,Ch$O (TM = Fe, Mn, Co :Ch = S, Se), deren reversible Multielektronenspeicherung pro Struktureinheit auf einer gekoppelten Redoxaktivität des Übergangsmetallkations und des Sulfid/Selenid-Anions beruht, verspricht hohe spezifische Kapazitäten [18]. Die Erforschung der lithiumreichen Antiperowskite sowie deren elektrochemischen Eigenschaften steht noch am Anfang. Bisher haben sich bereits viele positive Eigenschaften, aber auch einige Probleme in Bezug zu deren Tauglichkeit als Kathodenmaterial für LIB gezeigt.

Für einige Probleme von Lithium-Ionen-Batteriematerialien existieren bereits heute Lösungen oder Lösungsansätze. Ein Überblick über einige Lösungsansätze und deren Einfluss auf die Eigenschaften des Batteriematerials, wie zum Beispiel die Partikelgrößenskalierung, die Kompositherstellung und auch die Kohlenstoffummantelung, ist in Abb. 1.3 gegeben. Dies zeigt, dass nicht nur die Entdeckung von neuen Materialien von äußerster Wichtigkeit ist, sondern auch deren Optimierung. Die passenden Verbesserungsansätze können nur durch ein tiefgreifendes Verständnis der physikalischen Zusammenhänge zwischen Materialstruktur und den stattfindenden elektrochemischen Prozessen erlangt werden. Der einzige Weg, diese Zusammenhänge herzustellen, ist über eine Fülle von Charakterisierungsmessungen bezüglich der Materialeigenschaften. Das erlangte Verständnis kann dann genutzt werden, um Lösungsansätze für materialspezifische Probleme zu entwickeln.

Die vorliegende Arbeit beschäftigt sich zum einen mit konversionsbasierten Übergangsmetallverbindungen als potenzielle Anodenmaterialien in LIB. Hierbei liegt ein klarer Fokus auf der Untersuchung des Ursprungs und der Verbindung der auftretenden elektrochemischen Phänomene und den inhärenten physikalischen Eigenschaften des Materials.

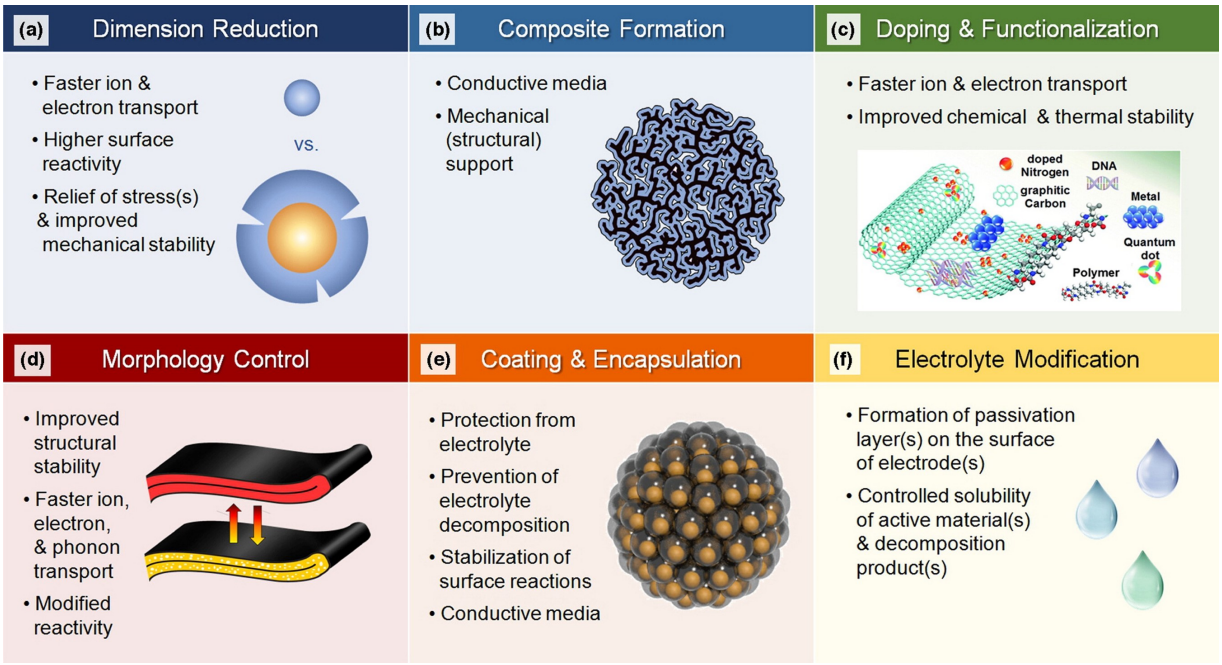

Abbildung 1.3: Allgemeine Optimierungsstrategien für LIB-Materialien (a) Skalierung der Partikelgröße, (b) Bildung von Verbundwerkstoffen, (c) Dotierung und Funktionalisierung, (d) Abstimmung der Morphologie, (e) Bildung von Beschichtungen/Einhüllen der Aktivmaterialien und (f) Modifizierung des Elektrolyten. Entnommen aus [4].

Zum anderen wird die vielversprechende Materialklasse der lithiumreichen Antiperowskite hinsichtlicher ihrer physikalischen und elektrochemischen Eigenschaften untersucht und deren Eignung als Kathodenmaterial für Lithium-Ionen-Batterien studiert.

Die Arbeit ist wie folgt gegliedert: In Kapitel 2 wird eine kurze Einführung in die relevanten Grundlagen und Messmethoden sowie eine kurze Literaturzusammenfassung der untersuchten Materialien gegeben. Kapitel 3 befasst sich mit den Konversionsmaterialien Fe_3O_4, MoO_2 sowie MoS_2, die als Kohlenstoffkomposite untersucht werden. Hierbei wird vor allem der Zusammenhang physikalischer und elektrochemischer Eigenschaften dieser Materialien untersucht und die auftretenden elektrochemischen Phänomene mittels *ex situ*-Messungen erforscht. Kapitel 4 widmet sich der Materialklasse der lithiumreichen Antiperowskite. Die Untersuchungen in diesem Abschnitt zeigen das Potential dieser Materialklasse am Beispiel von $(Li_2Fe)SeO$ und präsentieren ein umfassendes Bild der physikalischen und elektrochemischen Eigenschaften. Untersuchungen an $(Li_2Fe)SeO$, welches mit einem effizienten Mahlvorgang hergestellt wurde, zeigten einen bisher unbekannten Prozess im elektrochemischen Reaktionsmechanismus auf. Die Untersuchung dieses neuen Prozesses zeigen dessen Bedeutung für die Zyklenstabilität und ermöglichten darüber hinaus die

Verbesserung der elektrochemischen Performance. Im letzten Kapitel werden die wichtigsten Ergebnisse der einzelnen Abschnitte zusammengefasst und im Kontext diskutiert.

Kapitel 2 Grundlagen

2.1 Theoretische Grundlagen und experimentelle Durchführung physikalischer Messungen

Die Untersuchung der verwendeten Materialien für Batterieelektroden kann aufgrund der Komplexität nicht von einer einzigen Technik gelöst werden. Für ein umfassendes Bild müssen daher die Ergebnisse vieler verschiedener Charakterisierungstechniken zusammengefügt werden [19]. Im Folgenden wird eine kurze Einführung in die Theorie sowie die experimentelle Durchführung der dieser Arbeit zugrundeliegenden Messmethoden gegeben.

2.1.1 Pulver-Röntgendiffraktometrie (XRD)

Pulver-Röntgendiffraktometrie (XRD) dient der Phasenbestimmung von Pulver-Proben. Es handelt sich dabei um eine zerstörungsfreie Messung, die für ganz oder teilweise kristalline Materialien anwendbar ist.

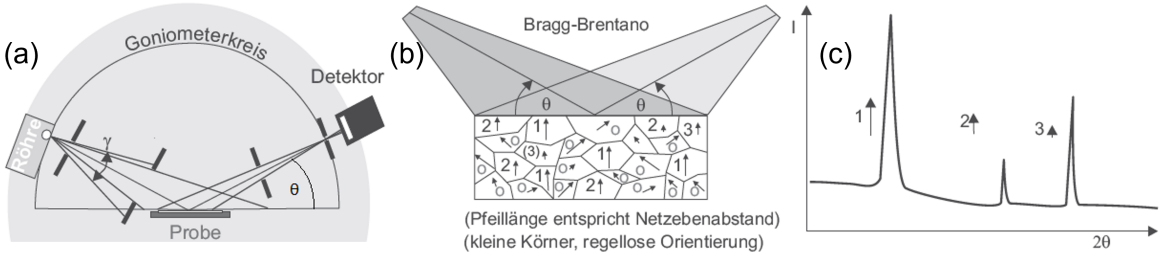

Abbildung 2.1: Vereinfachte Illustration der Bragg-Bretano-Geometrie für Pulver-Röntgendiffraktometrie (a, b), resultierendes Diffraktogramm (c). Adaptiert von [20].

Der experimentelle Aufbau und das Funktionsprinzip der in dieser Arbeit verwendeten

Pulver-Röntgendiffraktometrie in Bragg-Bretano-Geometrie ist schematisch vereinfacht in Abbildung 2.1a) dargestellt. Monochromatische Röntgenstrahlen werden in einem Winkel θ auf die Probe fokussiert. Der Detektor, auch im Winkel θ zur Probe, registriert ein messbares Signal (Abbildung 2.1c), wenn es Partikel mit einer Netzebenennormalen senkrecht zur Oberfläche gibt, deren Netzebenenabstände die Braggbedingung erfüllen. Siehe zum Beispiel Partikel mit der Markierung 1↑ in Abbildung 2.1b. Im Folgenden wird der Winkel θ verändert, um weitere Netzebenenabstände und Reflexe (2↑, 3↑) sichtbar zu machen. Für eine ausführliche Erklärung wird auf [20] verwiesen.

Die in dieser Arbeit gezeigten Messungen wurden größtenteils von Ilse Glass am Bruker D8 ADVANCE ECO Diffraktometer mit Kupfer-K_α-Strahlung ($\lambda(K_{\alpha1})$ = 0,15406 nm, $\lambda(K_{\alpha2})$ = 0,15444 nm) des Instituts für Geowissenschaften der Universität Heidelberg durchgeführt. Die Probenpräparation erfolgt in zwei Schritten. Um eine gleichmäßige Verteilung des Pulvers zu erhalten, wird zunächst das Pulver mit Isopropanol in einem Mörser händisch dispergiert. Daraufhin wird die erhaltene Dispersion auf einen Probenträger aus Silizium gleichmäßig aufgebracht. Die Messung erfolgt kontinuierlich und die pro Schrittweite (typischerweise $2\theta = 0{,}02°$) integrierte Intensität wird dabei aufgezeichnet.

Die Datenauswertung diente primär der Identifizierung und Zuweisung kristalliner Phasen in den Proben. Hierfür werden die auftretenden Bragg-Reflexe in den aufgenommenen Diffraktogrammen mit Referenzeinträgen der kristallografischen Datenbanken von ICSD [21] und COD [22] verglichen. Die untere Grenze der Quantifizierung bei einem Labor-Pulver-XRD-Gerät hängt stark von Faktoren wie der Vorzugsorientierung der Kristallite, der gemessenen Peaküberlappung im Diffraktogramm, dem amorphen Anteil in der Probe, usw. ab und ist somit von Probe zu Probe abhängig [23]. Als allgemein anerkannte Faustregel für die untere Grenze der Quantifizierung gelten allerdings 3-5 % Massenanteil in der Probe [23]. Die Größe der kleinsten in einem Diffraktogramm noch sichtbaren Nanopartikel, ist aus denselben Gründen stark probenabhängig. Hier gilt als Faustregel eine kristalline Ausdehnung von minimal 2-3 nm [24, 25].

Aus den gemessenen Diffraktogrammen lassen sich darüber hinaus Aussagen über die vorliegende Ausdehnung der Kristallite treffen, falls diese kleiner als 150-200 nm sind. Die endliche Ausdehnung der Kristallite führt zu einer Verbreiterung der Beugungsreflexe. Die Kristallitgröße (D_{hkl}) kann somit aus der Halbwertsbreite $\Delta(2\theta_{hkl})$ der Reflexe mittels der Scherer-Gleichung [26] abgeschätzt werden:

$$D_{hkl} = \frac{K\lambda}{\Delta(2\theta_{hkl})\cos\theta_{hkl}} \qquad \text{mit K } \approx 0.9 \,(\text{abhängig von der Kristallitform}) \tag{2.1}$$

Zu erwähnen ist, dass die Verbreiterung, die der instrumentelle Messaufbau verursacht, in unserem Fall unbekannt ist. Die berechneten Werte für die Kristallitgröße stellen daher keine verlässlichen Absolutwerte dar. Trotz alledem kann aber anhand der gewonnenen Kristallitgrößen ein Größenvergleich zwischen den Proben vorgenommen werden, da die instrumentelle Verbreiterung des Messaufbaus immer annähernd gleich sein sollte.

2.1.2 Rasterelektronenmikroskopie (REM) und Energiedispersive Röntgenspektroskopie (EDS)

Das Rasterelektronenmikroskop, kurz REM, basiert auf der elastischen und inelastischen Streuung von Elektronen an einer Probe [27]. Prinzipielle lassen sich aus der Vielzahl der Wechselwirkungen zwischen einem gerichteten Elektronenstrahl und Materie eine Reihe unterschiedlicher Informationen wie Topografie, Morphologie und atomare Komposition bestimmen. Der zugrundeliegende Aufbau hinter einem Rasterelektronenmikroskop (REM) ist, dass unter Vakuum mittels thermischer Feldemission freie Elektronen erzeugt werden. Diese Elektronen werden durch das Anlegen einer gewählten Hochspannung beschleunigt und mithilfe elektromagnetischer Optik gesteuert. Für die 2-dimensionale Auflösung wird eine gewisse Fläche mit einer zuvor gewählten Schnelligkeit rasternd aufgelöst. Für eine tiefere Einführung wird auf [27, 28] verwiesen, auf dem auch die hier gegebene Einführung basiert. Bei den detektierten Elektronen unterscheidet man generell zwischen elastisch gestreuten (Zurückgestreute Elektronen, kurz BSE) und inelastische gestreuten (Sekundärelektronen, kurz SE) Elektronen. Als Sekundärelektronen werden Elektronen bezeichnet, die aufgrund von Ionisation der Oberflächenatome durch den gerichteten Elektronenstrahl emittiert werden. Diese Elektronen besitzen eine geringe Energie von ein paar Elektronenvolt und können daher nur innerhalb ein paar Nanometer der Oberfläche entkommen. SE enthalten somit Informationen über die Oberfläche und eignen sich gut für die topografische und morphologische Untersuchung. Die Standardauflösung mittels SE wird allgemein als knapp unter 10 nm angegeben, allerdings kann bei spezielle Proben und unter gezielter Anwendung die Auflösung weiter verbessert werden. Zurückgestreute Elektronen haben aufgrund der elastischen Streuung eine deutlich höhere Energie als SE und können dadurch aus deutlich tieferen Schichten des Materials kommen. Da darüber hinaus der Wirkungsquerschnitt der

Streuung stark von der Kernladungszahl Z abhängt, enthalten BSE neben topografischen Informationen auch Informationen über die atomare Zusammensetzung des Materials. Die Information der Zusammensetzung ist als Kontrast sichtbar. Die laterale Auflösung der BSE ist aufgrund der höheren Energie deutlich geringer bei ungefähr 1 μm.

Eine genauere Untersuchung der elementaren Zusammensetzung kann mittels einer weiteren Wechselwirkung durchgeführt werden. Die Wechselwirkung zwischen dem gerichteten Elektronenstrahl und der Materie führt auch zur Entstehung von Röntgenstrahlung. Die Methodik hinter der Messung dieser Röntgenstrahlen nennt sich Energiedispersive Röntgenspektroskopie (EDS). EDS basiert auf der Detektion der entstehenden Röntgenstrahlung, die sich aus Bremsstrahlung und charakteristischer Strahlung zusammensetzt. Die Detektion dieser Röntgenstrahlung gibt über die charakteristische Strahlung, welche direkt verbunden ist, mit den charakteristischen Übergänge jedes Elements, Aufschluss über die elementare Zusammensetzung der Probe. Die laterale Auflösung hängt stark von der Beschleunigungsspannung ab und ist in aller Regel im Mikrometerbereich. Der Fehler in der atomaren Zusammensetzung ist sowohl Element als auch probenabhängig. Als Faustregel gilt ein Fehler von 5%, bei Sauerstoff und Kohlenstoff ist der Fehler aufgrund von Absorptionseffekten noch höher.

Im Rahmen dieser Arbeit wurden topografische Messungen an einem REM der Firma Zeiss (Typ LEO 1530) sowie an einem REM der Firma JEOL (Typ JSM-7610F) mit integriertem BSE- und EDS-Detektor des Physikalisch-Chemischen Institut der Universität Heidelberg durchgeführt. Primärziel jeder Messung ist es, die Morphologie und Größe der Partikeln der pulverförmigen Elektrodenmaterialien zu untersucht. Das LEO-REM ist mit zwei Sekundärelektronendetektoren zentral in und verkippt zur Elektronenstrahlachse ausgestattet.

Die Probenpräparation erfolgt, in dem zuerst selbstklebendes Kohlenstofftape (Plano) auf den jeweiligen gerätespezifischen Probenträger aufgebracht wird. Im Folgenden wird die Menge einer Pinzettenspitze des zu untersuchenden Pulvermaterials auf das klebendes Kohlenstofftape verteilt. Für eine möglichst gleichmäßige Verteilung wird mit einer zusätzlichen Pinzette leicht gegen die Pinzette mit dem Pulver geklopft, was zu einem gleichmäßigen herunterrieseln des Materials führt. Anschließend wird überschüssiges, nicht angeklebtes Material zuerst durch händisches Klopfen und dann mit der Hilfe eines leichten Druckluftstrahles entfernt. Im Falle einer elektrisch schlecht leitenden Probe wurde an einem Sputtergerät der Firma Blazers (Typ Union SCD 004) auf die Probe eine Schicht von circa 10 nm Gold (I=25 mA für die t=25 s) aufgebracht. Die Goldschicht reduziert die

elektrische Aufladung der Probe und minimiert dadurch auftretende Bildfehler.

2.1.3 Elementaranalyse (CHN)

Elementaranalyse oder auch CHN-Analyse ermöglicht die Messung des prozentualen Gehaltes der Elemente Kohlenstoff (C), Wasserstoff (H) und Stickstoff (N) einer Probe. Hierfür wird ein Teil der Probe, idealerweise mindestens 5 mg, explosionsartig in einer sauerstoffreichen Atmosphäre verbrannt. Die dabei entstehenden Gase (CO_2, H_2O, NO_x), werden daraufhin mittels des Trägergases, hier Helium abtransportiert. Zunächst wird das Gasgemisch über einen geheizten, hochreinen Wolframkontakt geführt, um den überschüssigen Sauerstoff zu entfernen und die enthaltenen Stickoxide in molekularen Stickstoff (N_2) umzuwandeln. Das Gasgemisch wird dann gaschromatografisch getrennt und die einzelnen Bestandteile einem Wärmeleitfähigkeitsdetektor zugeführt und analysiert. Der Wärmeleitfähigkeitsdetektor misst dabei kontinuierlich. Aus den voneinander getrennten, gemessenen Peakflächen, kann schlussendlich die Menge von C,H,N in der Probe quantifiziert werden [29].

Die in dieser Arbeit gezeigten CHN-Messungen wurden am Organisch-Chemischen Institut der Universität Heidelberg von C. Vetter mittels des Vario MICRO Cubes der Firma Elementar untersucht. Die Unsicherheit der Messung setzt sich aus der Einwaage sowie dem Gerätefehler zusammen. Der Fehler wurde insgesamt auf 0,5% abgeschätzt.

2.1.4 Röntgenphotoelektronenspektroskopie (XPS)

Röntgenphotoelektronenspektroskopie (XPS) ist eine zerstörungsfreie Methode zur Messung des chemischen Zustandes von Spezien im oberflächennahen Bereich ($\sim$10 nm) eines Festkörpers. XPS beruht auf der Messung von Kernniveau- oder Innenschalenelektronen, die durch den photoelektrischen Effekt emittiert werden [30, 31]. Hierfür werden monochromatische Laserstrahlen auf der Probe fokussiert. Aufgrund des photoelektrischen Effektes kommt es daraufhin zur Erzeugung eines Spektrums an Elektronen mit charakteristischen Energien. Jedes Element beziehungsweise jede Verbindung kann anhand der charakteristischen Bindungsenergien der ausgesandten Elektronen unterschieden werden. Unter Bindungsenergie versteht man die Energie, die erforderlich ist, um ein Elektron aus einem Atom auszustoßen. Diese Energie hängt unter anderem von dem Element, dem Orbital und der chemischen Umgebung ab [30, 31]. Die gemessenen Spektren können daraufhin

mit Literaturwerten verglichen werden. Anhand der Anzahl und Position der gemessenen Peaks können Rückschlüsse auf die enthaltenen Elemente, deren Oxidation und chemische Umgebung gezogen werden. Eine genaue Beschreibung sowie Referenzspektren können im Handbook of X-Ray Photoelectron Spectroscopy von Moulder *et al.* [31] nachgelesen werden.

Für die Probenpräparation wurde zunächst ein Probenträger aus Kupfer mithilfe von Schleifpapier angeraut. Daraufhin wird ein Streifen reines Indiummetall auf den Probenträger aufgebracht und an den Kanten mittels eines Spatels festgedrückt. Als Nächstes wird die oxidierte Oberfläche des Indiums mittels eines Skalpells entfernt. Auf die glänzende Indiumoberfläche wird gleichmäßig eine dünne Schicht der zu untersuchenden Pulverprobe aufgetragen. Diese dünne Schicht wird dann mithilfe des Spatels leicht in das Indium hineingedrückt, sodass ein möglichst gleichmäßiger Film entsteht. Um die Haftung zwischen Indium und dem Pulver weiter zu verbessern, wird der Pulverfilm mit Aluminiumfolie bedeckt und mithilfe einer Pressmatrix in einem Schraubstock handfest zusammengedrückt. Im letzten Schritt wird mittels eines feinen Pinsels sowie durch leichtes Klopfen, loses, überschüssiges Pulver entfernt. Das Endresultat ist ein Probenträger mit einem festen, gleichmäßigen Pulverprobenfilm auf der Indiumoberfläche.

Die in der vorliegenden Arbeit gezeigten XPS-Messungen wurden am Physikalisch-Chemischen Institut der Universität Heidelberg in der Arbeitsgruppe von Professor Michael Zharnikov mit einem MAX200-Spektrometer (Leybold-Heraeus) durchgeführt. Dieser besitzt eine Mg Kα Röntgenquelle (200 W) und einen hemisphärischen Analysator.

2.1.5 Magnetische Messungen

Eine weitere Charakterisierung kann durch magnetische Messungen erreicht werden. Der magnetische Zustand eines Übergangsmetallions steht in direktem Zusammenhang mit seiner elektronischen Konfiguration und der kristallinen Umgebung [19]. Für eine Einführung zum Magnetismus von Festkörpern wird auf das Buch „Magnetism in Condensed Matter“ [32] verwiesen. Die hier dargestellten relevanten Grundlagen sind ebenfalls an [32] und [33] angelehnt. Die magnetischen Eigenschaften eines Festkörpers sind durch die Magnetisierung bzw. die magnetische Suszeptibilität gekennzeichnet. Die Magnetisierung M wird als magnetisches Moment pro Volumen definiert. Die Abhängigkeit der Magnetisierung von einem externen Magnetfeld (H) ist durch die magnetische Suszeptibilität (χ) gekennzeichnet. Die zwei typischen magnetischen Charakterisierungsmessungen sind Temperatur-

(M von T) und Magnetfeldabhängigkeiten (M von B). Aus der Temperaturabhängigkeit der Magnetisierung lassen sich zum Beispiel Phasenübergänge ablesen oder Informationen über Fremdphasen gewinnen. Abhängig von den jeweiligen Materialien lassen sich dabei sehr hohe Sensitivitäten gegenüber Fremdphasen erzielen [19], zum Beispiel wenn magnetische Fremdphasen oder paramagnetische Ionen in einem diamagnetischen Material auftreten. Magnetisierungsmessung bei konstanter Temperatur und variablen Magnetfeldern erlauben ebenfalls Aussagen über die Art des in der Probe vorliegenden Magnetismus. Die Kristallinität der Probe lässt sich zusätzlich durch einen Vergleich zwischen der theoretischen und der gemessenen Sättigungsmagnetisierung abschätzen [19]. Bei einer sehr amorphen Probe kann die Aussagekraft magnetischer Messungen abnehmen, da die magnetischen Phasenübergänge unterdrückt werden. Für eine detaillierte Beschreibung über die Möglichkeiten und Grenzen von magnetischen Messungen an Elektrodenmaterialien für LIB wird auf Whittingham *et al.* , "What can we learn about battery materials from their magnetic properties?" [19] verwiesen.

Die Messungen wurden an einem Magnetic Properties Measurement System (MPMS3), einem SQUID-Magnetometer der Firma Quantum Design, durchgeführt. Im verwendeten Magnetometer können Messungen bis 7 Tesla durchgeführt werden. Der gemessene Temperaturbereich liegt zwischen 1.8 bis 400 Kelvin. Das Funktionsprinzip dieses Gerätes kann zum Beispiel in [34] nachgelesen werden. Die Probenpräparation erfolgt, indem die zu untersuchende Pulverprobe zunächst in den dazu vorhergesehen Zylinder, eine Polypropylen-Kapsel, eingewogen wird. Der zweite Teil der Kapsel ist ein Stempel, mit dessen Hilfe die Probe in die Kapsel gedrückt und fixiert wird. Die gefüllte Kapsel wird daraufhin in dem dafür vorhergesehen Kupferhalm fixiert.

2.2 Theoretische Grundlagen und experimentelle Durchführung der elektrochemischen Messungen

Im Folgenden wird eine kurze Einführung in die Elektrochemie gegeben. Zudem werden die im Rahmen dieser Arbeit genutzten elektrochemischen Messmethoden (zyklische Voltammetrie, galvanostatische Zyklierung, elektrochemische Impedanzspektroskopie) sowie der Versuchsaufbau vorgestellt.

2.2.1 Grundlagen der Elektrochemie

Die Elektrochemie beschäftigt sich generell mit den Gesetzmäßigkeiten zwischen chemischer und elektrischer Energie. Für detaillierte Ausführungen wird auf die folgenden Lehrbücher [35, 36] und auf [37] verwiesen. An dieser Literatur ist auch die folgende kurze Zusammenfassung der batteriespezifischen Grundlagen angelehnt.

Eine Batterie beruht auf der Umwandlung von chemischer in elektrische Energie und wieder zurück (Sekundärbatterie). Der generelle Aufbau einer Batterie besteht aus einer oder mehreren galvanischen Zellen. Die galvanische Zelle wiederum besteht aus zwei via eines Separators örtlich getrennten, elektrisch leitenden Elektroden. Die Elektroden befinden sich dabei in einem reinen Ionenleiter, dem Elektrolyten. Der innere Ionenstrom im Elektrolyten zwischen den Elektroden wird durch den äußeren Stromkreis, über den elektrische Arbeit verrichtet werden kann, geschlossen. Die Umwandlung der Energie erfolgt unter anderem mittels Redoxreaktionen:

$$\mathrm{Ox} + \mathrm{z} \cdot \mathrm{e}^- \underset{\text{Oxidation}}{\overset{\text{Reduktion}}{\rightleftharpoons}} \mathrm{Red} \tag{2.2}$$

O_x bezeichnet hierbei den oxidierten Zustand einer Spezies und Red den reduzierten Zustand. Z gibt die Anzahl der an der Reaktion beteiligten Elektronen an und wird als Äquivalenzzahl bezeichnet. Definitionsgemäß ist festgelegt, dass die Elektrode, an der die Oxidation abläuft, als Anode und diejenige, an der die Reduktion stattfindet, als Kathode bezeichnet wird. Die grundlegende thermodynamische Gleichung für eine reversible elektrochemische Umwandlung lautet:

$$\Delta G = \Delta H - T\Delta S \tag{2.3}$$

Dabei steht ΔG für die Änderung der Gibbs freien Energie bzw. die verfügbare Energie einer Reaktion zur Verrichtung von Arbeit. ΔH steht für die Enthalpieänderung bzw. die durch die Reaktion freigesetzte Energie, ΔS für die Änderung der Entropie und T für die absolute Temperatur. TΔS entspricht somit der entstehenden Wärme aufgrund der (elektrochemischen) Umwandlung der Materialien.

Die aus einer bestimmten Reaktion verfügbare Nutzenergie ΔG ist mit der elektrischen Energie, die aus dieser Reaktion in einer elektrochemischen Zelle entsteht, verbunden durch:

$$\Delta G = -nFE \tag{2.4}$$

Wobei n, die Anzahl der übertragenen Elektronen pro Mol Reaktant beschreibt, F die Faraday-Konstante und E die Spannung der Zelle, die aufgrund der spezifischen chemischen Reaktion entsteht. Die Spannung der Zelle ist für jedes Reaktionspaar durch die jeweiligen elektrochemischen Potentiale gegeben. Die Menge der erzeugten Elektrizität (nF) wird durch die Gesamtmenge der für die Reaktion verfügbaren Materialien bestimmt.

Da in der Realität nicht alle vorliegenden Spezien an einer Reaktion teilnehmen, eignet sich die Aktivität besser als die reine Konzentration zur Beschreibung von Reaktionen. Unter der Aktivität a versteht man die Anzahl der Spezien pro Lösungsvolumen, die an der Reaktion aktiv teilnehmen. Im Gleichgewicht kann die Veränderung der freien Energie abhängig von der Aktivität der involvierten Spezien wie folgt beschrieben werden:

$$\Delta G = \Delta G^0 + RT \ln(\frac{a_\mathrm{R}}{a_\mathrm{O}}) \tag{2.5}$$

Dabei bezeichnet $\Delta \mathrm{G}^0$ die freie Energie bei Standardbedingungen und R die molare Gaskonstante. Zusammen mit Gleichung 2.4, die eine Verbindung der Gibbs freien Energie und dem elektrochemischen Potential herstellt, ergibt sich die Nernst-Gleichung mit dem aktuellen Potential E und dem Standartpotential E^0:

$$E = E^0 + \frac{RT}{nF} \cdot \ln(\frac{a_\mathrm{R}}{a_\mathrm{O}}) \tag{2.6}$$

Die Klemmspannung einer galvanischen Zelle ist durch die Differenz der Galvanipotentiale von Kathode und Anode gegeben:

$$\phi_\mathrm{Zellle} = \phi_\mathrm{Anode} - \phi_\mathrm{Kathode} \tag{2.7}$$

2.2.2 Elektrochemische Charakterisierungsmessungen (CV, GCPL, EIS)

Zyklische Voltammetrie (CV)

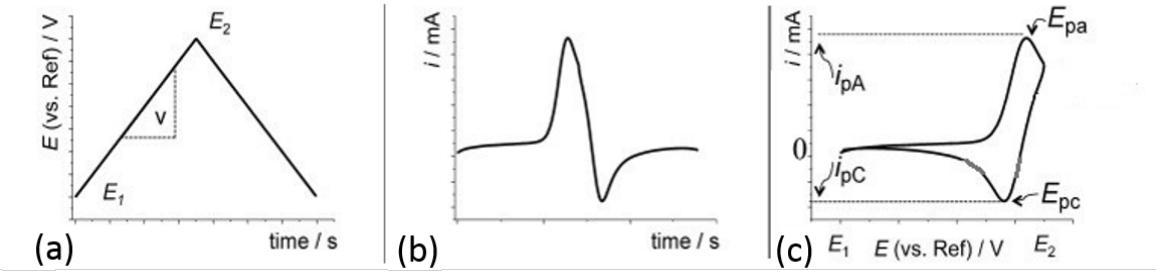

Abbildung 2.2: Beispielhafte Darstellung einer zyklischen Voltammetriemessung. A, die an die Zelle angelegte Dreiecksspannung, b, der daraus resultierende gemessene Strom gegenüber der Zeit und c, das finale Zyklovoltammogramm. Adaptiert aus [38].

Zyklische Voltammetrie ist eine der am meisten eingesetzten Methoden in der Elektrochemie, da mittels ihrer Hilfe eine Vielzahl an Informationen zu Reduktions- und Oxidationsprozessen zugänglich werden [39]. Hierfür wird an die Arbeitselektrode ein Potenzial (in Bezug auf die verwendete Referenzelektrode, in unserem Fall eine Lithiummetallelektrode) von außen angelegt (siehe Abbildung 2.2a). Die zyklische Voltammetriemessung beginnt dabei bei einem Anfangspotential E1, führt mittels angelegter Dreieckspannung zum Endpotential (Umkehrpotential) E2 und dann wieder zurück. Die angelegte, gewählte Scanrate v beträgt im Rahmen dieser Arbeit typischerweise 0.1 mV/s. Der daraus resultierende Strom wird dabei gemessen und ist exemplarisch als Funktion der Zeit in Abbildung 2.2b abgebildet. Die Darstellung der gemessenen Daten einer zyklischen Voltammetriemessung, bei der der gemessene Strom gegen die Spannung aufgetragen wird, bezeichnet man als Zyklovoltammogramm (CV) (siehe Abbildung 2.2c). Diese Arbeit folgt der IUPAC Konvention, die bei einer Oxidation des Elektrodenmaterials positiven Strom zeigt und bei reduktiven Prozessen einen negativen Strom [39]. Das Auftreten von Peaks in den charakteristischen Kurven eines CVs weist auf redoxaktive Prozesse hin. Anhand des Potentials, an dem diese Peaks auftreten (E_{pa},E_{pc} in Abb. 2.2c), können zum Beispiel mittels eines Vergleiches mit Literaturdaten Aussagen über die zugrundeliegende Reaktion gemacht werden. Die gemessene Halbwertsbreite der Peaks ist ein Indikator für die dem Prozess zugrundeliegende Kinetik und damit der Kristallinität der untersuchten Probe. Mit einer

zyklischen Voltammetriemessung lassen sich zusätzlich, wenn die Peaks/Reaktionen weit genug auseinanderliegen, einzelne Prozesse und deren Wirkung auf die Probe untersuchen. Hierfür werden die Potentialgrenzen so gewählt, dass sie nur einzelne Prozesse einschließen. Im weiteren Verlauf kann auf weitere Prozesse erweitert werden. Eine Einführung kann zum Beispiel in [39] gefunden werden.

Galvanostatische Zyklierung (GCPL)

Die klassische Untersuchung des Lade- bzw. Entladeverhaltens von Elektrodenmaterialien gelingt durch die galvanostatische Zyklierung. Hierfür wird an die Zellen ein konstanter Ent-/Ladestrom angelegt und die daraus resultierende Veränderung der Spannung (Potentialverlauf) gemessen. Die Stromstärke wird hierbei auch Zyklierrate genannt. Im Rahmen dieser Arbeit wird für die Vermeidung von Tiefenentladungs- und Überladungseffekten eine galvanostatische Zyklierung mit zusätzlicher potentieller Limitierung (GCPL) verwendet [40]. Informationen über die elektrochemischen Prozesse sind auf vielfältige Weise aus GCPL-Messungen ablesbar. Erstens lassen sich aus dem zeitlichen Potentialverlauf Informationen über die Art des Prozesses erhalten. Zum Beispiel flacht bei einem Nernstschen System das Potential in der Nähe des Gleichgewichtspotenzial des Redoxpaares, plateauartig ab. Plateaus in den Potentialkurven des GCPLs entsprechen daher den Peaks in einem CV. Zweitens lassen sich anhand der dabei umgesetzten Ladungsmenge Aussagen über die Effektivität einzelner Prozesse und dem Gehalt von Lithium im Elektrodenmaterial treffen. Die umgesetzte Ladungsmenge bezieht sich auf die effektive elektrochemisch aktive Menge im Elektrodenmaterial und wird spezifische Kapazität (C_{spez}) genannt. Für einen Ladezyklus der Zeit t mit Stromstärke I ergibt sich die spezifische Kapazität aus der Integration des geflossenen Stromes über die Zeit:

$$C_{\text{spez}} = \frac{1}{m} \int_0^t I(t)dt \tag{2.8}$$

Die theoretische, materialspezifische Kapazität eines Elektrodenmaterials lässt sich mithilfe des Faradayschen Gesetztes,

$$C_{\text{theo}} = \frac{z \cdot F}{M} \tag{2.9}$$

mit der molaren Masse M des Aktivmaterials und der Faraday-Konstante bestimmen

[35]. Die Normierung der Stromstärke und der Kapazität erfolgt auf die Masse der elektrochemisch aktiven Bestandteile der Elektrode. Für Anodenmaterialien (typischerweise untersucht im Spannungsbereich 0.01-3 V) bedeutet das, dass sowohl das Aktivmaterial als auch der verwendete Leitruß (elektrochemische Aktivität im Bereich von 0.01-1 V) [41] mit einbezogen werden muss. Der Strom wird in diesem Fall auf die Masse normiert und als Stromdichte der Einheit mA g^{-1} angegeben und die Kapazität in mAh g^{-1}. Im elektrochemisch aktiven Bereich von Kathodenmaterialien (typischerweise 1-4.5 V) ist der verwendete Leitruß nicht elektrochemisch aktiv und somit für Kapazitätsbetrachtungen vernachlässigbar [42]. Die verwendete Zyklierrate wird für Kathodenmaterialien typischerweise in C-Raten angegeben. Eine C/x-Rate entspricht dabei dem Strom, der benötigt wird, um die theoretische Kapazität des Materials in x-Stunden zu ent-/laden. Die Kapazität bezieht sich hierbei nur auf das verwendete Aktivmaterial und wird erneut in mAh g^{-1} angegeben.

Eine weitere wichtige Messgröße, die ein Maß für die Reversibilität der untersuchten elektrochemischen Prozesse darstellt, ist die Coulombische Effizienz (CE), die sich wie folgt ergibt [43]:

$$CE = \frac{\text{discharge capacity}}{\text{charge capacity}} = \frac{\text{Total number of } Li^+ \text{ ions back to cathode}}{\text{Total number of } Li^+ \text{ ions departing from cathode}} \quad (2.10)$$

Die Zyklenstabilität ist ein weiterer entscheidender Faktor, der angibt, welcher Anteil der ursprünglichen Kapazität nach mehrmaligem Laden und Entladen noch erreicht wird. Die Summe aus erreichter spezifischer Kapazität und Zyklenstabilität bezeichnet man im Allgemeinen als elektrochemische Performance, welche ein Hauptindikator für den möglichen positiven Ausblick aller Batteriematerialien ist.

Elektrochemische Impedanzspektroskopie (EIS)

Elektrochemische Impedanzspektroskopie (kurz: EIS) ist ein leistungsfähiges, nicht destruktives Verfahren zur Untersuchung der Kinetik in elektrochemischen Systemen [44]. Der Messansatz besteht dabei darin, eine sinusförmige Spannung (potentiostatischer Modus, PEIS) $U(t) = U \sin(\omega t)$ mit einer bestimmten Amplitude und Frequenz anzulegen und die Amplitude und Phasenverschiebung des resultierenden Stromes $I(t) = I \sin(\omega t + \phi)$ zu messen. Für die Validität der Messung müssen dabei immer folgende drei Grundvoraussetzungen erfüllt werden: Linearität, Kausalität und Stationarität. Die Linearität lässt

sich trotz der nicht linearen Natur elektrochemischer Systeme durch die Anwendung einer ausreichend kleinen Störung sicherstellen (im Allgemeinen hat sich eine Amplitude von 10 mV als noch im pseudolinearen Bereich bewährt) [45]. Der gemessene Antwort-Strom hat somit ungefähr die gleiche Frequenz wie die Störung [44]. Kausalität meint in diesem Zusammenhang, dass die Antwort des Systems komplett auf die Störung zurückgeführt werden kann. Die Bedingung der Stabilität bedeutet, dass das System, bis es durch einen äußeren Reiz angeregt wird, stabil ist und nach Beendigung der äußeren Störung, in der Lage ist, in seinen ursprünglichen Zustand zurückzukehren.

Die frequenzabhängige Impedanz beziehungsweise der Wechselstromwiderstand kann unter diesen Randbedingungen mithilfe des Ohmschen Gesetzes berechnet werden:

$$Z = \frac{F\{U(t)\}}{F\{I(t)\}} = \frac{\tilde{U}(w)}{\tilde{I}(w)} \tag{2.11}$$

Mit F{U(t)} der Fouriertransformierten der angelegten Spannung und F{I(t)} der Fouriertransformierten des gemessenen Stroms. Dieser Messvorgang wird bei einer Reihe von Frequenzen wiederholt, die in aller Regel von wenigen Hertz (Hz) bis in den MHz-Bereich reichen, um ein charakteristisches Impedanzspektrum zu erzeugen. Die Vielzahl an verschiedenen Frequenzbereichen ermöglicht es, Prozesse mit unterschiedlichen Zeitkonstanten innerhalb der Batterie anzuregen und zu untersuchen. Die gemessene Impedanz wird typischerweise in Nyquist-Darstellung (Imaginärteil der Impedanz gegen den Realteil) aufgetragen. Diese Darstellung ermöglicht die Zerlegung der auftretenden, charakteristischen Zellkomponenten und Zellprozesse bezüglich der jeweiligen Zeitkonstanten (siehe Abbildung 2.3a), wobei im Bereich des Diagramms bei kleinen Re(Z) schnelle Prozesse detektiert werden und bei großen Re(Z) (d.h. rechts in Abb.2.3) langsame Prozesse.

Die Analyse der Impedanzspektren erfolgt mittels Ersatzschaltkreisen (siehe Abbildung 2.3b), welche die jeweiligen Prozesse durch resistive, kapazitäre und induktive Elemente beschreibt. Für eine detailliertere Erläuterung der elektrochemischen Impedanz und deren Analyse wird auf [48] verwiesen. Auf [48] beruhen auch die hier dargelegten Grundlagen.

Für die in dieser Arbeit durchgeführten PEIS-Messungen wurde eine kleine Störung von 10 mV im Frequenzbereich von 200 kHz bis 1 mHz gewählt. Um die Reproduzierbarkeit der Messung sowie einen stabilen Zustand zu gewährleisten, wurde vor jeder PEIS-Messung die Zelle für mehrere Stunden im OVC (Leerlaufspannung) ruhen gelassen und nach der Messung eine zweite Kontroll-PEIS-Messung durchgeführt.

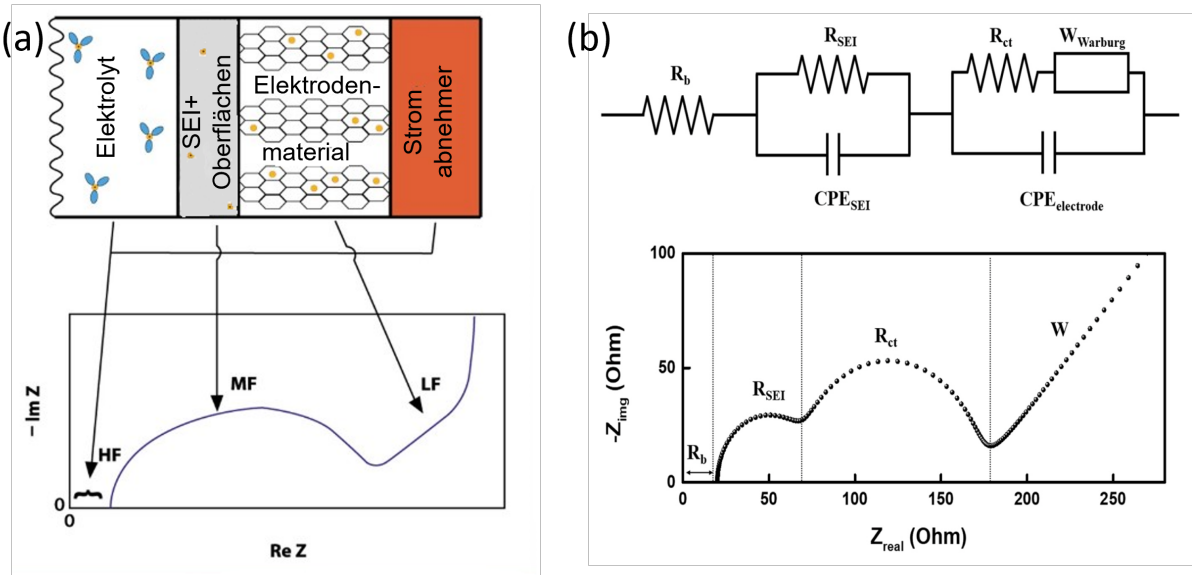

Abbildung 2.3: (a) Illustrative Darstellung eines typischen Impedanzspektrums eines Batteriematerials in Nyquistdarstellung, adaptiert von [46]. (b) Darstellung eines für ein Batteriematerial repräsentativen Ersatzschaltkreises, sowie das dazugehörige Impedanzspektrum in Nyquistdarstellung, entnommen aus [47].

Ex-situ Messungen

Für *ex situ* Charakterisierungsmessungen wie REM- und TEM-Messungen wurde für eine möglichst vollständige elektrochemische Ladungsumsetzung teilweise die Messmethode konstanter Strom konstante Spannung (CCCV) verwendet. Hierbei wird, nachdem die Endspannung erreicht wird, diese Spannung noch eine gewisse Zeit t gehalten, was zu einem zusätzlichen Stromfluss führen kann und damit zur zusätzlichen Ein-/Auslagerung von Lithiumionen. Um die zyklierten Elektroden weiter zu untersuchen, wurden die gemessenen Zellen in einer Argon-Glovebox zerlegt. Im Falle von Knopfzellen kam ein spezieller Decrimping-Aufsatz für die Presse zum Einsatz. Die erhaltenen Elektroden wurden dann gewaschen, um das hochreaktive Lithiumsalz zu entfernen. Hierfür wurden die Elektroden der Reihe nach in insgesamt drei mit Ethylencarbonat gefüllten Fläschchen getaucht und für jeweils fünf Minuten geschüttelt. Zum Schluss wurden die Elektroden über Nacht im Vakuum getrocknet. Zur Vermeidung von möglichen Reaktionen an Luft wurden die Elektroden nach dem Ausschleusen aus der Argon-Glovebox unter bestmöglichem Luftausschluss zu den jeweiligen Geräten transportiert.

2.2.3 Versuchsaufbau

Die elektrochemischen Messungen wurden mithilfe eines mehrkanaligen VMP3- [49], eines VSP- [50] Potentiostaten/Galvanostaten sowie einem Battery Cycler (BCS) [51] der Firma Biologic durchgeführt. Der VMP3-Galvanostat/Potentiostat verfügt über zwei Messmöglichkeiten für elektrochemische Impedanzspektroskopie. Die Potentiostaten besitzen drei Abgriffe zur Potentialmessung und zwei Stromanschlüsse. Die verwendete Software ist bei allen Geräten „EC-Lab“ der Firma BioLogic [52]. Die Software ermöglicht eine individuelle Anpassung der zuvor beschriebenen Messmethoden an die jeweiligen Anforderungen. Nach dem Einstellen der Parameter führt die Software die Messung automatisch durch. Für die Gewährleistung des Gleichgewichtszustandes wurde vor jeder Messung eine 12 h Leerlaufspannungsmessung durchgeführt. Die Anschlüsse des VMP3 befinden sich in einem Wärmeschrank der Firma Binder, der auf konstant 25 °C eingestellt ist. Die Anschlüsse des VSP und des BCS befinden sich bei Raumtemperatur (ungefähr 25 °C).

Elektrodenpräpration

Die Elektrodenpräparation erfolgte im Rahmen dieser Arbeit für Anoden- und Kathodenmaterialien unterschiedlich. Die Elektrodenpräparation für elektrochemische Impedanzmessungen sowohl von Anoden- als auch Kathodenmaterialien erfolgen nahezu identisch zu den jeweiligen Protokollen, allerdings wurde die Größe der Stromabnehmer auf ⌀ 18 mm angepasst.

Die Reproduzierbarkeit der gemessenen elektrochemischen Daten hängt maßgeblich von der Qualität der hergestellten Elektroden ab. Die für die Qualität der Elektroden entscheidenden Faktoren sind: Der Fehler der Einwaage, die Homogenität sowohl bei der Vermischung als auch beim Aufbringen auf die Netze sowie die erreichte Massenbeladung der Netze. Da diese Prozesse händisch durchgeführt werden, ist eine präzise Kontrolle dieser Parameter nicht vollumfänglich möglich. Abhängig von der Probe und der verwendeten Menge der Einwaage lässt sich die Ungenauigkeit der Messdaten auf durchschnittlich zwischen 5 und 10% abschätzen. Dieser Wert wurde anhand von Vergleichsmessungen ermittelt und ist typisch für vergleichbare Untersuchungen.

Anodenherstellung

Die Herstellung von Elektroden mit Anodenmaterialien erfolgte nach dem gruppeninternen Standardprotokoll [53]. Hierfür wird als Erstes das zu untersuchende Aktivmaterial AM, Carbon Black CB (Super C65, Timcal) und Polyvinylidenfluorid-Binder PVDF (Solvay Plastics) abgewogen. Das Gewichtsverhältnis von AM:CB:PVDF wurde im Rahmen dieser Arbeit auf 80:10:10 festgelegt. Im nächsten Schritt wird zuerst PVDF in N-Methyl-2-pyrrolidon (NMP) mittels eines Magnetrührers in Kombination mit einem Rührfischchen aufgelöst. Daraufhin wird Carbon Black und das Aktivmaterial hinzugegeben und die erhaltene Dispersion wird für weitere 24 h gerührt. Um die Viskosität und somit die Haftung zu erhöhen wird ein Teil des NMPs der Mischung in einem Vakuumtrockenschrank (65 °C, 12 mbar) verdampft. Nach dem Herstellen einer geeigneten Viskosität wird die Paste mittels eines Spatels händisch homogen auf den ⌀=10 mm (für CV-, GCPL-Messungen) oder ⌀=18 mm (für PEIS-Messungen) netzartigen Kupferstromabnehmer (Drahtdurchmesser: 0,115 mm, offene Fläche: 30,3 %, Dicke: 0,25 mm) aufgetragen. Die bestrichenen Elektroden werden dann im Vakuumofen für 24 h getrocknet, bevor sie mittels einer hydraulischen Presse bei 10 MPa gepresst werden. Vor dem Einschleusen in die Glovebox werden die Elektroden erneut mehrere Stunden getrocknet.

Kathodenherstellung

Die Herstellung der Kathoden erfolgte aufgrund der Luftsensitivität der untersuchten lithiumreichen Antiperowskite ausschließlich in einer Argon-Glovebox ($O_2 < 1$ ppm, $H_2O < 1$ ppm). Die Kathodenpräparation für lithiumreiche Antiperowskite beruht auf den Erkenntnissen aus den vorangegangenen Arbeiten von Özkara [54], Djendjur [55] und Hahn [56]. Am Anfang wird das zu untersuchende Aktivmaterial AM, Carbon Black CB (Super C65, Timcal) und Polyvinylidenfluorid-Binder PVDF (Solvay Plastics) in einem Massenverhältnis von AM:CB:PVDF von 70:15:15 abgewogen. Anschließend werden die Materialien mithilfe eines Fisherbrand Model 120 Dispergiergerätes für 2 h in trockenem Isopropanol vermischt. In einer Vakuumkammer wird daraufhin so lange Isopropanol verdampft, bis sich eine pastenartige Viskosität der Mischung einstellt. Die resultierende Paste wird dann mittels eines Spatels händisch homogen auf einen ⌀=10 mm (für CV-, GCPL-Messungen) oder ⌀=18 mm (für PEIS-Messungen) netzartigen Aluminiumstrom-abnehmer (Drahtdurchmesser: 0,1 mm, offene Fläche: 27 %) aufgetragen. Die erhaltenen

Elektroden werden danach über Nacht im Vakuum getrocknet, mit einer Spindelpresse händisch gepresst und erneut getrocknet.

Zellaufbau

Im Rahmen dieser Arbeit wurden für die elektrochemischen Messungen galvanostatische Zyklierung und zyklische Voltammetrie teilweise eine luftdichte Swagelog-Rohrverschraubung (siehe [53, 57]) oder ein CR2032 Knopfzellenaufbau (⌀= 20 mm, h= 3,2 mm) verwendet, der schematisch in Abbildung 2.4 dargestellt ist.

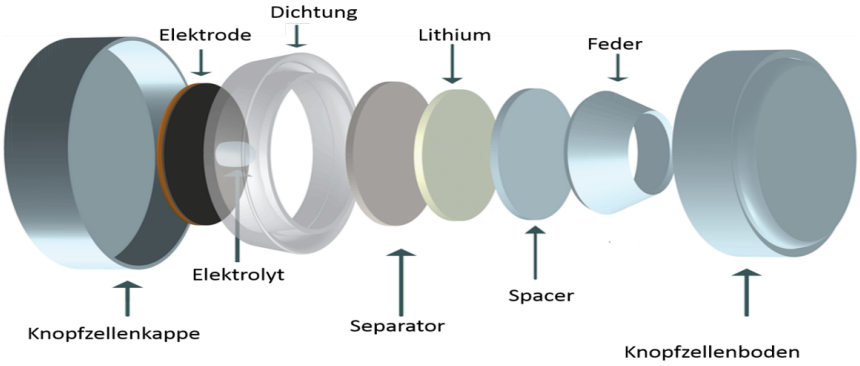

Abbildung 2.4: Schematische Illustration des Aufbaus einer Knopfzelle. Adaptiert von [58].

Der Knopfzellenboden (Edelstahl, SS316) mit integrierter Teflondichtung sowie die Knopfzellenkappe (Edelstahl, SS316) bilden das Gehäuse der Knopfzelle. In den Knopfzellenboden wird eine Edelstahlfeder platziert, die einen konstanten Druck auf die elektrischen Kontakte der Zellbestandteile aufbaut. Auf die Feder kommt der Stromabnehmer der Gegenelektrode aus SS316 Edelstahl, welcher auch Spacer genannt wird. Auf diesen wird wiederum die Gegenelektrode aus reinem Lithiummetall (⌀=10 mm, Alfa Aesar, Reinheit > 99,9 %) aufgebracht. Darauffolgend befinden sich zwei Lagen (Whatman GF/D, ⌀=16 mm) Separator, die beide jeweils mit 65 µl der Elektrolytlösung (1M LiPF6 in 1:1 Ehtylenecarbonat (EC) und Dimethylcarbonat (DMC) Elektrolyte LP30, Merck) getränkt wurden. Die letzte Komponente ist die Arbeitselektrode, bestehend aus einem mit dem zu untersuchenden Anoden-/Kathodenmaterial beschichteten netzartigen Stromabnehmer aus Kupfer/Aluminium (⌀=10 mm). Final wird zur Herstellung der Luftdichtheit die Knopfzelle in einem sogenannten Coin Cell Crimper zusammengepresst. Für eine ausführliche Beschreibung der Knopfzellenherstellung wird auf [59] verwiesen.

Die elektrochemischen Impedanzmessungen wurde mittels einer PAT-Zelle der Firma EL-

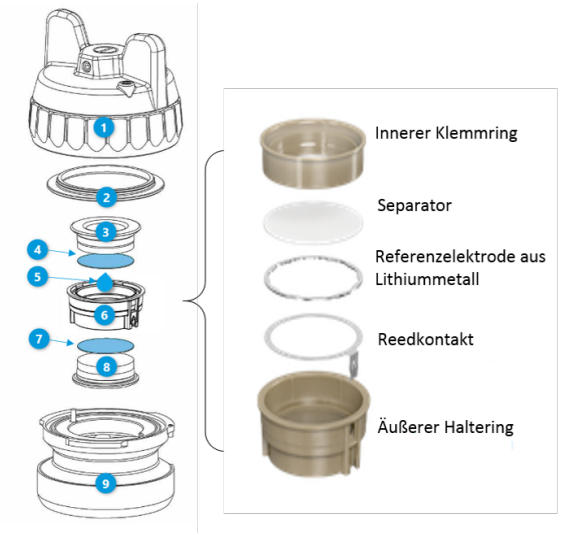

Abbildung 2.5: Schematische Abbildung des Aufbaus einer PAT-Zelle, sowie des PAT-Kerns, adaptiert von [60] und [61].

Cell, welche schematisch in Abbildung 2.5 dargestellt ist, durchgeführt. Die Zelle besteht aus einer Zwei-Komponenten-Edelstahlhülle (1) und (9), einer Dichtung aus Polyethylen (2), dem oberen und unteren Edelstahlstößel (3 und 8), der Lithiummetallgegenelektrode ⌀=18 mm (4), dem Pat-Kern (6) und der ⌀=18 mm Arbeitselektrode (7). Das Herzstück der Zelle ist der PAT-Kern, rechts dargestellt in Abbildung 2.5. Dieser besteht aus einem äußeren Haltering mit einem inneren, kreisrunden Absatz (⌀=21,6 mm) zur Platzierung des Reedkontakts und der Referenzelektrode aus Lithiummetall. Auf diese wird der Separator (⌀=21,6 mm) platziert und mit dem inneren Klemmring fixiert. Durch diesen Aufbau ist die Position der Arbeitselektrode fixiert und symmetrisch gegenüberliegend zur Gegenelektrode. Zusätzlich ist auch die Referenzelektrode nahe an der Arbeitselektrode positioniert, was zu einer Reduktion von Artefakten im Impedanzspektrum führt und insgesamt eine sehr hohe Qualität und Reproduzierbarkeit der elektrochemischen Impedanzdaten erlaubt [62–64]. Für eine tiefere Betrachtung entscheidender geometrischer Aspekte und deren Effekte auf die elektrochemische Impedanz wird auf [62–64] verwiesen.

Die hohe Reaktivität von Lithium und die Bildung von Flusssäure bei Kontakt des Elektrolyten mit Wasser erfordert, dass die gesamte Knopfzellenproduktion in einer Glovebox unter Argonatmosphäre ($O_2 < 1$ ppm, $H_2O < 1$ ppm) stattfindet.

2.3 Nanostrukturierte Übergangsmetallverbindungen als Anodematerialien

Übergangsmetallverbindungen werden aufgrund ihrer einfachen Handhabung und hohen erreichbaren Kapazitäten intensiv als neue Anodenmaterialien für Lithium-Ionen-Batterien untersucht [65]. Die untersuchten Übergangsmetallverbindungen mit Konversionsreaktionen besitzen allerdings eine geringe Lithiummobilität, schlechte elektronischer Leitfähigkeit, hohe volumetrische Ausdehnung und Zerbröseln des aktiven Materials bei wiederholter Lithiierung/Delithiierung.

Die typischen Lösungsansätze zum Vermeiden dieser Probleme sind in Abbildung 1.3 grafisch dargestellt. Im Rahmen dieser Arbeit wurde zum einen auf die Partikelgrößenskalierung bzw. Verkleinerung der Partikelgröße und zum anderen auf die Bildung von Kohlenstoffkompositen oft zusammen mit einer Beschichtungen/Einbettung der aktiven Materialien in die jeweiligen Kohlenstoffstrukturen zurückgegriffen. Der individuelle Einfluss dieser Strategien ist folgender: Durch die Verkleinerung der Partikelgröße, wird dem langsamen Elektronen- und Lithium-Ionen-Transport entgegenwirkt, da sich die Diffusionslängen verringern. Dieses Mitigieren der langsamen Transporteigenschaften ermöglicht eine insgesamt höhere Leistung und Kapazitätsausnutzung des Materials [66]. Verkleinerte Partikel zeigen zudem bei der Volumenausdehnung während der Aufnahme von Lithium einen geringeren Aufbau interner Spannungen. Das wiederum verhindert effektiv die Bildung von Rissen und das Zerbröseln des Materials und führt somit zu einer Erhöhung der Zyklenstabilität [67]. Die Bildung von Kohlenstoffkompositen und/oder das Einbetten der Aktivmaterialpartikel in eine gut leitende Kohlenstoffmatrix verbessert den elektrischen Transport [68]. Darüber hinaus kann die verwendete Kohlenstoffstruktur die Volumenausdehnung der Aktivmaterialkomponente während des Ladens und Entladens abfedern und begrenzen, was die strukturelle Stabilität des Materials weiter verbessert [69].

2.3.1 Magnetit (Fe_3O_4)

Fe_3O_4 oder auch Magnetit besitzt eine hohe magnetische Sättigungsmagnetisierung, vergleichbare hohe elektronische Leitfähigkeit, gute Verfügbarkeit sowie eine hohe Biokompatibilität [70]. Aufgrund dieser Eigenschaften gilt Fe_3O_4 nicht nur als einer der attraktivsten Kandidaten der nächsten Generation an Anodenmaterialien, sondern ist auch ein viel

untersuchtes Material in einer ganzen Reihe von Forschungs- und Anwendungsgebieten. Fe_3O_4 findet beispielsweise Anwendung als Pigment, Katalysator und als magnetokalorisches Kühlungsmaterial [71]. Speziell nanoskalierte Fe_3O_4-Partikel sind darüber hinaus in weiteren Anwendungsbereichen, wie beispielsweise in der Krebstherapie, von Bedeutung [72].

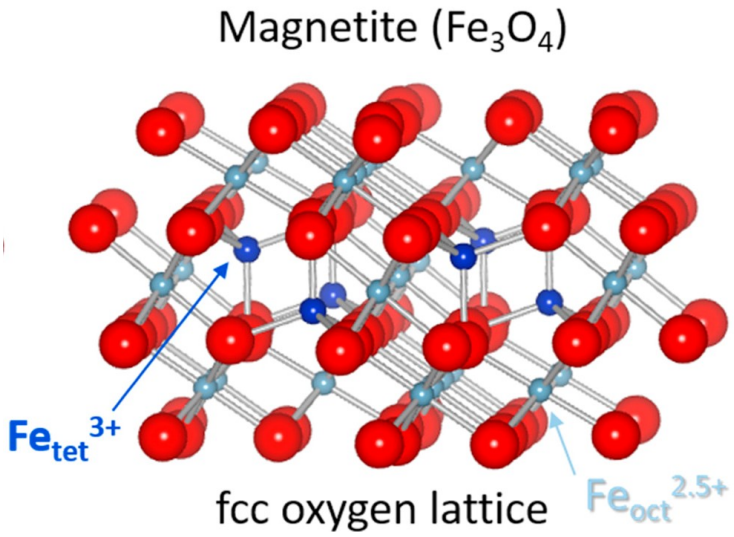

Abbildung 2.6: Schematische Darstellung der Kristallstruktur von Fe_3O_4. In Rot dargestellt Sauerstoff, hellblau die oktaedrisch besetzten Plätze von Fe und dunkelblau die tetraedrischen. Entnommen aus [73].

Magnetit besitzt eine kubische, inverse Spinell-Kristallstruktur basierend auf einem dicht gepacktem O^{2-}-Anionengitter [73]. Die kleineren Fe-Kationen besetzen zu einem 50:50 Anteil an Fe^{2+} und Fe^{3+} die oktaedrischen und zu 100% Fe^{3+} die tetraedrisch koordinierte Zwischenräume (siehe Abbildung 2.6). Die magnetischen Momente von Fe^{3+}- und Fe^{2+}-Kationen auf den oktaedrischen Plätzen sind ferromagnetisch gekoppelt. Die Fe^{3+}-Ionen auf den tetraedrischen Positionen sind jedoch zu den Fe^{3+} auf den oktaedrischen Plätzen antiferromagnetisch gekoppelt [73]. Fe_3O_4 ist daher ein ferrimagnetisches Material mit hoher Sättigungsmagnetisierung (MS) und niedriger Koerzitivfeldstärke (HC) [73]. Fe_3O_4-Nanopartikel mit einer Größe von unter 20 Nanometern zeigen superparamagnetische Eigenschaften [74].

Fe_3O_4 wurde als Anodenmaterial in Lithium-Ionen-Batterien erstmals 1982 von Thackeray *et al.* untersucht [75]. Für Fe_3O_4 als Anodenmaterial der nächsten Generation spricht die hohe Verfügbarkeit, die geringen Kosten, die Ungiftigkeit und die hohe theoretische spezifische Kapazität von 926 mAh g^{-1} für den ersten Zyklus und eine reversible theoretische Kapazität aufgrund der $Fe^{2+} \leftrightarrow Fe^0$ Reaktion von 694 mAh g^{-1} [76, 77].

Die gesamte elektrochemischen Reaktionen ist gegeben durch [76]:

$$Fe_3O_4 + 2Li^+ + 2e^- \rightarrow Li_2Fe_3O_4 \tag{2.12}$$

$$Li_2Fe_3O_4 + 2e^- + 2Li^+ \leftrightarrow 2(Li_2O \cdot FeO) + Fe \tag{2.13}$$

$$FeO + 2e^- + 2Li^+ \leftrightarrow Fe + Li_2O \tag{2.14}$$

$$Fe_3O_4 + 8Li^+ + 8e^- \rightarrow 3Fe + 4Li_2O \tag{2.15}$$

Fe_3O_4 besitzt allerdings die für Konversionsmaterialien typischen Nachteilen einer geringen Li-Mobilität, unzureichender elektronischer Leitfähigkeit sowie einer hohen volumetrischen Ausdehnung, die zu einer Zerbröckelung bei wiederholter Lithiierung/Delithiierung führt [78]. Viele dieser Nachteile konnten bereits durch die erwähnten Methodiken gelöst werden. In der Literatur findet man als potenzielle Anodenmaterialien viele nanostrukturierte Fe_3O_4-Morphologien wie Oktaeder [79], Nanowürfel [80] und Partikel [81]. Darüber hinaus gibt es eine Vielzahl an Fe_3O_4-Morphologien, die zudem in irgendeiner Form mit Kohlenstoffstrukturen verbunden wurden [82]. Einige Beispiele hierfür sind Nano Fe_3O_4@N-dotierte poröse Kohlenstoff-Nanokugeln [83], hierarchische 3D-Fe_3O_4@poröse Kohlenstoffmatrix [84] und hohle Fe_3O_4 Nanokugeln in wabenförmigem makroporösem Kohlenstoff [85], sowie vielen mehr [69]. All diese Materialien zeigen ganz unterschiedliche physikalische und elektrochemische Eigenschaften. Die jeweiligen Strukturen lösen dabei die oben genannten inhärenten Nachteile unterschiedlich gut. So erreichen zum Beispiel Fe_3O_4-Oktaeder eine anfängliche Ladekapazität von 700 mAh g^{-1} bei einem Strom von 50 mA g^{-1}. Nach 40 Zyklen fällt die Kapazität bei diesem Material auf 400 mAh g^{-1} ab [79]. Die hohlen Fe_3O_4 Nanokugeln in wabenförmigem makroporösem Kohlenstoff hingegen zeigen im fünften Zyklus bei einem Strom von 100 mA g^{-1} eine Kapazität von 1500 mAh g^{-1}. Im Zyklus 150 und einem Strom von 200 mA g^{-1} erreicht das Kompositmaterial eine Kapazität von 1050 mAh g^{-1} [85] und somit insgesamt Werte deutlich über der reversiblen theoretischen Kapazität. Insgesamt hat sich gezeigt, dass speziell nanoskalierte Fe_3O_4-Komposite in der Lage sind, Kapazitäten weit überhalb der theoretischen Kapazität zu erreichen. In der Literatur existieren zwei Hypothesen bezüglich des Ursprungs dieses noch nicht geklärten Speichermechanismus. Die erste Hypothese besagt, dass die Ladung aufgrund einer Oberflächenreaktion der gebildeten Fe-Nanopartikel mit der SEI/Li_2O gespeichert wird [78, 86]. Diese Hypothese beruht auf Hellfeldmikroskopieuntersuchungen von Poizot *et al.* [78], die zeigten, dass die gebildeten Metallnanopartikel sowie Li_2O-Strukturen von einer festen Elektrolyt-Grenzfläche umgeben sind. Zudem wurde deutlich, dass sich die Art und Zusammensetzung dieser Grenzfläche

während dem Zyklieren verändert. Festkörper-Kernspinresonanzspektroskopie von Hu *et al.* [86] deuten eine Konversionsreaktion von LiOH zu Li_2O und LiH, sowie eine reversible auf- und abbauende Oberflächenschicht an. Die dort angestellten *ab-initio* Berechnungen ergeben, dass hauptsächlich die Konversionsreaktion von LiOH zur elektrochemischen Speicherung beiträgt. Eine andere Erklärung geht von der Speicherung von Elektronen an der Oberfläche der gebildeten Eisenmetallteilchen in sogenannten Raumladungszonen als Ursprung der zusätzlichen Kapazität aus [87]. Die Raumladungszone bildet sich dabei zwischen der ionisch leitenden Li_2O-Matrix und den elektrisch leitenden Eisenpartikeln. Die Kapazität dieser Raumladungszone wird bestimmt von der Ionisierungsenergie von Lithium (der Energie, die benötigt wird, um ein Elektron aus einem Atom herauszulösen), der Elektronenaffinität des Eisens (der Energie, die erforderlich ist, um ein Elektron aus einem einfach negativ geladenen Anion zu entfernen und ein neutrales Molekül oder Atom zu bilden) und einem Coulomb-Term, der die Ladungswechselwirkung misst [87]. Bestätigung hat diese Theorie erst kürzlich durch *in situ* Magnetisierungsmessungen von Li *et al.* [88] erfahren. Die *in situ* Magentisierungsmessungen deuten daraufhin, dass das gebildete Fe-Metall weiterhin an der elektrisch angetriebenen Lithiierungsreaktion teilnimmt. Ausgehend von dieser Beobachtung und weiteren elektrochemischen Messungen wurde die zusätzliche Kapazität der Speicherung von spinpolarisierten Elektronen an der Oberfläche der Fe-Partikel zugeordnet [88].

2.3.2 Molybdändioxid (MoO_2)

Der Halbleiter Molybdändioxid (MoO_2) kristallisiert in der monoklinen primitiven Gitterstruktur der Raumgruppe $P2_{1/c}$.

Die verzerrte rutilartige Kristallstruktur (siehe Abbildung 2.7) kann als tunnelgerüstartig beschrieben werden. Die MoO_6-Oktaeder, welche über die Kanten miteinander verknüpft sind schließen zwischen sich entlang der kristallographischen a-Richtung eindimensionale Kanäle ein [89]. Auborn et al. [90] präsentierten MoO_2 im Jahr 1987 erstmals als potenzielles Anodenmaterial, das auf der Interkalation von Li^+-Ionen basiert. *In-situ*-Röntgendiffraktometrie-Studien zeigen, dass bei der Interkalation von 1 Li^+-Ion/f.u. die ursprüngliche monokline Phase in eine orthorhombische Phase (Pnnm) übergeht, bevor sie in eine andere monokline Struktur überführt wird [91] (siehe Gleichung 2.16). Die Speicherung oberhalb von 1 Li^+-Ion/f.u., die bei nanostrukturiertem MoO_2 beobachtbar ist, konnte durch Röntgenphotoelektronenspektroskopie-Untersuchungen einer Konversionsreaktion

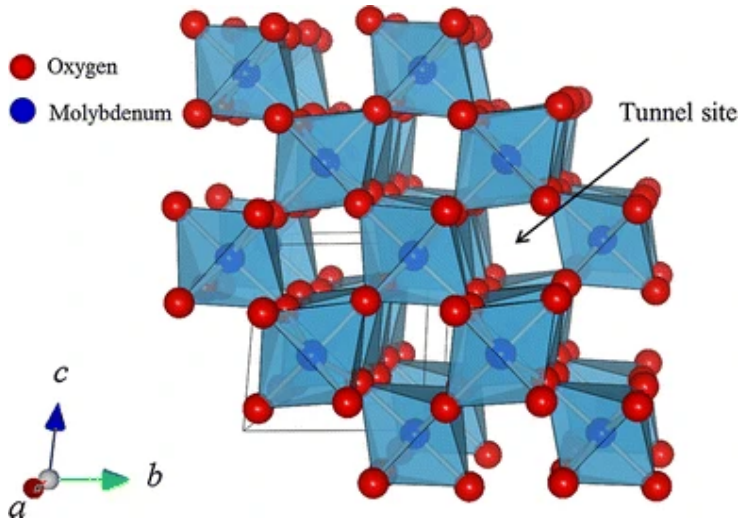

Abbildung 2.7: Schematische Darstellung der MoO_2-Struktur. Die roten Kugeln symbolisieren Sauerstoff, die blauen Kugeln Molybdän. Entnommen aus [89].

(Gleichung 2.17) zugeordnet werden [92].

Der gesamte elektrochemische Reaktionsmechanismus ist gegeben durch:

$$MoO_2 + xLi^+ + xe^- \leftrightarrow Li_xMoO_2 \qquad \text{für} \quad (0 \leq x \leq 0.98) \tag{2.16}$$

$$Li_xMoO_2 + (4-x)Li^+ + (4-x)e^- \leftrightarrow Mo + 2Li_2O \tag{2.17}$$

Die theoretische Kapazität von nanostrukturiertem MoO_2 beträgt 838 mAh g^{-1}. Die halbleitenden Eigenschaften verleihen MoO_2 darüber hinaus speziell im Bereich der TMOs eine vergleichsweise hohe elektrische Leitfähigkeit [93]. Zur Überwindung der bekannten Nachteile von Konversionsmaterialien, wurde auch im Fall von MoO_2 bereits verschiedene Arten von Nanomaterialstrukturen (z. B. Partikel [94], Röhren [95], Kugeln [96]) sowie verschiedene MoO_2-Kohlenstoff-Komposite mit unterschiedlicher Morphologie und Struktur hergestellt. Das ex-folierte Graphen Oxide/MoO_2-Komposit von Petnikota *et al.* [97] erreicht dabei eine Kapazität von 850 mAh g^{-1} nach 10 Zyklen bei 0,1 A g^{-1}, während das MoO_2/3D-Graphen-Komposit von Huang *et al.* [98] eine Kapazität von 975,4 mAh g^{-1} bei 0,05 A g^{-1} erreicht.

2.3.3 Molybdändisulfid (MoS_2)

Das Übergangsmetall-Dichalkogenid Molybdändisulfid (MoS_2) hat in den letzten Jahren große Aufmerksamkeit in Industrie und Wissenschaft auf sich gezogen. MoS_2 kristalli-

siert in drei Formen: 2H, 1T und 3R. Die 2H- und 1T-Phasen weisen eine signifikante Energiespeicher- und -umwandlungsleistung auf [99]. MoS_2-2H ist eine halbleitende Phase mit einer graphitähnlichen Schichtstruktur. Die Schichtstruktur besteht aus drei gestapelten Atomen S-Mo-S mit einem Schichtabstand von 6,2 Å und damit einem fast doppelt so großen wie der von Graphit (3,35 Å) [100].

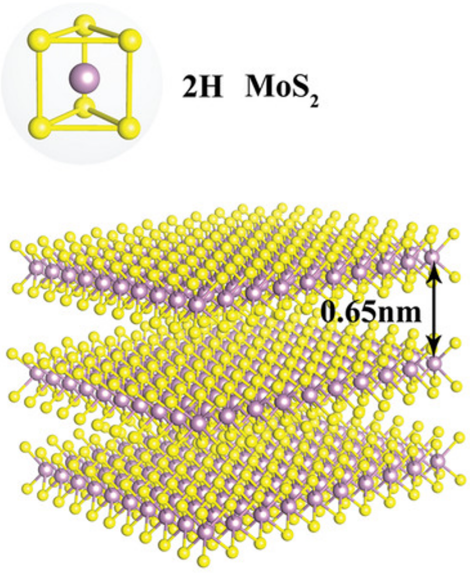

Abbildung 2.8: Schematische Darstellung der MoS_2-2H Schichtstruktur. Schwefel ist gelb dargestellt, Molybdän violett. Entnommen aus [100].

Eine hohe Verfügbarkeit sowie die hohe theoretische Kapazität von 669 mAh g^{-1} machen MoS_2 zu einem vielversprechenden Anodenmaterial für Lithium-Ionen-Batterien [101]. Die signifikante Volumenänderung beim Einlagern/Extrahieren von Li^+ sowie potenziell schädliche Nebenreaktionen verhinderten bislang aber eine Kommerzialisierung [99].

Der elektrochemische Reaktionsprozess ist gegeben durch [102]:

$$MoS_2 + xLi^+ + xe^- \leftrightarrow Li_xMoS_2 \tag{2.18}$$

$$Li_xMoS_2 + (4-x)Li^+ + (4-x)e^- \rightarrow Mo + 2Li_2S \tag{2.19}$$

$$Mo + 2Li_2S \leftrightarrow Mo + 2S + 4Li^+ + 4e^- \tag{2.20}$$

Während der Interkalation (Gleichung 2.18) erfolgt eine Umwandlung von MoS_2 von der 2H-Phase in die 1T-Phase, die metallische Eigenschaften aufweist. Während der weiteren Lithiumaufnahme tritt eine Konversionsreaktion auf, die zur Bildung von Li_2S- und Mo-Nanopartikeln führt. Die folgende Reaktion von Li_2S zu reinem Schwefel ist die dominante

reversible Reaktion [103]. Inwiefern sich MoS_2 nach der Konversionsreaktion zurückbilden kann, ist noch nicht geklärt [102].

Um die elektrochemischen Eigenschaften von MoS_2 weiter zu verbessern wurde eine Vielzahl an MoS_2-Kohlenstoffkompositen entwickelt. Eine vielversprechende Arbeit von Li *et al.* [104] über MoS_2/N-dotierte poröse Kohlenstoff-Nanostäbchen zeigt stabile Kapazitäten von 800 mAh g^{-1} bei 0.5 A g^{-1}. MoS_2-Nanoblätter im Inneren hohler mesoporöser Kugeln (HMCS) erreichen eine Kapazität von 993 mAh g^{-1} [105].

2.4 Lithiumreiche Antiperowskite als Kathodenmaterialien

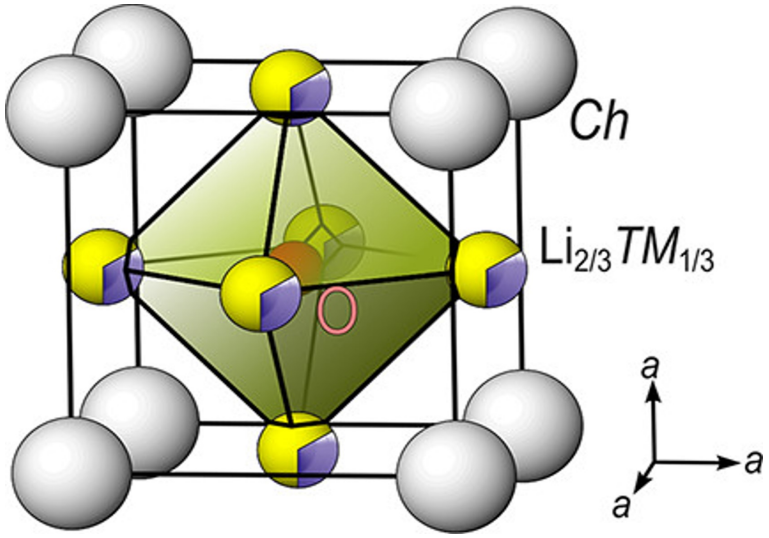

Abbildung 2.9: Schematische Darstellung der allgemeinen Struktur der Einheitszelle von lithiumreichen Antiperowskiten: $(Li_2TM)ChO$ (TM = Übergangsmetall und der Chalkogene Ch = S or Se). Die grauen Sphären in den Ecken repräsentieren die Chalkogene. In Gelb/Lila ist Lithium/TM dargestellt und in der Mitte in Rot, Sauerstoff. Entnommen aus [106].

Das Forschungsfeld der Kathodenmaterialien für Lithium-Ionen-Batterien (LIB) wurde 2017 durch die Entdeckung der Materialklasse der lithiumreichen Antiperowskite mit der allgemeinen Formel $(Li_2TM)ChO$ (TM = Fe, Mn, Co; Ch = S, Se) durch Lai *et al.* [18] erweitert. Im Gegensatz zur klassischen Perowskit-Struktur (ABX_3, wobei A und B Kationen sind und X ein anionisches Oxid (O^{2-})) wie zum Beispiel bei $CaTiO_3$ zeigen Antiperowskite eine umgekehrte Anordnung von Anionen und Kationen. Im Antiperowskit sind die Chalkogenid-Ionen die Ecken der kubischen Einheitszelle, während sich die Lithium-

und Übergangsmetall-Ionen zufällig auf der Würfeloberfläche verteilen. Das Sauerstoff-Ion ist in der Mitte des Würfels zu finden [18, 106] (siehe Abbildung 2.9). Die bisher untersuchten lithiumreichen Antiperowskite sind an Luft nicht stabil. Für $(Li_2Fe)SO$ ist folgende Zersetzung vorhergesagt [107]:

$$2Li_2FeSO \rightarrow FeS + Li_2S + Li_2FeO_2 \tag{2.21}$$

Aus der Batterieanwendungsperspektive zeigt die Materialklasse der lithiumreichen Antiperowskite vielversprechende Eigenschaften wie niedrige Herstellungskosten, die Verwendung ungiftiger Rohstoffe, hohe potentielle Lithiumdiffusionsraten sowie eine hohe theoretische Kapazität aufgrund der enthaltenen zwei Lithium pro Formeleinheit [18]. Darauffolgende Untersuchungen mittels Dichtefunktionaltheorie (DFT) und *ab-initio* Molekulardynamiksimulationen sagten zudem ein reversibles Regime für die Aus- und Einlagerung von 1.25 Lithium in die Antiperowskitstruktur voraus [107].

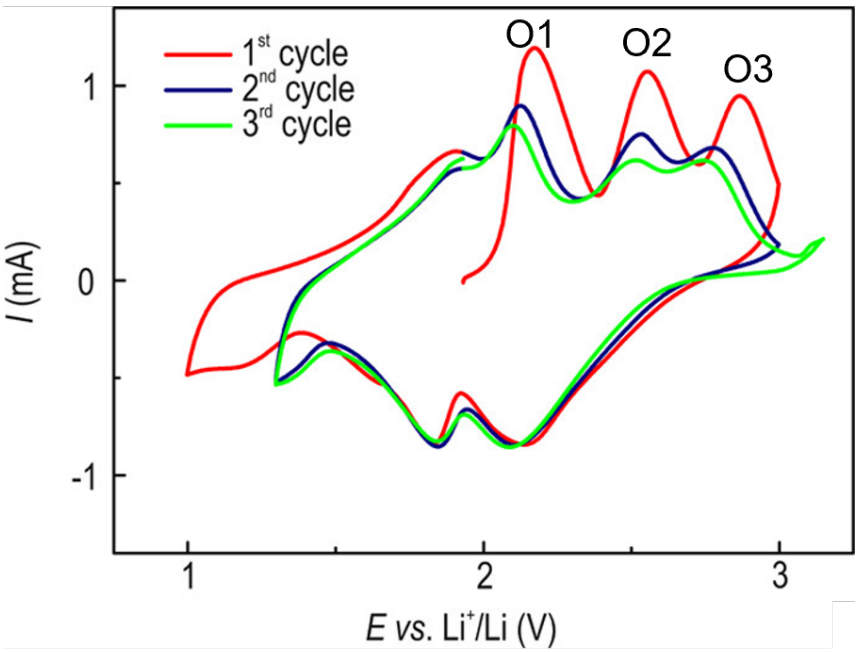

Abbildung 2.10: Zyklovoltammogramm von $(Li_2Fe)SO$ vs Li/Li^+ im Spannungsbereich zwischen 1 und 3 V. Adaptiert aus [108].

In-Operando-Messungen am lithiumreichen Antiperowskit Li_2FeSO, speziell *in situ* Röntgenabsorptionsspektroskopie (XAS), *in situ* XRD sowie *ex situ* XPS-Messungen und Mößbauerspektroskopie, ermöglichten eine erste Charakterisierung des elektrochemischen

Reaktionsmechanismus [108]. Im Rahmen dieser Ergebnisse konnte der kationische elektrochemische Oxidationsprozess Fe^{2+} zu Fe^{3+} zu den ersten zwei Peaks im CV (O1, O2) zugeordnet werden (siehe Abbildung 2.10). Darüber hinaus, deuten die *ex situ* XPS-Ergebnnisse auf ein anionischen Beitrag (S^{-2} zu S^0 bei ungefähr 2.9 V, Peak O3) zur elektrochemischen Kapazität an. Die vollständige Beschreibung des anionischen Prozesses, sowie Aussagen zu dessen Reversibilität sind mittels der erhobenen Daten allerdings nicht möglich. Die erreichte spezifische Kapazität für Li_2FeSO liegt in Zyklus 50 bei einem Strom von 0.1C bei 150 mAh g^{-1} [108]. Weitere Untersuchungen bezüglich des Einflusses des Übergangsmetalls an $(Li_2Fe_{0.9}Co_{0.1})SO$ und $(Li_2Fe_{1-x}Mn_x)SO$ zeigen weder eine starke Verschiebung der elektrochemischen Reaktionen aufgrund der verwendeten Dotierung noch zusätzliche Reaktionen im CV. Eine Abhängigkeit der Zyklenstabilität und Kapazität mit der Dotierung konnte hingegen festgestellt werden. Bei einer geringen Dotierung ist eine leicht verbesserte Performance beobachtbar. Bei höheren Mn (50%) Dotierungen wird die Performance hingegen wieder schlechter [109, 110]. So erreicht $(Li_2Fe_{0.9}Co_{0.1})SO$ bei einem Strom von 1C eine Kapazität von ungefähr 230 mAh g^{-1} [110], wohingegen $(Li_2Fe_{0.5}Mn_{0.5})SO$ bei einem Strom von 0.1C in Zyklus 50 nur eine Kapazität von 120 mAh g^{-1} erreicht [109]. Untersuchungen bezüglich des Einflusses des anionischen Selen-Gehalts in $(Li_2Fe)S_{1-x}Se_xO$ zeigen eine starke Abhängigkeit des O3-Prozesses. Je höher der Selen-Gehalt, desto mehr wandert O3 zu niedrigeren Spannungen. Auch hier scheint ein niedriger Gehalt an Selen (30%) für die umgesetzte Kapazität (245mAh g^{-1} bei 0.1C in Zyklus 5) von Vorteil zu sein [111]. Die bisher untersuchten lithiumreichen Antiperowskite demonstrieren somit vielversprechende spezifische Kapazitäten, mit allerdings nur moderaten Zyklenstabilitäten.

Kapitel 3 Nanostrukturierte Übergangsmetall-verbindungen

3.1 On the rising extra storage capacity of ultra-small Fe_3O_4 particles functionalised with HCS and their potential as high-performance anode material for electrochemical energy storage

Autoren:

Lennart Singer, Wojciech Kukułka, Elisa Thauer, Nico Gräßler,Andika Asyuda, Michael Zharnikov, Ewa Mijowska, Rüdiger Klingeler

veröffentlicht in: Electrochimica Acta, Volume 448, April 2023, 142155.

L. Singer ist Erst- und (zusammen mit R. Klingeler) korrespondierender Autor. L. Singer hat das Manuskript konzipiert und mit Ausnahme des experimentellen Teils zur Synthese verfasst. Alle Abbildungen außer S2, S3 wurden von ihm erstellt. Er hat folgende experimentelle Arbeiten und Analysen durchgeführt:

- Analyse Röntgendiffraktometrie (XRD)
- Rasterelektronenmikroskopie (REM): Durchführung und Analyse
- Magnetische Messungen: Durchführung und Analyse
- Analyse der Ergebnisse der Transmissionselektronenmikroskopie (TEM)
- Analyse der Ergebnisse der Röntgenphotoelektronenspektroskopie (XPS) (zusammen mit und unter Anleitung von M. Zharnikov)
- Elektrochemische Untersuchungen (CV, GCPL, PEIS): Durchführung und Analyse
- Ex-situ REM-Studien: Durchführung und Analyse

Beitrag der Koautoren:

W. Kukułka, E. Mijowska: Synthese der Materialien sowie Raman- und TEM (Abb.3e-h, S2, S3, S7e, f); Beschreibung der Synthese im Manuskripttext.

A. Asyuda, M. Zharnikov: XPS-Messungen (Abb. 2, S1).

N. Grässler, E. Thauer: Beratung und Diskussion über der Analyse der experimentellen Daten.

R. Klingeler: Projektplanung und -leitung, Beteiligung an der Interpretation und Beitrag zur Finalisierung des Manuskriptes.

Korrespondenz mit den Gutachtern: L. Singer, R. Klingeler.

Alle Autoren haben das Manuskript Korrektur gelesen.

Electrochimica Acta 448 (2023) 142155

Contents lists available at ScienceDirect

Electrochimica Acta

journal homepage: www.journals.elsevier.com/electrochimica-acta

On the rising extra storage capacity of ultra-small Fe_3O_4 particles functionalized with HCS and their potential as high-performance anode material for electrochemical energy storage

Lennart Singer [a,*], Wojciech Kukułka [b], Elisa Thauer [a], Nico Gräßler [c], Andika Asyuda [d], Michael Zharnikov [d], Ewa Mijowska [b], Rüdiger Klingeler [a,*]

[a] Kirchhoff Institute for Physics, Heidelberg University, Heidelberg, 69120, Germany
[b] Faculty of Chemical Technology and Engineering, West Pomeranian University of Technology, Szczecin, 71-065, Poland
[c] Leibniz Institute for Solid State and Materials Research Dresden e.V., Dresden, 01069, Germany
[d] Applied Physical Chemistry, Heidelberg University, Heidelberg, 69120, Germany

ARTICLE INFO

Keywords:
Fe_3O_4
Carbon composite
Extra storage capacity
Lithium-ion battery

ABSTRACT

We report a nanocomposite material exhibiting ultra-small Fe_3O_4 nanoparticles uniformly decorated on hollow carbon spheres (Fe_3O_4@HCS). The unique hierarchically-structured material displays excellent electrochemical cycling performance that exceeds the theoretical bulk capacity of Fe_3O_4 when used as an anode in lithium-ion batteries. In particular, it features increasing reversible capacity upon cycling yielding 1050 mAh g^{-1}at 0.1 A g^{-1} in cycle 250. Comprehensive scanning and transmission electron microscopy images combined with detailed electrochemical analysis demonstrate that the outstanding electrochemical performance can be traced back to the formation and decomposition of a capacitative surface layer during dis/charging.

1. Introduction

Over the past three decades, due to their high energy density, high Coulombic efficiency, and long cycle life, rechargeable lithium-ion batteries (LIBs) have been widely used in portable electronic devices, stationary energy storage devices, and electric vehicles. However, there is still a gap between existing batteries as well as their active electrode materials and, the enormous demand for batteries with ever higher energy density, cycle stability and environmental compatibility. Therefore, the development of alternative battery materials is imperative. Transition metal oxides (TMOs), with their attractive theoretical (bulk) capacities due to the multiple-electron transfer conversion reaction taking place with Li^+ ions are considered a promising alternative anode material for LIBs [1–8]. Among them, based on its low cost, environmentally friendly nature, and high theoretical capacity of 926 $mAhg^{-1}$, Fe_3O_4 is one of the most promising anode materials for the next-generation of LIBs [1,9–11]. However, large volume changes of Fe_3O_4 anodes during cycling, leading to particle cracking, electrode pulverization and premature electrode collapse, prevent full exploitation of Fe_3O_4 as a LIB anode material [12]. To address these issues, several strategies have been developed to improve the structural integrity of Fe_3O_4-based anode materials, like the fabrication of Fe_3O_4-carbon composites and particle size reduction to the nanometer-scale [13]. Particularly, downsizing of Fe_3O_4 particles into the few nanometer regime has been found to result in further positive effects such as the possibility to even exceed the proposed theoretical bulk capacity [10,14,15]. For the observed extra capacity, two different scenarios are discussed in the literature: (1) surface side reactions including the SEI [1,16] and/or (2) storage of spin polarized electrons at the surface of the formed iron metal particles [17] described by interfacial charge storage theory [18–20]. In both scenarios, the amount of additional stored charges strongly depends on the size and surface area of the electrochemically formed iron particles. The smaller the formed iron particles, the greater their combined surface area and surface to volume ratio, leading to more possible reaction sites. The size of the electrochemically formed iron particles in turn strongly depends on the size of the pristine Fe_3O_4 particles in the material [10,14,17]. Beyond the amount of additional capacity of nanoscaled Fe_3O_4, most of the materials do not reach maximum capacity directly, they instead exhibit an increasing capacity during cycling. The phenomenon of the increasing capacity during cycling is even less understood and discussed in literature as the origin behind the extra capacity of Fe_3O_4. One powerful way to investigate both, the origin and the rise of the extra capacity is electrochemical impedance spectroscopy (EIS). EIS allows to study complex electrochemical processes and kinetics with the

* Corresponding authors.
E-mail addresses: lennart.singer@kip.uni-heidelberg.de (L. Singer), klingeler@kip.uni-heidelberg.de (R. Klingeler).

https://doi.org/10.1016/j.electacta.2023.142155
Received 15 December 2022; Received in revised form 23 February 2023; Accepted 27 February 2023
Available online 2 March 2023

ability to deconvolute them into elementary processes according to the difference in the specific relaxation time constants [21–24]. This can particularly be used to invisible interfaces and surface layer, like the SEI and the double-layers [21–24]. Following the theories concerning the extra capacity EIS promises to be an ideal tool to get a deeper insight into the phenomenon of extra capacity and the rise of it. We report the hybrid material Fe_3O_4@HCS exhibiting exceptionally small Fe_3O_4 particles uniformly distributed on hollow carbon spheres. The presented Fe_3O_4@HCS impress not only with a compelling electrochemical performance of 1050 mAh g^{-1} at 0.1 A g^{-1} in cycle 250, it also displays an distinctive extra capacity with a constant increase during cycling. Our detailed electrochemical studies on Fe_3O_4@HCS combined with deep in situ electrochemical impedance spectroscopy measurements which are completed wit ex situ SEM und TEM images enabled to clarify the picture behind the extra capacity of Fe_3O_4 and its rise. Our results demonstrate, that the reversibly, growing extra capacity, reaching values well beyond the theoretical capacity can be traced back to an gradual formation and decomposition of a capacitive surface layer.

2. Experimental section

Synthesis of SiO_2–NH_2 template

To begin, a template for the growth of the final structure was prepared. For that, 6 ml of tetraethoxysilane (TEOS) was added drop wise, to a ethanol (200 ml), $NH_3{\cdot}H_2O$ (10 ml) mixture and stirred at room temperature for 24 h. In order to attach NH_2 groups to the silica, additional functionalization with (3-Aminopropyl)triethoxysilane (APTES) was performed. This was done by adding 0.6 ml of APTES to the prepared mixture and stirred for the next 4 h. Finally, the obtained sample was centrifuged and the sediment was dried at 60 °C overnight.

Synthesis of carbon spheres from glucose (HCS)

In order to cover the SiO_2-NH_2 with a glucose layer, 0.6 g of the SiO_2-NH_2 prepared in the previous step and 0.6 g of glucose were added to 100 ml of water and sonicated for 30 min. Coating was then done in an Teflon-lined autoclave at 180 °C for 12 h. After, the glucose-coated silica was placed in a tube furnace, carbonization was carried out at 800 °C for 2 h under nitrogen atmosphere. Finally, the silica was removed with HF to obtain hollow carbon spheres based on glucose.

Synthesis of carbon spheres functionalized with iron oxide nanoparticles (Fe_3O_4@HCS)

Functionalization of hollow carbon spheres with iron oxide nanoparticles was performed by mixing 100 mg of HCS and 50 mg of iron(III) acetylacetonate in 30 ml triethylenglycol followed by sonication for 30 min. The mixture was then heated under reflux and nitrogen atmosphere to 278 °C at a heating rate of 3 °C/min. After cooling the mixture to room temperature, the product was precipitated with ethanol, washed and dried at 60 °C overnight.

Characterization

X-ray diffraction (XRD) patterns were acquired on a Bruker AXS D8 Advance Eco using Cu Kα radiation with a step size of $2\theta = 0.02°$. The carbon content was determined by CHN analysis on a Elementar Vario MICRO Cube. The morphology of the powder was studied using a JEOL JSM-7610F scanning electron microscope (SEM) and a transmission electron microscope with EDS attachment (TEM, Tecnai F30). Raman spectra were measured using a Via Raman Microscope (Renishaw) with an excitation wavelength of 785 nm. X-ray photoelectron (XP) spectra were measured with a MAX200 (Leybold-Heraeus) spectrometer equipped with a non-monochromatized Mg Kα X-ray source (200 W) and a hemispherical analyzer. The powder materials were pressed into clean indium foil and thinned by a brush to suppress charging effects, following established methodology [25]. Magnetic measurements were performed on Fe_3O_4@HCS powder samples using an MPMS3 magnetometer (Quantum Design). Magnetization was measured by varying the temperature between 2 and 300 K using zero-field-cooled (ZFC) and field-cooled (FC) protocols at 0.05 T. Isothermal magnetization was studied at 2 and 200 K in magnetic fields up to ±7 T.

Electrochemical measurements

Electrochemical measurements were performed on a VMP3 potentiostat (BioLogic) at 25 °C. Working electrodes were prepared by mixing the active material 80%wt, carbon black (TIMCAL SUPER C65) 10%wt, and polyvinylidene fluoride (PVDF) 10%wt in N-methyl-2-pyrrolidinone (NMP). The mixture was then stirred for 24 h before spreading the resulting slurry on (Ø=10mm, thickness=0.25 mm, weight=53.8 mg) copper mesh current collectors (see [26]). The as-prepared electrodes were dried in a vacuum oven (80 °C, 10 mbar) overnight, then pressed and dried again. The active material mass loading of the prepared electrodes ranged between 0.9 and 1.7 mg cm^{-2}. Glass fiber (Whatman GF/D, 675 µm thickness) was used as the separator and pure lithium metal foil (Aldrich) as the counter electrode. As electrolyte 120 µl of 1 M $LiPF_6$ in a mixture of ethylene carbonate and dimethyl carbonate (1:1 by weight) was used. CR 2032 coin cells were used for cyclic voltammetry and galvanostatic cycle measurements with potential limitation (GCPL). For potentiostatic electrochemical impedance measurements (PEIS), a 3-electrode PAT-Cell from EL-CELL was used, with a ring-shaped lithium metal reference electrode close to the working electrode. Cell assembly was performed in an Ar-filled glovebox with controlled humidity and oxygen concentration. Cyclic voltammetry was performed at a scan rate of 0.1 mVs^{-1}, GCPL at specific currents, each in the voltage range of 0.01–3.0 V vs. Li/Li^+. For the normalization of the specific capacity, the mass of all electrochemically active materials is taken into account, i.e. carbon black plus Fe_3O_4@HCS. For the PEIS measurements, the small disturbance of 10 mV in the frequency range from 200 kHz to 1 mHz was selected. To ensure time invariance of the measurement as well as a steady state, a 16 h OVC (open circuit voltage) was performed before each PEIS measurement, and a second control PEIS measurement was performed directly afterwards. For monitoring the micro-structural changes of Fe_3O_4@HCS during cycling, ex-situ SEM, TEM images were acquired using a JEOL JSM-7610F scanning electron microscope and a Tecnai F30 TEM, respectively. The cycled electrodes were disassembled in an argon glove box, washed with ethylene carbonate, and then dried overnight.

3. Results and discussion

3.1. Structure, morphology, and composition of Fe_3O_4@HCS

Fig. 1 shows X-ray diffractograms of the synthesized materials, i.e., Fe_3O_4@HCS and pure HCS. For HCS, a broad diffraction peak is observed around $2\theta \approx 23.5°$, which is characteristic of graphite and can be attributed to the (002) planes of graphitic carbon. This broad shoulder is also seen in the XRD pattern of Fe_3O_4@HCS, where additional Bragg reflections are observed, signaling a cubic spinel iron oxide structure, namely Fe_3O_4 (magnetite) or $\gamma - Fe_2O_3$ (maghemite). Since the XRD patterns of magnetite and maghemite are very similar, the XRD data alone do not distinguish these structures [29,30]. We also note that the respective Bragg peaks are rather broad and of low-intensity which may be attributed to small crystal size and/or low crystallinity of Fe_xO_y-particles present in the composite [31]. The average primary crystallite size of the as-synthesized samples was estimated using Scherrer's equation [32],

$$D_{hkl} = \frac{K\lambda}{\Delta(2\theta_{hkl})\cos\theta_{hkl}} \quad (1)$$

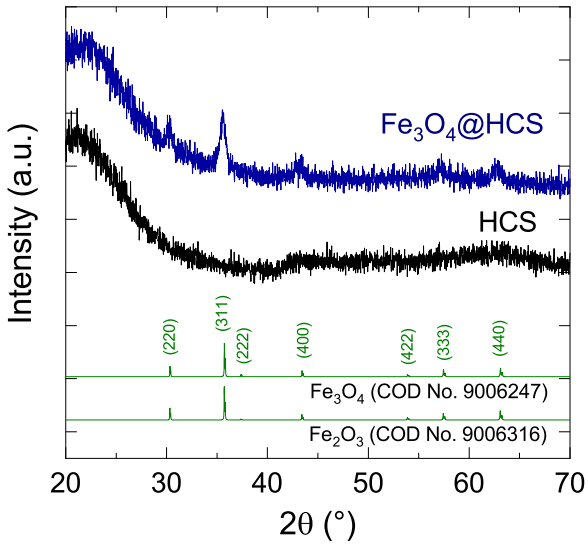

Fig. 1. XRD patterns of HCS and Fe_3O_4@HCS as well as indexed reference patterns for $\gamma - Fe_2O_3$ COD No. 9006316 [27] and Fe_3O_4 COD No. 9006247 [28].

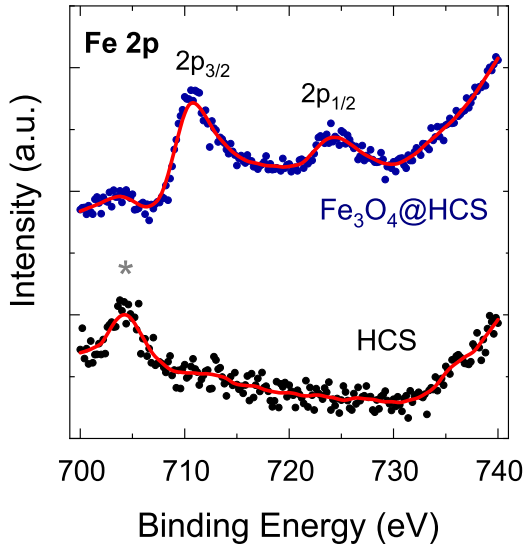

Fig. 2. Fe2*p* XP spectra of Fe_3O_4@HCS and HCS. The red solid lines show a binning of the data points. The peak marked by the asterisks originates from the used In substrate (In $3p_{1/2}$).

where D is the average crystal grain size based on the respective reflective crystal face direction (hkl), K a shape factor that can be approximated to 0.9, λ is the wavelength of the applied Cu K_α radiation, $\Delta(2\theta_{hkl})$ the full width at the half maximum of the diffraction peak, and θ_{hkl} the Bragg angle. The analysis of the (311) and (440) reflections yields the crystallite size $d_{XRD} \simeq 11(3)$ nm.

Elemental analysis of the sample Fe_3O_4@HCS shows a weight percentage of carbon of about 53.7(5) w%, as well as residuals of nitrogen of 2.7(5) w% and 1.5(5)w% of hydrogen. We hence conclude that the remaining mass fraction of 42.1w% amounts to the iron oxide content in the composite.

For the unambiguous determination of the iron oxide phase present, XPS measurements were performed which can differentiate the presence of Fe^{2+} and Fe^{3+} ions. Fig. 2 shows the XP spectra of Fe2*p* of Fe_3O_4@HCS and HCS. The spectra on Fe_3O_4@HCS display broad peaks at 710.6 ($2p_{3/2}$) and 724.2 eV ($2p_{1/2}$) which are typical of Fe_3O_4 [30]. In addition, Fe_2O_3 can be excluded since the characteristic satellite peak at 719.2 eV is not perceptible [33]. These findings clearly rule out the presence of Fe_2O_3 and imply that the formed oxide in the hybrid nanomaterial is Fe_3O_4. Note, that an additional peak at around 704 eV which is visible in both pure HCS and Fe_3O_4@HCS spectra is the characteristic In $3p_{1/2}$ line of the indium substrate used. Complementary XPS data can be found in the Supporting Information. In particular, the survey spectrum in S1a displays the presence of O, C, In and Fe without any detectable impurity. The comparison of C1s spectra of pure HCS and Fe_3O_4@HCS (S1b) as well as the respective Raman spectra (S2) show moreover no change of the carbon structure during the functionalization of HCS with the iron oxide nanoparticles, which demonstrates the HCS as a well-preserved, well-conducting carbon buffer matrix for the ultra-small magnetite nanoparticles.

The typical spherical shape of both as-synthesized HCS and Fe_3O_4@HCS is confirmed by SEM and TEM studies which visualize the morphology and micro-structure of the materials (see Fig. 3). In Fe_3O_4@HCS, in addition to bare HCS (Fig. 3a,b) which are about 150 nm in diameter, the images Fig. 3c to f show the presence of evenly dispersed nano-sized iron oxide particles. High-resolution TEM images (shown in Fig. 3f,h) additionally highlight that the iron oxide particles, are not loosely deposited on the HCS, they are embedded in the HCS framework. The observed crystalline region in Fig. 3h marked in red, displays a d-spacing of 0.25 nm an can hence be attributed to the (311)-plane of Fe_3O_4.

Additionally the TEM-EDX measurements (see Fig. S3 in the Supplement) furthermore prove the uniform distribution of Fe, O, and C. We note the exceptionally small size of the nanoparticles which display a maximum diameter well below 20 nm. This agrees to the results of the XRD analysis which implies crystallites with an average diameter of $d_{XRD} \simeq 11$ nm. One can hence conclude that most of the iron oxide particles are single crystalline.

3.2. Magnetic properties

The presence of ferromagnetism in Fe_3O_4 renders magnetic studies a meaningful tool to further investigate iron oxide nanoparticles in a hybrid nanomaterial [34]. While the weak diamagnetic contribution of carbon can be neglected, the magnetization curve in Fig. 4b confirms the overall ferromagnetic response of Fe_3O_4@HCS. Quantitatively, the observed saturation magnetization amounts to about 18 erg/$g_{Fe_3O_4}$ which is much lower than that of bulk Fe_3O_4 ($M_s = 92$ erg/$g_{Fe_3O_4}$) [35]. Reduced saturation magnetization of iron oxide nanoparticles is a known phenomenon and is attributed to surface effects, which, in nanoparticles, can dominate the properties due to the large surface to bulk ratio [30,36].

The difference in field-cooled (fc) and zero-field-cooled (zfc) magnetization data which is observed upon cooling below about 100 K confirms the presence of superparamagnetism in Fe_3O_4@HCS (Fig. 4b). This is also visible in the M vs. B curves in Fig. 4a which display a significant increase of the hysteresis, i.e., of the critical field, upon cooling to 2 K. The data allow to read-off the characteristic blocking temperature T_B which is particularly evident when the derivative of the difference of M_{fc} and M_{zfc} is considered (see the inset in Fig. 4b) [37,38]. The peak in $\partial(M_{fc} - M_{zfc})/\partial T$ at $T_B \approx 5$ K implies the characteristic blocking temperature. Note, that the observation of a small hysteresis above T_B suggests that few particles remain blocked up to about 100 K, which is also the maximum of the zfc curve and therefore implies another characteristic blocking temperature. As the blocking temperature depends on the particle size, this suggests a certain distribution of particle sizes with however a clear signature attributed to the mean. From T_B, the mean particle volume can be estimated as [39]

$$V = \frac{T_B 25 k_B}{K_u} \tag{2}$$

with k_B the Boltzman constant and K_u the magnetic anisotropy constant. Using the anisotropy constant of bulk Fe_3O_4 of 1.35×10^4 Jm^{-3} [40]

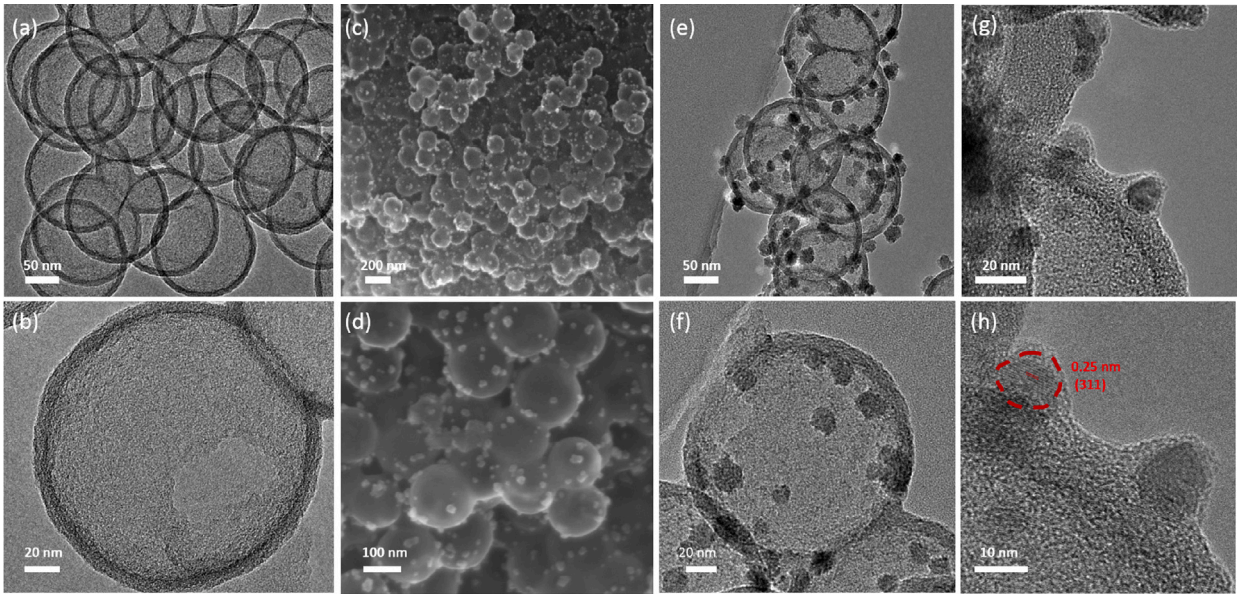

Fig. 3. TEM images of HCS (a,b) as well as SEM (c,d) and TEM (e-h) images of Fe_3O_4@HCS. The red color used marks a crystalline region.

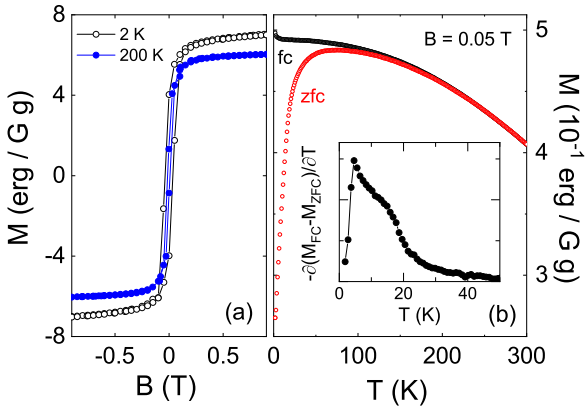

Fig. 4. (a) Magnetization of Fe_3O_4@HCS vs. magnetic field, at 2 K and 200 K and (b) vs. temperature at $B = 0.05$ T. The inset shows the derivative of the difference between field-cooled (fc) and zero-field-cooled (zfc) magnetization.

and the two characteristic temperatures, the average particle diameter can be roughly estimated to ~10 nm which agrees to the analysis of the TEM data and d_{XRD}. The sharp low-temperature peak at 5 K in particular indicates particles of 6 nm in diameter in the material.

3.3. Electrochemical studies

The hierarchical structure of Fe_3O_4@HCS featuring nano-sized particles of the oxide conversion material embedded in a hollow carbon matrix was studied by cyclic voltammetry and galvanostatic cycling (GCPL) in the voltage range of 0.01 – 3 V vs. Li/Li^+. In order to assess the effects of the carbon matrix, measurements were performed on pristine HCS under the same conditions. The complete electrochemical reaction path of bulk Fe_3O_4 can be expressed as follows [10,17,41]:

$$Fe_3O_4 + 2Li^+ + 2e^- \rightarrow Li_2Fe_3O_4 \quad (3)$$

$$Li_2Fe_3O_4 + 2e^- + 2Li^+ \leftrightarrow 2(Li_2O \cdot FeO) + Fe \quad (4)$$

$$FeO + 2e^- + 2Li^+ \leftrightarrow Fe + Li_2O \quad (5)$$

$$Fe_3O_4 + 8Li^+ + 8e^- \rightarrow 3Fe + 4Li_2O \quad (6)$$

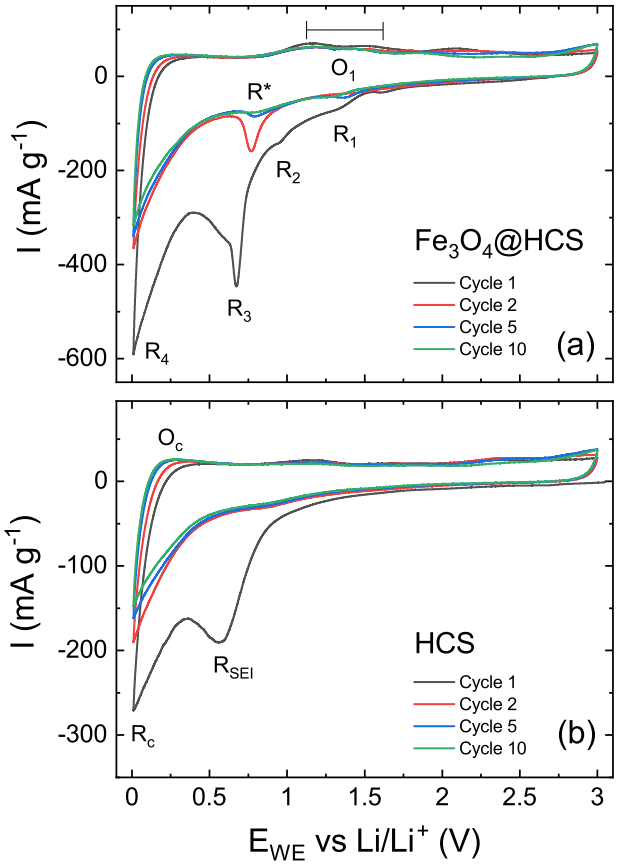

Fig. 5. Cyclic voltammogramms of cycle 1, 2, 5, and 10 of (a) Fe_3O_4@HCS and (b) HCS measured at a scan rate of 0.1 mV s^{-1}. The labels R/O mark distinct reduction and oxidation features.

Various processes can be identified in the cyclic voltammogramms (CVs) presented in Fig. 5. For pristine HCS (see Fig. 5b) the data indicate the formation of a passivating SEI (solid electrolyte interface) on the carbon surfaces as evidenced by the first-cycle reduction peak

(R_{SEI}) at 0.6 V [42]. Correspondingly, the SEI peak disappears upon further cycling. In addition, the data show a reduction/oxidation pair at 0.01/0.2 V (R_C/O_C) attributed to the reversible de-/lithiation into the carbon structures. Both the evolution of the features upon cycling, as well as tiny peaks around 0.8 V (reduction) and 1.2 V (oxidation), originating from lithium insertion/extraction into/from defects in the carbon structure, are typical for pristine HCS [43–47]. For Fe_3O_4@HCS, there are several additional features indicating the electrochemical activity of iron oxide (Fig. 5a). The first cycle is fundamentally different from the following ones and displays the irreversible transformation of Fe_3O_4 during the first lithiation in agreement with previous reports [9,10,41,48,49]. The first peak at 1.4 V is assigned to the initial incorporation of Li^+ cations into the Fe_3O_4 structure (Eq. (3)), the second peak at 1.0 V corresponds to the phase change from spinel Fe_3O_4 to rock salt FeO during additional Li^+ incorporation (Eq. (4)), and the third peak at 0.6 V is assigned to both the conversion reaction FeO to elemental Fe (Eq. (5)) and the formation of the SEI. Upon subsequent delithiation, Fe_3O_4 does not reappear but the FeO structure is formed in the O1 region [1,9,10]. In the subsequent cycles the reversible $Fe^{2+} \leftrightarrow Fe^0$ reaction is the remaining reaction happening in the R*/O1 region, leading to a theoretical reversible bulk capacity of Fe_3O_4 after the first cycle of 694 $mAhg^{-1}$ [10].

The galvanostatic cycling performance of Fe_3O_4@HCS with respect to pristine HCS-based electrodes is shown in Fig. 6a where dis-/charge capacities are presented. Fe_3O_4@HCS shows an initial discharge capacity of 1620 mAh g^{-1}. In contrast, the first charge yields only 600 mAh g^{-1}. The reason for the significantly higher discharge capacity can be traced back to firstly, the irreversible formation of the SEI and secondly, the irreversible conversion of Fe_3O_4, both taking place in the voltage region below 1 V (see the potential profile of the first cycle in Fig. 6b), which results in an irreversible capacity component of the first discharge cycle. In the next 20 cycles, a further slight decrease in the converted specific capacity towards 520 mAh g^{-1} is observed. Thereafter, the converted capacity increases steadily up to 1050 mAh g^{-1} in cycle 240 and then levels off slightly. Note, that the measured specific capacity of Fe_3O_4@HCS-based electrodes after 250 cycles significantly exceeds the postulated theoretical reversible capacity even for pure iron oxide of 694 mAh g^{-1}. As it will be discussed below, the exceedingly small size of the initial Fe_3O_4 nanoparticles presented here may be advantageous for the effect of additional capacity [10]. It is noteworthy that over the entire number of cycles, discharging converts more capacity than charging. The same trend is reflected in the Coulombic efficiency (see Fig. S4a), which displays an increase over the entire 250 cycles. The sharp increase in the first cycles is due to the step wise decrease of the irreversible components of the first discharge cycles. In the almost constant capacity range up to cycle 50, the coulombic efficiency increases to 96%, which is also clearly visible in the reduced gap between discharge capacity and charge capacity. In the next 200 cycles, the increase becomes smaller and smaller until finally a coulombic efficiency of 98.5% is reached in cycle 250. Meanwhile, pure HCS shows initial irreversibility and rather constant capacity upon cycling similar to previous reports [50,51]. An estimate of the contribution of only the Fe_3O_4 component in Fe_3O_4@HCS to the converted specific capacity can be made by subtracting the capacity of HCS according to its mass fraction. The resulting capacity of the ultrasmall Fe_3O_4-nanoparticles in the hybrid materials is shown in Fig. 6a. After a few cycles, it displays a reversible capacity of about 820 mAh $g^{-1}_{Fe_3O_4}$. As already qualitatively seen by the rather constant cycling performance of pure HCS, the increase in capacity of Fe_3O_4@HCS is due to the Fe_3O_4-subsystem which reaches more than 2000 mAh $g^{-1}_{Fe_3O_4}$ after 250 cycles. This value by far exceeds the theoretical reversible capacity associated with the electrochemical reactions shown above, clearly insinuating an enormous additional mechanism of charge storage.

Further insight into this phenomenon is gained by considering the corresponding potential curves in cycles 50, 100 and 200 shown in Fig. 6b. The potential curves of the discharge cycles imply due to the large overlap of the curves at high voltages that the increase in the achieved specific capacity upon cycling is mostly achieved in the low voltage range below 1 V. Since a low average discharge potential is considered as the main criterion for the positive prospect of industrial

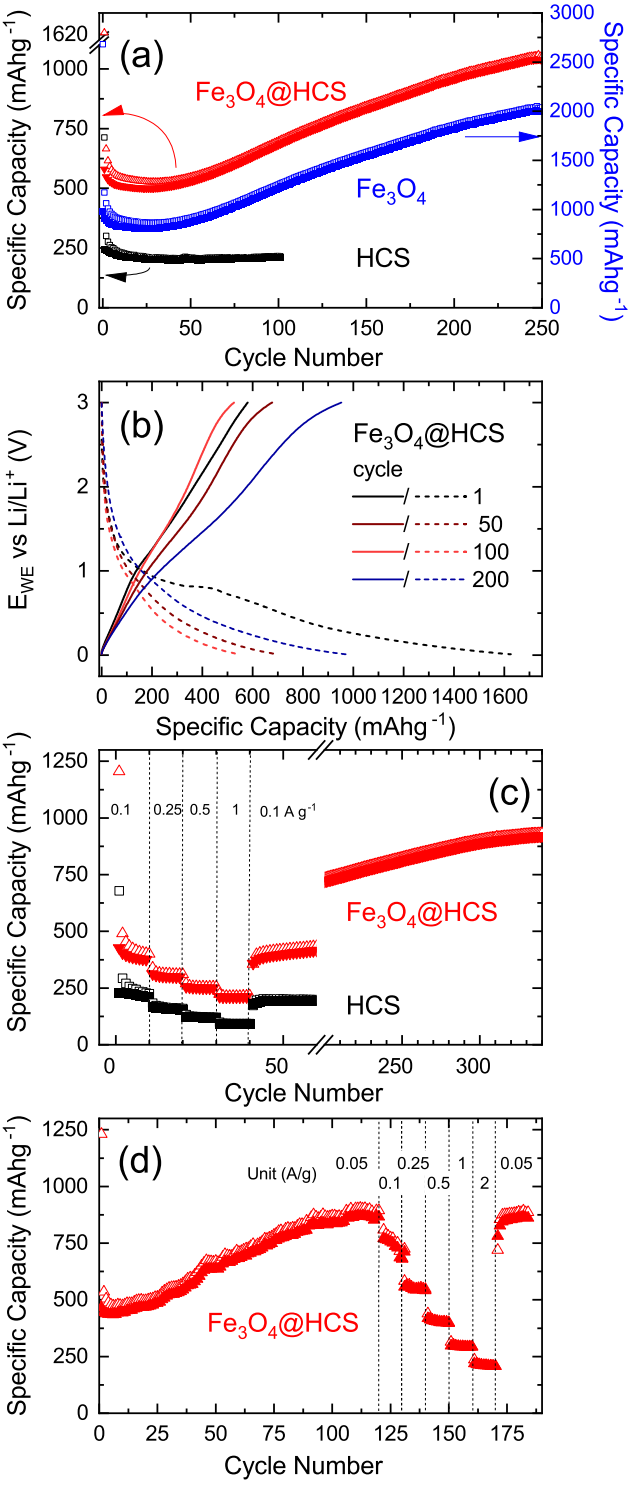

Fig. 6. (a) Specific charge/discharge capacities of Fe_3O_4@HCS and HCS electrodes at 100 mA g^{-1} between 0.01 and 3 V. (b) Selected corresponding potential profiles of Fe_3O_4@HCS electrodes. (c) Rate capacities with different cycling rates of Fe_3O_4@HCS and HCS electrode. (d) Rate capacities obtained at different cycling rates of Fe_3O_4@HCS after 120 cycles at 0.05 Ag^{-1}. Full/open markers indicate de/lithiation.

application, the result that the pronounced additional storage process occurs at low voltages is of utmost importance [52]. The low average discharge potential of our Fe_3O_4@HCS of about 0.5 V makes it again stand out compared to other Fe_3O_4 composites whose average discharge potential is around 1 V [9,53–56] and demonstrates its outstanding properties also from this point of view. From the charge curves it becomes apparent that strong differences upon charging in different cycles appear only in the range of more than one volt. These findings indicate a large voltage hysteresis of the underlying process, which is a common phenomenon in conversion based materials [57].

In Fig. 6c the superior performance of Fe_3O_4@HCS is shown by the rate capability test. It yields a reversible capacity of 400, 310, 250 and 200 mAh g^{-1}, respectively, for Fe_3O_4@HCS and 230, 170, 130, 100 mAh g^{-1} for HCS at currents of 0.1, 0.25, 0.5, 1 A g^{-1}. When the current density is set again to 0.1 A g^{-1}, the reversible capacity reaches 400 mAh g^{-1} demonstrating excellent reversibility of the Fe_3O_4@HCS-based electrode. Notably, as cycling continues, the capacity begins to immediately increases. Just shortly before the 300th cycle, the capacity hardly increases further and remains constant at a value of around 1000 mAh g^{-1} for the next 40 cycles.

To investigate the rate capability of Fe_3O_4@HCS in the regime where the capacity has increased upon cycling, a rate capability study was performed after 120 cycles at 0.05 Ag^{-1} when the reversible capacity reached 900 mAh g^{-1} (see Fig. 6d). The achieved capacity in the entire current range is about twice as high as compared to the rate measurements done in the beginning of cycling, so that at 0.1, 0.25, 0.5, 1 and 2 A g^{-1} a capacity of 750, 550, 400, 300 and 220 mAh g^{-1} is achieved, respectively. While the attained capacity increased significantly due to the decrease at higher current rates, the kinetic behavior remains similar to that observed in the initial cycles. Fig. S4a in the Supplement further shows that, at a consistently high current rate of 1 A g^{-1}, there is no large increase in capacity over 500 cycles. This indicates that the process which yields increasing capacity has slow kinetics or is unable to take place at high current rate. In contrast, in a constant current constant voltage (CCCV) measurement, the capacity gain per cycle significantly increases to around 20 mAh g^{-1} as shown in Fig. S4b. Note, that in this measurement the difference between charge and discharge is larger, too. In order to study whether and to which extent the capacity increases in the low voltage range alone, the voltage was limited from 0.01 to 1 V after the lithiation in cycle 13. The data in Fig. S4b after 13 cycles show that the capacity only increases minimally in the limited potential range from 0.01 to 1 V. The increase in capacity during cycling is therefore taking place over the entire voltage range.

Electrochemical impedance measurements on Fe_3O_4@HCS provide further insights into the electrochemical processes and their kinetics. The measurements have been performed at specific states of charge at frequencies between 200 kHz and 0.1 Hz (see Fig. S5). In Fig. 7 the corresponding Nyquist diagrams are displayed as well as fits to the data performed using the function Z Fit of the software EC-Lab (Bio-Logic) and the equivalent circuit shown in Fig. S6. The obtained fitting parameters are shown in Table S1.

After OCV, the Nyquist plot features a depressed semicircle in the high to medium frequency range reflecting the charge transfer (CT) resistance between electrolyte and electrode material. This is followed by a steep increase in the low-frequency range which slope represents the Li^+ diffusion impedance. The EIS after the first discharge displays an elevated high-frequency semicircle and in addition, a further, clearly visible semicircle starts to appear in the medium frequency range. Upon first charging, the 2nd semicircle disappears. The same trend, with an even more pronounced effect, is also detected after 10 cycles. Here again, it is evident that when fully charged, only a small semicircle is visible, whereas after complete discharge, two, now very pronounced semicircles are present. A quantitative analysis by fitting the data with the appropriate equivalent circuit (see Fig. S6) yields the enables to assess the effect of cycling on the electrolyte and CT resistances (R_E and R_{ct}), and double layer capacitance (Q_{ct}) (Table S1). The results

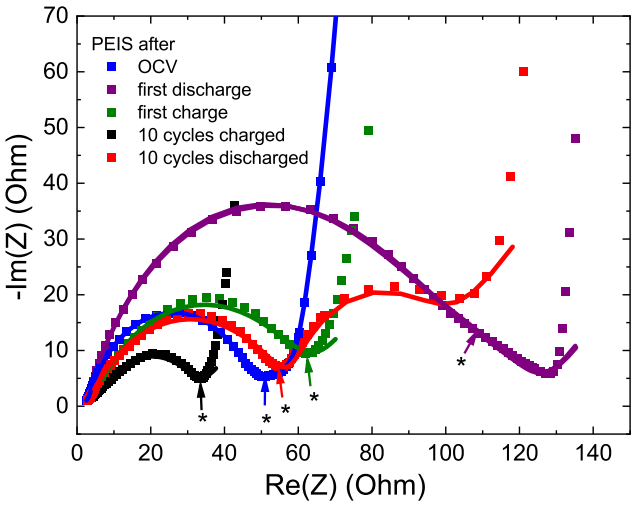

Fig. 7. Nyquist plot for Fe_3O_4@HCS measured at different state of charge. Solid lines show fits according to the equivalent circuit used (see the text). The arrows/asterisks mark the measured impedance at the frequency 10 Hz.

confirm and specify the qualitative conclusions. In particular, the data yield $R_E \sim 3\ \Omega$ while the CT resistance amounts to around ~50 Ω and Q_{ct} ~5 μF. R_{ct} as well as Q_{ct} are of the same magnitude as reported in Ref. [48]. A main observation in the EIS profiles is the appearance of the additional depressed semicircle in the discharged state which in the equivalent circuit is modeled by R_2 and Q_2. Such a feature is normally attributed to an additional capacitance surface layer. Our data imply that this surface layer is successively formed and disappearing as well as growing upon cycling. This scenario is corroborated by the fact that it is associated with a much slower process as can be nicely seen when considering the impedance response at a certain frequency, i.e., here 10 Hz, which is illustrated by the asterisks in Fig. 7. Specifically, the impedance response at 10 Hz always is in the minimum following the first semicircle. This observation allows two conclusions: (1) The newly appearing 2nd semicircle clearly is associated with a distinct and slower process with an innate time constant. (2) For all states under study, the high-frequency semicircle is characterized by a similar kinetics and can be assigned to the same layer. In addition, the observation that the 2nd semicircle becomes much more pronounced upon cycling indicates a possible explanation for the increase of converted specific capacity because the associated capacitance Q_2 increases from 0.4 mF in the first cycle to 12 mF in cycle ten. The slower time constant of the evolving 2nd semicircle may also be the reason behind the observed slow-down of the observed rate-dependence of extra capacity at higher current rates in the GCPL and GCPL rate measurements. As will be further discussed below and following the literature, the second semicircle can be either associated with reactions including the SEI [1,16] or with deposited spin-polarized electrons at the iron nanoparticles surfaces [17], or both. Our results render the usual SEI as the sole explanation for the respective process very unlikely. Firstly, the fact that the 2nd semicircle largely recedes upon charging would indicate nearly complete regression of the SEI which is not very plausible. SEI-related processes are usually in the high-frequency regime while the 2nd semicircle at hand appears at intermediate time scales. Exemplarily, graphite shows two semicircles in the fully charged state which do not regress and from which the distinct high frequency semicircle corresponds to the SEI [58]. In Fe_3O_4@HCS, the PEIS response of the SEI may be merged in the first semicircle but a distinct process cannot be extracted from the data which we attribute to similar kinetics of both processes. Though usual SEI formation can be ruled out, surface side reactions of the SEI and the formed iron metal nanoparticles which may result in the reversible

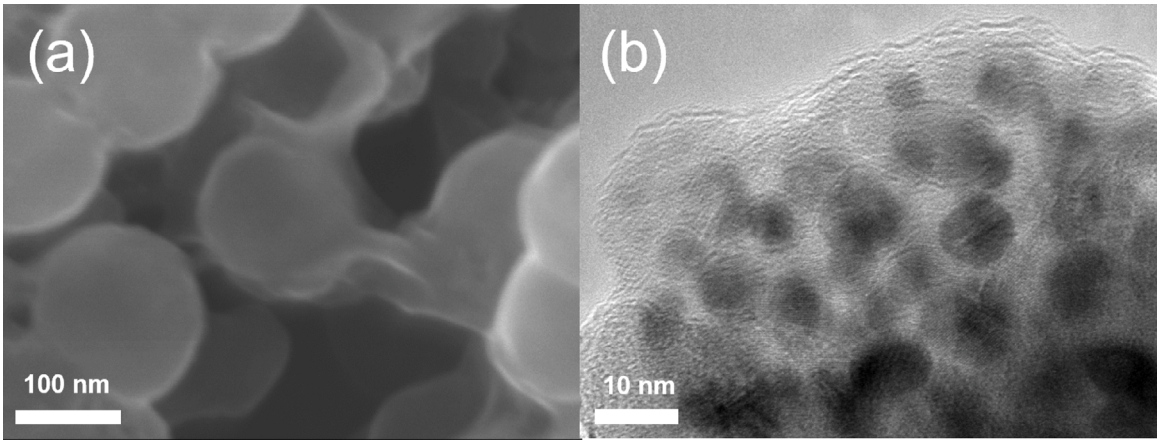

Fig. 8. (a) *Ex-situ* SEM and (b) *ex-situ* TEM images of a discharged Fe_3O_4@HCS-electrode.

Table 1
Electrochemical performance of various Fe_3O_4/carbon nanocomposites in LIBs.

Active material	Current (A g^{-1})	Cycle number	Capacity (mAh g^{-1})	Ref.
Fe_3O_4 nanoflakes-RGO	0.1	150	900	[60]
Yolk-double shell Fe_3O_4@C@C	0.5	250	800	[61]
Fe_3O_4@-tubular mesoporous carbon	0.2	60	850	[56]
Fe_3O_4@-N-doped porous carbon nanospheres	0.1	100	1240	[15]
Hierarchical 3D Fe_3O_4@porous carbon matrix	0.2 C	100	1077	[54]
Fe_3O_4 hollow nanospheres in honeycomb macroporous carbon	0.2	150	1050	[62]
Fe_3O_4@graphene quantum dots	0.1	200	900	[63]
Cake-like porous Fe_3O_4/C	0.1	100	600	[64]
Ultra-small Fe_3O_4@hollow carbon spheres	0.1	250	1050	This work

growth of a polymeric gel-like film are a possible explanation of the observed second semicircle [59].

A scenario involving interfacial storage theory suggests charge storage at the surface/contact area between the ionically conducting Li_2O-matrix (Li^+ storage) and the electrically conducting iron centers (e^- storage). In this scenario, an additional semicircle appearing in the mid frequency range of the EIS spectrum is proposed to signal such a capacitative storage mechanism [65,66]. Qualitatively, our observation of the mid-frequency extra semicircle only after charging seem to support this assignment. However, a rough estimate of the associated capacity based on geometrical considerations [67] questions this hypothesis, too (for details see the Supplemental Information, section Sd). Our measurements show that the reversibly accessible specific capacity associated with Fe_3O_4-nanoparticles in our material is about 1300 mAh g^{-1} larger than the postulated bulk capacity of Fe_3O_4. Since our data show that the formed iron nanoparticles are at least $d \sim 6$ nm in diameter, in a surface charge model the measured extra capacity would be associated with a surface capacitance of more than 10 mF cm^{-2}. This value is orders of magnitude larger than the maximum double layer capacitance of pure iron which is about 100 μF cm^{-2} [65,68]. We hence exclude a significant impact of the interfacial storage mechanism and, therefore, as an explanation for the observed strongly enhanced capacity [65,69]. We hence must conclude that surface side reactions of the formed iron metal nanoparticles and the SEI are most likely the dominant effect behind the high extra capacity as well as the observed additional medium frequency semicircle.

The effect of cycling on the materials microstructure is illustrated by Fig. 8 and Fig. S7 which displays *ex-situ* SEM and TEM images of Fe_3O_4@HCS-based electrodes after complete discharge. The SEM images (see Figs. 8a and Fig. S7a-d) show that the HCS substructure is practically unchanged even after 70 cycles, which confirms that the HCS matrix forms a very stable framework. The iron oxide nanoparticles on the contrary are no longer recognizable in the SEM image (Fig. 8a). We conclude that the formed iron nanoparticles are too small to be resolved by SEM. Instead, a new layer is observed which may be SEI and/or Li_2O [54] that spans over the HCS and even connects them (see Fig. S7c,d). This is also visible in corresponding TEM images in Fig. 8b and Fig. S7e,f which illustrate the material at complete discharge and a converted capacity of 800 mAh g^{-1}. Here, the formed iron particles are visible (black dots) and their size can be estimated to well below 10 nm. It is again noticeable that the iron particles are covered by some kind of layer, i.e., SEI or Li_2O, as was already seen by SEM. The layer even connects distant HCS with each other (see Fig. S7e).

To relate the electrochemical performance of Fe_3O_4@HCS presented here with other state-of-the-art Fe_3O_4 carbon composites from the literature, Table 1 shows the electrochemical properties of different Fe_3O_4 carbon composites. The table shows compatible or superior electrochemical performance of the Fe_3O_4@HCS composite as compared to other state-of-the-art Fe_3O_4 carbon composites.

4. Conclusions

In summary, a Fe_3O_4@HCS carbon composite is achieved by straightforward low-temperature synthesis, which avoids Oswald ripening of the ultra-small Fe_3O_4-particles (~10 nm) and furthermore yields a uniform dispersion of the nanoparticles on the stable HCS structure. The resulting hierarchical structure not only effectively prevents the disadvantages of Fe_3O_4 such as pulverization due to the large volume expansion upon electrochemical cycling, but moreover provides access to extra capacity resulting from the nano-nature of Fe_3O_4. As a result, the designed Fe_3O_4@HCS exhibits a high specific capacity of 1050 mAh g^{-1} at 0.1 C and a stable cycling performance well above 300 cycles. Furthermore demonstrates our detailed electrochemical analysis combined with ex situ imaging that the process of the extra capacity and its increase originates from a gradual formation and disappearance of

a capacitive surface layer, hinting to reversible reactions between the formed iron metal particles and the SEI. Notably, the design strategy and the synthesis route have great potential to be extended to construct other remarkable transition metal based carbon composites.

CRediT authorship contribution statement

Lennart Singer: Conceptualization, Methodology, Investigation, Writing – original draft, Review & editing. **Wojciech Kukułka:** Synthesis, Investigation, Review & editing. **Elisa Thauer:** Investigation, Validation, Review & editing. **Nico Gräßler:** Validation, Review & editing. **Andika Asyuda:** Investigation. **Michael Zharnikov:** Investigation, Review & editing. **Ewa Mijowska:** Conceptualization, Synthesis, Review & editing, Supervision. **Rüdiger Klingeler:** Conceptualization, Methodology, Review & editing, Supervision.

Declaration of competing interest

Authors have no conflicts of interest to disclose.

Data availability

Data will be made available on request.

Acknowledgments

We are grateful for access to the instrument and technical support for SEM studies provided by J. Zaumseil's group at Heidelberg University. Support by Deutsche Forschungsgemeinschaft (DFG) through project KL 1824/12-1, by BMBF via the project SpinFun (13XP5088) and within the framework of the Excellence Strategy of the Federal and State Governments of Germany is acknowledged. We are also grateful for support via project UMO-2016/23/G/ST5/04200 (Beethoven 2) by the National Science Centre Poland. A.A. acknowledges financial support by the DAAD-ACEH Scholarship of Excellence.

Appendix A. Supplementary data

Supplementary material related to this article can be found online at https://doi.org/10.1016/j.electacta.2023.142155.

References

[1] M.M. Thackeray, W. David, J.B. Goodenough, Structural characterization of the lithiated iron oxides $Li_xFe_3O_4$ and $Li_xFe_2O_3$ (0<x<2), Mater. Res. Bull. 17 (6) (1982) 785–793.
[2] P. Poizot, S. Laruelle, S. Grugeon, L. Dupont, J.M. Tarascon, Nano-sized transition-metal oxides as negative-electrode materials for lithium-ion batteries, Nature 407 (6803) (2000) 496–499.
[3] S. Gu, A. Zhu, Graphene nanosheets loaded Fe_3O_4 nanoparticles as a promising anode material for lithium ion batteries, J. Alloys Compd. 813 (2020) 152160.
[4] X. Yan, H. Ge, Y. Fang, Q. Liu, J. Gu, In situ ion–exchange synthesis of Fe_3O_4 nanosheets with 3D hierarchically porous carbon frameworks for high–performance energy storage, Energy Technol. 10 (7) (2022) 2200207.
[5] J. Cabana, L. Monconduit, D. Larcher, M.R. Palacín, Beyond intercalation-based Li-ion batteries: The state of the art and challenges of electrode materials reacting through conversion reactions, Adv. Mater. 22 (35) (2010) E170–92.
[6] D. Vernardou, M. Apostolopoulou, N. Katsarakis, E. Koudoumas, C. Drosos, I.P. Parkin, Electrochemical properties of APCVD α-Fe_2O_3 nanoparticles at 300 °C, ChemistrySelect 1 (10) (2016) 2228–2234.
[7] D. Vernardou, A. Kazas, M. Apostolopoulou, N. Katsarakis, E. Koudoumas, Cationic effect on the electrochemical characteristics of the hydrothermally grown manganese dioxide, J. Electron. Mater. 46 (4) (2017) 2232–2240.
[8] M. Valvo, C. Floraki, E. Paillard, K. Edström, D. Vernardou, Perspectives on iron oxide-based materials with carbon as anodes for Li- and K-ion batteries, Nanomaterials 12 (9) (2022) 1436.
[9] L. Li, H. Wang, Z. Xie, C. An, G. Jiang, Y. Wang, 3D graphene-encapsulated nearly monodisperse Fe_3O_4 nanoparticles as high-performance lithium-ion battery anodes, J. Alloys Compd. 815 (2020) 152337.
[10] D.C. Bock, A.C. Marschilok, K.J. Takeuchi, E.S. Takeuchi, Deliberate modification of the solid electrolyte interphase (SEI) during lithiation of magnetite, Fe_3O_4: Impact on electrochemistry, Chem. Commun. 53 (98) (2017) 13145–13148.
[11] J. Wang, Q. Hu, W. Hu, W. Zhu, Y. Wei, K. Pan, M. Zheng, H. Pang, Preparation of hollow core-shell Fe_3O_4/nitrogen-doped carbon nanocomposites for lithium-ion batteries, Molecules 27 (2) (2022) 396.
[12] M.D. Bhatt, J.Y. Lee, High capacity conversion anodes in Li-ion batteries: A review, Int. J. Hydrogen Energy 44 (21) (2019) 10852–10905.
[13] Y. Lu, L. Yu, X.W. Lou, Nanostructured conversion-type anode materials for advanced lithium-ion batteries, Chem 4 (5) (2018) 972–996.
[14] L. Fu, C.-C. Chen, J. Maier, Interfacial mass storage in nanocomposites, Solid State Ionics 318 (2018) 54–59.
[15] J. Mao, D. Niu, N. Zheng, G. Jiang, W. Zhao, J. Shi, Y. Li, Fe_3O_4-embedded and N-doped hierarchically porous carbon nanospheres as high-performance lithium ion battery anodes, ACS Sustain. Chem. Eng. 7 (3) (2019) 3424–3433.
[16] Y.-Y. Hu, Z. Liu, K.-W. Nam, O.J. Borkiewicz, J. Cheng, X. Hua, M.T. Dunstan, X. Yu, K.M. Wiaderek, L.-S. Du, K.W. Chapman, P.J. Chupas, X.-Q. Yang, C.P. Grey, Origin of additional capacities in metal oxide lithium-ion battery electrodes, Nat. Mater. 12 (12) (2013) 1130–1136.
[17] Q. Li, H. Li, Q. Xia, Z. Hu, Y. Zhu, S. Yan, C. Ge, Q. Zhang, X. Wang, X. Shang, S. Fan, Y. Long, L. Gu, G.-X. Miao, G. Yu, J.S. Moodera, Extra storage capacity in transition metal oxide lithium-ion batteries revealed by in situ magnetometry, Nat. Mater. 20 (1) (2021) 76–83.
[18] J. Jamnik, J. Maier, Nanocrystallinity effects in lithium battery materials, Phys. Chem. Chem. Phys. 5 (23) (2003) 5215.
[19] J. Maier, Mass storage in space charge regions of nano-sized systems (nano-ionics. Part V), Faraday Discuss. 134 (2007) 51–66, discussion 103–18, 415–9.
[20] Y.F. Zhukovskii, P. Balaya, E.A. Kotomin, J. Maier, Evidence for interfacial-storage anomaly in nanocomposites for lithium batteries from first-principles simulations, Phys. Rev. Lett. 96 (5) (2006) 058302.
[21] S. Klink, E. Madej, E. Ventosa, A. Lindner, W. Schuhmann, F. La Mantia, The importance of cell geometry for electrochemical impedance spectroscopy in three-electrode lithium ion battery test cells, Electrochem. Commun. 22 (2012) 120–123.
[22] M. Ender, J. Illig, E. Ivers-Tiffée, Three-electrode setups for lithium-ion batteries, J. Electrochem. Soc. 164 (2) (2017) A71–A79.
[23] H. Nara, D. Mukoyama, R. Shimizu, T. Momma, T. Osaka, Systematic analysis of interfacial resistance between the cathode layer and the current collector in lithium-ion batteries by electrochemical impedance spectroscopy, J. Power Sources 409 (2019) 139–147.
[24] M. Gaberšček, Understanding Li-based battery materials via electrochemical impedance spectroscopy, Nat. Commun. 12 (1) (2021) 6513.
[25] Y. Zubavichus, A. Shaporenko, M. Grunze, M. Zharnikov, Innershell absorption spectroscopy of amino acids at all relevant absorption edges, J. Phys. Chem. A 109 (32) (2005) 6998–7000.
[26] G.S. Zakharova, L. Singer, Z.A. Fattakhova, S. Wegener, E. Thauer, Q. Zhu, E.V. Shalaeva, R. Klingeler, MoO_2/C composites prepared by tartaric acid and glucose-assisted sol-gel processes as anode materials for lithium-ion batteries, J. Alloys Compd. 863 (2021) 158353.
[27] C. Pecharromn, T. Gonzlez-Carreo, J. Iglesias, The infrared dielectric properties of maghemite, γ-Fe_2O_3, from reflectance measurement on pressed powders, Phys. Chem. Minerals 22 (1) (1995) 21–29.
[28] H.C. St. O'Neill, W.A. Dollase, Crystal structures and cation distributions in simple spinels from powder XRD structural refinements: $MgCr_2O_4$, $ZnCr_2O_4$, Fe_3O_4 and the temperature dependence of the cation distribution in $ZnAl_2O_4$, Phys. Chem. Minerals 20 (8) (1994) 541–555.
[29] R. Chalasani, S. Vasudevan, Form, content, and magnetism in iron oxide nanocrystals, J. Phys. Chem. C 115 (37) (2011) 18088–18093.
[30] J. Su, M. Cao, L. Ren, C. Hu, Fe_3O_4-graphene nanocomposites with improved lithium storage and magnetism properties, J. Phys. Chem. C 115 (30) (2011) 14469–14477.
[31] G.S. Zakharova, E. Thauer, A.N. Enyashin, L.F. Deeg, Q. Zhu, R. Klingeler, V_2O_3/C composite fabricated by carboxylic acid-assisted sol–gel synthesis as anode material for lithium-ion batteries, J. Sol-Gel Sci. Technol. 12 (2021) 700.
[32] A.L. Patterson, The scherrer formula for X-Ray particle size determination, Phys. Rev. 56 (10) (1939) 978–982.
[33] T. Radu, C. Iacovita, D. Benea, R. Turcu, X-Ray photoelectron spectroscopic characterization of iron oxide nanoparticles, Appl. Surf. Sci. 405 (2017) 337–343.
[34] K. Lipert, M. Ritschel, A. Leonhardt, Y. Krupskaya, B. Büchner, R. Klingeler, Magnetic properties of carbon nanotubes with and without catalyst, J. Phys. Conf. Ser. 200 (7) (2010) 072061.
[35] J. Popplewell, L. Sakhnini, The dependence of the physical and magnetic properties of magnetic fluids on particle size, J. Magnet. Magn. Mater. 149 (1–2) (1995) 72–78.
[36] G.C. Papaefthymiou, Nanoparticle magnetism, Nano Today 4 (5) (2009) 438–447.
[37] H. Mamiya, M. Ohnuma, I. Nakatani, T. Furubayashim, Extraction of blocking temperature distribution from zero-field-cooled and field-cooled magnetization curves, IEEE Trans. Magn. 41 (10) (2005) 3394–3396.
[38] S. Dietrich, S. Chandra, C. Georgi, S. Thomas, D. Makarov, S. Schulze, M. Hietschold, M. Albrecht, D. Bahadur, H. Lang, Design, characterization and magnetic properties of Fe_3O_4-nanoparticle arrays coated with PEGylated-dendrimers, Mater. Chem. Phys. 132 (2–3) (2012) 292–299.

[39] C.P. Bean, J.D. Livingston, Superparamagnetism, J. Appl. Phys. 30 (4) (1959) S120–S129.

[40] D.J. Dunlop, O. Oezdemir, Rock Magnetism: Fundamentals and Frontiers, 1. paperback ed. with corr., 2. ed., reprinted., in: Cambridge studies in magnetism, vol. 3, Cambridge Univ. Press, Cambridge, 2013.

[41] W. Zhang, D.C. Bock, C.J. Pelliccione, Y. Li, L. Wu, Y. Zhu, A.C. Marschilok, E.S. Takeuchi, K.J. Takeuchi, F. Wang, Insights into ionic transport and structural changes in magnetite during multiple-electron transfer reactions, Adv. Energy Mater. 6 (10) (2016) 1502471.

[42] P. Novák, F. Joho, M. Lanz, B. Rykart, J.-C. Panitz, D. Alliata, R. Kötz, O. Haas, The complex electrochemistry of graphite electrodes in lithium-ion batteries, J. Power Sources 97–98 (2001) 39–46.

[43] K. Wenelska, A. Ottmann, P. Schneider, E. Thauer, R. Klingeler, E. Mijowska, Hollow carbon sphere/metal oxide nanocomposites anodes for lithium-ion batteries, Energy 103 (2016) 100–106.

[44] J. Eom, D. Kim, H. Kwon, Effects of ball-milling on lithium insertion into multi-walled carbon nanotubes synthesized by thermal chemical vapour deposition, J. Power Sources 157 (1) (2006) 507–514.

[45] Y. Zhang, Q. Ma, S. Wang, X. Liu, L. Li, Poly(vinyl alcohol)-assisted fabrication of hollow carbon spheres/reduced graphene oxide nanocomposites for high-performance lithium-ion battery anodes, ACS Nano 12 (5) (2018) 4824–4834.

[46] K. Tang, R.J. White, X. Mu, M.-M. Titirici, P.A. van Aken, J. Maier, Hollow carbon nanospheres with a high rate capability for lithium-based batteries, ChemSusChem 5 (2) (2012) 400–403.

[47] X. Yue, W. Sun, J. Zhang, F. Wang, Y. Yang, C. Lu, Z. Wang, D. Rooney, K. Sun, Macro-mesoporous hollow carbon spheres as anodes for lithium-ion batteries with high rate capability and excellent cycling performance, J. Power Sources 331 (2016) 10–15.

[48] Y. Liu, J. Chen, Z. Liu, H. Xu, Y. Zheng, J. Zhong, Q. Yang, H. Tian, Z. Shi, J. Yao, C. Xiong, Facile fabrication of Fe_3O_4 nanoparticle/carbon nanofiber aerogel from fe-ion cross-linked cellulose nanofibrils as anode for lithium-ion battery with superhigh capacity, J. Alloys Compd. 829 (6058) (2020) 154541.

[49] Q. Peng, C. Guo, S. Qi, W. Sun, L.-P. Lv, F.-H. Du, B. Wang, S. Chen, Y. Wang, Ultra-small Fe_3O_4 nanodots encapsulated in layered carbon nanosheets with fast kinetics for lithium/potassium-ion battery anodes, RSC Adv. 11 (3) (2021) 1261–1270.

[50] K. Wenelska, A. Ottmann, D. Moszyński, P. Schneider, R. Klingeler, E. Mijowska, Facile synthesis N-doped hollow carbon spheres from spherical solid silica, J. Colloid Interf. Sci. 511 (2018) 203–208.

[51] E. Thauer, X. Shi, S. Zhang, X. Chen, L. Deeg, R. Klingeler, K. Wenelska, E. Mijowska, Mn_3O_4 encapsulated in hollow carbon spheres coated by graphene layer for enhanced magnetization and lithium-ion batteries performance, Energy 217 (2021) 119399.

[52] H. Zhang, L. Wang, H. Li, X. He, Criterion for identifying anodes for practically accessible high-energy-density lithium-ion batteries, ACS Energy Lett. 6 (10) (2021) 3719–3724.

[53] W. Deng, S. Ci, H. Li, Z. Wen, One-step ultrasonic spray route for rapid preparation of hollow Fe_3O_4/C microspheres anode for lithium-ion batteries, Chem. Eng. J. 330 (2017) 995–1001.

[54] S. Hao, B. Zhang, Y. Wang, C. Li, J. Feng, S. Ball, M. Srinivasan, J. Wu, Y. Huang, Hierarchical three-dimensional Fe_3O_4@porous carbon matrix/graphene anodes for high performance lithium ion batteries, Electrochimica Acta 260 (2018) 965–973.

[55] Y. Zhao, J. Wang, C. Ma, L. Cao, Z. Shao, A self-adhesive graphene nanoscroll/nanosheet paper with confined $Fe_{1-x}S/Fe_3O_4$ hetero-nanoparticles for high-performance anode material of flexible Li-ion batteries, Chem. Eng. J. 370 (2019) 536–546.

[56] Z. Cao, X. Ma, Encapsulated Fe_3O_4 into tubular mesoporous carbon as a superior performance anode material for lithium-ion batteries, J. Alloys Compd. 815 (2020) 152542.

[57] L. Li, R. Jacobs, P. Gao, L. Gan, F. Wang, D. Morgan, S. Jin, Origins of large voltage hysteresis in high-energy-density metal fluoride lithium-ion battery conversion electrodes, J. Am. Chem. Soc. 138 (8) (2016) 2838–2848.

[58] P. Zhang, T. Yuan, Y. Pang, C. Peng, J. Yang, Z.-F. Ma, S. Zheng, Influence of current density on graphite anode failure in lithium-ion batteries, J. Electrochem. Soc. 166 (3) (2019) A5489–A5495.

[59] X. Li, L. Qiao, D. Li, X. Wang, W. Xie, D. He, Three-dimensional network structured α-Fe_2O_3 made from a stainless steel plate as a high-performance electrode for lithium ion batteries, J. Mater. Chem. A 1 (21) (2013) 6400.

[60] Y.-H. Shi, K. Wang, H.-H. Li, H.-F. Wang, X.-Y. Li, X.-L. Wu, J.-P. Zhang, H.-M. Xie, Z.-M. Su, J.-W. Wang, H.-Z. Sun, Fe_3O_4 nanoflakes-RGO composites: A high rate anode material for lithium-ion batteries, Appl. Surf. Sci. 511 (2020) 145465.

[61] X. Wang, J. Wang, Z. Chen, K. Yang, Z. Zhang, Z. Shi, T. Mei, J. Qian, J. Li, X. Wang, Yolk-double shell Fe_3O_4@C@C composite as high-performance anode materials for lithium-ion batteries, J. Alloys Compd. 822 (2020) 153656.

[62] L. Wang, H. Zheng, X. Jin, Y. Yuan, Fe_3O_4 hollow nanospheres grown in situ in three-dimensional honeycomb macroporous carbon boost long-life and high-rate lithium ion storage, J. Electron. Mater. 52 (1) (2023) 10–22.

[63] F. Shi, Q. Liu, Z. Jin, G. Huang, B. Xing, J. Jia, C. Zhang, A facile method to prepare Fe_3O_4@CTP QDs composite as advanced anode material for lithium ion batteries, J. Alloys Compd. 890 (2022) 161911.

[64] J. Huang, Q. Dai, C. Cui, H. Ren, X. Lu, Y. Hong, S. Woo Joo, Cake-like porous Fe_3O_4@C nanocomposite as high-performance anode for Li-ion battery, J. Electroanalyt. Chem. 918 (2022) 116508.

[65] F. Baumann, J. Fleig, H. Habermeier, J. Maier, Impedance spectroscopic study on well-defined $(La,Sr)(Co,Fe)O_{3-\delta}$ model electrodes, Solid State Ionics 177 (11–12) (2006) 1071–1081.

[66] J. Jamnik, J. Maier, Treatment of the impedance of mixed conductors equivalent circuit model and explicit approximate solutions, J. Electrochem. Soc. 146 (11) (1999) 4183–4188.

[67] A. Ponrouch, P.-L. Taberna, P. Simon, M.R. Palacín, On the origin of the extra capacity at low potential in materials for Li batteries reacting through conversion reaction, Electrochimica Acta 61 (2012) 13–18.

[68] O.E. Barcia, O.R. Mattos, Reaction model simulating the role of sulphate and chloride in anodic dissolution of iron, Electrochimica Acta 35 (10) (1990) 1601–1608.

[69] R. Usiskin, J. Maier, Interfacial effects in lithium and sodium batteries, Adv. Energy Mater. 11 (2) (2021) 2001455.

Supplementary Information:
On the rising extra storage capacity of ultra-small Fe_3O_4 particles functionalised with HCS and their potential as high-performance anode material for electrochemical energy storage

Lennart Singer*[a], Wojciech Kukułka[b], Elisa Thauer[a], Nico Gräßler[c], Andika Asyuda[d], Michael Zharnikov[d], Ewa Mijowska[b], Rüdiger Klingeler*[a]

[a] *Kirchhoff Institute for Physics, Heidelberg University, 69120 Heidelberg, Germany*
[b] *Faculty of Chemical Technology and Engineering, West Pomeranian University of Technology, 71-065, Szczecin, Poland*
[c] *Leibniz Institute for Solid State and Materials Research Dresden e.V., 01069 Dresden, Germany*
[d] *Applied Physical Chemistry, Heidelberg University, 69120 Heidelberg, Germany*

Email addresses: lennart.singer@kip.uni-heidelberg.de (Lennart Singer*), klingeler@kip.uni.heidelberg.de (Rüdiger Klingeler*)

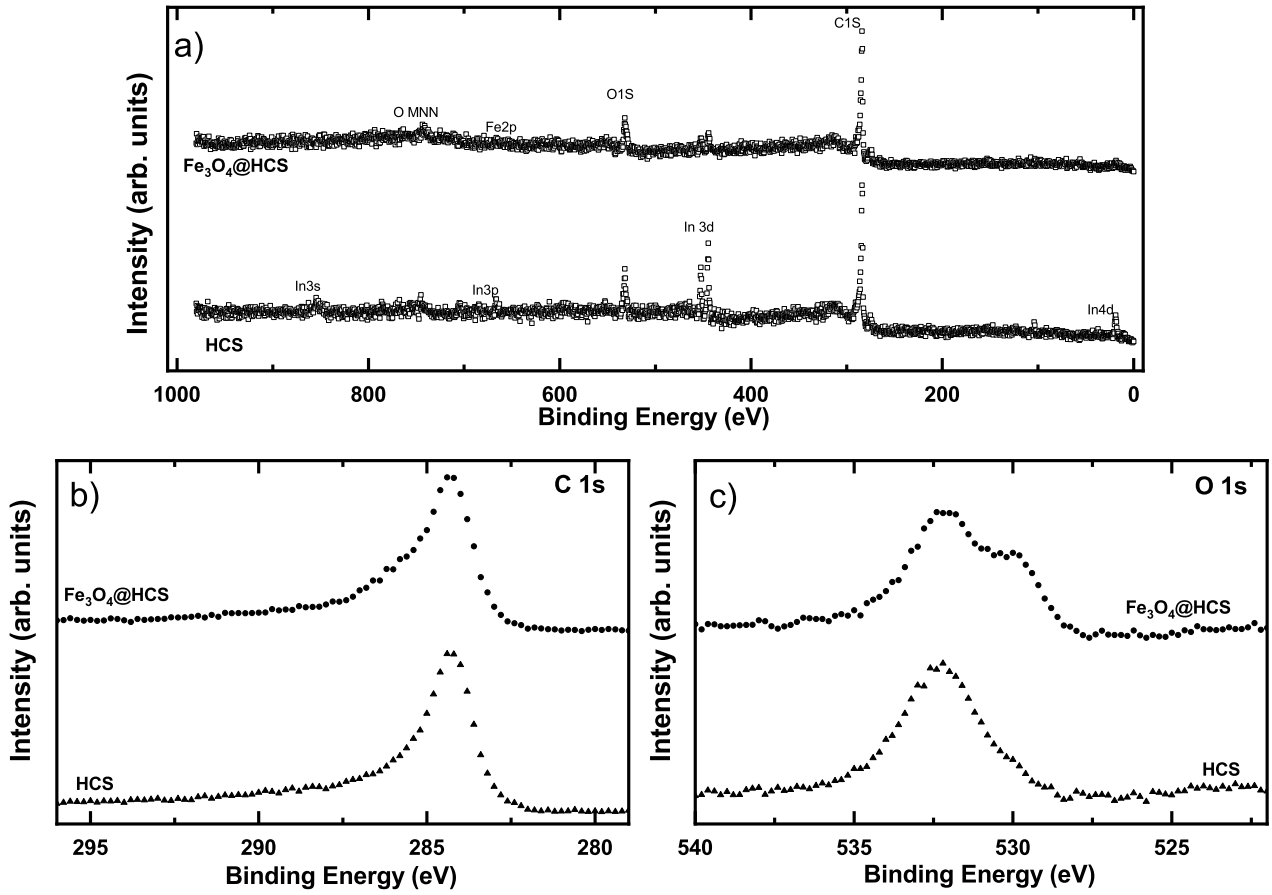

Figure S1: (a) Survey XP spectra of Fe_3O_4@HCS and HCS displaying the presence of O, C, and Fe as well as In from the used substrate. No detectable impurities are perceptible. (b) C1s XP spectra of Fe_3O_4@HCS and HCS, showing that the carbon structure remains unchanged upon functionalisation with Fe_3O_4 nanoparticles. (c) O1s XP spectra of Fe_3O_4@HCS and HCS featuring peaks at around 532 eV attributed to absorbed oxygen-containing functional groups of C-O, C=O, and O-H on HCS. Fe_3O_4@HCS furthermore displays a contribution of anionic oxygen in Fe_3O_4 at around 529.2 eV [1, 2].

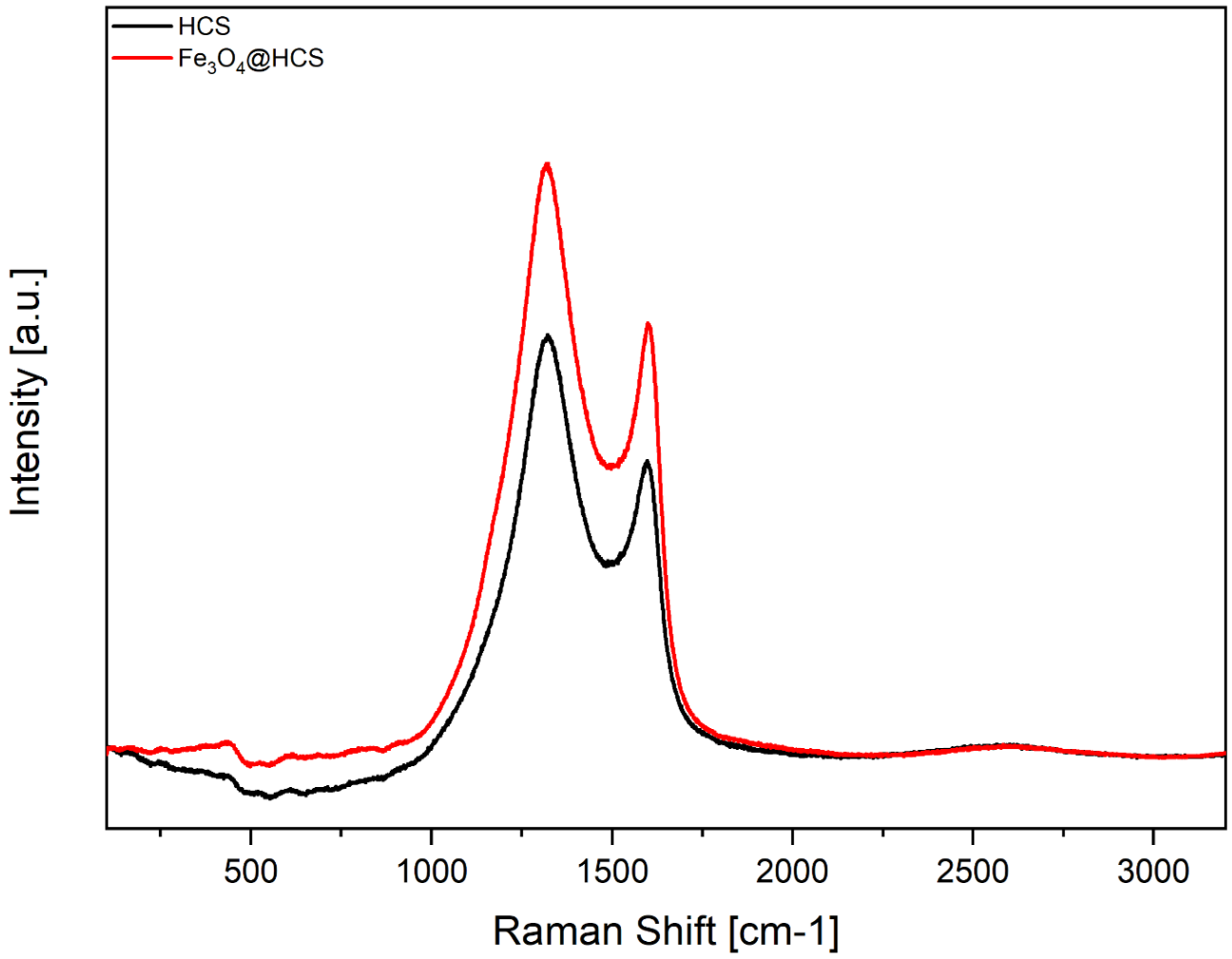

Figure S2: Raman spectra of HCS and Fe_3O_4@HCS. The Raman spectra indicate two strong peaks at around 1320 and 1600 cm^{-1} corresponding to the carbon D- and G-bands, respectively. The D-band is ascribed to the vibration of carbon atoms with dangling bonds in the plane and therefore contains information about defects in the graphitic structure. The G-band corresponds to the E2g mode of hexagonal graphite and is related to the vibration of the sp_2-hybridized carbon atoms or in other words the graphitic content [3]. The spectra of both samples are similar suggesting that functionalization with iron oxide does not induce additional defects to the structure of hollow carbon spheres. Specifically is the I_D/I_G ratio for pure HCS 1.34 and for Fe_3O_4@HCS 1.36. Both values indicate a high degree of graphitic content which is desirable for application in Li-ion electrodes as it supports high electrical conductivity.

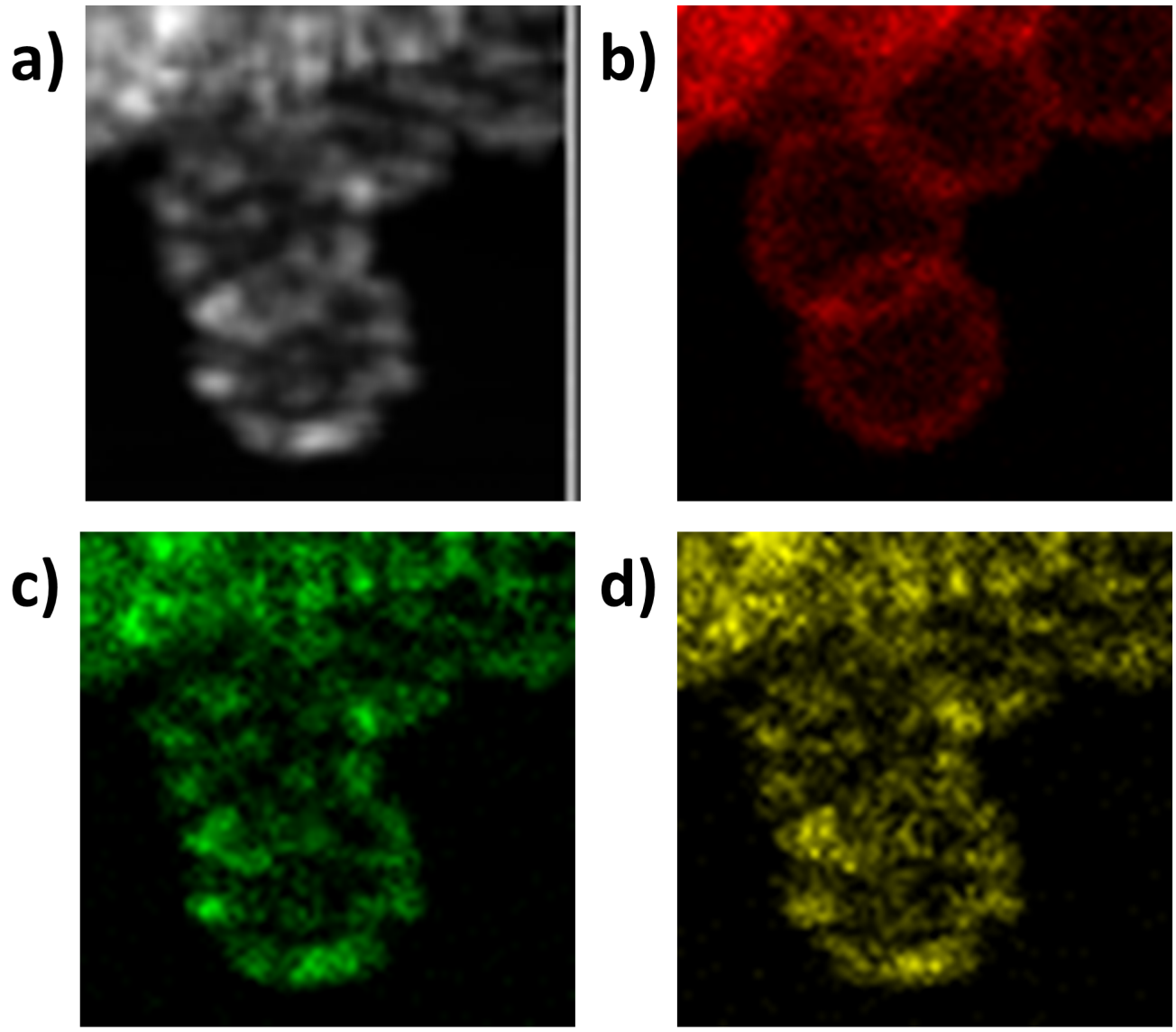

Figure S3: STEM images of HCS (a) and EDS signal from carbon (b), iron (c) and oxygen (d). Elemental composition of the sample was confirmed by EDS mapping of few spheres indicating the presence of only carbon, iron and oxygen elements.

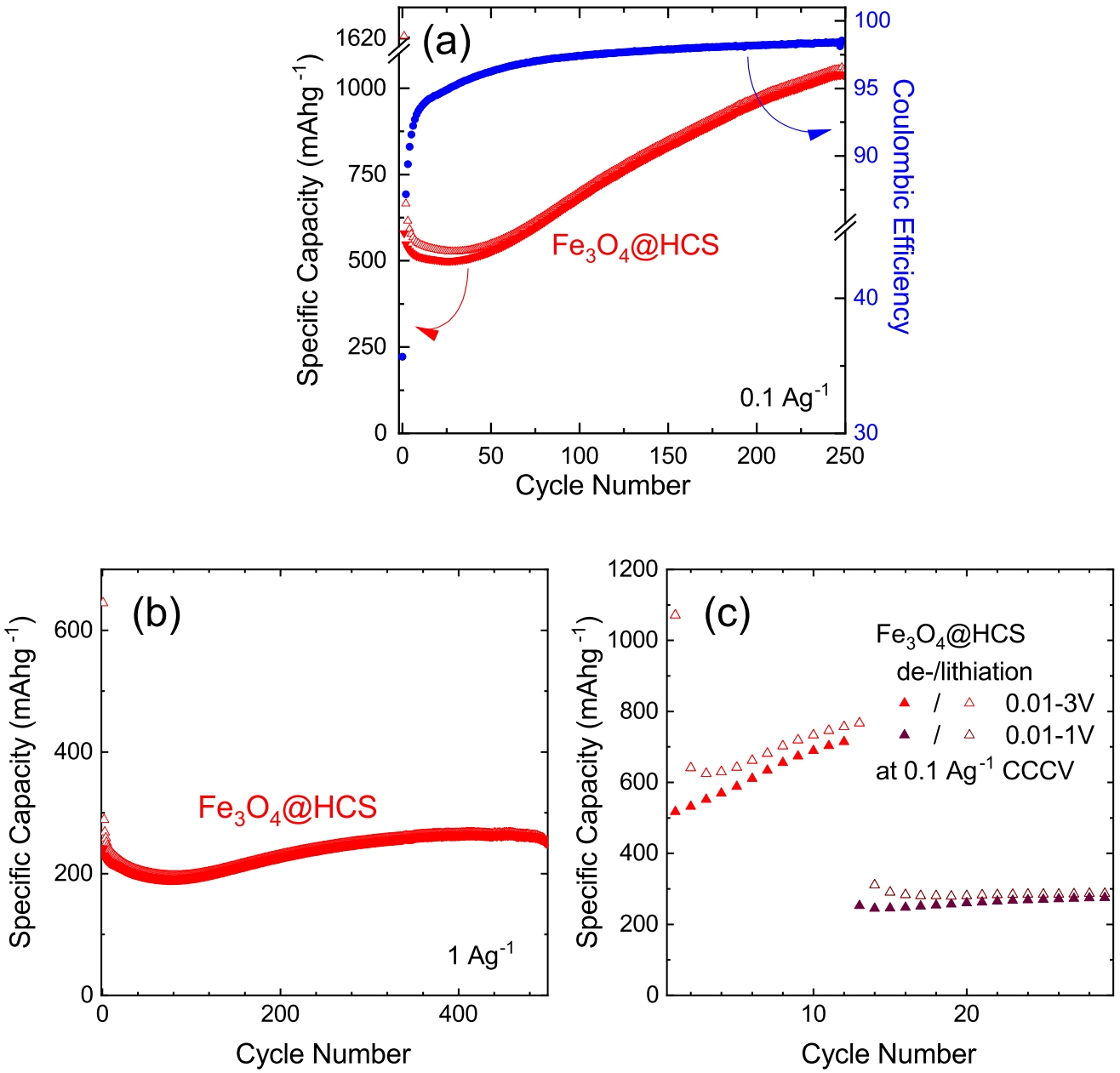

Figure S4: (a) Specific charge/discharge capacities as well as coulombic efficiency of Fe_3O_4@HCS electrodes at 0.1 A g^{-1} (b) Specific charge/discharge capacities of Fe_3O_4@HCS electrodes at 1 A g^{-1}. (c) Specific charge/discharge capacities of Fe_3O_4@HCS electrodes at 0.1 A g^{-1} and 5 hour constant voltage (CCCV). The first 12 cycles were done in the voltage range between 0.01 and 3 V, thereafter, cycling was reduced to the voltage range 0.01 to 1 V.

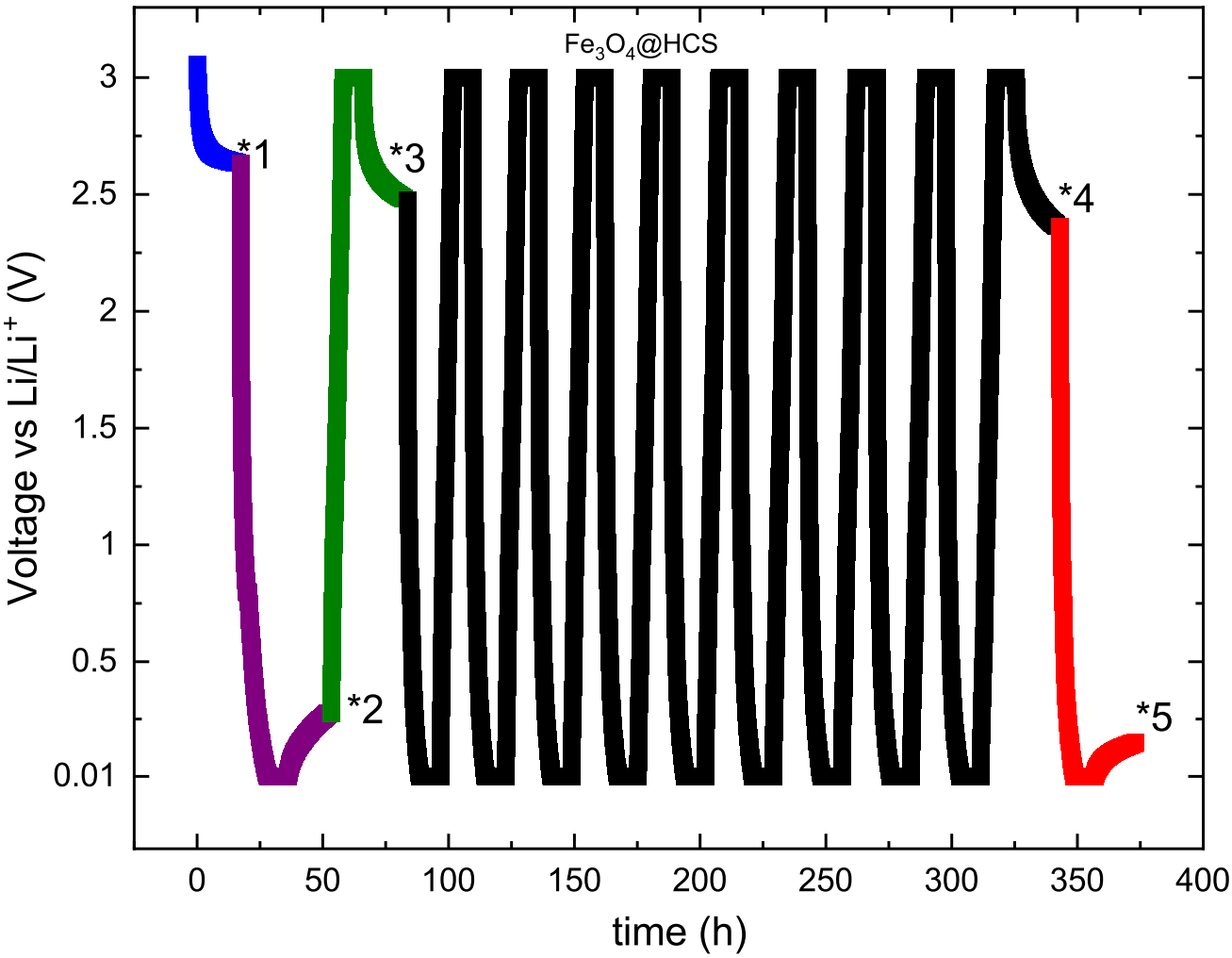

Figure S5: Specific Voltage vs. time illustrating the specific state of charge where PEIS measurements presented in Fig. 7 have been performed. The colours have been used to display the charge/discharge process in front of the corresponding PEIS measurement. The numbers show where the PEIS measurements have been done.

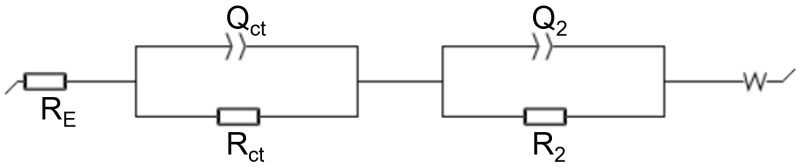

Figure S6: Equivalent circuit used to model the measured impedance. R_{E} reflects the electrolyte resistance, R_{ct} and Q_{ct} the charge transfer contributions. R_2 and Q_2 are used to model a 2nd semicircle (see the main text).

Table S1: Best fitting parameter obtained by modelling PEIS data shown in Fig. 7 by means of the equivalent circle Fig. S6. The parameters reflect the average values with standard deviation from three fits with slightly different boundaries.

SOC	R_E (Ω)	R_{ct} (Ω)	Q_{ct} (10^{-6} F)	R_2 (Ω)	Q_2 (10^{-3} F)
OCV	2.5(3)	46.5(3)	3.0(2)		
first discharge	2.7(7)	89(4)	3.3(2)	30(10)	0.4(1)
first charge	3.8(2)	57(2)	7.8(3)		
10 cycles charged	3(1)	31(3)	14(3)		
10 cycles discharged	2.6(2)	55.1(2)	8.9(1)	33.7(3)	12(1)

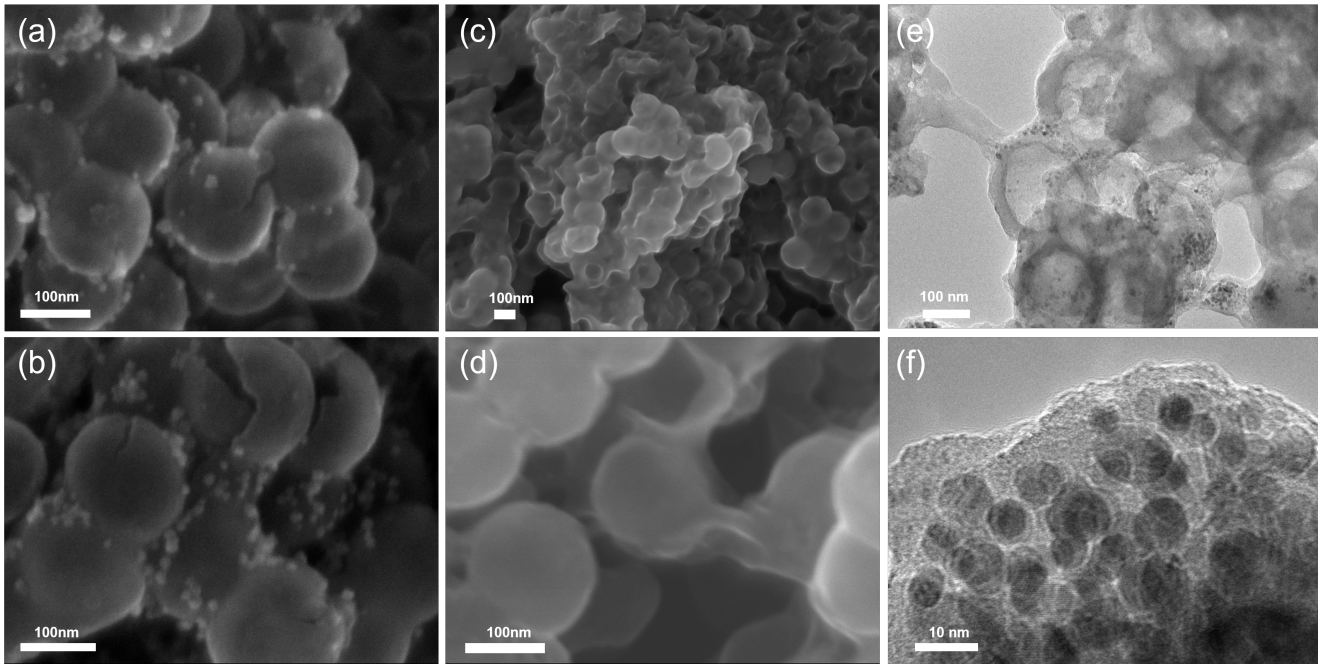

Figure S7: *Ex-situ* SEM images of an Fe_3O_4@HCS-electrode after OCV (a,b) and after 70 galvanostatic cycles at 100 mA/g (c,d) as well as *ex-situ* TEM images after reaching a discharge capacity of 800 mAh g^{-1}(e,f).

Estimate of surface capacity of iron nanoparticles

For a typical formed iron metal nanoparticle of $r = 3$ nm in radius, the volume is given through:

$$V_{\mathrm{NP}} = \frac{4\pi}{3} \cdot r^3 = \frac{4\pi}{3} \cdot (3 \cdot 10^{-9}\ m)^3 = 1.13 \times 10^{-25}\ \mathrm{m}^3$$

Using the density of iron of $7.87{\cdot}10^6\ \frac{\mathrm{g}}{\mathrm{m}^3}$, the mass of one iron nanoplarticle (m_{NP}) can be estimated.

$$m_{\mathrm{NP}} = \rho \times V_{\mathrm{NP}} = 8.89 \times 10^{-19}\ \mathrm{g}$$

The number of iron metall nanoparticles (# $\mathrm{NP_{Fe}}$) in 1 g of Fe_3O_4 hence amounts to:

$$\#NP_{\mathrm{Fe}} = \frac{0.72g}{8.89 \times 10^{-19}g} = 8.13 \times 10^{17}$$

The associated total surface for the iron nanoparticles ($r \sim 3$ nm) is then estimated as

$$A = \pi r^2 \cdot \#NP \approx 23\ \mathrm{m}^2$$

From the GCPL measurement shown in Fig. 6a) and after subtracting the contribution of HCS, a converted capacity of only the Fe_3O_4 component can be obtained of ∼2000 mah $g^{-1}_{Fe_3O_4}$ in cycle 250. Based on the predicted reversible theoretical electrochemical capacity of Fe_3O_4 ∼ 700 mAh $g^{-1}_{Fe_3O_4}$, our data evidence an capacity of ∼1300 mAh g^{-1} or 4680 $Cg^{-1}_{Fe_3O_4}$. Assuming that most of the capacity is converted in the range of 2 to 0.01 V as confirmed by the potential curves in Fig. 6b), we conclude that the charge stored at the interface amounts to 2340 $Fg^{-1}_{Fe_3O_4}$. Using the calculated iron surface for 1 g iron oxide nanoparticles of 23 m^2, this leads to a iron surface capacitance of more than 10 mF cm^{-2} needed to explain the measured extra capacity.

References

[1] S. R. Chowdhury, E. K. Yanful, A. R. Pratt, Arsenic removal from aqueous solutions by mixed magnetite–maghemite nanoparticles, Environmental Earth Sciences 64 (2) (2011) 411–423.

[2] S. R. Chowdhury, E. K. Yanful, A. R. Pratt, Chemical states in XPS and Raman analysis during removal of Cr(VI) from contaminated water by mixed maghemite-magnetite nanoparticles, Journal of Hazardous Materials 235-236 (2012) 246–256.

[3] A. C. Ferrari, J. Robertson, Interpretation of Raman spectra of disordered and amorphous carbon, Physical Review B 61 (20) (2000) 14095–14107.

3.2 MoO_2/C composites prepared by tartaric acid and glucose-assisted sol-gel processes as anode materials for lithium-ion batteries

Autoren:

G.S. Zakharova, L. Singer, Z.A. Fattakhova, S.A. Wegener, E. Thauer, Q. Zhu, E.V. Shalaeva und R. Klingeler

Veröffentlicht im: Journal of Alloys and Compounds 863, 2021, 158353.

abgedruckt mit freundlicher Genehmigung des Elsevier Verlags

L. Singer ist zusammen mit G.S. Zakharova (SSC UB RAS) zu gleichen Teilen Erstautor des Artikels. L. Singer erstellte den Abschnitt über die elektrochemischen Ergebnisse sowie die Abb. 6 - 7 und Abb. S1 - S4. L. Singer hat folgende experimentelle Arbeiten und Analysen durchgeführt:

- Rasterelektronenmikroskopie (REM) an dem nachbehandelten MoO2/C: Durchführung und Analyse.
- Elektrochemischen Untersuchungen (CV, GCPL) an dem nachbehandelten Material: Durchführung und Analyse.
- Ex-situ Rasterelektronenmikroskopie Untersuchungen (REM): Durchführung und Analyse.

Beitrag der Koautoren:

G.S. Zakharova: Konzeptualisierung und Verfassen des Manuskriptes, mit Ausnahme der Teile zu den elektrochemischen Untersuchungen. Anfertigung von Abb. 1 - 5. Durchführung der Charakterisierungsmessungen: XRD, Raman- und Infrarot-Spektroskopie sowie die thermogravimetrische Analyse (TGA).

Z.A. Fattakhova: Synthese.

E. Thauer federführend mit dem Bachelorstudent S.A. Wegener: Elektrochemische Charakterisierung der unbehandelten Materialien. E. Thauer unterstützte bei der finalen Korrektur des Manuskripts.

Q. Zhu, E.V. Shalaeva: TEM-Messungen (Abb. 3).

R. Klingeler: Projektplanung und -leitung, Beteiligung an der Interpretation und Beitrag zur Finalisierung des Manuskripts.

Korrespondenz mit den Gutachtern: G.S. Zakharova, L. Singer, R. Klingeler.

Alle Autoren haben das Manuskript Korrektur gelesen.

Journal of Alloys and Compounds 863 (2021) 158353

Contents lists available at ScienceDirect

Journal of Alloys and Compounds

journal homepage: www.elsevier.com/locate/jalcom

MoO_2/C composites prepared by tartaric acid and glucose-assisted sol-gel processes as anode materials for lithium-ion batteries

G.S. Zakharova[a,1], L. Singer[b,1], Z.A. Fattakhova[a], S. Wegener[b], E. Thauer[b], Q. Zhu[c], E.V. Shalaeva[a], R. Klingeler[b,d,*]

[a] Institute of Solid State Chemistry, Ural Division, Russian Academy of Sciences, Yekaterinburg, Russia
[b] Kirchhoff Institute of Physics, Heidelberg University, Heidelberg, Germany
[c] Institute of Material Science and Engineering, Wuhan University of Technology, Wuhan, PR China
[d] Centre for Advanced Materials (CAM), Heidelberg University, Heidelberg, Germany

ARTICLE INFO

Article history:
Received 28 October 2020
Received in revised form 10 December 2020
Accepted 11 December 2020
Available online 9 January 2021

Keywords:
Molybdenum dioxide
Composite
Tartaric acid
Glucose
Sol-gel method
Lithium-ion battery

ABSTRACT

MoO_2/C-composites have been fabricated for the first time by a tartaric acid/glucose-assisted sol-gel method with post-annealing at 500 °C for 1 h in N_2 flow. The synthesized materials were fully characterized with respect to structure, morphology, and electrochemical properties. Compared with tartaric acid-assisted products, the adoption of glucose as carbon source effectively increases the carbon content in the composites. Irrespective of the organic component, the composites exhibit low crystallinity and small grain size. This results in good electrochemical performance of the anode materials as confirmed for the glucose-assisted materials which after additional post treatment delivers a competitive electrochemical capacity.

1. Introduction

Molybdenum dioxide (MoO_2), as an important semiconductor, has great potential applications in the production of chemical sensors [1], catalysts [2], field emission devices [3,4], and solar cells [5]. Additionally, MoO_2 has attracted considerable attention as electrode material for lithium ion batteries (LIB) because of its relatively large theoretical capacity (838 mA h g^{-1}) [6] and its high metallic conductivity ($6.04 \cdot 10^3$ S cm^{-1} for the individual rods) [7]. However, several of its intrinsic material properties limit the practical application of bulk MoO_2, namely strong capacity fading and poor cycling stability originated by the huge volume changes during the charge/discharge processes as well as poor rate performance caused by the slow kinetics [8,11]. A variety of strategies have been employed to overcome this issue such as preparation of nanosized materials with different morphologies [9], doping with nitrogen [10], copper [11], and design of 3D hierarchically structures nanomaterials providing shorter lithium ion/electron diffusion distances and accommodating strain associated with strong volume changes upon cycling [12,13]. Additionally, incorporating MoO_2 with functional conductive carbonaceous materials like hollow carbon spheres [14], graphene [15], graphite oxide [16], is regarded as an effective strategy. A further way which advantageously yields homogeneous distribution of the carbon component, thereby increasing cycling stability of the materials is to introduce the carbonaceous phase during calcination of many different organic precursors such as aniline [17], dopamine [18,19], polyethylene glycol [20], alginate [21], ascorbic acid [22], glucose [23], or sucrose [24]. All functionalized materials display enhanced Li-retention performance in comparison with bulk MoO_2, based on their higher surface areas, more actives sites, shorter ion diffusion paths, and functioning carbon buffer which accommodate the strain.

Various techniques, such as a hydrothermal method [25,26], thermolysis [27], and electrospinning [28], have been developed to prepare composites based on MoO_2. Herein, we present a new sol-gel synthesis approach to obtain MoO_2/C composites. This method provides a molecular level-mixing of the starting materials and leads to better chemical homogeneity of the final products. Carbon coated MoO_2 particles have been produced by using glucose or tartaric acid

* Corresponding author at: Kirchhoff Institute of Physics, Heidelberg University, Heidelberg, Germany.
E-mail address: r.klingeler@kip.uni-heidelberg.de (R. Klingeler).
[1] Both authors contributed equally.

https://doi.org/10.1016/j.jallcom.2020.158353
0925-8388/

as both reducing agents and carbon sources and the electrochemical performance of the resulting MoO_2/C composites as electrodes for Li-ion batteries was investigated.

2. Experimental

Molybdenum powder Mo (99.95% metal, Alfa Aesar), hydrogen peroxide H_2O_2 (30%, Merck), tartaric acid $C_4H_6O_6$ (AppliChem), and glucose $C_6H_{12}O_6$ (Sigma-Aldrich) were utilized for the synthesis. Firstly, 1.0 g of Mo powder was dissolved in 35 ml H_2O_2 at 10–15 °C to form a clear yellow solution of peroxomolybdic acid. Secondly, tartaric acid was dissolved in distilled water and stirred for 10 min. The molar ratio of tartaric acid to molybdenum metal was 1: 1. Then, the solution of tartaric acid was slowly added into the solution of peroxomolybdic acid. To get a gel, the solution was heated at 60 °C under continuous stirring. The resulting gel was dried at 60 °C in air and calcinated at 500 °C for 1 h in N_2 flow to yield the MoO_2/C composite. At lower annealing temperatures, the materials were amorphous while annealing at 500 °C yields crystalline samples. The as-prepared product is labeled as MoO_2/C-T. For comparison, MoO_2/C was produced in a glucose-assisted process at a molar ratio of Mo: glucose = 1: 1 and denoted as MoO_2/C-G. To study the effect of pounding on the electrochemical activity, MoO_2/C-G powder was colloidally grinded (300 Us^{-1}) in ethanol using **Ø** 1 mm ZrO_2 balls in a PM 100 planetary mill (Retsch) for 6 h, later annealed at 500 °C for 1 h in N_2 and afterwards hand grinded in a mortar for 15 min; this sample is labeled as MoO_2/C-G(M).

X-ray diffraction (XRD) patterns were obtained on a Bruker AXS D8 Advance Eco using Cu Kα radiation with a step size of Δ2θ = 0.02°. The morphology of the powder was determined by a ZEISS Leo 1530 and a JEOL JSM-7610F scanning electron microscope (SEM), a JEOL JEM 2100 and a JEMe200 CX transmission electron microscope (TEM), respectively. In order to monitor the microstructural changes of MoO_2 upon cycling, ex-situ SEM studies were performed using a JEOL JSM-7610F scanning electron microscope. The cycled electrodes were disassembled in an Argon glove box, washed with ethylene carbonate and then dried overnight.

Fourier transform infrared (FT-IR) spectra were recorded using Spectrum One B (Perkin-Elmer) with an automatic diffuse reflectance accessory. A thoroughly ground sample was applied as a thin layer to a purpose-designed holder plate. Thermogravimetric analysis (TG-DSC-MS) with a heating rate of 10 K min^{-1} starting from room temperature up to 750 °C under flowing air was carried out using STA 449 F_3 Jupiter thermoanalyzer (Netzsch) coupled with a QMS 403 mass spectrometer. Raman spectra were measured with a Renishaw U1000 spectrometer at a laser wavelength of 532 nm.

Electrochemical measurements were carried out in Swagelok-type cells (see [29]). Working electrodes were prepared by mixing the active material, carbon black and polyvinylidene fluoride (PVDF) in N-methyl-2-pyrrolidinone (NMP) and stirred for 24 h before the resulting slurry was pasted on copper net current collectors. The as-prepared electrodes were dried in a vacuum oven (80 °C, 10 mbar) overnight, pressed and dried again. Fiberglass (Whatman GF/D) was used as separator and pure lithium metal foil (Aldrich) as counter electrode. The electrolyte was 1 M $LiPF_6$ in a mixture of ethylene carbonate and diethyl carbonate (1: 1 by weight). Cell assembly was carried out in an Ar-filled glovebox with controlled moisture and oxygen concentration. Cyclic voltammetry (CV) at a scan rate of 0.1 mV s^{-1} and galvanostatic cycling with potential limitation (GCPL) at specific currents of 100 mA g^{-1}, both in the voltage range of 0.01–3.0 V vs. Li/Li^+, were carried out on a VMP3 potentiostat (Bio-Logic) at 25 °C.

3. Results and discussion

Fig. 1 shows X-ray diffractograms of the synthesized materials, i.e., MoO_2/C-G, MoO_2/C-G(M), and MoO_2/C-T. All observed peaks correspond to monoclinic MoO_2 and are accordingly indexed in a monoclinic lattice system with space group $P2_1/c$. The post treatment of the as-prepared composite does not change its structure. The experimentally determined lattice parameters of MoO_2 in the composite MoO_2/C materials are in a good agreement with theoretical values from JCSD no. 72-4534 (cf. Table 1).

The XRD data exhibit broad diffraction peaks with rather weak intensity which suggests that MoO_2 formed in the composites displays poor crystallinity and small crystal size. The mean primary crystallite size of the as-synthesized samples can be estimated using Scherrer's equation [30]:

$$D = K\lambda/\Delta(2\theta)\cos\theta, \quad (1)$$

where D is the average grain size based on the particular reflecting crystal face (hkl) direction, K is a shape factor which can be approximated to 0.9, λ is the wavelength of the applied Cu Kα radiation, $\Delta(2\theta)$ is the full width at half-maximum of the diffraction peak, and θ is the Bragg angle. Analysis[2] of the (011), (200), and (022) peaks yield to a mean primary crystallite size of around 6 nm for MoO_2/C-G, MoO_2/C-G(M), and MoO_2/C-T composites under study. The crystal structure of monoclinic MoO_2 is depicted in Fig. 1. It consists of

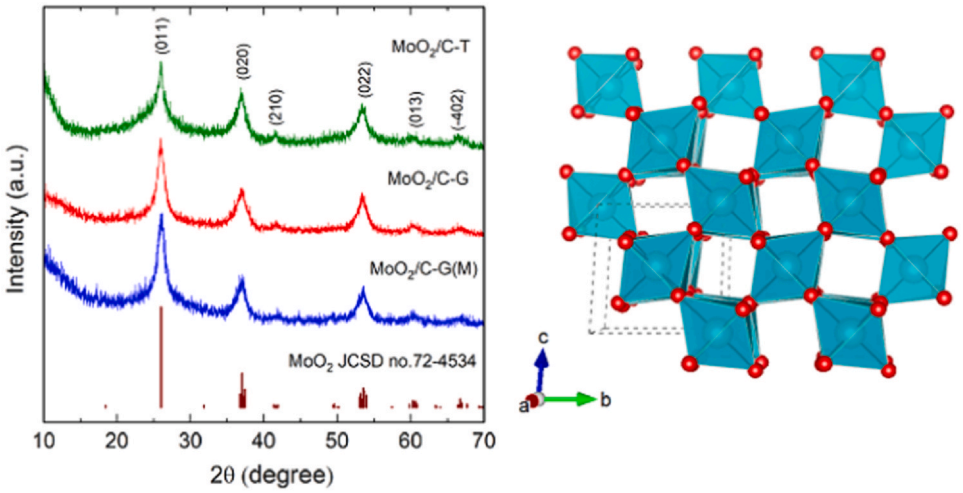

Fig. 1. XRD patterns of the MoO_2/C-G and the MoO_2/C-T composites (left), and a schematic of the corresponding crystal structure of MoO_2 (right).

Table 1
Experimentally determined lattice parameters of MoO_2 in MoO_2/C-G, MoO_2/C-G(M), and MoO_2/C-T as well as values from JCSD no. 72-4534.

	a (Å)	b (Å)	c (Å)	β (deg.)	V (Å^3)
MoO_2/C-G	5.652(6)	4.832(5)	5.594(7)	120.39(6)	131.7(3)
MoO_2/C-G(M)	5.679(5)	4.808(9)	5.619(8)	120.48(2)	132.2(3)
MoO_2/C-T	5.648(3)	4.912(6)	5.609(1)	119.24(7)	135.8(2)
MoO_2	5.6109	4.8562	5.6285	120.95	131.53

MoO_6 octahedrons which form channels along the *a*-axis which are supposed to facilitate Li^+ transport during electrochemical cycling.

Scanning electron microscopy images in Fig. 2 show the morphology of the as-prepared composites. Both as-prepared composite materials MoO_2/C-T and -G consist of irregular micro-sized agglomerates (Fig. 2a, c). The underlying primary particles, which are well visible in the high-magnification SEM images in Fig. 2b and d, in both composites consist of round grains with an average particle size of less than 20 nm. A further post treatment of the sample results in a visible size reduction of the agglomerates (Fig. 2e-f).

Additional detailed information on MoO_2/C-G is obtained from the TEM images in Fig. 3a. The images show the presence of MoO_2/C-G nanocrystallites forming large agglomerates that are dispersed in an amorphous carbon matrix. Lattice fringes visible in the high-resolution TEM (HR-TEM) image (Fig. 3b) indicate lattice display spacings of approximately 0.35 nm. This value corresponds well with the (011) plane of MoO_2 which according to our XRD analysis has a plane distance of 0.3417(3) nm in MoO_2/C-G. Fig. 3b also shows carbon layers of around 10 nm in thickness around the crystallites. Selected area electron diffraction (SAED) confirms the crystalline structure of MoO_2 in the MoO_2/C-G nanocomposite (Fig. 3c). Debye rings from the SAED pattern demonstrate the ultrafine structure of crystalline MoO_2 without any preferred orientation of the individual crystallites. The Debye rings can be attributed to the monoclinic phase of MoO_2 with $P2_1/c$ space group symmetry, which agrees with the XRD results.

Raman spectra of the MoO_2/C composites shown in Fig. 4a provide information on both the MoO_2 and the carbon components of the nanocomposite as the observed Raman peaks refer to Mo-O as well as carbon modes. The prominent carbon modes are the G-band which corresponds to the sp^2-bonded carbon atoms and the D-band associated with defects or disorder mainly due to sp^3-hybridization of carbon atoms [31]. The D- and G-bands of MoO_2/C-G composite arise at 1372 cm^{-1} and 1586 cm^{-1}, respectively. In comparison, the G- and D-bands of MoO_2/C-T are at slightly lower wavenumbers of 1365 and 1575 cm^{-1}. The ratio of the maximum intensities of these peaks, I_D/I_G, was calculated as 0.78 and 0.71 for MoO_2/C-G and MoO_2/C-T composites, respectively. This indicates that in comparison with tartaric acid, glucose promotes the formation of defects and disorder in the carbon component of the composite. In comparison with the pure MoO_2 phase [32], a richer Raman spectrum of MoO_2/C composites with intensive bands below 1000 cm^{-1} resulting from different vibration modes of Mo-O is observed. The presence of the peaks located at 819 and 993 cm^{-1} corresponding to the stretching vibrations of Mo=O bonds indicates the formation of the layered structure of the compounds similar to MoO_3 [33]. This phenomenon has been reported by Camacho-Lopez et al. [34] who associated it with the oxidation of MoO_2 to $MoO_{2+\delta}$ by laser irradiation.

FT-IR spectra of the MoO_2/C composites are shown in Fig. 4b. There are two typical vibration modes belonging to the MoO_2 phase [35]. The stretching vibrations of Mo=O bonds are demonstrated by the characteristic bands at 957 and 955 cm^{-1} for MoO_2/C-T and MoO_2/C-G composites, respectively. The bridge stretching vibration of Mo-O-Mo bonds are displayed by the bands at 718 and 693 cm^{-1} for MoO_2/C-T and MoO_2/C-G composites, respectively. The peaks at 1598 cm^{-1} (MoO_2/C-T) and 1600 cm^{-1} (MoO_2/C-G) are assigned to the C–O stretching vibration in the carboxylic group which may result from incomplete decomposition of the organic groups in the carbon component. The weak bands located at around 3400 cm^{-1} and 1640 cm^{-1} are associated with the stretching and bending vibrations of O–H, respectively, originating from trace amounts of adsorbed water in the powder. It is worth noting that the peaks which are attributed to pure glucose [36] and tartaric acid [37] are not part of the respective spectra.

In order to determine the thermal stability of MoO_2/C composites in air and to quantify the amount of carbon within the materials, TG-DSC-MS studies of as-prepared materials were carried out (Fig. 5). The TG curve of the MoO_2/C-G composite evidences two steps of weight loss (Fig. 5a). We attribute the first weight loss of 5.7 wt% in the temperature regime from 70 °C to 300 °C mainly to evaporation of water. It appears as a weak and broad endothermic process centered at 115 °C. The second weight loss of 23.7 wt% from 300 °C to 690 °C is caused by oxidation of carbon components and the release of CO_2 gases. The mass spectrometry curve (ion current versus temperature) indicates that the main gaseous product of MoO_2/C-G decomposition is CO_2 (m/z = 44 a.m.u.). However, the carbon component of MoO_2/C-G was not completely oxidized to CO_2 at 690 °C. Despite the appearance of a two-step process somehow similar to what is observed in MoO_2/C-G, the TG curve of MoO_2/C-T shown in Fig. 5b shows several differences. Again, a first stage from 25 to 300 °C with corresponding weight loss of 3.6 wt% can be assigned to evaporation of surface-adsorbed water. The second region of mass loss (2.4 wt%) from 300 to 514 °C is accompanied by a broad exothermal peak. It is attributed to the decomposition and full oxidation of organics. From the mass spectrometry curve, it can be revealed that the main gaseous product of MoO_2/C-T decomposition is CO_2 (m/z = 44 a.m.u.). Additionally, the three steps observed in TGA suggest that the carbon component in the MoO_2/C-T composite has three states differently bound to the main phase (MoO_2). At around 550 °C, the TG data indicate an increase of sample weight by 2.9 wt%. This process is attributed to the oxidation of Mo^{4+} to Mo^{6+} and results in the formation of MoO_3 as a final thermolysis product. Based on the assumptions made above, the calculated carbon contents in MoO_2/C-T and MoO_2/C-G composites are 2.4 and more than 23.7 wt %, respectively.

The electrochemical properties of the composite materials obtained as described are investigated with respect to their applicability as electrode materials in LIB by means of CV and GCPL. Fig. 6 displays the first, second, fifth CV curve of MoO_2/C-G and MoO_2/C-T. The reversible reactions of MoO_2 with lithium are described by the following electrochemical reactions [16,38]:

$$MoO_2 + xLi^+ + xe^- \leftrightarrow Li_xMoO_2, \quad (0 \le x \le 0.98) \tag{2}$$

$$Li_xMoO_2 + (4 - x)Li^+ + (4 - x)e^- \leftrightarrow Mo + 2Li_2O. \tag{3}$$

Due to the deliberate low crystallinity of the samples, mainly extended areas of electrochemical activity instead of well-defined peaks are visible in the CV. In the first reductive sweep of MoO_2/C-G, four different cathodic features are observed. The elevation at around 1.25 V (R1) can be attributed to the phase transition between the orthorhombic and the monoclinic phase upon lithium insertion (Eq. (2)) as suggested by Dahn et al. [39]. Due to the absence of the peak R2 at around 0.6 V in further cycles, it is most likely assigned to the solid electrolyte interface (SEI) formation which is consistent with reports by Luo et al. [40] and Xu et al. [41]. The reversible conversion reaction (Eq. (3)) can be assigned to the reduction peak R3, parts of R4 and the elevation O3 [38]. The two overlapping oxidation peaks O2 and O1 can be ascribed to the phase transitions (monoclinic-orthorhombic-monoclinic) in partially lithiated

[2] Additional contributions to peak broadening are neglected.

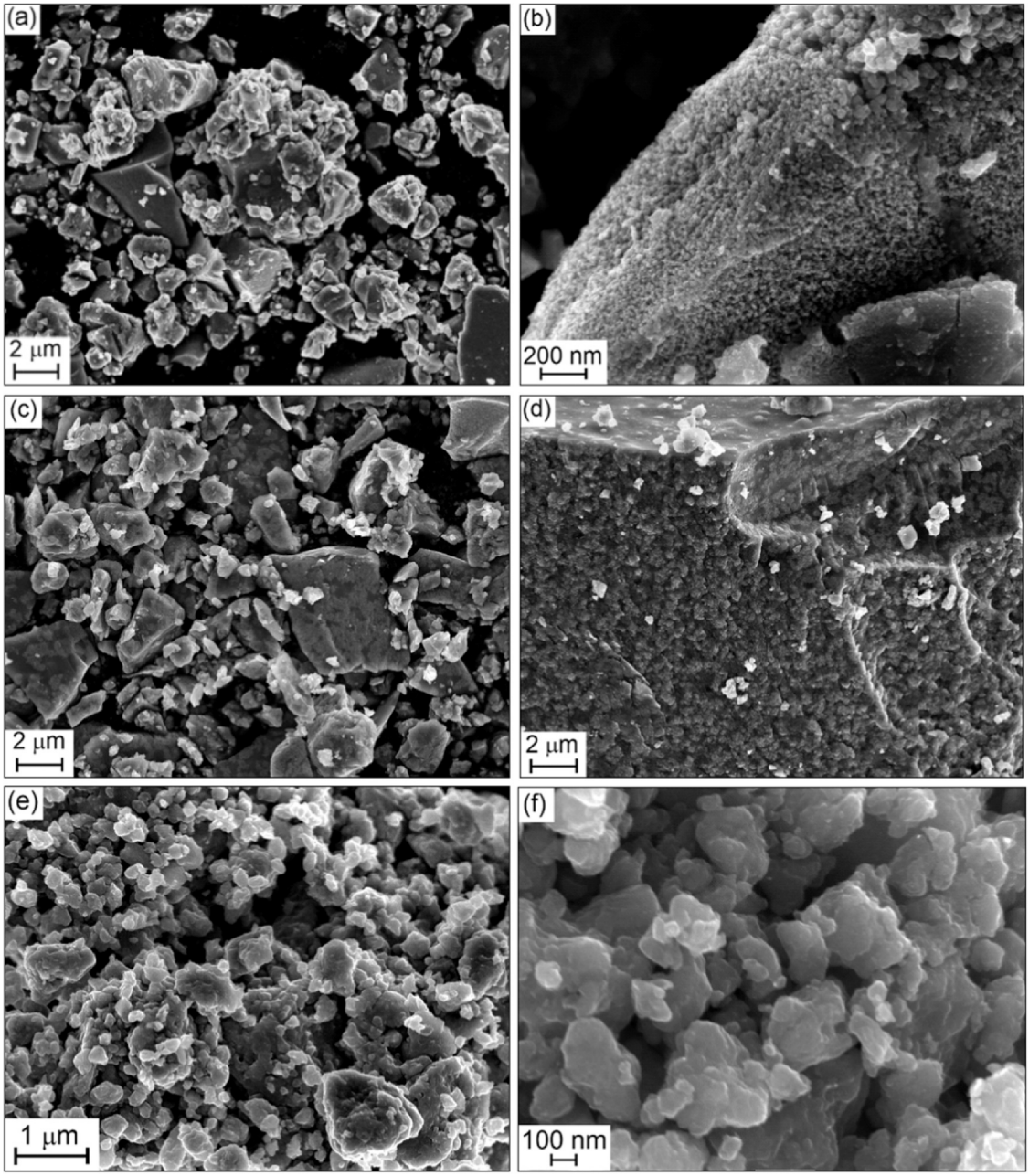

Fig. 2. SEM and high-magnification SEM images of (a, b) MoO_2/C-T, (c, d) MoO_2/C-G, and (e, f) MoO_2/C-G(M) obtained by a post treatment (see the text).

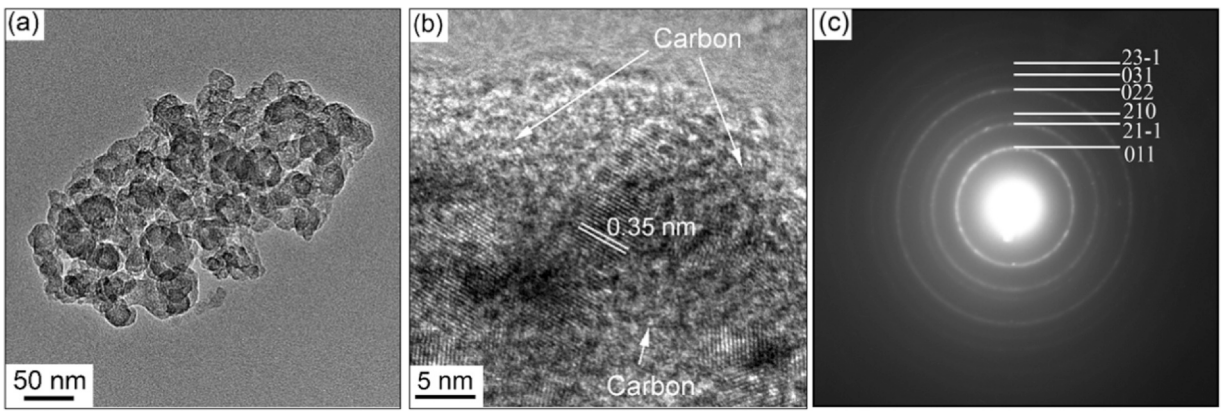

Fig. 3. (a) TEM image, (b) HRTEM image, and (c) SAED pattern of MoO_2/C-G composite.

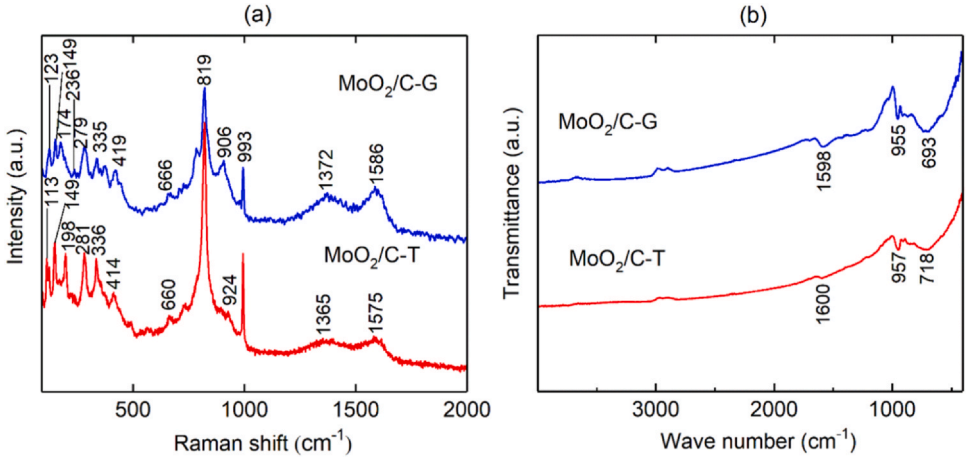

Fig. 4. (a) Raman and (b) FT-IR spectra of MoO_2/C-G and MoO_2/C-T composites.

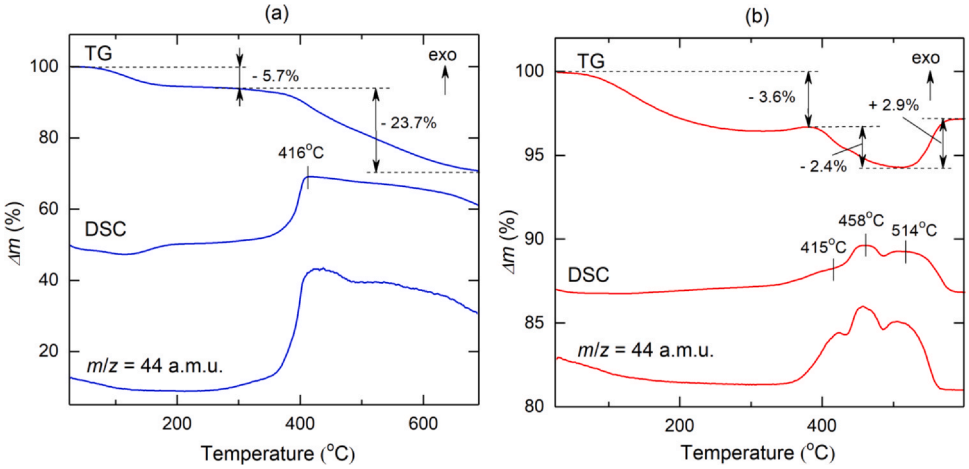

Fig. 5. Thermogravimety, DSC, and mass spectroscopy curves of (a) MoO_2/C-G and (b) MoO_2/C-T composites.

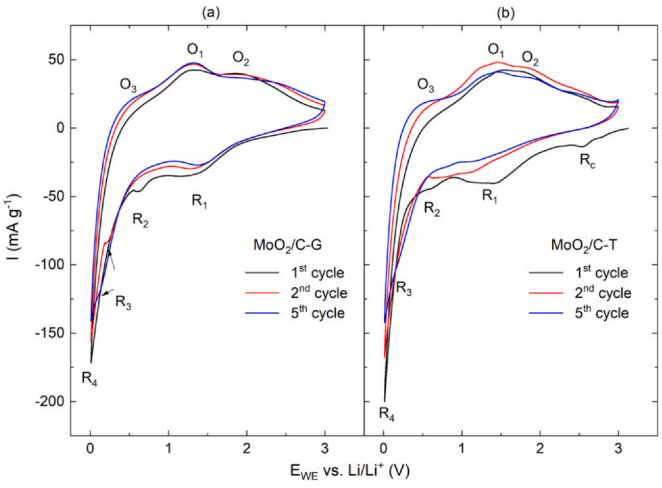

Fig. 6. Cyclic voltammograms of (a) MoO_2/C-G and (b) MoO_2/C-T composites recorded at a scan rate of 0.1 mV s^{-1}.

Li_xMoO_2 [42]. The main difference between the CV of MoO_2/C-G (Fig. 6a) and MoO_2/C-T (Fig. 6b) is the presence of the feature Rc at around 2.5 V in the first reductive sweep of the latter. In the literature, Rc is sometimes observed [27,43] and sometimes not [42,44] and its origin is yet unclear.

The cycling performance of as-prepared MoO_2/C-G- and MoO_2/C-T- as well as of MoO_2/C-G(M)-based electrodes is presented in Fig. 7a. The corresponding potential profiles are shown in Figs. S1-S3. The electrochemical performance of the MoO_2/C composites show strong differences. The highest discharge capacity in the first and twentieth cycle of 928 mAh g^{-1} and 610 mAh g^{-1} is reached by the post treated sample MoO_2/C-G(M). In contrast, the as-prepared material MoO_2/C-G achieves 516/195 mAh g^{-1}, respectively. Coulombic efficiencies also shown in Fig. 7a confirm significant irreversible effects not only for MoO_2/C-T but also for MoO_2-/C-G. All materials display reduced Coulombic efficiency in the first cycles which is attributed to common irreversible processes as electrolyte decomposition and formation of the SEI [22,40,41]. Similarly to what is concluded from the evolution of capacity upon cycling, Coulombic efficiencies for MoO_2/C-G(M) are highest and amount to about 98%. MoO_2/C-T has in comparison to MoO_2/C-G a high initial discharge capacity of 617 mAh g^{-1} but shows a much severe drop in capacity already in the second cycle. We attribute this to the much lower (i.e., by more than 20%) carbon content. Such a low carbon content may result in an increased contact loss between the active material and the current collector during cycling. This degeneration process is well known for conversion-type materials and occurs due to the volume expansion and the associated induced pulverization during the conversion reaction [45–47]. Comparison of the treated and untreated MoO_2/C-G samples shows that the post treated sample MoO_2/C-G(M), which features a reduced size of the agglomerates (Fig. 2e-f), achieves nearly 2 times the capacity of MoO_2/C-G over all

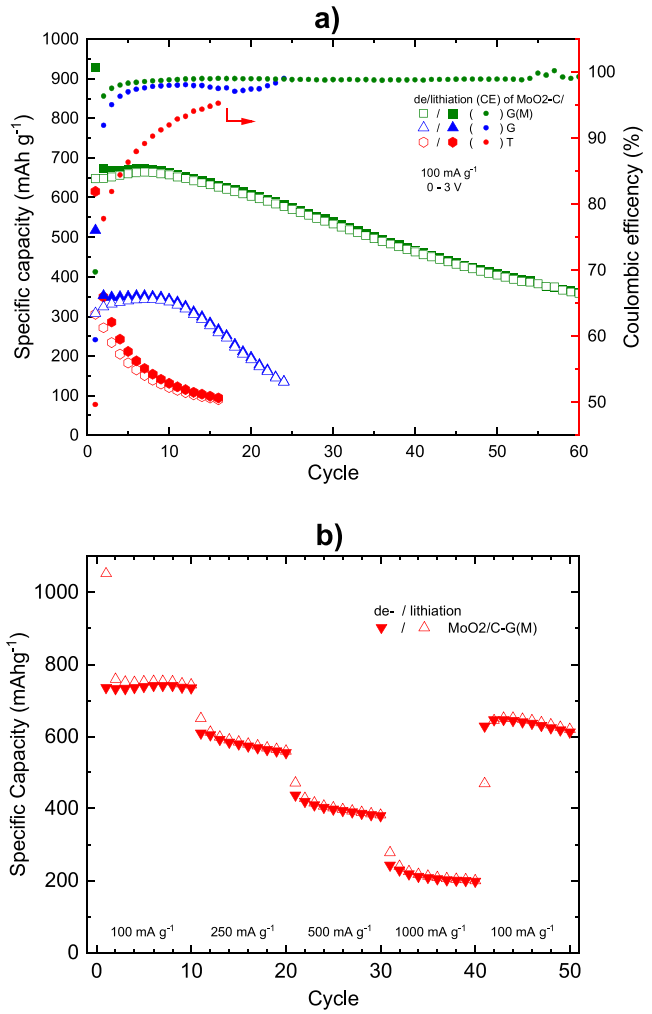

Fig. 7. a) Specific charge/discharge capacities and associated coulombic efficiencies of MoO_2/C electrodes and b) rate capability test with different cycling rates of MoO_2/C-G(M) electrode measured by GCPL between 0.01 V and 3 V.

cycles. As expected, the size reduction of the agglomerates by the post treatment and the associated surface enlargement leads to an increased electrochemical activity of MoO_2/C-G as electrolyte diffusion is facilitated [48]. The initial increase in capacity of the MoO_2/C-G samples may be attributed to a gradual decomposition of Li_xMoO_2 in the conversion reaction during cycling, the formation of crystalline defects which is a common phenomenon in oxide anodes resulting in increasing capacity, and/or a reaction including the SEI [43,49,50]. The rate capability of MoO_2/C-G(M) at cycle rates between 100 and 1000 mA g^{-1} displayed in Fig. 7b implies a reversible capacity of 740, 580, 400, and 210 mA h g^{-1}, at a current density of 100, 250, 50 and 1000 mA g^{-1}, respectively. The reversible capacitance reaches 650 mA h g^{-1} when the current density is set again to 100 mA g^{-1}, which proves good reversibility of the electrode. To characterize the microstructure details of the MoO_2/C-G(M) based electrode before and after galvanostatic cycling, *ex-situ* SEM measurements were performed (Fig. S4). The comparison of the SEM images before (Fig. S4a) and after (Fig. S4b) cycling reveals that the individual particles change their surface texture, which is likely due to the known degeneration mechanisms such as SEI formation [51] and/or agglomeration. Pulverization as a possible degeneration phenomenon for MoO_2/C-G(M) seems to be less critical as the high-resolution SEM images show that even after 60 cycles the binder network is intact and no clear cracks are visible.

To relate the electrochemical performance of the here presented MoO_2/C-G(M) composite to the literature, Table 2 lists the discharge capacities of various MoO_2/C composite anodes. The MoO_2/C-G(M)-based electrode studied at hand exhibits a superior electrochemical capacity compared to the materials obtained by Che *et al.* [21], Yoon *et al.* [52] and Luo *et al.* [40] and is slightly better than the materials reported by Sun et al. [53] and Hu *et al.* [54]. However, MoO_2/graphene oxide composite materials generally show higher capacities [16,41,55]. In contrast to these materials, the MoO_2/C-G(M) composite reported here benefits from a straightforward, environment-friendly, and well-controllable synthesis process, which is based on cost-effective starting materials. Evidently, the electrochemical performance of MoO_2/C composites mainly depends on morphological features as carbon coating, particle size and surface texture which are directly affecting the transport path length of electrons as well as Li-ions.

4. Conclusions

In summary, a tartaric acid and glucose based sol–gel method combined with thermal reduction has been utilized to synthesize hybrid MoO_2/C nanocomposites. This synthetic strategy is simple, cost-effective, and promising for large-scale industrial production of MoO_2/C composites. In the as-prepared composites, MoO_2 nanoparticles with a size of about 20 nm are embedded into a ~10 nm thick amorphous carbon matrix, which serves as a buffer layer preventing the degradation of MoO_2 nanoparticles during charge/discharge processes.

The observed electrochemical performances of the prepared materials underline the relevance of the used carbon source and the received morphology for the application in LIB. Compared to untreated MoO_2/C-G, post treated MoO_2/C-G(M) shows a clearly improved capacity. The post treated MoO_2/C-G(M) features a remarkably enhanced, competitive specific capacity of 660 mAh g^{-1} at 100 mA g^{-1} in the tenth cycle. Therefore, the results show that this simple and cost-effective synthesis approach may also be successfully applied to other metal oxides.

Table 2
Comparison of the electrochemical cycling performance of MoO_2 -based composites obtained by various synthesis methods.

Material	Synthesis method	Current (mA g^{-1})	Discharge capacity (mAh g^{-1})/cycle no[a]	Ref.
MoO_2/C-G(M) nanoparticles	Glucose-assisted sol-gel	100	660/10	this work
MoO_2/C nanoparticles	Alginate-assisted sol-gel	200	300/10	[21]
Nitrided MoO_2	hydrothermal	120	310/10	[52]
MoO_2/C nanofibers	Electrospinning	100	500/10	[40]
MoO_2/C nanoparticles	Impregnation of carbon matrix	100	600/10	[53]
MoO_2/graphite oxide nanoparticles	Solvothermal	100	620/10	[54]
MoO_2/graphite oxide nanoparticles	Solvothermal	100	800/10	[16]
MoO_2/C cage-like particle	Hydrothermal reduction	200	800/10	[22]
MoO_2/exfoliated graphene oxide	Solid-state graphenothermal reduction	100	850/10	[55]
MoO_2/graphene oxide	Decomposition	100	1200/10	[41]

[a] For better comparison, data from the same cycle number are shown as read-off from reported figures.

CRediT authorship contribution statement

G.Z.: Conceptualization, Investigation, Methodology, Writing - original draft, Writing - review & editing. **L.S.:** Investigation, Methodology, Writing - original draft, Writing - review & editing. **Z.F.**: Investigation. **S.W.**: Investigation. **E.T.**: Writing - review & editing. **Q.Z.**: Investigation. **E.V.:** Investigation. **R.K.:** Conceptualization, Supervision, Writing - review & editing.

Declaration of Competing Interest

The authors declare that they have no known competing financial interests or personal relationships that could have appeared to influence the work reported in this paper.

Acknowledgements

This work was supported by the Deutsche Forschungsgemeinschaft through projects KL 1824/12-1 and KL 1824/14-1. G.Z. acknowledges support of the state order via the Ministry of Science and High Education of Russia (Theme no. AAAA-A19-119031890025-9). Partial support by the BMWi through project 03ET6095C (HiKoMat) is acknowledged. The authors thank I. Glass for experimental support.

Appendix A. Supporting information

Supplementary data associated with this article can be found in the online version at doi:10.1016/j.jallcom.2020.158353.

References

[1] T. Yunusi, C. Yang, W. Cai, F. Xiao, J. Wang, X. Su, Synthesis of MoO_3 submicron belts and MoO_2 submicron spheres via polyethylene glycol-assisted hydrothermal method and their gas sensing properties, Ceram. Int. 39 (2013) 3435–3439.
[2] A. Bento, A. Sanches, E. Medina, C.D. Nunes, P.D. Vaz, MoO_2 nanoparticles as highly efficient olefin epoxidation catalysts, Appl. Catal. A 504 (2015) 399–407.
[3] J. Liu, Z. Zhang, C. Pan, Y. Zhao, X. Su, Y. Zhou, D. Yu, Enhanced field emission properties of MoO_2 nanorods with controllable shape and orientation, Mater. Lett. 58 (2004) 3812–3815.
[4] S.T. Nishanthi, A. Baruah, K.K. Yadav, D. Sarker, S. Ghosh, A.K. Ganguli, M. Jha, New low temperature environmental friendly process for the synthesis of tetragonal MoO_2 and its field emission properties, Appl. Surf. Sci. 467–468 (2019) 1148–1156.
[5] L. Li, H. Sui, K. Zhao, W. Zhang, X. Li, S. Liu, K. Yang, M. Wu, Y. Zhang, Preparation of carbon nanofibers supported MoO_2 composites electrode materials for application in dye-sensitized solar cells, Electrochim. Acta 259 (2018) 188–195.
[6] G. Xu, P. Liu, Y. Ren, X. Huang, Z. Peng, Y. Tang, H. Wang, Three-dimensional MoO_2 nanotextiles assembled from elongated nanowires as advanced anode for Li ion batteries, J. Power Sources 361 (2017) 1–8.
[7] Q. Xie, X. Zheng, D. Wu, X. Chen, J. Shi, X. Han, X. Zhang, G. Peng, Y. Gao, H. Huang, High electrical conductivity of individual epitaxially grown MoO_2 nanorods, Appl. Phys. Lett. 111 (2017) 093505.
[8] L.C. Yang, Q.S. Gao, Y. Tang, Y.P. Wu, R. Holze, MoO_2 synthesized by reduction of MoO_3 with ethanol vapor as an anode material with good rate capability for the lithium ion battery, J. Power Sources 179 (2008) 357–360.
[9] Y. Liang, Z. Yi, S. Yang, L. Zhou, J. Sun, Y. Zhou, Hydrothermal synthesis and lithium-intercalation properties of MoO_2 nano-particles with different morphologies, Solid State Ion. 177 (2006) 501–505.
[10] Huanhuan Sun, Yu Zhang, Huanyan Liu, Xingyuan Zhang, Jian-Gan Wang, Constructing hierarchical MoO2/N-doped carbon hydrangea-like spheres with superior lithium storage properties, J. Alloy. Compd. 787 (2019) 45–52.
[11] L. Zhang, W. He, M. Ling, K. Shen, Y. Liu, S. Guo, Cu@MoO_2@C nanocomposite with stable yolk-shell structure for high performance lithium-ion batteries, J. Alloy. Compd. 768 (2018) 714–721.
[12] X. Li, Q. Xiao, Y. Gao, H. Zhang, H. Xu, Y. Zhang, Hierarchical MoO_2/C microspheres: preparation and application as anode materials for lithium ion batteries, J. Alloy. Compd. 723 (2017) 1113–1120.
[13] P. Zhang, L. Zou, H. Hu, M. Wang, J. Fang, Y. Lai, J. Li, 3D hierarchical carbon microflowers decorated with MoO_2 nanoparticles for lithium ion batteries, Electrochim. Acta 250 (2017) 219–227.
[14] Xingyuan Zhanga, Jian-Gan Wanga, Wei Huaa, Hongzhen Liua, Bingqing Weiaa, Hierarchical nanocomposite of hollow carbon spheres encapsulatingnano-MoO_2 for high-rate and durable Li-ion storage, J. Alloy. Compd. 787 (2019) 301–308.
[15] K.H. Seng, G.D. Du, L. Li, Z.X. Chen, H.K. Liu, Z.P. Guo, Facile synthesis of graphene–molybdenum dioxide and its lithium storage properties, J. Mater. Chem. 22 (2012) 16072–16077.
[16] Y. Xu, R. Yi, B. Yuan, X. Wu, M. Dunwell, Q. Lin, L. Fei, S. Deng, P. Andersen, D. Wang, H. Luo, High capacity MoO_2/graphite oxide composite anode for lithium-ion batteries, J. Phys. Chem. Lett. 3 (2012) 309–314.
[17] Q. Gao, L. Yang, X. Lu, J. Mao, Y. Zhang, Y. Wu, Y. Tang, Synthesis, characterization and lithium-storage performance of MoO_2/carbon hybrid nanowires, J. Mater. Chem. 20 (2010) 2807–2812.
[18] Y. Qi, B. Zhou, X. Yang, Y. Zhou, W. Jin, J. Zhou, W. Chen, 3D microstructures with MoO_2 nanocrystallines embedded into interpenetrated carbon nanosheets for lithium ion batteries, J. Mater. Sci. Mater. Electron. 29 (2018) 11521–11528.
[19] P. Zhang, L. Zou, H. Hu, M. Wang, J. Fang, Y. Lai, J. Li, 3D hierarchical carbon microflowers decorated with MoO_2 nanoparticles for lithium ion batteries, Electrochim. Acta 250 (2017) 219–227.
[20] X. Li, Q. Xiao, Y. Gao, H. Zhang, H. Xu, Y. Zhang, Hierarchical MoO_2/C microspheres: preparation and application as anode materials for lithium ion batteries, J. Alloy. Compd. 723 (2017) 1113–1120.
[21] Y. Che, X. Zhu, J. Li, J. Sun, Y. Liu, C. Jin, C. Dong, Simple synthesis of MoO_2/carbon aerogel anodes for high performance lithium ion batteries from seaweed biomass, RSC Adv. 6 (2016) 106230–106236.
[22] B. Liu, X. Zhao, Y. Tian, D. Zhao, C. Hu, M. Cao, A simple reduction process to synthesize MoO_2/C composites with cage-like structure for high performance lithium-ion batteries, Phys. Chem. Chem. Phys. 15 (2013) 8831–8837.
[23] J. Ni, Y. Zhao, L. Li, L. Mai, Ultrathin MoO_2 nanosheets for superior lithium storage, Nano Energy 11 (2015) 129–135.
[24] W. Cho, J.H. Song, J. Kim, G. Jeong, E.Y. Lee, Y. Kim, Electrochemical characteristics of nano-sized MoO_2/C composite anode materials for lithium-ion batteries, J. Appl. Electrochem. 42 (2012) 909–915.
[25] J. Jiang, W. Yang, Hao Wang, Y. Zhao, J. Guo, J. Zhao, M. Beidaghi, L. Gao, Electrochemical performances of MoO_2/C nanocomposite for sodium ion storage: an insight into rate dependent charge/discharge mechanism, Electrochim. Acta 240 (2017) 379–387.
[26] K. Palanisamy, Y. Kim, H. Kim, J.M. Kim, W. Yoon, Self-assembled porous MoO_2/graphene microspheres towards high performance anodes for lithium ion batteries, J. Power Sources 275 (2015) 351–361.
[27] L. Guo, Y. Wang, Standing carbon-coated molybdenum dioxide nanosheets on graphene: morphology evolution and lithium ion storage properties, J. Mater. Chem. A 3 (2015) 4706–4715.
[28] J. Xianga, Z. Wu, X. Zhang, S. Yao, Enhanced electrochemical performance of an electrospun carbon/MoO_2 composite nanofiber membrane as self-standing anodes for lithium-ion batteries, Mater. Res. Bull. 100 (2018) 254–258.
[29] A. Ottmann, G.S. Zakharova, B. Ehrstein, R. Klingeler, Electrochemical performance of single crystal belt-like $NH_4V_3O_8$ as cathode material for lithium-ion batteries, Electrochim. Acta 174 (2015) 682–687.
[30] A.L. Patterson, The Scherrer formula for X-Ray particle size determination, Phys. Rev. Lett. 56 (1939) 978–982.
[31] V. Wang, D.C. Alsmeyer, R.L. McCreery, Raman spectroscopy of carbon materials: structural basis of observed spectra, Chem. Mater. 2 (1990) 557–563.
[32] L. Kumari, Y.-R. Ma, C.-C. Tsai, Y.-W. Lin, S.Y. Wu, K.-W. Cheng, Y. Liou, X-ray diffraction and Raman scattering studies on large-area array and nanobranched structure of 1D MoO_2 nanorods, Nanotechnology 18 (2007) 115717.
[33] G.S. Zakharova, Ch Schmidt, A. Ottmann, E. Mijowska, R. Klingeler, Microwave-assisted hydrothermal synthesis and electrochemical studies of α- and h-MoO_3, J. Solid State Electrochem. 22 (2018) 3651–3661.
[34] M.A. Camacho-Lypez, L. Escobar-Alarcyn, M. Picquart, R. Arroyo, G. Cyrdoba, E. Haro-Poniatowski, Micro-Raman study of the m-MoO_2 to α-MoO_3 transformation induced by cw-laser irradiation, Opt. Mater. 33 (2011) 480–484.
[35] X. Wang, Y. Liu, J. Zeng, C. Peng, R. Wang, MoO_2/C hollow nanospheres synthesized by solvothermal method as anode material for lithium-ion batteries, Ionics 25 (2019) 437–445.
[36] F.O. Libnau, A.A. Christy, O.M. Kvalheim, Resolution of infrared spectra and kinetic analysis of mutarotation of D-glucose in water by sequential rank analysis, Vib. Spectrosc. 7 (1994) 139–148.
[37] N. Chumha, S. Kittiwachana, T. Thongtem, S. Thongtem, S. Kaowphong, Synthesis and characterization of $GdVO_4$ nanostructures by a tartaric acid-assisted sol–gel method, Ceram. Int. 40 (2014) 16337–16342.
[38] L. Yang, X. Li, Y. Ouyang, Q. Gao, L. Ouyang, R. Hu, J. Liu, M. Zhu, Hierarchical MoO_2/Mo_2C/C hybrid nanowires as high-rate and long-life anodes for lithium-ion batteries, ACS Appl. Mater. Interfaces 8 (2016) 19987–19993.
[39] J. Dahn, W. Mckinnon, Structure and electrochemistry of Li_xMoO_2, Solid State Ion. 23 (1987) 1–7.
[40] W. Luo, X. Hu, Y. Sun, Y. Huang, Electrospinning of carbon-coated MoO_2 nanofibers with enhanced lithium-storage properties, Phys. Chem. Chem. Phys. 13 (2011) 16735–16740.
[41] Z. Xu, K. Yao, H. Fu, X. Shen, X. Duan, L. Cao, J. Huang, H. Wang, Constructing MoO_2 porous architectures using graphene oxide flexible supports for lithium ion battery anodes, Glob. Chall. 1 (2017) 1700050.
[42] L. Zhou, H. Wu, Z. Wang, X. Lou, Interconnected MoO_2 nanocrystals with carbon nanocoating as high-capacity anode materials for lithium-ion batteries, ACS Appl. Mater. Interfaces 3 (2011) 4853–4857.
[43] B. Guo, X. Fang, B. Li, Y. Shi, C. Ouyang, Y. Hu, Z. Wang, G. Stucky, L. Chen, Synthesis and lithium storage mechanism of ultrafine MoO_2 nanorods, Chem. Mater. 24 (2012) 457–463.

[44] Y. Sun, X. Hu, W. Luo, Y. Huang, Self-assembled hierarchical MoO_2/graphene nanoarchitectures and their application as a high-performance anode material for lithium-ion batteries, ACS Nano 5 (2011) 7100–7107.
[45] J. Li, S. Hwang, F. Guo, S. Li, Z. Chen, R. Kou, K. Sun, C. Sun, H. Gan, A. Yu, E. Stach, H. Zhou, D. Su, Phase evolution of conversion-type electrode for lithium ion batteries, Nat. Commun. 10 (2019) 2224.
[46] M. Ebner, F. Marone, M. Stampanoni, V. Wood, Visualization and quantification of electrochemical and mechanical degradation in Li ion batteries, Science 342 (2013) 716–720.
[47] A. Ottmann, M. Scholz, E. Thaue, P. Schneider, M. Gellesch, C. Nowka, S. Wurmehl, S. Hampel, R. Klingeler, Electrochemical magnetization switching and energy storage in manganese oxide filled carbon nanotubes, Sci. Rep. 7 (2017) 13625.
[48] C. Delacourt, P. Poizot, S. Levasseur, C. Masquelier, Size effects on carbon-free $LiFePO_4$ powders: the key to superior energy density, Electrochem. Solid State Lett. 9 (2006) A352–A355.
[49] Kun Chang, Dongsheng Geng, Xifei Li, Jinli Yang, Yongji Tang, Mei Cai, Ruying Li, Xueliang Sun, Ultrathin MoS_2/nitrogen-doped graphene nanosheets with highly reversible lithium storage, Adv. Energy Mater. 3 (2013) 839–844.
[50] Yan-Yan Hu1, Zigeng Liu, Kyung-Wan Nam, Olaf J. Borkiewicz, Jun Cheng, Xiao Hua1, Matthew T. Dunstan, Xiqian Yu, Kamila M. Wiaderek, Lin-Shu Du, Karena W. Chapman, Peter J. Chupas, Xiao-Qing Yang2, Clare P. Grey, Origin of additional capacities in metal oxide lithium-ion battery electrodes, Nat. Mater. 12 (2013).
[51] Fanyan Zeng, Maohui Yu, Wanting Cheng, Wenxiu He, Yang Pan, Yaohui Qu, Cailei Yuan, Tunable surface selenization on MoO_2-based carbon substrate for notably enhanced sodium-ion storage properties, Small 16 (2020) 2001905.
[52] Sukeun Yoon, Kyu-Nam Jung, Chang Soo Jin, Kyung-Hee Shin, Synthesis of nitrided MoO_2 and its application as anode materials for lithium-ion batteries, J. Alloy. Compd. 536 (2012) 179–183.
[53] Y. Sun, X. Hu, W. Luo, Y. Huang, Ultrafine MoO_2 nanoparticles embedded in a carbon matrix as a high-capacity and long-life anode for lithium-ion batteries, J. Mater. Chem. 22 (2012) 425–431.
[54] S. Hu, F. Yin, E. Uchaker, W. Chen, M. Zhang, J. Zhou, Y. Qi, G. Cao, Facile and green preparation for the formation of MoO_2-GO composites as anode material for lithium-ion batteries, J. Phys. Chem. C 118 (2014) 24890–24897.
[55] S. Petnikota, K.W. Teo, L. Chen, A. Sim, S.K. Marka, M.V. Reddy, V.V.S.S. Srikanth, S. Adams, B.V.R. Chowdari, Exfoliated graphene oxide/MoO_2; composites as anode materials in lithium-ion batteries: an insight into intercalation of Li and conversion mechanism of MoO_2, ACS Appl. Mater. Interfaces 8 (2016) 10884–10896.

Supplement Information:

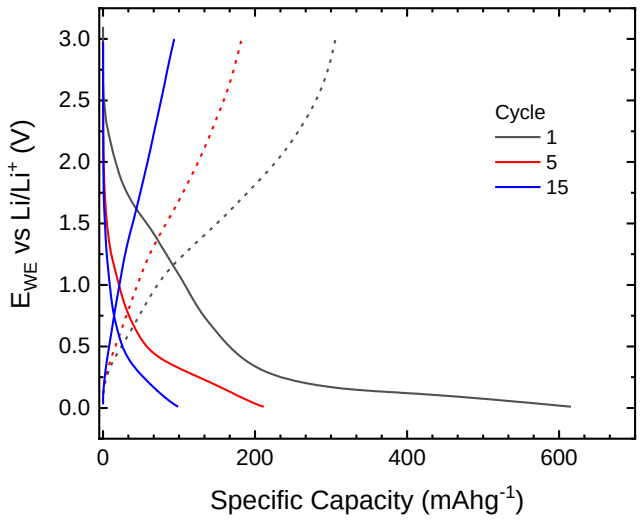

.

Fig. S1. Potential profile of MoO_2/C-T at current densities of 100 mA g^{-1}.

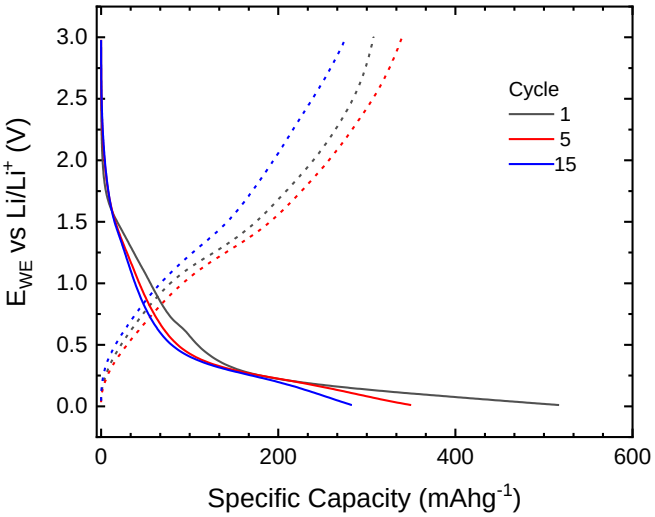

Fig. S2. Potential profile of MoO_2/C-G at current densities of 100 mA g^{-1}.

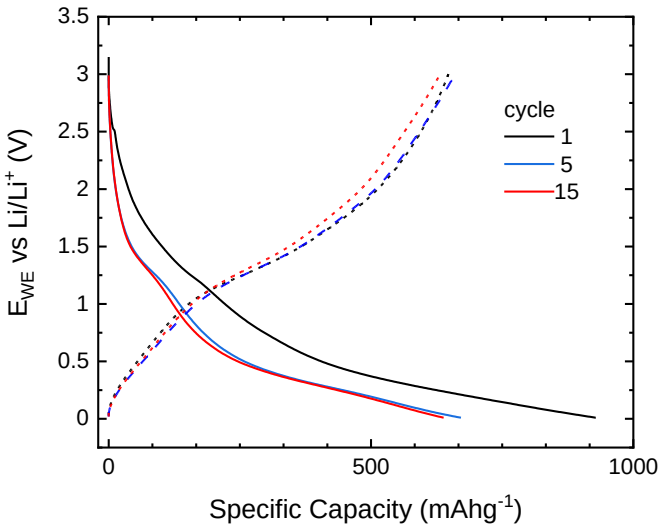

Fig. S3. Potential profile of MoO_2/C-G(M) at current densities of 100 mA g^{-1}.

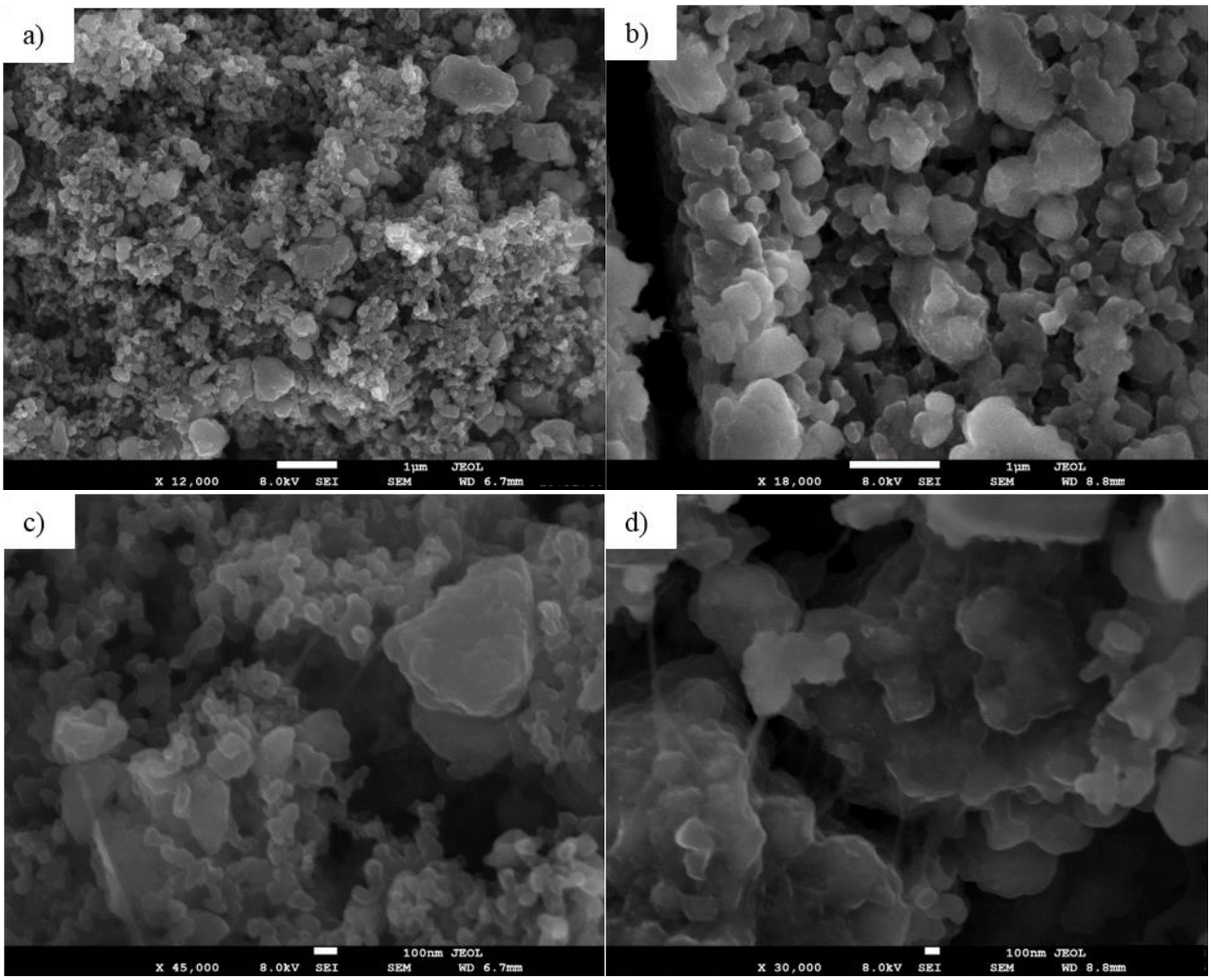

Fig. S4. Ex-situ SEM pictures of a MoO2-C/G(M) electrode after OCV (a,c) and after 60th times galvanostatically cycled at 100 mA/g (b,d).

3.3 Fabrication of 3D graphene/MoS_2 spherical heterostructure as anode material in Li-ion battery

Autoren:

K. Wenelska, V. Adam, E. Thauer, L. Singer, R. Klingeler, X. Chen und E. Mijowska

Veröffentlicht im: Front. Energy Res., Volume 10, August 2022, Sec. Electrochemical Energy Conversion and Storage.

abgedruckt mit freundlicher Genehmigung von Frontiers Media SA

L. Singer stand den elektrochemischen Messungen von V. Adam und E. Thauer beratend zur Seite und unterstützte beim Schreiben des dazugehörigen Abschnittes (Abb. 4). Die *ex situ* elektrochemischen REM-Messungen (Abb. 5) wurden von L. Singer initiiert, durchgeführt und der dazugehörige Abschnitt geschrieben.

Beitrag der Koautoren:

K. Wenelska: Erst- und Korrespondenzautorin des Artikels. K. Wenelska konzipierte und verfasste das Manuskript mit Ausnahme der Teile zu den elektrochemischen Untersuchungen und erstellte bis auf Abb. 4, 5 alle Abbildungen. Die Synthese der Materialien, die Röntgendiffraktometrie, SEM, TGA, Raman und die BET-Messung erfolgten von K. Wenelska.

E. Thauer federführend mit dem Masterstudent V. Adam: Elektrochemische Charakterisierung: Durchführung und Analyse sowie Verfassen des dazugehörigen Abschnittes (Abb.4).

R. Klingeler: stand beratend zur Seite, und unterstützte bei der Durchsicht und Überarbeitung des Manuskripts.

E. Mijowska: Projektplanung und -leitung, Beteiligung an der Interpretation und Beitrag zur Finalisierung des Manuskripts.

Alle Autoren haben das Manuskript Korrektur gelesen.

frontiers | Frontiers in Energy Research

TYPE Original Research
PUBLISHED 29 August 2022
DOI 10.3389/fenrg.2022.960786

OPEN ACCESS

EDITED BY
Fei Zhang,
The Chinese University of Hong Kong, Shenzhen, China

REVIEWED BY
Lingqi Huang,
Zhejiang University of Science and Technology, China
Tong Liu,
Hong Kong Polytechnic University, Hong Kong SAR, China

*CORRESPONDENCE
K. Wenelska,
kwenelska@zut.edu.pl

SPECIALTY SECTION
This article was submitted to Electrochemical Energy Conversion and Storage, a section of the journal Frontiers in Energy Research

RECEIVED 03 June 2022
ACCEPTED 14 July 2022
PUBLISHED 29 August 2022

CITATION
Wenelska K, Adam V, Thauer E, Singer L, Klingeler R, Chen X and Mijowska E (2022), Fabrication of 3D graphene/MoS_2 spherical heterostructure as anode material in Li-ion battery. *Front. Energy Res.* 10:960786. doi: 10.3389/fenrg.2022.960786

Fabrication of 3D graphene/MoS_2 spherical heterostructure as anode material in Li-ion battery

K. Wenelska[1]*, V. Adam[2], E. Thauer[2], L. Singer[2], R. Klingeler[2,3], X. Chen[1] and E. Mijowska[1]

[1]Szczecin Faculty of Chemical Technology and Engineering, Department of Nanomaterials Physicochemistry, West Pomeranian University of Technology, Szczecin, Poland, [2]Kirchhoff Institute of Physics, Heidelberg University, Heidelberg, Germany, [3]Centre for Advanced Materials (CAM), Heidelberg University, Heidelberg, Germany

Three-dimensional (3D) graphene-based nanocomposites have received considerable attention in both fundamental research and industrial applications, as they combine the functionalities of well-controlled nano-architectures and the integrity of bulk materials. Actually, among these materials, spherical structures are attracting more and more attention worldwide due to their excellent performance in various fields such as drug delivery, heterogeneous catalysis, encapsulation of support, and electrode materials for lithium-ion batteries. Herein, a facile route to fabricate a three-dimensional hierarchical graphene/MoS_2 nanocomposite is presented. The molecular heterostructure is derived from graphene oxide flakes and precursors of molybdenum ($(NH_4)_2Mo_7O_4{\cdot}4H_2O$) and sulfur (L-cysteine). Spherical morphology (GO/MoS_2) is obtained *via* self-assembly of the precursor. This 3D nanocomposite exhibits MoS_2-nanosheets strongly linked to graphene oxide flakes, which renders it particularly suited to exploit the conversion reaction of MoS_2 for electrochemical energy storage. When assembled into an electrode in lithium-ion batteries, as-prepared GO/MoS_2 electrodes indeed deliver a high initial charge capacity of 783 mA h g^{-1} at a current density of 100 mA/g and Coulombic efficiency of more than 96% from the second cycle on exceeding the theoretical capacity of the pristine 2D MoS_2 and graphene. Overall, the study sheds some light on the design of 3D heterostructure as a promising anode material in Li-ion batteries.

KEYWORDS

molybdenum disulfide (MoS) 2, graphene, lithium-ion batteries, electrochemistry (113), anode

Introduction

Motivated by recent rapid advancements and considering the constraints of two-dimensional (2D) graphene, the research on graphene-based materials has been directed toward the exploration of different graphene-like morphologies, with appropriate and attractive contributions from physics, chemistry, and materials science, among others (Novoselov et al., 2004; Novoselov et al., 2005; Zhu et al., 2014). The actual application

performance achieved using 2D materials is always less than that anticipated based on its ideal properties such as high surface area, high charge carrier mobility, premier mechanical strength, and excellent thermal conductivity.

Functional carbon nanospheres with controllable size, surface area, pore diameter, surface morphology, and chemical composition are an appealing topic. They reveal enhanced performance in a wide variety of applications, such as electrode materials for electrochemical energy storage, absorbents, or catalysts (Zheng et al., 2014; Wang et al., 2021). Graphene spheres and reshaped structures with good chemical and mechanical properties are among the most promising candidates to overcome the obstacles associated with 2D nanosheets. They exhibit plentiful porous channels with enhanced electrical conductivity and superb structural stability (Liu et al., 2020a; Ji et al., 2020).

Various nanostructured MoS_2 and carbon composites have triggered intensive interest due to their intriguing physicochemical properties. Hou et al. reported molybdenum disulfide nanoparticles with spherical structures prepared *via* a hydrothermal method of about 190 nm in diameter (Koroteev et al., 2021). Cui and co-workers prepared a novel carbon-coated MoS_2 nanobowl structure by a solvothermal method, followed by an annealing process (Cui et al., 2015). Zhou et al. reported on carbon nanofibers decorated with molybdenum disulfide sheets (Liu et al., 2020b). To optimize links between MoS_2 and carbon, a variety of approaches have been explored, such as exploiting the high wettability of N-doped graphitic surface and electrostatic attraction between thiomolybdate precursor anion and N-doped sites to fabricate amorphous molybdenum sulfide layers directly bound at vertical N-doped carbon nanotube forest surface (Li et al., 2014; Long et al., 2014). Further approaches have yielded MoS_2@C nanotubes (Zhang et al., 2016a), C/MoS_2/C sandwiched hollow spheres (Li et al., 2017), carbon-sheathed MoS_2 on CNT (Zhang et al., 2018), and MoS_2/N-doped carbon porous nanorods.

A particularly promising application of MoS_2/C composite heterostructures is testing them as anode material in lithium-ion batteries (LIB). While their unique and layered structure and high theoretical lithium storage capacity of 670 mA h g^{-1} imply great prospects of MoS_2 for LIB in general (Gao et al., 2013; Hu et al., 2016), semi-conductivity and large volume changes associated with the conversion reaction process are severe drawbacks for the actual application (Stephenson et al., 2014). Increasing conductivity and mechanical strength by fabrication of 3D MoS_2/C composite structures have, however, resulted in various materials with good cycling stability in LIB (Zhang et al., 2016a; Zhang et al., 2018; Li et al., 2019a) and sodium-ion batteries (David et al., 2018; Xiong et al., 2018; Li et al., 2019b). In particular, structures are expected to offer several benefits (Li et al., 2009; Wu et al., 2018). The proposed 3D heterostructures exhibit a high contact area with the electrolyte providing more active sites for de-/lithiation and favorable Li^+ transport kinetics. Also, it is proposed that the internal cross-linkage of nanosheets can prevent their aggregation and ensure good structural stability.

We present a facile and highly reproducible route to prepare a spherical 3D structure based on graphene and MoS_2 in a solution phase. MoS_2 and graphene oxide were self-assembled from structures to spherical heterostructures at a high-temperature reaction in a line-Teflon autoclave. A mechanism for reshaping the spherical structure is proposed. Furthermore, we report on the electrochemical performance of designed GO/MoS_2-based when used as electrodes in Li-ion battery.

Experimental section

Preparation of graphene oxide

The graphene oxide was synthesized by a modified Hummers method (Hummers and Offeman, 1958). Shortly, 1 g of graphite was mixed with 6 g of $KMnO_4$ in a flask. Concentrated sulfur acid and orthophosphoric acid (90:10 ml) were added to the flask and then heated to 50°C while stirring. After 24 h, the mixture was poured into ice (100 ml) and H_2O_2 (30%, 1 ml) and then filtered using a polycarbonate membrane. The solid product was washed twice with water, 10% HCl, and ethanol and, finally, vacuum-dried for 12 h.

Preparation of MoS_2 and GO-based heterostructures (GO/MoS_2)

A total of 30 mg of GO was introduced to 820 mg of ammonium molybdate tetrahydrate $(NH_4)_2Mo_7O_4{\bullet}4H_2O$ mixed with 120 ml of DI water and sonicated for 30 min. In the next step, a source of sulfur (2.4 g of l-cysteine) was added. The mixture was transferred into a Teflon-lined steel autoclave and heated to 240°C for 24 h. Afterward, the sample was washed with ethanol and dried at 60°C for 24 h.

Characterization

The crystallographic information regarding the as-synthesized samples was established by X-ray diffraction (XRD), performed using Philips X'Pert PRO X-ray diffractometer a Cu Ka radiation. The morphology of the samples was obtained using transmission electron microscopy (Tecnai F20-based at 200 kV) and scanning electron microscopy (TESCAN VEGA 3). For monitoring the microstructural changes of the GO/MoS_2-electrode after cycling, *ex situ* SEM studies were performed using a JEOL JSM-7610F scanning electron microscope. The cycled electrodes were disassembled in an Argon glove box, washed with ethylene carbonate, and then

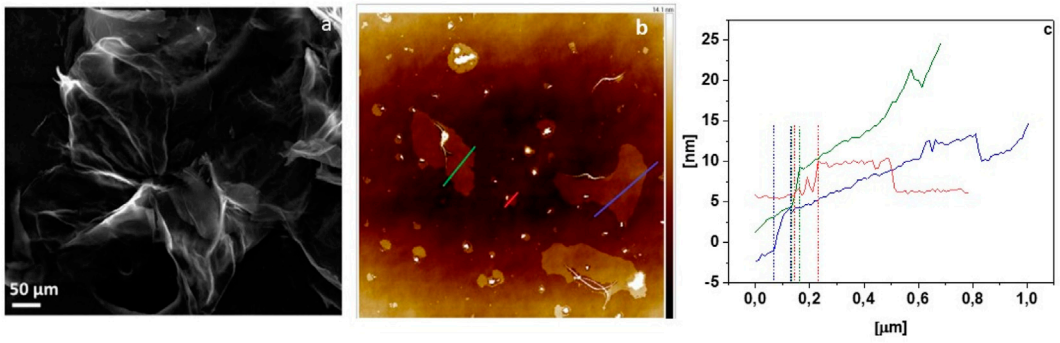

FIGURE 1
SEM image **(A)**, AFM image **(B),** and height profile **(C)** of GO flakes.

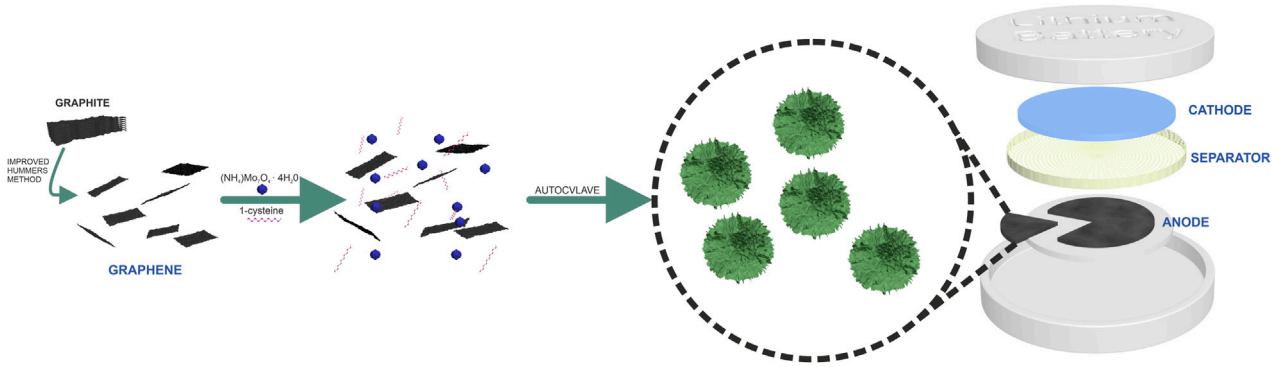

SCHEME 1
Schematic illustration of synthesis and application of GO/MoS_2.

dried overnight. Atomic Force Microscopy (AFM NTEGRA Aura (NT-MTD) microscope) was employed to obtain the thickness and number of layers of GO. Thermogravimetric analysis (TGA) was carried out using an SDT Q6000 thermoanalyzer instrument (TA Instruments Inc.) under airflow of 100 ml/min. The samples were heated from room temperature to 900°C at a linear heating rate of 10°C/min. Raman spectroscopy was applied with a microscope mode (InViaRenishaw) with a 785 nm laser. N_2 adsorption/desorption isotherms were obtained at liquid nitrogen temperature (77 K) using a Micromeritics ASAP 2010M instrument. The Brunauer–Emmett–Teller (BET) and Barrett–Joyner–Halenda (BJH) methods were adopted to calculate the specific surface area and pore size distribution.

Electrochemical studies on GO/MoS_2 have been performed by means of Swagelok-type cells (Ottmann et al., 2015) at 25°C. Working electrodes were prepared by mixing 80 wt% active material, 10 wt% carbon black (Super C65, Timcal), and 10 wt% polyvinylidene fluoride (PVDF, Sigma-Aldrich, 99%) in anhydrous 1-methyl-2-pyrrolidinone (NMP, Sigma-Aldrich, 99%) for 12 h. After pasting the slurry on a circular copper mesh of 10 mm diameter, the electrodes were vacuum dried overnight at 65°C and pressed subsequently. The procedure resulted in an active mass loading of about 4 mg cm^{-2}. The cells were assembled in an Ar-Glovebox using the as-prepared working electrodes, two layers of glass fiber (Whatman GF/D) as a separator and lithium foil pressed on a nickel plate as a counter electrode. A total of 200 µL of a 1 M $LiPF_6$ salt solution in 1:1 ethylene carbonate (EC) and dimethyl carbonate (DMC) (Merck Electrolyte LP30) was used as the electrolyte. Electrochemical measurements were performed between 0.01 and 3.0 V *versus* Li/Li^+ at a scan rate of 0.05 mV/s for cyclic voltammetry and 100 mA/g as the

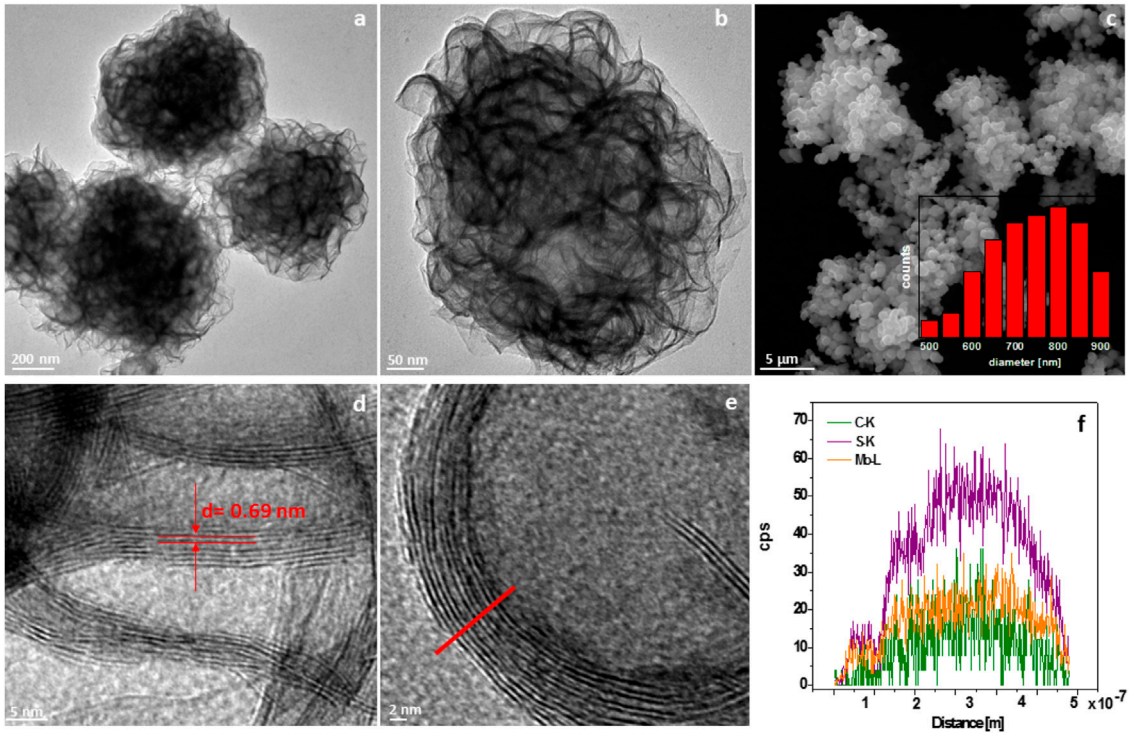

FIGURE 2
TEM images **(A,B)**, SEM image **(C)**, HRTEM images **(D,E),** and line profile **(F)** of GO/MoS_2.

current rate for galvanostatic cycling using a VMP3 multichannel potentiostat (Bio-Logic SAS). The carbon content was examined by elemental analysis using Vario MICRO Cubes (Elementar).

Results and discussion

The morphology of GO investigated by SEM and AFM microscopes is presented in Figures 1A,B, respectively. Figure 1A shows that few-layered GO was successfully obtained by a modified Hummers method. The Tapping-mode of AFM used to determine the thickness of GO (Figure 1C) implies a thickness of ~4.3–5.4 nm of the resulting sheets corresponding to 7–9 layers of GO (Wang et al., 2017).

The schematic illustration of synthesis and the application for GO/MoS_2 is present in Scheme 1.

Figure 2 shows TEM and SEM images of the obtained spherical material. Specifically, Figures 2A,B present the TEM images of structure based on GO and MoS_2 (GO/MoS_2). The SEM image (Figure 2C) reveals that the composite is in the form of irregular spheres with diameters of ~800 ± 70 nm. Further investigations by means of TEM (Figures 2A,C) allow determining the morphology in greater detail. The irregular spheres are formed by flowerlike structures. A high-resolution transmission electron microscopy image (Figures 2D,E) enables reading off the distance between the layers to be 0.69 nm which is slightly larger than the (002) plane spacing of 0.62 nm in bulk MoS_2. As shown in Figure 2F, EDS line scans taken across the wall of the sphere (see red line in Figure 2E clearly prove the elemental composition: C, Mo, and S are evenly distributed throughout the wall.

TGA studies performed in the temperature range from 25 to 1,000°C under air gas flow (Figure 3A) observed a gradual weight loss occurring in three steps. A first weight loss of 9% observed in the range of 320–400°C is associated with oxidation of MoS_2 to MoO_3. The next significant weight loss of 58% appears above 680°C and corresponds to graphite burning. After burning at around 900°C, the ash content in the ceramic cap is about 1.5%, corresponding to MoO_3.

The presence of crystalline MoS_2 in GO/MoS_2 is revealed by powder XRD as shown in Figure 3B. The diffraction peaks at 2Θ of 14°, 33°, 39°, and 59.8° can be unambiguously assigned to the (002), (100), (103), and (110) planes in hexagonal MoS_2, respectively (Zhang et al., 2016b). The (002) peak indicates the formation of the well-stacked layered structure of MoS_2 (Chhowalla and Amaratunga, 2000).

No obvious XRD peaks from a carbon phase are detected, which might be due to its lower content (<10 wt%), its rather

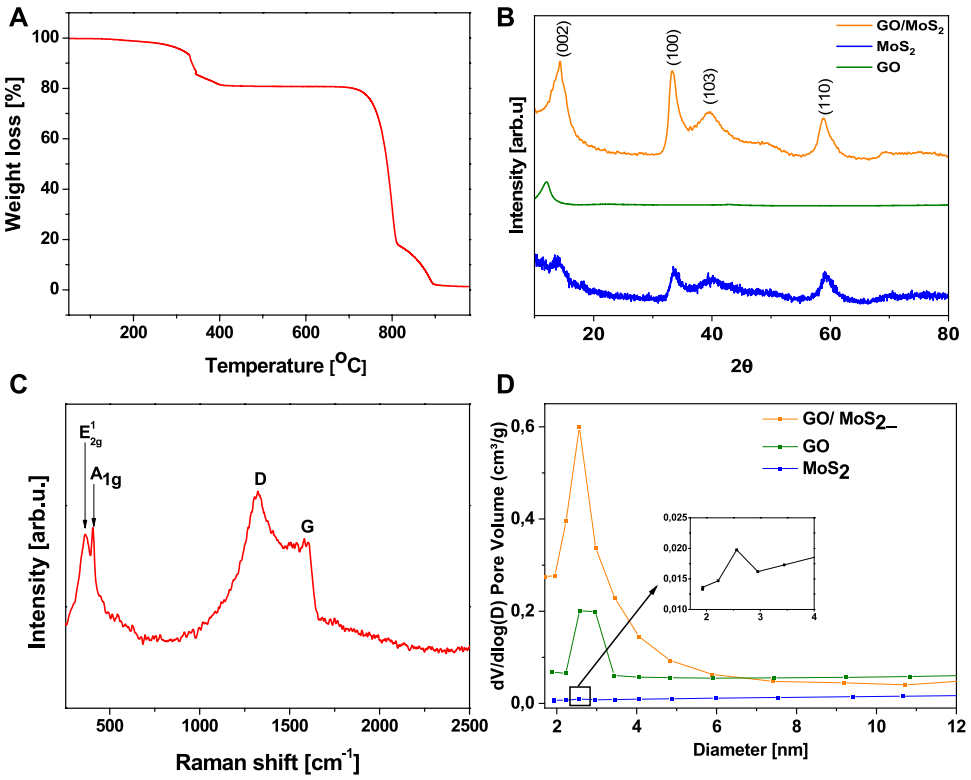

FIGURE 3
TGA profile **(A)**, XRD pattern **(B)**, Raman spectrum **(C)** and BJH pore size distribution of GO, MoS_2, and GO/MoS_2 **(D)**.

amorphous nature, and the high background signal. The presence of carbon is, however, confirmed *via* Raman spectroscopy (Figure 3C), which is one of the most sensitive techniques to characterize carbon materials. The spectrum shows the G-mode at about 1,583 cm^{-1} arising from the stretching of the C-C bond in graphitic materials, and it is common to all sp^2-carbon systems (Novoselov et al., 2004), whereas the D band at about 1,353 cm^{-1} is assigned the so-called breathing vibrations, which are mainly enabled by defects and disorder. Raman data of GO/MoS_2 present strong signals of $E_{2g}{}^1$ and A_{1g} modes of MoS_2 (Wieting and Verble, 1971).

The surface area and pore volume of GO/MoS_2 andthe intermediate products, i.e., the pure GO flakes and exfoliated MoS2 are presented on Figure 3D. The nanocomposite GO/MoS_2 features the largest surface area of 68 m^2/g. For the pure GO flakes and exfoliated MoS_2, much smaller surface areas of 10 and 11 m^2/g were observed, respectively. The pore volume in GO/MoS_2 is strongly enhanced to 0.52 cm^3/g, whereas GO and the exfoliated MoS_2 exhibit pore volumes of 0.002 and 0.01 cm^3/g, correspondingly. According to the pore distribution of the three materials calculated by means of the Barrett–Joyner–Halenda (BJH) analysis, GO/MoS_2 is characterized by a uniform mesostructured with narrow pore size distribution with a diameter of ~2.5 nm (Figure 3D).

We believe that GO flakes might serve as building blocks in the self-assembly process triggered by reducing agent L-cysteine. This effect was already observed previously by Xu et al. (2021). During this process, GO is functionalized by sulfur and molybdenum. In the next step, at the temperature of 240°C, the sulfur and molybdenum deposited on the spherical structure of GO reacted, forming MoS_2 sheets evenly distributed in the bulk heterostructure.

Electrochemical measurements

$$MoS_2 + xLi^+ + xe^- \rightarrow Li_xMoS_2 \quad (1)$$

The electrochemical properties of GO/MoS_2 are investigated by means of cyclic voltammetry (CV) and galvanostatic cycling with potential limitation (GCPL). Figure 4A shows the first, second, and tenth cycles of the CV of GO/MoS_2-based electrodes. The initial reductive sweep shows an extended region of activity

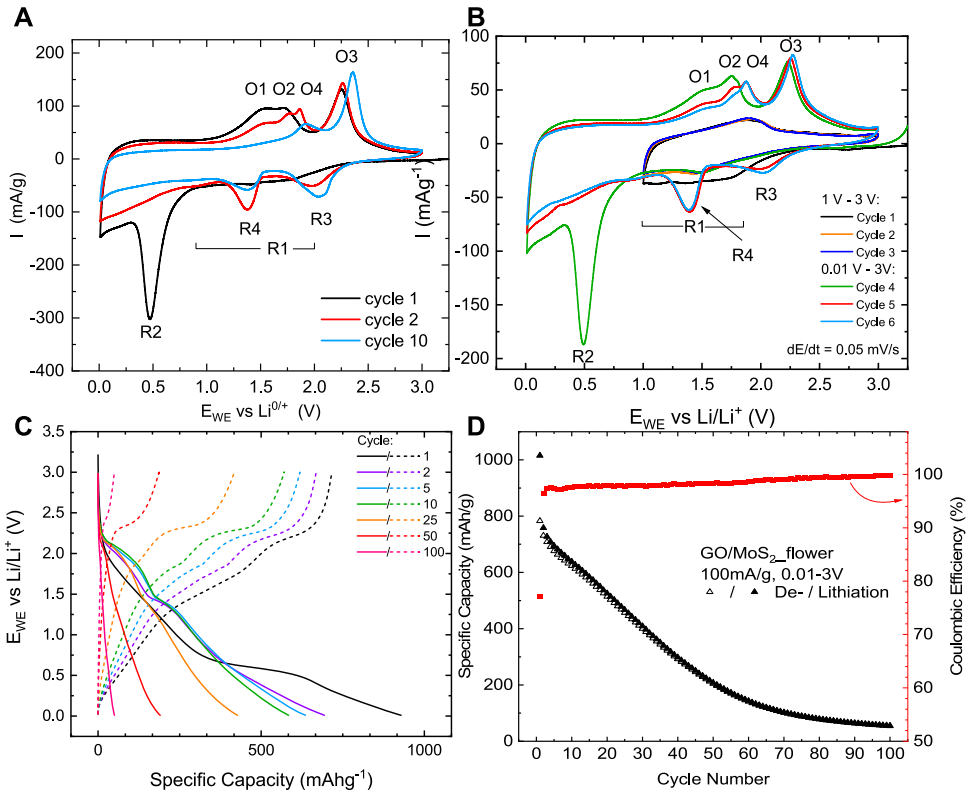

FIGURE 4
(A) Cyclic voltammograms of GO/MoS_2-type electrodes recorded at a scan rate of 0.05 mV/s, **(B)** CV of GO/MoS_2 at a scan rate of 0.05 mV/s in the potential range from 1.0 to 3 V in the first three cycles and subsequently in the potential range of 0.01 to 3 V of cycles 4, 5 and 6. **(C)** Potential profile of galvanostatic cycling of GO/MoS_2 at 100 mA/g between 0.01 and 3 V at specific cycles. **(D)** Specific charge/discharge capacities and associated Coulombic efficiencies during the first hundred cycles studied by GCPL at 100 mA/g.

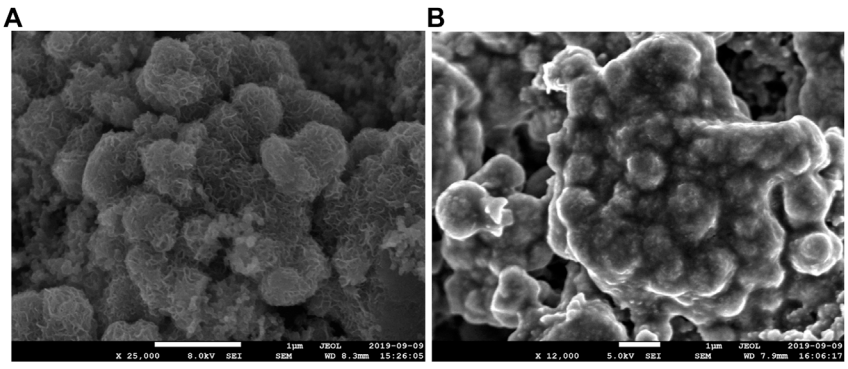

FIGURE 5
SEM images of GO/MoS_2-based electrodes before **(A)** and after 100 times, galvanostatically cycled at 100 mA/g **(B)**.

R1 in the potential range from 1 to 2 V corresponding to the intercalation of Li^+ into the layered structure of MoS_2 (Li et al., 2016) accompanied by a phase transition from trigonal prism structure (2H) into the octahedral structure (1T) (Chang and Chen, 2011; Teng et al., 2016). The absence of a well-defined redox peak agrees with the low crystallinity of MoS_2 in the material, which is also inferred from the XRD data (Figure 3B). The following peak R2 at 0.5 V represents the

subsequent conversion reaction of Li_xMoS_2 into metallic Mo and Li_2S (Li et al., 2016):

$$Li_xMoS_2 + (4 - x)Li^+ + (4 - x)e^- \rightarrow 2Li_2S + Mo. \quad (2)$$

In the first oxidative scan, a broad double peak O1/O2 around 1.5/1.7 V is visible. The corresponding reaction processes are controversially discussed in the literature. On the one hand, O1/O2 has been associated with partial oxidation of Mo, including possible re-formation of MoS_x (Yang et al., 2013; Tang et al., 2014; Wu et al., 2018). However, our CV studies in a restricted potential range (Figure 4B) indicate that peak O1 is linked to the conversion reaction (Eq. 2). The oxidative peak O3 at 2.3 V corresponds to the reversible conversion reaction of Li_2S to elemental S (Li et al., 2016):

$$Li_2S \leftrightarrow S + 2Li^+ + 2e^- \quad (3)$$

The associated reduction peak R3 emerges from the second cycle on at 2.0 V. Figure 4B shows that the reversible de-/lithiation process with the participation of the electrochemical active couple Li_2S/S is enabled by the conversion reaction (Eq. 2), which provides the reactant Li_2S. The main lithium storage mechanism for the following cycles is the reversible sulfur conversion reaction (Eq. 3). This is also visible up to the 100th cycle in the potential profiles (Figure 4C). Starting from the second cycle on, another pronounced reduction peak R4 (1.4 V) and an oxidation peak O4 (1.9 V) emerge. These peaks were also observed by Li et al. (2016), but the underlying processes remain unclear.

The cycling performance of GO/MoS_2-type electrodes studied by GCPL measurements at a current density of 100 mA/g over 100 cycles is displayed in Figure 4D. The dis-/charge capacities in the first cycle are 1,015/783 mA h/g. The capacity loss in the first cycle is mainly attributed to the partially irreversible conversion reaction (Eq. 2) and the formation of a solid electrolyte interface (SEI). Based on the reaction mechanism of Li_2S/S (Eq. 3) with a theoretical capacity of 1,675 mA h/g, for MoS_2, a maximal capacity of 672 mA h/g is expected. Initially, the measured capacities of GO/MoS_2 even exceed this value, suggesting that the complete MoS_2 is involved in the Li^+-ion storage process. The dis-/charge capacities start to decrease constantly from 758/730 mA h/g in the second cycle and stabilize at around 55 mA h/g after 100 cycles. Strong fading effects are expected to arise from mechanical stress associated with the conversion reaction and the dissolution of polysulfides (shuttle effect) during electrochemical cycling. SEM images of a GO/MoS_2-type electrode extracted after the 100th cycle (Figure 5) show that the structure seems to be destroyed after cycling. The same observation has been reported in previous works (Das et al., 2012; Ren et al., 2017a; Ren et al., 2017b), where it is attributed to aggregation of MoS_2 during electrochemical cycling. Moreover, SEM studies confirm that a coating, for example, with TiO_2 or carbon, can prevent structural degradations and thus enhances the cycling stability.

By combining spherical structured MoS_2 nanosheets with graphene oxide, a composite with a large surface area and conductive network is obtained, enabling high accessibility of the active material. The GO/MoS_2 composite initially reaches the full theoretical capacity, but degradation effects lead to poor cycle stability. Comparison with the electrochemical performance of other reported MoS_2/C-composites shows promising options to optimize the cycling stability. The GO/MoS_2 composite studied by Jiao et al. exhibits similar electrochemical properties as the composite studied at hand. N-plasma treatment improves the cycling stability. Another effective strategy to inhibit structural degradation and thus capacity fading is coating MoS_2 with carbon, for example. Das et al. showed that while uncoated MoS_2/C composite delivers a performance like that of the material presented at hand, C-coated MoS_2/C exhibits superior cycling stability. (Das et al., 2012).

Conclusion

In summary, this study presents a facile and reproducible fabrication route of 3D graphene and molybdenum disulfide heterostructure with spherical morphology and their potential application as electrode material in Li-ion batteries. The mechanism of spherical structure formation was proposed. As anode material for Li-ion batteries, the spherical GO/MoS_2 initially delivers an excellent capacity by complete conversion. The high surface area attained by the proposed heterostructure and the presence of graphene oxide, providing a conductive network, enable the high theoretical capacity of MoS_2. Therefore, we believe this material shows considerable promise from both a scientific viewpoint and practical applications.

Data availability statement

The raw data supporting the conclusion of this article will be made available by the authors without undue reservation.

Author contributions

Conceptualization, KW, EM, and RK; methodology and formal analysis, ET,XC and KW; writing–original draft preparation, KW, LS, VA, and ET; writing–review and editing, EM, RK, XC, visualization, KW, ET; funding acquisition, EM, RK, XC. All authors have read and agreed to the published version of the manuscript.

Acknowledgments

The authors are grateful for the financial support from National Science Centre Poland OPUS 10 UMO-2015/19/B/ST8/00648 and Beethoven UMO-2016/23/G/ST5/04200. This

work was partly supported by Deutsche Forschungsgemeinschaft DFG *via* KL 1824/12-1.

Conflict of interest

The authors declare that the research was conducted in the absence of any commercial or financial relationships that could be construed as a potential conflict of interest.

Publisher's note

All claims expressed in this article are solely those of the authors and do not necessarily represent those of their affiliated organizations or those of the publisher, the editors, and the reviewers. Any product that may be evaluated in this article, or claim that may be made by its manufacturer, is not guaranteed or endorsed by the publisher.

References

Chang, K., and Chen, W. (2011). l-Cysteine-Assisted synthesis of layered MoS2/graphene composites with excellent electrochemical performances for lithium ion batteries. *ACS Nano* 5 (6), 4720–4728. doi:10.1021/nn200659w

Chhowalla, M., and Amaratunga, G. A. (2000). Thin films of fullerene-like MoS 2 nanoparticles with ultra-low friction and wear. *Nature* 407, 164–167. doi:10.1038/35025020

Cui, C., Li, X., Hu, Z., Xu, J., Liu, H., and Ma, J. (2015). Growth of MoS2@C nanobowls as a lithium-ion battery anode material. *RSC Adv.* 5, 92506–92514. doi:10.1039/C5RA17992K

Das, S. K., Mallavajula, R., Jayaprakash, N., and Archer, L. A. (2012). Self-assembled MoS2–carbon nanostructures: Influence of nanostructuring and carbon on lithium battery performance. *J. Mat. Chem.* 22 (26), 12988. doi:10.1039/C2JM32468G

David, L., Bhandavat, R., and Singh, G. (2018). MoS2/graphene composite paper for sodium-ion battery electrodes. *ACS Nano* 8 (2), 1759–1770. doi:10.1021/nn406156b

Gao, M.-R., Xu, Y.-F., Jiang, J., and Yu, S.-H. (2013). Nanostructured metal chalcogenides: Synthesis, modification, and applications in energy conversion and storage devices. *Chem. Soc. Rev.* 42 (7), 2986–3017. doi:10.1039/C2CS35310E

Hu, Z., Liu, Q., Sun, W., Li, W., Tao, Z., Chou, S.-L., et al. (2016). MoS2 with an intercalation reaction as a long-life anode material for lithium ion batteries. *Inorg. Chem. Front.* 3 (4), 532–535. doi:10.1039/C5QI00237K

Hummers, W. S., and Offeman, R. E. (1958). Preparation of graphitic oxide. *J. Am. Chem. Soc.* 80, 1339. doi:10.1021/ja01539a017

Ji, S., Kim, S. K., Song, W., Yoon, Y., Myung, S., Lim, J ., et al. (2020). Extraordinary lithium storage capacity and lithiation mechanism of partially amorphous molybdenum sulfide on chemically exfoliated graphene. *Electrochimica Acta* 354, 136636. doi:10.1016/j.electacta.2020.136636

Koroteev, V. O., Stolyarova, S. G., Kotsun, A. A., Modin, E., Makarova, A. A., Shubin, Y., et al. (2021). Nanoscale coupling of MoS2 and graphene via rapid thermal decomposition of ammonium tetrathiomolybdate and graphite oxide for boosting capacity of Li-ion batteries. *Carbon* 173, 194–204. doi:10.1016/j.carbon.2020.10.097

Li, H., Li, W., Ma, L., Chen, W., and Wang, J. (2009). Electrochemical lithiation/delithiation performances of 3D flowerlike MoS2 powders prepared by ionic liquid assisted hydrothermal route. *J. Alloys Compd.* 471 (1-2), 442–447. doi:10.1016/j.jallcom.2008.03.133

Li, D. J., Maiti, U. N., Lim, J., Choi, D. S., Lee, W. J., Oh, Y., et al. (2014). Molybdenum sulfide/N-doped CNT forest hybrid catalysts for high-performance hydrogen evolution reaction. *Nano Lett.* 14 (3), 1228–1233. doi:10.1021/nl404108a

Li, Z., Liu, S., Vinayan, B. P., Zhao-Karger, Z., Diemant, T., Wang, K., et al. (2019). Hetero-layered MoS2/C composites enabling ultrafast and durable Na storage. *Energy Storage Mater.* 21, 115–123. doi:10.1016/j.ensm.2019.05.042

Li, Z., Ottmann, A., Sun, Q., Kast, A. K., Wang, K., Zhang, T., et al. (2019). Hierarchical MoS 2–carbon porous nanorods towards atomic interfacial engineering for high-performance lithium storage. *J. Mat. Chem. A Mat.* 7 (13), 7553–7564. doi:10.1039/C8TA12293H

Li, Z., Ottmann, A., Thauer, E., Neef, C., Sai, H., Sun, Q., et al. (2016). A facile synthesis method and electrochemical studies of a hierarchical structured MoS2/C-nanocomposite. *RSC Adv.* 6 (79), 76084–76092. doi:10.1039/C6RA11214E

Li, Z., Ottmann, A., Zhang, T., Sun, Q., Meyer, H.-P., Vaynzof, Y., et al. (2017). Preparation of hierarchical C@MoS2@C sandwiched hollow spheres for lithium ion batteries. *J. Mat. Chem. A Mat.* 5 (8), 3987–3994. doi:10.1039/C6TA10439H

Liu, C. L., Bai, Y., Zhao, Y., Yao, H., and Pang, H. (2020). MoS2/graphene composites: Fabrication and electrochemical energy storage. *Energy Storage Mater.* 33, 470–502. doi:10.1016/j.ensm.2020.06.020

Liu, Y. M., Zhang, C. L., Cui, J. H., and Wei, W. (2020). Graphene enwrapped molybdenum disulfide for long life rechargeable batteries. *Mat. express* 10, 1358–1363. doi:10.1166/mex.2020.1748

Long, F., Chen, Y., Wu, C. H., Wang, J. L., Mo, S. Y., Zou, Z. G., et al. (2014). Unique three-dimensional hierarchical heterogeneous MoS2/graphene structures as a high-performance anode material for lithium-ion batteries. *IONICS* 27, 1977–1986. doi:10.1007/s11581-021-03936-y

Novoselov, K. S., Geim, A. K., Morozov, S. V., Jiang, D., Zhang, Y., Dubonos, S. V., et al. (2004). Electric field effect in atomically thin carbon films. *Science* 306, 666–669. doi:10.1126/science.1102896

Novoselov, K. S., Jiang, D., Schedin, F., Booth, T. J., Khotkevich, V. V., Morozov, S. V., et al. (2005). Two-dimensional atomic crystals. *Proc. Natl. Acad. Sci. U. S. A.* 102, 10451–10453. doi:10.1073/pnas.0502848102

Ottmann, A., Zakharova, G. S., Ehrstein, B., and Klingeler, R. (2015). Electrochemical performance of single crystal belt-like NH4V3O8 as cathode material for lithium-ion batteries. *Electrochim. Acta* 174, 682–687. doi:10.1016/j.electacta.2015.06.027

Ren, W., Zhang, H., Guan, C., and Cheng, C. (2017). Ultrathin MoS2Nanosheets@Metal organic framework-derived N-doped carbon nanowall arrays as sodium ion battery anode with superior cycling life and rate capability. *Adv. Funct. Mat.* 27 (32), 1702116. doi:10.1002/adfm.201702116

Ren, W., Zhou, W., Zhang, H., and Cheng, C. (2017). ALD TiO2-coated flower-like MoS2 nanosheets on carbon cloth as sodium ion battery anode with enhanced cycling stability and rate capability. *ACS Appl. Mat. Interfaces* 9 (1), 487–495. doi:10.1021/acsami.6b13179

Stephenson, T., Li, Z., Olsen, B., and Mitlin, D. (2014). Lithium ion battery applications of molybdenum disulfide (MoS2) nanocomposites. *Energy Environ. Sci.* 7, 209–231. doi:10.1039/C3EE42591F

Tang, Y., Wu, D., Mai, Y., Pan, H., Cao, J., Yang, C., et al. (2014). A two-dimensional hybrid with molybdenum disulfide nanocrystals strongly coupled on nitrogen-enriched graphene via mild temperature pyrolysis for high performance lithium storage. *Nanoscale* 6 (24), 14679–14685. doi:10.1039/C4NR05519E

Teng, Y., Zhao, H., Zhang, Z., Li, Z., Xia, Q., Zhang, Y., et al. (2016). MoS2 nanosheets vertically grown on graphene sheets for lithium-ion battery anodes. *ACS Nano* 10 (9), 8526–8535. doi:10.1021/acsnano.6b03683

Wang, J., Ma, F., and Sun, M. (2017). Graphene, hexagonal boron nitride, and their heterostructures: Properties and applications. *RSC Adv.* 7, 16801–16822. doi:10.1039/C7RA00260B

Wang, W. W., Guo, S. Z., Zhang, P. L., Liu, J. Z., Zhou, C. C., Zhou, J. J., et al. (2021). Interlayer expanded MoS2/nitrogen-doped carbon hydrangea nanoflowers assembled on nitrogen-doped three-dimensional graphene for high-performance lithium and sodium storage. *ACS Appl. Energy Mat.* 4, 5775–5786. doi:10.1021/acsaem.1c00609

Wieting, T., and Verble, J. (1971). Infrared and Raman studies of long-wavelength optical phonons in hexagonal MoS2. *Phys. Rev. B* 3, 4286–4292. doi:10.1103/PhysRevB.3.4286

Wu, M., Xia, S., Ding, J., Zhao, B., Jiao, Y., Du, A., et al. (2018). Growth of MoS2 nanoflowers with expanded interlayer distance onto N-doped graphene for reversible lithium storage. *ChemElectroChem* 5 (16), 2263–2270. doi:10.1002/celc.201800520

Xiong, P., Ma, R., Sakai, N., Nurdiwijayanto, L., and Sasaki, T. (2018). Unilamellar metallic MoS2/graphene superlattice for efficient sodium storage and hydrogen evolution. *ACS Energy Lett.* 3 (4), 997–1005. doi:10.1021/acsenergylett.8b00110

Xu, M., Wu, T., Qi, J., Zhou, D., and Xiao, Z. (2021). V2C/VO2 nanoribbon intertwined nanosheet dual heterostructure for highly flexible and robust lithium–sulfur batteries. *J. Mat. Chem. A Mat.* 9, 21429–21439. doi:10.1039/D1TA05693J

Yang, L., Wang, S., Mao, J., Deng, J., Gao, Q., Tang, Y., et al. (2013). Hierarchical MoS(2)/polyaniline nanowires with excellent electrochemical performance for lithium-ion batteries. *Adv. Mat.* 25 (8), 1180–1184. doi:10.1002/adma.201203999

Zhang, F., Tang, Y., Liu, H., Ji, H., Jiang, Ch., Zhang, J., et al. (2016). Uniform incorporation of flocculent molybdenum disulfide nanostructure into three-dimensional porous graphene as an anode for high-performance lithium ion batteries and hybrid supercapacitors. *ACS Appl. Mat. Interfaces* 8, 4691–4699. doi:10.1021/acsami.5b11705

Zhang, X., Li, X., Liang, J., Zhu, Y., and Qian, Y. (2016). Synthesis of MoS2@ C nanotubes via the kirkendall effect with enhanced electrochemical performance for lithium ion and sodium ion batteries. *Small* 12 (18), 2484–2491. doi:10.1002/smll.201600043

Zhang, Z., Zhao, H., Teng, Y., Chang, X., Xia, Q., Li, Z., et al. (2018). Carbon-sheathed MoS2 nanothorns epitaxially grown on CNTs: Electrochemical application for highly stable and ultrafast lithium storage. *Adv. Energy Mat.* 8 (7), 1700174. doi:10.1002/aenm.201700174

Zheng, L. X., O'Connell, M. J., Doorn, S. K., Liao, X. Z., Zhao, Y. H., Akhadov, E. A., et al. (2014). Ultralong single-wall carbon nanotubes. *Nat. Mat.* 3, 673–676. doi:10.1038/nmat1216

Zhu, J., Yang, D., Yin, Z., Yan, Q., and Zhang, H. (2014). Graphene and graphene-based materials for energy storage applications. *Small* 10, 3480–3498. doi:10.1002/smll.201303202

Kapitel 4 Lithiumreiche Antiperowskite

4.1 Lithium-rich antiperovskite $(Li_2Fe)SeO$: a high-performance cathode material for lithium-ion batteries

Autoren:

M.A.A. Mohamed, L. Singer, H. Hahn, D. Djendjur, A. Özkara, E. Thauer, I.G. Gonzalez-Martinez, M. Hantusch, B. Büchner, S. Hampel, R. Klingeler und N. Grässler

Veröffentlicht in: Journal of Power Sources, Volume 558, February 2023, 232547.

abgedruckt mit freundlicher Genehmigung des Elsevier Verlags

L. Singer ist zusammen mit M.A.A. Mohamed (IFW Dresden) zu gleichen Teilen Erstautor des Artikels. L. Singer hat das Kapitel über die elektrochemischen Eigenschaften sowie zusammen mit M.A.A. Mohamed den Abstract, die Einleitung, die Zusammenfassung und den Abschnitt über die physikalischen Eigenschaften verfasst. L. Singer erstellte die Abbildungen 6-9, S3 und S5, S6 sowie die grafische Zusammenfassung und führte folgende experimentelle Arbeiten und Analysen durch:

- Analyse der Transmissionselektronenmikroskopie (TEM) und Röntgenphotoelektronenspektroskopie (XPS) (zusammen mit M.A.A. Mohamed)
- Magnetische Messungen: Durchführung und Analyse
- Elektrochemische Untersuchungen (CV, GCPL, PEIS): Durchführung und Analyse entweder alleine oder zusammen mit den von ihm angeleiteten Bachelorstudenten A. Özkara, H. Hahn oder dem Masterstudent D. Djendjur.

Beitrag der Koautoren:

M.A.A. Mohamed: Synthese der Materialien sowie die XRD, DTA, SEM-Messungen (Abb.1-5 sowie S1, S2, S4). Beschreibung der Materialsynthese im Manuskript sowie zusammen mit L. Singer den Abstract, die Einleitung, die Zusammenfassung und den Abschnitt über die physikalischen Eigenschaften.

I.G. Gonzalez-Martinez: TEM-Messungen (Abb. 4).

M. Hantusch: XPS-Messungen (Abb. 5,S4).

H. Hahn, D. Djendjur, A. Özkara: Unter der Anleitung von L. Singer Mitarbeit an den elektrochemischen Messungen (Abb. 6-9, S3, S5-7).

E. Thauer, B. Büchner, S. Hampel: Projektplanung, Beratung bei den Experimenten bzw. Diskussion der Ergebnisse

R. Klingeler und N. Grässler: Projektplanung und -leitung, Beteiligung an der Interpretation und Beitrag zur Finalisierung des Manuskriptes.

Korrespondenz mit den Gutachtern: L. Singer, R. Klingeler.

Alle Autoren haben das Manuskript Korrektur gelesen.

Journal of Power Sources 558 (2023) 232547

Contents lists available at ScienceDirect

Journal of Power Sources

journal homepage: www.elsevier.com/locate/jpowsour

Lithium-rich antiperovskite (Li_2Fe)SeO: A high-performance cathode material for lithium-ion batteries

M.A.A. Mohamed [a,c,1], L. Singer [b,1], H. Hahn [b], D. Djendjur [b], A. Özkara [b], E. Thauer [b], I.G. Gonzalez-Martinez [a], M. Hantusch [a], B. Büchner [a], S. Hampel [a], R. Klingeler [b,*], N. Gräßler [a,*]

[a] Leibniz Institute for Solid State and Materials Research Dresden e.V., 01069 Dresden, Germany
[b] Kirchhoff Institute for Physics, Heidelberg University, 69120 Heidelberg, Germany
[c] Department of Physics, Faculty of Science, Sohag University, 82524 Sohag, Egypt

HIGHLIGHTS

- Synthesis of antiperovskite (Li_2Fe)SeO using one-step solid-state method.
- Demonstrating its potential as Lithium ion battery cathode material.
- High capacity of ~150 mAh g^{-1}at 0.1 C and high current capability of 100 mAh g^{-1}at 1 C.
- (Li_2Fe)SeO displays outstanding cycling stability and storage per formula unit.

GRAPHICAL ABSTRACT

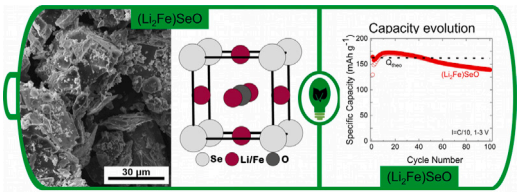

ARTICLE INFO

Keywords:
Antiperovskites
Lithium-ion battery
Lithium-rich cathode material

ABSTRACT

Lithium-rich antiperovskite cathode materials with cationic and anionic redox bi-functionality are promising candidates for lithium-ion batteries (LIB) with high energy density. Here, we report the synthesis of antiperovskite (Li_2Fe)SeO by means of an one-step solid-state method which results in phase pure material consisting of predominantly micrometer-sized particles. Thermodynamic investigations confirm high thermal stability of (Li_2Fe)SeO up to 1200 °C without any indication of phase decomposition. Electrochemical studies of (Li_2Fe)SeO-based cathodes show a multi-step redox process involving electrochemical activity of cationic Fe and anionic Se. Rate capability tests yield a discharge capacity of 150 mAh g^{-1} and 100 mAh g^{-1} at 0.1 C and 1 C, respectively. In-depth kinetic analyses by *in-situ* electrochemical impedance spectroscopy indicate a considerable structural change primarily in the first cycle, however, the structure stabilizes afterwards in the following cycles. Accordingly, we observe superior high cycling stability. Upon cycling, the material displays only a slight capacity fading while still delivering 140 mAh g^{-1}after 100 cycles at 0.1 C. Our findings highlight the high performance and compelling cycling stability of (Li_2Fe)SeO as cathode material in lithium-ion batteries.

1. Introduction

In current commercial cathode materials, maximum capacity is limited to one or less electron transfer per formula unit [1]. The class of lithium-rich cathode materials promises to surpass this barrier as they exhibit multi-electron redox activity [2]. In general, multi-electron charge transfer can be obtained by (i) multi-stage redox processes of transition metal cations or (ii) the coupled redox processes of transition metal cations and anions [1,3]. One class that can exhibit such advantage are Li-rich oxides [2]. However, storing more than one electron per formula unit is difficult to actually implement in materials

* Corresponding authors.
E-mail addresses: klingeler@kip.uni.heidelberg.de (R. Klingeler), n.graessler@ifw-dresden.de (N. Gräßler).
[1] Both authors contributed equally.

https://doi.org/10.1016/j.jpowsour.2022.232547
Received 6 May 2022; Received in revised form 14 November 2022; Accepted 17 December 2022
Available online 5 January 2023
0378-7753/

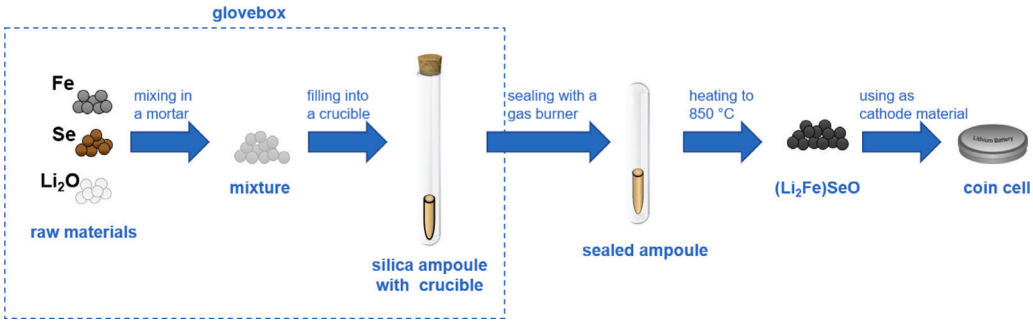

Fig. 1. Schematic diagram of the $(Li_2Fe)SeO$ synthesis.

in practice due to the redox activity of oxygen at high potentials which leads to irreversible O_2 release and decomposition of current commercial electrolytes [4,5]. Therefore, the pursuit of further, more convenient Li-rich cathode materials without such disadvantage is high. Recently, a novel class of Li-rich antiperovskite-structured cathode materials with the general composition $(Li_2TM)ChO$ (TM = Fe, Mn, Co :Ch = S, Se) was reported [6,7]. This class circumvents the problems appearing in Li-rich oxides by the lower redox potentials of the anionic sulfides/selenides [8]. In fact, their reversible multi-electron storage originates from the coupled redox activity of transition metal cation and the sulfide/selenide anion [9]. First measurements on the antiperovskite cathode material $(Li_2Fe)SO$ already proved its promising electrochemical performance by showing discharge capacity of ~285 mAh g^{-1} at 0.1 C and high rate capability (~200 mAh g^{-1} at 1 C) when cycled between 1.2 and 3 V [9]. However up to now only a limited cycling stability of the antiperovskite cathodes was achieved [9]. Some progress was made by the partial anionic substitution of S^{2-} with Se^{2-}, which was found to tune the cycling stability and the working potential in the $(Li_2Fe)S_{1-x}Se_xO$ series (x = 0.1–0.9) [10]. The antiperovskite-structured cathode material $(Li_2Fe)SeO$ was initially electrochemically characterized by Lai et al. [6] by means of a few-cycle experiment using homemade plastic bag batteries (vs. graphite). However, only modest electrochemical properties have been reported, including the initial discharge capacity of ~120 mAh g^{-1} at ~0.18 C and in particular pronounced capacity fading to 98 mAh g^{-1} after only 5 cycles (~18 percent capacity fade) [6].

Here, we report on the actually outstanding performance that $(Li_2Fe)SeO$ can display. We show that $(Li_2Fe)SeO$-based electrodes exhibit an initial specific discharge capacity of 164 mAh g^{-1} at 0.1 C. During cycling the here presented $(Li_2Fe)SeO$ exhibits only a slight capacity loss leading to still ~140 mAh g^{-1}after 100 cycles. Furthermore, even at the rate of 1 C, $(Li_2Fe)SeO$ delivers a reversible capacity of around 100 mAh g^{-1}. These findings highlight the great potential of $(Li_2Fe)SeO$ as a cathode material for LIB, especially in terms of cycling stability, and promotes further work on Se containing antiperovskite cathode materials.

2. Experimental section

2.1. Synthesis

The material $(Li_2Fe)SeO$ was prepared by a solid-state reaction method. For this process, stoichiometric amounts of Li_2O, Fe and Se (Alfa Aesar) were mixed in an Ar-filled glovebox (MBraun, Germany, H_2O and O_2 levels < 1 ppm), and filled in a corundum crucible (Aliaxis, Frialit-Degussit, AL23). The crucible was placed inside a silica ampoule (QSILAG; Quarzschmelze, Ilmenau) and temporarily closed with a rubber stopper. Outside the glovebox, the ampoule was evacuated, filled with Ar to adjust the pressure to 200 mbar, and finally melt-sealed. The sealed ampoule was heated to 850 °C (heating rate: 50 °C/h) in a furnace and held at this temperature for 3 h. Afterwards the ampoule was quenched in water to prevent the formation of other phases such as transition metal oxides and selenides [6]. Finally, the ampoule was opened inside the glovebox and the final product was used for further characterization and measurements. A schematic diagram showing the synthesis procedure is displayed in Fig. 1

2.2. Characterization

X-ray diffraction (XRD) studies were performed using a STADI P diffractometer (STOE) in Debye–Scherrer geometry using Co $K_{\alpha 1}$ radiation (λ = 1.79026 Å) and a Mythen 1K detector (Dectris). The sample was placed into glass capillary inside the glove box and melt-sealed outside in order to prevent any air exposure during the XRD investigations. Inductively coupled plasma optical emission spectroscopy (ICP-OES) (iCAP 6500 Duo View, Fa. Thermo Fisher Scientific GmbH) was used for elemental analysis. Differential thermal analysis (DTA) up to 1200 °C was performed by means of a Setaram DTA92-2400 (alumina container) under helium atmosphere (heating rate: 10 °C/min). Scanning electron microscopy (Nova-NanoSEM 200) coupled with energy dispersive spectroscopy (EDS) was used to investigate the morphology and composition of the compound. X-ray photoelectron spectroscopy (XPS) was performed with a PHI 5600 spectrometer (Physical Electronics) equipped with a hemispherical analyzer with 29.35 eV pass energy for high resolution spectra, using monochromatic Al-K_α radiation (200 W). To prevent any air exposure the sample was transferred in a special transfer chamber. The estimated spot size on the sample is about 0.4 mm. To avoid charging effects, an electron gun is used as a neutralizer. All binding energies refer to the Li 1s peak at 54.0 eV. Transmission Electron Microscopy (TEM) studies were conducted on a FEI Titan 300-80 TEM with third-order spherical aberration correction. The sample was loaded by direct contact onto Cu 300 mesh TEM grids (Agar) and holey carbon film (Plano). High-resolution imaging was performed at 300 kV.

2.3. Electrochemical studies

Electrochemical measurements were carried out using a VMP3 potentiostat (BioLogic) at 25 °C. Slurry preparation as well as cell assembly have been performed in an Argon-filled glovebox with controlled humidity and oxygen concentration. Working electrodes were prepared by mixing the active material 70%wt, carbon black (TIMCAL SUPER C65) 15%wt, and 15%wt polyvinylidene fluoride (PVDF) in dry isopropanol using a Fisherbrand Model 120 before spreading the resulting mixture onto a (Ø = 10 mm) aluminum mesh (thickness 0.125 mm). Afterwards the obtained electrodes were dried over night in vacuum, pressed and dried again. The mass loading ranged between 3 and 4.5 mg cm^{-2}. For assembling the cells, glass fiber (Whatman GF/D, 675 μm thickness) was used as the separator, pure lithium metal foil (Aldrich) as the counter electrode and 1M $LiPF_6$ in a mixture of ethylene carbonate and dimethyl carbonate (1:1 by weight) as electrolyte [11]. Cyclic voltammetry (CV) and galvanostatic cycling measurements

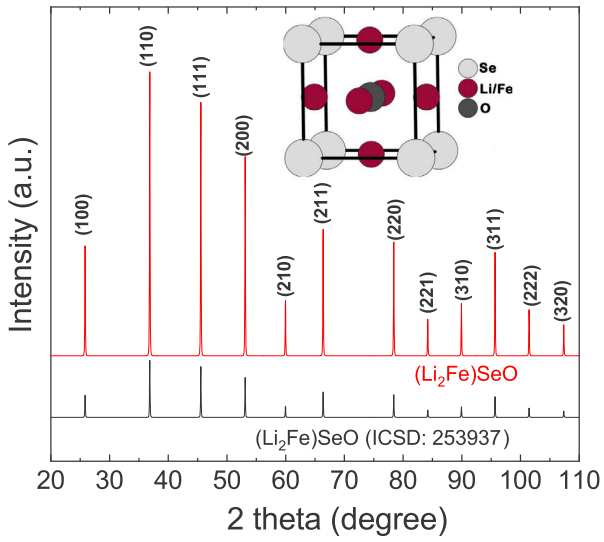

Fig. 2. XRD pattern of $(Li_2Fe)SeO$ (top) with the corresponding reference pattern (ICSD: 253937) [6] and a schematic image of the crystallographic unit cell.

with potential limitation (GCPL) in the voltage range 1 to 3 V were performed in coin cell housing. A 3-electrode PAT-Cell from EL-CELL was used for potentiostatic electrochemical impedance measurements (PEIS). For the PEIS measurements, a small perturbation of 10 mV was applied. In order to ensure the time invariance of the measurement as well as a stable condition, an OVC (open circuit voltage) was performed before each PEIS measurement. Note, the theoretical capacity of $(Li_2Fe)SeO$ for the remove/introduce of 1 Li^+ is 162.8 mAh $g^{-1}$and we attribute the rate 1C to the charge/discharge current required to remove/introduce 1 Li^+ from/into the antiperovskite material within one hour.

3. Results and discussion

Fig. 2 shows the XRD pattern obtained on $(Li_2Fe)SeO$ produced by the solid state reaction method. All diffraction peaks can be identified at the expected Bragg positions for the cubic antiperovskite structure with the *Pm-3m* space group. The XRD pattern does not indicate any additional impurities within its detection limit. The XRD analysis (see Supplemental Information) suggests high crystallinity of the material and shows a large crystallite size combined with a low lattice strain. We obtain the lattice parameter $a = 4.0028(6)$ Å which matches well with the reported value (4.0025 Å) [6].

The ICP-OES analysis of the sample (see Table S1) shows a good agreement of the calculated elemental composition with the nominal composition of the material. Two consecutive cycles of DTA measurements confirm the congruent melting of $(Li_2Fe)SeO$ without indication of intermediate phase decomposition/transition (see Fig. S2). Note, that the absence of additional thermal processes in addition to main melting/crystallization further confirms high purity of the obtained sample. The DTA data imply a melting peak temperature at 1037(2) °C and a crystallization peak at 1008(2) °C. This thermal behavior suggests higher thermal stability of $(Li_2Fe)SeO$ compared to $(Li_2Fe)SO$ [6] and coincides well with the reported thermal trend for the series $(Li_2Fe)S_{1-x}Se_xO$ [10]. The better thermal stability may be attributed to the higher tolerance factor (~0.897) of $(Li_2Fe)SeO$ compared to $(Li_2Fe)SO$ (~0.85) [6,12].

3.1. Physicochemical properties

SEM images of $(Li_2Fe)SeO$ (see Fig. 3(a) and (e)) show that the sample exhibits non-uniform particle shape with large size distribution. The particle size ranges from several tens of micrometers up to submicrometer. Due to the high ionic conductivity of antiperovskites [13], even micrometer-sized $(Li_2Fe)SeO$ particles can be used in actual electrodes for lithium-ion batteries. A large particle size distribution in turn allows for a high tapping density, which is one of the key criteria for a positive industrial outlook [14]. In addition, a homogeneous distribution of Fe, Se and O elements is observed from SEM-EDS mapping images (as seen in Fig. 3 (b–d)), while Li could not be detected by EDS due to its low radiation energy.

High-resolution TEM images (Fig. 4(a) and (b)) provide further insight into the material under study. The images show lattice fringes of the atomic planes of only few crystalline domains. However, the thickness of the shown particle in some areas causes significant overlapping of the lattice fringes of some domains stacked along the optical axis. The average d-spacing for the (110) plane is found to be ~0.301(1) nm which is larger than the expected value from XRD (0.28309(2) nm).

This discrepancy may be attributed to the effect of dislocations and lattice strain on the lattice fringes as observed in the inverse Fourier Transformation FFT in the inset of Fig. 4(a) and (b), which leads to a slight error in the estimation of the d-spacing value from the TEM images. In contrast, the average d-spacing for (210) is found to be close (0.184(7) nm) to the expected XRD value (0.178992(9) nm). Regions with unexpectedly large d-spacings (0.56(3) nm) appeared in a few particles. Such regions may suggest the presence of minor FeSe or $FeSe_{1-x}$ impurities. Due to their characteristic magnetic properties [15], from magnetization data (see Fig. S3 in the Supplemental Information) we infer the presence of small amounts of β–$Fe_{1-x}Se$ with $x \approx 0.25$ ($\lesssim$1 w%) and possibly γ–$Fe_{1-x}Se$ with $x \approx 0.13$. The invisibility of such impurities in the XRD pattern indicates their negligible content.

XPS analyses were performed to investigate the composition and chemical states of the as prepared $(Li_2Fe)SeO$. Fig. S4 shows the full XPS spectrum with clear photoemission peaks for the expected elements. The large background observed at high binding energies is attributed to the increased effect of inelastic photoemission [16]. To get a deeper insight into the oxidation states present, Fig. 5 displays the high resolution spectra of Li 1s, Se 3d and Fe 3p (a) and Fe (b). The similar binding energies of Li 1s, Se 3d and Fe 3p [17] and the observed strong merging of them into only one clearly visible peak (see Fig. 5(a)), impedes a precise quantification of the surface composition. This is especially true since the relative sensitivity factor of Fe 3p is 30 times higher than Li 1s which further complicates the separation process [18]. Nevertheless, the Li 1s peak at 54 eV was adjusted as reference for charge correction which can result in underestimation of the observed binding energies compared to the real ones. The Fe 2p high resolution spectrum (Fig. 5(b)) shows two distinct features due to spin–orbit splitting corresponding to Fe $2p_{3/2}$ and Fe $2p_{1/2}$, respectively [18,19]. The clear appearance of satellite feature for Fe $2p_{1/2}$ combined with multiple splitting of the Fe $2p_{1/2}$ and $2p_{3/2}$ suggests a high-spin state for Fe^{2+} as reported previously for $(Li_2Fe)SO$ based on Moessbauer spectroscopy [9,20]. To further analyze the selenium oxidation state present in our $(Li_2Fe)SeO$ sample, Fig. 5(c) displays the high-resolution Se 3p spectrum. Spin–orbit coupling leads to a splitting of the Se 3p peak into two peaks at 160.12 eV ($3p_{3/2}$) and 165.75 eV ($3p_{1/2}$). The observed binding energies of Se $3p_{3/2}$ and Se $3p_{1/2}$ are close to the values reported for Se^{2-} in other compounds such as CdSe [21] and ZnSe [22]. The slight difference between the here obtained binding energies of Se 3p compared to the values of CdSe and ZnSe can be attributed to the different chemical environment. This finding confirms the existence of Se with oxidation state −2 in $(Li_2Fe)SeO$. Accordingly, the XPS results support the successful formation of $(Li_2Fe)SeO$ with high spin Fe^{2+}.

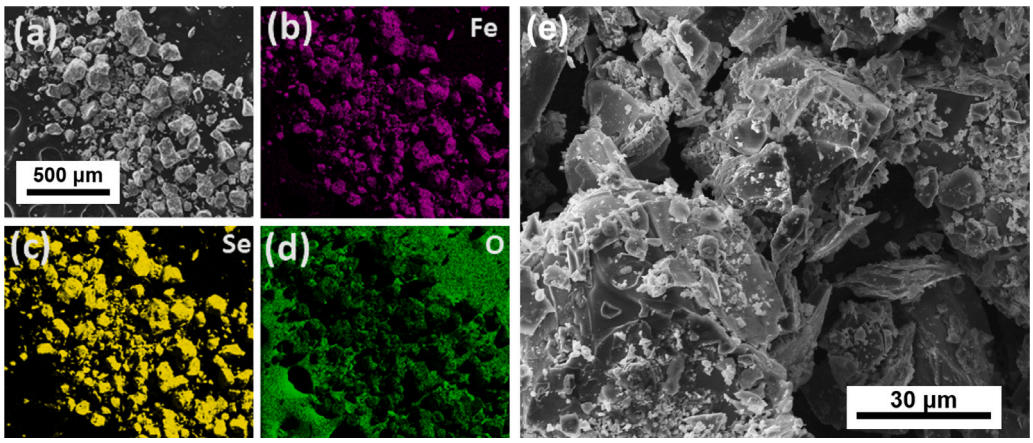

Fig. 3. SEM images of $(Li_2Fe)SeO$ at low (a) and high (e) magnifications as well as (b–d) the EDS-mapping images corresponding to (a).

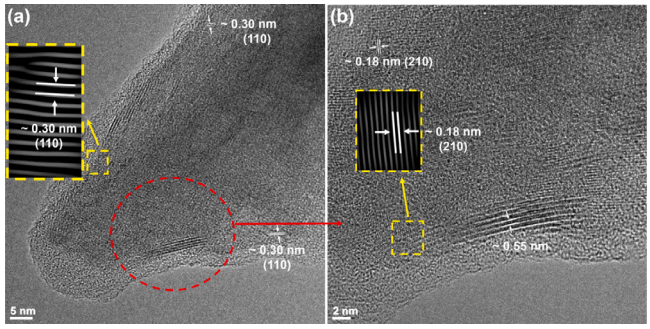

Fig. 4. TEM pictures and analysis of a representative $(Li_2Fe)SeO$ particle. (a) Survey TEM image of one selected $(Li_2Fe)SeO$ particle and (b) enlarged section of the red marked area in (a). The yellow dashed framed insets display the inverse FFT images for specific regions. The *d*-spacing and the corresponding crystal planes are marked in white. (For interpretation of the references to color in this figure legend, the reader is referred to the web version of this article.)

3.2. Electrochemical performance

The electrochemical properties of $(Li_2Fe)SeO$ are investigated with regard to its applicability as an cathode material in LIB. The cyclic voltammograms in Fig. 6 demonstrate that $(Li_2Fe)SeO$ undergoes a multistage Lithium extraction process (see the peaks O1, O2, O*) during the first charge, which shares similarities with the behavior observed in mixed phase $(Li_2Fe)S_{1-x}Se_xO$ [10]. The multistage oxidation behavior observed can be traced back to cationic as well as anionic processes. The first initial oxidation peaks O1 and O2 are typically assigned to the two-stage cationic oxidation process Fe^{2+} to Fe^{3+} [9,10,23]. In a previous report on the related material $(Li_2Fe)SO$, the high voltage process O* was ascribed to the anionic process ($S^{2-} \rightarrow S^0$) by means of XPS and XAS studies [9]. Up to now this reaction could not be further clarified and the reversibility of the process is also still under discussion. During incorporation of Lithium (discharge), much broader peaks (R1, R2, R3) appear in the cyclic voltammogramms. The main double peak (R1/R2) at ~2 V can be attributed to the reversible reduction of iron. Notably is the much smaller voltage difference between R1/R2 compared to the voltage difference of O1/O2 in the oxidation cycle. In addition, the low voltage region shows a small reduction peak R3 at ~1.5 V and an oxidation peak O3 at 1.7 V. The origin of these peaks remains unclear, even though previous reports on similar compounds $(Li_2Fe)SO$ $(Li_2Fe_{0.9}Mn_{0.1})SO$, $(Li_2Fe_{0.9}Co_{0.1})SO$ and $(Li_2Fe_{0.5}Mn_{0.5})SO$ have already shown similar low voltage features [10,23,24]. In the following cycles the reduction peaks (R1,R2,R3) and the oxidation peak O3 increase in height without significant broadening. The high voltage oxidation peaks however shift to lower voltages, broaden and decrease in height, which indicates a changing reaction mechanism and a different kinetics between charge and discharge. The hypothesis of a different kinetics during charge/discharge is supported by the GITT measurements on $(Li_2Fe)SO$ [9].

In Fig. 7(a) the superior performance of $(Li_2Fe)SeO$ is shown by a rate capability test. It yields a reversible capacity of 150, 140, 125 and 100 mAh g^{-1}, at currents rates of C/10, C/4, C/2, and C. When the current density is set again to C/10 in cycle 40, the capacity reaches again 150 mAh g^{-1} which proves good reversibility of the $(Li_2Fe)SeO$-based electrodes. A deeper insight into the underlying processes and their dependence on the charge/discharge rate is provided by the potential curves in Fig. 7(b). The charge curve in cycle 5 recorded at the current rate of C/10 shows that approximately a capacity of 50 mAh g^{-1} is converted within the low voltage process O3 below 2 V while a capacity of 100 mAh g^{-1} is associated with the high voltage processes (above 2 V) O1, O2, and O*. With increasing current, the capacity

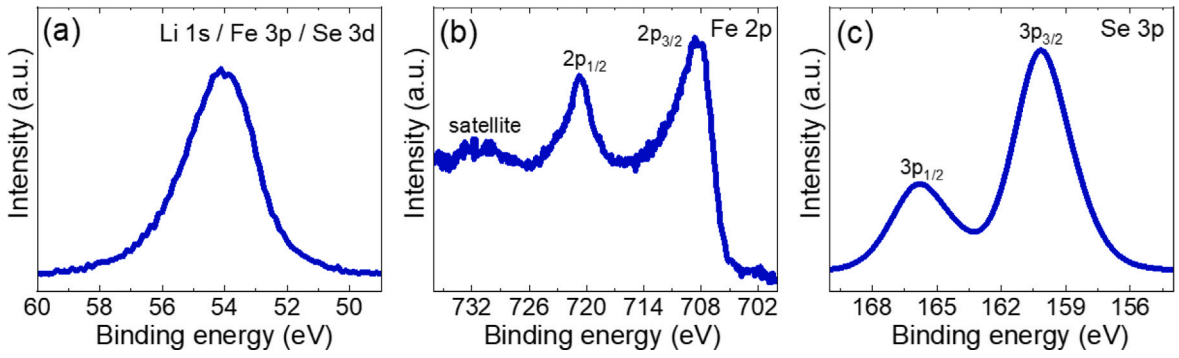

Fig. 5. High-resolution $(Li_2Fe)SeO$ XPS spectra for (a) Li 1s, Se 3d and Fe 3p, (b) Fe 2p and (c) Se 3p.

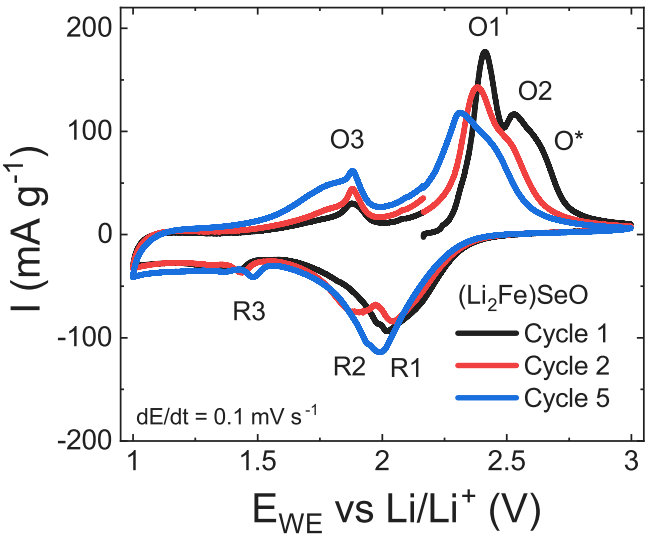

Fig. 6. Cyclic voltammograms of $(Li_2Fe)SeO$ of cycles 1, 2 and 5 recorded at a scan rate of 0.1 mV s^{-1}.

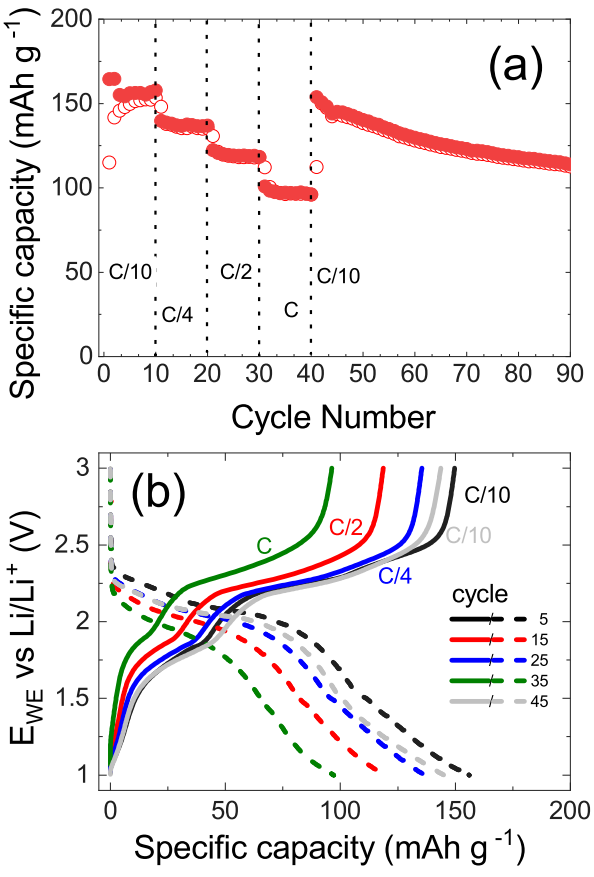

Fig. 7. (a) Evolution of the specific charge/discharge capacities of $(Li_2Fe)SeO$ during rate capability tests with cycling rates between $C/10$ and C and (b) selected corresponding potential profiles of $(Li_2Fe)SeO$. Open/full markers indicate de/lithiation.

associated with the high voltage processes increases (~67% at C/10 to ~79% at 1 C) indicating the high voltage processes to exhibit faster kinetics then the low voltage ones. Returning to a rate of C/10 in cycle 45 results in an increase of the contribution of the low voltage process at the expense of the high voltage one. This observation suggests that

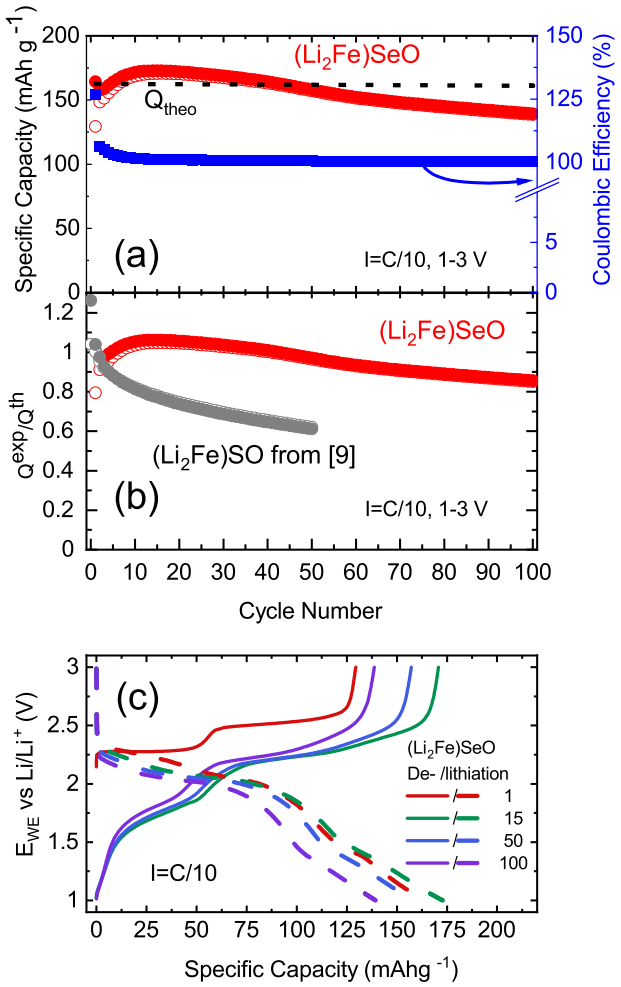

Fig. 8. (a) Specific charge/discharge capacities obtained at C/10 for 100 cycles. (b) Relative specific charge/discharge capacities with respect to the theoretical capacity of one Li insertion/extraction. Grey data markers show results on $(Li_2Fe)SO$ from Ref. [9]. Open/full markers indicate de/lithiation. In (c) selected potential profiles of the $(Li_2Fe)SeO$-electrode are displayed.

the capacity fading is mainly attributed to the high voltage processes O1, O2, and O* as these processes show a regression during cycling.

Long-term galvanostatic cycling performance of $(Li_2Fe)SeO$-cathodes at C/10 is displayed in Fig. 8(a) where dis-/charge capacities are presented. $(Li_2Fe)SeO$ shows an initial charge/discharge capacities of 128/164 mAh g^{-1}. In the next 10 cycles the converted capacity increases to around 170 mAh g^{-1}. Thereafter, a slight monotonous decrease in converted specific capacity to 139 mAh g^{-1} in cycle 100 is observed. The large difference between charge and discharge capacity in the first cycle is also evident in the Coulombic efficiency, which is for the first cycle 126%. Values over 100% strongly point to an irreversible process happening in the first cycle. Afterwards the Coulombic Efficiency decreases to a value slightly above 100% demonstrating the stability of $(Li_2Fe)SeO$.

Fig. 8(b) compares the relative specific capacity (Q experimental/theoretical) of $(Li_2Fe)SeO$ (current study) with the reported $(Li_2Fe)SO$ antiperovskite cathode [9] during removal/insertion of Li into the corresponding structure. Fig. 8(b) reveals that although $(Li_2Fe)SO$ can initially (first five cycles) insert/extract more lithium than $(Li_2Fe)SeO$, $(Li_2Fe)SeO$ is significantly more stable. $(Li_2Fe)SeO$ demonstrates the possibility to reversibly remove/insert 0.85 lithium even after 100 cycles, which is superior to 0.6 found for $(Li_2Fe)SO$ in cycle 50. Consequently, the results show that $(Li_2Fe)SeO$ is a competitive antiperovskite cathode material particularly in terms of cycling

stability and volumetric capacity. The observed higher stability of $(Li_2Fe)SeO$ upon cycling is accompanied by the higher structural stability of $(Li_2Fe)SeO$ compared to $(Li_2Fe)SO$. The intrinsic higher structural stability of selenium containing li-rich antiperovskites is also reinforced by the higher Goldschmidt factor as well as thermal analysis and XRD studies in air [10]

Further insight into charge storage during cycling can be obtained from the potential profiles in Fig. 8(c). The curves show that the increase in the converted capacity in the first 10–15 cycles can be attributed to the low voltage process. The following decrease in the achieved charge capacity from cycles 15 to 50 is ascribed to the decline of the high-voltage anionic selenium reaction. The slight decrease in converted capacity in cycles 50 to 100 is associated with the whole charging regime with however still a dominant loss in the anionic high voltage region. Sulfur-containing lithium-rich antiperovskites display an even higher loss in the high voltage anionic reaction, which is displayed in the CV [24] and potential profiles [23] of sulfur-containing lithium-rich antiperovskite cathodes. The higher electrochemical reactivity of sulfur also explains the initially higher storage per formula unit of $(Li_2Fe)SO$. We therefore attribute the superior cycling stability of Se-containing lithium-rich antiperovskite cathodes to the less pronounced anionic reaction of selenium compared to sulfur in this materials [25]. The conclusion that the sulfur/selenium reaction is of great importance is furthermore supported by studies on $(Li_2Fe)S_{1-x}Se_xO$ [10] which show a shift of the high voltage peak in the reported first cycle CV as a function of selenium content, i.e., the anionic reaction in the first cycle distinctly changes with x. The high-voltage anionic reaction is hence critical for the obtained electrochemical performance. Introducing additional protective coating or the use of different electrolytes could enhance the stability further. A further comparison of our work in terms of electrochemical performance and especially of cycling stability with the recently reported lithium-rich antiperovskites cathodes [10] is not applicable. The here presented galvanostatic study applies a standard protocol as described above which is in contrast to the cycling protocol used in the previous reports [10] where the maximum capacity seems to be limited to a theoretically predicted decomposition value [26]. The latter approach may lead to a severe overestimation of the cycling stability so that comparison of the electrochemical performance from Ref. [10] with our data is not feasible.[2]

To examine the kinetics present in $(Li_2Fe)SeO$ in more detail, potentiostatic electrochemical impedance measurements (PEIS) were carried out at a specific state of charge in different cycles at frequencies between 200 kHz and 5 mHz (see Fig. S5). The corresponding Nyquist plots as well as the fits applied to the data using the Z Fit function of the EC-Lab (Bio-Logic) software are presented in Fig. 9. Qualitative analysis by fitting the data with the corresponding equivalent circuit (see Fig. S6) enables to evaluate the impact of cycling on the electrolyte resistance R_e, on the charge transfer resistance between electrolyte and electrode material R_{ct}, and on the double layer capacitance C_{dl}. The obtained fit parameters are listed in the table S2. After OCV, the Nyquist diagram exhibits a small depressed semicircle in the high to medium frequency range representative for charge transfer followed by a steep rise in the low-frequency range, whose slope is representative for the diffusion impedance of Li^+ ions inside the cathode. Qualitative analysis yields an electrolyte resistance of 2.0(3) Ω, a rather small charge transfer resistance of 15.4(4) Ω and a double layer capacitance of 3.2(3) μF. After one cycle the impedance response of $(Li_2Fe)SeO$ is

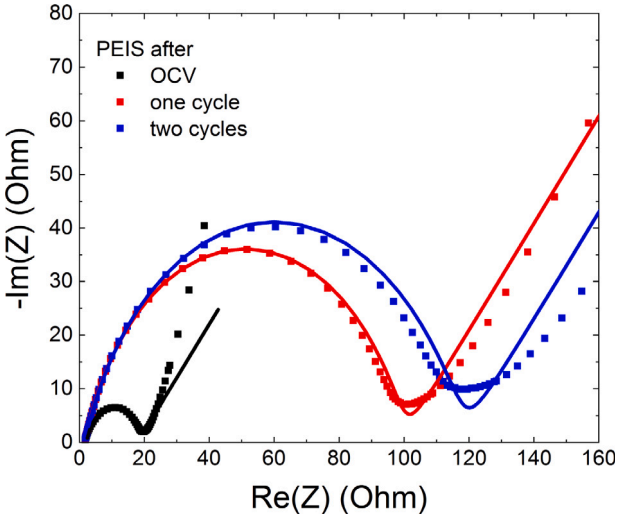

Fig. 9. Nyquist plots for $(Li_2Fe)SeO$ measured at different cycles. Solid lines show fits according to the equivalent circuit used (see the text).

practically unchanged with respect to R_e and C_{dl} while R_{ct} strongly increases to around 98 Ω. This strong increase of R_{ct} implies a major change of $(Li_2Fe)SeO$ in the first cycle. After cycle 2, the PEIS data again confirm quasi unchanged R_e and C_{dl} values and a further, but significantly smaller increase of R_{ct} to ~115 Ω indicating further slight change of $(Li_2Fe)SeO$. Examination of the measured low-frequency impedance response, which reflects the diffusion, reveals a significantly higher slope than the 45-degree slope predicted by the Warburg element. The higher slope of the measured low frequency impedance after OCV indicates that ion diffusion in $(Li_2Fe)SeO$ is likely multi-dimensional [27]. During cycling, a flattering of the slope of the low frequency response during cycling is visible which is indicative for structural change. Again the most significant change occurs within the first cycle. In conclusion, the PEIS Data demonstrated that $(Li_2Fe)SeO$ undergoes strong structural changes during the first cycle and then stabilizes more and more. The observation of structural changes during the first cycle is consistent to data shown in previous reports [9,24].

4. Conclusions

In summary, phase pure $(Li_2Fe)SeO$ was synthesized via a solid-state method with particles in the range of several tens of micrometers up to sub-micrometer in size. A thermally stable behavior with congruent melting is confirmed by differential thermal analysis. Electrochemical characterizations demonstrate a multistage extraction/insertion mechanism of $(Li_2Fe)SeO$ based on cation Fe as well as anion Se activity. Further electrochemical performance test on $(Li_2Fe)SeO$ displayed not only a high current capability of 100 mAh g^{-1} at 1 C but also high cycling stability cooperated by high coulombic efficiency. These promising results persist leading to an overall superior cycling stability and storage per formula unit of $(Li_2Fe)SeO$ compared to its isostructural $(Li_2Fe)SO$. In addition, the electrochemical impedance spectroscopy measurements shed a light onto the kinetics of $(Li_2Fe)SeO$ and the respective changes during cycling. The results displayed major structural change primarily in the first cycle with a strong trend in the next cycle towards more structural stability. The here realized electrochemical performance makes the antiperovskite $(Li_2Fe)SeO$ a competitive cathode material for Lithium ion batteries and nominates Se containing antiperovskites for further optimization and investigations. One attractive option for further improvement involves reduction

[2] Specifically, in our protocol there are no predefined constraints regarding the converted capacity. When limiting the maximum capacity to a defined value, in an initial cycling regime the experimentally obtained capacity values may just reflect the chosen constraint parameters. Even though, the limitation of the capacity may not prevent irreversible processes in general but rather allows them to gradually proceed while the protocol yields seemingly stable capacity values.

of the particle size to shorten the ionic diffusion length inside the bulk cathode, and hence, improve the ionic conductivity for high current rate applications.

CRediT authorship contribution statement

M.A.A. Mohamed: Conceptualization, Experiments, Original draft preparation, Visualization. **L. Singer:** Conceptualization, Experiments, Original draft preparation, Visualization. **H. Hahn:** Experiments. **D. Djendjur:** Experiments. **A. Özkara:** Experiments. **E. Thauer:** Experiments. **I.G. Gonzalez-Martinez:** Experiments. **M. Hantusch:** Experiments. **R. Klingeler:** Conceptualization, Original draft preparation, Visualization, Supervision. **N. Gräßler:** Conceptualization, Original draft preparation, Visualization, Supervision.

Declaration of competing interest

The authors declare that they have no known competing financial interests or personal relationships that could have appeared to influence the work reported in this paper.

Data availability

Data will be made available on request.

Acknowledgments

Financial support by Deutsche Forschungsgemeinschaft (DFG) through project KL 1824/12-1 and by BMBF via the project SpinFun (13XP5088) is acknowledged. Work has also been supported within the framework of the Excellence Strategy of the Federal and State Governments of Germany via Heidelberg University's flagship EMS initiative. M.A.A. Mohamed thanks the IFW excellence program for financial support. N. Gräßler acknowledges funding from the European Regional Development Fund through Sächsische Aufbaubank and project LUKSIAK (Project number 100350438). S. Hampel acknowledges the financial support by the German Research Foundation (DFG) within project VA831/4-1. The authors thank Andrea Voss and Anne Voidel (IFW Dresden) for performing ICP-OES measurements.

Appendix A. Supplementary data

The Supplemental Material presents ICP-OES results, a detailed explanation how d_{XRD} was determined, DTA thermograms, magnetization data, XPS survey spectrum, and further information on PEIS measurements and their analysis.

Supplementary material related to this article can be found online at https://doi.org/10.1016/j.jpowsour.2022.232547.

References

[1] G. Assat, J.-M. Tarascon, Fundamental understanding and practical challenges of anionic redox activity in Li-ion batteries, Nature Energy 3 (5) (2018) 373–386.
[2] W. Zuo, M. Luo, X. Liu, J. Wu, H. Liu, J. Li, M. Winter, R. Fu, W. Yang, Y. Yang, Li-rich cathodes for rechargeable Li-based batteries: reaction mechanisms and advanced characterization techniques, Energy Environ. Sci. 13 (12) (2020) 4450–4497.
[3] C.J. Hansen, J.J. Zak, A.J. Martinolich, J.S. Ko, N.H. Bashian, F. Kaboudvand, A. van der Ven, B.C. Melot, J. Nelson Weker, K.A. See, Multielectron, cation and anion redox in lithium-rich iron sulfide cathodes, J. Am. Chem. Soc. 142 (14) (2020) 6737–6749.
[4] E. McCalla, A.S. Prakash, E. Berg, M. Saubanère, A.M. Abakumov, D. Foix, B. Klobes, M.-T. Sougrati, G. Rousse, F. Lepoivre, S. Mariyappan, M.-L. Doublet, D. Gonbeau, P. Novak, G. van Tendeloo, R.P. Hermann, J.-M. Tarascon, Reversible Li-intercalation through oxygen reactivity in Li-rich Li-Fe-Te oxide materials, J. Electrochem. Soc. 162 (7) (2015) A1341–A1351.
[5] E. McCalla, M.T. Sougrati, G. Rousse, E.J. Berg, A. Abakumov, N. Recham, K. Ramesha, M. Sathiya, R. Dominko, G. van Tendeloo, P. Novák, J.-M. Tarascon, Understanding the roles of anionic redox and oxygen release during electrochemical cycling of lithium-rich layered Li_4FeSbO_6, J. Am. Chem. Soc. 137 (14) (2015) 4804–4814.
[6] K.T. Lai, I. Antonyshyn, Y. Prots, M. Valldor, Anti-perovskite Li-battery cathode materials, J. Am. Chem. Soc. 139 (28) (2017) 9645–9649.
[7] K.T. Lai, I. Antonyshyn, Y. Prots, M. Valldor, Extended chemical flexibility of cubic anti-perovskite lithium battery cathode materials, Inorg. Chem. 57 (21) (2018) 13296–13299.
[8] M. Chen, Y. Liu, Y. Zhang, G. Xing, Y. Tang, Lithium-rich sulfide/selenide cathodes for next-generation lithium-ion batteries: challenges and perspectives, Chem. Commun. 58 (22) (2022) 3591–3600.
[9] D. Mikhailova, L. Giebeler, S. Maletti, S. Oswald, A. Sarapulova, S. Indris, Z. Hu, J. Bednarcik, M. Valldor, Operando studies of antiperovskite lithium battery cathode material $(Li_2Fe)SO$, ACS Appl. Energy Mater. 1 (11) (2018) 6593–6599.
[10] M.A.A. Mohamed, M.V. Gorbunov, M. Valldor, S. Hampel, N. Gräßler, D. Mikhailova, Tuning the electrochemical properties by anionic substitution of Li-rich antiperovskite $(Li_2Fe)S_{1-x}Se_xO$ cathodes for Li-ion batteries, J. Mater. Chem. A 9 (40) (2021) 23095–23105.
[11] G.S. Zakharova, L. Singer, Z.A. Fattakhova, S. Wegener, E. Thauer, Q. Zhu, E.V. Shalaeva, R. Klingeler, MoO_2/C composites prepared by tartaric acid and glucose-assisted sol-gel processes as anode materials for lithium-ion batteries, J. Alloys Compd. 863 (2021) 158353.
[12] H. Zhong, C. Feng, H. Wang, D. Han, G. Yu, W. Xiong, Y. Li, M. Yang, G. Tang, S. Yuan, Structure-composition-property relationships in antiperovskite nitrides: Guiding a rational alloy design, ACS Appl. Mater. Interfaces 13 (41) (2021) 48516–48524.
[13] Z. Deng, D. Ni, D. Chen, Y. Bian, S. Li, Z. Wang, Y. Zhao, Anti–perovskite materials for energy storage batteries, 2021, InfoMat.
[14] R. Jain, A.S. Lakhnot, K. Bhimani, S. Sharma, V. Mahajani, R.A. Panchal, M. Kamble, F. Han, C. Wang, N. Koratkar, Nanostructuring versus microstructuring in battery electrodes, Nat. Rev. Mater. 7 (9) (2022) 736–746.
[15] P. Terzieff, K.L. Komarek, The antiferromagnetic and ferrimagnetic properties of iron selenides with NiAs-type structure, Monatsh. Chem. 109 (5) (1978) 1037–1047.
[16] B. Spencer, S. Maniyarasu, B. Reed, D. Cant, R. Ahumada-Lazo, A. Thomas, C. Muryn, M. Maschek, S. Eriksson, T. Wiell, et al., Inelastic background modelling applied to hard X-ray photoelectron spectroscopy of deeply buried layers: A comparison of synchrotron and lab-based (9.25 keV) measurements, Appl. Surf. Sci. 541 (2021) 148635.
[17] J. Chastain, J.F. Moulder, W.F. Stickle, P.E. Sobol, K.D. Bomben, R.C. King Jr., Handbook of X-ray Photoelectron Spectroscopy: A Reference Book of Standard Spectra for Identification and Interpretation of XPS Data, Physical Electronics, Eden Prairie, Minn., 1995.
[18] R. Dedryvere, M. Maccario, L. Croguennec, F. Le Cras, C. Delmas, D. Gonbeau, X-ray photoelectron spectroscopy investigations of carbon-coated Li_xFePO_4 materials, Chem. Mater. 20 (22) (2008) 7164–7170.
[19] S. Lu, H. Wu, S. Xu, Y. Wang, J. Zhao, Y. Li, A.M. Abdelkader, J. Li, W. Wang, K. Xi, et al., Iron selenide microcapsules as universal conversion-typed anodes for alkali metal-ion batteries, Small 17 (8) (2021) 2005745.
[20] A. Grosvenor, B. Kobe, M. Biesinger, N. McIntyre, Investigation of multiplet splitting of Fe 2p XPS spectra and bonding in iron compounds, Surf. Interface Anal. 36 (12) (2004) 1564–1574.
[21] R. Ospina, S.A. Rincón-Ortiz, J. Rodriguez-Pereira, Cadmium selenide by XPS, Surf. Sci. Spectra 27 (1) (2020) 014021.
[22] J.R. Shallenberger, N. Hellgren, Zinc selenide analyzed by XPS, Surf. Sci. Spectra 27 (1) (2020) 014020.
[23] M.V. Gorbunov, S. Carrocci, S. Maletti, M. Valldor, T. Doert, S. Hampel, I.G. Gonzalez Martinez, D. Mikhailova, N. Gräßler, Synthesis of $(Li_2Fe_{1-y}Mn_y)$so antiperovskites with comprehensive investigations of $(Li_2Fe_{0.5}Mn_{0.5})SO$ as cathode in Li-ion batteries, Inorg. Chem. 59 (21) (2020) 15626–15635.
[24] M.V. Gorbunov, S. Carocci, I.G. Gonzalez Martinez, V. Baran, D. Mikhailova, Studies of $Li_2Fe_{0.9}M_{0.1}SO$ antiperovskite materials for lithium-ion batteries: The role of partial Fe^{2+} to M^{2+} substitution, Front. Energy Res. 9 (2021) 360.
[25] A. Eftekhari, The rise of lithium–selenium batteries, Sustain. Energy Fuels 1 (1) (2017) 14–29.
[26] Z. Lu, F. Ciucci, Anti-perovskite cathodes for lithium batteries, J. Mater. Chem. A 6 (12) (2018) 5185–5192.
[27] X. Zhang, X. Zhang, X. Sun, Y. An, S. Song, C. Li, K. Wang, F. Su, C.-M. Chen, F. Liu, Z.-S. Wu, Y. Ma, Electrochemical impedance spectroscopy study of lithium-ion capacitors: Modeling and capacity fading mechanism, J. Power Sources 488 (2021) 229454.

Supplemental Information: Lithium-rich antiperovskite $(Li_2Fe)SeO$: a high-performance cathode material for lithium-ion batteries

M.A.A. Mohamed[a,c,**], L. Singer[b,**], H. Hahn[b], D. Djendjur[b], A. Özkara[b], E. Thauer[b], I. G. Gonzalez-Martinez[a], M. Hantusch[a], B. Büchner[a], S. Hampel[a], R. Klingeler[b,*], N. Gräßler[a,*]

[a] *Leibniz Institute for Solid State and Materials Research Dresden e.V., 01069 Dresden, Germany*
[b] *Kirchhoff Institute for Physics, Heidelberg University, 69120 Heidelberg, Germany*
[c] *Department of Physics, Faculty of Science, Sohag University, 82524 Sohag, Egypt*

*Corresponding authors.
**Both authors contributed equally.
Email addresses: klingeler@kip.uni.heidelberg.de (R. Klingeler), n.graessler@ifw-dresden.de (N. Gräßler)

Table S1: ICP-OES results for $(Li_2Fe)SeO$

compound	Mass %			Molar ratios[1]			
	Li	Fe	Se	Li	Fe	Se	O
$(Li_2Fe)SeO$	7.96± 0.17	33.68±0.67	45.54±1.2	1.874±0.041	1.012±0.02	1.04±0.026	1.067

[1]Molar ratios are scaled to sum up to about 5

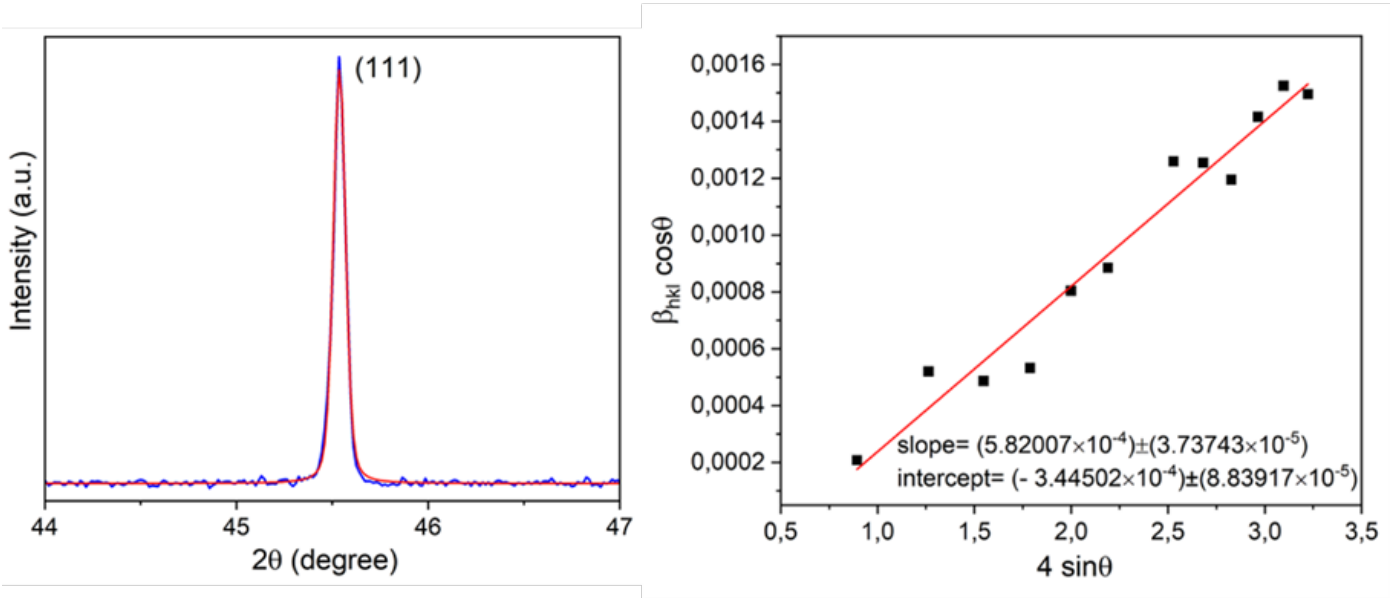

Figure S1: Voigt fitting (left) for (111) plane and W-H plot (right) for $(Li_2Fe)SeO$ compound. Direct application of scherrer's equation to calculate the crystallite size is based on determination of the peak full width at half maximum (FWHM), excluding the instrumental effect and then presuming that all residual broadening comes only from the crystallite size. This simplification is only valid in specific cases where the crystallite size has the major effect on the peak broadening such as nanoparticles. However, in most cases, disregarding the effect of lattice strain is not correct and results in underestimation of the crystallite size. To overcome this issue, Williamson-Hall (W-H) model is used. According to that model, the lattice strain and crystallite size are independent and the total peak broadening can be represented as: $\beta_{hkl}\ \cos(\theta_{hkl}) = \frac{k\lambda}{D} + 4\epsilon \sin\theta_{hkl}$ where β_{hkl} is the FWHM after excluding the instrumental effect, θ_{hkl} is the Bragg angle, k is the shape factor, λ is the wavelength for the XRD source, D is the crystallite size and ϵ is the lattice strain. It was found that all XRD diffraction peaks fit non-linearly well with the Voigt function as highlighted for (111) peak in Fig. S1. Therefore, this function was used for estimating the average full width at half maximum (FWHM) and then the instrumental broadening was excluded by recording the XRD data for a standard Si and then eliminated from the observed pattern. By plotting a graph between $\beta_{hkl}\ \cos(\theta_{hkl})$ and $4\ \sin\theta_{hkl}$, D and ϵ can be estimated from the y-intercept and the slope of the straight line, respectively as seen in Fig. S1. W-H plot gave unphysical value of the crystallite size of – 519 nm while Sheerer's equation yielded a crystallite size of ∼ 260 nm. This negative value for the crystallite size results from intrinsic errors in case of large crystallite size that can lead W-H line intercepts negative value of the y axis[1] . The lattice strain (ϵ) was extracted from W-H plot to be ∼ 0.00058. This finding of large crystallite size combined with low lattice strain reflects the high crystallinity of the obtained sample.

0.1. Voigt function

Voigt function represents a combination of Gaussian (strain effect) and Lorentzian (crystallite size effect) functions. Based on this function, the full width at half maximum (FWHM) can be calculated as follows[2]:

$$\beta_0 = 0.5346 \times W_L + \sqrt{(0.2166 \times W_L^2 + W_G^2)} \tag{S1}$$

where β_0 is the (FWHM), W_L is the Gaussian width and W_G is the Lorentzian width. The broadening due to instrument (β_i) is excluded by recording XRD data for a standard material and then using this expression:

$$\beta_{hkl} = \sqrt{(\beta_0 - \beta_i)(\beta_0^2 - \beta_i^2)^{0.5}} \tag{S2}$$

0.2. Williamson-Hall (W-H) model [2]:

The average crystallite size (D) can be estimated from Scherre' s equation as follows:

$$D = \frac{k\lambda}{\beta_D \cos(\theta_{hkl})} \tag{S3}$$

Where D is the crystallite size, k is the shape factor, λ is the wavelength for the XRD source, β_D is the broadening due to crystallite size and θ_{hkl} is the Bragg angle. While the lattice strain is given by Wilson equation as follows:

$$\epsilon = \frac{\beta_\epsilon}{4\tan(\theta_{hkl})} \tag{S4}$$

Where β_ϵ is the broadening due to lattice strain. According to W-H model[2], the total XRD broadening (β_{hkl}) due to both crystallite size and lattice strain can be given by simple addition as:

$$\beta_{hkl} = \beta_D + \beta_\epsilon \tag{S5}$$

By substituting equations S3 and S4 in S5, the following expression can be obtained for W-H model:

$$\beta_{hkl}\cos(\theta_{hkl}) = \frac{k\lambda}{D} + 4\epsilon\sin(\theta_{hkl}) \tag{S6}$$

By plotting a graph between $\beta_{hkl}\cos(\theta_{hkl})$ and $4\ \epsilon\sin(\theta_{hkl})$, D and ϵ can be estimated from the y-intercept and the slope of the straight line, respectively.

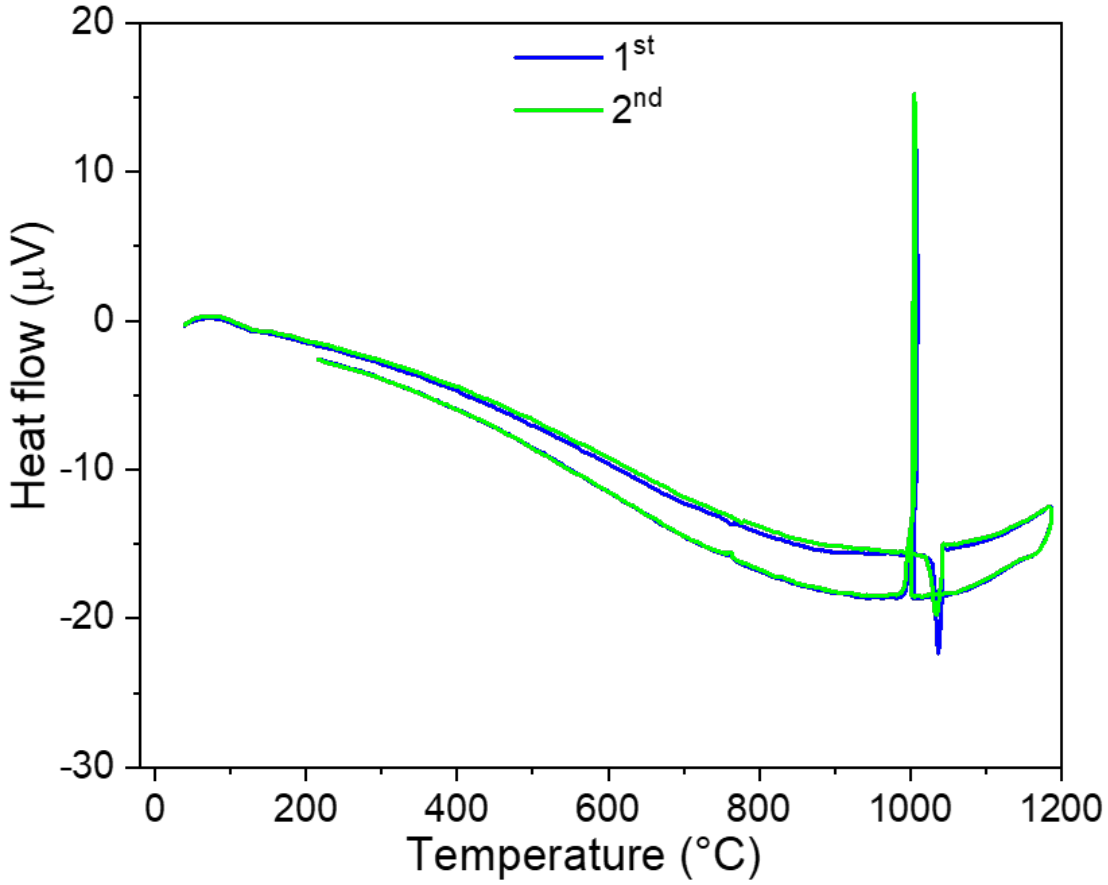

Figure S2: DTA thermograms during the 1^{st} and 2^{nd} cycles for (Li_2Fe)SeO compound. Thermogram revealed a congruent melting for (Li_2Fe)SeO without any intermediate phase change. Indeed, this finding agrees with the reported thermal behavior for (Li_2Fe)SeO [3].

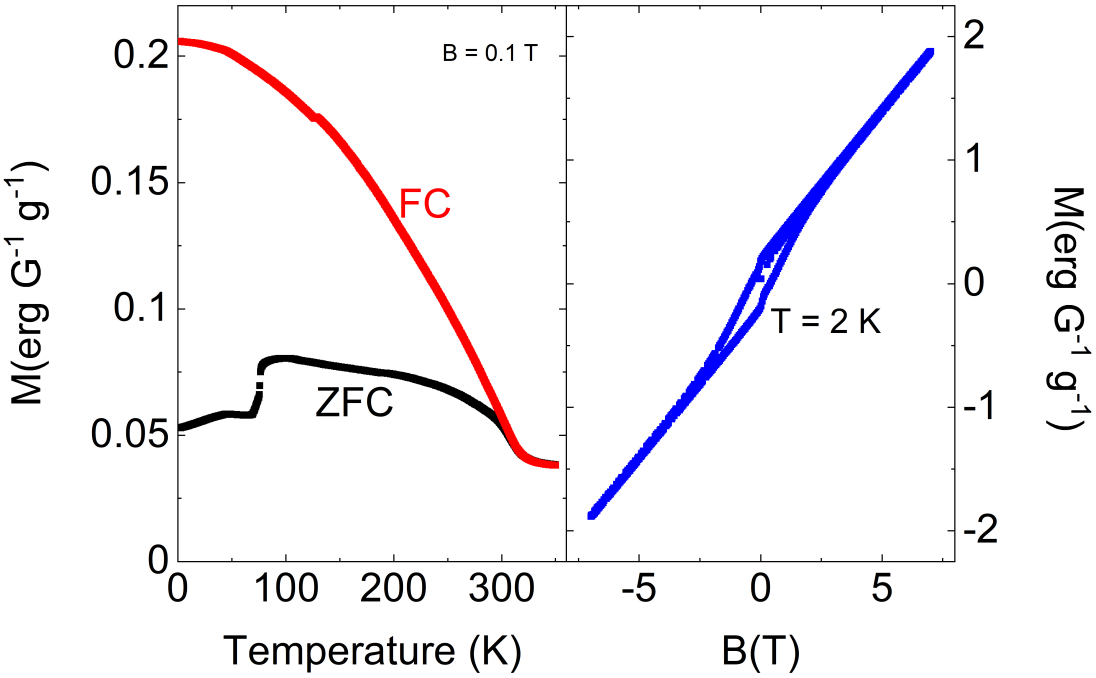

Figure S3: Magnetization of $(Li_2Fe)SeO$ vs. temperature at $B = 0.1$ T (a), and vs. magnetic field at $T = 2$ K (b). The data indicate a small ferrimagnetic impurity phase of $\beta-Fe_{1-x}Se$ with $x \approx 0.25$ ($T_C \simeq 320$ K; $\lesssim 1$w%) and suggest an antiferromagnetic transition around 130 K indicative of $\gamma-Fe_{1-x}Se$ with $x \approx 0.13$ [4]

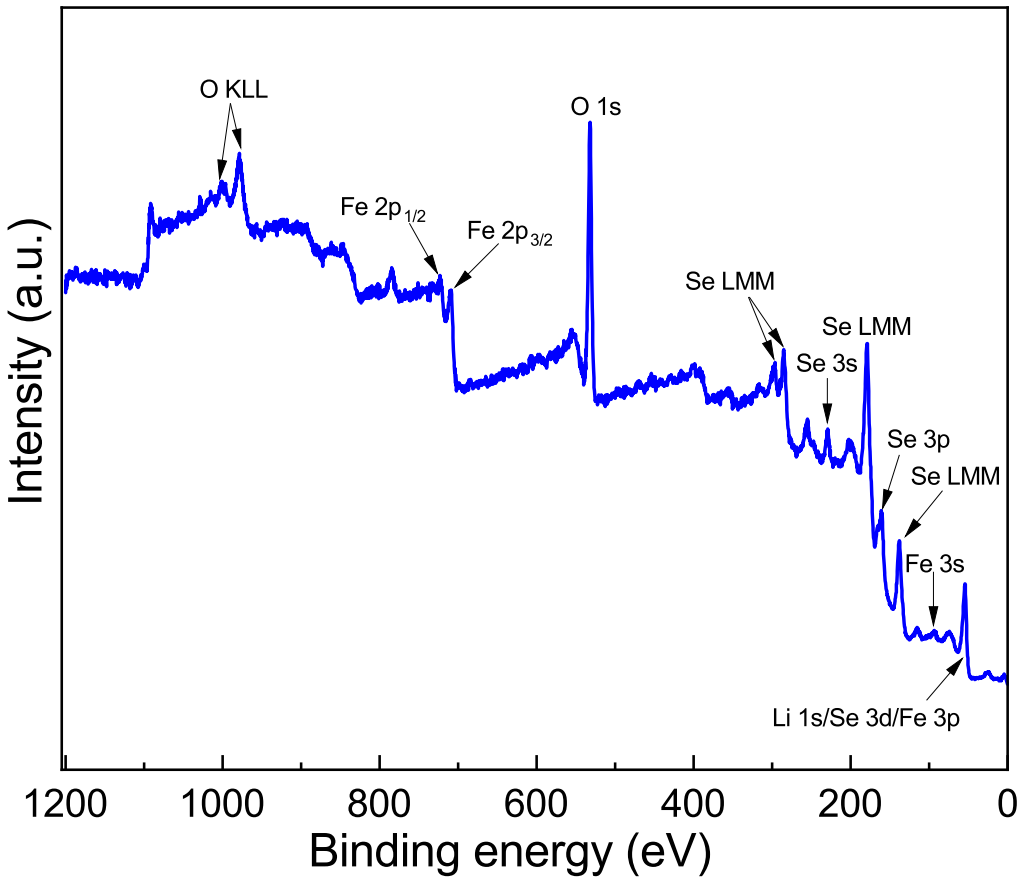

Figure S4: Full XPS survey spectrum of (Li_2Fe)SeOwith markers for all relevant elemental binding energies

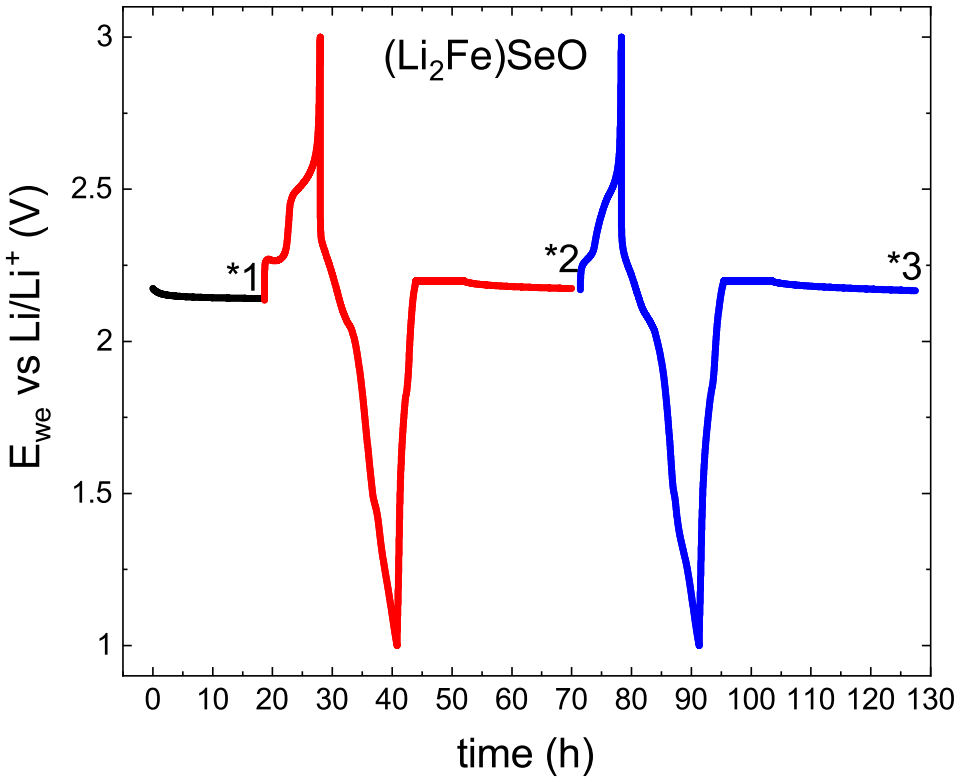

Figure S5: Voltage vs. time illustrating the specific state of charge where the PEIS measurements presented in have been performed. The colours have been used to display the charge/discharge process in front of the corresponding PEIS measurement. The numbers show where the PEIS measurements have been done.

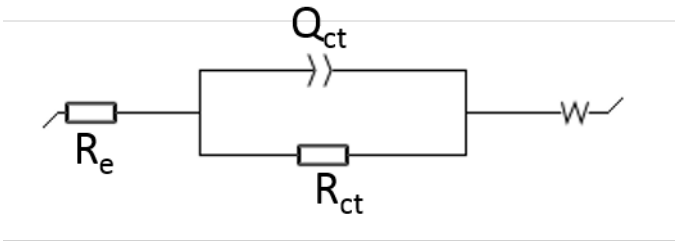

Figure S6: Equivalent circuit used to model the measured impedance. R_e reflects the electrolyte resistance, R_{ct} and Q_{ct} the charge transfer contributions.

Table S2: Best fitting parameter obtained by modelling shown PEIS data by means of the equivalent circuit Fig. S6. The parameters reflect the average values with standard deviation from three fits with slightly different boundaries.

SOC	R_E (Ω)	R_{ct} (Ω)	C_{dl} (10^{-6} F)
OCV	2.0(3)	15.4(4)	3.2(3)
after first cycle	1.3(5)	98(1)	3.1(1)
after second cycle	1.3(3)	115(1)	3.4(1)

References

[1] Y.-Y. Kim, A. S. Schenk, J. Ihli, A. N. Kulak, N. B. Hetherington, C. C. Tang, W. W. Schmahl, E. Griesshaber, G. Hyett, F. C. Meldrum, A critical analysis of calcium carbonate mesocrystals, Nature Communications 5 (1) (2014) 1–14.

[2] P. Muhammed Shafi, A. Chandra Bose, Impact of crystalline defects and size on X-ray line broadening: A phenomenological approach for tetragonal SnO_2 nanocrystals, AIP Advances 5 (5) (2015) 057137.

[3] K. T. Lai, I. Antonyshyn, Y. Prots, M. Valldor, Anti-Perovskite Li-Battery Cathode Materials, Journal of the American Chemical Society 139 (28) (2017) 9645–9649.

[4] P. Terzieff, K. L. Komarek, The antiferromagnetic and ferrimagnetic properties of iron selenides with NiAs-type structure, Monatshefte für Chemie 109 (5) (1978) 1037–1047.

4.2 Elucidating the electrochemical reaction mechanism of lithium-rich antiperovskite cathodes for lithium-ion batteries as exemplified by $(Li_2Fe)SeO$

Autoren:

Lennart Singer, M.A.A. Mohamed, Henrik Hahn, Ignacio G. Gonzalez-Martinez, Martin Hantusch, Bernd Büchner, Silke Hampel, Nico Gräßler, Rüdiger Klingeler

Akzeptiert vom Journal of Materials Chemistry A

L. Singer ist zusammen mit M.A.A. Mohamed (IFW Dresden) zu gleichen Teilen Erstautor des Artikels. L. Singer hat den Abstract, die Einleitung, das Kapitel zu den elektrochemischen Eigenschaften und die Zusammenfassung sowie zusammen mit M.A.A. Mohamed den Abschnitt über die physikalischen Eigenschaften erstellt. L. Singer fertigte die finalen Abbildungen 1, 3, sowie Abbildung 4-7, S4, S6-S7 und S9-S11 sowie zusammen mit M.A.A. Mohamed den graphical Abstract an. L. Singer hat folgende experimentelle Arbeiten und Analysen durchgeführt:

- Analyse der Röntgendiffraktometrie (XRD), Transmissionselektronenmikroskopie (TEM) und Röntgenphotoelektronenspektroskopie (XPS) (zusammen mit M.A.A. Mohamed)
- Magnetische Messungen: Durchführung und Analyse
- Elektrochemische Untersuchungen (CV, GCPL): Durchführung und Analyse entweder alleine oder zusammen mit dem von ihm angeleiteten Bachelorstudenten H. Hahn.

Beitrag der Koautoren:

M.A.A. Mohamed: Synthese der Materialien sowie XRD, DTA, SEM-Messungen (Abb.1,3 sowie S2, S3, S5, S8). Verfassen der Synthesebeschreibung sowie zusammen mit L. Singer der physikalischen Charakterisierung.

I.G. Gonzalez-Martinez: TEM-Messungen (Abb. 4).

M. Hantusch: XPS-Messungen (Abb. 5,S4).

H. Hahn: Unter der Anleitung von L. Singer Mitarbeit an den elektrochemischen Messungen.

B. Büchner, S. Hampel: Projektplanung, Beratung bei den Experimenten bzw. Diskussion der Ergebnisse.

R. Klingeler und N. Grässler: Projektplanung und -leitung, Beteiligung an der Interpretation und Beitrag zur Finalisierung des Manuskriptes.

Korrespondenz mit den Gutachtern: L. Singer, R. Klingeler.

Alle Autoren haben das Manuskript Korrektur gelesen.

Journal Name

ARTICLE TYPE

Cite this: DOI: 00.0000/xxxxxxxxxx

Elucidating the electrochemical reaction mechanism of lithium-rich antiperovskite cathodes for lithium-ion batteries as exemplified by $(Li_2Fe)SeO$.

Lennart Singer,[‡a] M.A.A. Mohamed,[‡b,d] Henrik Hahn,[a] Ignacio G. Gonzalez-Martinez, [b] Martin Hantusch, [b] Karolina Wenelska,[c] Ewa Mijowska,[c] Bernd Büchner,[b] Silke Hampel,[b] Nico Gräßler,[*b] and Rüdiger Klingeler[*a]

Received Date
Accepted Date

DOI: 00.0000/xxxxxxxxxx

We report in the context of lithium-rich antiperovskite cathode materials outstanding electrochemical properties of $(Li_2Fe)SeO$, which for the first time was synthesized via direct ball-milling. The unique structured material displays a electrochemical cycling performance of 250 mAh g^{-1} at 0.1 C when used as a cathode in lithium-ion batteries. Comprehensive electrochemical analysis combined with detailed transmission electron microscopy studies reveal that, above 2.5 V, the multi electron storage mechanism involves conversion of $(Li_2Fe)SeO$ to $Fe_{1-x}Se_x$. Our results furthermore demonstrate the general relevance of our findings to the whole class of antiperovskite cathode materials and present a route to strongly enhance their cell performance by avoiding the degradation path deciphered by our studies.

1 Introduction

The recent discovery of lithium-rich antiperovskite with the general formula $(Li_2TM)ChO$ (TM = Fe, Mn, Co; Ch = S, Se) has extended the field of cathode materials for lithium-ion batteries (LIB). The new class of lithium-rich antiperovskites exhibits promising properties like low cost, non-toxic raw materials used, high lithium-diffusion and the possibility of multi-electron storage per formula unit which renders them a promising alternative cathode material for LIB [1,2]. Among them, based on its superior multi-electron storage and cycling stability, selenium-containing lithium-rich antiperovskites such as $(Li_2Fe)SeO$ are regarded as particularly compelling, competitive cathode candidates. The full potential of antiperovskite-based cathodes could however, up to now, not completely be unleashed [2–4]. Two major obstacles are restraining the antiperovskite cathodes. First, the high-temperature solid-state synthesis method previously applied yields rather large particles, which in turn limits the high-current capability, and the synthesis technique is difficult to scale up [5]. Second, while high-voltage anionic electrochemical activity limits the accessible capacity, the associated processes are yet unclear which hinders the development of appropriate strategies to overcome this issue. Our approach to surpass these barriers exploits a novel mechanochemical synthesis method for the lithium-rich antiperovskite $(Li_2Fe)SeO$ which is based on direct ball milling. This method benefits from a controllable, low-temperature, solvent-free process and can be easily scaled-up to the industrial level. Mechanochemical synthesis furthermore allows to vary the synthesis parameters in a wide regime and thereby to tune relevant material properties such as the particle size [6]. This is particularly relevant as the particle size is directly linked to the required ion transport lengths so that tuning the size in turn yields significant changes of the electrochemical properties [7–9]. Importantly, a more detailed look at the occurring high-voltage processes is provided by our purposefully fabricated, unique $(Li_2Fe)SeO$ samples, elucidating the mechanism of multi-electron storage of the lithium-rich antiperovskites. In the previous literature, lithium storage was discussed as a multi-electron storage process involving cationic and anionic contributions [2–4,10]. In particular, $(Li_2Fe)SO$, $(Li_2Fe)SeO$, and the mixed systems $(Li_2Fe)S_{1-x}Se_xO$ have been studied. By means of *in-situ* XAS, *in-situ* XRD and Mössbauer spectroscopy, the first two oxidation peaks in the cyclovolta mmograms were attributed to the oxidation of Fe^{2+} to Fe^{3+} [2]. In contrast, the exact anionic process associated with sulfur/selenium has not been fully elucidated despite many investigations. Mikhailova *et al.* [2] have proposed that in the region of

[a] *Kirchhoff Institute for Physics, Im Neuenheimer Feld 227, Heidelberg University, 69120 Heidelberg, Germany.*
[b] *Leibniz Institute for Solid State and Materials Research Dresden e.V., 01069 Dresden, Germany.*
[c] *Nanomaterials Physicochemistry Department, Faculty of Chemical Technology and Engineering, West Pomeranian University of Technology, 71-065 Szczecin, Poland*
[d] *Department of Physics, Faculty of Science, Sohag University, 82524 Sohag, Egypt*
† Electronic Supplementary Information (ESI) available: [details of any supplementary information available should be included here]. See DOI: 00.0000/00000000.
‡ *Both authors contributed equally.* * *Corresponding author. E-mail: n.graessler@ifw-dresden.de and klingeler@kip.uni.heidelberg.de*

high voltages (∼2.9 V) an anionic sulfur reaction S^{-2} to S^0 takes place. The data however did not allow to unambiguously conclude whether this involves an irreversible phase transformation of the antiperovskite (formation of pure amorphous sulfur), or a reversible reaction of the antiperovskite material itself[2]. Further investigations on this issue are essential as knowledge of the complete underlying reaction mechanism is of utmost importance for possible improvement of the electrochemical performance.

Here, we report on two differently synthesized (Li_2Fe)SeO materials with different physical and electrochemical properties. Our studies on the one hand yield insight into the effect and the great potential of mechanochemical synthesis and, on the other hand, elucidate the electrochemical reaction mechanism of antiperovskites in general. The mechanisms are studied by comprehensive electrochemical analyses with a particular focus on the distinct electrochemical processes and their interrelationships accompanied by in-depth transmission electron microscopy. Comparing studies on (Li_2Fe)SO and (Li_2Fe)SeO show that our findings concerning the high-voltage process can be generalised to the whole class of antiperovskites. The such obtained knowledge on the influence of the high voltage process yields a strategy to strongly improve cycling stability and high current capability as demonstrated by our studies on (Li_2Fe)SeO. In particular, the here presented (Li_2Fe)SeO does not only display high specific capacity of 250 mAh g^{-1} at 0.1 C but also exhibits outstanding high-current performance of 150 mAh g^{-1} after 100 cycles at 1 C. Our results hence show the route to improve lithium-rich antiperovskites cathode materials in general, thereby opening the field for further research and improvements in this whole class of materials.

2 Experimental section

Synthesis

Quantities of Li_2O, Fe and Se as starting materials (purchased from Alfa Aesar), were loaded into a stainless-steel jar inside an argon-filled glovebox according to the desired stoichiometry. The mixture (in total 2 g) was ball-milled using high-energy SPEX SamplePrep 8000D with hardened stainless-steel balls (2 balls 12 mm diameter and 2 balls 6 mm diameter) for 8 h. The powder-to-ball mass ratio was ∼1:10. After milling, the jar was opened inside the glovebox and a black powder was taken out for further characterization. For the heat treatment of the sample after ball milling, a certain amount of the sample was filled in a corundum crucible (Aliaxis, Frialit-Degussite, AL23) in the glovebox. The crucible was placed into a silica tube (QSILAG; Quarzschmelze, Ilmenau) and temporarily closed with a rubber stopper. Outside the glovebox, the tube was evacuated to a pressure of less than 10^{-3} mbar, refilled with Ar to adjust the internal pressure to 0.2 bar, and sealed with a gas burner. Finally, the closed ampoule was placed into a furnace and heated up to 600 °C (heating rate: 50 °C h^{-1}) for 3 h. The materials obtained by ball milling will be labeled by the suffix '-BM' (i.e., (Li_2Fe)SeO-BM) and the potential post-heat treatment temperature may be added, i.e., (Li_2Fe)SeO-BM600 refers to a ball-milled material subsequently heated at 600 °C.

X-ray diffraction (XRD)

The purity and crystallinity of the prepared (Li_2Fe)SeO samples were studied by XRD (STOE STADI P diffractometer) using Debye-Scherrer mode with Co $K_{\alpha 1}$ radiation source (λ = 1.788965 Å) and a Mythen 1 K detector (Dectris). To prevent any air exposure during XRD measurements, the samples were filled into glass capillaries (diameter: 0.6 mm) inside the Ar-filled glovebox and subsequently melt-sealed outside. The XRD patterns were fitted by Voigt function and the sample broadening β_s was derived by subtracting the instrumental broadening β_i from the total broadening β_t as described elsewhere[11]. The average crystallite size (D_{XRD}) was calculated from Debye-Scherrer equation $D_{\mathrm{XRD}} = K\lambda/\beta_s \cos(\theta)$, where K is the shape factor, λ is the wavelength of the XRD source, β_s is the full width at half maximum, and θ is the Bragg position[12].

Elemental analysis

To estimate the stoichiometry of the produced compositions in terms of molar ratios of the elements, inductively coupled plasma-optical emission spectroscopy (ICP-OES) (iCAP 6500 Duo View, Fa. Thermo Fisher Scientific GmbH) was used.

X-ray photoelectron spectroscopy (XPS)

X-ray photoelectron spectroscopy (XPS) was performed with a PHI 5600 spectrometer (Physical Electronics) using monochromatic Al-K_α radiation (250 W) equipped with a hemispherical analyzer with 29.35 eV pass energy for high-resolution spectra. To prevent any air exposure the sample was transferred from the glovebox to the XPS device in a special transfer chamber. The estimated spot size on the sample is about 0.4 mm. To avoid charging effects, an electron gun is used as a neutralizer for each measurement.

Electron Microscopy

Scanning electron microscopy (Nova-NanoSEM 200) coupled with energy dispersive spectroscopy (EDS) was used to evaluate the morphology and composition for the compounds under study. High-resolution transmission Electron Microscopy (HR-TEM) studies were performed using a FEI Titan 80-300, equipped with a C_s corrector and operated at 300 kV. The sample was loaded by direct contact onto Cu 300 mesh TEM grids (Agar) and holey carbon film (Plano). For monitoring the micro-structural changes of (Li_2Fe)SeO during cycling, TEM images were acquired using a FEI Titan 80-300 transmission electron microscope, respectively. The d-spacings between the atomic fringes in TEM images were evaluated using Digital Micrograph software from Gatan[13]. For each crystalline domain, the average value for the d-spacing was calculated from multiple lines at various locations. As uncertainty, the maximum deviation of the measured d-spacings to the mean was used. The cycled electrodes were disassembled in an Ar-filled glovebox, washed with ethylene carbonate, and then dried overnight. To prevent air exposure the sample was transferred from the glovebox to the device in a special air-tight transfer box.

Magnetic measurements

Magnetic measurements were performed on $(Li_2Fe)SeO$ powder samples using an MPMS3 magnetometer (Quantum Design). Magnetisation was measured by varying the temperature between 2 and 300 K using zero-field-cooled (ZFC) and field-cooled (FC) protocols at 0.1 T. Isothermal magnetisation was studied at 2 K in magnetic fields up to ±7 T.

Thermodynamic investigations

Differential thermal analysis (DTA) up to 1200 °C was performed by means of a Setaram DTA 92-2400 (alumina container) under helium atmosphere (heating rate: 10 °C min^{-1}).

Surface area analysis

N_2 adsorption/desorption measurements of the samples were conducted to analyse the surface area using ASAP 2460 at a relative pressure of P/Po = 0.1 - 1.0. Prior to the measurements, samples were degassed at 100 °C under vacuum for 12 h. The specific surface area was calculated by the Brunauer-Emmett-Teller (BET) method.

Electrochemical measurements

Electrochemical measurements were carried out using a VMP3 potentiostat (BioLogic) at 25 °C. Slurry preparation as well as cell assembly have been performed in an Argon-filled glovebox with controlled humidity and oxygen concentration due to the moisture sensitivity of $(Li_2Fe)SeO$. Working electrodes were prepared by mixing the active material (70%wt), carbon black (15%wt) and polyvinylidene fluoride (PVDF, 15%wt) in dry isopropanol. Afterwards the resulting mixture was spread onto a (Ø=10 mm) aluminum mesh (thickness 0.125 mm). The obtained electrodes were thereafter dried overnight in vacuum, pressed and dried again. The active material mass loading ranged between 3 and 4.5 mg cm^{-2}. During cell assembly Glass fiber (Whatman GF/D) as the separator, pure lithium metal foil (Aldrich) as the counter electrode and as electrolyte 1M $LiPF_6$ in a mixture of ethylene carbonate and dimethyl carbonate (1:1 by weight) have been used. Cyclic voltammetry (CV) and galvanostatic cycle measurements with potential limitation (GCPL) were performed in a coin cell housing (see[14]). Note, the theoretical capacity of $(Li_2Fe)SeO$ for the remove/introduce of 1 Li^+ is 162.8 mAh g^{-1} and we attribute the rate 1 C to the charge/discharge current required to remove/introduce 1 Li^+ from/into the antiperovskite material within one hour.

3 Results and discussion

3.1 Structure, morphology, and composition

Figure 1 displays the XRD patterns of the mechanochemical synthesized $(Li_2Fe)SeO$-BM and $(Li_2Fe)SeO$-BM600 together with the reference pattern of $(Li_2Fe)SeO$[1]. For both samples, all observed peaks correspond to the cubic antiperovskite structure with *Pm-3m* space group. The absence of any additional peak in both patterns excludes, within the detection limit, the presence of crystalline impurities in both $(Li_2Fe)SeO$ samples. The heat treatment leads to an increase in the crystallinity as evident from the higher signal-to-noise ratio for $(Li_2Fe)SeO$-BM600 compared to $(Li_2Fe)SeO$-BM. The lattice parameter in $(Li_2Fe)SeO$-BM amounts to 4.009(2) Å which slightly decreases upon subsequent heat treatment to 4.005(1) Å in $(Li_2Fe)SeO$-BM600. Both values agree well with 4.0025(3) Å reported for $(Li_2Fe)SeO$ prepared by solid-state reaction[1]. The small reduction of the lattice parameter upon heat treatment can likely be attributed to strain relaxation and the vanishing of intrinsic defects such as stacking faults and grain boundaries. By considering the peak broadening and using Debye Scherrer formula[12], the crystallite size of 5.2(9) nm for $(Li_2Fe)SeO$-BM and 41(2) nm for $(Li_2Fe)SeO$-BM600 was calculated; the changes upon heat treatment coincides with the expectation on thermal grain-size growth.

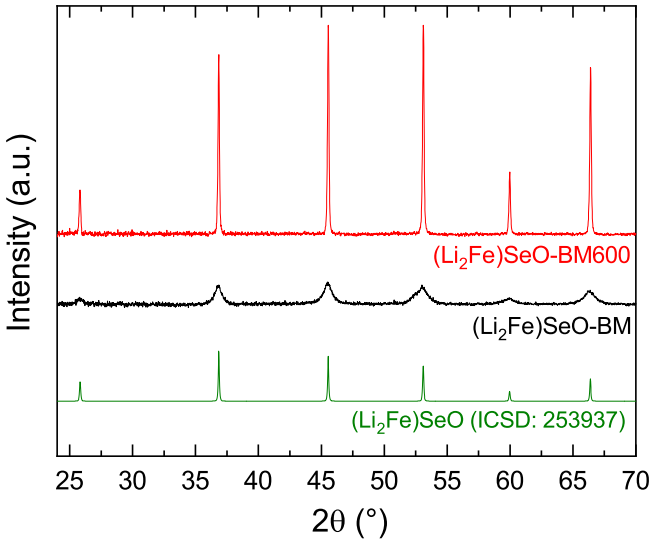

Fig. 1 XRD patterns of $(Li_2Fe)SeO$-BM and $(Li_2Fe)SeO$-BM600 as well as the reference pattern for $(Li_2Fe)SeO$[1].

To further confirm the formation of $(Li_2Fe)SeO$ and to exclude the presence of other oxidation states, XPS analyses were carried out on $(Li_2Fe)SeO$-BM and $(Li_2Fe)SeO$-BM600. The full XP survey spectra (see Fig. S1 in the Supplemental Material) for both samples confirm the presence of Li, Fe ,Se , and O with only a slight contribution of adsorbed atmospheric carbon, which is typical and hard to avoid[15]. For further insight, Fig. 2 shows high-resolution spectra of (a) Li 1*s*, Se 3*d* and Fe 3*p* (b) Fe 2*p* and (c) Se 3*p*, Se LMM Auger-peak, and (d) O 1*s*. The measured spectra in Fig. 2a consist of a combination of the Li 1*s*, Se 3*d*, and Fe 3*p* lines which are all in the energy range between 53 and 56 eV[16]. Due to the strong mixing of these lines, into only one clearly visible peak, it is not possible to accurately quantify the actual surface composition and oxidation state of these elements from the recorded spectra. The fact that the relative sensitivity factor of Fe 3*p* is 30 times higher than for Li 1*s* further hinders separation[17]. Fig. 2b presents the Fe 2*p* spectra and their splitting into two characteristic peaks at 709 eV (Fe $2p_{3/2}$) and 722.2 eV (Fe $2p_{1/2}$) due to spin-orbit coupling. The clearly visible satellite features at higher binding energies compared to the main Fe $2p_{3/2}$ and Fe $2p_{1/2}$ peaks strongly suggest the high-spin state of Fe^{2+} in both materials under study[18,19]. For both materials, the Se 3*p* and Se LMM peaks shown in Fig. 2c appear in

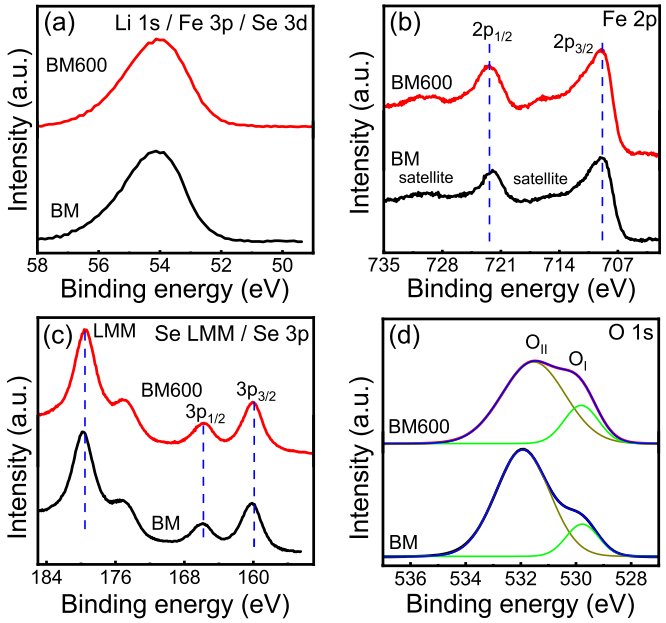

Fig. 2 High-resolution XP spectra of $(Li_2Fe)SeO$-BM and $(Li_2Fe)SeO$-BM600 of the (a) Li 1*s*, Se 3*d* and Fe 3*p*, (b) Fe 2*p*, (c) Se LMM Auger-peak, and (d) O 1*s*.

the energy range from 155 eV to 185 eV. The very similar spectra indicate that heat treatment at 600 °C does not significantly affect the selenium oxidation state. The measured binding energies of Se $3p_{3/2}$ (160.2 ev) and Se $3p_{1/2}$ (165.8 eV) are close to reported values for Se^{2-} in CdSe [20] and ZnSe [21], thereby confirming the oxidation state -2 of selenium in both materials studied at hand. The O 1*s* spectra of $(Li_2Fe)SeO$-BM and $(Li_2Fe)SeO$-BM600 are separated into two peaks, i.e., O_{I} and O_{II} (see Fig. 2d). The first peak (O_{I}) appears for both materials at 529.8 eV, while O_{II} locates at 531.9 eV for $(Li_2Fe)SeO$-BM and at 531.5 eV for $(Li_2Fe)SeO$-BM600. We attribute O_{I} to the oxygen lattice, while O_{II} most likely corresponds to chemisorbed oxygen species[22]. The higher relative expression of O_{II} for $(Li_2Fe)SeO$-BM may indicate a higher amount of absorbed oxygen species due to the smaller particle size and higher specific surface of the material. The hypothesis of a higher specific surface area of $(Li_2Fe)SeO$-BM compared to -BM600 was confirmed by N_2 adsorption measurements (see Fig. S2), which show that while both materials exhibit a low surface area, $(Li_2Fe)SeO$-BM, with 1.2(4) $m^2\ g^{-1}$, has more than twice the surface area of -BM600, with 0.5(1) $m^2\ g^{-1}$. The XPS analysis in summary confirms the successful formation of $(Li_2Fe)SeO$ in both materials. In addition, we observe quasi-identical XP spectra which imply no significant differences in the oxidation states of the contained Se, Li, Fe, and O due to heat treatment. In particular, our data exclude the presence of impurities with different oxidation in both samples.

The morphology and micro-structure of $(Li_2Fe)SeO$-BM and $(Li_2Fe)SeO$-BM600 are investigated by SEM and TEM images (see Fig. 3). The SEM image of $(Li_2Fe)SeO$-BM (Fig. 3a) displays irregular, nearly spherical dominantly sub-micrometer-sized primary particles. Compared to $(Li_2Fe)SeO$ prepared by solid-state synthesis [23], $(Li_2Fe)SeO$-BM displays a strongly reduced particle size along with a narrower size distribution. In addition, minor particle agglomeration is visible in the SEM images of $(Li_2Fe)SeO$-BM which we attribute to the cold welding phenomenon during the milling process[24]. Additional heat treatment leads to strong sintering of the primary fine particles into larger agglomerates (see Fig. 3e of $(Li_2Fe)SeO$-BM600) which we attribute to the Ostwald repining effect[25]. To confirm the uniform distribution of the elements and the nominal composition, EDS measurements were performed as shown in Fig. S3 and Fig. S4. The EDS analyses reveal uniform distribution of the elements and that both $(Li_2Fe)SeO$-BM and $(Li_2Fe)SeO$-BM600 consist entirely of Fe, Se, and O with comparable relative atomic percentages coinciding with the expected stoichiometry. Moreover, no indication of impurities or contamination are detected. The stoichiometric composition of the material is further proven by ICP-OES analysis whose results are presented in Table S1 in the Supplemental Material. The good agreement between the measured and nominal values in addition excludes non-stoichiometric extraneous phases.

TEM images in Fig. 3 provide a closer insight into the morphology and lattice spacings of $(Li_2Fe)SeO$-BM (b-d) and $(Li_2Fe)SeO$-BM600 (f-h). The selected area electron diffraction (SAED) pattern of $(Li_2Fe)SeO$-BM (inset of Fig. 3b) shows that the Bragg peaks are arranged in circles of different diameters. We conclude that the SAED spot area covers several crystallites which is in agreement with the cristallite size of $d_{\mathrm{XRD}} \simeq 5$ nm obtained from the Scherrer analysis as well as from crystalline regions in Fig. 3c. The TEM images of $(Li_2Fe)SeO$-BM furthermore reveal not only multiple crystallites inside a given mircoscaled particle, they also show the existence of two kinds of crystalline regions. The dominant one (Fig. 3c) consists entirely of crystalline domains related to the $(Li_2Fe)SeO$ phase, as evidenced by the appearance of average interplanar spacing of 0.21(1) nm and 0.29(1) nm between the atomic fringes corresponding to (200) and (110) planes of $(Li_2Fe)SeO$. The data also indicate a second kind of crystalline regions in $(Li_2Fe)SeO$-BM (see Fig. 3d) that clearly differ from the *d*-spacing values of the $(Li_2Fe)SeO$ phase (Fig. 3d). Specifically, the observed *d*-spacings between 0.54 to 0.56, and 0.31(1) nm can not be associated with the $(Li_2Fe)SeO$ phase so that we conclude the presence of an impurity phase. As the associated layer distances of 0.55(2) and 0.31(1) nm deduced from Fig. 3d match well with the (001) and (101) spacings in tetragonal FeSe[26], we infer the presence of a FeSe impurity phase in $(Li_2Fe)SeO$-BM. Note, that crystalline regions with spacings of 0.29(1) and 0.19(1) nm could either correspond within the uncertainty to the (110) and (200) planes in $(Li_2Fe)SeO$ or to the (002) and (112)/(200) planes of FeSe. In addition, the presence of non-stoichiometric FeSe can based on our analysis not be excluded since some regions display a slight deviation of the lattice *d*-spacing of 0.55 nm corresponding to stoichiometric Fese. As a result of heat treatment after milling ($(Li_2Fe)SeO$-BM600 sample), the crystallinity improves as indicated by the observation of aligned dots in SEAD (see inset in Fig. 3f) and an increase in the size of the crystalline domain corresponding to (110) plane of $(Li_2Fe)SeO$ (Fig. 3g). In addition to crystalline domains corresponding to $(Li_2Fe)SeO$ with a *d*-spacing of 0.29(2) nm, $(Li_2Fe)SeO$-BM600 displays only rarely, small crystalline domains

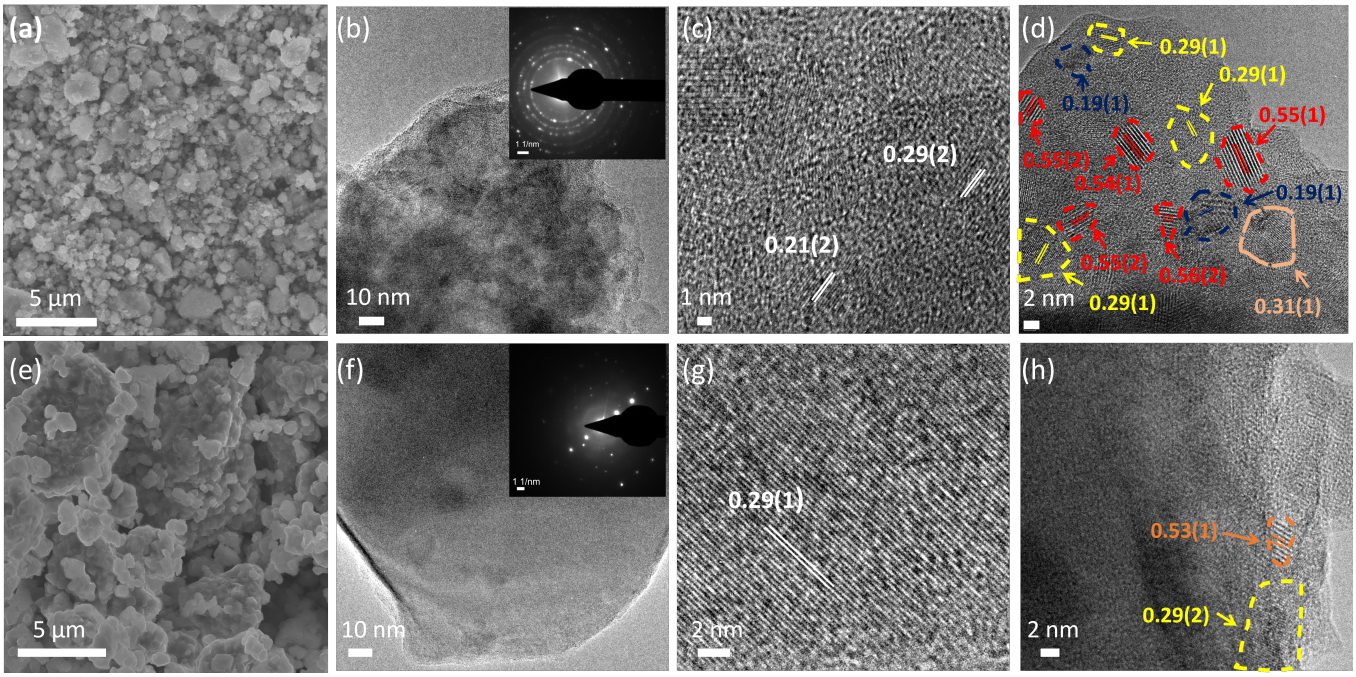

Fig. 3 SEM and HR-TEM images of $(Li_2Fe)SeO$-BM (a-d) and $(Li_2Fe)SeO$-BM600 (e-h). The inset (b),(f) displays the obtained SAED pattern. The depicted d-spacings are given in the unit nanometer. Differently colored dashed lines in (d),(h) mark regions with different lattice spacing.

with 0.53(1) nm interplanar spacing (Fig. 3h). Regions with a d-spacing of 0.53(1) nm may indicate the presence of non-stoichiometric FeSe. The observation that the number as well as the d-spacing of crystallite domains corresponding to $Fe_{1-x}Se_x$ decrease in $(Li_2Fe)SeO$-BM600, further supports its assignment to FeSe in $(Li_2Fe)SeO$-BM as tetragonal FeSe is reported to be thermally unstable at high temperatures[27].

Owing to its characteristic magnetic properties[28], the presence of small amounts of $Fe_{1-x}Se_x$ is unambiguously confirmed by magnetic studies (see Fig. S5 in the Supplemental Material). Specifically, from the magnetization data we infer the presence of $\beta-Fe_{1-x}Se$ with $x \approx 0.26$ and of ferromagnetic $Fe_{1-x}Se$ with $x \approx 0.21 - 0.11$[28,29]. Since magnetic order is supposed to appear in crystalline structures, these results indicate crystalline magnetic impurity phases in the low single-digit % regime. In addition, there may be amorphous regions of the same phases.

DTA measurements in the temperature range between room temperature (RT) and 1200 °C show the thermal behavior and stability of ball-milled $(Li_2Fe)SeO$-BM (see Fig. S6a in the Supplemental Material). The DTA results indicate a single endothermic (at 1039(2) °C) and exothermic (at 1018(2) °C) peak corresponding to the melting and re-solidification process of $(Li_2Fe)SeO$, respectively. The absence of any additional process, even though some $Fe_{1-x}Se_x$ is expected from the TEM and magnetisation analysis, may refer to impurity content below the resolution limit of the DTA, its mainly amorphous nature, or both. Similar thermal behavior in the first and the second thermal cycles proves thermal reversibility of the material. In addition, XRD after heating the sample above its melting point and cooling it to room temperature (see Fig. S6b) confirms congruent melting of $(Li_2Fe)SeO$-BM without any phase transition/decomposition. The observed thermal properties of $(Li_2Fe)SeO$-BM are therefore in good agreement with the reported properties of $(Li_2Fe)SeO$ prepared by the solid-state reaction method[23]. We particularly note that our data imply that $(Li_2Fe)SeO$ antiperovskites possess superior thermal stability as compared to other commercial cathode materials[30] which may be advantageous for Li-ion battery performance at high operating temperatures.

3.2 Electrochemical studies

The mechanochemically synthesized $(Li_2Fe)SeO$-BM as well as the temperature-treated $(Li_2Fe)SeO$-BM600 are studied as cathode material in LIB. The corresponding cyclic voltammograms in the potential range 1 to 3 V vs. Li/Li^+ shown in Fig. 4 demonstrate that the two $(Li_2Fe)SeO$ materials exhibit a comparable multistage lithium extraction and insertion mechanism which is also similar to the previous report on $(Li_2Fe)SeO$ produced by the solid state reaction (SSR) method[23]. The open circuit voltage (OCV) of $(Li_2Fe)SeO$-BM (2.1 V) and -BM600 (2.2 V) is in the middle of the electrochemical reactions. Note, a full cyclic voltammetry cycle starts and ends at OCV. For both materials at hand, the two initial oxidation peaks O_1 and O_2 appear at about $\sim$ 2.3 V and 2.5 V and signal the two-stage cationic Fe^{2+} to Fe^{3+} oxidation process[2,10]. We note the lower voltage of these features compared to $(Li_2Fe)SeO$-SSR[23]. This shift towards lower voltages can be attributed to lower polarization due to the smaller particle sizes and corresponding smaller diffusion path length for Li^+[31–33]. An anionic reaction of the contained chalcogen is proposed to take place in the high-voltage region O_2, O_*[2,10]. During the first intercalation (discharge), both samples display distinct

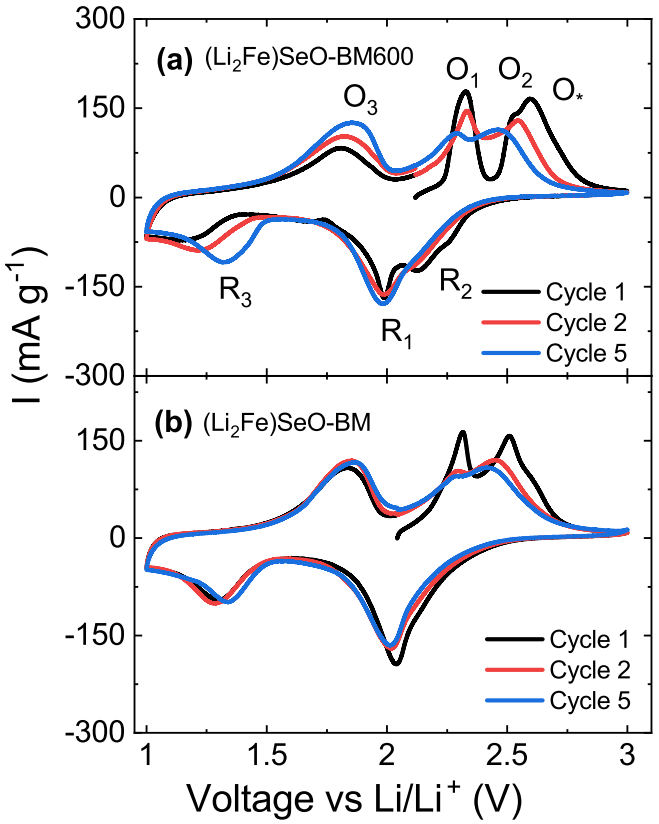

Fig. 4 Cyclic voltammograms of cycle 1, 2 and 5 of (a) $(Li_2Fe)SeO$-BM600 and (b) $(Li_2Fe)SeO$-BM measured at a scan rate of 0.1 mV s^{-1}. The labels R/O mark distinct reduction and oxidation features.

reduction peaks (R_1, R_2, R_3) in the CV. Note, the lower distinctness and the higher broadness of the peaks in the cyclic voltammogram of $(Li_2Fe)SeO$-BM can, in accordance with the XRD data, be attributed to the lower crystallinity. By comparing the first cycle with the following ones, it becomes evident that the first cycle is fundamentally different regarding the number, positions and curvature of the peaks, which seems to be a general phenomenon of $(Li_2Fe)SeO$ and other similar antiperovskite compounds. This is particularly visible by the appearance of a fourth pronounced peak O_3 at about ~ 1.8 V in the second delithiation cycle. This fourth peak is more pronounced in $(Li_2Fe)SeO$-BM600 than in $(Li_2Fe)SeO$-BM and increases in the subsequent cycles. The other peaks (O_1, O_2, O_*) strongly decrease in height upon cycling with a concomitantly increasing overlap. In fact, from the CVs it cannot be unambiguously seen whether O_* is still present after cycle 1 since it becomes indiscernible but might be hidden by O_2. In the intercalation cycles, the change of the subsequent cyclic voltammetry curves is less dominant and mainly visible at the peak R_3. Notably, the peaks R_3/O_3 not only shift but also clearly increase for BM600 whereas for $(Li_2Fe)SeO$-BM the peak height does not change significantly. Overall, upon cycling the CV curves of both materials become more and more similar. This may indicate strong irreversible structural changes of $(Li_2Fe)SeO$ in the initial cycle exceeding the initial effect of a post-synthesis heat treatment.

To investigate the electrochemical processes and their interrelationships, as well as the differences between both materials in more detail, CV measurements in three limited potential ranges (row a, b, and c of Fig. 5) were carried out for both $(Li_2Fe)SeO$ materials. As will be discussed in detail below, these measurements demonstrate the effect and stability of the distinct processes in each regime and allow us to identify the interdependencies between them. Firstly, the CVs with initial lithiation (discharge) to 1 V and restriction of the maximum voltage to OCV (Fig. 5, row a) show the electrochemical behavior upon initial intercalation of the cathode material, thereby allowing to investigate possible lithium vacancies or reactive anodic impurity phases. In phase-pure cathode material without defects and void space, it is not possible to directly incorporate further lithium into the material, which holds especially for the here presented $(Li_2Fe)SeO$ as their stoichiometric and structural composition is confirmed by XRD, XPS, EDS and ICP-EOS. The results for $(Li_2Fe)SeO$-BM however display not only electrochemical activity but also a clearly visible reduction peak R_3 at around 1.4 V and an oxidation peak O_3 at around 1.8 V. The observation of such a redox pair in the CV imply the presence of an electrochemical active foreign phase. Moreover, the process appears to be very stable, which is represented by quasi-perfect overlapping CV curves of $(Li_2Fe)SeO$-BM. For BM600 on the other hand this process is only negligibly pronounced. As the only difference between BM and BM600 is the post-temperature treatment to 600 °C, this implies that the electrochemical active foreign phase is not stable up to this temperature. Both this observation and the peak positions which match literature values for $Fe_{1-x}Se_x$ [34,35] confirm the presence of an electrochemically active $Fe_{1-x}Se_x$ phase as suggested by the TEM and magnetisation studies discussed above. Extending the upper voltage limit to ≈ 2.4 V (see row b of Figure 5) includes the peak O_1 and hence allows us to examine the processes associated with the reaction pair O_1/R_1, which is considered to be a part of the reversible redox process ($Fe^{2+} \leftrightarrow Fe^{3+}$). As expected for a reversible intercalation process, an almost perfect overlap of the CV curves of the following cycles can be seen, proving the excellent reversibility of this process. Note, there is also no discernible change in the O_3/R_3 peaks in $(Li_2Fe)SeO$-BM. The CVs extending to the full potential range of 1 to 3 V and thereby including the two high voltage processes O_2 and O_* are displayed in row c of Fig. 5. For both samples, the data imply significant changes driven by the high-voltage processes which in particular involve pronounced non-reversible behavior and the appearance of a new redox pair in $(Li_2Fe)SeO$-BM600. Specifically, the pair R_3/O_3 evolves in the low voltage regime and in both materials it increases and shifts upon cycling. Furthermore, especially for $(Li_2Fe)SeO$-BM600, there is a significant decrease and broadening of O_1, O_2 and O_* in the subsequent cycles after passing through O_2/O_*. It is noteworthy that for $(Li_2Fe)SeO$-BM, the previously visible peak pair R_3/O_3 is also clearly enhanced after passing O_2/O_*. Based on our observations, these results demonstrate that passing through the high voltage oxidation processes O_2/O_* triggers an irreversible process that partly converts $(Li_2Fe)SeO$ to a different phase which is electrochemically active as demonstrated by the redox pair R_3/O_3. The peak positions at

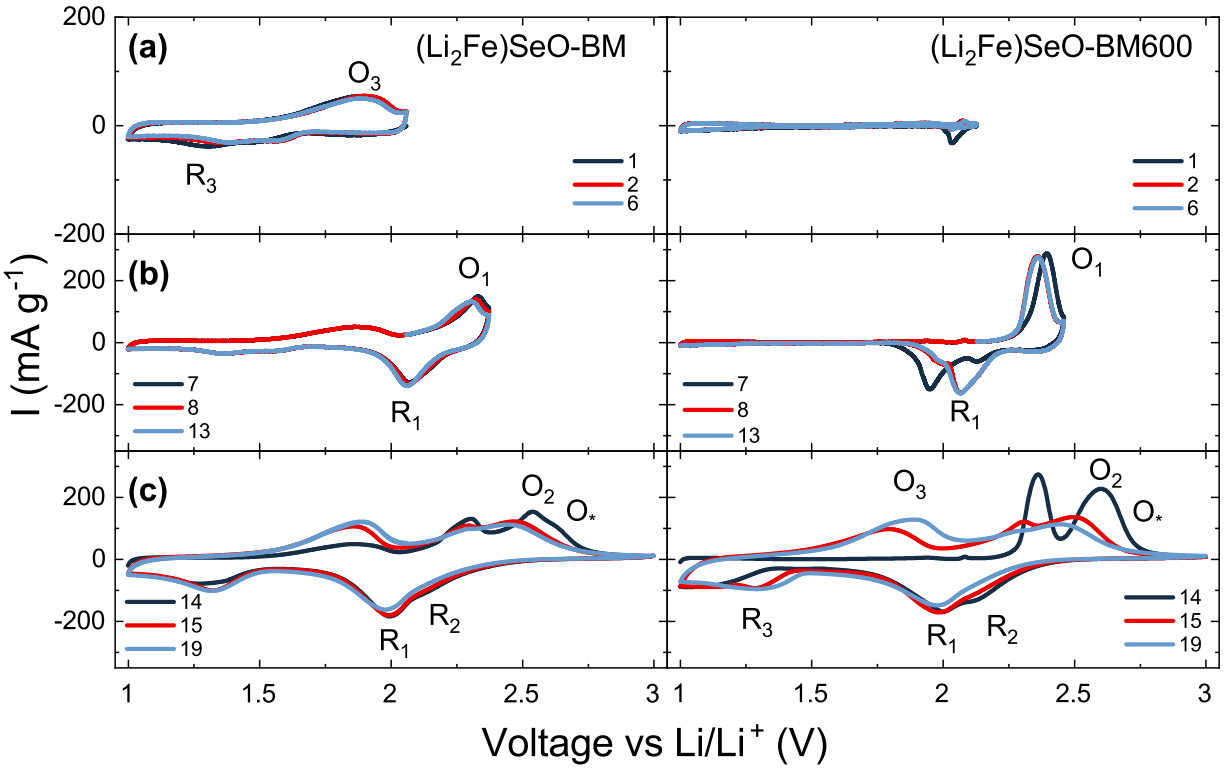

Fig. 5 Cyclic voltammograms of $(Li_2Fe)SeO$-BM and $(Li_2Fe)SeO$-BM600 in the potential range from (a) 1 V to OCV, (b) 1 to 2.38/2.48 V respectively, and (c) 1 to 3 V vs. Li/Li^+ measured at a scan rate of 0.1 mV s^{-1}. The labels R/O correspond to the ones in Fig. 4.

$\sim$ 1.4 and 1.8 V, respectively, in both samples strongly suggest that $Fe_{1-x}Se_x$ is formed during the high voltage processes. This is confirmed by the corresponding presence of R_3 in $(Li_2Fe)SeO$-BM signaling the $Fe_{1-x}Se_x$ impurity phase. The additional activity signaled by R_3/O_3 agrees to the expected behaviour of $Fe_{1-x}Se_x$ and further corroborates this conclusion.

To gain detailed information on the charge converted in each of the above-discussed processes and to precisely determine the voltage regime where the irreversible processes O_* start, the maximum potential in GCPL measurements was step-wise increased from OCV to 3 V with a 0.1 V step size (see Fig S7 in the Supplemental Material). For $(Li_2Fe)SeO$-BM600, the capacity stored by direct discharge from OCV is very small and amounts to only 6 mAh g^{-1} . This agrees to the CVs which show negligible electrochemical activity in this regime. The same measurements on $(Li_2Fe)SeO$-BM however yield the sizable capacity of $\sim$ 60 mAh g^{-1} for the first three cycles (see Fig. S7a,c in the Supplemental Material). The quasi-linear behaviour of the potential curves hints to the amorphous nature of the electrochemical active $Fe_{1-x}Se_x$. Upon subsequent increase of the potential range, in $(Li_2Fe)SeO$-BM600 a change of the potential lines and the development of a plateau-like feature indicating the low-voltage process R_3/O_3 is seen when the maximum voltage of 2.5 V is exceeded (see Fig. S7d). For $(Li_2Fe)SeO$-BM the boundary voltage is due to the already initially existing $Fe_{1-x}Se_x$ impurity phase harder to estimate. However, one also observes a change in the potential line profile and an increase of the plateau-like feature (R_3/O_3) in the 2.5 V boundary voltage region. The data, therefore, imply that, at C/10, the limiting voltage to avoid the irreversible transformation of $(Li_2Fe)SeO$ to $Fe_{1-x}Se_x$ is around 2.5 V.

In order to further confirm the formation of $Fe_{1-x}Se_x$ in $(Li_2Fe)SeO$-BM600 during cycling, *ex-situ* TEM measurements of $(Li_2Fe)SeO$-BM600 have been performed after charging the material to 3 V using a constant current constant voltage (CCCV) protocol. The TEM results in Fig. 6a-c show that the cycled material again exhibits two kinds of particles. Firstly, there are particles with crystalline structures similar to those observed in the pristine material with lattice spacings corresponding to $(Li_2Fe)SeO$ (Fig. 6a). In addition, the TEM images (Fig. 6b and c) display particles with mixed crystalline/amorphous regions where the crystalline parts exhibit a lattice spacing of 0.55(1) nm corresponding to FeSe[26]. It has to be mentioned that crystalline regions with a large lattice d-spacing of 0.53(1) nm are also present in pristine $(Li_2Fe)SeO$-BM600 but very rarely which is in agreement with the electrochemical data. We hence conclude that the highlighted area in (c) correspond to regions where $(Li_2Fe)SeO$ was converted to $Fe_{1-x}Se_x$.

To verify whether the high voltage process O_* and its effects are general, synthesis-independent phenomena in antiperovskite cathodes, similar measurements were also performed for $(Li_2Fe)SeO$-SSR and $(Li_2Fe)SO$-SSR (see Fig. S8 in the Supplemental Material). X-ray diffractograms as well as SEM images of the SSR samples can be found in the Supplemental Material Fig. S9 and display their purity and particle size. The obtained

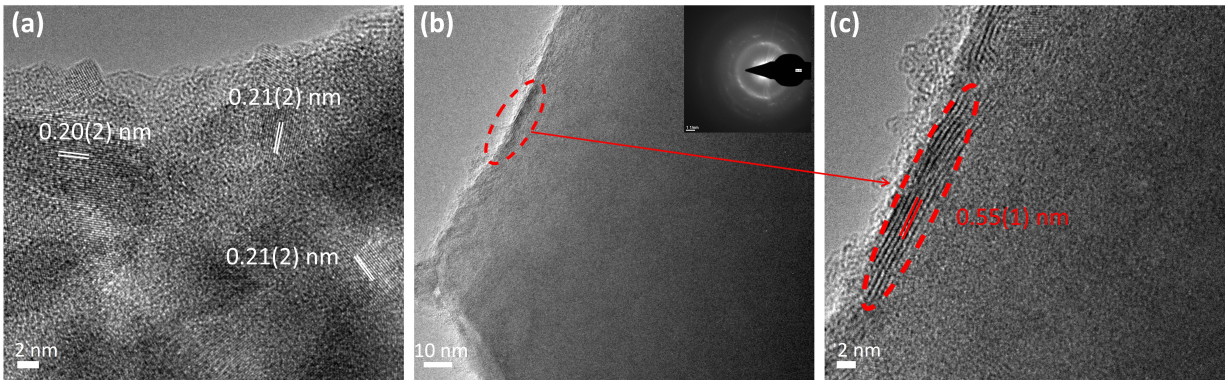

Fig. 6 *Ex-situ* TEM images of an $(Li_2Fe)SeO$-BM600 electrode charged to 3 V using a CCCV protocol (see the text).

CVs are very similar to the ball-milled $(Li_2Fe)SeO$ and confirm a highly reversible behaviour when the voltages are limited below the high voltage process O_*. Significant irreversibility appears again only when the high-voltage processes are included. The fact that this observation holds for all presented antiperovskite materials independent on synthesis and composition demonstrates that the process O_* is a general feature of antiperovskite cathodes which strongly hinders reversible cycling.

In summary, we conclude two major results. (1) We find a new process in the high voltage range that leads to the progressive, irreversible phase transformation of $(Li_2Fe)SeO$ to $Fe_{1-x}Se_x$. (2) We discover the severe effect of the process (O_*) on the electrochemical properties of lithium-rich antiperovskites and prove its generic nature.

The current capability of $(Li_2Fe)SeO$-BM and $(Li_2Fe)SeO$-BM600 is displayed in Fig. 7. To determine the influence of O_* on the high-current capability and stability, measurements were conducted both up to 3 V and in a limited potential range (up to 2.5 V) avoiding O_*. At cycle 1, two characteristics stand out. Firstly, in the entire potential range, 1-3 V, both samples convert an enormous initial capacity of around 300 mAh g^{-1} at a current rate of C/10, which is up to now the highest capacity ever reported for any Li-rich antiperovskite and therefore confirms the huge advantage and potential of mechanochemical synthesis. Secondly, in the restricted potential regime a capacity of still 220 mAh g^{-1} is reached for $(Li_2Fe)SeO$-BM and around 150 mAh g^{-1} for $(Li_2Fe)SeO$-BM600. The following nine cycles (see Fig. 7a) illustrate that capacity fading even in the initial cycles is completely different when cycling $(Li_2Fe)SeO$ at up to 3 V and 2.5 V, respectively. For the former range, both $(Li_2Fe)SeO$ samples display a strong decrease in capacity whereas in the restricted potential range $(Li_2Fe)SeO$-BM shows stable capacity and $(Li_2Fe)SeO$-BM600 even an increase to 240 mAh g^{-1} in cycle 10. At higher current rates, these effects become more pronounced: In $(Li_2Fe)SeO$-BM, we observe average capacities of 205, 170, and 136 mAh g^{-1} at C/4, C/2 and 1 C in the full potential range and 204, 190, and 163 mAh g^{-1} in the limited one. In $(Li_2Fe)SeO$-BM600, the same measurements yield 150, 108, and 75 mAh g^{-1} (full range) and 196, 145, and 95 mAh g^{-1} (limited range). The major findings are as following: (1) $(Li_2Fe)SeO$-BM exhibits a better overall high current capability than BM600. (2) The limited potential range is beneficial for both samples, leading to a higher converted capacity at higher currents and improved cycling stability. In particular, in the limited potential regime the reversibly accessibly capacity in $(Li_2Fe)SeO$ exceeds the one accessible when cycling up to 3 V after a few cycles. We hence also conclude, that the hybrid $(Li_2Fe)SeO/Fe_{1-x}Se_x$ material in $(Li_2Fe)SeO$-BM displays a superior electrochemical performance compared to the pure material present in $(Li_2Fe)SeO$-BM600. However, a part of the converted capacity for $(Li_2Fe)SeO$-BM is associated with the contained $Fe_{1-x}Se_x$-phase. In both cases, application of a limited potential range is beneficial for the electrochemical performance.

The evolution of the potential profiles provides further insight into the differences appearing for the two materials and voltage regimes and in particular where the capacity is actually converted (see Fig. S10 in the Supplemental Material). In agreement with the expected formation of $Fe_{1-x}Se_x$ at high voltages, the associated capacity to the converted capacity of cycle one for the samples $(Li_2Fe)SeO$-BM and BM600 in the full potential range (see S10a,c) is already highly increased 112 mAh g^{-1} ($(Li_2Fe)SeO$-BM) and 118 mAh g^{-1} ($(Li_2Fe)SeO$-BM600) compared to the capacity attributed to the $Fe_{1-x}Se_x$-phase which can be obtained by direct discharge (60 mAh g^{-1} and 6 mAh g^{-1} for $(Li_2Fe)SeO$-BM and BM600). The formed $Fe_{1-x}Se_x$-phase however cannot compensate for the capacity losses of $(Li_2Fe)SeO$, hence resulting in the observed fading. The data also imply that in $(Li_2Fe)SeO$-BM the process O_3/R_3 attributed to $Fe_{1-x}Se_x$ does not increase when cycling in the limited voltage range from 1 to 2.5 V while a clear increase of this process is evident in $(Li_2Fe)SeO$-BM600 already after the fifth cycle. One might speculate that already at 2.5 V a small portion of $Fe_{1-x}Se_x$ is formed in $(Li_2Fe)SeO$-BM600 in contrast to $(Li_2Fe)SeO$-BM which may explain its lower cycling stability in the restricted potential range. This result again indicates the dependence on and importance of the boundary voltage, as slight changes lead to huge effects on the electrochemical performance. Note, that the reversible regime depends on the kinetics present and especially the current rate as all processes shift to higher voltages for higher currents. Comparing the positions of the plateaus in the potential profiles at 1 C and C/10 leads to

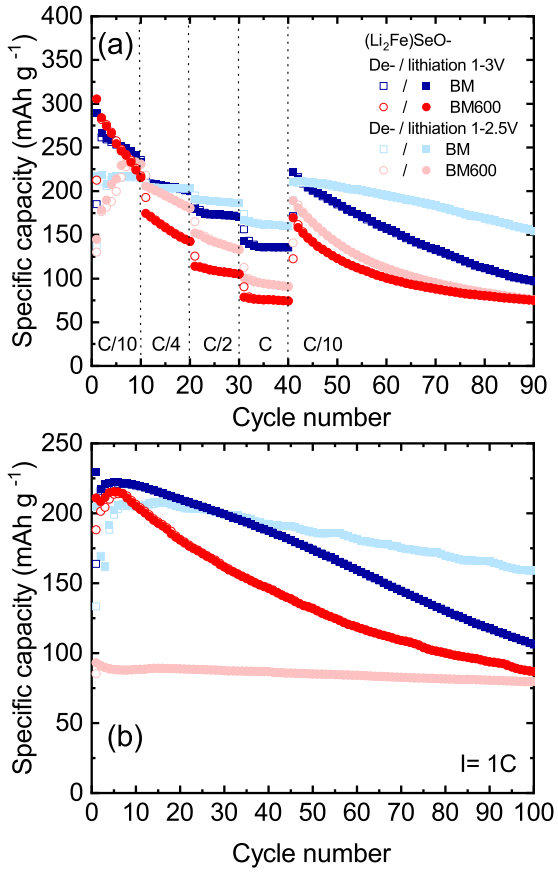

Fig. 7 Rate performance (a) and specific dis-/charge capacities at 1 C (b) of $(Li_2Fe)SeO$-BM and -BM600 in the potential window 1-3 V and 1-2.5 V, respectively.

an estimated shift of 0.1 to 0.2 V.

Galvanostatic cycling studies at 1 C (Fig. 7b) confirm excellent electrochemical performance of mechanochemically synthesized $(Li_2Fe)SeO$. As already mentioned above, the data in particular imply superior performance of $(Li_2Fe)SeO$-BM when limiting the voltage to a maximum of 2.5 V. Specifically, while the initial capacity amounts to around 200 mAh g^{-1} , cycling at 1 C only yields moderate capacity fading resulting in 158 mAh g^{-1} , after 100 cycles. When cycling to 3 V, slightly higher initial capacity of ~220 mAh g^{-1} is achieved with however much stronger fading to 105 mAh g^{-1} in cycle 100. For the same voltage regime, findings for $(Li_2Fe)SeO$-BM600 are similar, i.e., there is a rather larger decrease of capacity from initially 210 mAh g^{-1} to 90 mAh g^{-1} in cycle 100. Whereas, in the limited potential range a quasi-constant capacity of 90 mAh g^{-1} is reached. The latter observation is in full accordance with our conclusion that presence and conversion to $Fe_{1-x}Se_x$ triggers capacity fading in $(Li_2Fe)SeO$ as in $(Li_2Fe)SeO$-BM600 there is no $Fe_{1-x}Se_x$ and due to the slight shift of O_* towards higher voltages (see Fig. S11 in the Supplemental Material) conversion to $Fe_{1-x}Se_x$ starts at 1 C well above 2.5 V. Long-term galvanostatic cycling studies of $(Li_2Fe)SeO$-BM and $(Li_2Fe)SeO$-BM600 in the restricted potential range to 2.5 V and over 500 cycles can be found in Fig. S12 in the Supplemental Material. For $(Li_2Fe)SeO$-BM600, the data at 1 C show only a small drop in capacity over more than 500 cycles when limiting the maximum voltage to 2.5 V, thereby confirming negligible fading when the formation of the $Fe_{1-x}Se_x$-phase is completely prevented. The results hence clearly show that capacity fading appearing in all previous reports on antiperovskite cathodes can be practically circumvented when the fading channel via $Fe_{1-x}Se_x$ is avoided.

4 Conclusions

In summary, we report for the first time a straightforward low-temperature, easy-to-scale mechanochemical synthesis method for the antiperovskite $(Li_2Fe)SeO$. Moreover, we propose a new electrochemical reaction mechanism for $(Li_2Fe)SeO$ which is generalized to all up-to-now investigated antiperovskite cathodes. Our data in particular prove the progressive partial conversion of $(Li_2Fe)SeO$ to $Fe_{1-x}Se_x$ at high voltages. While $Fe_{1-x}Se_x$ is electrochemically active its formation still reduces the overall capacity of the material and in particular opens a channel to capacity fading. Notably, completely avoiding this channel in a post-synthesis heat-treated material practically prevents capacity fading appearing in all previous reports on antiperovskite cathodes. Pristine mechanochemically synthesised $(Li_2Fe)SeO$ with more dispersed and smaller primary particles even achieves an outstanding reversible specific capacity of 200 mAh g^{-1} at the high current rate of 1 C. The results and achievements presented at hand further elucidate the electrochemical reaction mechanism in antiperovskites and show a route how to increase their cycling stability. The success of this approach is already proven by the drastic performance improvements of $(Li_2Fe)SeO$ demonstrated at hand.

Author Contributions

Conceptualization, L.S., M.M., N.G., R.K.; Synthesis and materials characterisation M.M., B.B., S.H., N.G.; TEM studies I.G.G.M.; XPS studies M.H.; BET studies K.W., E.M.; Electrochemical and magnetic studies L.S., H.H.; writing—original draft preparation, L.S., M.M., R.K.; Writing - Review & Editing, L.S., M.M., N.G., R.K.; visualization, L.S., M.M.; supervision, R.K. and N.G.; All authors have read and agreed to the published version of the manuscript.

Conflicts of interest

There are no conflicts to declare.

Acknowledgements

The authors thank Andrea Voss and Anne Voidel (IFW Dresden) for performing ICP-OES measurements. Financial support by Deutsche Forschungsgemeinschaft (DFG) through projects KL 1824/20-1 and GR 5987/2-1 and by BMBF via the project SpinFun (13XP5088) is acknowledged. Work has also been supported within the framework of the Excellence Strategy of the Federal and State Governments of Germany via Heidelberg University's flagship EMS initiative. M.A.A. Mohamed thanks the IFW excellence program for financial support. S. Hampel acknowledges the financial support by the German Research Foundation (DFG) within project VA831/4-1.

Notes and references

1 K. T. Lai, I. Antonyshyn, Y. Prots and M. Valldor, *Journal of the American Chemical Society*, 2017, **139**, 9645–9649.

2 D. Mikhailova, L. Giebeler, S. Maletti, S. Oswald, A. Sarapulova, S. Indris, Z. Hu, J. Bednarcik and M. Valldor, *ACS Applied Energy Materials*, 2018, **1**, 6593–6599.

3 M. V. Gorbunov, S. Carrocci, S. Maletti, M. Valldor, T. Doert, S. Hampel, I. G. Gonzalez Martinez, D. Mikhailova and N. Gräßler, *Inorganic chemistry*, 2020, **59**, 15626–15635.

4 M. V. Gorbunov, S. Carocci, I. G. Gonzalez Martinez, V. Baran and D. Mikhailova, *Frontiers in Energy Research*, 2021, **9**, 360.

5 A. Banik, T. Famprikis, M. Ghidiu, S. Ohno, M. A. Kraft and W. G. Zeier, *Chemical Science*, 2021, **12**, 6238–6263.

6 J. Zhang, J. Qiao, K. Sun and Z. Wang, *Particuology*, 2022, **61**, 18–29.

7 A. S. Aricò, P. Bruce, B. Scrosati, J.-M. Tarascon and W. van Schalkwijk, *Nature Materials*, 2005, **4**, 366–377.

8 Y. Sun, N. Liu and Y. Cui, *Nature Energy*, 2016, **1**, 366â€“– 377.

9 R. Jain, A. S. Lakhnot, K. Bhimani, S. Sharma, V. Mahajani, R. A. Panchal, M. Kamble, F. Han, C. Wang and N. Koratkar, *Nature Reviews Materials*, 2022, **7**, 736–746.

10 M. A. A. Mohamed, M. V. Gorbunov, M. Valldor, S. Hampel, N. Gräßler and D. Mikhailova, *Journal of Materials Chemistry A*, 2021, **9**, 23095–23105.

11 P. Muhammed Shafi and A. Chandra Bose, *AIP Advances*, 2015, **5**, 057137.

12 A. L. Patterson, *Physical Review*, 1939, **56**, 978–982.

13 `http://www.gatan.com/products/tem-analysis/gatan-microscopy-suite-software`.

14 G. S. Zakharova, L. Singer, Z. A. Fattakhova, S. Wegener, E. Thauer, Q. Zhu, E. V. Shalaeva and R. Klingeler, *Journal of Alloys and Compounds*, 2021, **863**, 158353.

15 X. Zhang, X. Zhang, X. Sun, Y. An, S. Song, C. Li, K. Wang, F. Su, C.-M. Chen, F. Liu, Z.-S. Wu and Y. Ma, *Journal of Power Sources*, 2021, **488**, 229454.

16 J. F. Moulder, W. F. Stickle, W. M. Sobol and K. D. Bomben, Handbook of X-Ray Photoelectron Spectroscopy, 1992.

17 R. Dedryvère, M. Maccario, L. Croguennec, F. Le Cras, C. Delmas and D. Gonbeau, *Chemistry of Materials*, 2008, **20**, 7164–7170.

18 T. Radu, C. Iacovita, D. Benea and R. Turcu, *Applied Surface Science*, 2017, **405**, 337–343.

19 A. P. Grosvenor, B. A. Kobe, M. C. Biesinger and N. S. McIntyre, *Surface and Interface Analysis*, 2004, **36**, 1564–1574.

20 R. Ospina, S. A. Rincón-Ortiz and J. Rodriguez-Pereira, *Surface Science Spectra*, 2020, **27**, 014021.

21 J. R. Shallenberger and N. Hellgren, *Surface Science Spectra*, 2020, **27**, 014020.

22 J.-C. Dupin, D. Gonbeau, P. Vinatier and A. Levasseur, *Physical Chemistry Chemical Physics*, 2000, **2**, 1319–1324.

23 M. Mohamed, L. Singer, H. Hahn, D. Djendjur, A. Özkara, E. Thauer, I. G. Gonzalez-Martinez, M. Hantusch, B. Büchner, S. Hampel, R. Klingeler and N. Gräßler, *Journal of Power Sources*, 2023, **558**, 232547.

24 D. L. Zhang, *Progress in Materials Science*, 2004, **49**, 537–560.

25 P. W. Voorhees, *Journal of Statistical Physics*, 1985, **38**, 231–252.

26 M. Shi, N. Wang, B. Lei, J. Ying, C. Zhu, Z. Sun, J. Cui, F. Meng, C. Shang, L. Ma *et al.*, *New Journal of Physics*, 2018, **20**, 123007.

27 F. Nitsche, T. Goltz, H.-H. Klauss, A. Isaeva, U. Muller, W. Schnelle, P. Simon, T. Doert and M. Ruck, *Inorganic chemistry*, 2012, **51**, 7370–7376.

28 P. Terzieff and K. L. Komarek, *Monatshefte für Chemie*, 1978, **109**, 1037–1047.

29 T. Hirone, S. Maeda and N. Tsuya, *Journal of the Physical Society of Japan*, 1954, **9**, 496–499.

30 S. Muhammad, S. Lee, H. Kim, J. Yoon, D. Jang, J. Yoon, J.-H. Park and W.-S. Yoon, *Journal of Power Sources*, 2015, **285**, 156–160.

31 P. Poizot, S. Laruelle, S. Grugeon, L. Dupont and J. M. Tarascon, *Nature*, 2000, **407**, 496–499.

32 M. C. Menard, A. C. Marschilok, K. J. Takeuchi and E. S. Takeuchi, *Electrochimica Acta*, 2013, **94**, 320–326.

33 D. C. Bock, C. J. Pelliccione, W. Zhang, J. Timoshenko, K. W. Knehr, A. C. West, F. Wang, Y. Li, A. I. Frenkel, E. S. Takeuchi, K. J. Takeuchi and A. C. Marschilok, *Physical chemistry chemical physics : PCCP*, 2017, **19**, 20867–20880.

34 Du Zhong, J. Chen, J. Zhang, Y. Luo, Z. Li, L. Cheng, Y. Chen, G. Wang and R. Wang, *Materials Research Express*, 2019, **6**, 085058.

35 Y. Lan, J. Zhou, K. Xu, Y. Lu, K. Zhang, L. Zhu and Y. Qian, *Chemical communications (Cambridge, England)*, 2018, **54**, 5704–5707.

Elucidating the electrochemical reaction mechanism of lithium-rich antiperovskite cathodes for lithium-ion batteries as exemplified by $(Li_2Fe)SeO$.

Lennart Singer[a,**], M.A.A. Mohamed[b,d,**], Henrik Hahn[a], Ignacio G. Gonzalez-Martinez[b], Martin Hantusch[b], Karolina Wenelska[c], Ewa Mijowska[c], Bernd Büchner[b], Silke Hampel[b], Nico Gräßler[b,*], Rüdiger Klingeler[a,*]

[a] *Kirchhoff Institute for Physics, Heidelberg University, 69120 Heidelberg, Germany*
[b] *Leibniz Institute for Solid State and Materials Research Dresden e.V., 01069 Dresden, Germany*
[c] *Nanomaterials Physicochemistry Department, Faculty of Chemical Technology and Engineering, West Pomeranian University of Technology, 71-065 Szczecin, Poland*
[d] *Department of Physics, Faculty of Science, Sohag University, 82524 Sohag, Egypt*

*Corresponding authors.
**Both authors contributed equally.
Email addresses: n.graessler@ifw-dresden.de (Nico Gräßler), klingeler@kip.uni.heidelberg.de (Rüdiger Klingeler)

Preprint submitted to Journal of Materials Chemistry A *May 10, 2023*

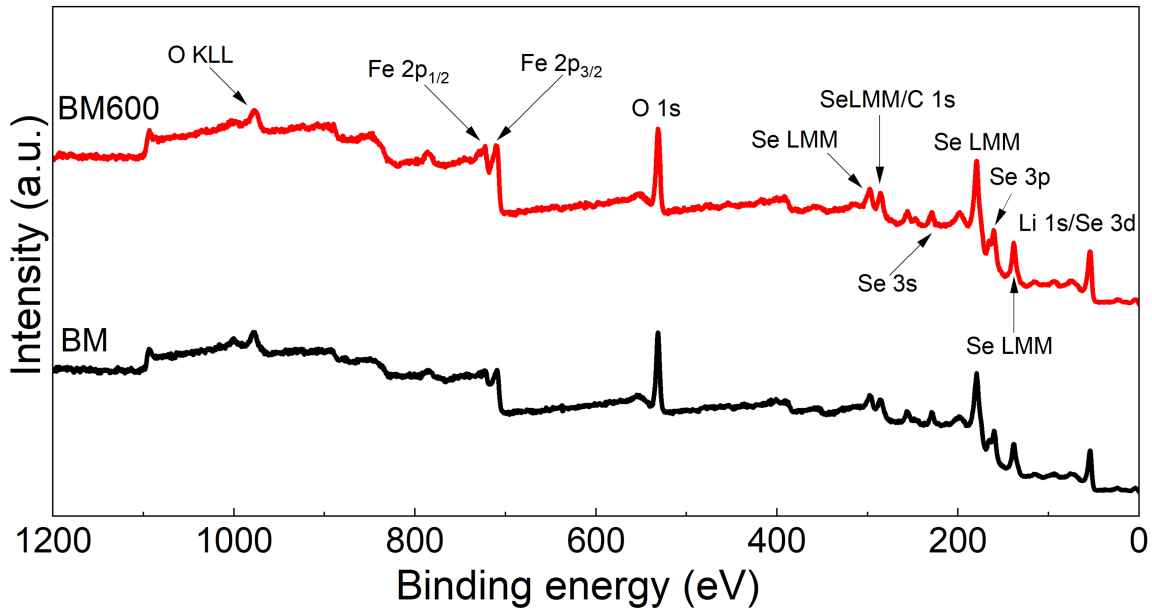

Figure S1 Full XPS spectra of (Li_2Fe)SeO-BM and (Li_2Fe)SeO-BM600

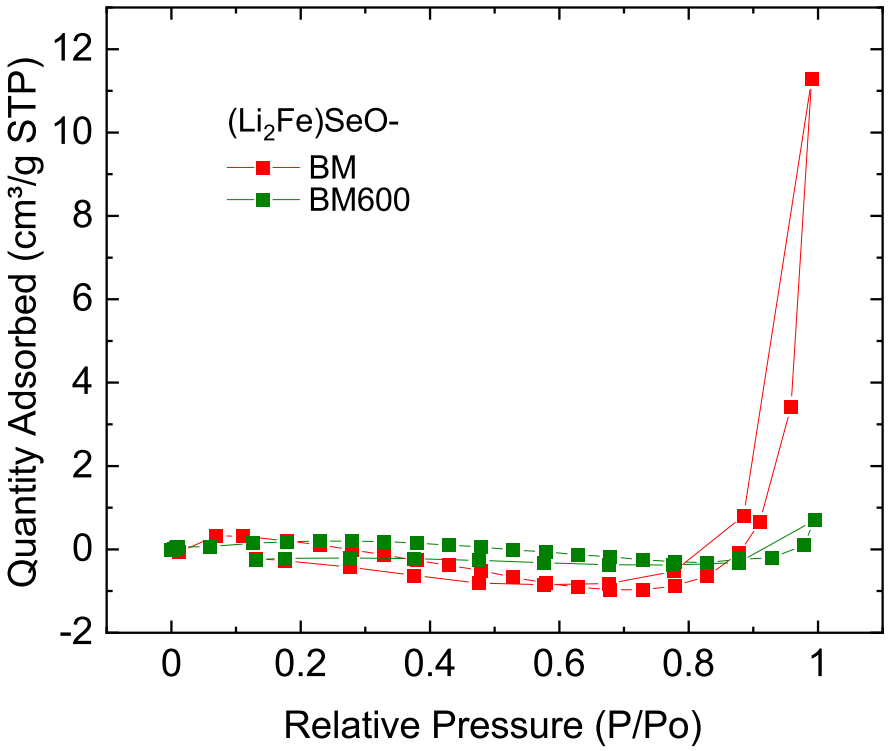

Figure S2 Nitrogen adsorption/desorption isotherms of $(Li_2Fe)SeO$-BM and $(Li_2Fe)SeO$-BM600.

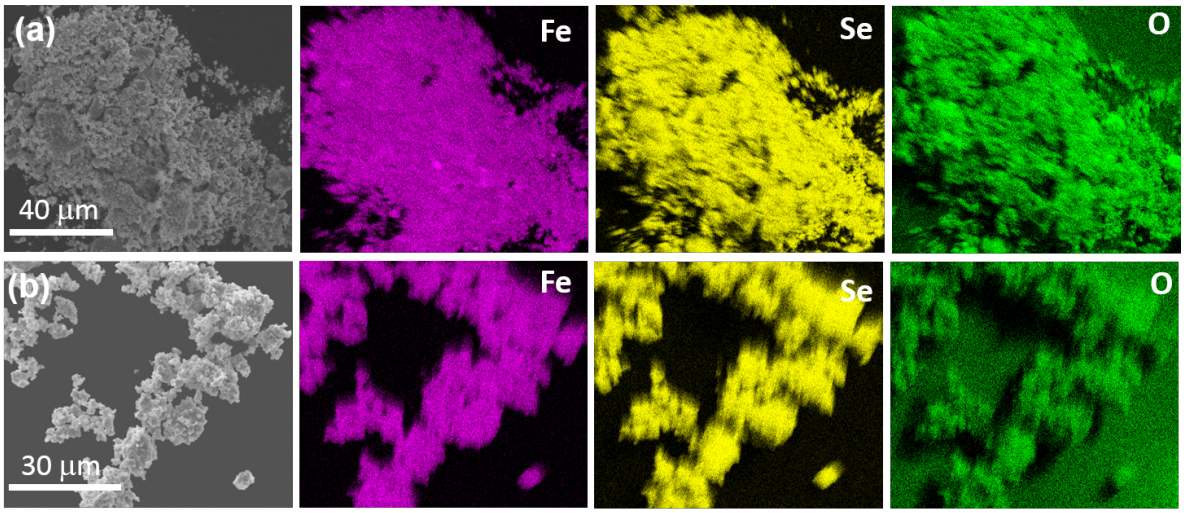

Figure S3 EDS mapping of iron, selenium and oxygen for $(Li_2Fe)SeO$-BM (a) and $(Li_2Fe)SeO$-BM600 (b). The two materials both possess a uniform distribution of the investigated elements.

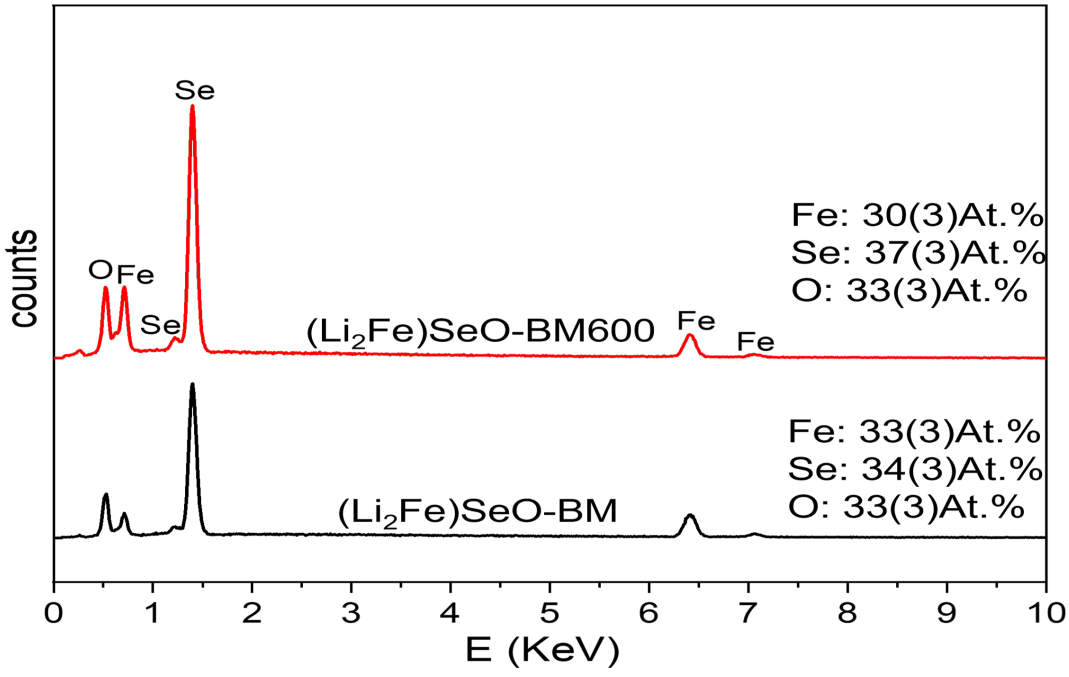

Figure S4 EDS spectra of $(Li_2Fe)SeO$-BM and $(Li_2Fe)SeO$-BM600 together with the atomic percent ratio of the existing elements. The results confirm within uncertainty the expected nominal composition of the materials.

Table S1 ICP-OES results for $(Li_2Fe)SeO$-BM and $(Li_2Fe)SeO$-BM600

compound	Mass %			Molar ratios[1]			
	Li	Fe	Se	Li	Fe	Se	O
$(Li_2Fe)SeO$-BM	8.36±0.13	33.92 ±0.49	47.87±0.55	1.971±0.031	0.994±0.014	0.992±0.011	1.043±0.003
$(Li_2Fe)SeO$-BM600	8.34±0.08	33.81±0.28	47.49±0.49	1.996±0.019	1.006±0.008	0.999±0.01	0.999±0.007

[1]Molar ratios are scaled to sum up to about 5

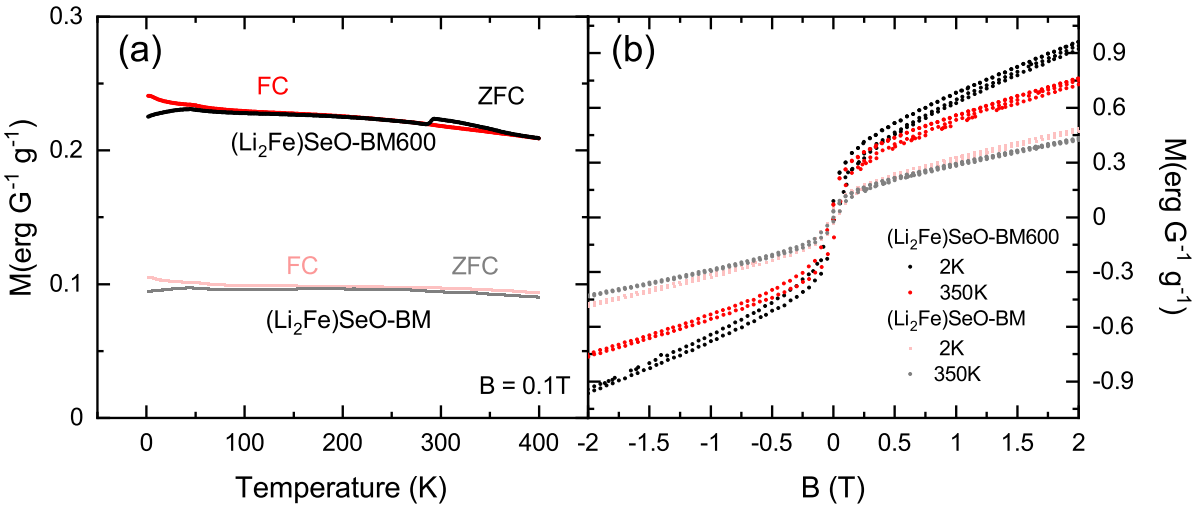

Figure S5 Magnetization of $(Li_2Fe)SeO$ vs. temperature at $B = 0.1$ T (a), and vs. magnetic field at $T = 2$ K (b). The data indicate a antiferromagnetic transition f at ($T_N \simeq 290$ K;) and a ferri or ferromagentic transition at 50 K. Both hint to the existence of $\beta-Fe_{1-x}Se$ with $x \approx 0.26$ as impurity phase present [1, 2].

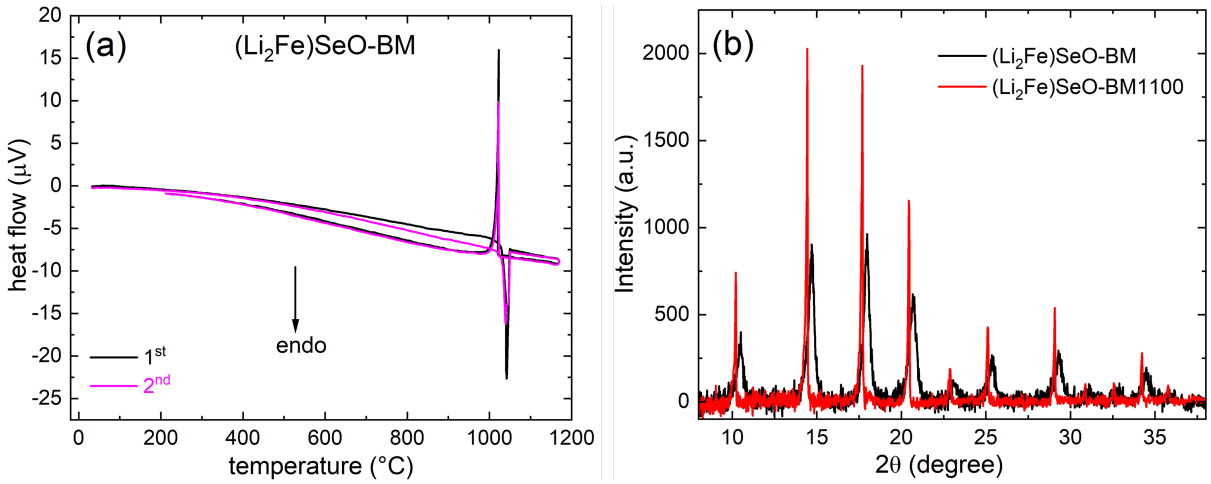

Figure S6 DTA for (Li_2Fe)SeO-BM (a) and XRD patterns (b) for pristine (Li_2Fe)SeO-BM and after its heat treatment at 1100 °C ((Li_2Fe)SeO-BM1100). To prove that no phase decomposition occurs, the (Li_2Fe)SeO-BM was heat-treated at 1100 °C (higher than its melting point) and then cooled normally to room temperature (we refer to this sample as ((Li_2Fe)SeO-BM1100). The XRD patterns using Mo $K_{\alpha 1}$ radiation source ($\lambda = 0.709300$ Å) show that by heating the sample above its melting point, the peaks increase in intensity and becomes sharper. This effect can be attributed to an improvement of crystallinity and long-range atomic order. In addition, a noticeable shift in the peaks position to lower 2θ angle is remarked, which corresponds to an expansion in the lattice parameter. The expansion of the lattice parameter may be attributed to strain relaxation and vanishing of the internal defects.

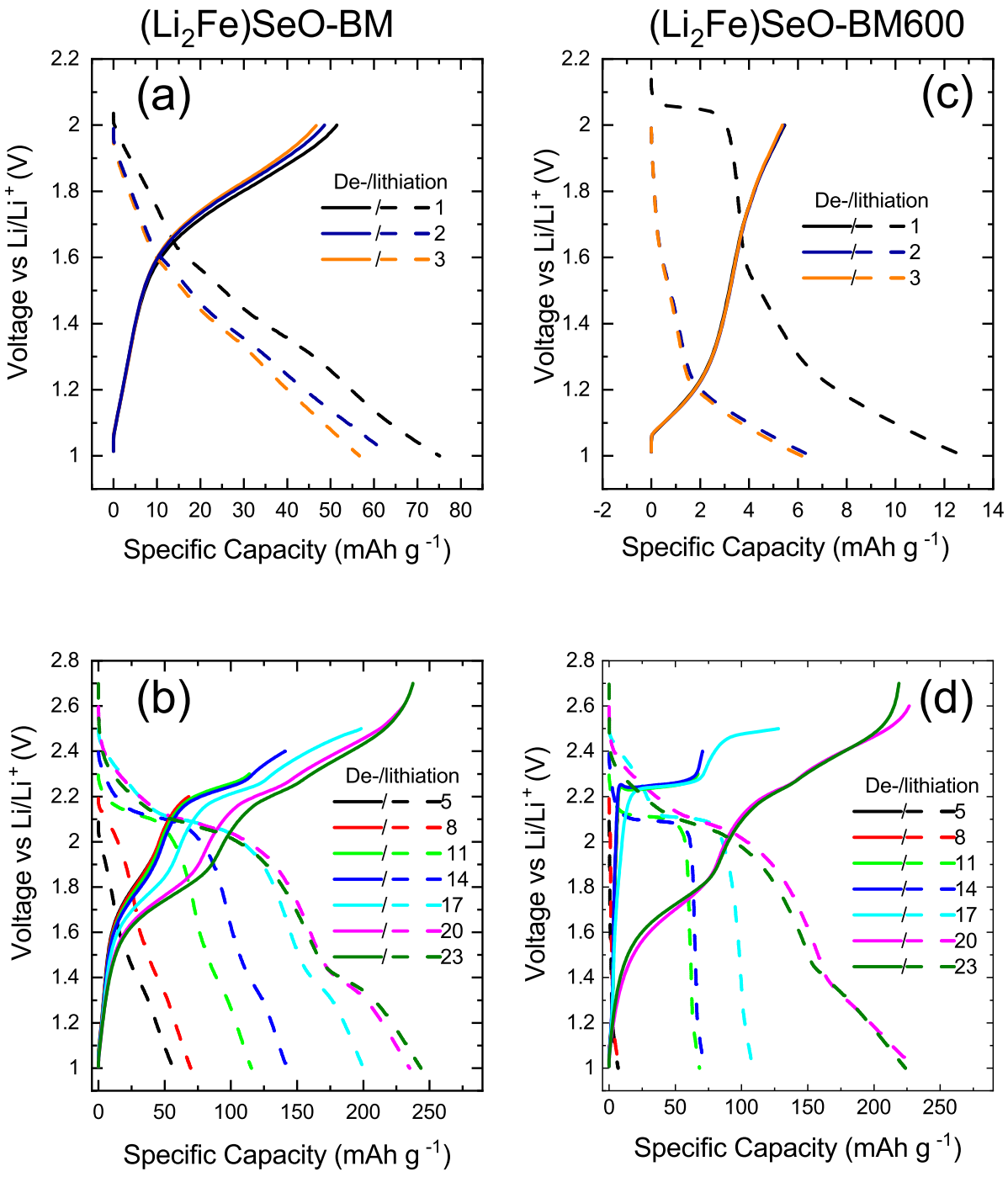

Figure S7 Potential profiles of $(Li_2Fe)SeO$-BM (a,b) and $(Li_2Fe)SeO$-BM600 (c,d) in specific potential ranges at a C/10 current rate. At each potential step, 3 discharge/charge cycles were recorded. At direct discharge $(Li_2Fe)SeO$-BM displays a pronounced capacity of around 75 mAh g^{-1} whereas $(Li_2Fe)SeO$-BM600 (c) shows a much lower capacity of around 12 mAh g^{-1} . By increasing the potential range in 0.1 V steps (b,d) a decisive increase of the low voltage feature R3/O3 is for both samples only visible at 2.6 V, leeding to a boundary voltage of 2.5 V.

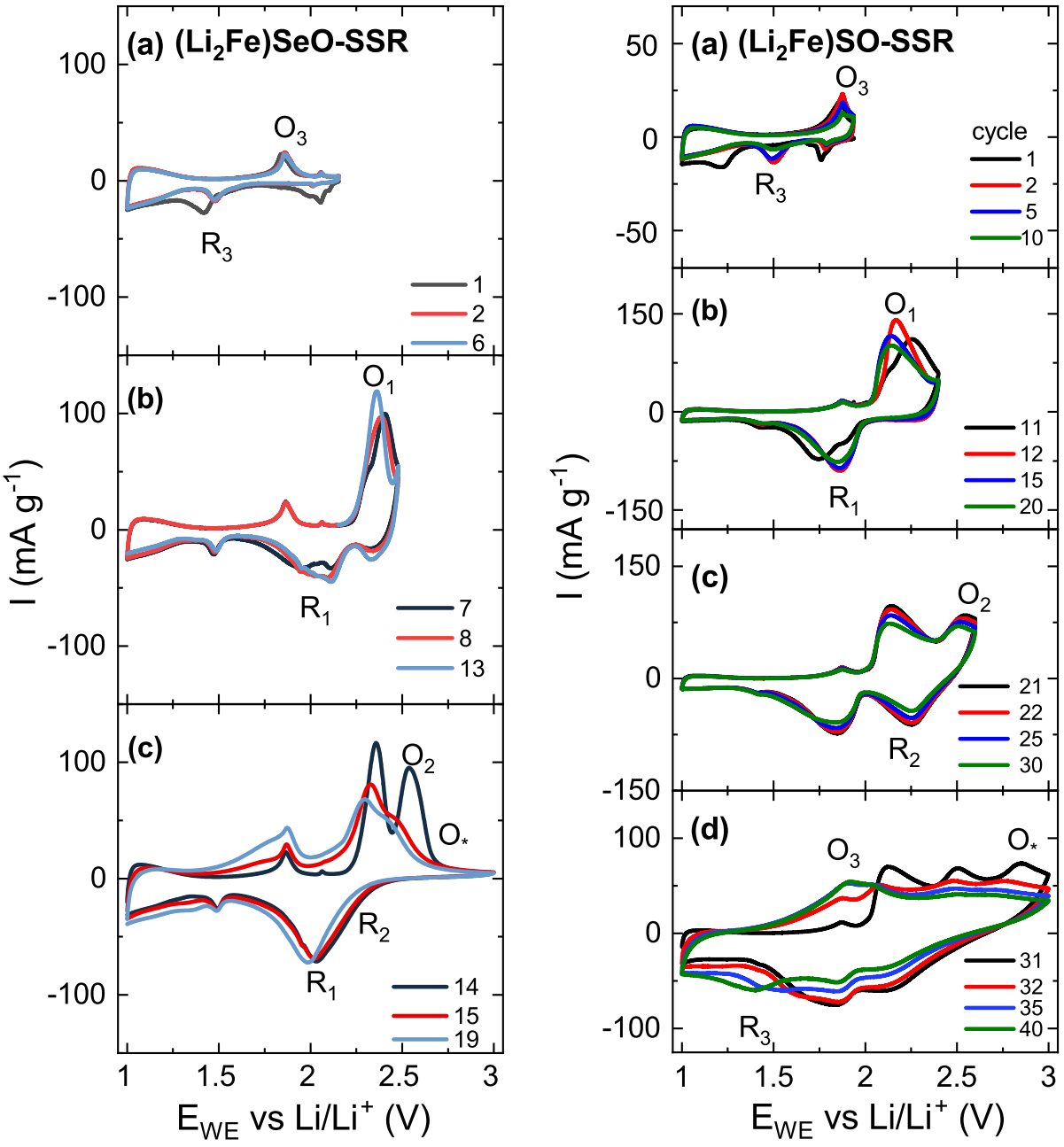

Figure S8 Cyclic voltammograms of (left) $(Li_2Fe)SeO$-SSR in the potential range from (a) 1 to OCV, (b) 1 to 2.4 V, (c) 1-3 V and (right) $(Li_2Fe)SO$-SSR in the potential range from (a) 1 to OCV, (b) 1 to 2.4 V, (c) 1 to 2.6 V and (d) 1 to 3 V vs Li/Li^+ measured at a scan rate of 0.1 mV s^{-1}. The cyclic voltammograms for both materials show, similar to the data shown for $(Li_2Fe)SeO$-BM and BM600 a pronounced increase in the low voltage O3/R3 feature only after the voltage range was extended and include the high voltage process O*. Note, the lower expression of O_3/R_3 after the first cycle for the $(Li_2Fe)SeO$-SSR samples compared to the ball-milled samples can likely be attributed to the much larger particles obtained through the SSR synthesis which reduces the number of active sites.

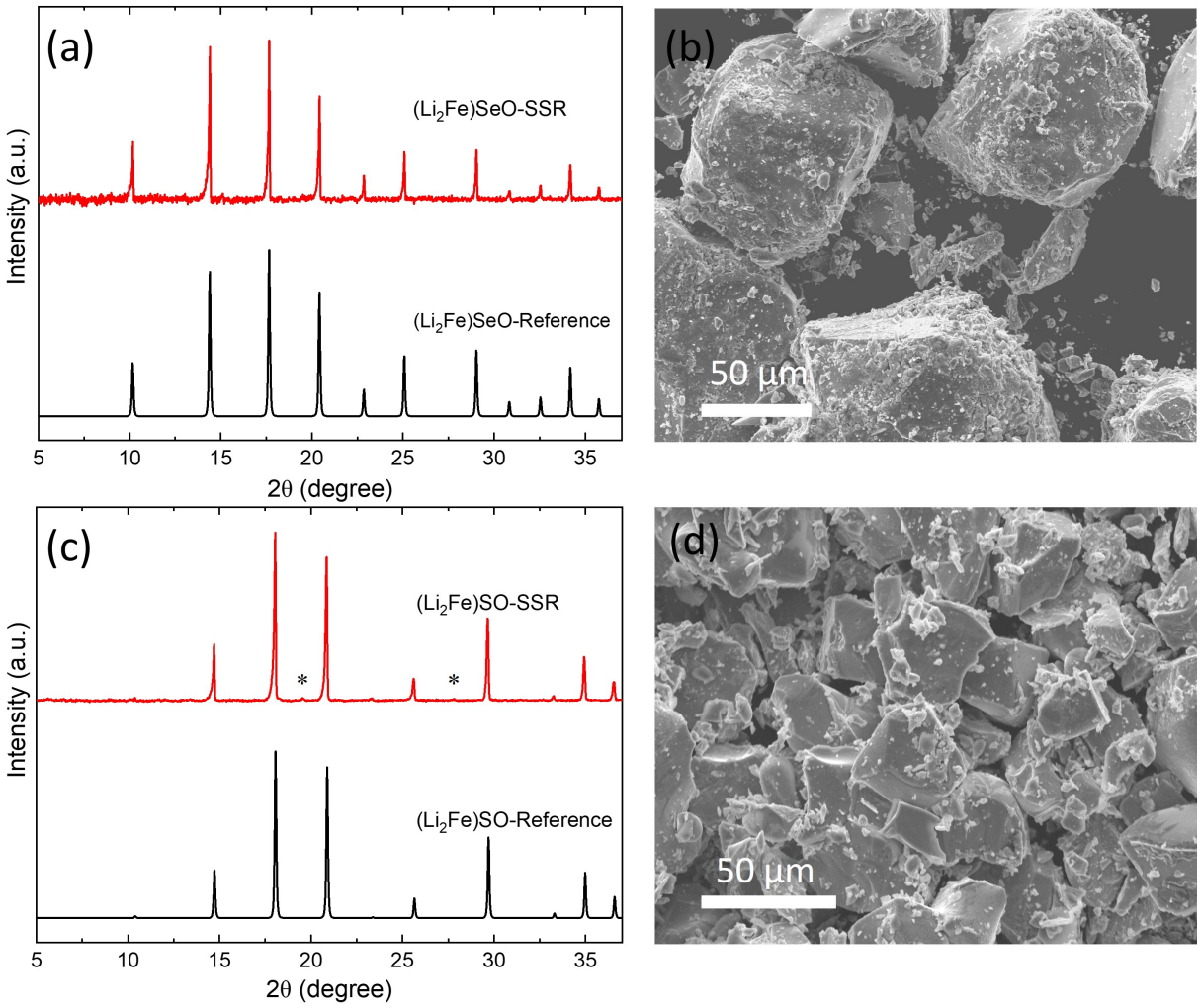

Figure S9 XRD (using Mo $K_{\alpha 1}$ radiation source ($\lambda = 0.709300$ Å)) and SEM image of $(Li_2Fe)SeO$ (a,b) and $(Li_2Fe)SO$ (c,d) prepared by solid-state reaction method. The synthesis was reproduced using the synthesis conditions from Ref.[3]. The asterisks in c refer to minor $LiFeO_2$ secondary phase.

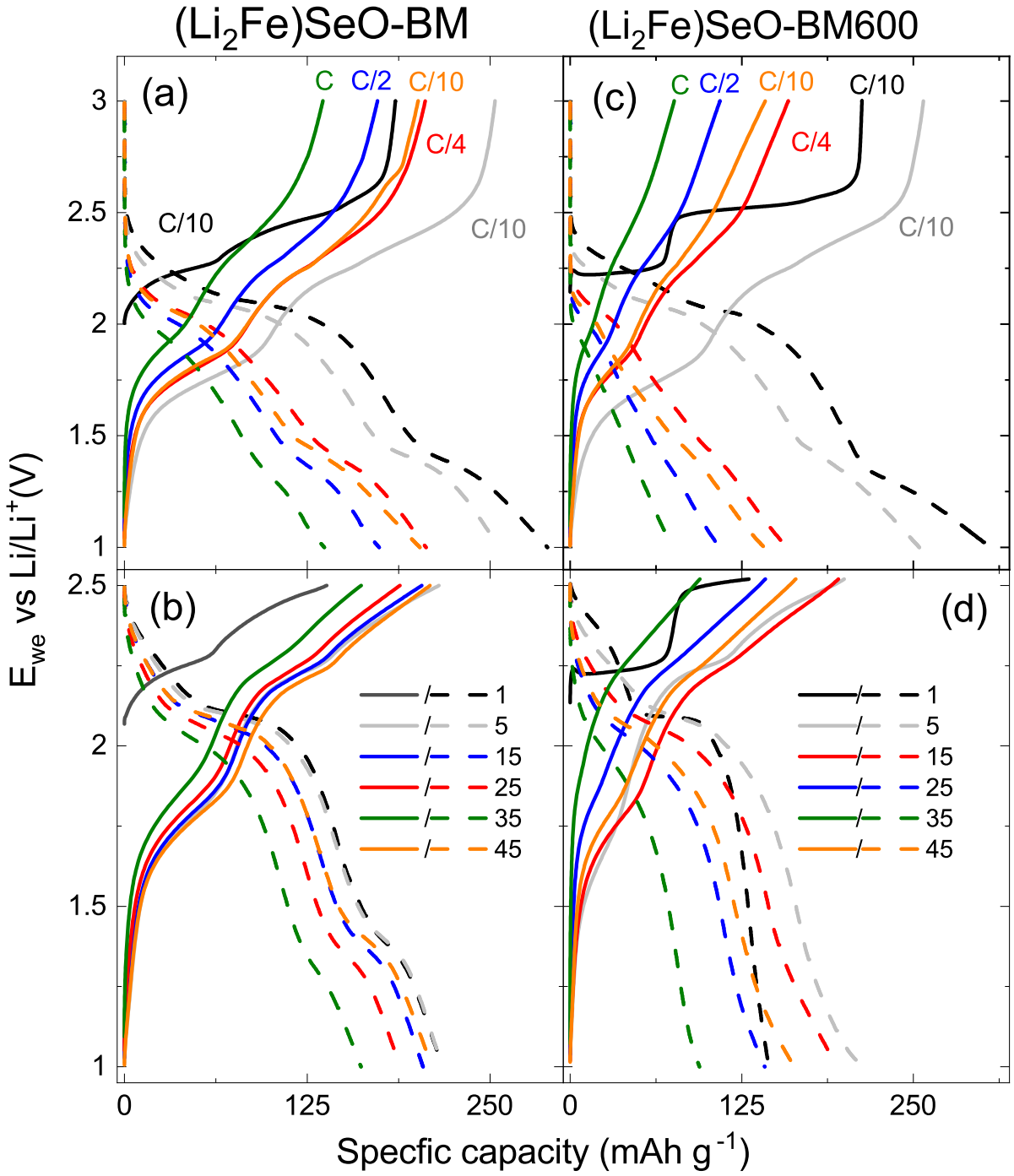

Figure S10 Potential profiles of $(Li_2Fe)SeO$-BM (a,b) and $(Li_2Fe)SeO$-BM600 (c,d) at different current rates of C/10, C/4, C/2 and C. The colors used symbolize distinct cycles and currents.

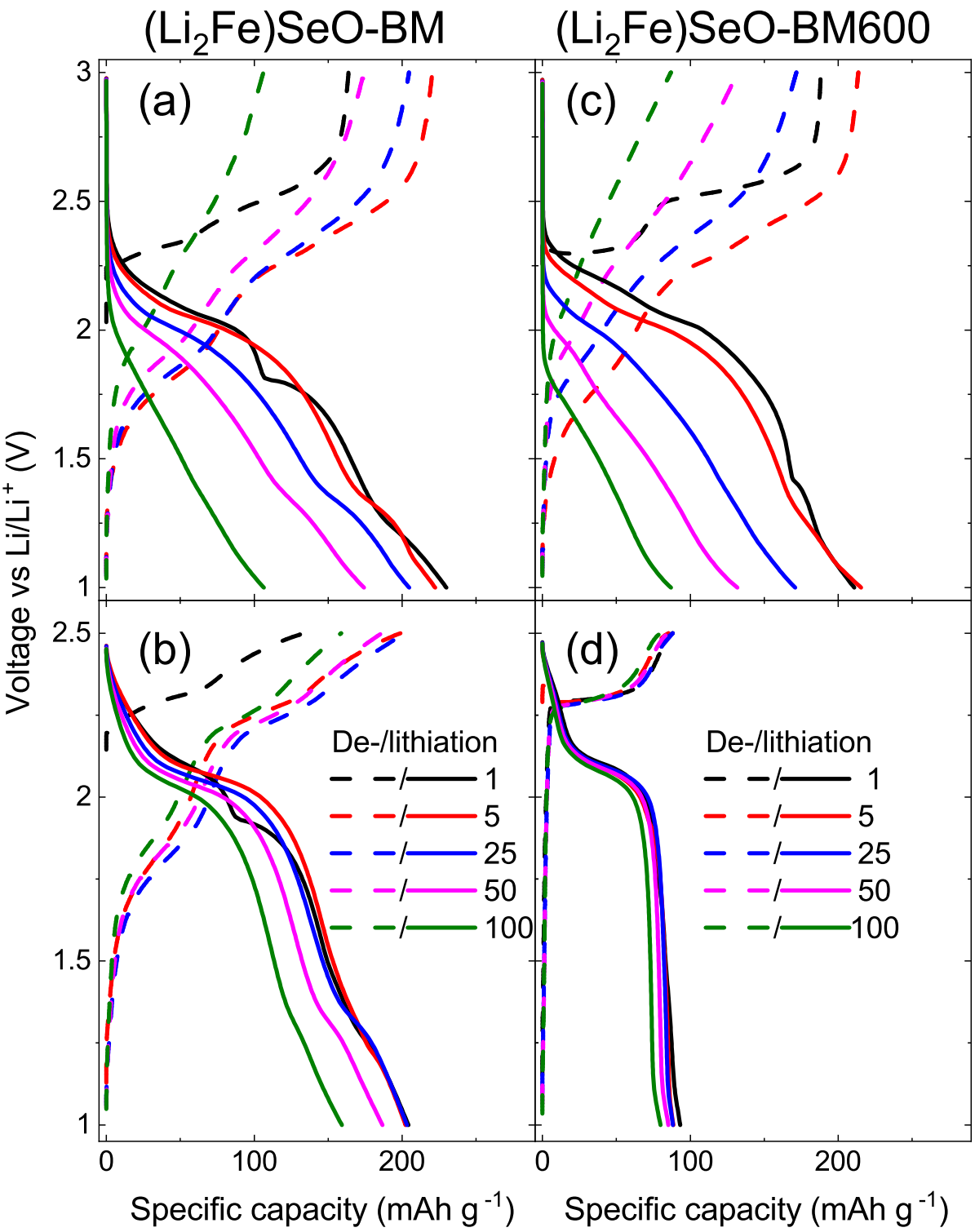

Figure S11 Potential profiles of $(Li_2Fe)SeO$-BM (a,b) and $(Li_2Fe)SeO$-BM600 (c,d) at a current rate of 1 C. The colors used symbolize distinct cycles.

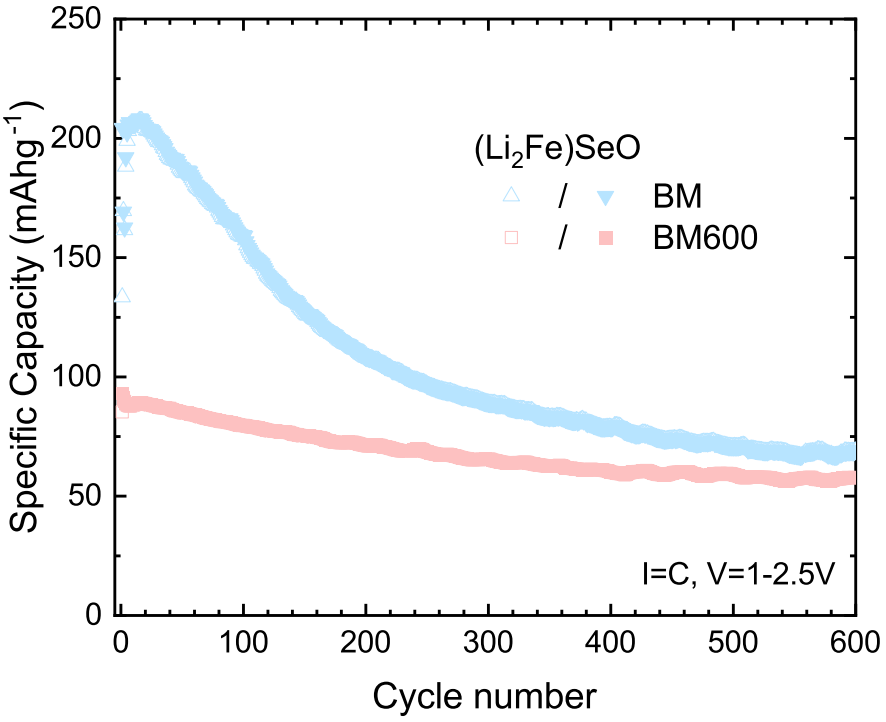

Figure S12 Longterm GCPL of $(Li_2Fe)SeO$-BM and $(Li_2Fe)SeO$-BM600 in the limited potential range from 1 to 2.5 V at 1C.

References

[1] P. Terzieff and K. L. Komarek, *Monatshefte für Chemie*, 1978, **109**, 1037–1047.
[2] T. Hirone, S. Maeda and N. Tsuya, *Journal of the Physical Society of Japan*, 1954, **9**, 496–499.
[3] K. T. Lai, I. Antonyshyn, Y. Prots and M. Valldor, *Journal of the American Chemical Society*, 2017, **139**, 9645–9649.

Kapitel 5 Abschliessende Diskussion

Die vorliegende Arbeit beschäftigt sich mit potenziellen Anoden- und Kathodenmaterialien für Lithium-Ionen-Batterien. Die hergestellten Materialien wurden dafür hinsichtlich ihrer physikalischen und elektrochemischen Eigenschaften untersucht, mit dem Ziel, den Zusammenhang zwischen physikalischen und elektrochemischen Eigenschaften zu verstehen. Um dieses Ziel zu erreichen, wurde ein breites Spektrum an Charakterisierungsmessungen eingesetzt. So wurde die Struktur sowie Kristallitgröße mittels Röntgendiffraktometrie untersucht und die Morphologie und Partikelgröße mittels Rasterelektronenmikroskopie bestimmt. Die chemische Zusammensetzung ergab sich sowohl aus energiedispersiven Röntgenspektroskopie- als auch aus CHN-Analysen. Die vorliegenden Oxidationsstufen der jeweiligen Elemente wurden mittels Röntgenphotoelektronenspektroskopie bestimmt und die magnetischen Eigenschaften der Materialien mittels SQUID-Magnetometrie studiert. Die elektrochemischen Charakterisierungsmethoden zyklische Voltammetrie, galvanostatische Zyklierung und elektrochemische Impedanzspektroskopie kamen zur Bestimmung der elektrochemischen Eigenschaften zum Einsatz. Darüber hinaus wurden in Zusammenarbeit mit Kooperationspartner*innen auch Transmissionselektronenmikroskopie (TEM), Ramanspektroskopie, optische Emissionsspektrometrie mit induktiv gekoppeltem Plasma (ICP-EOS) sowie Differenz-Thermoanalyse (DTA) eingesetzt, um die Materialien weiter zu charakterisieren.

Anhand des Kohlenstoffkomposites Fe_3O_4@HCS wurde der Ursprung sowie die Eigenschaften des zusätzlichen, noch nicht aufgeklärten Speichermechanismuses von Nano-Fe_3O_4-Partikeln untersucht. Das Anodenmaterial Fe_3O_4@HCS wurde dafür mittels Hydrothermalsynthese hergestellt. Das erlangte Kompositmaterial zeichnete sich durch gleichmäßig verteilte, sehr kleine Fe_3O_4-Partikel ($\sim$ 10 nm) auf hohlen Kohlenstoff-Nanopshären ($\sim$ 150 nm) aus. Speziell die sehr kleinen Fe_3O_4-Partikel verleihen Fe_3O_4@HCS interessante elektrochemische Eigenschaften. So zeigt Fe_3O_4@HCS nicht nur eine während des Zyklierens stetig steigende spezifische Kapazität, sondern erreicht auch Werte (1050 mAh g^{-1} in

Zyklus 250 bei einem Strom von 0.1 A g^{-1}) deutlich über der reversiblen theoretischen Kapazität von Bulk-Fe_3O_4 von 694 mAh g^{-1}. Da die gesamte zusätzliche Kapazität auf die enthaltene Fe_3O_4-Komponente zurückgeht, ist die tatsächliche spezifische Kapazität auf die Fe_3O_4-Komponente gerechnet sogar 2000 mAh $g^{-1}_{Fe_3O_4}$. Die zusätzliche Kapazität und ihr Anstieg sind im Fall von Fe_3O_4@HCS aufgrund der besonders kleinen Größe der Fe_3O_4-Partikel stark ausgeprägt. Zwar ist das Erreichen von Kapazitäten über der theoretischen Kapazität ein bekanntes Phänomen für TMOs, die genaue Ursache dahinter ist allerdings noch Gegenstand unzähliger Studien.

Im Rahmen dieser Arbeit kamen sowohl elektrochemische Impedanzmessungen als auch *ex situ*-SEM- und TEM-Messungen für die Untersuchung des zugrundeliegenden, unbekannten Prozesses sowie dessen kontinuierlicher Anstieg zum Einsatz. Die elektrochemischen Impedanzdaten zeigen, dass sich während des Ladens/Entladens eine kapazitive Oberflächenschicht auf- und abbaut, die während des Zyklierens weiter anwächst. Eine Abschätzung des Beitrags des zusätzlichen Speichermechanismuses zur Gesamtkapazität, ausgehend von der Theorie der Speicherung spinpolarisierter Elektronen [88], wurde anhand der Größe der gebildeten Fe-Partikel (*ex situ*-TEM Messungen) und der maximalen Kapazität der Doppelschicht dieser Partikel (Literatur [112]) durchgeführt. Die im Rahmen dieser Arbeit durchgeführte Abschätzung ergab, dass der postulierte Speichermechanismus, im Vergleich zur gemessenen spezifischen Kapazität, mehrere Größenordnungen zu klein ist und somit nicht verantwortlich sein kann. Eine weitere Hypothese [86] hinter der zusätzlichen Kapazität vermutet, dass die zusätzliche Speicherung unter anderem in einer sich kontinuierlichen auf- und abbauenden gelartigen Oberfläche begründet liegt. Die Bildung dieser Oberfläche wiederum kommt in diesem Szenario aus einer reversiblen Reaktion der elektrochemischen gebildeten Fe-Partikel und der SEI. Die Impedanzdaten, die eine sich auf- und abbauende kapazitäre Oberfläche zeigen, lassen diese Theorie als Ursprung durchaus plausibel erscheinen. Darüber hinaus zeigen die Impedanzdaten, dass die beobachtete Abnahme der zusätzlichen Kapazität bei hohen Lade-/Entladeströmen auf die vergleichsweise langsame Zeitkonstante des Prozesses zurückzuführen ist. Die folgende Arbeit konnte somit eine häufig diskutierte Erklärung für die zusätzliche Kapazität ausschließen und fand Indizien für die Speicherung mittels einer sich auf- und abbauenden kapazitären Oberfläche, die vermutlich aufgrund einer Reaktion der gebildeten Fe-Partikeln und der SEI entsteht. Die genaue Reaktion ist allerdings nach wie vor unbekannt und bedarf weiterer Untersuchungen. Die Größe der Kapazität von 1300 mAh $g^{-1}_{Fe_3O_4}$ und deren niedriges Redoxpotential von ungefähr 0.5 V macht diesen Mechanismus aus der Perspektive der Energiespeicherung

besonders interessant. Zum einen wird die theoretische Kapazität von Fe_3O_4 fast verdreifacht und zum anderen auch die durchschnittliche Entladespannung reduziert. Mögliche potenziell hilfreiche Charakterisierungsmessungen für weitere Untersuchungen wären *in situ*-Neutronenstreuung und/oder Kernspinresonanzspektroskopie (NMR). Der Vorteil beider Methoden ist, dass sie, anders als Techniken, die auf Röntgenstrahlen basieren, sensitiv gegenüber Lithium sind.

Im Rahmen einer Sol-Gel-Synthese wurde mittels zweier verfügbarer, preisgünstiger Kohlenstoffquellen (Glukose und Weinsäure) MoO_2/C-Komposite (MoO_2/C-G und MoO_2/C-T) hergestellt. Anschließende Charakterisierungsmessungen zeigen, dass der Kohlenstoffanteil der Komposite maßgeblich von der verwendeten Kohlenstoffquelle abhängt. MoO_2/C-G zeigt einen Kohlenstoffgehalt von 23,7(5)wt% und MoO_2/C-T von 2,4(5) wt%. Die morphologischen Eigenschaften hingegen sind nahezu unbeeinflusst von der verwendeten Kohlenstoffquelle. Elektrochemische Untersuchungen ergaben, dass ein höherer Kohlenstoffanteil prinzipiell zu einer verbesserten elektrochemischen Performance führt. Für den folgenden Vergleich wird, aufgrund der irreversiblen Bildung der SEI im ersten Lithiierungszykluses und der schwierigen Abschätzung dessen Einflusses, immer die Delithiierung betrachtet. Beide MoO_2-Kohlenstoffkomposite zeigen zwar im ersten Delithiierungszyklus eine spezifische Kapazität von 300 mAh g^{-1}, jedoch ist ihre Zyklenstabilität sehr unterschiedlich. Das Komposit mit dem niedrigeren Kohlenstoffanteil (MoO_2/C-T) zeigt nach 15 Zyklen eine spezifische Kapazität 100 mAh g^{-1} und somit einen Verlust von 67%. MoO_2/C-G mit seinem höheren Kohlenstoffanteil hingegen erreicht 280 mAh g^{-1} nach 15 Zyklen und zeigt somit lediglich einen Verlust von 7%. Um den Effekt der Größenskalierung studieren zu können, wurde das Komposit MoO_2/C-G mit seiner vorliegenden Agglomerategröße von 1-3 µm nachbehandelt. Dieser Prozess beinhaltete eine nachträgliche Kolloidvermahlung und eine darauffolgende Temperaturbehandlung bei 500°C für 1 Stunde unter N_2-Atmosphäre. Die Nachbehandlung erwirkte eine Verkleinerung der Agglomerate auf 0,5-0,1 μm (MoO_2/C-G(M)). Die elektrochemischen Untersuchungen zeigen, dass die Sekundärpartikelgröße einen signifikanten Einfluss auf die elektrochemischen Eigenschaften hat. Die nachbehandelte Probe MoO_2/C-G(M) erreicht eine spezifische Kapazität von 650 mAh g^{-1} im ersten Delithiierungszyklus. Dies entspricht 78% der theoretischen spezifischen Kapazität und ist somit mehr als das Doppelte der Kapazität des ersten Zyklus des Ursprungsmaterials MoO_2/C-G von 300 mAh g^{-1}. Die Kapazitätsabnahme nach 15 Zyklen ist allerdings bei beiden Proben quasi identisch und liegt bei 7%. Insgesamt lässt sich für die hergestellten MoO_2-Strukturen festhalten, dass sich sowohl ein höherer Kohlenstoffgehalt

als auch eine Verkleinerung der Agglomerate positiv auf die elektrochemische Performance auswirken. Die Verkleinerung der Agglomerate erhöht die erreichte spezifische Kapazität und ein höherer Kohlenstoffanteil verbessert die Zyklenstabilität.

Als weiteres Konversionsmaterial wurde ein hydrothermal synthetisiertes dreidimensionales hierarchisches blütenartiges Graphen/MoS_2-Nanokomposit vorgestellt. Die Ergebnisse der elektrochemischen Untersuchungen zeigen die typischen Redoxmerkmale von MoS_2 auf. Das blütenartige Graphen/MoS_2-Nanokomposit präsentiert eine vielversprechende spezifische Entladekapazität im ersten Zyklus von 1015 mAh g^{-1}. In den folgenden Zyklen zeigt sich jedoch ein relativ starker Abfall der Kapazität auf 55 mAh g^{-1} in Zyklus 100 und somit eine starke Degeneration des Materials. Zur Untersuchung dieser wurden *ex situ* SEM-Untersuchungen an einer Elektrode nach 100 Zyklen durchgeführt. Diese demonstrieren, dass sich die Kohlenstoffstruktur nahezu nicht verändert, wohingegen die MoS_2-Struktur nach 100 Zyklen vollständig zerstört ist. Die verlorene MoS_2-Struktur deutet auf ein Zerbröseln der Partikel aufgrund der auftretenden großen Volumenänderung sowie Aggregation der Partikel hin. Es ist unklar, inwiefern ein mögliches Herauslösen von Polysulfiden (Shuttle-Effekt) während des Entladevorgangs zusätzlich eine Rolle gespielt hat. Aus Anwendungssicht muss daher festgestellt werden, dass das hergestellte dreidimensionale hierarchische blütenartige Graphen/MoS_2-Nanokomposit alleine nicht die inhärenten Probleme von MoS_2 löst. Eine zusätzliche weitere Beschichtung mit Kohlenstoff oder TiO_2 könnte möglicherweise helfen, die auftretende Degeneration zu reduzieren.

Zusammengefasst wurde im Rahmen der vorliegenden Untersuchungen drei vielversprechende konversionsbasierte Kohlenstoffkomposite Fe_3O_4@HCS, MoO_2/C sowie Graphen-MoS_2 für die potenziell nächste Generation von Anodenmaterialien für Lithium-Ionen-Batterien vorgestellt. Von diesen Materialien sticht vor allem Fe_3O_4@HCS mit seiner sehr hohen spezifischen Kapazität von 1050 mAh g^{-1} nach 250 Zyklen heraus. Die Fe_3O_4@HCS-Struktur verhindert nicht nur am effektivsten die klassischen Nachteile der Konversionsreaktion, wie die Volumenausdehnung während dem zyklieren, sondern ermöglicht aufgrund der Nano-Natur der Fe_3O_4-Partikel darüber hinaus den Zugang zu einem zusätzlichen Speichermechanismus. Unter den hergestellten MoO_2-Kohlenstoffkompositen zeigt das nachbehandelte MoO_2 mit verkleinerten Agglomeraten und höchstem Kohlenstoffgehalt die beste elektrochemische Performance von 650 mAh g^{-1} im ersten Delithiierungszyklus. Die Nachbehandlung des Materials verbesserte dabei die erreichte spezifische Kapazität deutlich. Der Kapazitätsverlust konnte jedoch nicht weiter verbessert werden. Dies führte dazu, dass das nachbehandelte MoO_2-Kohlenstofkomposit nach 100 Zyklen eine Kapazität

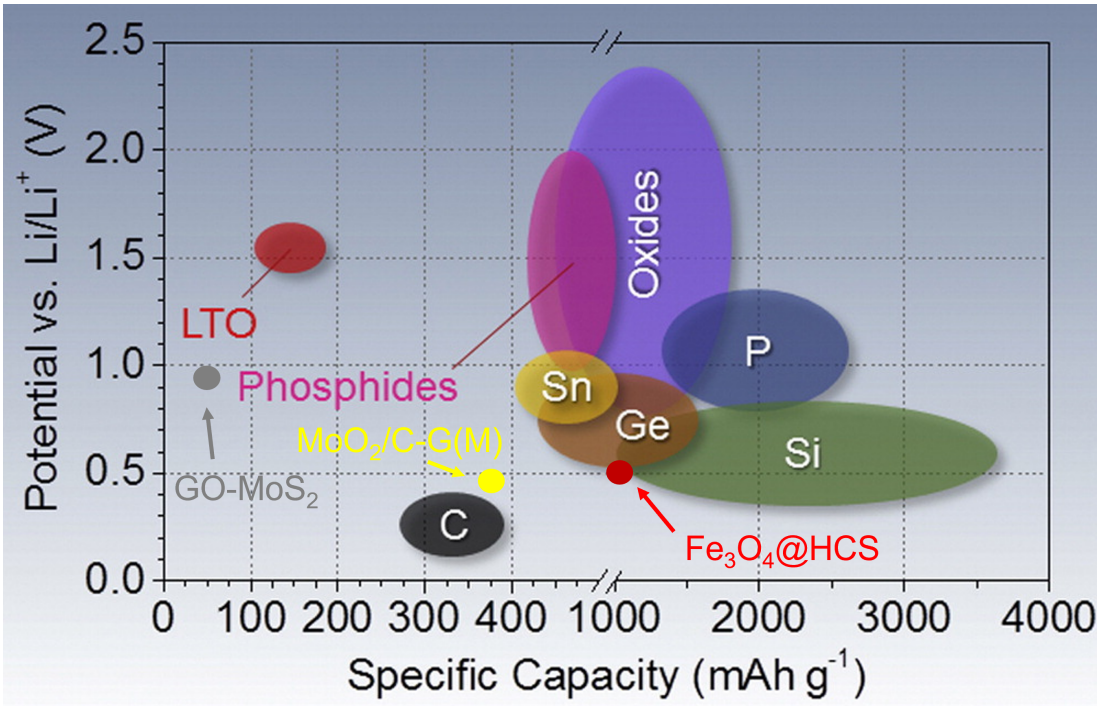

Abbildung 5.1: Vergleich der mittleren Redoxspannungen und spezifischen Kapazitäten von verschiedenen Anodenmaterialien. Die im Rahmen dieser Arbeit vorgestellten Konversionsmaterialien sind in Rot (Fe_3O_4@HCS), Gelb (MoO_2C-G(M)), Grau (GO-MoS_2) eingetragen. LTO steht für $Li_4Ti_5O_12$. Sn, Gn, Si und P stehen für die legierungsbildenden Elemente Zinn, Germanium, Silizium und Phosphor. Oxide stehen für Materialien mit Sauerstoff und Phosphide für Materialien mit Phosphor als Anion. C steht für Graphit, das am häufigsten verwendete Anodenmaterial. Entnommen aus [4].

von 350 mAh g^{-1} umsetzt. Die vorgestellte MoS_2-Kohlenstoff-Struktur zeigt zwar eine hohe Kapazität von 1015 mAh g^{-1} im ersten Zyklus, allerdings löst die vorgestellte Struktur die inhärenten Nachteile des Materials nicht vollständig, was zu einem starken Abfall in der spezifischen Kapazität auf 55 mAh g^{-1} in Zyklus 100 führt.

Eine Übersicht über die spezifischen Kapazitäten und die durchschnittlichen Redoxspannungen der vorgestellten Materialien im Vergleich zu bereits kommerzialisierten und anderen aktiv erforschten Anodenmaterialien ist in Abbildung 5.1 zu finden. Um die Zyklenstabilität der Materialien zu berücksichtigen, wurde die Kapazität am letzten gemessenen Zyklus eingetragen. Für MoO_2/C-G(M) und das blütenartige Graphen/MoS_2 entspricht das der Kapazität bei Zyklus 100. Bei Fe_3O_4@HCSist es die Kapazität bei Zyklus 250.

Abbildung 5.1 zeigt erneut, dass Fe_3O_4@HCS unter den hier untersuchten Anodenmaterialien die vielversprechendsten Eigenschaften für eine potenzielle Kommerzialisierung aufweist. Generell ist zu beachten, dass es sich bei dem durchgeführten Vergleich nur um eine Mo-

mentaufnahme handelt. Die Fortschritte, die für ein Material möglicherweise erzielt werden können, lassen sich schlicht nicht abschätzen. Zum Beispiel ist das tatsächliche Maximum des zusätzlichen Speichermechanismuses von Fe_3O_4 noch nicht bestimmt und liegt vermutlich deutlich über dem hier gemessenen Wert. Zudem existieren weitere Faktoren, die dieser Vergleich nicht berücksichtigt, aber für eine praktische Anwendung von großer Bedeutung sind. Diese Faktoren betreffen alle konversionsbasierten nanostrukturierten Materialien und sind daher von genereller Relevanz [113]. Einer dieser Faktoren ist die geringe Coulombische Effizienz von Konversionsmaterialien aufgrund irreversibler Vorgänge in den ersten Zyklen. Im Fall der Vollzelle führt diese dazu, dass auf Kathodenseite zusätzliches Aktivmaterial vorgesehen werden muss, um die Verluste auszubalancieren. Die Energiedichte wird somit sowohl von der Kathoden- als auch Anodenseite verringert. Ein weiterer Faktor ist die geringe Schüttdichte von Nanomaterialien, die die praktisch erreichbare Energiedichte deutlich reduzieren, da eine geringere Materialmenge pro Volumen eine geringere erreichbare volumetrische Energiedichte nach sich zieht. Für die genannten Probleme existieren teilweise bereits Lösungsansätze. Die geringe Schüttdichte kann zum Beispiel durch eine hierarchische Strukturierung der Primärpartikel zu größeren Sekundärpartikel verbessert werden [114, 115]. Studien haben zudem gezeigt, dass die Coulombische Effizienz der ersten Zyklen durch Elektrolytadditive [116, 117], einer zusätzlichen Beschichtung [118], sowie Prelithiation [119, 120], weiter verbessert werden kann [121]. All diese Faktoren machen aussagekräftige Statements über das Potenzial von Batteriematerialien schwierig. Die Community hat dieses Problem erkannt und ist sehr bestrebt, Metriken zu entwickeln, die diese Faktoren mit einbeziehen [113, 122].

Die Materialklasse der lithiumreichen Antiperowskite und speziell der Vertreter $(Li_2Fe)SeO$ wurde hinsichtlich seines Einsatzes als Kathodenmaterial für Lithium-Ionen-Batterien untersucht. Das mittels Festkörpersynthese hergestellte lithiumreiche Antiperowskit $(Li_2Fe)SeO$ hat dabei in den Charakterisierungsmessungen vielversprechende physikalische Eigenschaften für die praktische Anwendung als Kathodenmaterial in LIB wie eine hohe Kristallinität und Phasenreinheit, eine hohe thermische Stabilität und eine durchschnittliche Partikelgröße von mehreren Mikrometern gezeigt. Die elektrochemischen Untersuchungen an Li_2FeSeO resultierten darüber hinaus in zwei Hauptergebnissen. $(Li_2Fe)SeO$ hat eine deutlich vielversprechendere elektrochemische Performance von 150 mAh g^{-1} in Zyklus 1 und 125 mAh g^{-1} in Zyklus 100 bei einem Strom von 0.1C gezeigt, als die ersten 5 Zyklen Vollzellenmessungen von Lai *et al.* [18] von 120 mAh g^{-1} im ersten Zyklus bei einem Strom von 0.18C sowie einem Abfall von 18 % nach bereits 5 Zyklen, erhoffen ließen. Auch der Vergleich mit dem

isostrukturellen $(Li_2Fe)SO$ zeigt trotz anfänglich geringerer absoluter Kapazität eine höhere Speicherung pro Formeleinheit sowie eine bessere Zyklenstabiltät von $(Li_2Fe)SeO$. Die bessere Zyklenstabilität ist dabei vermutlich auf die geringere elektrochemische Aktivität von Selen zurückzuführen. Das zweite Hauptergebnis resultiert aus den elektrochemischen Impedanzmessungen, welche eine starke Veränderung des Ladungstransferwiderstandes zwischen dem ersten und zweiten Zyklus zeigen. Diese Veränderung deutet eine starke strukturelle Veränderung von $(Li_2Fe)SeO$ im ersten Zyklus an. Die strukturelle Veränderung scheint allerdings nach dem ersten Zyklus bereits abgeschlossen, da sich im Folgenden der Ladungstranferwiderstand stabilisiert. Insgesamt blieb aber offen, inwiefern diese strukturelle Veränderung die Zyklenstabilität beeinflusst. Im Folgenden wurde zunächst eine neue, besser zu skalierende Synthese mittels Kugelvermahlen (BM) und Kugelvermahlen plus nachträglicher Hitzebehandlung bei 600 °C (BM600) für $(Li_2Fe)SeO$ vorgestellt. Das so hergestellte Material besitzt eine deutlich kleinere Partikelgröße und zeigt nach XRD, ICP-EOS, DTA und XPS ähnliche physikalische Eigenschaften. Hochauflösende TEM-Messungen sowie magnetische Messungen weisen allerdings auf $Fe_{1-x}Se_x$ als Fremdphase in der Probe hin. Mit der Vermutung, dass die strukturelle Veränderung die Grundlage für die beobachtete Zyklenstabilität ist, wurden zielgerichtet weitere Untersuchungen durchgeführt, um die Hypothese zu bestätigen. Elektrochemische Messungen im begrenzten Potentialbereich und direktem Entladen enthüllten die reduktive elektrochemische Aktivität von $Fe_{1-x}Se_x$. Ein Teil der gemessenen Kapazität entfällt somit auf die enthaltene Fremdphase. Darüber hinaus, konnte gezeigt werden, dass es erst durch den Hochspannungsprozess O* zu einer starken strukturellen Veränderung kommt. Diese strukturelle Veränderung enthält dabei die teilweise Zerstörung der Antiperowskitstruktur sowie die zeitgleiche Formation von $Fe_{1-x}Se_x$. Die Hochspannungsreaktion hat somit einen maßgeblichen Einfluss auf die beobachtbare Zyklenstabilität. Messungen, die den Hochspannungsprozess durch eine Begrenzung der Maximalspannung vermeiden, haben im Vergleich eine drastisch verbesserte Zyklenstabilität nachgewiesen. Die generelle Relevanz für die Klasse der lithiumreichen Antiperowskite konnte durch identische Messungen an festkörpersyntethisiertem $(Li_2Fe)SO$ und $(Li_2Fe)SeO$ bewiesen werden. Insgesamt präsentieren die Ergebnisse der vorliegenden Arbeit somit essenzielle physikalische als auch elektrochemische Eigenschaften der Materialklasse der lithiumreichen Antiperowskite, wie zum Beispiel den Ursprung der bisher beobachteten schlechten Zyklenstabilität sowie einen Weg, wie diese deutlich verbessert werden kann.

Aus einer weitreichenderen Perspektive auf die lithiumreichen Antiperowskite bleibt al-

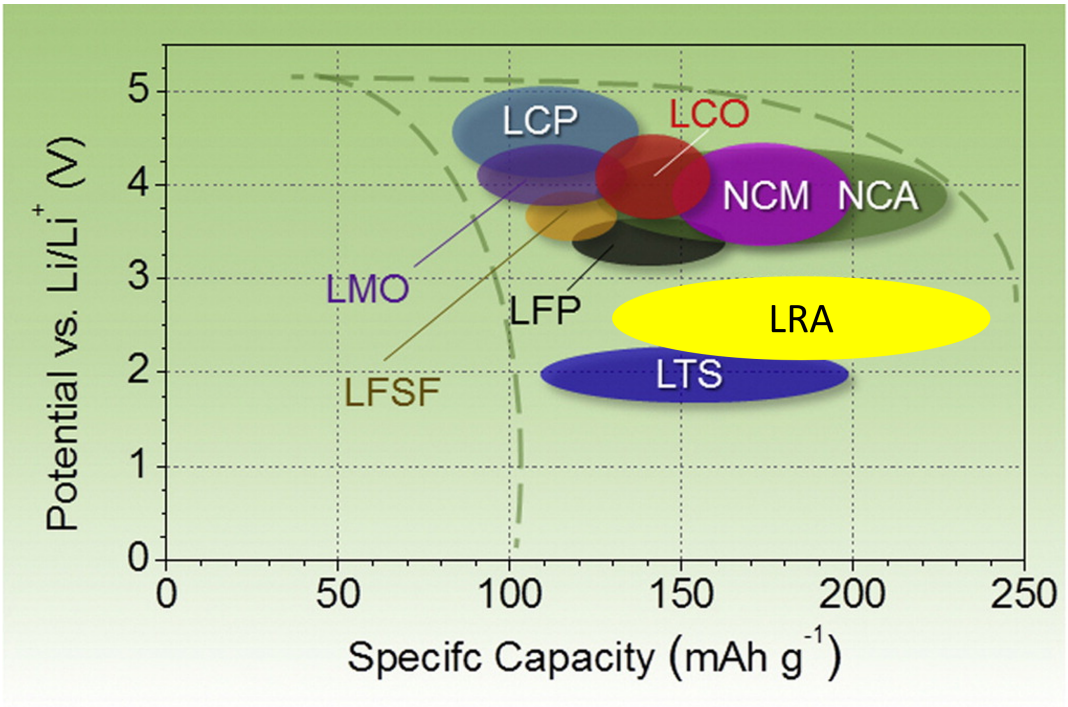

Abbildung 5.2: Vergleich der mittleren Redoxspannungen und spezifischen Kapazitäten von verschiedenen Kathodenmaterialien. Die in dieser Arbeit untersuchten lithiumreichen Antiperowskite sind in Gelb eingetragen und mit LRA abgekürzt. LCO steht für Lithium-Kobalt-Oxid, LMO für Lithium-Mangan-Oxid, NCM für Nickel-Kobalt-Mangan-Oxid, NCA für Nickel-Kobalt-Aluminium-Oxid, LCP für Lithium-Kobalt-Phosphat, LFP für Lithium-Eisen-Phosphat, LFSF für Lithium-Eisen-Fluorosulfat und LTS für Lithium-Titan-Sulfid. Adaptiert aus [4].

lerdings die Problematik der nicht vollständig verstandenen Hochspannungsreaktion, der Luftsensitivität und der insgesamt nicht sehr hohen Redoxspannungen, die es noch zu überwinden gilt. Weitere Untersuchungen bezüglich der Hochspannungsreaktion werden benötigt, da nur mit dem Wissen um den gesamten elektrochemischen Reaktionsmechanismus ein Weg zu höheren Kapazitäten entwickelt werden kann. Die DFT-Kalkulation von Lu *et al.* sagen einen Zerfall der $(Li_2Fe)SeO$-Struktur ab einer Entnahme von 1.25 Lithium voraus [107]. Es kann daher spekuliert werden, ob die beobachtete Umwandlung im Hochspannungsbereich auf diesem Prozess beruht. Eine mögliche Erklärung könnte sein, dass es aufgrund der ungleichmäßigen Partikelgrößen, zu einer unregelmäßigen Entnahme von Lithium in einzelnen Partikeln kommt, die punktuell über 1.25 Lithium liegt. Allerdings sind weitere Studien notwendig, um diese Hypothese zu bestätigen, wie zum Beispiel *in situ* XRD, Paarverteilungsfunktionsanalyse (PDF) sowie differenzielle elektrochemische Massenspektrometrie (DEMS). Mit *in situ* XRD und/oder PDF kann die sich elektroche-

misch formende Struktur nachvollzogen werden. Mittels DEMS ist es möglich, den aus der Struktur lösenden Sauerstoff zu quantifizieren, um darauf aufbauend Rückschlüsse über die Reaktion zu treffen. Dotierung könnte ein Weg sein, der die Zersetzung an Luft verhindert, sowie die geringen elektrochemischen Redoxpotentiale erhöht. Eine Dotierung kann unter Umständen die Struktur stabilisieren und die Redoxpotentiale zu höheren Spannungen verschieben. Um diese Hypothese zu bestätigen sind erneut weitere Untersuchungen an weiteren, gedopten lithiumreichen Antiperowskiten nötig.

Inwiefern die spezifischen Kapazitäten und Redoxspannungen lithiumreicher Antiperowskite (LRA) zu anderen, teilweise bereits kommerzialisierten Kathodenmaterialien vergleichbar sind, zeigt Abbildung 5.2. Der Vergleich legt dar, dass die Redoxspannungen der LRA im Verhältnis zu anderen Kathodenmaterialien geringer sind, die erreichbaren Kapazitäten sind hingegen durchaus vielversprechend. Mit dem Blick auf die erreichbaren Energiedichten sind die lithiumreichen Antiperowskite somit durchaus kompetitiv. Zum jetzigen Zeitpunkt lässt es sich allerdings nicht vorhersagen, wie sich die LRA entwickeln. Zuerst müssen die vorher genannten Probleme gelöst werden, da ansonsten alleine die Luftsensitivität ein zentrales Gegenargument gegen die tatsächliche Verarbeitung der LRA sein wird. Insgesamt bleibt jedoch anzumerken, dass in der Klasse der Lithiumreichen Antiperowskite (LRA) noch beträchtliches Optimierungspotenzial vorhanden ist, welches höchstwahrscheinlich zu einer Neubewertung dieser Materialklasse führen wird. Die bisherige Forschung im Bereich der Entwicklung und Optimierung von Lithium-Ionen-Batteriematerialien verbreitet Optimismus, da sie gezeigt hat, dass sie für zahllose Probleme unzählige Lösungen finden kann.

Kapitel 6 Publikationsliste

An den folgenden, in dieser Arbeit verwendeten, eingereichten oder nach dem Peer-Review-Verfahren veröffentlichten Artikeln, hat der Autor der vorliegenden Arbeit maßgeblich mitgearbeitet:

L. Singer, W. Kukułka, E. Thauer, N. Gräßler, A. Asyuda, M. Zharnikov, E. Mijowska, R. Klingeler, „On the rising extra storage capacity of ultra-small Fe_3O_4 particles functionalised with HCS and their potential as high-performance anode material for electrochemical energy storage “, *Electrochimica Acta* Volume 448, April 2023, 142155. https://doi.org/10.1016/j .electacta.2023.142155

G.S. Zakharova, **L. Singer**, Z.A. Fattakhova, S. Wegener, E. Thauer, Q. Zhu, E.V. Shalaeva, R. Klingeler, „MoO_2/C composites prepared by tartaric acid and glucose-assisted sol-gel processes as anode materials for lithium-ion batteries“, *Journal of Alloys and Compounds*, Volume 863, May 2021, 158353. https://doi.org/10.1016/j .jallcom.2020.158353 .

K. Wenelska, V. Adam, E. Thauer, **L. Singer**, R. Klingeler, X. Chen, E. Mijowska, „Fabrication of 3D graphene/MoS_2 spherical heterostructure as anode material in Li-ion battery “, *Front. Energy Res.* Volume 10, August 2022, Sec. Electrochemical Energy Conversion and Storage. https://doi.org/10.3389/fenrg.2022.960786

A.A. Mohamed, **L. Singer**, H. Hahn, D. Djendjur, A. Özkara, E. Thauer, I.G. Gonzalez-Martinez, M. Hantusch, B. Büchner, S. Hampel, R. Klingeler und N. Grässler, „Lithium-rich antiperovskite $(Li_2Fe)SeO$: a high-performance cathode material for lithium-ion batteries “, *Journal of Power Sources*, Volume 558, February 2023, 232547. https://doi.org/10.1016/j .jpowsour.2022.232547

L. Singer, M.A.A. Mohamed, H. Hahn, I. G. Gonzalez-Martinez, M. Hantusch, B. Büchner, S. Hampel, N. Gräßler, R. Klingeler, „Elucidating the electrochemical reaction mechanism of lithium-rich antiperovskite cathodes for lithium-ion batteries as exemplified by $(Li_2Fe)SeO$ “, akzeptiert vom *Journal of Materials Chemistry A*.

Weitere Veröffentlichungen die bereits in Peer-Review-Journalen veröffentlicht oder eingereicht sind mit Beiträgen des Autoren, die als Doktorand angefertigt, aber nicht für die vorliegende Arbeit verwendet wurden; diese Arbeiten befinden sich im Anhang:

E. Thauer, G.S. Zakharova, E.I. Andreikov, V. Adam, S.A. Wegener, J.-H. Nölke, **L. Singer**, A. Ottmann, A. Asyuda, M. Zharnikov, D.M. Kiselkov, Q. Zhu, I.S. Puzyrev, N.V. Podval'naya, R. Klingeler, „Novel synthesis and electrochemical investigations of ZnO/C composites for lithium-ion batteries", *Journal of Material Science*, Volume 56, May 2021, 13227–13242. https://doi.org/10.1007/s10853-021-06125-4 .

M. Trukawka, K. Wenelska, **L. Singer**, R. Klingeler, X. Chen, E. Mijowska, „Hollow carbon spheres loaded with uniform dispersion of copper oxide nanoparticles for anode in lithium-ion batteries ", *Journal of Alloys and Compounds*, Volume 853, February 2021, 156700. https://doi.org/10.1016/j .jallcom.2020.156700

A. Elghandour, L. Gries, **L. Singer**, K. Dey, R. Klingeler, „Magnetic anisotropy, magnetoelastic coupling and the phase diagram of $Ni_{0.25}Mn_{0.75}TiO_3$ ". Eingereicht bei *Physical Review B*.

P. Guo, **L. Singer**, Z. Zhao, W. Kukułka, F. Sebastian, E. Mijowska, M. Zharnikov, P. Comba, R. Klingeler, „A facile preparation method and proof of cycle-stability of carbon-coated metal oxide and disulfide battery materials ". Akzeptiert in *Electrochimica Acta*.

Kapitel 7 Anhang

J Mater Sci (2021) 56:13227–13242

Energy materials

Novel synthesis and electrochemical investigations of ZnO/C composites for lithium-ion batteries

E. Thauer[1,*], G. S. Zakharova[2,3], E. I. Andreikov[4], V. Adam[1], S. A. Wegener[1], J. -H. Nölke[1], L. Singer[1], A. Ottmann[1], A. Asyuda[5], M. Zharnikov[5], D. M. Kiselkov[6], Q. Zhu[7], I. S. Puzyrev[4], N. V. Podval'naya[2], and R. Klingeler[1,8]

[1] *Kirchhoff Institute of Physics, Heidelberg University, Heidelberg, Germany*
[2] *Institute of Solid State Chemistry, Ural Division, Russian Academy of Sciences, Yekaterinburg, Russia*
[3] *Ural Federal University, Yekaterinburg, Russia*
[4] *I.Ya. Postovskii Institute of Organic Synthesis, Ural Division, Russian Academy of Sciences, Yekaterinburg, Russia*
[5] *Applied Physical Chemistry, Heidelberg University, Heidelberg, Germany*
[6] *Institute of Technical Chemistry, Ural Division, Russian Academy of Sciences, Perm, Russia*
[7] *School of Material Science and Engineering, Wuhan University of Technology, Wuhan, China*
[8] *Centre for Advanced Materials, Heidelberg University, Heidelberg, Germany*

Received: 16 February 2021
Accepted: 21 April 2021
Published online: 12 May 2021

ABSTRACT

For the first time, ZnO/C composites were synthesized using zinc glycerolate as a precursor through one-step calcination under a nitrogen atmosphere. The effect of the heat treatment conditions on the structure, composition, morphology as well as on the electrochemical properties regarding application in lithium-ion batteries are investigated. The products obtained by calcination of the precursor in nitrogen at 400—800 °C consist of zinc oxide nanoparticles and amorphous carbon that is *in-situ* generated from organic components of the glycerolate precursor. When used as anode material for lithium-ion batteries, the as-prepared ZnO/C composite synthesized at a calcination temperature of 700 °C delivers initial discharge and charge capacities of 1061 and 671 mAh g^{-1} at a current rate of 100 mA g^{-1} and hence 1.5 times more than bare ZnO, which reaches only 749/439 mAh g^{-1}. The native carbon improves the conductivity, allowing efficient electronic conductivity and Li-ion diffusion. By means of *ex-situ* XRD studies a two-step storage mechanism is proven.

Handling Editor: Mark Bissett.

Address correspondence to E-mail: elisa.thauer@kip.uni-heidelberg.de

https://doi.org/10.1007/s10853-021-06125-4

Introduction

ZnO has attracted attention of a large community of researchers as an electrode material for lithium-ion batteries (LIBs) due to its low cost, environmental friendliness and high theoretical capacity in particular [1–4]. Assuming a two-step reaction mechanism that involves a conversion Eq. (1) and alloying process Eq. (2), as proposed by previous studies [5–7], up to 3 Li^+/f.u. can be reversibly stored corresponding to a theoretical capacity of 978 mAh/g:

$$ZnO + 2Li^+ + 2e^- \leftrightarrow Zn + Li_2O, \quad (1)$$

$$Zn + Li^+ + e^- \leftrightarrow LiZn. \quad (2)$$

However, there are some challenges to overcome. One issue is the large volume change of ZnO during the dis-/charge process resulting in pulverization of the electrode material [8]. Furthermore, the studies of Pelliccione et al. [6] and Park et al. [9] revealed the limited reversibility of the conversion reaction Eq. (1), which depends on the size of the electrochemically formed zinc particles, as additional reason behind the rapid capacity fading. Li_2O can only be partially decomposed due to its poor reactivity and low lithium ion conductivity [10]. Another factor that limits the practical application of ZnO for electrochemical energy storage is its poor electrical conductivity [11]. To overcome these difficulties and to enhance the electrochemical performance of ZnO-based anodes, hybridizing ZnO with varieties of conductive carbon materials is frequently employed. Carbonaceous materials can prevent the aggregation of ZnO nanoparticles and maintain the structural stability of the anode during charge/discharge processes. ZnO nanoparticles anchored on the surface of carbon nanotubes (CNT) have been shown to deliver a reversible capacity of 602 mAh g^{-1} at 100 mA g^{-1} for up to 50 cycles, i.e., superior cycling and rate performances [12]. Similarly, a ZnO/graphene anode exhibits an initial specific capacity of 850 mAh g^{-1} at 0.1 C and good cycling stability (capacity decay ~8% after 50 cycles) [13]. Also, films of ZnO nanosheets coated with 350 Å thick graphite layers showed specific capacity values of ~ 600 mAh g^{-1} at 1 A g^{-1} after 100 cycles [14].

Various synthesis methods and approaches have been used in the literature to fabricate ZnO/C composites. Yang et al. [15] reported the synthesis of porous carbon coated ZnO quantum dots by the carbonization of metal–organic frameworks. As-obtained composites exhibit a reversible capacity of 919 mAh g^{-1} over 100 cycles at 100 mA g^{-1}. The porous ZnO/C microboxes prepared by annealing of the analogous metal–organic framework carboxylate groups deliver an initial discharge capacity of 1290 mAh g^{-1} and reach a high reversible capacity of 716 mAh g^{-1} after 100 cycles at a current density of 100 mA g^{-1} [16]. Bai et al. [17] have synthesized ZnO/C nanospheres by a one-step co-pyrolysis method using Zn powder and acetylacetone as starting materials. As-prepared ZnO/C nanospheres show a reversible capacity of 440 mAh g^{-1} at a current density of 100 mA g^{-1} after 50 cycles. Electrospinning and subsequent thermal treatment by Zhao et al. yielded a ZnO/carbon nanofiber composite, which delivers a reversible capacity of 702 mAh g^{-1} at a current density of 200 mA g^{-1} [18]. Hydrothermally fabricated core–shell ZnO/C nanospheres by Liu et al. [19] obtained from Zn-resorcinol–formaldehyde polymer followed by carbonization at 650 °C under inert atmosphere show a capacity of 496 mAh g^{-1} after 200 cycles at a current density of 82.5 mA g^{-1}. Microwave-assisted solvothermal synthesis permitting to reduce the time of reaction was performed to produce ZnO/C composites using sucrose as carbon source [20]. However, these methods always need multi-step or strict experimental conditions which increase the costs and limit large-scale production.

There are, however, one-step methods as well, with calcination under a nitrogen atmosphere for the synthesis of ZnO/C composites being probably the most efficient, easily implementable, and low-cost approach. In this case, organometallic complexes suggested for thermal treatment such as zinc citrate dihydrate $(C_6H_5O_7)_2Zn_3{\cdot}2H_2O$ [21–24] and zinc tartrate $C_4H_4ZnO_6$ [25] can serve as precursors for both, ZnO and carbon.

Summarizing, although a significant progress has already been achieved, developing a facile route to synthesize carbon coated nanosized materials remains an important task to further improve the performance of ZnO-based anode materials. In the present paper, based on the results of our previous work [26], a synthetic route involving a thermal treatment of organometallic compounds was developed to prepare carbon-composited metal oxide. The formation of ZnO/C composites has been

successfully realized by heat treatment of zinc glycerolate (ZnGly) under inert atmosphere. The organic component of ZnGly partially transformed into carbon resulting in the formation of ZnO/C composites. Additionally, potential applications of the ZnO/C composites as anode materials for lithium-ion batteries were investigated.

Experimental

Materials preparation

Zinc acetate dihydrate $(CH_3COO)_2Zn{\cdot}2H_2O$ and freshly distilled glycerol (analytical grade) were used as the starting materials for the synthesis of zinc glycerolate $ZnC_3H_6O_3$. The ZnGly precursor was prepared via a polyol-mediated synthesis based on Dong's work [27]. Typically, 2.0 g $(CH_3COO)_2Zn{\cdot}2H_2O$ and 1 ml of distilled water were added to 50 mL of glycerol in a 100-mL round-bottom flask. This solution was heated to 160 °C and refluxed under Ar flow for 1 h. After cooling to room temperature, the resulting colorless precipitate, zinc glycerolate, was collected using centrifugation, washed with ethanol, and dried at 80 °C for 60 min. Finally, ZnO/C composites were prepared by annealing of the as-obtained ZnGly in a tube furnace at different temperatures between 400 and 800 °C for 2 h under N_2 flow at an initial heating rate of 5 °C min^{-1}. The carbonized products are termed as ZnO/C-X, where X is the annealing temperature. For the purpose of comparison, a bare ZnO sample was prepared by annealing of the ZnO/C-800 composite at 600 °C for 1 h in air.

Materials characterization

The synthesized ZnO/C-X composites were characterized by a variety of complementary experimental techniques, as described in detail below. X-ray diffraction (XRD) patterns were obtained with a Bruker AXS D8 Advance Eco diffractometer using Cu K_α radiation and a step size of $\Delta(2\theta) = 0.02°$ at the angular scan. The morphology of the samples was investigated using a ZEISS Leo 1530 scanning electron microscope (SEM) and a JEOL JEM 2100 transmission electron microscope (TEM). Raman spectra of the samples were recorded on a Bruker Senterra spectrometer equipped with Olympus BX-51 optical microscope using a 532 nm laser. To avoid damage to the samples, the emitted power was limited to 2 mW. All spectra were obtained at room temperature at a wavelength range from 100 to 4000 cm^{-1} using a 400 lines mm^{-1} grid and 25 × 1000 µm aperture. X-ray photoelectron (XP) spectra of the samples were measured with MAX200 (Leybold-Heraeus) spectrometer equipped with a non-monochromatized Mg Kα X-ray source (200 W) and a hemispherical analyzer. The powder materials were pressed into clean indium foil and thinned by a brush to suppress charging effects, following the established methodology [28]. Thermogravimetric analysis (TG/DTA) was performed on a Mettler Toledo TGA/DSC1 analyzer with a heating rate of 5 °C min^{-1} in air and Ar. The content of carbon was examined by elemental analysis using Vario MICRO Cubes (Elementar). Nitrogen sorption isotherms were determined on a Micromeritics Gemini VII 2390 Surface Area Analyzer. Prior to N_2 physisorption data collection, the samples were degassed at 150 °C under vacuum for 4 h. The specific surface area, pore size distribution, and pore volumes were obtained by means of the Brunauer–Emmett–Teller (BET) method and the Barrett-Joyner-Halenda model from the adsorption branches of the isotherms.

Electrochemical measurements

Electrochemical studies were performed in Swagelok-type two electrode cells at 25 °C by using a VMP3 potentiostat (Bio-Logic SAS) (see [26]). The preparation procedure of the working electrodes is as follows. A mixture of 80% ZnO/C, 15% carbon black (Super C65, Timcal), and 5% polyvinylidene fluoride binder (PVDF, Solvay Plastics) dissolved in N-methyl-2-pyrrolidone (NMP, Sigma-Aldrich) was stirred for at least 12 h. In order to obtain a spreadable slurry most of the NMP was evaporated in a vacuum oven (10 mbar, 65 °C). The resulting electrode slurry was applied on circular Cu meshes (diameter 10 mm) with a mass loading of about 2 mg cm^{-2}. Afterward, the electrodes were dried at 80 °C under vacuum, mechanically pressed at 10 MPa, and then dried again. The working electrode and the counter electrode, consisting of a lithium metal foil disk (Alfa Aesar) pressed on a nickel current collector, were separated by two layers of glass fiber separator (Whatman GF/D). As electrolyte 200 µL of a 1 M $LiPF_6$ salt solution in 1:1 ethylene

carbonate (EC) and dimethyl carbonate (DMC) (Merck Electrolyte LP30) was used. The cells were assembled in a glove box under argon atmosphere ($O_2/H_2O < 5$ ppm). For *ex-situ* XRD measurements the cells were galvanostatically cycled at 10 mA g^{-1} and disassembled at various dis-/charged states in the glove box. The electrodes were washed in DMC and dried under vacuum conditions overnight. The XRD measurement of the post-cycled electrode material was performed using an airtight sample carrier.

Results and discussion

The structure of the ZnO/C-X composites was analyzed by XRD (Fig. 1a). For comparison, the XRD pattern of ZnO obtained by annealing the ZnO/C-800 composite in air at 600 °C is also included. All diffraction peaks can be assigned to a hexagonal phase of wurtzite-type ZnO according to JCPDS # 36–1451, space group P63mc. Lattice parameters determined by means of full-profile analyses with the FullProf Suite (see Table 1) are in good agreement with the literature. The intensities of the characteristic peaks of ZnO increase with rising annealing temperatures. For ZnO/C composites prepared by heat treatment below 600 °C, the diffraction peaks are rather broad which is attributed to nanosized ZnO crystallites. The crystallite sizes of ZnO in the ZnO/C-X (X = 400, 500, 600) samples are calculated using the Scherrer equation:

$$D_{hkl} = K\lambda/\Delta(2\theta_{hkl})\cos\theta_{hkl}, \quad (3)$$

where D_{hkl} is the average grain size based on the particular reflecting crystal face (*hkl*) direction, K is a shape factor which can be approximated to 0.9, λ is the wavelength of the applied Cu Kα radiation, $\Delta(2\theta_{hkl})$ is the full width at half-maximum of the diffraction peak and θ_{hkl} is the Bragg angle. The analysis of the peaks below $2\theta_{hkl} = 65°$ yields the averaged crystallite size for the ZnO/C-X samples. Both, ZnO/C-400 and ZnO/C-500 composites, exhibit similar particle size of around 12 nm. By contrast, the ZnO/C-600 composite is characterized by a larger size of 19 ± 3 nm.

Raman spectra collected from the ZnO/C-X (X = 400 − 700) samples display two prominent peaks which are attributed to the carbon D- and G-bands (see Fig. 1b). The G-band corresponds to sp^2-bonded carbon atoms, while the D-band is associated with defects or disorders mainly due to sp^3 hybridization [29]. The D- and G-bands of the ZnO/C-400 composite are located at 1359 cm^{-1} and 1591 cm^{-1}, respectively. In comparison, the D-and G-peaks of the ZnO/C-700 sample are slightly red-shifted by 23 and 20 cm^{-1} toward 1314 and 1571 cm^{-1}, respectively. The same shift toward higher binding energy indicating the strong chemical interaction between the surface carbon and Zn atoms was observed by XPS on ZnO/C composite [23]. Similar shifts have been reported for TiO_2/C composites [30, 31]. These shifts are attributed to the stress induced by the chemical anchoring of ZnO atoms on the carbon surface. Obviously, such an interaction can change the Raman shifts describing the carbon bond energy. The ratio of the maximum intensities, I_D/I_G, was calculated as 0.73 and 0.91 for

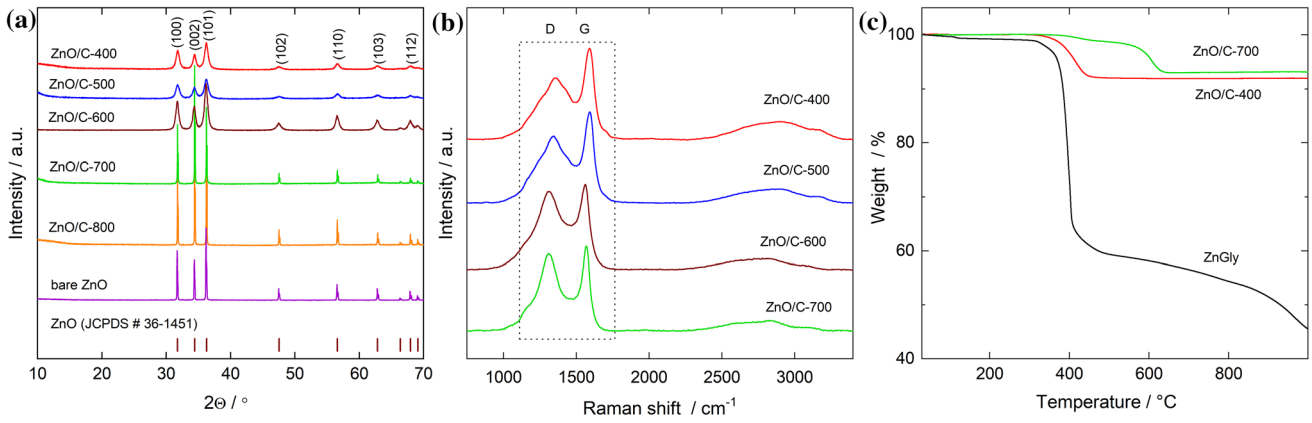

Figure 1 **a** XRD patterns and **b** Raman spectra of the ZnO/C-X composites and bare ZnO sample as well as (**c**) TG curves for the ZnGly precursor heated in an inert atmosphere and ZnO/C-400(700) composites heated in air.

Table 1 Lattice parameters obtained from Rietveld refinement, results of BET analysis, and carbon content for the ZnO/C-X composites and bare ZnO

Sample	Lattice parameters		S_{BET} (m g^{-1})	Total pore volume (cm^3 g^{-1})	Carbon content (wt%)	
	a (Å)	*c* (Å)			TG	Chemical analysis
ZnO/C-400	34.80	52.05	54.8	0.18	8.0	8.7(5)
ZnO/C-500	32.49	52.06	59.8	0.16	7.1	8.2(5)
ZnO/C-700	32.55	52.16	100.9	0.36	5.7	6.0(5)
ZnO/C-800	32.53	52.11	93.1	0.29	–	5.8(5)
ZnO	32.49	52.05	6.6	0.02	–	–

the ZnO/C-400 and ZnO/C-700 composite, respectively. According to the model proposed by Ferrari and Robertson, the ratio I_D/I_G is proportional to the crystallite size, when it is less than 2 nm for amorphous carbon [32]. The increasing intensity of the D-band with rising annealing temperature is characteristic of the carbonization process and implies less disorder and a lower number of defects in the carbon component due to a growing crystallite size [33, 34]. The peaks associated with ZnO were not observed by Raman spectroscopy using a laser wavelength of 532 nm.

TG/TGA analysis (Fig. 1c) of the ZnGly precursor illustrates its conversion into carbon containing zinc oxide upon annealing in a nitrogen atmosphere. A significant weight loss of ca. 40% at heating from 400 to 1000 °C can be explained by the total decomposition of the ZnGy precursor with simultaneous formation of zinc oxide, volatile products with low molecular weight and products of condensation of organic compounds, similar to titanium glycerolate [26]. Furthermore, the products of the condensation also undergo a disproportionation with the formation of volatile low molecular weight substances and the carbonaceous part of the ZnO composite. Therefore, 400 °C was selected as the start reaction temperature to calcine the ZnGly precursor under nitrogen environment to produce the ZnO/C composites. The carbon content in the as-prepared ZnO/C-X composites was determined by the TG/TGA measurements in air, performed in the temperature range up to 1000 °C to ensure the complete oxidation of carbon into carbon dioxide (cf. Table 1). As a result, the carbon contents in the ZnO/C-400 and ZnO/C-700 composites were estimated at 8.0 and 5.7 wt%, respectively. These values were additionally verified by the chemical analysis, with good agreement of the results (Table 1).

To confirm the formation of the ZnO/C composites and to exclude other oxidation states of Zn, XPS analyses were carried out on ZnO/C-400 and ZnO/C-700. The XPS survey spectrum and core level spectra of the Zn 2p, O 1 s and C 1 s peaks for both samples are shown in Fig. 2. The survey spectrum in Fig. 2a displays the presence of Zn, O, C without any detectable impurities. The Zn 2p spectra of both samples in Fig. 2b exhibit a single Zn $2p_{3/2,1/2}$ doublet, with the positions of the Zn $2p_{3/2}$ and Zn $2p_{1/2}$ components, 1021.6 eV and 1044.7 eV, respectively, corresponding to Zn^{2+} [11, 23]. This assignment is additionally supported by the kinetic energy position of the most intense Zn LMM Auger peak at 988 eV (Fig. S1), which corresponds to ZnO. The O 1 s spectrum, as shown in Fig. 2c, was resolved and the lower binding energy component at 530.7 for the ZnO/C-400 sample and 530.6 eV for the 700 sample can be attributed to the hexagonal close packing of O_2 in the wurtzite-ZnO structure. The peak at 532.3 eV for both samples is associated with surface hydroxyl groups (OH) and/or C=O. The peak at 533.9 and 534.2 eV corresponds to single bonds between oxygen and carbon (C-O) and/or absorbed water [35]. The C 1 s spectra, which are shown in Fig. 2d, can be fitted by four sub-peaks, the aliphatic C–C, the C–O, C=O, and O–C=O peak [35]. For ZnO/C-400 the positions of these peaks are at 284.8, 286.2, 287.9, and 289.9 eV and for ZnO/C-700 the peaks are located at 284.4, 286.6, 287.9, and 289.8 eV. The shift of the C–C peak from ZnO/C-400 to ZnO/C-700 towards lower binding energies indicates, in accordance with the Raman data, a more graphitic state for the carbon component of the ZnO/C-700 composite [36].

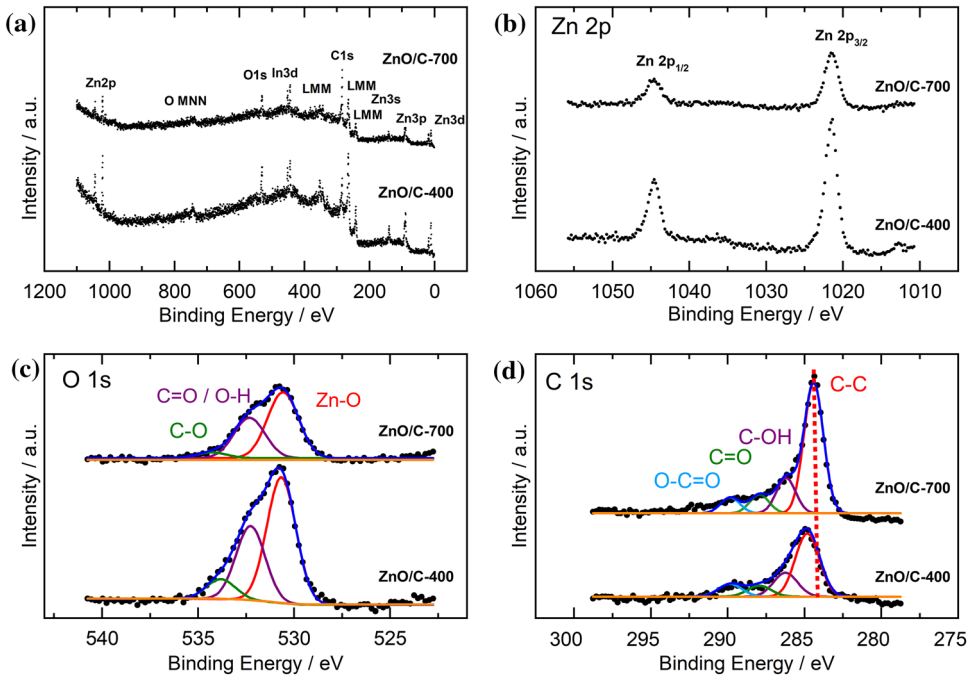

Figure 2 XPS spectra of ZnO/C-400 and ZnO/C-700: **a** survey spectrum, **b** Zn 2p, **c** O 1 s and **d** C 1 s.

SEM images of the ZnO/C-X composites in Fig. 3 show the drastic effect of the calcination temperature on the morphology of the samples. The pristine ZnGly precursor is mainly composed of irregularly shaped sheets with several micrometers in length (Fig. 3a). The ZnO/C composites fabricated via annealing of the precursor at a temperature below 500 °C consist of sheets with an average size of few micrometers, which are primarily composed of nanosized grains of ZnO (Fig. 3b, c). Probably, carbon acts as a cross-linking agent that holds the ZnO nanoparticles together. The cross-sectional SEM images of the sheets show that their thickness changes from 270 to 800 nm for ZnO/C-500 and ZnO/C-400 composites, respectively (Fig. 3b, c, insert). In contrast, the ZnO/C-700 and ZnO/C-800 composites consist of many thin sheets and several large particles of about 1 − 7 μm in diameters (Fig. 3d, e). As shown in Fig. 3f, the bare, carbon-free ZnO particles, obtained by the heat treatment of the ZnO/C-800 composite in air, represent hexagonal ZnO prisms with an average size of about 1–7 μm.

Further information on the morphology and structural features of the sheets in the ZnO/C-700 composite was obtained by TEM studies. The TEM images shown in Fig. 4a exhibit well crystallized ZnO nanoparticles which are dispersed in a carbon matrix. The corresponding high-resolution TEM (HRTEM) image in Fig. 4b exhibits lattice fringes with spacings of 0.26 and 0.28 nm, which correspond to the distances between the (002) and (100) planes of ZnO, respectively. Furthermore, the crystalline structure of the ZnO/C-700 composite is confirmed through the selected area electron diffraction (SAED) pattern as shown in Fig. 4c. Several clear diffraction rings from the SAED pattern can be assigned to the (100), (002), (101), (102), (110), (103), and (200) planes of hexagonal ZnO, suggesting a polycrystalline nature of the ZnO component in the composite.

The porous nature and the specific surface area of the as-prepared samples were investigated by nitrogen adsorption–desorption isotherms. Corresponding pore size distribution plots of the samples are shown in Fig. 5. The ZnO/C-X composites display isotherms of type IV, according to the IUPAC classification, with a H3 hysteresis loop (Fig. 5a) [37]. The isotherms of the bare ZnO powder are close to type II, which is typical for non-porous or macroporous materials. The BET specific surface area and the respective pore volumes of the samples are displayed in Table 1. The BET surface area of the ZnO/C-X composites is rather high which is attributed to the presence of mesopores, in contrast to the bare ZnO which displays a very low value of this parameter (6.7 $m^2 g^{-1}$). In the case of the ZnO/C-X hybrid materials, the annealing temperature of the ZnGly precursor affects the specific surface area significantly as this parameter increases with the increasing

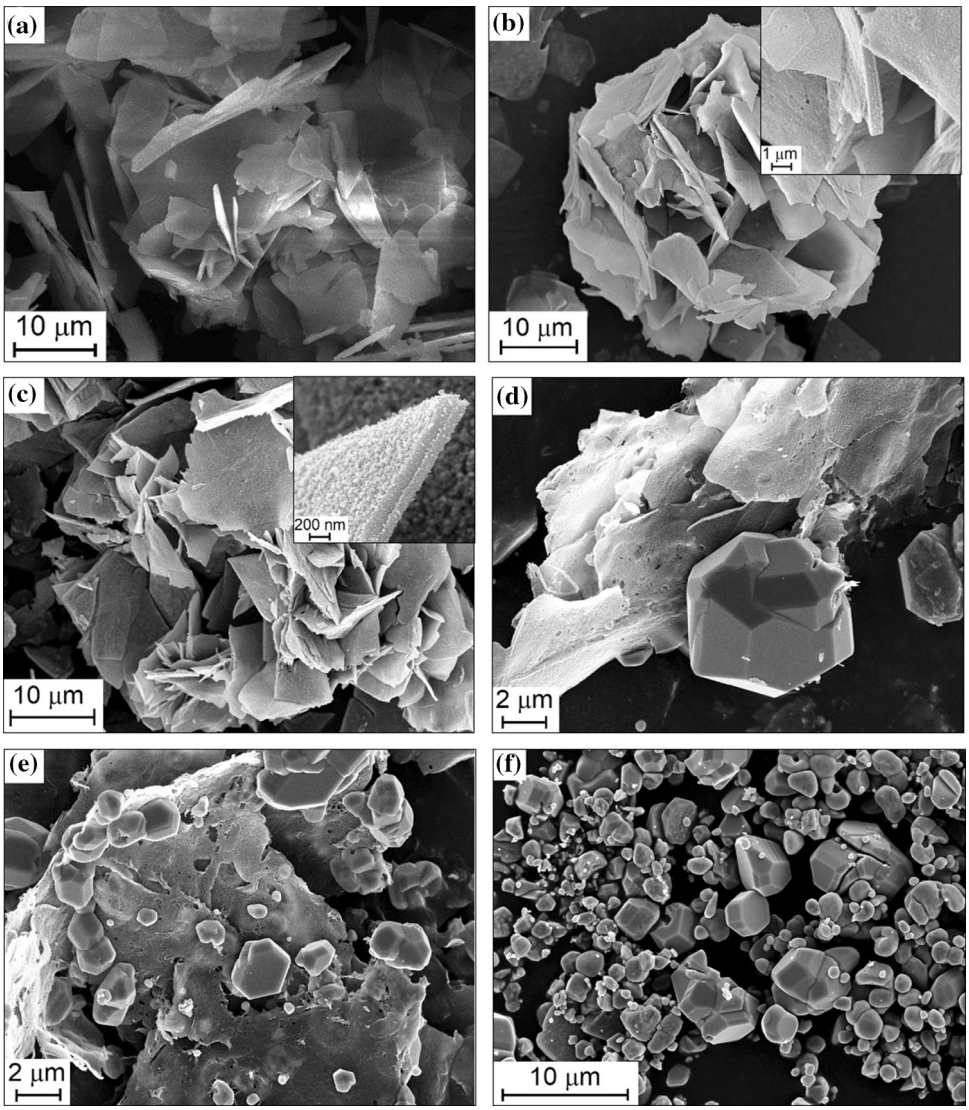

Figure 3 SEM images of (**a**) ZnGly precursor, **b** ZnO/C-400, **c** ZnO/C-500, **d** ZnO/C-700, **e** ZnO/C-800 composites, and **f** bare ZnO sample. Insets show high-magnification SEM images of cross sections of ZnO/C-400(500) composites.

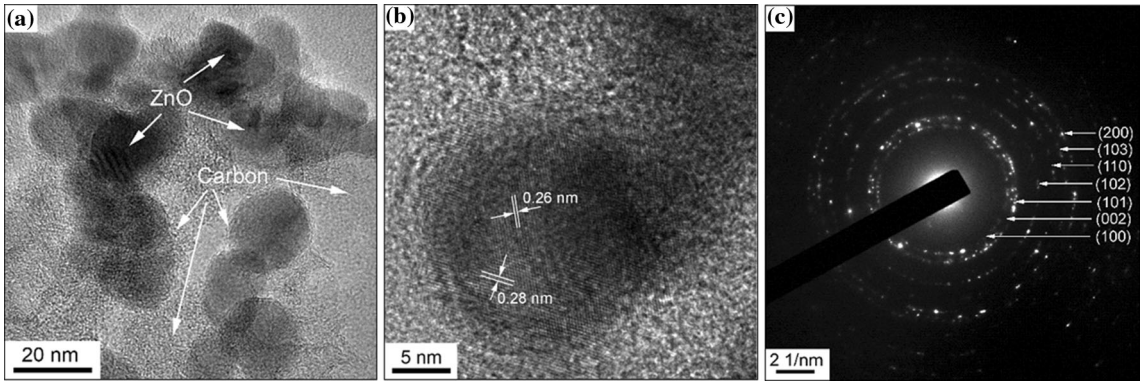

Figure 4 **a** TEM image, **b** HRTEM image, and **c** SAED pattern of ZnO/C-700 composite.

annealing temperature, from 400 to 700 °C. We attribute this behavior to the formation of defects in the composite structure during their annealing under N_2. The decrease in the specific surface area of the ZnO/C-800 composite compared to the ZnO/C-700 composite is attributed to the appearance of large

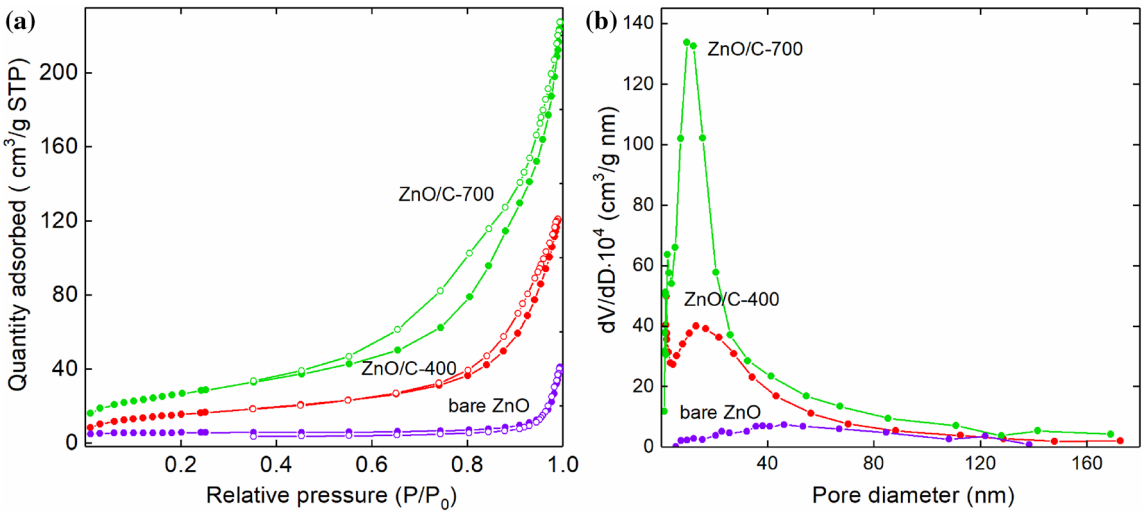

Figure 5 **a** N2 adsorption–desorption isotherms and **b** BJH pore size distribution curves of as-prepared ZnO/C composites and bare ZnO powder.

ZnO particles, as demonstrated by the SEM images (Fig. 3). Note, the ZnO/C-700 composite shows the highest BET surface of 100.9 $m^2\ g^{-1}$. From the pore size distribution plots (Fig. 5b), it is obvious that mesoporous structures are predominant in the fabricated ZnO/C-X composite materials.

The fabricated hybrid nanomaterials were studied with respect to their applicability as electrode materials in LIBs. Note, that the mesoporous nature of these materials is supposed to facilitate penetration of the electrolyte, thereby securing good electrical contact with the electrode and accelerating the diffusion kinetics. The electrochemical properties were investigated by cyclic voltammetry (CV) and galvanostatic cycling with potential limitation (GCPL). Figure 6a shows the first, second, third and tenth CV cycles for the ZnO/C-400 composite at a scan rate of 0.1 mV s^{-1} in a voltage range of 0.01–3.0 V. During the first reductive sweep the irreversible formation of the solid electrolyte interphase (SEI) occurs at around 0.6 V (R3). The peak R1 at the lower voltage limit of 0.01 V originates in part from the lithiation process related to carbon [38]. Since no corresponding oxidative peak is visible, we conclude that the delithiation process takes place over an extended voltage range. The reduction peak R2 and the oxidation peaks O1–O4 can be assigned to the Li^+ storage in ZnO [5, 6]. In the initial scan the reduction peak R2 at 0.3 V can be ascribed to both electrochemical reactions, the conversion and the alloying process [6]. After the second cycle R2 splits up in $R2_A$ (0.4 V) and $R2_C$ (0.7–0.8 V) which may be explained by a reduced overpotential of the conversion reaction at $R2_C$ due to structural changes during the initial cycle as compared to the conversion reaction at R2 while the alloying reaction at $R2_A$ is not significantly affected. Such a behavior is also observed for other conversion materials, such as Mn_3O_4 [38]. The oxidation peaks O1–O3 located between 0.3 and 0.7 V are assigned to the dealloying of LiZn alloy. The occurrence of several peaks suggests a multi-step process with various LiZn intermediate stages, such as Li_2Zn_3, $LiZn_2$ and Li_2Zn_5 [39, 40]. The peaks O1–O3 as well as $R2_A$ corresponding to the alloying process show good cycling stability. The oxidation feature O4 at around 1.3 V finally signals conversion to ZnO [6, 9]. Upon further cycling, the redox peak pair $R2_C$/O4 quickly decreases in intensity indicating an inactivation of the conversion reaction of ZnO Eq. (1). In contrast to the CV curve of the ZnO/C-400 composite, in case of the ZnO/C-700 composite (Fig. 6b) and bare ZnO (Fig. 6c) the oxidation peaks O1—O4 have lower intensity in the first cycle, while an additional oxidation peak at 2.6 V, labeled as O5, can be observed. The latter feature was also observed in several previous studies [3, 6, 7, 41, 42] but its origin still remains unclear. Huang et al. [3] and Pelliccione et al. [6] have speculatively assigned it to the back formation of ZnO Eq. (2) and the oxidation peak O4 to the dealloying process Eq. (1). In contrast, Mueller et al. [7] showed by means of *in-situ* XRD studies that the dealloying process is completed even before the oxidation process O4 starts and that ZnO is formed only afterwards, at O4. However, while these

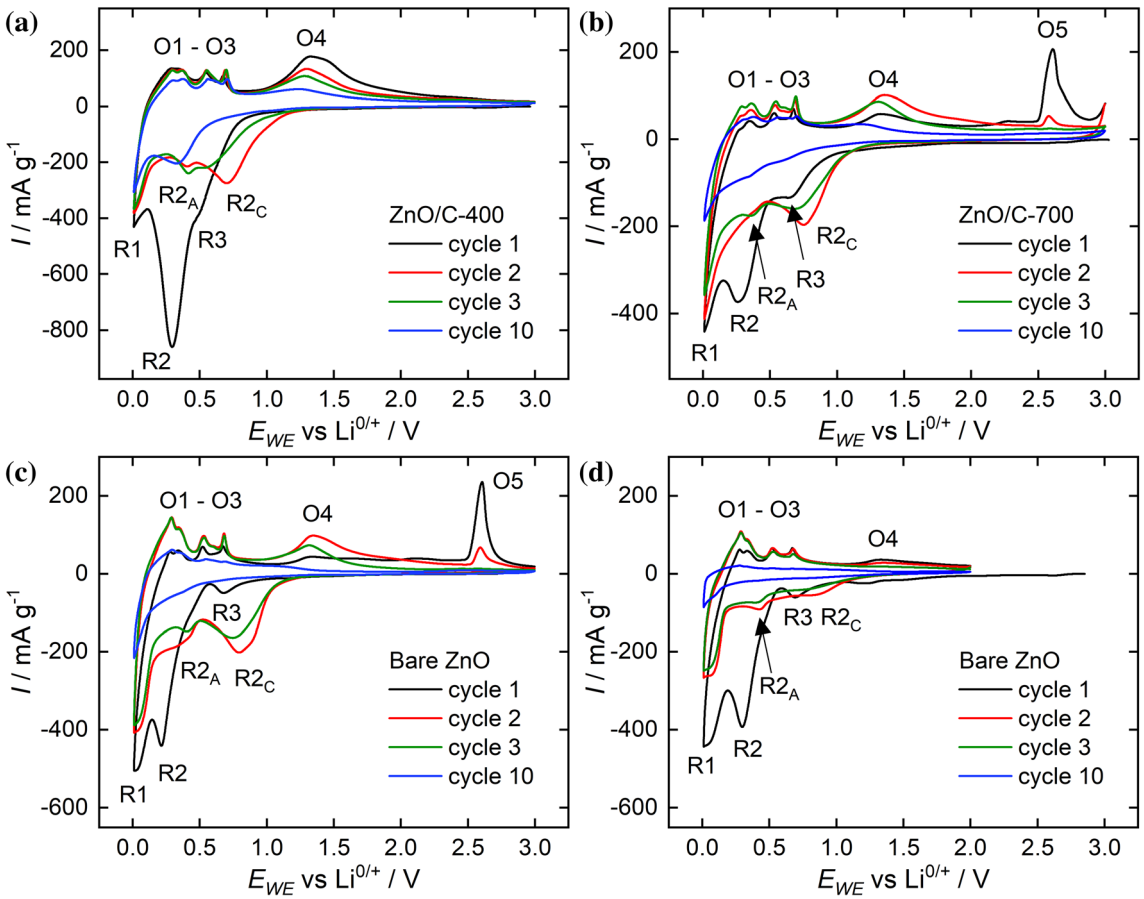

Figure 6 Cyclic voltammograms of (**a**) ZnO/C-400, **b** ZnO/C-700, and bare ZnO in the range of **c** 0.01–3 V and **d** 0.01–2 V at a scan rate of 0.1 mV s^{-1}. O1–O5 and R1–R4 label oxidation/reduction features as discussed in the text.

results exclude the above-mentioned assignment of O5, Mueller et al. make no further statements about this oxidation process. Hence, for understanding of the latter process we recorded a CV of the bare ZnO anode in a restricted potential range of 0.01–2.0 V (Fig. 6d), excluding O5. The comparison of this CV curve with the full range scans shows that the electrochemical activity steadily and strongly decreases in case of O5 exclusion, whereas otherwise, i.e., when the oxidation O5 takes place, the intensities of the subsequent features are significantly higher. Apparently, the oxidation process O5 plays a decisive role in the reversibility of Li^+ storage processes.

Ex-situ XRD measurements were performed in order to get insight into the structural changes of ZnO/C composites during electrochemical cycling. The XRD patterns of the ZnO/C-700 electrode at different dis-/charge states are shown in Fig. 7. In the initial state, the hexagonal ZnO phase (JCPDS #36–1451) is identified. The additional peaks at 44° and 51° originate from the Cu current collector. After discharging to 0.6 V the XRD pattern is similar to that of the as-prepared electrode. As expected, this implies that the electrode material does not undergo any structural transformation during the SEI formation. By further discharging to 0.3 V, the hexagonal ZnO phase completely transforms into a Zn phase (COD #9,008,522), which goes along with the conversion reaction according to Eq. (1). As can be seen from the expanded view of the 27–41° 2θ range in the inset of Fig. 7, a broad low intensity peak located at 33.7° indicates the presence of Li_2O (ICSD #54,368). It can be observed for all the following charge states as exemplarily shown by the XRD patterns of the fully charged and discharged state in the inset of Fig. 7. The XRD pattern of the completely discharged electrode (i.e., at 0.01 V) exhibits the characteristics of a single LiZn phase (COD #1,539,519), resulting from the alloying process described by Eq. (2). The observed structural changes upon cycling are in good

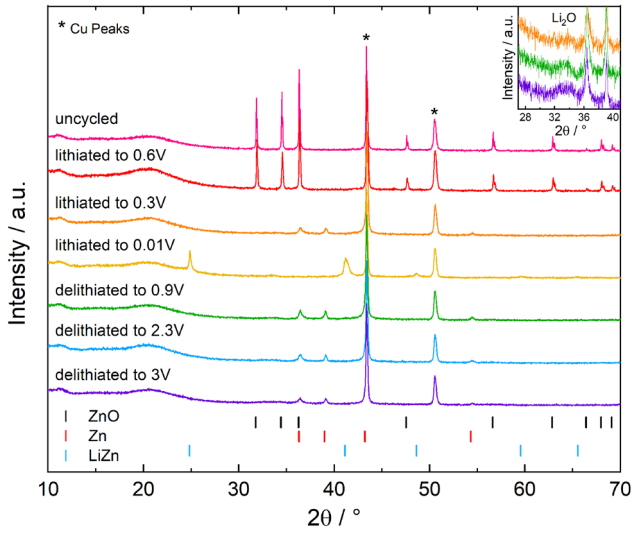

Figure 7 *Ex-situ* XRD patterns of a ZnO/C-700 electrode recorded at different stages of electrochemical Li^+ de-/insertion. The reflexes marked with * originate from the Cu current collector. In addition, the Bragg peak positions for ZnO (JCPDS # 36–1451), Zn (COD #9,008,522), and LiZn (COD #1,539,519) are shown. The inset shows the expanded view of XRD patterns of the samples lithiated up to 0.01 V (fully discharged), 0.9 V, and 3 V (fully charged) in the 27–41° 2θ range.

agreement with the reported results for a two-step mechanism for Li^+ storage in ZnO including a conversion and an alloying process [5, 40]. During the subsequent charging to 0.9 V, the peaks associated with LiZn vanish and the Zn phase reappears, confirming the reversibility of the alloying process. As charging proceeds to 3 V, the peaks associated with the Zn phase diminish in intensity, while no other crystalline phase shows up. Apparently, no structural changes are associated with the oxidation processes reflected by O4 and O5. Against expectation, there is no indication of crystalline ZnO in the completely charged electrode (i.e., at 3 V). This might be explained either by the amorphous structure or nanosize of the electrochemically formed ZnO or by the irreversibility of the conversion reaction Eq. (1). The lattice parameters of the Zn and LiZn phases appearing at various charging stages during the electrochemical cycling were determined by means of full-profile analyses with the FullProf Suite (Table S1). *Ex-situ* XRD studies on ZnO/C-400 show similar results (Fig. S2).

GCPL measurements at a current density of 100 mA g^{-1} in the range of 0.01–3.0 V enable assessing the cycling performance of the composite

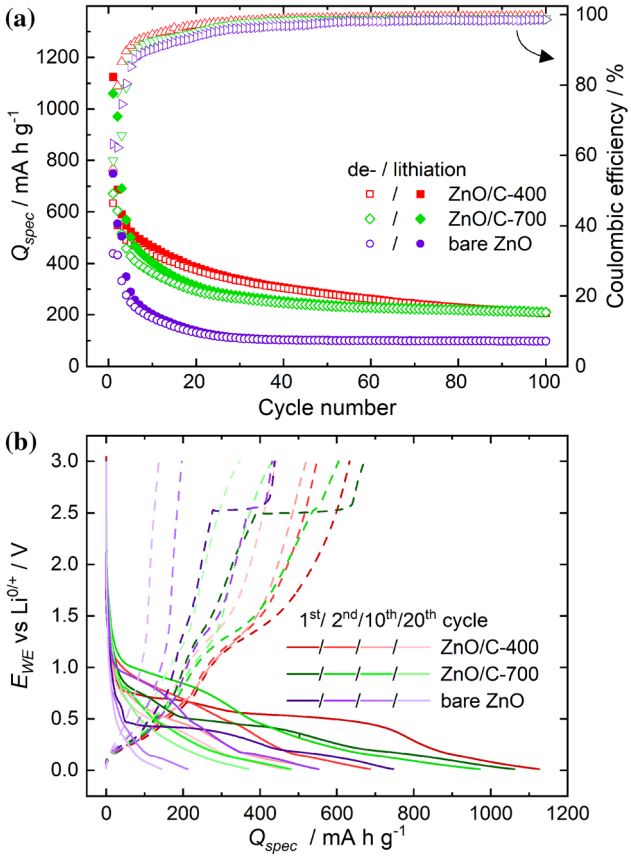

Figure 8 a Specific dis-/charge capacities and coulombic efficiencies of the ZnO/C-400 and ZnO/C-700 composites and of bare ZnO for galvanostatic cycling in the potential range between 0.01 and 3 V at 100 mA g^{-1} as well as (**b**) the respective potential profiles for the first, second, tenth and twentieth cycles.

nanomaterials under study. Figure 8a shows specific dis-/charge capacities and coulombic efficiencies for the first 100 cycles of the ZnO/C-400 and ZnO/C-700 composite as well as of the bare ZnO electrode. In the first cycle specific dis-/charge capacities of 1126/633 mAh g^{-1} (ZnO/C-400), 1061/671 mAh g^{-1} (ZnO/C-700) and 749/439 mAh g^{-1} (ZnO) were measured. One reason for the large capacity loss in the first cycle is the irreversible SEI formation during discharge. As can be seen from the potential profiles of the first lithiation (Fig. 8b), for bare ZnO the SEI contribution is quite small with less than 50 mAh g^{-1}, whereas for the composites it is larger due to the fact that the irreversible charge loss is roughly linearly proportional to the specific surface area of carbonaceous materials [43]. Cracking and fracture of the electrode material due to large volume changes can lead to an unstable SEI and irreversible capacity losses beyond

the first cycle [44], which also might explain the unexpected high second discharge capacity of ZnO/C-700 compared to the first charge capacity. Based on the reaction mechanism of ZnO Eqs. (1) and (2), a maximal theoretical specific capacity of 978 mAh g^{-1} can be reached. Considering the capacity from the SEI formation, it can be concluded that in the case of the composites the ZnO almost fully reacts with Li^+ according to the expected reaction mechanism, while this is not the case for the bare ZnO electrode. After 20 cycles 293 mAh g^{-1} can be charged from ZnO/C-700 and a slightly higher capacity of 374 mAh g^{-1} from ZnO/C-400, corresponding to a capacity fading of 44% and 41% relative to the first cycle. The poor coulombic efficiencies and rapid capacity fading during the first twenty cycles might be explained by the limited reversibility of the conversion reaction Eq. (1). This is supported by the results of *ex-situ* XRD studies. Under the assumption that the back formation to ZnO Eq. (1) is irreversible and the reversible lithiation reaction is a single alloying process Eq. (2) a maximal capacity of only 329 mAh g^{-1} can be expected. Obviously, the charge capacities exceed this value for about the first twenty cycles indicating that the reoxidation of Zn to ZnO is at least partly reversible as also observed by Pelliccione et al. [6] and Mueller et al. [7]. Interestingly, during further cycling the coulombic efficiencies are increasingly converging at 100% and simultaneously the cycling stabilities get much better. Exemplarily, the ZnO/C-700 composite delivers a discharge capacity of 212 mAh g^{-1} after 100 cycles exhibiting excellent cycle stability with an average capacity loss of only 0.04% per cycle over the last 80 cycles. The potential profiles of the first, second, tenth and twentieth cycle in Fig. 8b provide an insight into the origins of the capacity fading. Comparing the potential profiles, it is noticeable that the capacity loss can be mainly traced back to an inactivation of the conversion reaction Eq. (1), which can also be observed in the CV curves (Fig. 6). During the first cycles both processes, viz. the conversion and the alloying, take place but in the further course the alloying mainly contributes to the Li^+ storage, which might be due to the incomplete back formation of ZnO. In addition, the loss of electrical connectivity to the active material due to changes in the electrode structure, such as particle aggregation or pulverization, results in capacity losses. Comparing the two composites, indeed, the capacities of the ZnO/C-700 composite fade more rapidly in the first cycles with lower coulombic efficiency than for ZnO/C-400 but stabilize faster in the further course. It should be noted, that the evolution of the capacities of the ZnO/C-500 sample is similar to that of ZnO/C-400 while the evolution of the capacities of the ZnO/C-800 sample is similar to that of ZnO/C-700 (Fig. S3), who each have similar crystallographic and morphological properties, respectively. The worse cycling stability of the ZnO/C-700 composite in the first twenty cycles might be attributed to the presence of microscaled polyhedrons, whereas the ZnO/C-400 composite consists only of nanoscaled primary particles. For one thing, the reversibility of the conversion reaction depends on the crystallite size of the transition metal particles formed during electrochemical cycling [45]. Park et al. [9] have shown that the back formation of ZnO

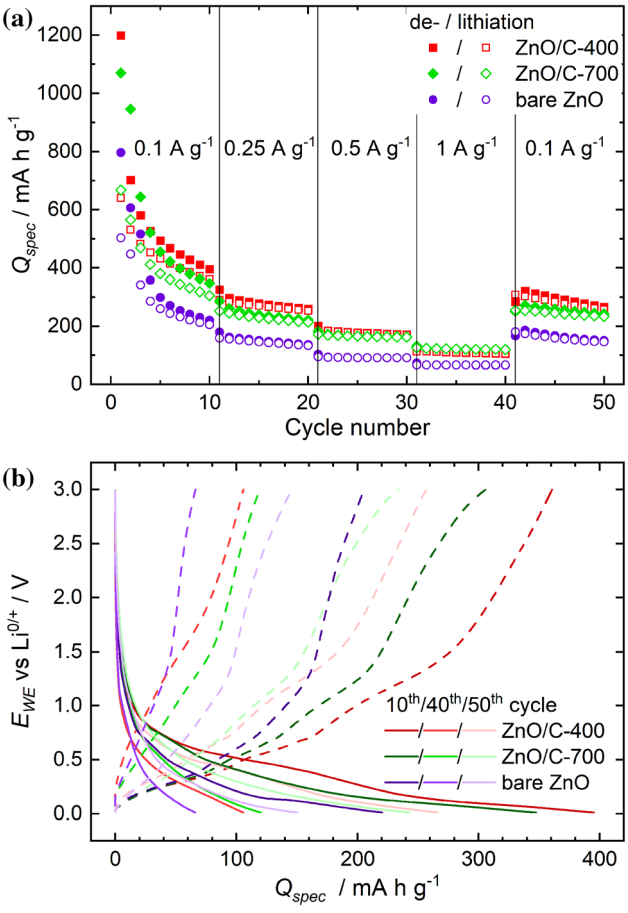

Figure 9 **a** Rate capability test of the ZnO/C-400 and ZnO/C-700 composites and of bare ZnO at current rates between 100 and 1000 mA g^{-1} as well as (**b**) the respective potential profiles of cycle 10 at 100 mA g^{-1}, cycle 40 at 1000 mA g^{-1} and cycle 50 again at 100 mA g^{-1}.

only occurs for extremely small Zn nanocrystallites. In addition, nanosized particles can better accommodate the strain caused by the volume changes during electrochemical cycling [46]. Looking at the comparison between the ZnO/C composites and the bare ZnO sample, it is remarkable that over the whole measurement the composites reach about twice the capacities of the bare sample. In cycle 20 and 100, the bare ZnO compound reaches specific capacities of 131 mAh g^{-1} and 97 mAh g^{-1}, respectively. The higher capacities of the composite materials can be probably traced back to the larger surface area offering more active sides as well as a better electronic connection of the ZnO particles due to the conductive network provided by the carbon. Furthermore, the stabilized coulombic efficiency and the cycling stability of the bare ZnO electrode is with a capacity loss of 70% in cycle 20 relative to the first cycle worse than for the composites. We conclude that degradation effects such as structural changes of the electrode material leading to the electrical disconnection of the active material as well as an unstable SEI can be at least partly prevented by the carbon. The carbon matrix can effectively suppress the nanoparticle aggregation and pulverization of the electrode material due to large volume changes maintaining the structural stability and, moreover, helping stabilize SEI formation [23, 47–49]. In addition, the electrochemical properties of bare ZnO and the ZnO/C-400 and ZnO/C-700 composites were also investigated by galvanostatic cycling with various current densities between 100 and 1000 mA g^{-1}. The specific dis-/charge capacities are shown in Fig. 9a along with the potential profiles of cycle 10 at 100 mA g^{-1}, cycle 40 at 1000 mA g^{-1} and cycle 50 again at 100 mA g^{-1} in Fig. 9b. The ZnO/C-400 composite reaches a charge capacity of 113 mAh g^{-1} at a high current rate of 1000 mA g^{-1} while for ZnO/C-700 a charge capacity of 125 mAh g^{-1} is measured and for bare ZnO 67 mAh g^{-1}. The inferior rate capability of the sample ZnO/C-400 compared to ZnO/C-700 is caused by a more severe polarization resistance due to kinetic effects. As can be seen from the potential profiles, at a high current rate of 1000 mA g-1, the potential gap between charge and discharge increases more for ZnO/C-400 than for ZnO/C-700. The reduced polarization resistance in case of ZnO/C-700 might be associated with better conductivity of the less disordered carbon as shown by Raman spectroscopy and the XPS analysis. When the current density is reset to 100 mA g^{-1} charge capacities of ca. 83%, 86% and even 88% relative to cycle 10 can be regained for the ZnO/C-400, ZnO/C-700 and bare ZnO samples, respectively.

Table 2 Comparison of the electrochemical performance of ZnO and ZnO/C electrodes prepared via different synthesis methods as reported in the literature

Sample	Method of synthesis	Current density (mA g^{-1})	Discharge capacity (mAh g^{-1})/cycle no	References
ZnO spheres	Hydrothermal	100	109/100	[2]
ZnO/C nanoparticles	Thermal decomposition of $Zn_3(C_6H_5O_7)_2$	100	850/200	[22]
ZnO/C spheres	Thermal decomposition of $Zn_3(C_6H_5O_7)_2$	100	520/150	[24]
ZnO/C nanoparticles	Thermal decomposition of $C_4H_4ZnO_6$	100	610/300	[25]
ZnO/C nanocages	Pyrolysis	100	750/100	[50]
ZnO/C spheres	Pyrolysis	100	750/100	[51]
ZnO/C nanoparticles	Ball milling	100	610/500	[52]
ZnO/C tetrahedron	Calcination	110.7	518/300	[53]
ZnO/C nanoparticles	Calcination	100	610/50	[54]
ZnO/C spheres	Coprecipitation	500	659/300	[55]
ZnO/C-400	Thermal decomposition of $ZnC_3H_6O_3$	100	208/100	This work
ZnO/C-700		100	212/100	
ZnO		100	98/100	

Interestingly, the comparison with the measurement consistently at 100 mA g^{-1} (Fig. 8) reveals that the capacity fading seems to be more serious for electrochemical cycling at lower rates accompanied with higher Li^+ storage capacity. For ZnO/C-400, ZnO/C-700 and bare ZnO which were continuously cycled at 100 mA g^{-1}, charge capacities of only 68%, 67% and 54% were obtained in cycle 41 relative to cycle 10. Higher degradation effects for a more comprehensive dis-/charge process might be explained as a result of more serious structural damages of the electrode material. For comparison purposes, Li storage performance of the as-prepared ZnO/C anodes and those of ZnO and ZnO/C materials reported in literature are summarized in Table 2. The results show that the cycling performance of ZnO/C composites compared with bare ZnO is much better owing to positive effects of carbon. The differences of the specific capacities of ZnO/C composites produced by various methods can be attributed to the morphology, crystal size, specific surface area as well as porosity which influence the electrochemical properties of the electrode materials. The lower electrochemical activity of the ZnO/C composites in this work compared to most of ZnO materials in literature can be explained by their morphological features and carbon content in the compounds. The as-prepared composites are composed of ZnO particles with relatively large dimensions. Small-sized particles have a large surface area, which provides more active sides resulting in high specific dis-/charge capacities. The good electrochemical performance of the electrodes prepared by the thermal decomposition of the different organometallic complexes [22, 24, 25] can be attributed to the distinctive carbon content in the products.

Conclusions

In conclusion, a facile method to synthesize ZnO/C composites, involving a thermal treatment of zinc glycerolate as a source of both carbon and zinc, was demonstrated. This one-pot method allows the synthesis of a variety of controllable ZnO/C composites with distinctive nano/microscaled arrays of ZnO particles. When used as anode material for lithium-ion batteries, the ZnO/C composite synthesized at a calcination temperature of 700 °C achieves high initial discharge and charge capacities of 1061 and 671 mAh g^{-1} at a current rate of 100 mA g^{-1}. As compared to the bare ZnO, the composites exhibit significantly better electrochemical properties, such as higher specific capacities and superior cycling stability. The carbon acts as a conductive network that runs through the material leading to the prevention of inactive areas and thus to a higher electrochemical activity. *Ex-situ* XRD studies confirm a two-step mechanism for lithiation of ZnO including a conversion and alloy process.

Acknowledgements

This work was supported by the Deutsche Forschungsgemeinschaft through projects KL1824/12-1 and KL 1824/14-1. G.Z. acknowledges support of the state order via the Ministry of Science and Higher Education of Russia (No AAAA-A19-119031890025-9). E.T. acknowledges support by the BMWi through project 03ET6095C (HiKoMat). The authors thank I. Glass for experimental support.

Funding

Open Access funding enabled and organized by Projekt DEAL.

Declarations

Conflict of interest The authors declare that they have no conflict of interest.

Supplementary Information: The online version contains supplementary material available at https://doi.org/10.1007/s10853-021-06125-4.

Supplementary Information: The online version contains supplementary material available at https://doi.org/10.1007/s10853-021-06125-4.

References

[1] Wang Y, Deng Q, Xue W, Jian Z, Zhao R, Wang J (2018) ZnO/rGO/C composites derived from metal–organic framework as advanced anode materials for Li-ion and Na-ion batteries. J Mater Sci. https://doi.org/10.1007/s10853-018-2003-3

[2] Wu G, Jia Z, Cheng Y, Zhang H, Zhou X, Wu H (2019) Easy synthesis of multi-shelled ZnO hollow spheres and their conversion into hedgehog-like ZnO hollow spheres with superior rate performance for lithium ion batteries. Appl Surf Sci. https://doi.org/10.1016/j.apsusc.2018.09.115

[3] Huang XH, Guo RQ, Wu JB, Zhang P (2014) Mesoporous ZnO nanosheets for lithium ion batteries. Mater Lett. https://doi.org/10.1016/j.matlet.2014.02.012

[4] Kundu S, Sain S, Yoshio M, Kar T, Gunawardhana N, Pradhan SK (2015) Structural interpretation of chemically synthesized ZnO nanorod and its application in lithium ion battery. Appl Surf Sci. https://doi.org/10.1016/j.apsusc.2014.12.152

[5] Fu Z-W, Huang F, Zhang Y, Chu Y, Qin Q-Z (2003) The electrochemical reaction of zinc oxide thin films with lithium. J Electrochem Soc. https://doi.org/10.1149/1.1570410

[6] Pelliccione CJ, Ding Y, Timofeeva EV, Segre CU (2015) In Situ XAFS study of the capacity fading mechanisms in ZnO anodes for lithium-ion batteries. J Electrochem Soc. https://doi.org/10.1149/2.1011509jes

[7] Mueller F, Geiger D, Kaiser U, Passerini S, Bresser D (2016) Elucidating the impact of cobalt doping on the lithium storage mechanism in conversion/alloying-type zinc oxide anodes. ChemElectroChem. https://doi.org/10.1002/celc.201600179

[8] Hao Y, Wang S, Zeng J, Li H, Yang P, Liu B, Zhang S, Xing Y (2018) A peapod-like ZnO@C design with internal void space to relieve its large-volume-change as lithium-ion battery anode. Ceram Int. https://doi.org/10.1016/j.ceramint.2017.08.088

[9] Park M-G, Sung G-K, Sung N-E, Kim J-H, Park C-M (2016) Partially reversible Li2O formation in ZnO: a critical finding supporting realization of highly reversible metal oxide electrodes. J Power Sources. https://doi.org/10.1016/j.jpowsour.2016.08.053

[10] Jamnik J, Maier J (2003) Nanocrystallinity effects in lithium battery materials. Phys Chem. https://doi.org/10.1039/b309130a

[11] Xiao L, Li E, Yi J, Meng W, Wang S, Deng B, Liu J (2018) Enhancing the performance of nanostructured ZnO as an anode material for lithium-ion batteries by polydopamine-derived carbon coating and confined crystallization. J Alloy Compd. https://doi.org/10.1016/j.jallcom.2018.06.081

[12] Abbas SM, Hussain ST, Ali S, Ahmad N, Ali N, Abbas S (2013) Structure and electrochemical performance of ZnO/CNT composite as anode material for lithium-ion batteries. J Mater Sci. https://doi.org/10.1007/s10853-013-7336-3

[13] Hsieh C-T, Lin C-Y, Chen Y-F, Lin J-S (2013) Synthesis of ZnO@Graphene composites as anode materials for lithium ion batteries. Electrochim Acta. https://doi.org/10.1016/j.electacta.2013.07.197

[14] Quartarone E, Dall'Asta V, Resmini A, Tealdi C, Tredici IG, Tamburini UA, Mustarelli P (2016) Graphite-coated ZnO nanosheets as high-capacity, highly stable, and binder-free anodes for lithium-ion batteries. J Power Sources. https://doi.org/10.1016/j.jpowsour.2016.04.107

[15] Yang T, Liu Y, Huang Z, Liu J, Bian P, Ling CD, Liu H, Wang G, Zheng R (2018) In situ growth of ZnO nanodots on carbon hierarchical hollow spheres as high-performance electrodes for lithium-ion batteries. J Alloy Compd. https://doi.org/10.1016/j.jallcom.2017.11.125

[16] Shen L, Wang C (2015) ZnO/C microboxes derived from coordination polymer particles for superior lithium ion battery anodes. RSC Adv. https://doi.org/10.1039/C5RA18254A

[17] Bai Z, Zhang Y, Fan N, Guo C, Tang B (2014) One-step synthesis of ZnO@C nanospheres and their enhanced performance for lithium-ion batteries. Mater Lett. https://doi.org/10.1016/j.matlet.2013.12.060

[18] Zhao Q, Xie H, Ning H, Liu J, Zhang H, Wang L, Wang X, Zhu Y, Li S, Wu M (2018) Intercalating petroleum asphalt into electrospun ZnO/Carbon nanofibers as enhanced free-standing anode for lithium-ion batteries. J Alloy Compd. https://doi.org/10.1016/j.jallcom.2017.12.091

[19] Liu Y, Li Y, Zhong M, Hu Y, Hu P, Zhu M, Li W, Li Y (2016) A facile synthesis of core-shell structured ZnO@C nanosphere and their high performance for lithium ion battery anode. Mater Lett. https://doi.org/10.1016/j.matlet.2016.02.112

[20] Rangel-Mendez JR, Matos J, Cházaro-Ruiz LF, González-Castillo AC, Barrios-Yáñez G (2018) Microwave-assisted synthesis of C-doped TiO_2 and ZnO hybrid nanostructured

materials as quantum-dots sensitized solar cells. Appl Surf Sci. https://doi.org/10.1016/j.apsusc.2017.10.236

[21] Xue J, Ma S, Zhou Y, Zhang Z (2015) Facile synthesis of ZnO-C nanocomposites with enhanced photocatalytic activity. Chem New J. https://doi.org/10.1039/C4NJ02004A

[22] Xiao C, Zhang S, Wang S, Xing Y, Lin R, Wei X, Wang W (2016) ZnO nanoparticles encapsulated in a 3D hierarchical carbon framework as anode for lithium ion battery. Electrochim Acta. https://doi.org/10.1016/j.electacta.2015.11.045

[23] Liu H, Shi L, Li D, Yu J, Zhang H-M, Ullah S, Yang B, Li C, Zhu C, Xu J (2018) Rational design of hierarchical ZnO@Carbon nanoflower for high performance lithium ion battery anodes. J Power Sources. https://doi.org/10.1016/j.jpowsour.2018.03.047

[24] Xie Q, Zhang X, Wu X, Wu H, Liu X, Yue G, Yang Y, Peng D-L (2014) Yolk-shell ZnO-C microspheres with enhanced electrochemical performance as anode material for lithium ion batteries. Electrochim Acta. https://doi.org/10.1016/j.electacta.2014.02.003

[25] Wei D, Xu Z, Wang J, Sun Y, Zeng S, Li W, Li X (2017) A one-pot thermal decomposition of C 4 H 4 ZnO 6 to ZnO@carbon composite for lithium storage. J Alloy Compd. https://doi.org/10.1016/j.jallcom.2017.04.214

[26] Zakharova GS, Ottmann A, Möller L, Andreikov EI, Fattakhova ZA, Puzyrev IS, Zhu Q, Thauer E, Klingeler R (2018) TiO2/C nanocomposites prepared by thermal annealing of titanium glycerolate as anode materials for lithium-ion batteries. J Mater Sci. https://doi.org/10.1007/s10853-018-2488-9

[27] Dong H, Feldmann C (2012) Porous ZnO platelets via controlled thermal decomposition of zinc glycerolate. J Alloy Compd. https://doi.org/10.1016/j.jallcom.2011.10.004

[28] Zubavichus Y, Shaporenko A, Grunze M, Zharnikov M (2005) Innershell absorption spectroscopy of amino acids at all relevant absorption edges. J Phys Chem. https://doi.org/10.1021/jp0535846

[29] Wang Y, Alsmeyer DC, McCreery RL (1990) Raman spectroscopy of carbon materials: structural basis of observed spectra. Mater Chem. https://doi.org/10.1021/cm00011a018

[30] Kumar R, Singh RK, Kumar Dubey P, Singh DP, Yadav RM, Tiwari RS (2015) Hydrothermal synthesis of a uniformly dispersed hybrid graphene–TiO_2 nanostructure for optical and enhanced electrochemical applications. RSC Adv. https://doi.org/10.1039/C4RA06852A

[31] Akhavan O, Abdolahad M, Esfandiar A, Mohatashamifar M (2010) Photodegradation of graphene oxide sheets by TiO_2 nanoparticles after a photocatalytic reduction. J Phys Chem C. https://doi.org/10.1021/jp103472c

[32] Ferrari AC, Robertson J (2000) Interpretation of Raman spectra of disordered and amorphous carbon. Rev B Phys. https://doi.org/10.1103/PhysRevB.61.14095

[33] Cho NH, Veirs DK, Ager JW, Rubin MD, Hopper CB, Bogy DB (1992) Effects of substrate temperature on chemical structure of amorphous carbon films. J Appl Phys. https://doi.org/10.1063/1.351122

[34] Deldicque D, Rouzaud J-N, Velde B (2016) A Raman–HRTEM study of the carbonization of wood: a new Raman-based paleothermometer dedicated to archaeometry. Carbon. https://doi.org/10.1016/j.carbon.2016.02.042

[35] Yan Y, Wang B, Yan C, Kang DJ (2019) Decorating ZnO nanoflakes on carbon cloth: free-standing, highly stable lithium-ion battery anodes. Ceram Int. https://doi.org/10.1016/j.ceramint.2019.05.097

[36] Chen X, Wang X, De Fang K (2020) A review on C1s XPS-spectra for some kinds of carbon materials. Fullerenes Nanotubes Carbon Nanostruct. https://doi.org/10.1080/1536383X.2020.1794851

[37] Rouquerol J, Avnir D, Fairbridge CW, Everett DH, Haynes JM, Pernicone N, Ramsay JDF, Sing KSW, Unger KK (1994) Recommendations for the characterization of porous solids (Technical Report). Pure Appl Chem. https://doi.org/10.1351/pac199466081739

[38] Ottmann A, Scholz M, Haft M, Thauer E, Schneider P, Gellesch M, Nowka C, Wurmehl S, Hampel S, Klingeler R (2017) Electrochemical magnetization switching and energy storage in manganese oxide filled carbon nanotubes. Sci Rep. https://doi.org/10.1038/s41598-017-14014-7

[39] Fujieda T, Takahashi S, Higuchi S (1992) Cycling behaviour of electrodeposited zinc alloy electrode for secondary lithium batteries. J Power Sources. https://doi.org/10.1016/0378-7753(92)80016-5

[40] Wang J, King P, Huggins R (1986) Investigations of binary lithium-zinc, lithium-cadmium and lithium-lead alloys as negative electrodes in organic solvent-based electrolyte. Solid State Ionics. https://doi.org/10.1016/0167-2738(86)90212-2

[41] Zhang CQ, Tu JP, Yuan YF, Huang XH, Chen XT, Mao F (2007) Electrochemical performances of Ni-coated ZnO as an anode material for lithium-ion batteries. J Electrochem Soc. https://doi.org/10.1149/1.2400609

[42] Xiao L, Mei D, Cao M, Qu D, Deng B (2015) Effects of structural patterns and degree of crystallinity on the performance of nanostructured ZnO as anode material for lithium-ion batteries. J Alloy Compd. https://doi.org/10.1016/j.jallcom.2014.11.195

[43] Winter M (1998) Graphites for lithium-ion cells: the correlation of the first-cycle charge loss with the Brunauer-

Emmett-Teller surface area. J Electrochem Soc. https://doi.org/10.1149/1.1838281

[44] Pender JP, Jha G, Youn DH, Ziegler JM, Andoni I, Choi EJ, Heller A, Dunn BS, Weiss PS, Penner RM, Mullins CB (2020) Electrode degradation in lithium-ion batteries. ACS Nano. https://doi.org/10.1021/acsnano.9b04365

[45] Poizot P, Laruelle S, Grugeon S, Dupont L, Tarascon JM (2000) Nano-sized transition-metal oxides as negative-electrode materials for lithium-ion batteries. Nature. https://doi.org/10.1038/35035045

[46] Guo Y-G, Hu J-S, Wan L-J (2008) Nanostructured materials for electrochemical energy conversion and storage devices. Mater Adv. https://doi.org/10.1002/adma.200800627

[47] Li H, Zhou H (2012) Enhancing the performances of Li-ion batteries by carbon-coating: present and future. Chem Commun 2:10. https://doi.org/10.1039/c1cc14764a

[48] Ge Y, Jiang H, Zhu J, Lu Y, Chen C, Hu Y, Qiu Y, Zhang X (2015) High cyclability of carbon-coated TiO_2 nanoparticles as anode for sodium-ion batteries. Electrochim Acta. https://doi.org/10.1016/j.electacta.2015.01.086

[49] Zhang W-M, Wu X-L, Hu J-S, Guo Y-G, Wan L-J (2008) Carbon coated Fe3O4 nanospindles as a superior anode material for lithium-ion batteries. Funct Mater Adv. https://doi.org/10.1002/adfm.200801386

[50] Song Y, Chen Y, Wu J, Fu Y, Zhou R, Chen S, Wang L (2017) Hollow metal organic frameworks-derived porous ZnO/C nanocages as anode materials for lithium-ion batteries. J Alloy Compd. https://doi.org/10.1016/j.jallcom.2016.10.110

[51] Fu Y, Zhong B, Chen Y, Song Y, Zhou R, Song Y, Chen S (2017) Porous ZnO@C core–shell nanocomposites as high performance electrode materials for rechargeable lithium-ion batteries. J Porous Mater. https://doi.org/10.1007/s10934-016-0297-6

[52] Yu M, Shao D, Lu F, Sun X, Sun H, Hu T, Wang G, Sawyer S, Qiu H, Lian J (2013) ZnO/graphene nanocomposite fabricated by high energy ball milling with greatly enhanced lithium storage capability. Electrochem Commun. https://doi.org/10.1016/j.elecom.2013.07.013

[53] Ren Z, Wang Z, Chen C, Wang J, Fu X, Fan C, Qian G (2014) Preparation of carbon-encapsulated ZnO tetrahedron as an anode material for ultralong cycle life performance lithium-ion batteries. Electrochim Acta. https://doi.org/10.1016/j.electacta.2014.09.038

[54] Li P, Liu Y, Liu J, Li Z, Wu G, Wu M (2015) Facile synthesis of ZnO/mesoporous carbon nanocomposites as high-performance anode for lithium-ion battery. Chem Eng J. https://doi.org/10.1016/j.cej.2015.02.077

[55] Fan H, Yu H, Zhang Y, Guo J, Wang Z, Wang H, Hao X, Zhao N, Geng H, Dai Z, Yan Q, Xu J (2017) From zinc-cyanide hybrid coordination polymers to hierarchical yolk-shell structures for high-performance and ultra-stable lithium-ion batteries. Nano Energy. https://doi.org/10.1016/j.nanoen.2017.01.043

Supplementary Materials

Table S1 Rietveld refinement data of Zn and LiZn appearing at various charging stages during electrochemical cycling.

Phase	Charging stage	Lattice parameters	
	(V)	*a* (Å)	*c* (Å)
Zn	0.3	2.66(1)	4.93(1)
LiZn	0.01	6.18(4)	6.18(4)
Zn	0.9	2.664(6)	4.934(8)
Zn	3.0	2.661(4)	4.94(1)

Figure S1: XPS Zn Auger spectra of ZnO/C-400 and ZnO/C-700

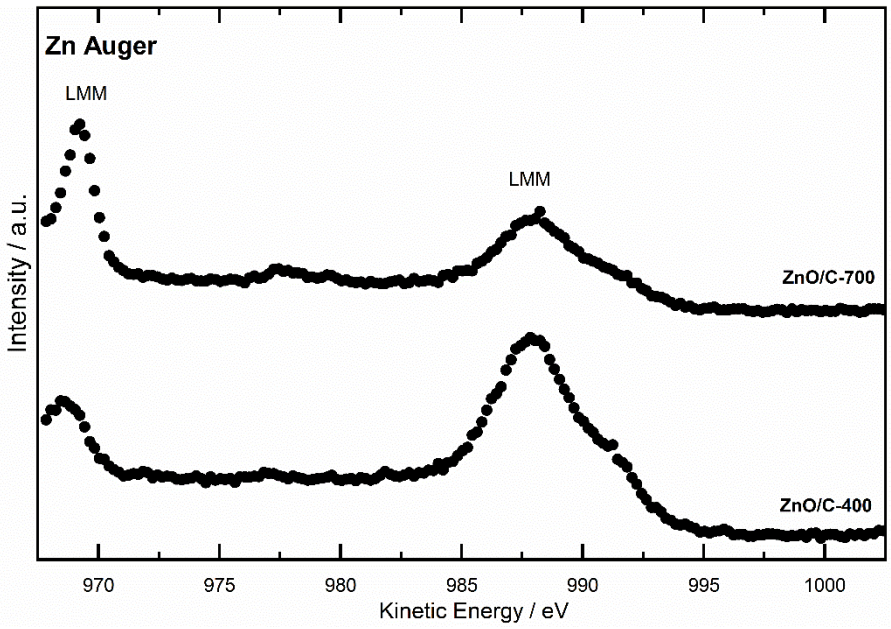

Figure S2 *Ex-situ* XRD patterns of an uncycled, fully discharged (0.01 V) and charged (3 V) ZnO/C-400 electrode. The reflexes marked with * originate from the Cu current collector. In addition, the Bragg peak positions for ZnO (JCPDS # 36-1451), Zn (COD #9008522), LiZn (COD #1539519) and Li2O (ICSD #54368) are shown.

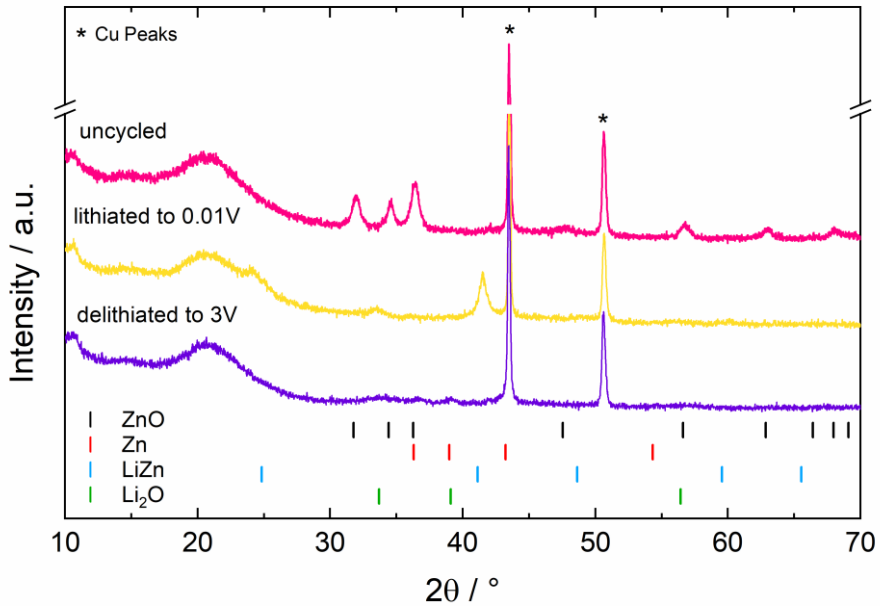

Figure S3 Specific dis-/charge capacities of the composites ZnO/C-X and of bare ZnO for galvanostatic cycling in the potential range between 0.01 and 3 V at 100 mA g^{-1}.

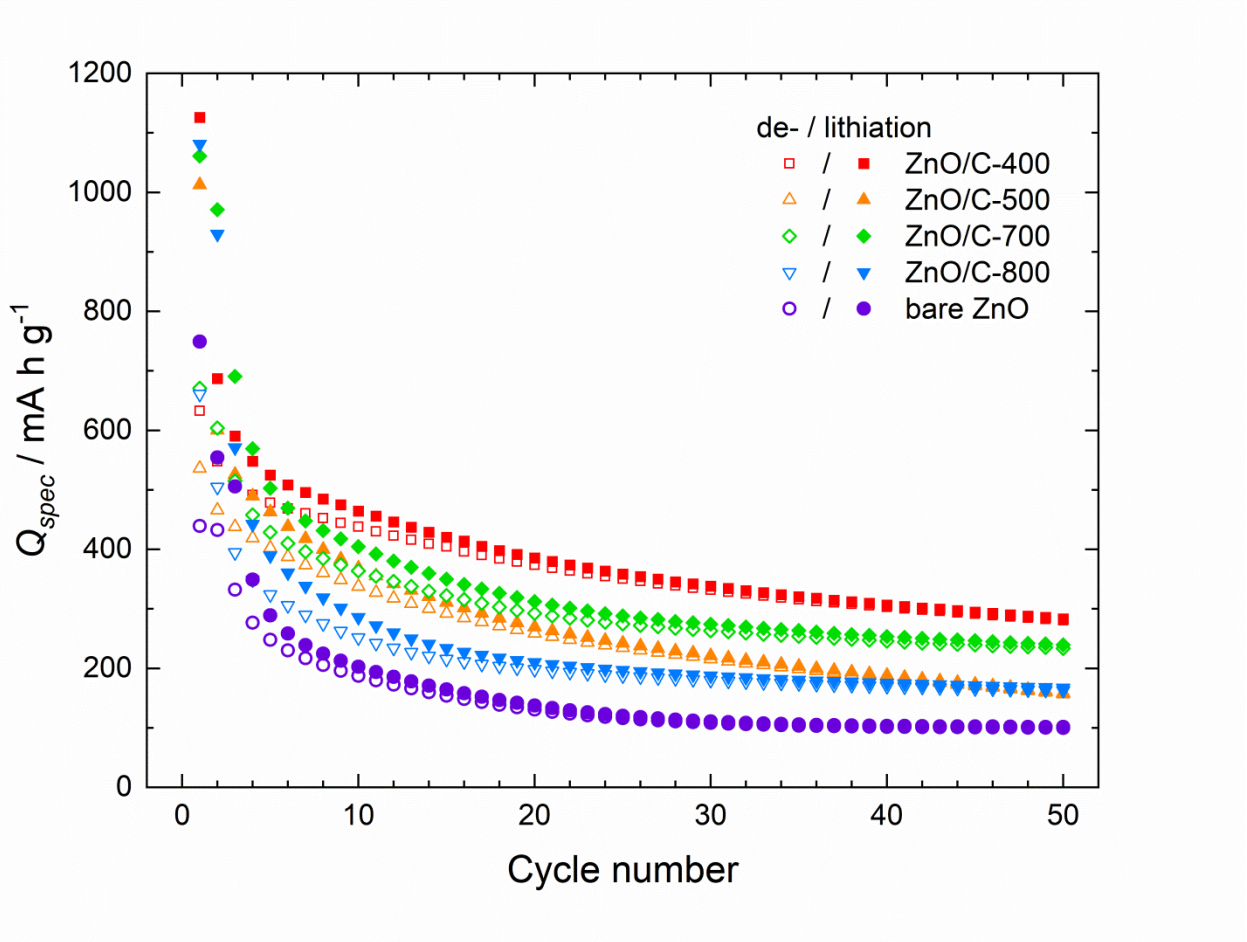

Journal of Alloys and Compounds 853 (2021) 156700

Contents lists available at ScienceDirect

Journal of Alloys and Compounds

journal homepage: http://www.elsevier.com/locate/jalcom

Hollow carbon spheres loaded with uniform dispersion of copper oxide nanoparticles for anode in lithium- ion batteries

Martyna Trukawka [a], Karolina Wenelska [a, *], Lennart Singer [b], Rüdiger Klingeler [b, c], Xuecheng Chen [a, **], Ewa Mijowska [a]

[a] Faculty of Chemical Technology and Engineering, West Pomeranian University of Technology, Szczecin, Piastow Ave. 42, 71-065, Szczecin, Poland
[b] Kirchhoff Institute of Physics, Heidelberg University, INF 227, 69120, Heidelberg, Germany
[c] Centre for Advanced Materials (CAM), Heidelberg University, INF 225, 69120, Heidelberg, Germany

ARTICLE INFO

Article history:
Received 16 April 2020
Received in revised form
3 August 2020
Accepted 12 August 2020
Available online 11 September 2020

Keywords:
Hollow carbon spheres
Coper oxide
Spheres
Anode material
Lithium-ion batteries

ABSTRACT

Lithium ion batteries are well established as a prominent option for electrical energy storage due to their high-power and high-energy density. Here, we demonstrate fully reversible conversion in hollow carbon spheres (HCSs) functionalized with copper oxide when applied as an anode material for lithium ion batteries. HCSs have been produced with hard template and glucose as a carbon precursor. Copper oxide has been prepared via thermal decomposition of copper precursor. The spherical structure is uniform in diameter of 160 nm and shell thickness of ~10 nm. Copper oxide (Cu_2O) nanoparticles of about 25 nm in diameter are homogeneously distributed inside HCSs. The carbon structure between Cu_2O nanoparticles buffers the volume change and prevents aggregation of Cu_2O nanoparticles. Clearly, it provides also unobstructed pathways for electron transport and Li^+ diffusion during charge/discharge processes. When evaluated as anode material for lithium ion batteries, HCSs with Cu_2O nanoparticles deliver an enhanced high specific capacity of 682 mAh/g at a current density of 50 mA/g and super stable cycling performances even at higher current rates in comparison with HCSs. Therefore, these findings reveal a great potential of HCS/Cu_2O nanoparticles as high-energy anode materials for LIBs.

1. Introduction

In recent years there is an ever-increasing demand for portable electronics for consumer as well as for professional applications which results in increasing energy demand of these devices. Currently, the dominant energy storage technology for portable electronic devices is rechargeable Li-ion batteries (LIBs), which is mainly due to their high energy density and superior rate performances but also because of their long cycling stability and low manufacturing cost compared to other secondary batteries[1-4]. However, the energy density of conventional graphite-based lithium ion battery cells is greatly limited because the stoichiometric limit of Li^+ intercalation restricts the theoretical capacitance of graphite to about 372 mAh/g (about 837 mAh/cm^3). Therefore, researchers are aiming at alternative high-capacitance anode materials. It seems that the carbon-based composite nanomaterials are well-suited for this purpose, since they increase the capacity of the anode even up to 1000 mAh/g[5]. A number of carbonaceous materials including graphene, nanotubes, fullerenes, nanosheets and nanofibers have been previously reported[6-17]. In most of the cited examples, high specific surface area and associated high reactivity with the electrolyte leads to ineffectiveness during the first cycle and the materials often suffer from severe capacity fading upon long-term cycling. A crucial parameter of electrode materials is its porosity. It is important in terms of material contact with the electrolyte solution which allows interfacial diffusion of Li ions, and thus determines the overall electrochemical efficiency. For this reason, it is considered that, the spherical morphology is advantageous for the electrode material as it facilitates homogeneous distribution of current, thereby reducing the electrolyte distribution and preventing growth of dendrites from lithium, i.e., improving the safety of LIBs. In the case of hollow carbon nanospheres (HCS) there is another advantage: the short diffusion distance for Li ions. It is also worth mentioning that the void space in the hollow particles can buffer against the volume change during Li

* Corresponding author.
** Corresponding author.
E-mail addresses: kwenelska@zut.edu.pl (K. Wenelska), xchen@zut.edu.pl (X. Chen).

https://doi.org/10.1016/j.jallcom.2020.156700
0925-8388/

ions insertion/desertion and thus achieve better electrochemical performance[18]. The above-mentioned properties of HCS can be used to create composites with transition metal oxides (TMO), because they have high theoretical capacities[19-22]. Especially, the use of only TMO as active material is hindered by their poor rate performance and low cycling life resulting from the large volume changes during the conversion processes as well as often limited transport of electrons and ions in the materials. Hence, when designing such carbon/TMO composite one should aim at rather small TMO nanoparticles in order to reduce the Li^+ diffusion distance[23-25]. Therefore, much work has been done to develop strategies that would alleviate these problems. One of them is combining TMO with carbon materials such as carbon nanotubes [26-29] or graphene[30-32] because carbon materials can enable fast electron transport, stabilize the system and act as elastic buffers.

Furthermore, there are many reports that the combination of carbonaceous material and copper oxide is characterized by high capacity and improved cyclability when used as anodes in LIBs. Liu *et al* published results for onion-like carbon coated Cu_2O nanocapsules which maintained a reversible capacity of 629 mAh/g after 50 cycles[33]. Zhang *et al* have reported Cu_2O nanowires/functionalized graphene composite. This material exhibited good cyclic stability and decent specific capacity of 677 mAh/g after 50 cycles [34]. There are also records reporting on other combinations of carbonaceous material and copper oxide such as nano-structured carbon-coated Cu_2O hollow spheres[35,36] mesoporous Cu_2O particles threaded with CNTs[37] or multi-yolk-shell copper oxide@-carbon octahedral[38].

Herein, we report a facile and reproducible route to prepare HCSs functionalized by Cu_2O nanoparticles as advanced anode material for high performance LIBs as illustrated in Scheme 1. Hollow carbon spheres were obtained on a template of silica nanospheres using glucose as carbon source. Carbon structure between Cu_2O nanoparticles can buffer the volume change, preventing aggregation of the Cu_2O nanoparticles, and also providing unobstructed pathways for electron transport and Li^+ diffusion during charge/discharge processes. The electrochemical performance of HCS/Cu_2O was evaluated by cyclic voltammograms (CV) and galvanostatic charge-discharge (GCD). The results imply that HCS/Cu_2O electrodes possess large capacity, good capability and superior rate cycle stability.

2. Experimental section

2.1. Synthesis of SiO_2 sphere template

Silica spheres were prepared by the modified Stöber method. In a typical synthesis 4.5 mL of tetraethylorthosilicate (TEOS) was added to a mixture of ethanol (150 mL) and concentrated ammonia (25%, 6 mL). The solution was subsequently stirred for 16 h. Then, 0.45 mL of (3-Aminopropyl) triethoxysilane (APTES) was added and stirred for another 4 h. Finally, the product was dried in air at 90 °C for 24 h.

2.2. Synthesis of HCS

Above-prepared solid silica structures were used as a template to get HCSs. 0.5 g of silica spheres were dispersed in 80 mL of water. Then 0.5 g of glucose was added and stirred for 30 min. The mixture was placed in 100 mL autoclave at 180 °C for 12 h. In the next step, the product was separated by filtration, washed with ethanol, dried and annealed in inert gas at 800 °C for 2 h. Finally, to get HCS the product was washed with hydrofluoric acid to remove the silica.

2.3. Functionalization of HCS with copper oxide nanoparticles (HCS/Cu_2O)

The HCS modified by metal oxide nanoparticles (HCS/Cu_2O) were prepared according to the following procedure: 50 mg copper (II) sulfate were dispersed in 20 mL of ethanol and added dropwise to 50 mg of HCS while stirring and heating at 50 °C. Afterwards, the mixture was dried in air at 80 °C for 24 h. Then, the product was annealed in inert gas at 400 °C for 2 h.

2.4. Characterization

HR-TEM micrographs were collected using an FEI Tecnai G2 F20 S Twin with a field emission gun operating at 200 kV. The morphology of the samples was investigated by scanning electron microscopy (Hitachi SU8000), with an acceleration voltage of 30 kV. Raman scattering was conducted on a Renishaw micro-Raman spectrometer (λ = 720 nm). X-ray diffraction (XRD) was conducted on a Philips diffractometer (X'Pert PRO Philips diffractometer, Almelo, Holland) using Cu Kα radiation. The N_2 adsorption/desorption isotherms were acquired at liquid nitrogen temperature (77 K) via Micromeritics ASAP 2420 instrument, and the specific surface area was calculated by the Brunauer-Emmett-Teller (BET) method. The pore-size distribution (PSD) was determined by the Barret-Joner-Halenda (BJH) method. Thermogravimetric analysis (TGA) was carried out on 10 mg samples using a DTA-Q600 SDT TA at a heating rate of 10 C/min from room temperature to 900 °C under air.

2.5. Electrochemical measurements

The as-prepared HCS/Cu_2O nanomaterials were used as electrode materials for LIBs. The active materials, acetylene black and PVDF were mixed in a weight ratio of 85:10:5, respectively. Subsequently, *N*-methyl-pyrrolidone (NMP) was dropped to the powder in order to form a slurry. The working electrodes were fabricated by coating the slurry onto copper foam and dried in a vacuum at 80 °C overnight. The testing coin cells were assembled with the working electrode, metallic lithium foil as a counter

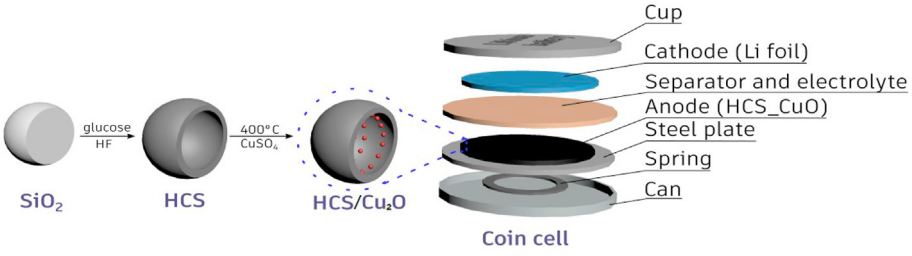

Scheme 1. Graphical illustration of HCS/Cu_2O synthesis route and coin cell composition.

electrode, NKK TK4350 film as separator, and 200 μl $LiPF_6$ in 1:1 ethylene carbonate (EC)/dimethyl carbonate (DMC) as the electrolyte. The assembly of the cells was carried out in an argon-filled glovebox (German, M. Braun Co.). Electrochemical studies were carried out by means of cyclic voltammetry (CV) and galvanostatic cycling with potential limitation (GCPL). The measurements were performed on a VMP3 multichannel potentiostat (BioLogic) at room temperature.

3. Results and discussion

Fig. 1 shows the XRD patterns of HCS/Cu_2O and HCS samples, respectively. In HCS, two broad diffraction peaks are observed at 24° and 44° which can be attributed to the (002) and (100) planes of graphitic carbon[39]. In addition to these broad features, several clear diffraction peaks in HCS/Cu_2O imply the presence of crystalline Cu_2O. Specifically, according to COD 1000063, diffraction peaks at 2θ values of 36.5, 42.5, 61.6, 73.8 and 77.6° can be assigned to the (111), (200), (220), (221), and (222) planes of cubic Cu_2O, respectively. The cubic lattice parameters of Cu_2O were calculated from the (111), (200), and (220) diffraction peaks using Bragg's law. The resulting value of $a = 4.252(2)$ Å agrees well with literature reports [40].

To further investigate the as-prepared samples, the morphology of the materials was studied by TEM and SEM (Fig. 2). Pristine hollow carbon nanospheres obtained from glucose on silica spheres template is shown in Fig. 2A. They are uniform in diameter of ~160 nm with the shells thickness ~10 nm. The size of copper oxide nanoparticles is in the range of 2–5 nm (see inset Fig. 2 D). SEM images indicated the maintaining of the spherical structure of the sample. Fig. 2C clearly shows that the surface of HCS/Cu_2O sample is smooth, demonstrating Cu_2O nanoparticles are supported inside of HCS instead of outside of HCS. No impurities or agglomerates were noticed. As discussed above, HR-TEM of the HCS/Cu_2O sample (Fig. 2D) shows only one kind of periodicity of lattice fringe with a spacing of 0.234 nm. This value nicely agrees to the separation of the (111) planes in Cu_2O as determined by XRD (see Fig. 1). Quantitatively, our XRD analysis yields 0.245(1) nm.

To further demonstrate the existence of Cu_2O nanoparticles supported in HCS, EDS mapping was used to characterize the prepared sample of HCS/Cu_2O. Fig. 3 presents the STEM image and EDS mapping of HCS/Cu_2O. It proves that Cu and O elements are evenly distributed in the sample of HCS/Cu_2O, further implying that Cu_2O nanoparticles have been successfully incorporated in HCS.

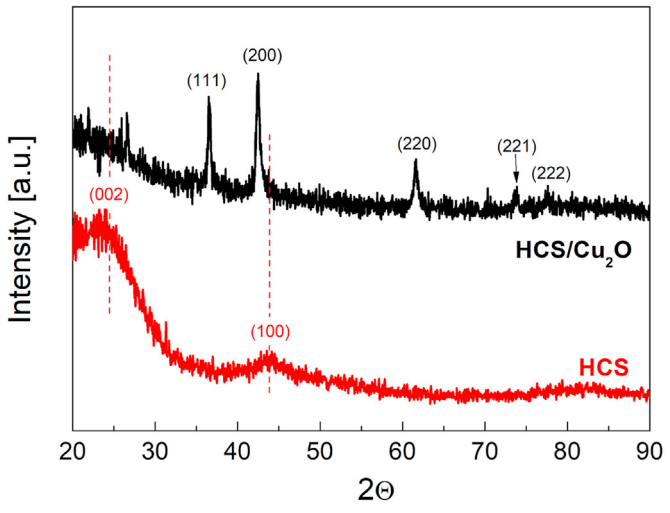

Fig. 1. XRD patterns of HCS (red) and HCS/Cu_2O (black). (For interpretation of the references to colour in this figure legend, the reader is referred to the Web version of this article.)

The N_2 adsorption/desorption measurements for HCS and HCS/Cu_2O shown in Fig. 4 imply typical type-IV profiles within relative pressure of 0–1, which suggests the presence of different pore sizes ranging from micro- to macropores. HCS exhibits larger specific surface area which decreases after modification with metal oxide nanoparticles. The parameter decrease upon Cu_2O functionalization indicates the presence of Cu_2O nanoparticles in the pores and their good distribution in the HCS. For HCS, the specific surface area is 1159 m^2/g with total a pore volume of 0.33 cm^3/g. After modification with Cu_2O nanoparticles, the specific surface area and the total pore volume decreased to 790 m^2/g and 0.18 cm^3/g, respectively (see Table 1).

Further information on the structure/defects of the materials is obtained by Raman spectroscopy (Fig. 5). The Raman spectra of the HCS and HCS/Cu_2O nanomaterials show two bands, i.e., the G- and D-band, which are characteristic for all graphitic materials. They are observed at ~1320 cm^{-1} (D) and ~1598 cm^{-1} (G). The G-band is associated with stretching of the C–C bond in graphitic materials which is common in all sp^2 carbon systems. The D-band is associated with the vibration of carbon atoms with dangling bonds in the plane with termination by disordered graphite. The intensity of the D-band measures the presence of such defects of the graphitic structure. To quantify disorder in carbon material, the I_D/I_G intensity ratio is estimated. The value of I_D/I_G for HCS/Cu_2O (~1.40) is not significantly higher than for HCS (~1.38), which may be associated with no changes in order of sp^2 bonded graphitic domains during decoration by Cu_2O nanoparticles[41].

The TGA measurements in Fig. 5 enable to reveal the carbon content and the quality of carbon nanospheres. Pristine HCS starts to decompose at 520 °C in air and the weight loss stops at 720 °C. This suggests that carbon spheres are less stable than pure graphite, which starts to burn above 600 °C[42]. There was no ash after combustion, which indicates high purity of HCS. TGA of HCS/Cu_2O reveals that the Cu_2O content is ~23 wt%. In addition, the data imply that the interaction of the metal oxide and the carbon induces lower stability of HCS. The main weight loss for HCS/Cu_2O starts at around 215 °C and ends at 400 °C.

3.1. Electrochemical measurements

To confirm the potential of the newly developed material (HCS/Cu_2O), lab-scale lithium cell prototypes were assembled using a HCS/Cu_2O-based electrode as anode. The cyclic performance of HCS/Cu_2O shows a variety of reversible redox reactions as well as irreversible processes, all of which governed by the electrochemical properties of both carbon and Cu_2O. Fig. 6A shows the initial discharge–charge curves from HCS/Cu_2O electrode in a half cell with a Li metal counter-electrode at the current density of 50 mAg^{-1}. In the reduction scan of the 1st cycle, the sample exhibits irreversible reactions at 0.6 V.

$$Cu_2O\cdot + \cdot 2Li^+\cdot + \cdot 2e^-\cdot \rightarrow \cdot Cu\cdot + \cdot Li_2O \quad (1)$$

and the formation of solid electrolyte interface (SEI) at below 0.8 V. In this case the Cu_2O is reduced into Cu during the discharge process. In the oxidation scan, the decomposition of SEI occurred at below 2.0 V and the Cu metal is then re-oxidized into Cu_2O and partially into CuO at 2.0–2.7 V during the charge process.

$$2Cu\cdot + \cdot Li_2O\cdot \rightarrow \cdot Cu_2O\cdot + \cdot 2Li\cdot + \cdot Cuo \quad (2)$$

In the reduction region of the 2nd cycle, the CuO phase is reduced to Cu_2O at 2.4 V.

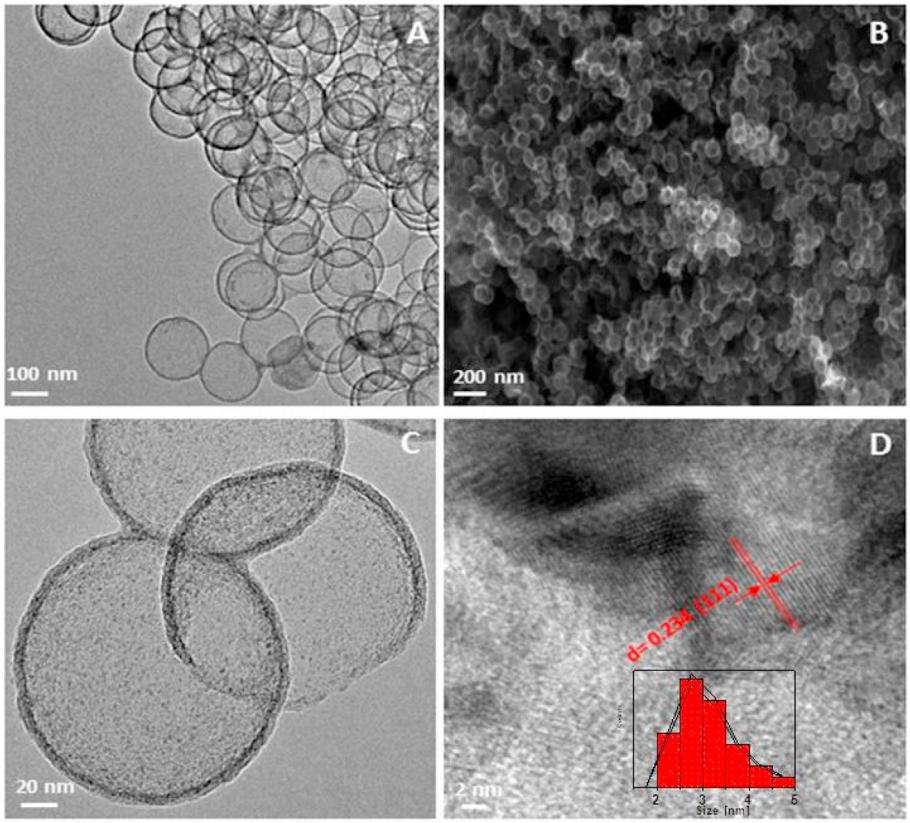

Fig. 2. (A) TEM images of HCS, (B) SEM, (C) TEM, (D) HRTEM images of HCS/Cu_2O, and Cu_2O nanoparticles size distribution as obtained from statistical analysis of the TEM images (inset).

$$Cuo \cdot + \cdot Li^{+} \cdot + \cdot e^{-} \cdot \rightarrow \cdot Cu_2O \quad (3)$$

and the Cu_2O phase is then reduced to the Cu metal at 1.4 V [43,44].

$$Cu_2O \cdot + \cdot 2Li^{+} \cdot + \cdot 2e \cdot \rightarrow \cdot Cu \cdot + \cdot Li_2O \quad (4)$$

Fig. 6B shows the first, the second and the fifth galvanostatic discharge–charge curves of the HCS/Cu_2O between 0.05 and 3.0 V (versus Li/Li+). The orange line shows the potential profile of the first charge and discharge cycle of HCS/Cu_2O (376 mA h g^{-1} and 860 mA h g^{-1}, respectively). The difference between the charge and discharge capacity in the first cycle can be assigned to irreversible effects such as the formation of the SEI layer. Thin SEI is formed on the HCS/Cu_2O electrode after cycling, and more mesopores are generated in the hollow structure, leading to the formation of interconnected spaces, which are favorable to fast transport of lithium ions and electrons. The stable SEI layer and hollow space on electrodes can stabilize lithiation/delithiation and mitigate the mechanical degradation originating from large volume expansion during discharge. The Cu_2O having dominant (111) facets, the enhanced of performance may be attributed to facilitating lithium ion transport during the discharging/ charging process. The capacity data in crystal planes of the Cu_2O play an important role in searching for high performance lithium-ion. The Cu_2O phase is easily oxidized to the CuO phase in this cell system. In addition, atom rearrangement and lattice/unit cell reconstruction were needed when the formation of monoclinic CuO from Cu2O phase occurred. However, on the (111) surfaces, which are a mixture of Cu and O atoms, it is difficult for the oxidation reaction to occur.

Multiple plateaus are clearly observed on both discharge/charge profiles, which are in good accordance with the CV curves. A sequential decay in reversible capacities as the rate increase can be observed. The electrode delivered capacities of 860 $mAhg^{-1}$, 487 $mAhg^{-1}$, 334 $mAhg^{-1}$, 219 $mAhg^{-1}$, 168 m hg^{-1} and 112 $mAhg^{-1}$ at current densities from 50 to 1000 mAg^{-1}. As shown in Fig. 6D, the new anode material exhibits good Li^{+} storage capacity and cyclic stability at each current density from 50 to 1000 mA g^{-1}. Notably, the fused HCS/Cu_2O presents much higher capacities at each stage in comparison to pristine HCS[45]. Even at a very high current density of 1000 mAg^{-1}, a satisfying capacity value of ~112 $mAhg^{-1}$ is measured. It is interesting to note that even at a current density of 50 mAg^{-1} (second time), the capacity quickly returned to 590 $mAhg^{-1}$. These results indicate an excellent rate capability of the HCS/Cu_2O-based electrode.

The Cu_2O and its composites have been studied widely in LIBs and attained prominent achievements. The specific properties of Cu_2O and its composites for LIBs are given in Table 2. The ability of Cu_2O to retain its electrochemical capacity is significant and is strongly dependent on the second component of composite.

From the above results, it is confirmed that Cu_2O nanoparticles stored inside hollow carbon spheres exhibit excellent performance when used as anode material of lithium ion battery. Due to the synergistic effect between Cu_2O nanoparticles and hollow carbon spheres, the hybrid HCS/Cu_2O material shows enhanced capacities in which the void space in HCS can buffer against the volume change during Li^{+} insertion/desertion.

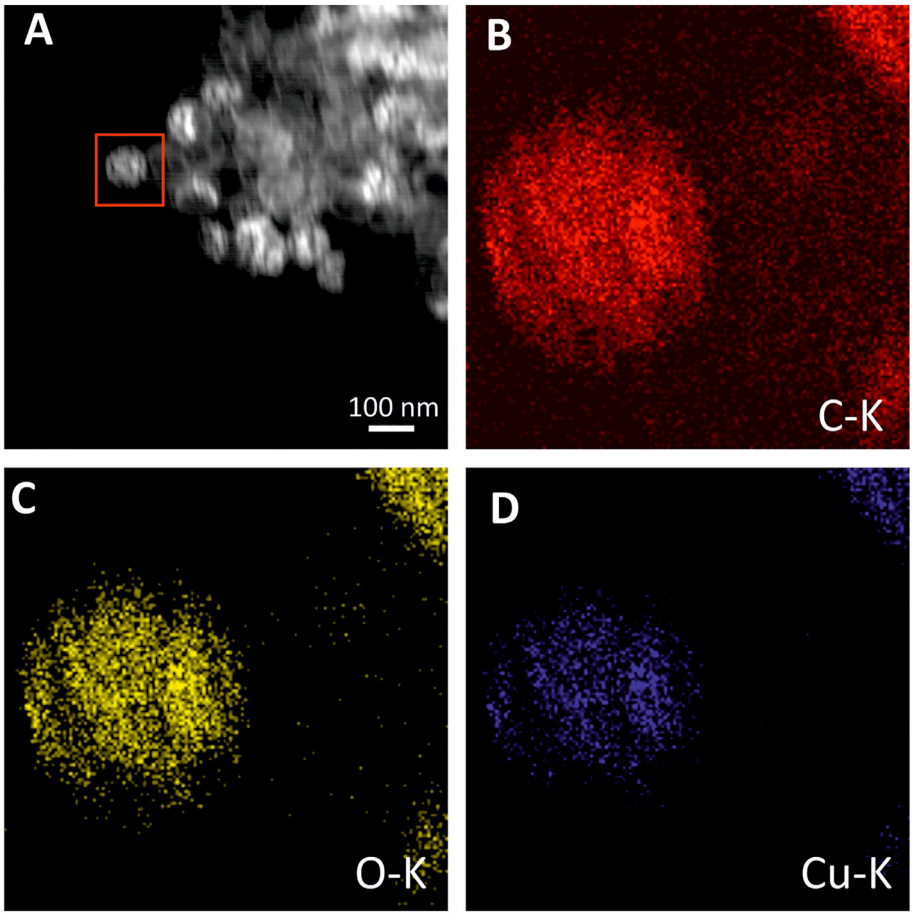

Fig. 3. (A) high-angle annular dark-field scanning transmission electron microscopy (STEM) and energy-dispersive X-ray spectroscopy (HAADF-STEM-EDS) mapping of (B) carbon, (C) oxygen, (D) copper of HCS/Cu_2O. The red square in (A) illustrates the region studied in (B) to (D). (For interpretation of the references to colour in this figure legend, the reader is referred to the Web version of this article.)

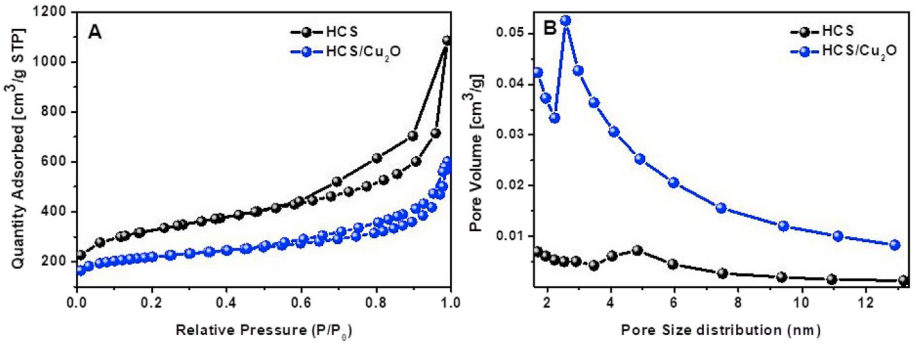

Fig. 4. N_2 adsorption/desorption isotherms (A) and pore size distribution profiles of HCS and HCS/Cu_2O.

Table 1
Specific surface area, total pore volume, and main pore size of HCS and HCS/Cu_2O as obtained by analysis of the N_2 adsorption/desorption isotherms in Fig. 4.

Sample	S_{BET} (m^2/g)	V_{TOTAL} (cm^3/g)	Pore Size (nm)
HCS	1159 ± 6.9	0.33	5.0
HCS/Cu_2O	791 ± 3.7	0.18	4.8

4. Conclusion

The contribution provides a facile route to prepare uniform hollow carbon nanospheres loaded with copper oxide nanoparticles. The spheres were obtained by the deposition of carbon from glucose onto silica sphere templates. Then, metal nanoparticles were selectively deposited inside HCS by precursor decomposition. The obtained HCSs were 160 nm in diameter with a shell thickness of about 10 nm. Based on TGA measurements, it was determined that the content of copper oxide was ~23 % wt. Also a slight decrease in order of sp^2 bonded graphitic domains with decoration of Cu_2O nanoparticles was noticed. High capacities and a good cycle performance make HCS/Cu_2O a promising anode material for rechargeable lithium ion batteries.

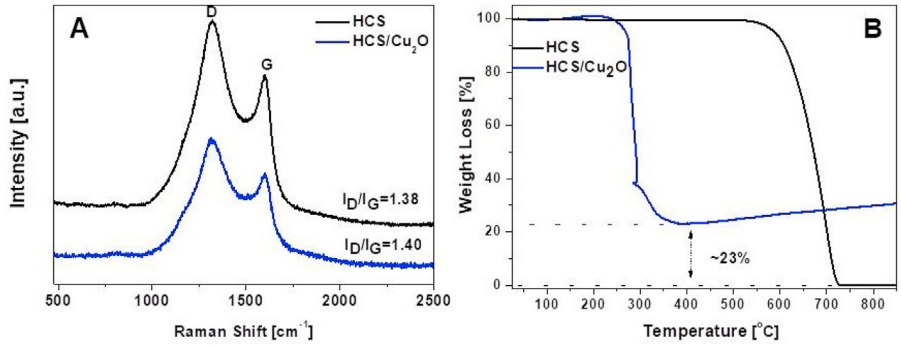

Fig. 5. (A) Raman spectroscopy and (B) TGA profile of HCS and HCS/Cu_2O.

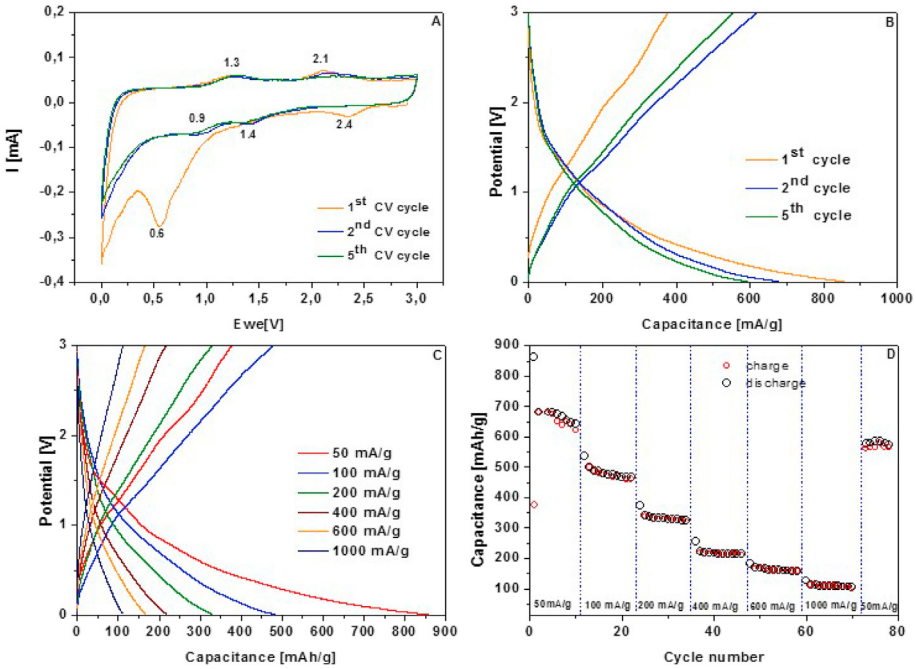

Fig. 6. (A) Cyclic voltammograms recorded over a potential window from 0.05 to 3 V at a scan rate from 0.5 mV s^{-1}, (B) galvanostatic charge/discharge profiles at a current density of 50 mA g^{-1} in the voltage range of 0.05–3.0 V, (C) voltage-capacity curves, (D) gravimetric specific capacities vs. cycle number of HCS/Cu_2O.

Table 2
Cu_2O and its composite materials for LIBs.

Materials	Disharge capacity [mAh g-1]	Ref.
Cu_2O/graphene hierarchical nanohybrids	857	[46]
Graphene oxide nanosheets Cu_2O	1326	[47]
Cu_2O/MXene	143	[48]
Cu_2O embedded in porous carbon	882.6	[49]
This work	**860**	
Core–shell structure morphology of Cu_2O 120 °C	351	[50]
Cubic shape Cu_2O	390	[51]

CRediT authorship contribution statement

Martyna Trukawka: Writing - original draft. **Karolina Wenelska:** Writing - original draft. **Lennart Singer:** Resources. **Rüdiger Klingeler:** Writing - review & editing. **Xuecheng Chen:** Conceptualization. **Ewa Mijowska:** Supervision.

Declaration of competing interest

The authors declare that they have no known competing financial interests or personal relationships that could have appeared to influence the work reported in this paper.

Acknowledgment

The authors acknowledge financial support from the National Science Centre, Poland, within Beethoven UMO-2016/23/G/ST5/04200 and by the Beethoven DFG project KL1824/12-1.

References

[1] J.B. Goodenough, Y. Kim, Challenges for rechargeable batteries, J. Power Sources 196 (2011) 6688–6694.
[2] V.G. Pol, M.M. Thackeray, Spherical carbon particles and carbon nanotubes prepared by autogenic reactions: evaluation as anodes in lithium electrochemical cells Energy, Environ. Sci. 4 (2011) 1904–1912.
[3] A. Manthiram, Materials challenges and opportunities of lithium ion batteries, J. Phys. Chem. Lett. 2 (2011) 176–184.
[4] S. Huang, J. Zhang, L. Yang, Ch Gong, J. Guo, P. Zhang, Q. Li, K. Huo, L. Mai, J. Yang, J. Zhang, Inward lithium-ion breathing of hollow carbon spheres-encapsulated Fe3O4@C nanodisc with superior lithium ion storage performance, J. Alloys Compd. (2019) 800.
[5] W. Wang, Z. Favors, C.L. Li, C. Liu, R. Ye, C.Y. Fu, K. Bozhilov, J.C. Guo, M. Ozkan, C.S. Ozkan, Silicon and carbon nanocomposite spheres with enhanced electrochemical performance for full cell lithium ion batteries, Sci. Rep. 7 (2017) 44838.
[6] L. Chen, Z. Wang, C. He, N. Zhao, C. Shi, E. Liu, A.J. Li, Uniform ultrasmall graphene oxide nanosheets with low cytotoxicity and high cellular uptake, ACS Appl. Mater. Interfaces 5 (2013) 9537–9545.
[7] R. Song, H. Song, J. Zhou, X. Chen, B. Wu, H.Y. Yang, Hierarchical porous carbon nanosheets and their favorable high-rate performance in lithium ion batteries, J. Mater. Chem. 22 (2012) 12369–12374.
[8] B.J. Landi, M.J. Ganter, C.D. Cress, R.A. Di Leo, R.P. Raffaelle, Carbon nanotubes for lithium ion batteries, Energy Environ. Sci. 2 (2009) 638–654.
[9] H.F. Xiang, Z.D. Li, K. Xie, J.Z. Jiang, J.J. Chen, P.C. Lian, J.S. Wu, Y. Yu, H.H. Wang, Graphene sheets as anode materials for Li-ion batteries: preparation, structure, electrochemical properties and mechanism for lithium storage, RSC Adv. 2 (2012) 6792–6799.
[10] D. Bhattacharjya, H.Y. Park, M.S. Kim, H.S. Choi, S.N. Inamdar, J.S. Yu, Nitrogen-Doped carbon nanoparticles by flame synthesis as anode material for rechargeable lithium-ion batteries, Langmuir 30 (2014) 318–324.
[11] W. Sun, Y. Wang, Graphene-based nanocomposite anodes for lithium-ion batteries, Nanoscale 6 (2014) 11528–11552.
[12] Z. Li, A. Ottmann, Q. Sun, A.K. Kast, T. Zhang, H.-P. Meyer, C. Backes, R. Schröder, J. Xiang, Y. Vaynzof, R. Klingeler, Hierarchical MoS_2-carbon porous nanorods towards atomic interfacial engineering for high-performance lithium storage, J. Phys. Chem. 7 (2019) 7553–7564.
[13] E. Thauer, A. Ottmann, P. Schneider, L. Möller, L. Deeg, R. Zeus, F. Wilhelmi, L. Schlestein, C. Neef, R. Ghunaim, et al., Molecules 25 (2020) 1064.
[14] G. Wang, J. Deng, T. Yan, J. Zhang, L. Shi, D. Zhang, Turning on electrocatalytic oxygen reduction by creating robust Fe–Nx species in hollow carbon frameworks via in situ growth of Fe doped ZIFs on g-C3N4, Nanoscale 12 (2020) 5601–5611.
[15] J. Zhang, J. Fang, J. Han, T. Yan, L. Shi, D. Zhang, P. N, S co-doped hollow carbon polyhedra derived from MOF-based core–shell nanocomposites for capacitive deionization, J. Mater. Chem. 6 (2018) 15245–15252.
[16] P. Liu, Y. Liu, J. Jiang, S. Ashraf, X. Wu, G. Han, J. Gao, K. Zhang, B. Li, Co-, Fe-, and N-modified carbon composites for excellent catalytic performances toward electrochemical reduction reaction, ACS Sustain. Chem. Eng. 7 (9) (2019) 8744–8754.
[17] L. Yan, D. Li, T. Yan, G. Chen, L. Shi, Zhongxun an, D. ZhangN,P,S-Codoped hierarchically porous carbon spheres with well-balanced gravimetric/volumetric capacitance for supercapacitors, ACS Sustain. Chem. Eng. 6 (4) (2018) 5265–5272.
[18] V. Etacheri, C. Wang, M.J. O'Connell, C.K. Chan, V.G. Pol, Porous carbon sphere anodes for enhanced lithium-ion storage, J. Mater. Chem. 3 (2015) 9861–9868.
[19] S. Hao, B. Zhang, S. Ball, B. Hu, J. Wu, Y. Huang, Porous and hollow NiO microspheres for high capacity and long-life anode materials of Li-ion batteries Mater, DES 92 (2016) 160–165.
[20] X. Qian, Q. Xu, T. Hang, S. Shanmugam, M. Li, Electrochemical deposition of Fe_3O_4 nanoparticles and flower-like hierarchical porous nanoflakes on 3D Cu-cone arrays for rechargeable lithium battery anodes Mater, DES 121 (2017) 321–334.
[21] S.Z. Huang, J. Jin, Y. Cai, Y. Li, H.Y. Tan, H.E. Wang, G. Van Tendeloo, B.-L. Su, Engineering single crystalline Mn_3O_4 nano-octahedra with exposed highly active {011} facets for high performance lithium ion batteries, Nanoscale 6 (2014) 6819–6827.
[22] H. Yuan, J. Li, W. Yang, Z. Zhuang, Y. Zhao, L. He, L. Xu, X. Liao, R. Zhu, L. Mai, Oxygen vacancy-determined highly efficient oxygen reduction in NiCo2O4/hollow carbon spheres, ACS Appl. Mater. Interfaces 10 (19) (2018) 16410–16417.
[23] S. Zhu, J.J. Li, X.Y. Deng, C. He, E.Z. Liu, F. He, C. Shi, N. Zhao, Ultrathin-nanosheet-induced synthesis of 3D transition metal oxides networks for lithium ion battery anodes, Adv. Funct. Mater. 27 (2017) 1605017.
[24] P. Poizot, S. Laruelle, S. Grugeon, L. Dupont, J.-M. Tarascon, Nano-sized transition-metal oxides as negative-electrode materials for lithium-ion batteries, Nature 407 (2000) 496–499.
[25] L. Martin, H. Martinez, D. Poinot, B. Pecquenard, F. Le Cras, Direct observation of important morphology and composition changes at the surface of the Cu_2O conversion material in lithium batteries, J. Power Sources 248 (2014) 861–873.
[26] X. Cui, Y. Wang, Z. Chen, H. Zhou, Q. Xu, P. Sun, J. Zhou, L. Xia, Y. Sun, Y. Lu, Preparation of pompon-like MnO/carbon nanotube composite microspheres as anodes for lithium ion batteries Electrochim, Acta 180 (2015) 858–865.
[27] R. Wu, D.P. Wang, X. Rui, B. Liu, K. Zhou, A.W.K. Law, Q. Yan, J. Wei, Z. Chen, In-Situ formation of hollow hybrids composed of cobalt sulfides embedded within porous carbon polyhedra/carbon nanotubes for high-performance lithium-ion batteries, Adv. Mater. 27 (2015) 3038–3044.
[28] X. Cui, Y.Q. Wang, Q.Y. Xu, P.P. Sun, X.Z. Wang, T. Wei, Y.M. Sun, Carbon nanotube entangled Mn_3O_4 octahedron as anode materials for lithium-ion batteries, Nanotechnology 28 (2017) 255402.
[29] A. Ottmann, M. Scholz, M. Haft, E. Thauer, P. Schneider, M. Gellesch, C. Nowka, S. Wurmehl, S. Hampel, R. Klingeler, Electrochemical magnetization switching and energy storage in manganese oxide filled carbon nanotubes, Sci. Rep. 7 (2017) 13625.
[30] B. Rangasamy, J.Y. Hwang, W. Choi, Multi layered Si-Cu_2O quantum dots wrapped by graphene for high-performance anode material in lithium-ion battery, Carbon 77 (2014) 1065–1072.
[31] G.D. Park, Y. Kang, Superior lithium-ion storage properties of mesoporous Cu_2O–reduced graphene oxide composite powder prepared by a two-step spray-drying process, Chem. Eur J. 21 (2015) 9179–9184.
[32] J. Xu, J. Wu, L. Luo, X. Chen, H. Qin, V. Dravid, S. Mi, C. Jia, Co_3O_4 nanocubes homogeneously assembled on few-layer graphene for high energy density lithium-ion batteries, J. Power Sources 274 (2015) 816–822.
[33] X. Liu, N. Bi, C. Feng, S.W. Or, Y. Sun, C. Jin, W. Li, F. Xiao, Onion-like carbon coated Cu_2O nanocapsules: a highly reversible anode material for lithium ion batteries, J. Alloys Compd. 587 (2014) 1–5.
[34] J. Zhang, B. Wang, J. Zhou, R. Xia, Y. Chu, J. Huang, Preparation of advanced Cu_2O nanowires/functionalized graphene composite anode material for lithium ion batteries, Materials 10 (2017) 72.
[35] Y. Xu, G. Jian, M.R. Zachariah, C. Wang, Nano-structured carbon-coated Cu_2O hollow spheres as stable and high rate anodes for lithium-ion batteries, J. Mater. Chem. 1 (2013) 15486.
[36] Z. Deng, Y. Li, Z. Ma, J. Zhao, J. Cao, D. Zhang, Facile one-pot synthesis of hollow Cu2O spheres with porous shells as high-performance anode materials for lithium ion batteries, Curr. Nanosci. 11 (4) (2015) 470–474.
[37] S. Ko, J.-I. Lee, H.S. Yang, S. Park, U. Jeong, Mesoporous Cu_2O particles threaded with CNTs for high-performance lithium-ion battery anodes, Adv. Mater. 24 (2012) 4451–4456.
[38] T. Chen, Y. Hu, B. Cheng, R. Chen, H. Lv, L. Ma, G. Zhu, Y. Wang, C. Yan, Z. Tie, Z. Jin, J. Liu, Multi-yolk-shell copper oxide@carbon octahedra as high-stability anodes for lithium-ion batteries, Nano Energy 20 (2016) 305–314.
[39] Y. Lu, X. Wen, X. Chen, P.K. Chu, T. Tang, E. Mijowska, Nitrogen-Doped porous carbon embedded with cobalt nanoparticles for excellent oxygen reduction reaction, J. Colloid Interface Sci. 546 (2019) 344–350.
[40] M.C. Neuburger, Präzisionsmessung der Gitterkonstante von Cuprooxyd Cu_2O, Z. Phys. 67 (1931) 11–12.
[41] S. Mildred, A.J. Dresselhaus, H. Mario, D. Gene, S. Riichiro, Perspectives on carbon nanotubes and graphene Raman spectroscopy, Nano Lett. 10 (2010) 751–758.
[42] Y. Devrim, A. Albostan, Graphene-supported platinum catalyst-based membrane electrode assembly for PEM fuel cell, J. Electron. Mater. 45 (2016) 8.
[43] X. Zhang, L. Yu, L. Wang, R. Ji, G. Wang, B. Geng, High electrochemical performance based on ultrathin porous CuO nanobelts grown on Cu substrate as integrated electrode, Chem. Phys. 15 (2013) 521–525.
[44] C.Q. Zhang, J.P. Tu, X.H. Huang, Y.F. Yuan, X.T. Chen, F. Mao, Preparation and electrochemical performances of cubic shape Cu_2O as anode material for lithium ion batteries, J. Alloys Compd. 441 (2007) 52–56.
[45] X. Shi, S. Zhang, X. Chen, T. Tang, R. Klingeler, E. Mijowska, Ultrathin NiO confined within hollow carbon sphere for efficient electrochemical energy storage, J. Alloys Compd. 797 (2019) 702–709.
[46] Y. Zhang, X. Wang, L. Zeng, S. Song, D. Liu, Green and controlled synthesis of Cu2O–graphene hierarchical nanohybrids as high-performance anode materials for lithium-ion batteries via an ultrasound assisted approach, Dalton Trans. 41 (2012) 4316.
[47] Y. Xu, Y. Guo, C. Li, X. Zhou, M.C. Tucker, X. Fu, R. Sun, C. Wong, Enhanced performance of lithium-ion batteries with copper oxide microspheres @ graphene oxide micro/nanocomposite electrodes, Nano Energy 11 (2015) 38.
[48] H. Zhang, H. Dong, X. Zhang, Y. Xu, J. Fransaer, Cu2O hybridized titanium carbide with open conductive frameworks for lithium-ion batteries, Electrochim. Acta 202 (2016) 24.
[49] X. Shen, S. Chen, D. Mu, B. Wu, F. Wu, Novel synthesis and electrochemical performance of nano-structured composite with Cu2O embedment in porous carbon as anode material for lithium ion batteries, J. Power Sources 238 (2013) 173.
[50] L.J. Fu, J. Gao, T. Zhang, Q. Cao, L.C. Yang, Y.P. Wu, R. Holze, H.Q. Wu, Preparation of Cu2O particles with different morphologies and their application in lithium ion batteries, J. Power Sources 174 (2007) 1197.
[51] C.Q. Zhang, J.P. Tu, X.H. Huang, Y.F. Yuan, X.T. Chen, F. Mao, Preparation and electrochemical performances of cubic shape Cu2O as anode material for lithium ion batteries, J. Alloys Compd. 441 (2007) 52.

A facile preparation method and proof of cycle-stability of carbon-coated metal oxide and disulfide battery materials

Peng Guo [a, b], Lennart Singer [a], Zhiyong Zhao [c], Wojciech Kukułka [d], Finn Sebastian [a], Ewa Mijowska [d], Michael Zharnikov [c], Peter Comba [b,*], Rüdiger Klingeler [a,*]

[a] Kirchhoff Institute for Physics, Heidelberg University, Im Neuenheimer Feld 227, D-69120 Heidelberg, Germany

[b] Anorganisch Chemisches Institut, Universität Heidelberg, Im Neuenheimer Feld 270, D-69120 Heidelberg, Germany

[c]Angewandte Physikalische Chemie, Universität Heidelberg, Im Neuenheimer Feld 253, D-69120, Heidelberg Germany

[d] Nanomaterials Physicochemistry Department, West Pomeranian University of Technology, Piastów Av. 45, Szczecin 70-311, Poland

ABSTRACT

Constructing composites of metal oxides and disulfides with carbonaceous materials is considered a useful approach to improve their lithium-ion storage performance. However, complicated synthesis processes and high-cost carbonaceous materials usually used hinder the commercialization of such composites. Here, as an example, carbon-coated tungsten oxides and disulfides are prepared using a facile and simple method on the basis of two kinds of low-cost carbon sources (CTAB and PVP). Following our postulated synthesis route, a variety of carbon-coated WO_x, WS_2, as well as mixed-phase WO_x-WS_2 is presented. The CTAB-assisted WO_x/C (c-WO_x/C), WS_2/C (c-WS_2/C), and mixed-phase (c-WO_x/C-WS_2/C) electrodes exhibit outstanding capacity retention of 74%, 99%, and 95%, respectively, which still have 420 mAh g^{-1}, 460 mAh g^{-1}, and 525 mAh g^{-1} capacity left after 200 cycles at 100 mA g^{-1}. Particularly, the c-WS_2/C electrode exhibits superior long-term cycle stability of 97% retention after 500 cycles. Similarly, the PVP-assisted WS_2/C (p-WS_2/C) electrode displays a capacity retention of 80% after 500 cycles. This work provides an easy and versatile route to fabricate carbon-coated tungsten oxides and disulfides with compelling battery performance and can be easily implemented for other metal oxides and disulfides.

Keywords: lithium ion batteries, tungsten-based materials, a facile method, metal oxides, metal disulfides

[*] Corresponding author

E-mail address: peter.comba@aci.uni-heidelberg.de

klingeler@kip.uni-heidelberg.de

1. Introduction

The energy crisis arising from the depletion of fossil fuels, and environmental pollution force people to develop clean, renewable energy like solar and wind energy. To effectively use these energies, significant worldwide interest has been raised to have access to appropriate energy conversion and energy storage devices [1-4]. In particular, rechargeable lithium-ion batteries (LIBs) are promising energy storage systems for electric vehicles and electric grids due to their high energy density and super-long cycle life [5-7]. However, limited by the low theoretical capacity of graphite (372 mA h g^{-1}), which cannot meet the ever-growing demand for anode materials of next-generation LIBs, many endeavors have been placed on exploring alternative anode materials for LIBs [8-12]. Among them, metal oxides and sulfides, like tungsten oxide and tungsten disulfide, are promising candidates because of their high theoretical capacity (WO_3 - 693 mAh g^{-1}, WS_2 - 432 mAh g^{-1}), high intrinsic density, low cost, and environment friendliness [13-16].

However, fast capacity fading and poor rate performance caused by low electrical conductivity and large volume expansion during cycling hinder practical applications of these compounds. To solve these issues, constructing composite with carbonaceous materials has proven to be a promising strategy [17-19]. In previous work, most papers reported composites of metal oxides and sulfides with carbonaceous materials including graphene, carbon nanotubes (CNTs), and carbon fiber which worked as a substrate via in-situ growth or liquid assembly method [20-22]. In particular, Park et al. prepared a hierarchically structured composite consisting of reduced graphene oxide and WO_3 via hydrothermal and heating treatment. The composite showed a good reversible capacity of 487 mAh g^{-1} under 150 mA g^{-1} over 100 cycles [23]. Kim et al. fabricated the onion-like crystalline WS_2 nanoparticles anchored on graphene sheets [24]. This material exhibited a specific capacity of 356.5 mAh g^{-1} at 100 mA g^{-1} after 100 cycles. Pang and their coworkers grew WS_2 nanosheets on mesoporous carbon CMK-3 by hydrothermal approach; the resulting composite delivered a good specific capacity of 720 mAh g^{-1} at 100 mA g^{-1} after 100 cycles [25].

Although the above composites exhibited better battery performance than the bare ones, complicated synthesis methods and high-cost carbonaceous materials still limit their practical application. Therefore, it is urgently needed to develop an easier and low-cost method to prepare composites of carbonaceous materials with metal oxides and sulfides. Polyvinyl pyrrolidone (PVP) and cetyltrimethylammonium bromide (CTAB) have been reported as low-cost carbon sources for various composites for many applications. For example, PVP was used as a carbon source to prepare MoS_2/C composites [26-28], carbon-coated SiO [29], SiO_2/C composite nanofibers [30], C@CoFe layered double hydroxides arrays [31], and V_2O_3@carbon nanofiber [32]. In the case of CTAB, it also worked as a carbon source for the preparation of carbon-coated TiO_2 [33], carbon-coated NaV_6O_{15} flower [34], nitrogen-doped Mo_2C@C composites [35], $Li_4Ti_5O_{12}$/C [36], and Ni-Mo_2C/graphene aerogel [37].

Here, we report a facile and scalable approach to fabricating carbon-coated metal oxides and sulfides by taking tungsten oxide and sulfide as an example. Two kinds of carbon sources, PVP and CTAB, were adopted to verify our approach. Important synthesis conditions, such as carbonization temperature, sulfurization temperature, and the amount of the carbon source, were adjusted. As a result, carbon-coated tungsten oxide and tungsten disulfide synthesized with two different carbon sources exhibit excellent battery performance. The reported approach provides an easy and versatile route that can be extended to the preparation of other metal oxides and disulfides.

2. Experimental Section

2.1 Synthesis of WO_x/C composite

WO_x/C composites were synthesized by a hydrothermal process and subsequent carbonization. Firstly, 600 mg Na_2WO_4 was dissolved in 25 ml deionized water at room temperature, then 9 M HCl solution was added dropwise to adjust the pH of the mixture to 1.5. 200 mg or 500 mg carbon source (CTAB, PVP) was subsequently added to the solution. The mixture was transferred to a 50 ml stainless steel autoclave lined with PTFE and heated at 180℃ for 24h and then cooled to room temperature. The precipitate was collected after centrifugation, washed several times with water and ethanol, and dried in an oven at 80℃ for 24 h. Finally, the powder was sintered under a flow of Argon gas at 400 – 800℃ for two hours to obtain WO_x/C composites, which are denoted as c-WO_x/C and p-WO_x/C respectively (x is a value varying from 2 to 3) according to the carbon source (CTAB or PVP) used for the synthesis. Pristine WO_3 was fabricated using the same reaction conditions without adding a carbon source.

2.2 Synthesis of WS_2/C composite

In the giving step, WO_x/C composites were used as precursors and further sulfurized to WS_2/C. 100 mg WO_x/C composite was ground with 500 mg thiourea and then loaded into an alumina crucible which was put in the downstream of a tube furnace; other alumina boat containing 500 mg thiourea was put in the upstream. The tube furnace was then kept at 600 or 800℃ for 2 h under argon flow. Pristine WS_2 was fabricated using the same reaction conditions by sulfurization of pristine WO_3. Depending on the initial carbon source, either CTAB (c) or PVP (p), the obtained products are denoted as c/p-WS_2/C. Mixed-phase composites are labeled as c/p-WO_x/C-WS_2/C.

2.3 Material Characterization

X-ray diffraction (XRD) patterns were obtained with a Bruker AXS D8 Advance Eco diffractometer using Cu K_α radiation and a step size of $\Delta(2\Theta) = 0.02°$ at the angular scans. Scanning electron microscopy (SEM) was carried out with a ZEISS Leo 1530 scanning electron microscope. Transmission electron microscopy (TEM) and high-resolution TEM (HR-TEM) were performed on a Tecnai F30 transmission electron microscope (FEI Corporation, USA) at an acceleration voltage of 200 kV. The elemental mapping was performed on a scanning transmission electron microscope (STEM) unit with a high-angle annular dark-field (HAADF) detector (FEI, Tecnai F30) operating at an acceleration voltage of 200 kV. Thermogravimetric analysis (TGA) was conducted on a DTA-Q600 SDT TA at a heating rate of 10℃ min^{-1} from room temperature to 800℃ under flowing air. X-ray photoelectron spectroscopy (XPS) measurements were conducted using a MAX 200 (Leybold-Heraeus) spectrometer equipped with a hemispherical analyzer (EA 200; Leybold-Heraeus) and a Mg Kα X-ray source. The XP spectra were acquired in normal emission geometry with an energy resolution of ~0.9 eV. The binding energy (BE) scale of the spectra was referenced to the Au $4f_{7/2}$ peak at 84.0 eV.

2.4 Battery Assembly and Electrochemical Measurements

The electrochemical performance of the fabricated materials was evaluated using coin cells (CR2032). The working electrodes were prepared by mixing the active material with carbon black and polyvinylidene difluoride (PVDF, Solvay Plastics) at a mass ratio of 7:2:1 in 1-methyl-2-pyrrolidone (NMP, Sigma Aldrich) by magnetic stirring for at least 12 h [38]. The mixed slurry was then applied on circular Cu meshes (diameter 10 mm) with a mass loading of about 1.5-2 mg cm^{-2}. Afterward, the electrodes were dried at 80℃ under vacuum, mechanically pressed at 10 MPa, and then dried again. The cells were assembled in a glove box under argon atmosphere (O_2/H_2O < 5 ppm) by using two layers of glass microfibre separator (WhatmanGF/D) soaked with 130 µl of a1 M solution of $LiPF_6$ in ethylene carbonate

(EC)/dimethyl carbonate (DMC) (1:1 by volume) (LP30, Merck) and a lithium foil (Sigma Aldrich) pressed on a nickel plate as the counter electrode. The electrochemical properties were investigated by cyclic voltammetry and galvanostatic cycling with potential limitation (GCPL) in the voltage range from 0.01 to 3 V. The measurements were performed with a VMP3 potentiostat (BioLogic) at room temperature.

3. Results and discussion

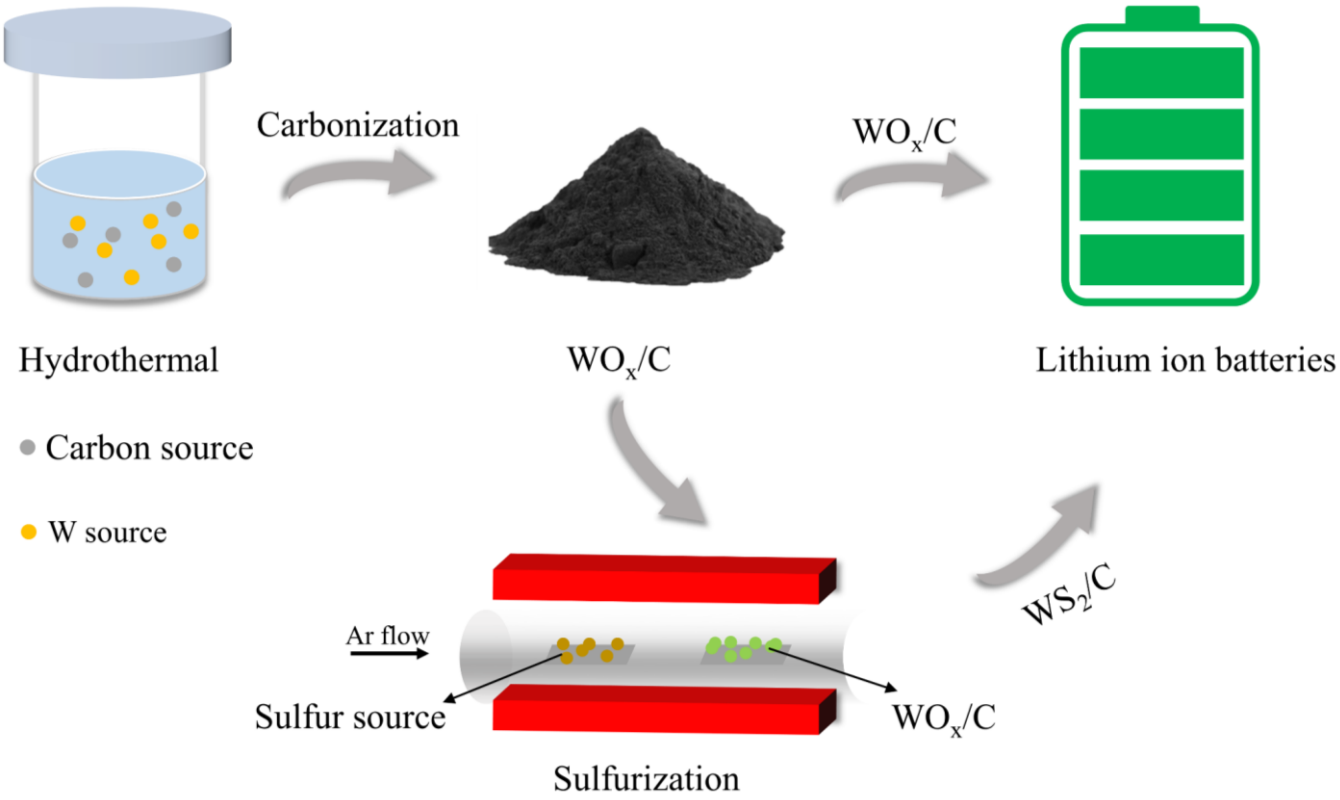

Scheme 1. Schematic illustration of the preparation of WO_x/C and WS_2/C composites.

The experimental synthesis procedure of WO_x/C and WS_2/C composites is illustrated in **Scheme 1**. The WO_x/C was obtained based on a hydrothermal process and a post-carbonization procedure. After a further sulfurization step, the WS_2/C was fabricated. It is noted that instead of high-cost carbonaceous materials like graphene, mesoporous carbon, and carbon nanotubes, the commonly used and inexpensive carbon source (CTAB and PVP) were introduced. Both carbon-coated tungsten oxides and disulfides could be easily obtained without the involvement of any sacrificial template and complex preparation steps. The effects of crucial synthesis parameters, such as the amount of carbon source, carbonization temperature, and sulfurization temperature, on the crystal structure, morphology, and battery performance of the above composite materials were investigated. We will first discuss the composites produced with the CTAB source, which was generally set to 500 mg.

3.1. c-WO_x/C, c-WO_x/C-WS_2/C, and c-WS_2/C

3.1.1. Morphology and Structure of c-WO_x/C, c-WO_x/C-WS_2/C, and c-WS_2/C

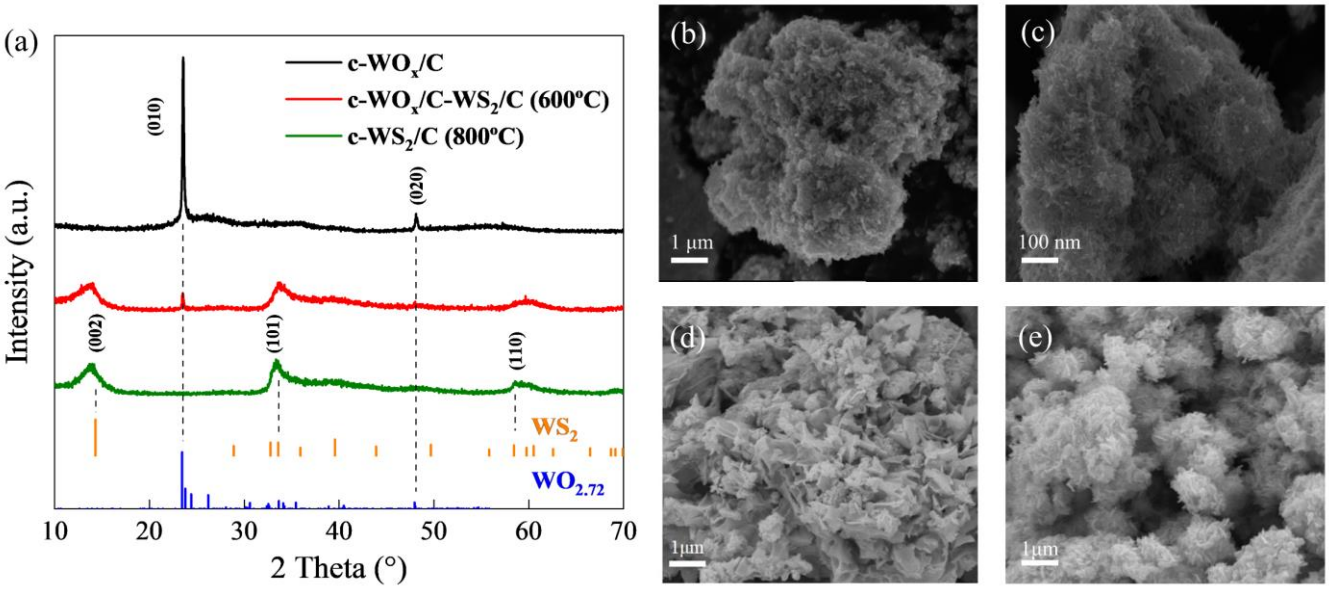

Fig. 1. (a) XRD patterns of c-WO_x/C, c-WO_x/C-WS_2/C (sulfurization at 600°C) and c-WS_2/C (sulfurization at 800°C). Vertical ticks show the reference patterns according to JCPDS No. 08-0237 and JCPDS No.71-2450. (b-e) SEM images of (b, c) c-WO_x/C, (d) c-WO_x/C-WS_2/C and (e) c-WS_2/C.

XRD patterns of pristine c-WO_x/C, sulfurized at 600 and 800 °C, respectively, are shown in Fig. 1a. The pattern of pristine c-WO_x/C exhibit distinct peaks at 23° and 48°, characteristic of $WO_{2.72}$ (JCPDS No. 71-2450) [39]. The influence of the amount of CTAB and the carbonization temperature on the obtained phase are presented in the Supplementary Information. A reduction of the amount of CTAB (200 mg) still results in the production of $WO_{2.72}$. Whereas without the addition of CTAB, the growth of pure WO_3 occurred (Fig. S1a). Besides, a high carbonization temperature (800 °C) causes the formation of WO_2 (Fig. S1b). Thus, we conclude that CTAB also acts as a reducing agent during the carbonization in addition to serving as a carbon source, and this effect becomes stronger at higher temperatures.

Upon sulfurization, the characteristic $WO_{2.72}$-diffraction peaks are suppressed and new features at 13°, 32°and 60° appear, pointing to the presence of WS_2 (JCPDS No. 08-0237). When the sulfurization process is performed at 800 °C, the resulting product is c-WS_2/C as indicated by the complete absence of the $WO_{2.72}$ diffraction peaks. By comparison, if the sulfurization temperature is 600 °C, a mixture of two components (c-WO_x/c-WS_2/C) is formed (see Fig. 1a). It can thus be concluded that the degree of sulfurization is controlled by the sulfurization temperature [40]. Moreover, all peaks associated with WS_2 are rather broad, indicating poor crystallinity. The phase of WS_2 was maintained when a small amount of CTAB (200 mg) was added (Fig. S3a), which is similar to the case of $WO_{2.72}$.

The effect of sulfurization on the microstructure of the resulting composites is demonstrated by SEM images in Fig. 1b-e and TEM images in Fig. 2a-e. Pristine c-WO_x/C exhibits a nanocluster-like structure of agglomerated nanorods with 100 – 200 nm in length (Fig. 1b, c). For comparison, the mixed-phase c-WO_x/C-WS_2/C is composed of curled nanosheets as well as nanoparticles which are assumed to be c-WO_x/C and c-WS_2/C, respectively (Fig. 1d). After the complete sulfurization at 800 °C, only curled nanosheets are observed in the resulting c-WS_2/C (Fig. 1e). Moreover, as shown in Fig. S2a, b and S3b, c, the morphology of c-WO_x/C and c-WS_2/C does not change noticeably at a small amount of CTAB added (200 mg). However, a low carbonization temperature (400 °C) caused the production of irregular c-WO_x/C (Fig. S2c).

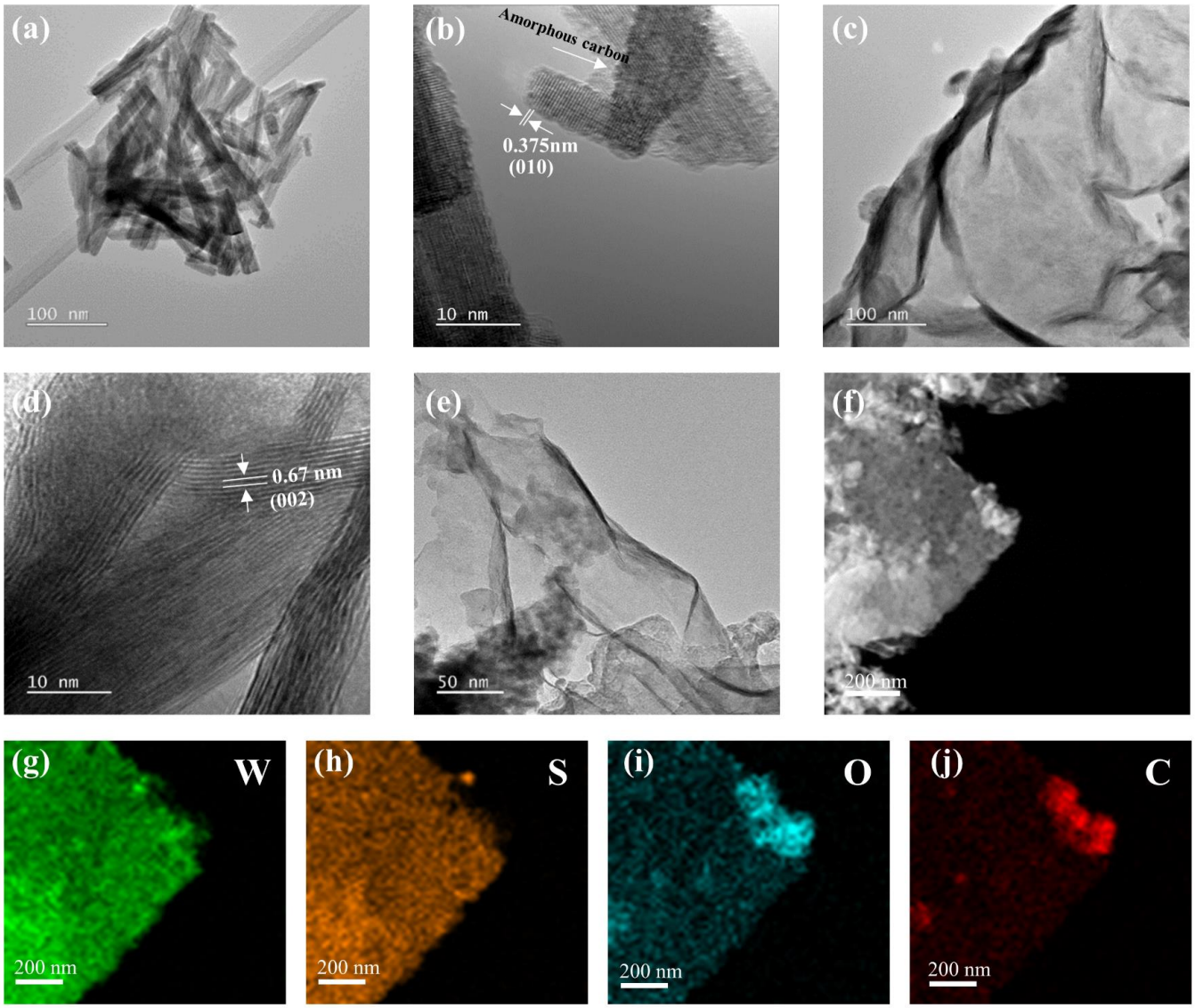

Fig. 2. TEM images and HR-TEM images of c-WO_x/C (a, b) and c-WS_2/C (c, d). TEM images (e, f) and elemental mapping images (g-j) of c-WO_x/C-WS_2/C.

As the TEM ad HRTEM images shown in Fig. 2a, b, the c-WO_x/C nanorods are coated by amorphous carbon which agrees with its SEM images. The lattice fringes with a spacing of 0.375 nm can be indexed to the (010) planes, corresponding to the main peak of $WO_{2.72}$ in the XRD patterns. The TEM and HRTEM images of the resulting c-WS_2/C (Fig. 2c-d) exhibit curled nanosheets with an interlayer spacing of 0.675 nm, which can be attributed to the (002)

plane of WS_2 [41, 42]. The elemental mappings of c-WS_2/C by energy dispersive spectroscopy (EDS) shown in Fig. S4 confirm the uniform distribution of W, S, and C in this composite. In the mixed-phase, c-WO_x/C-WS_2/C, both WS_2 nanosheets and WO_x nanoparticles are observed, as seen in Fig. 2e, which is consistent with the corresponding SEM images. EDS elemental mapping, presented in Fig. 2g-j, further illustrates the homogenous distribution of W, O, S, and C within randomly selected areas in Fig. 2f, indicating the coexistence of c-WO_x/C and c-WS_2/C, which is in good agreement with the XRD data. Thermogravimetric analysis (TGA) curves (Fig. S5) demonstrate that the specific carbon contents in c-WO_x/C, c-WO_x/C-WS_2/C, and c-WS_2/C are about 2.0, 2.1, and 2.0 ($\pm$0.5) wt%, respectively.

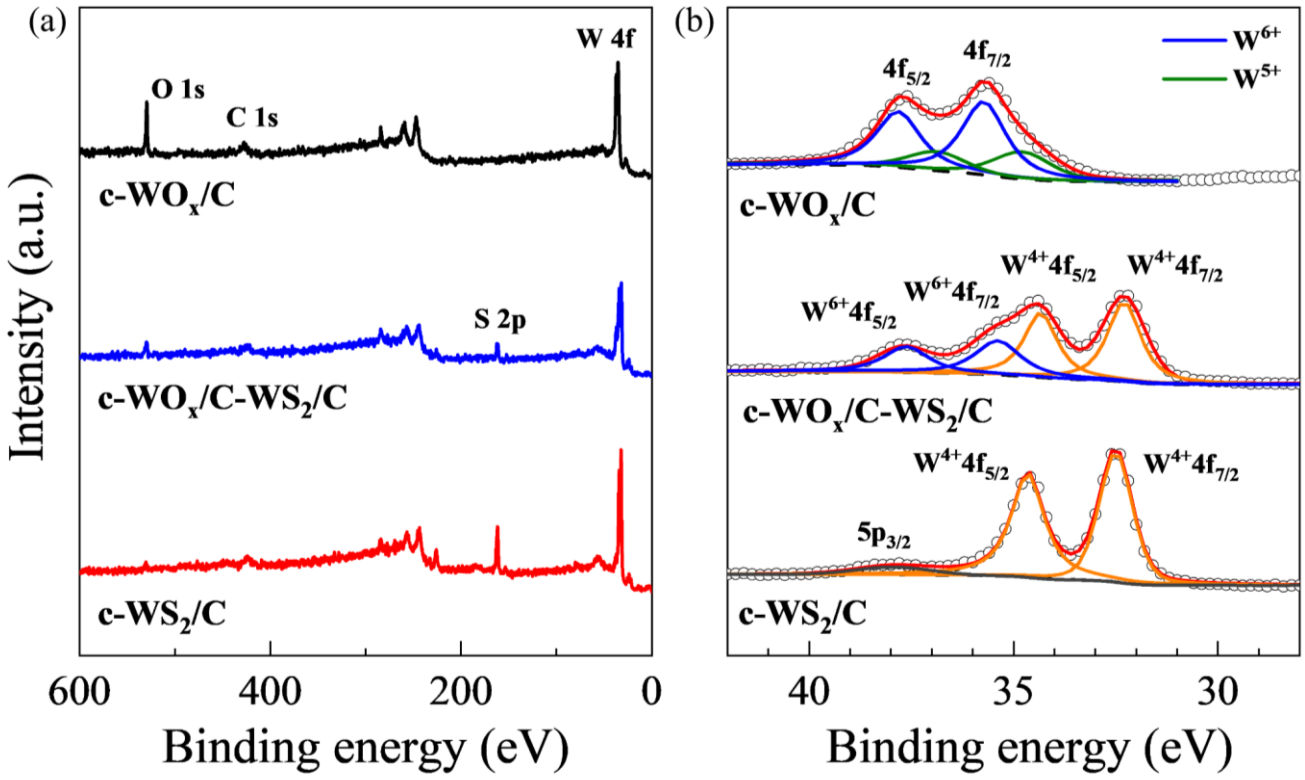

Fig. 3. Wide-scan XP spectra (a) and W 4f XP spectra (b) of c-WO_x/C, c-WO_x/C-WS_2/C, and c-WS_2/C. Characteristic peaks and doublet components are marked.

Chemical states and compositions of c-WO_x, c-WO_x/C-WS_2/C, and c-WS_2/C were monitored by XPS. The wide-scan XP spectrum of c-WO_x/C shown in Fig. 3a confirms the presence of W, O, and C in this material. After the sulfurization, there is a clear signature of S, as seen in the wide-scan spectra of c-WO_x/C-WS_2/C and c-WS_2/C. Simultaneously, the signal of O gradually decreases in intensity due to the sulfurization treatment. All these observations agree well with the results of the EDS elemental mapping.

The W 4f XP spectrum of the c-WO_x/C composite shown in Fig. 3b exhibits a superposition of two W $4f_{7/2,5/2}$ doublets. The first doublet, with the component peaks at ~35.7 and ~37.8 eV, is attributed to W^{6+}. The second, comparably weak doublet, with the component peaks at ~34.9 eV and ~36.9 eV, is assigned to W^{5+}. One can thus conclude that c-WO_x/C is composed of W^{5+} and W^{6+}, in good agreement with the literature data [43]. In contrast, in the W 4f XP spectrum of c-WS_2/C, a single W $4f_{7/2,5/2}$ doublet, with the component peaks at 32.5 eV and 34.6 eV, is found, corresponding to the W^{4+} oxidation state [44]. This doublet is accompanied by a broad W $5p_{3/2}$ peak at 37.8 eV. Complementary information is provided by the S 2p XP spectrum of c-

WS_2/C. The characteristic S $2p_{3/2,1/2}$ doublet, with the component peaks at 161.8 eV and 162.9 eV (Fig. S6), can be assigned to S–W bond, confirming the presence of WS_2. Moreover, the very low intensity of the O 1s peak in the spectrum of c-WS_2/C (Fig. 3a) verifies a nearly complete conversion of WO_x/C to WS_2/C. Significantly, the W 4f XP spectrum of the mixed-phase, c-WO_x/C-WS_2/C, confirms the presence of both W^{4+} and W^{6+}. Specifically, this spectrum exhibits two W $4f_{7/2,\ 5/2}$ doublets, with the component peaks at 32.2 eV and 34.4 eV for the first one and the component peaks at 5.5 eV and 37.7 eV for the second one. A coexistence of WO_x/C and WS_2/C in c-WO_x/C-WS_2/C is thus confirmed.

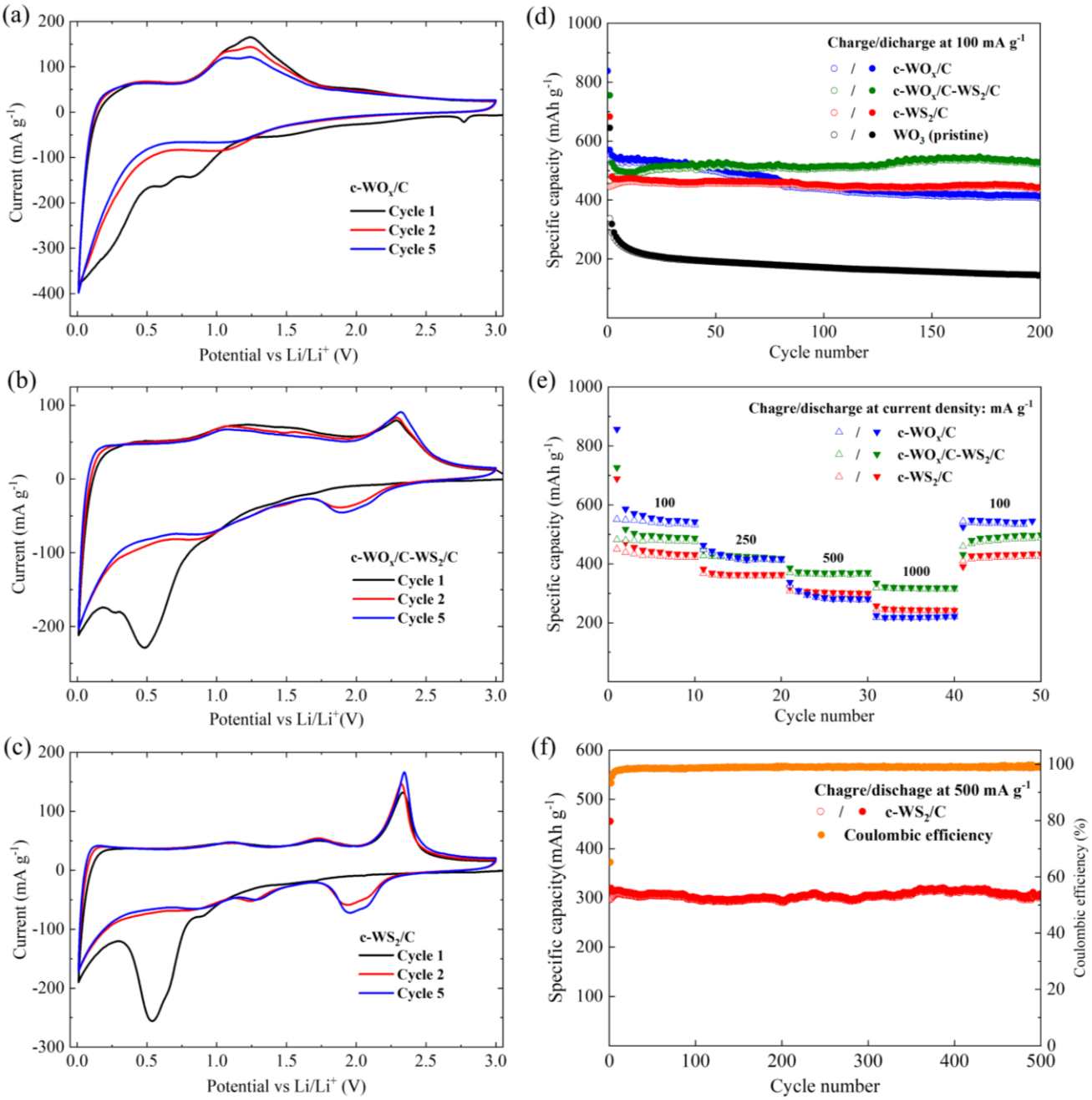

Fig. 4. CV curves for (a) c-WO_x/C, (b) c-WO_x/C-WS_2/C, and (c) c-WS_2/C electrodes for the first, second, and fifth cycles at a scan rate of 0.1 mV s^{-1} and in a potential range of 0.01–3 V vs. Li/Li^+. (d) Cycling performance at 100 mA g^{-1} and (e) rate performance of the above electrodes at the current densities ranging from 100 to 1000 mA g^{-1}. (f) Long-term cycling performance and Coulombic efficiency of c-WS_2/C at a high current density of 500 mA g^{-1}. In (d), the values for the pristine WO_3 are also shown for comparison.

3.1.2. Lithium Ion Storage Performance of c-WO_x/C, c-WO_x/C-WS_2/C, and c-WS_2/C

To investigate the electrochemical behaviors of c-WO_x/C, c-WO_x/C-WS_2/C, and c-WS_2/C electrodes, cyclic voltammetry (CV) at a scan rate of 0.1 mV s^{-1} and galvanostatic cycling with potential limitation (GCPL) were performed. The current density was set to either 100 or 500 mA g^{-1} and the potential window was set from 0.01 V to 3 V.

Fig. 4a shows the first, second, and fifth CV cycles of the c-WO_x/C electrode. The first cathodic scan displays five reduction peaks. Peaks at 2.8 and 0.6 V correspond to irreversible reactions and the formation of solid electrolyte interface (SEI) which disappear in the subsequent cycles. Other two reduction peaks at 1.5 and 0.8 V can be assigned to the lithium intercalation into $WO_{2.72}$ (Equation 1). The peak located at 0.3 V is attributed to the conversion reaction of $Li_xWO_{2.72}$ (Equation 2). During the first anodic process, an oxidation peak appears at 1.25 V which is associated with the delithiation process of Li_2O (Equation 3) [41, 45].

In the second discharge cycle, only one reduction peak at 1.1 V, corresponding to the lithium insertion into $WO_{2.72}$ (Equation 1), is visible. This peak is representative of a similar electrochemical reaction as the reduction peaks in the first cathodic scan but its position is slightly different, which can be attributed to structural changes caused by irreversible conversion reactions during the initial cycling [45]. The second and fifth CV cycles are mostly overlapping, implying high reversibility of Li^+ storage in the c-WO_x/C electrode after the second cycle.

The relevant electrochemical reactions for c-WO_x/C can be expressed below [45]:

$$WO_{2.72} + xLi^+ + xe^- \leftrightarrow Li_x WO_{2.72} \quad (1)$$

$$Li_x WO_{2.72} + (5.44 - x)Li^+ + (5.44 - x)e^- \rightarrow W + 2.72Li_2O \quad (2)$$

$$Li_2O + W \rightarrow xWO_{2.72} + (2 - x)W + zLi_2O + (2 - 2z)Li^+ + (2 - 2z)e^- \quad (3)$$

The c-WS_2/C electrode exhibits a completely different electrochemical behavior as shown by the respective CV curves in Fig. 4c. In the first cathodic scan, three reduction peaks are observed. The ones at 1.6 and 0.9 V can be attributed to the lithiation of WS_2 to form Li_xWS_2 (Equation 4). The third reduction peak, centered at 0.6 V, corresponds to the conversion reaction from Li_xWS_2 to metallic W (Equation 5) as well as to the generation of SEI [46, 47]. Also, in the first anodic scan, three oxidation peaks are recorded. Two of them, at 1.1 and 1.7 V, are fingerprints of the delithiation of Li_xWS_2 to form WS_2 (Equation 4). The pronounced oxidation peak at 2.3 V is associated with the oxidation of Li_2S to S (Equation 6) [47]. In the subsequent cathodic scan, three new reduction peaks appear which are ascribed to the lithiation of WS_2 (features at 0.9 and 1.3 V) (Equation 4) and the formation of Li_2S (1.9 V). At the same time, the reduction peak at 0.6 V disappears, indicating the irreversibility of the conversion reaction.

The electrochemical processes for c-WS_2/C can be described as follows:

$$WS_2 + xLi^+ + xe^- \leftrightarrow Li_x WS_2 \quad (4)$$

$$Li_x WS_2 + (4 - x)Li^+ + (4 - x)e^- \rightarrow 2Li_2 S + W \quad (5)$$

$$2Li_2 S \leftrightarrow 4Li^+ + 4e^- + 2S \quad (6)$$

The oxidation peaks in the second anodic scan are overlapping with the ones in the first cycle. Besides, the CV profiles remain fairly consistent and steady in the fifth cycle, suggesting good reversibility and stability of lithium ion transport.

For the mixed-phase, c-WO_x/C-WS_2/C, the CV profile in Fig. 4b displays the fingerprints of both constituting materials. Specifically, three reduction peaks in the first cathodic scan at 1.0, 0.5, and 0.3 V emphasize the intercalation of lithium ions into $WO_{2.72}$ and WS_2, the formation of an SEI, and the conversion reactions of WS_2 and $WO_{2.72}$, respectively. Oxidation peaks in the first anodic scan correspond to the delithiation of Li_xWO_x and Li_xWS_2 (1.1 V) and the delithiation of WS_2 (2.3 V). Similarly, in the further cycles, features related to WO_x/C as well as to WS_2/C are observed thereby showing that both materials in this mixed phase contribute to the electrochemical behavior. Again, the good matching of the redox peaks in the second and fifth cycles indicates high reversibility of Li^+ storage in the c-WO_x/C-WS_2/C electrode.

Fig. S7 shows the galvanostatic charge-discharge profiles for the 1st, 2nd, 10th, 100th and 200th cycles of c-WO_x/C, c-WO_x/C-WS_2/C, and c-WS_2/C electrodes at a current density of 100 mA g^{-1}. The observed potential plateaus are in good agreement with the CV results. The corresponding cycling performances and Coulombic efficiency are shown in Fig. 4d and Fig. S8 where the data of the pristine WO_3 electrode are also presented for comparison. The pristine electrode shows an initial specific discharge/charge capacity of 645/338 mAh g^{-1} which decreases gradually to 198/197 mAh g^{-1} after 200 cycles. The reason behind this decrease is typically assigned to the volume expansion effects and poor electric conductivity [39]. In contrast, the carbon-coated c-WO_x/C electrode not only delivers a higher initial specific discharge/charge capacity of 840/560 mAh g^{-1} but also exhibits noticeably better capacity retention (74%) which still amounts to 420 mAh g^{-1} after 200 cycles. For comparison, if a relatively small amount of CTAB (200 mg) is used, the initial specific discharge/charge capacity (860/630 mAh g^{-1}) is slightly higher than for the "standard" amount of CTAB (500 mg) but the capacity retention value (48%) is noticeably lower (Fig. S9). This can be explained by the lower carbon content resulting from the smaller amount of CTAB, which is not enough to completely cover WO_x. By contrast, the sufficiently high carbon content (500 mg) provides the full carbon coating on the WO_x surface, which not only promotes the electron and lithium ion diffusion kinetics but also alleviates the pulverization and volume expansion of WO_x [48].

The c-WO_x/C electrode exhibits a faster capacity fading in the first 20 cycles (Fig. S10) and the specific capacity is gradually maintained in the following cycles if the carbonization temperature is set to 400°C. Interestingly, a capacity retention of 88% is observed after nearly 100 cycles for the c-WO_x/C electrode synthesized at the high carbonization temperature (800°C), but the low initial specific discharge/charge capacity of 630/420 mAh g^{-1} hinders its application. The above results imply that the parameters of the preparation procedure, such as carbonization temperature and the amounts of carbon source, play crucial roles in the battery performance of the synthesized c-WO_x/C.

After sulfurization at 600°C, c-WO_x/C was partially converted to c-WS_2/C, and the mixed-phase, c-WO_x/C-WS_2/C, was obtained. In comparison with the c-WO_x/C electrode, the c-WO_x/C-WS_2/C electrode shows enhanced cycling stability as well as slightly lower initial specific discharge/charge capacities of 760/530 mAh g^{-1}. After 200 cycles, the specific discharge capacity of this electrode is remarkably maintained at 525 mAh g^{-1} (99% capacity retention) and no obvious capacity fading is observed during the cycling.

The full sulfurization of c-WO_x/C to c-WS_2/C at 800°C provides an electrode with an initial discharge/charge capacity of 680/483 mAh g^{-1}. Besides, this electrode shows remarkable cycling stability (95% capacity retention) and a high discharge capacity of 460 mAh g^{-1}, which is close to the theoretical capacity of WS_2 (462 mAh g^{-1}), after 200 cycles.

The pristine WS_2 and c-WS_2/C electrodes prepared with a small amount of CTAB (200 mg) were also tested to verify the importance of carbon coating. The respective pristine WS_2 electrode displays a fast discharge capacity fading from 836 to 248 mAh g^{-1} after 60 cycles (Fig.

S11). The c-WS_2/C electrode has a high initial capacity but shows a significant capacity drop from 763 to 428 mAh g^{-1} after 100 cycles (Fig. S11). Hence, optimization of the amounts of CTAB for the c-WS_2/C is of importance.

In brief, the electrodes of c-WO_x/C and c-WS_2/C as well as mixed-phase c-WO_x/C-WS_2/C all exhibit better cycling performance and higher specific capacities than the pristine WO_3 and WS_2 electrodes implying the usefulness of the facile composite preparation method described here.

Additionally, as shown in Fig. 4e, the rate capabilities of the c-WO_x/C, c-WO_x/C-WS_2/C, and c-WS_2/C electrodes were tested under different current densities ranging from 100 to 250, 500, and 1000 mA g^{-1}. The c-WS_2/C electrode delivers average specific discharge/charge capacities of 440, 360, 300, and 250 mAh g^{-1}, respectively. As the current density is returned to 100 mAg^{-1}, the specific discharge/charge capacity quickly recovers to 435 mAh g^{-1}. Similar superior rate performances are also observed for the c-WO_x/C-WS_2/C electrode which shows slightly higher average specific discharge/charge capacities of 500, 420, 380, and 320 mAh g^{-1}, respectively, at the same current densities. Consequently, both c-WS_2/C and c-WO_x/C-WS_2/C electrodes display high reversibility and excellent rate capability. By comparison, the c-WO_x/C electrode exhibits slightly inferior rate capability, delivering specific capacities of 550, 420, 280, and 220 mAh g^{-1}, respectively.

Motivated by the excellent stability and rate performance of the c-WS_2/C electrode, its long-term stability was evaluated at a high current density of 500 mA g^{-1}. Remarkably, as shown in Fig. 4f, even over 500 cycles, a high capacity retention of 97% is obtained and the electrode delivers a capacity of 307 mAh g^{-1}.

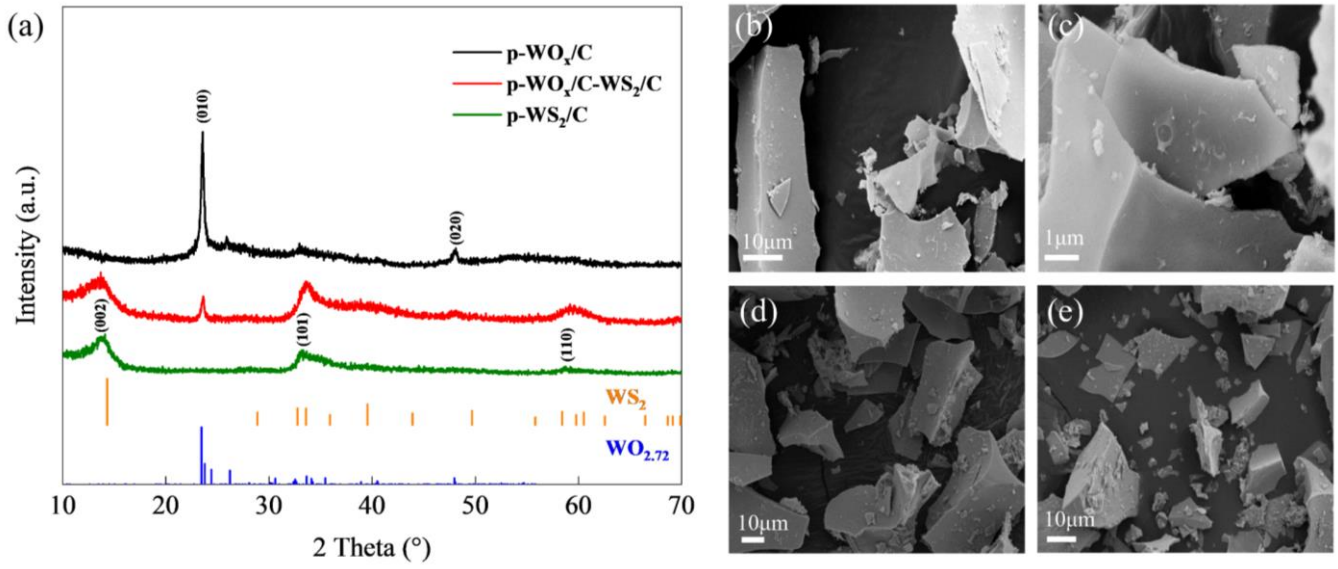

Fig. 5. (a) XRD patterns of p-WO_x/C, p-WO_x/C-WS_2/C (sulfurization at 600°C), and p-WS_2/C (sulfurization at 800 °C). Vertical ticks show the reference patterns according to JCPDS No. 08-0237 and JCPDS No.71-2450. (b-e) SEM images of (b, c) p-WO_x/C, (d) p-WO_x/C-WS_2/C, and (e) p-WS_2.

3.2. p-WO_x/C, p-WO_x/C-WS_2/C, and p-WS_2/C

3.2.1. Morphology and Structure of p-WO_x/C, p-WO_x/C-WS_2/C, and p-WS_2/C

In order to confirm the general applicability of the presented preparation method, PVP was used as an alternative carbon source to prepare carbon-coated tungsten-based oxide and disulfide. Analogously to the case of CTAB, p-WO_x/C was firstly synthesized via a hydrothermal and carbonization process, and then sulfurized at 600 and 800 °C to be converted into p-WO_x/C-WS_2/C and p-WS_2/C, respectively.

Fig. 5a shows the XRD patterns of p-WO_x/C, p-WO_x/C-WS_2/C, and p-WS_2/C. In the case of p-WO_x/C, two main peaks at 23° and 48° are observed, corresponding to the (010), and (020) planes of $WO_{2.72}$, respectively. It is noteworthy that, similar to CTAB, PVP worked as a carbon source as well as a reducing agent. After p-WO_x/C was further sulfurized at 600°C, three new peaks located at 13°, 32°, and 60° appeared which are attributed to the (002), (102), and (110) planes of WS_2. When the sulfurization temperature was elevated to 800°C, the peaks characteristic of $WO_{2.72}$ disappeared, while the peaks characteristic of WS_2 remained. It can then be concluded that the use of CTAB and PVP results in similar products, which confirms the general character of the preparation method. Some differences were however recorded. In contrast to the regular structure of the c-WO_x/C particles, the morphology of p-WO_x/C turned out to be quite irregular exhibiting microparticles ranging from 2 to 50 μm as well as some microplates (Figs. 5b, c). It is notable that this irregular morphology is maintained after sulfurization to p-WO_x/C-WS_2/C and p-WS_2/C (Figs. 5d, e), which differs noticeably from the behavior of the CTAB-based composites for which the morphology changed from nanorods to nanosheets after the sulfurization. The TEM and HRTEM images (Fig. S12) confirm the SEM data. Moreover, TEM-EDS mappings (Figs. S13 and S14), show a uniform distribution of the elements, including W, O, S, and C as well as W, S, and C in p-WO_x/C-WS_2/C and p-WS_2/C, respectively. As shown in Fig. S15, the carbon contents in p-WO_x/C, p-WO_x/C-WS_2/C, and p-WS_2/C amount to 11.6, 13.9, and 12.1 ($\pm$0.5) wt% respectively. Accordingly, we conclude that PVP provides more carbon coating than CTAB under identical preparation conditions.

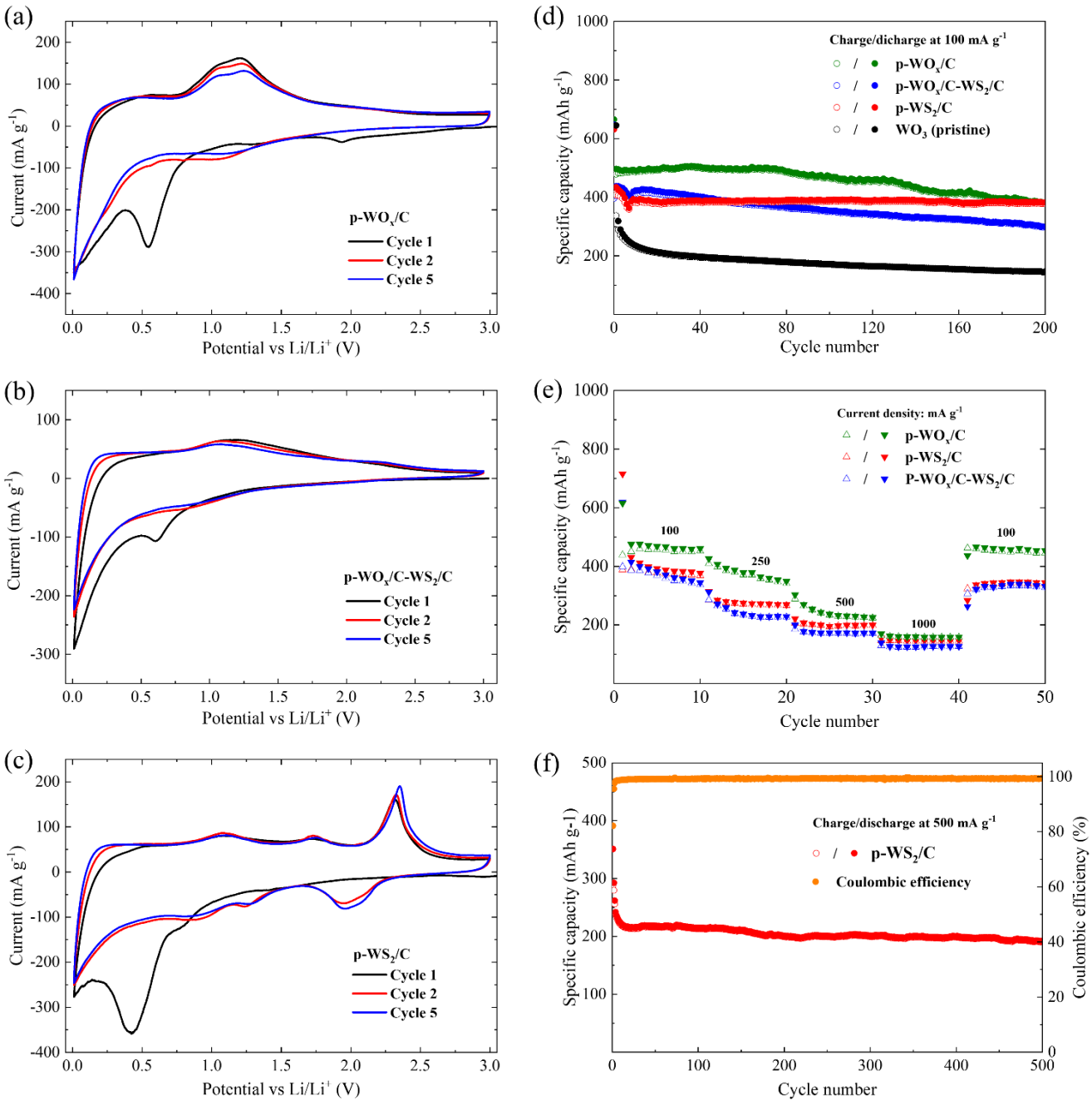

Fig. 6. CV curves for (a) p-WO_x/C, (b) p-WO_x/C-WS_2/C, and (c) p-WS_2/C electrodes for the first, second, and fifth cycles at a scan rate of 0.1 mV s^{-1} in a potential range of 0.01–3 V versus Li/Li^+. (d) Cycling performance at 100 mA $g^{-1}$and (e) rate performance of the above electrodes at current densities ranging from 100 to 1000 mA g^{-1}. (f) Long-term cycling performance and Coulombic efficiency of p-WS_2/C at a high current density of 500 mA g^{-1}.

3.2.2. Lithium Ion Storage performance of p-WO_x/C, p-WO_x/C-WS_2, and p-WS_2/C

The electrochemical behaviors of p-WO_x/C, c-WO_x/C-WS_2/C, and p-WS_2/C electrodes, as studied by CV (Figs. 6a, b, and c) and GCPL measurements (Figs. S16a, b, and c) in analog to section 3.1.2, is very similar to the materials obtained by the CTAB-assisted syntheses. The

cycling performance and Coulombic efficiency of pristine WO_3, p-WO_x/C, p-WO_x/C-WS_2/C, and p-WS_2/C electrodes were studied and the results are shown in Fig. 6d and Fig. S17. Compared with the pristine WO_3 electrode, the p-WO_x/C electrode delivers a lower initial discharge/charge specific capacity of 660/480 mAh g^{-1}, but exhibits more stable cycling performance (80% capacity retention after 200 cycles) at 100 mA g^{-1}. The mixed-phase p-WO_x/C-WS_2/C electrode, however, does not show an obvious improvement in battery performance compared with the p-WO_x/C electrode. It delivers an initial discharge/charge specific capacity of 630/440 mAh $g^{-1}$and a capacity retention of 67% after 200 cycles at 100 mA g^{-1}. In the case of the CTAB-assisted mixed-phase, c-WO_x/C-WS_2/C, the big improvement in the cycling stability can be explained by the synergetic effect of c-WO_x/C and c-WS_2/C. However, the micro-scale structure of p-WO_x/C-WS_2/C might mitigate the impact of this effect and lead to worse capacity retention. As p-WO_x/C completely converted to p-WS_2/C at 800 °C, the p-WS_2/C electrode delivers a comparatively low initial discharge/charge specific capacity of 654/420 mAh g^{-1} but shows excellent stability, viz. a capacity retention of 90% after 200 cycles at 100 mA g^{-1}.

To evaluate the rate capabilities, the p-WO_x/C, p-WO_x/C-WS_2/C, and p-WS_2/C electrodes were cycled at various current densities ranging from 100 mA g^{-1} to 1000 mA g^{-1} with 10 cycles for each (Fig. 6e). The p-WO_x/C and p-WO_x/C-WS_2/C electrodes show a pronounced capacity decrease along with increasing current densities. In contrast, the p-WS_2/C electrode exhibits an excellent rate performance, delivering high reversible capacities of 390, 280, 200, and 150 mAh g^{-1} and fast recovering to 360 mAh g^{-1} as the current density returns to 100 mA g^{-1}. In addition, the long-life cycling performance of p-WS_2/C electrode was tested at a current density of 500 mA g^{-1} to further verify its cycling stability. As displayed in Fig. 6f, a capacity retention of 80% is attained after 500 cycles, suggesting a superior cycling performance.

In the context of the above results, it is worth noting that CTAB works as a growth controller, setting the preferential orientation of WO_x and causing the formation of nanorods [49]. And the subsequent sulfurization process leads to the growth of the WS_2 curled nanosheets. These unique nanostructures provide both short lithium-ion diffusion paths and high surface areas [21]. Meanwhile, the carbon coating of around 2wt% (Table S1) can not only accommodate the volume expansion of WO_x and WS_2 during the cycling process but also improve the electrical conductivity of composites [24]. As a consequence, the unique structures and carbon coating result in outstanding cycling stability and the excellent rate capability of CTAB-assisted composites. Besides, in the mixed phase c-WO_x/C-WS_2/C, the content of WS_2 is estimated two times higher than that of WO_x (Table S1), leading to more electrochemical contribution from WS_2 and thus the comparatively lower capacity for the mixed phase than that for c-WO_x/C. By comparison, the PVP-assisted composites show a higher carbon content of 11wt%-14wt% (Table S1) and the high-content carbon coating hinders the lithium-ion diffusion, causing low capacity [48]. Although a similar ratio of WO_x and WS_2 was realized in the mixed phase p-WO_x/C-WS_2/C to the CTAB-assisted counterpart, the capacity retention is comparatively unstable. This might be because the unfavorable morphology of microparticles and microplates makes the volume expansion difficult to be alleviated even with the help of carbon coating and this effect works strongly in tungsten oxides instead of tungsten disulfide due to the moderate volume expansion of metal sulfides [15]. But both CTAB and PVP-assisted composites exhibit significantly enhanced lithium storage performance compared to the bare tungsten oxide and disulfide. To highlight the improvement, Table 1 compares the previously reported electrochemical performances of various tungsten oxides and sulfides composites when used as electrode materials in LIBs. The table implies competitive specific capacities and superior cycling stability of the carbon-coated tungsten oxides and sulfides produced in our work exhibit.

Table 1

Electrochemical performance of various tungsten oxides and sulfides composites in LIBs

Active material	Current ($mA\ g^{-1}$)	Cycle number	Capacity ($mAh\ g^{-1}$)	Ref.
WO_{3-x}/C nanosheets	200	100	662	17
m-WO_x /C	250	100	443	18
Cauliflower-like WO_3@C composites	50	50	650	50
WS_2/carbon nanotube-reduced graphene oxide	200	100	556	21
Polygonal WS_2@graphene multilayer films	100	100	430	51
WS_2@Super P nanocomposites	100	200	389	52
WS_2 nanoflowers@carbon nanotube vines	1000	140	455	53
WS_2 nanosheets@cabon composites	100	100	322	54
Carbon coated WO_x	100	200	420	
Carbon coated WO_x-WS_2	100	200	525	This work
Carbon coated WS_2	100/500	200/500	460/307	

4. Conclusion

In summary, we developed a facile and useful method for the synthesis of carbon-coated tungsten oxides and disulfides. Two kinds of carbon sources (PVP, CTAB) were adopted to obtain WO_x/C, WS_2/C, and mixed-phase, WO_x/C-WS_2/C. The respective composite electrodes exhibit excellent lithium-ion battery performance. Specifically, the c-WO_x/C electrode delivers a high initial discharge/charge capacity of 840/560 mAh g^{-1} at 100 mA g^{-1} and a 74% capacity retention after 200 cycles. Significantly, the c-WO_x/C-WS_2/C and c-WS_2/C electrodes show outstanding cycling stability with capacity retention of 99% and 95% respectively, after 200 cycles at 100 mA g^{-1}. Besides, the c-WS_2/C electrode also features a capacity retention of 97% after 500 cycles at a high current density of 500 mA g^{-1}. In addition, the p-WO_x/C, p-WS_2/C, and WO_x/C-WS_2/C electrodes exhibit high potential for high-performance lithium-ion storage. In particular, p-WS_2/C shows a capacity retention of 80% after 500 cycles at 500 mA g^{-1}. Hence, the proposed fabrication method provides a simple and low-cost way to prepare carbon-coated tungsten oxides and disulfides, useful in the context of high-performance lithium storage.

Declaration of Competing Interest

The authors declare that they have no known competing financial interests or personal relationships that could have appeared to influence the work reported in this paper.

Acknowledgments

This work was supported by the Deutsche Forschungsgemeinschaft DFG via KL 1824/12-1, within the framework of the Excellence Strategy of the Federal and State Governments of Germany, and through the China Scholarship Council (CSC). The authors thank I. Glass for experimental support.

References

[1] S. Koohi-Fayegh, M.A. Rosen, A review of energy storage types, applications and recent developments, Journal of Energy Storage 27 (2020).

[2] W. Li, X. Guo, P. Geng, M. Du, Q. Jing, X. Chen, G. Zhang, H. Li, Q. Xu, P. Braunstein, H. Pang, Rational Design and General Synthesis of Multimetallic Metal-Organic Framework Nano-Octahedra for Enhanced Li-S Battery, Adv. Mater. 33 (2021) e2105163.

[3] P. Geng, L. Wang, M. Du, Y. Bai, W. Li, Y. Liu, S. Chen, P. Braunstein, Q. Xu, H. Pang, MIL-96-Al for Li-S Batteries: Shape or Size?, Adv. Mater. 34 (2022) e2107836.

[4] J. Gu, Y. Peng, T. Zhou, J. Ma, H. Pang, Y. Yamauchi, Porphyrin-based framework materials for energy conversion, Nano Research Energy. 1 (2022) e9120009

[5] N. Nitta, F. Wu, J.T. Lee, G. Yushin, Li-ion battery materials: present and future, Materials Today 18 (2015) 252-264.

[6] P. Roy, S.K. Srivastava, Nanostructured anode materials for lithium ion batteries, Journal of Materials Chemistry A 3 (2015) 2454-2484.

[7] A. Manthiram, An Outlook on Lithium Ion Battery Technology, ACS Cent Sci 3 (2017) 1063-1069.

[8] Z. Li, A. Ottmann, T. Zhang, Q. Sun, H.-P. Meyer, Y. Vaynzof, J. Xiang, R. Klingeler, Preparation of hierarchical C@MoS_2@C sandwiched hollow spheres for lithium ion batteries, Journal of Materials Chemistry A 5 (2017) 3987-3994.

[9] X. Yu, C. Pei, W. Chen, L. Feng, 2 dimensional WS_2 tailored nitrogen-doped carbon nanofiber as a highly pseudocapacitive anode material for lithium-ion battery, Electrochim. Acta 272 (2018) 119-126.

[10] L. Zhang, H.B. Wu, X.W.D. Lou, Iron-Oxide-Based Advanced Anode Materials for Lithium-Ion Batteries, Advanced Energy Materials 4 (2014).

[11] B. Xiao, G. Wu, T. Wang, Z. Wei, Y. Sui, B. Shen, J. Qi, F. Wei, J. Zheng, High-entropy oxides as advanced anode materials for long-life lithium-ion Batteries, Nano Energy 95 (2022).

[12] Y. Zhang, P. Wang, Y. Yin, N. Liu, N. Song, L. Fan, N. Zhang, K. Sun, Carbon coated amorphous bimetallic sulfide hollow nanocubes towards advanced sodium ion battery anode, Carbon 150 (2019) 378-387.

[13] M. Zheng, H. Tang, Q. Hu, S. Zheng, L. Li, J. Xu, H. Pang, Tungsten-Based Materials for Lithium-Ion Batteries, Advanced Functional Materials 28 (2018).

[14] W. Dang, W. Wang, Y. Yang, Y. Wang, J. Huang, X. Fang, L. Wu, Z. Rong, X. Chen, X. Li, L. Huang, X. Tang, One-step hydrothermal synthesis of 2D WO_3 nanoplates@graphene nanocomposite with superior anode performance for lithium ion battery, Electrochim. Acta 313 (2019) 99-108.

[15] Y. Zhang, P. Wang, Y. Yin, X. Zhang, L. Fan, N. Zhang, K. Sun, Heterostructured SnS-ZnS@C hollow nanoboxes embedded in graphene for high performance lithium and sodium ion batteries, Chem. Eng. J. 356 (2019) 1042-1051.

[16] Z. Li, F. Yuan, M. Han, J. Yu, Atomic-Scale Laminated Structure of O-Doped WS_2 and Carbon Layers with Highly Enhanced Ion Transfer for Fast-Charging Lithium-Ion Batteries, Small 18 (2022) e2202495.

[17] K. Bao, W. Mao, G. Liu, L. Ye, H. Xie, S. Ji, D. Wang, C. Chen, Y. Li, Preparation and electrochemical characterization of ultrathin WO_{3-x} /C nanosheets as anode materials in lithium ion batteries, Nano Research 10 (2016) 1903-1911.

[18] C. Jo, W.-G. Lim, A.H. Dao, S. Kim, S. Kim, S. Yoon, J. Lee, Tracking the confinement effect of highly dispersive carbon in a tungsten oxide/carbon nanocomposite: conversion anode materials in lithium ion batteries, Journal of Materials Chemistry A 5 (2017) 24782-24789.

[19] K. Shiva, H.S.S. Ramakrishna Matte, H.B. Rajendra, A.J. Bhattacharyya, C.N.R. Rao, Employing synergistic interactions between few-layer WS_2 and reduced graphene oxide to improve lithium storage, cyclability and rate capability of Li-ion batteries, Nano Energy 2 (2013) 787-793.

[20] R. Chen, T. Zhao, W. Wu, F. Wu, L. Li, J. Qian, R. Xu, H. Wu, H.M. Albishri, A.S. Al-Bogami, D.A. El-Hady, J. Lu, K. Amine, Free-standing hierarchically sandwich-type tungsten disulfide nanotubes/graphene anode for lithium-ion batteries, Nano Lett 14 (2014) 5899-5904.

[21] Y. Wang, D. Kong, W. Shi, B. Liu, G.J. Sim, Q. Ge, H.Y. Yang, Ice Templated Free-Standing Hierarchically WS_2/CNT-rGO Aerogel for High-Performance Rechargeable Lithium and Sodium Ion Batteries, Advanced Energy Materials 6 (2016).

[22] T. Li, R. Guo, Y. Luo, F. Li, L. Meng, X. Sun, Z. Yang, H. Luo, Y. Wan, Improved lithium and sodium ion storage properties of WS_2 anode with three-layer shell structure, Electrochimica Acta 331 (2020).

[23] S.K. Park, H.J. Lee, M.H. Lee, H.S. Park, Hierarchically structured reduced graphene oxide/WO_3 frameworks for an application into lithium ion battery anodes, Chem. Eng. J. 281 (2015) 724-729.

[24] I. Kim, S.-W. Park, D.-W. Kim, Onion-like crystalline WS_2 nanoparticles anchored on graphene sheets as high-performance anode materials for lithium-ion batteries, Chemical Engineering Journal 375 (2019).

[25] Q. Pang, Y. Gao, Y. Zhao, Y. Ju, H. Qiu, Y. Wei, B. Liu, B. Zou, F. Du, G. Chen, Improved Lithium-Ion and Sodium-Ion Storage Properties from Few-Layered WS_2 Nanosheets Embedded in a Mesoporous CMK-3 Matrix, Chemistry 23 (2017) 7074-7080.

[26] Y. Li, L. Zan, J. Chen, Improving the Reaction Kinetics by Annealing MoS_2/PVP Nanoflowers for Sodium-Ion Storage, Molecules 28 (2023).

[27] M. Liu, N. Li, S. Wang, Y. Li, C. Liang, K. Yu, 3D nanoflower-like MoS_2 grown on wheat straw cellulose carbon for lithium-ion battery anode material, J. Alloys Compd. 933 (2023).

[28] J. Shao, Q. Qu, Z. Wan, T. Gao, Z. Zuo, H. Zheng, From Dispersed Microspheres to Interconnected Nanospheres: Carbon-Sandwiched Monolayered MoS_2 as High-Performance Anode of Li-Ion Batteries, ACS Appl Mater Interfaces 7 (2015) 22927-22934.

[29] Z. Huang, G. Dang, W. Jiang, Y. Sun, M. Yu, Q. Zhang, J. Xie, A Low-Cost and Scalable Carbon Coated SiO-Based Anode Material for Lithium-Ion Batteries, ChemistryOpen 10 (2021) 380-386.

[30] A. Belgibayeva, I. Taniguchi, Synthesis and characterization of SiO_2/C composite nanofibers as free-standing anode materials for Li-ion batteries, Electrochim. Acta 328 (2019).

[31] S.M. Xu, X. Liang, X.Y. Wu, S.L. Zhao, J. Chen, K.X. Wang, J.S. Chen, Multistaged discharge constructing heterostructure with enhanced solid-solution behavior for long-life lithium-oxygen batteries, Nat Commun 10 (2019) 5810.

[32] C. Busacca, O. Di Blasi, N. Briguglio, M. Ferraro, V. Antonucci, A. Di Blasi, Electrochemical performance investigation of electrospun urchin-like V_2O_3-CNF composite nanostructure for vanadium redox flow battery, Electrochim. Acta 230 (2017) 174-180.

[33] Y. Li, C. Chen, M. Wang, W. Li, Y. Wang, L. Jiao, H. Yuan, Excellent sodium storage performance of carbon-coated TiO_2: Assisted with electrostatic interaction of surfactants, J. Power Sources 361 (2017) 326-333.

[34] Y. Dong, J. Xu, M. Chen, Y. Guo, G. Zhou, N. Li, S. Zhou, C.-P. Wong, Self-assembled NaV_6O_{15} flower-like microstructures for high-capacity and long-life sodium-ion battery cathode, Nano Energy 68 (2020).

[35] Y. Liu, B. Huang, X. Hu, Z. Xie, Surfactant-assisted hydrothermal synthesis of nitrogen doped Mo_2C@C composites as highly efficient electrocatalysts for hydrogen evolution reaction, Int. J. Hydrogen Energy 44 (2019) 3702-3710.

[36] K. Liu, J. Cui, J. Yin, J. Man, Y. Cui, Z. Wen, J. Sun, Ultra-long life core-shell structure $Li_4Ti_5O_{12}$/C nanocomposite anode materials for lithium ion batteries, J. Alloys Compd. 765 (2018) 229-235

[37] P. Kumar, M. Arumugam, G. Maia, S. Praserthdam, P. Praserthdam, Double role of CTAB as a surfactant and carbon source in Ni-Mo_2C/GA composite: As a highly active electrocatalyst for hydrogen evolution reaction, Electrochim. Acta 441 (2023).

[38] E. Thauer, G.S. Zakharova, L.F. Deeg, Q. Zhu, R. Klingeler, Hierarchically structured V_2O_3/C microspheres: Synthesis, characterization, and their electrochemical properties, Electrochimica Acta 390 (2021).

[39] W. Zhang, L. Yue, F. Zhang, Q. Zhang, X. Gui, R. Guan, G. Hou, N. Xu, One-step in situ synthesis of ultrathin tungsten oxide@carbon nanowire webs as an anode material for high performance, Journal of Materials Chemistry A 3 (2015) 6102-6109.

[40] B. Zhang, C. Luo, Y. Deng, Z. Huang, G. Zhou, W. Lv, Y.B. He, Y. Wan, F. Kang, Q.H. Yang, Optimized Catalytic WS_2–WO_3 Heterostructure Design for Accelerated Polysulfide Conversion in Lithium–Sulfur Batteries, Advanced Energy Materials 10 (2020).

[41] Y. Sun, W. Wang, J. Qin, D. Zhao, B. Mao, Y. Xiao, M. Cao, Oxygen vacancy-rich mesoporous $W_{18}O_{49}$ nanobelts with ultrahigh initial Coulombic efficiency toward high-performance lithium storage, Electrochimica Acta 187 (2016) 329-339.

[42] L. Yin, D. Pham-Cong, I. Jeon, J.-P. Kim, J. Cho, S.-Y. Jeong, H. Woo Lee, C.-R. Cho, Electrochemical performance of vertically grown WS_2 layers on $TiNb_2O_7$ nanostructures for lithium-ion battery anodes, Chemical Engineering Journal 382 (2020).

[43] L. Sinha, P.M. Shirage, Surface Oxygen Vacancy Formulated Energy Storage Application: Pseudocapacitor-Battery Trait of $W_{18}O_{49}$ Nanorods, Journal of The Electrochemical Society 166 (2019) A3496-A3503.

[44] J. Li, H. Yan, W. Wei, X. Li, L. Meng, Enhanced Lithium Storage Performance of Liquid-Phase Exfoliated Graphene Supported WS_2 Heterojunctions, ChemElectroChem 5 (2018) 3222-3228.

[45] Z. Chen, K. Ye, M. Li, S. Zhao, J. Luo, B. Wu, Lithiation mechanism of $W_{18}O_{49}$ anode material for lithium-ion batteries: Experiment and first-principles calculations, Journal of Electroanalytical Chemistry 880 (2021).

[46] H. Liu, D. Su, G. Wang, S.Z. Qiao, An ordered mesoporous WS_2 anode material with superior electrochemical performance for lithium ion batteries, Journal of Materials Chemistry 22 (2012).

[47] H.T. Huu, H.T.T. Le, V.P. Nguyen, T.T. Huong Nguyen, T.X. Dieu Nguyen, V.T. Nguyen, S.-J. Kim, V. Vo, Facile one-step synthesis of g–C_3N_4–supported WS_2 with enhanced lithium storage properties, Electrochimica Acta 341 (2020).

[48] W. Sun, Z. Hu, C. Wang, Z. Tao, S.L. Chou, Y.M. Kang, H.K. Liu, Effects of Carbon Content on the Electrochemical Performances of MoS_2-C Nanocomposites for Li-Ion Batteries, ACS Appl Mater Interfaces 8 (2016) 22168-22174.

[49] X.L. Xu, Y. Chen, S.Y. Ma, S.H. Yan, Y.Z. Mao, T. Wang, H.Q. Bian, CTAB-assisted synthesis of unique 3D ZnO and the acetone sensing performances, Materials Letters 151 (2015) 5-8.

[50] S. Yoon, S.-G. Woo, K.-N. Jung, H. Song, Conductive surface modification of cauliflower-like WO_3 and its electrochemical properties for lithium-ion batteries, J. Alloys Compd. 613 (2014) 187-192.

[51] Y. Dong, S. Chen, J. Liu, J. Lei, F. Liu, W. Yang, J. Wang, Polygonal WS_2-decorated-graphene multilayer films with microcavities prepared from a cheap precursor as anode materials for lithium-ion batteries, Mater. Lett. 254 (2019) 73-76.

[52] J. Huang, X. Wang, J. Li, L. Cao, Z. Xu, H. Wei, WS_2-Super P nanocomposites anode material with enhanced cycling stability for lithium ion batteries, J. Alloys Compd. 673 (2016) 60-66.

[53] X. Li, J. Zhang, Z. Liu, C. Fu, C. Niu, WS_2 nanoflowers on carbon nanotube vines with enhanced electrochemical performances for lithium and sodium-ion batteries, J. Alloys Compd. 766 (2018) 656-662.

[54] J. Li, X. Shi, J. Fang, J. Li, Z. Zhang, Facile Synthesis of WS_2 Nanosheets-Carbon Composites Anodes for Sodium and Lithium Ion Batteries, ChemNanoMat 2 (2016) 997-1002.

Supporting Information

A facile preparation method and proof of cycle-stability of carbon-coated metal oxide and disulfide battery materials

Peng Guo [a,b], Lennart Singer [a], Zhiyong Zhao [c], Wojciech Kukułka [d], Finn Sebastian [a], Ewa Mijowska [d], Michael Zharnikov [c], Peter Comba [b,*], Rüdiger Klingeler [a,*]

[a] Kirchhoff Institute for Physics, Heidelberg University, Im Neuenheimer Feld 227, D-69120 Heidelberg, Germany

[b] Anorganisch Chemisches Institut, Universität Heidelberg, Im Neuenheimer Feld 270, D-69120 Heidelberg, Germany

[c]Angewandte Physikalische Chemie, Universität Heidelberg, Im Neuenheimer Feld 253, D-69120, Heidelberg Germany

[d] Nanomaterials Physicochemistry Department, West Pomeranian University of Technology, Piastów Av. 45, Szczecin 70-311, Poland

[*] Corresponding author

E-mail address: peter.comba@aci.uni-heidelberg.de

klingeler@kip.uni-heidelberg.de

The Supporting Material provides additional XRD patterns of the resulting materials under various synthesis conditions, SEM and TEM images, EDS elemental mappings, TGA and XPS data, as well as galvanostatic charge-discharge curves, Coulombic efficiency and capacity studies.

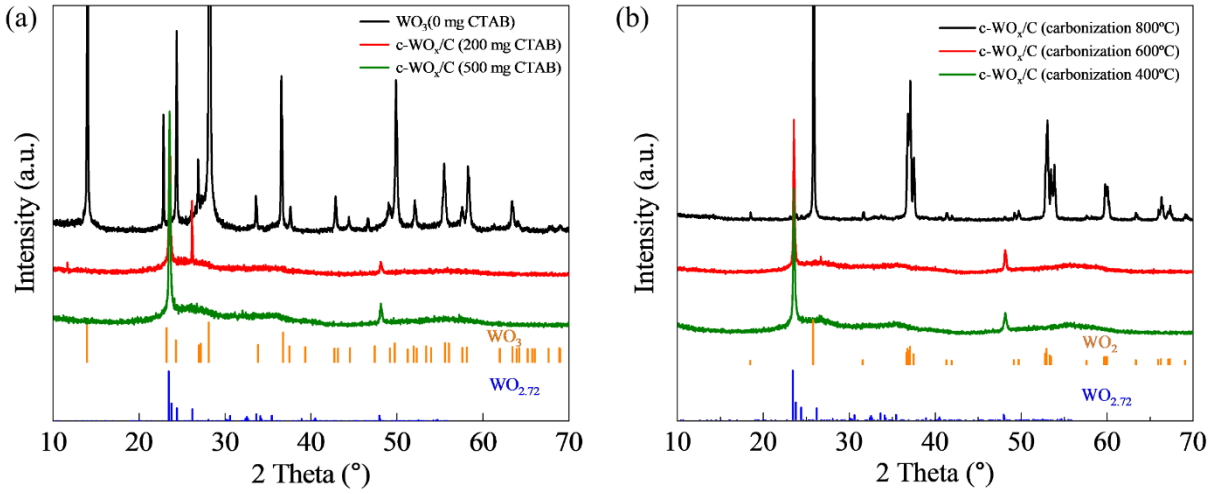

Figure S1. XRD patterns of c-WO_x/C with various carbonization temperatures and amounts of CTAB

(a) 600℃ carbonization and 0 mg CTAB, 600℃ carbonization and 200 mg CTAB, 600℃ carbonization and 500 mg CTAB. Vertical ticks show the reference patterns according to JCPDS No. 75-2187 (WO_3) and JCPDS No.71-2450 ($WO_{2.72}$)

(b) 400℃ carbonization and 500 mg CTAB, 600℃ carbonization and 500 mg CTAB, 800℃ carbonization and 500 mg CTAB. Vertical ticks show the reference patterns according to JCPDS No. 32-1393 (WO_2) and JCPDS No.71-2450 ($WO_{2.72}$)

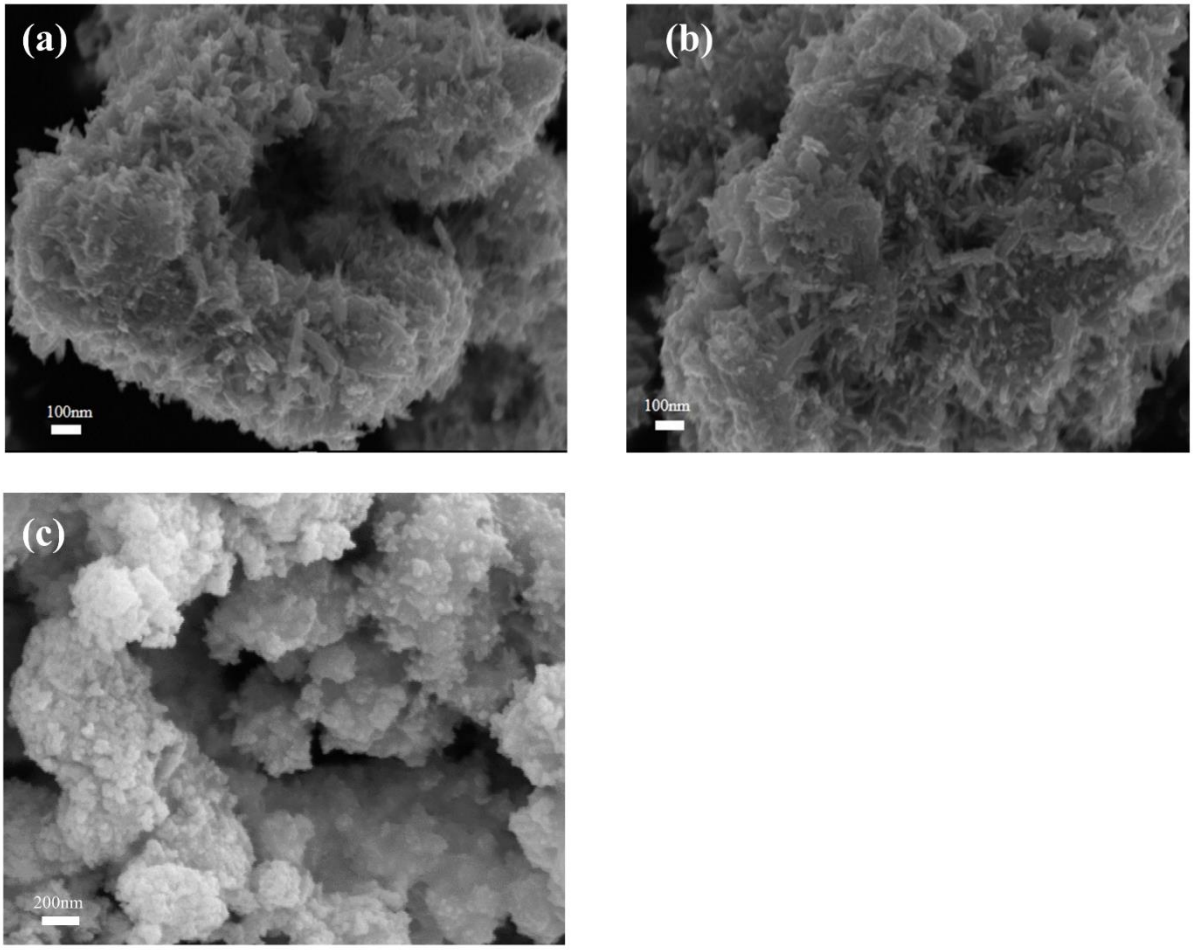

Figure S2. SEM images of c-WO_x/C with various carbonization temperatures and amounts of CTAB

(a) 600℃ carbonization and 200 mg CTAB. (b) 600℃ carbonization and 500 mg CTAB. (c) 400℃ carbonization and 500 mg CTAB.

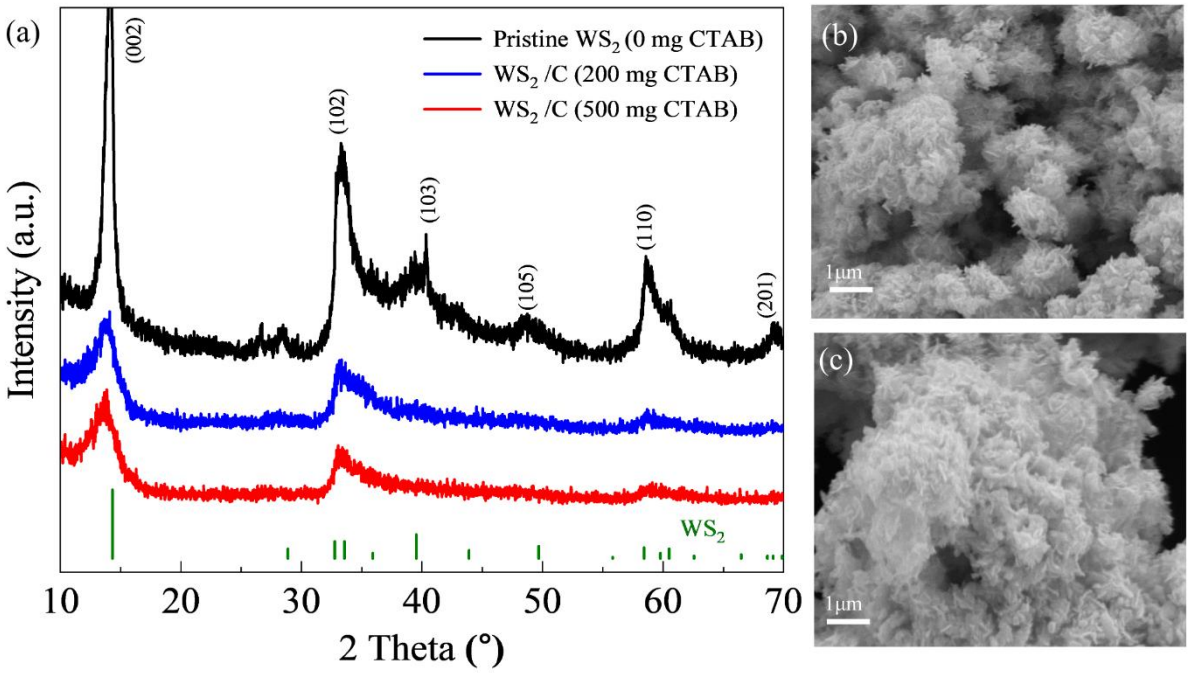

Figure S3. (a) XRD patterns of c-WS_2/C (sulfurization at 800℃) with 0, 200, and 500 mg CTAB. SEM images of c-WS_2/C with (b) 200 mg CTAB, (c) 500mg CTAB.

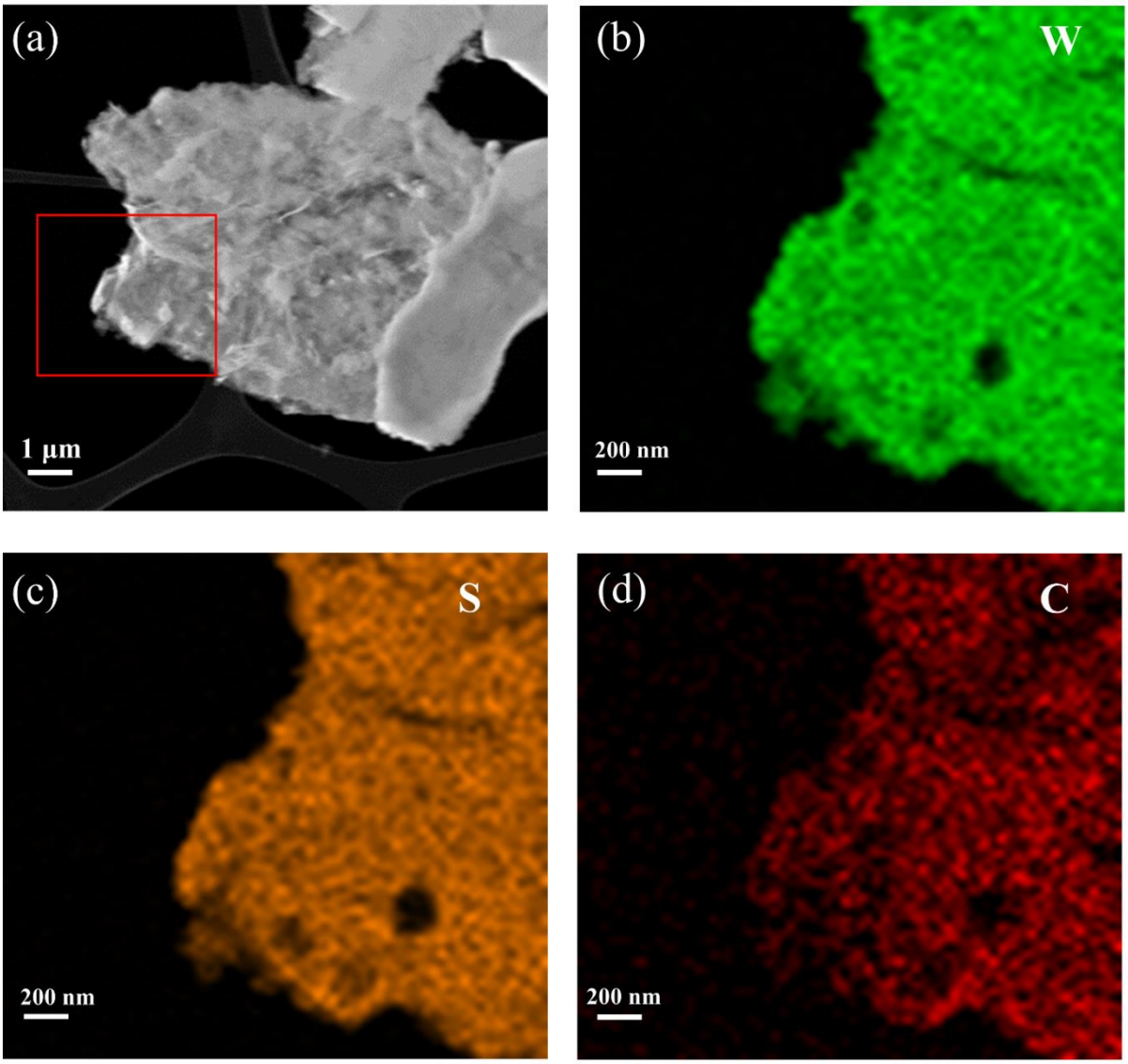

Figure S4. TEM image (a) and EDS elemental mappings (b-d) of c-WS_2/C

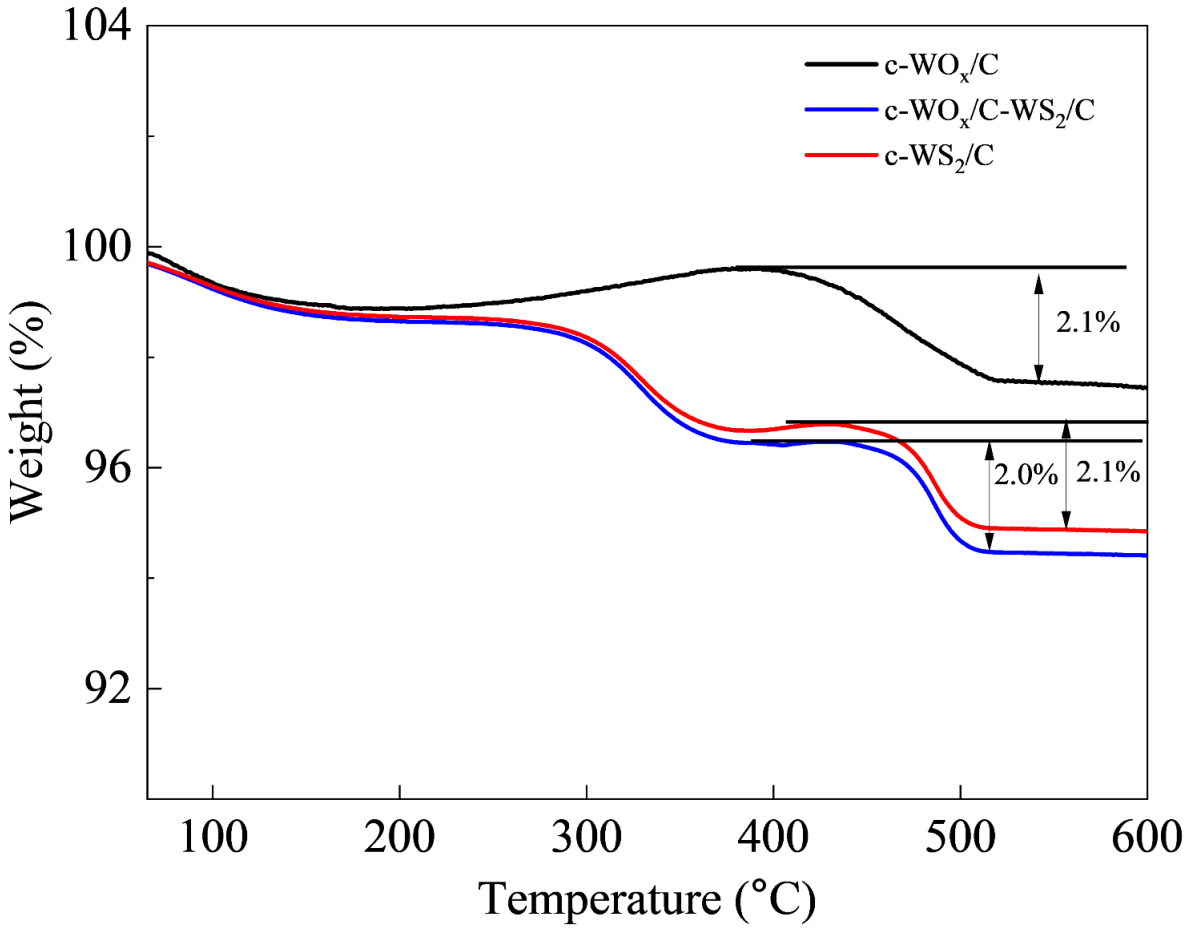

Figure S5. TGA curves of c-WO_x/C, c-WO_x/C-WS_2/C, and c-WS_2/C.

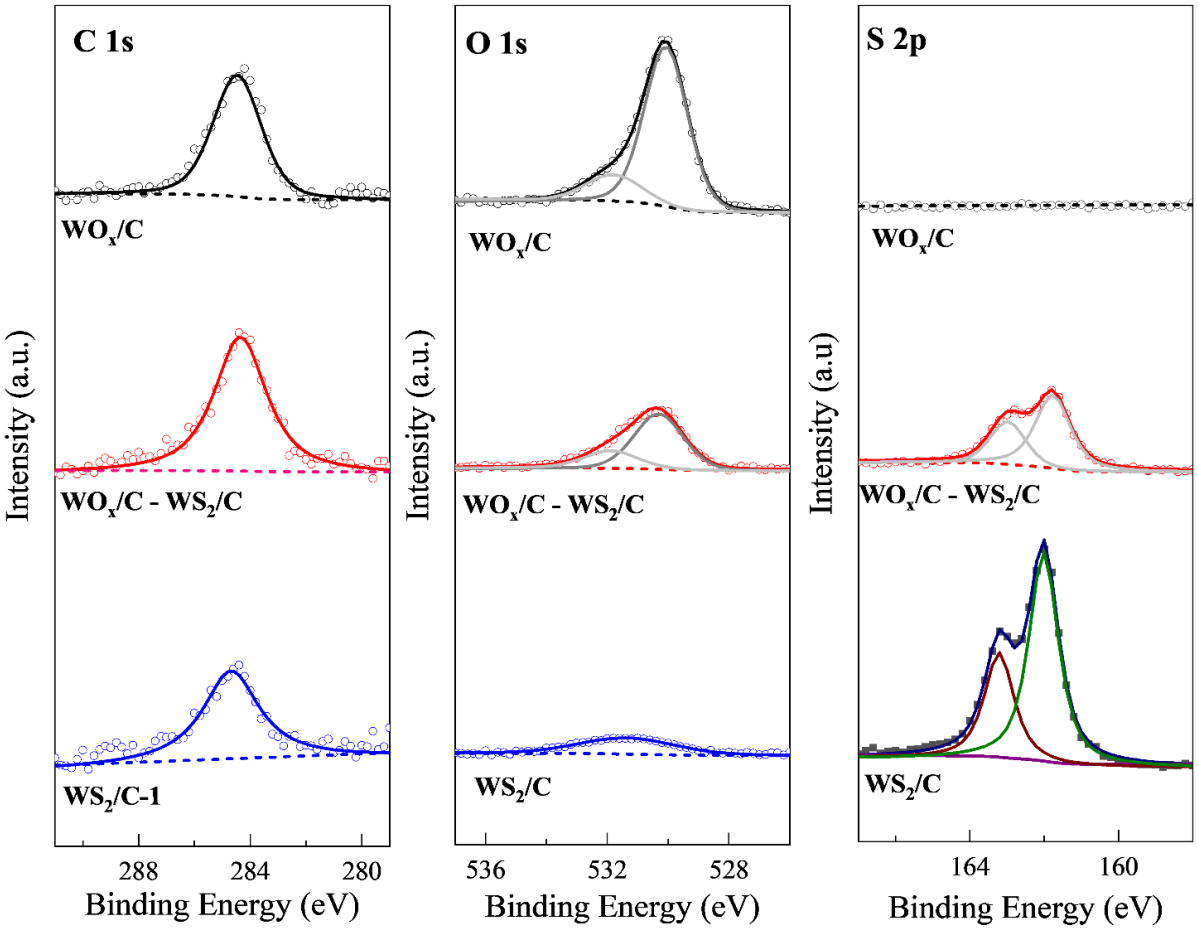

Figure S6. C 1s (a), O 1s, (b) and S 2p (c) XP spectra of c-WO_x/C, c-WO_x/C-WS_2/C, and c-WS_2/C

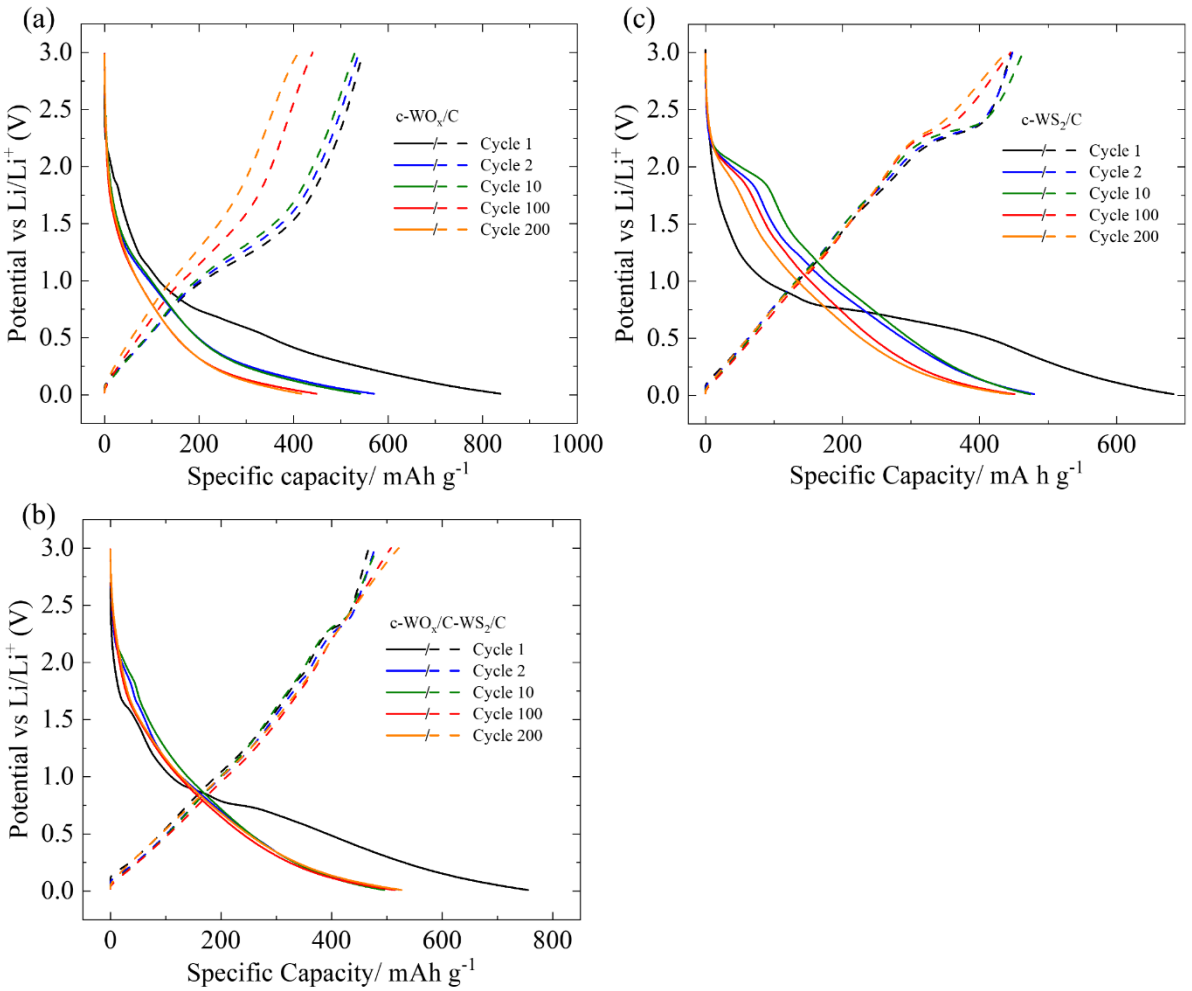

Figure S7. Galvanostatic charge-discharge curves of the c-WO_x (a), c-WO_x-WS_2/C (b), and c-WS_2/C (c) electrodes at a current density of 100 mA g^{-1} for the specific cycles.

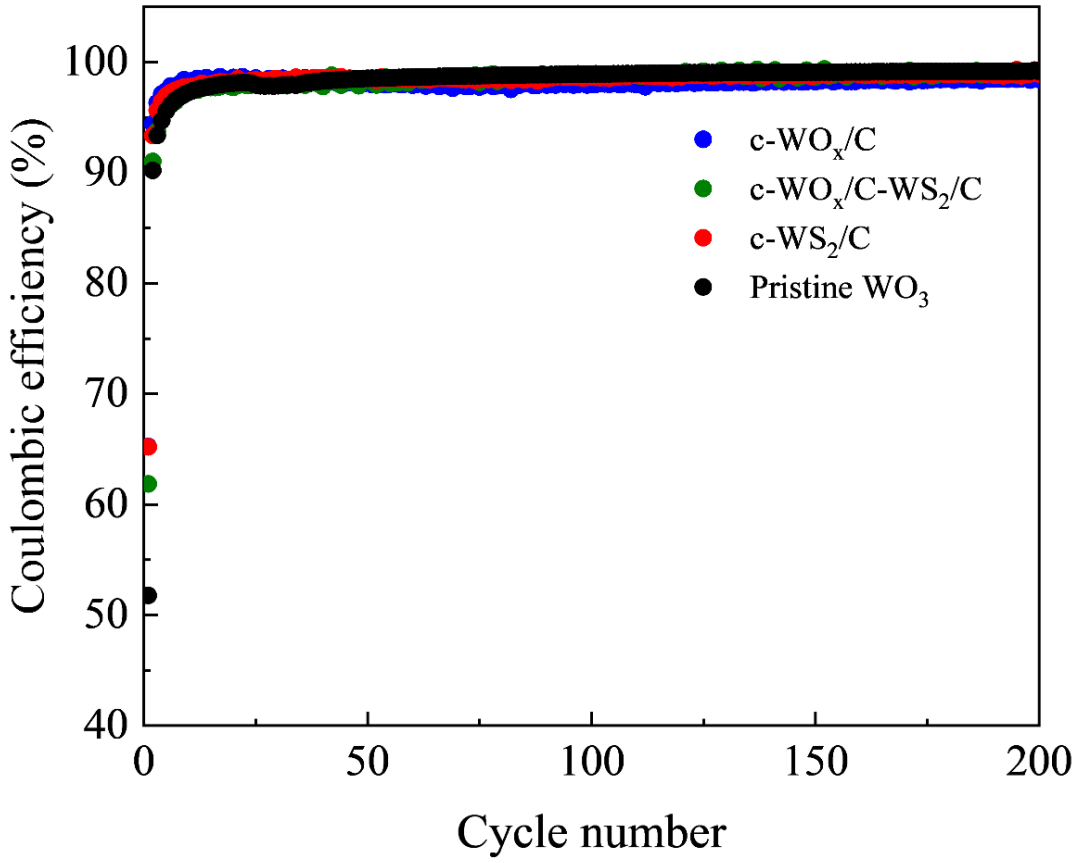

Figure S8. Coulombic efficiency of the c-WO_x, c-WO_x-WS_2/C, c-WS_2/C, and pristine WO_3 electrodes in the first 200 cycles at a current density of 100 mA g^{-1}.

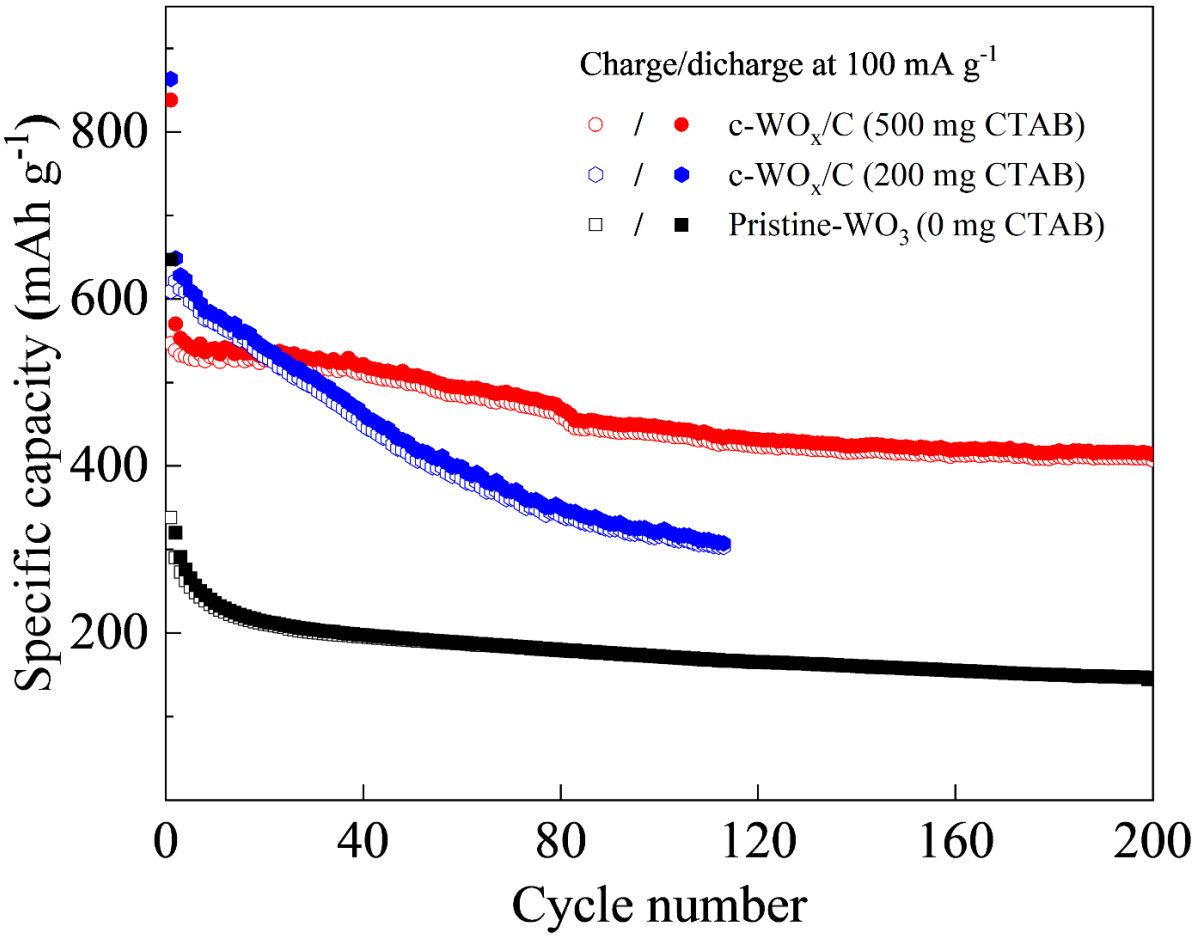

Figure S9. Cycling performance of c-WO_x/C with 0, 200, and 500 mg CTAB and fixed carbonization temperature 600℃.

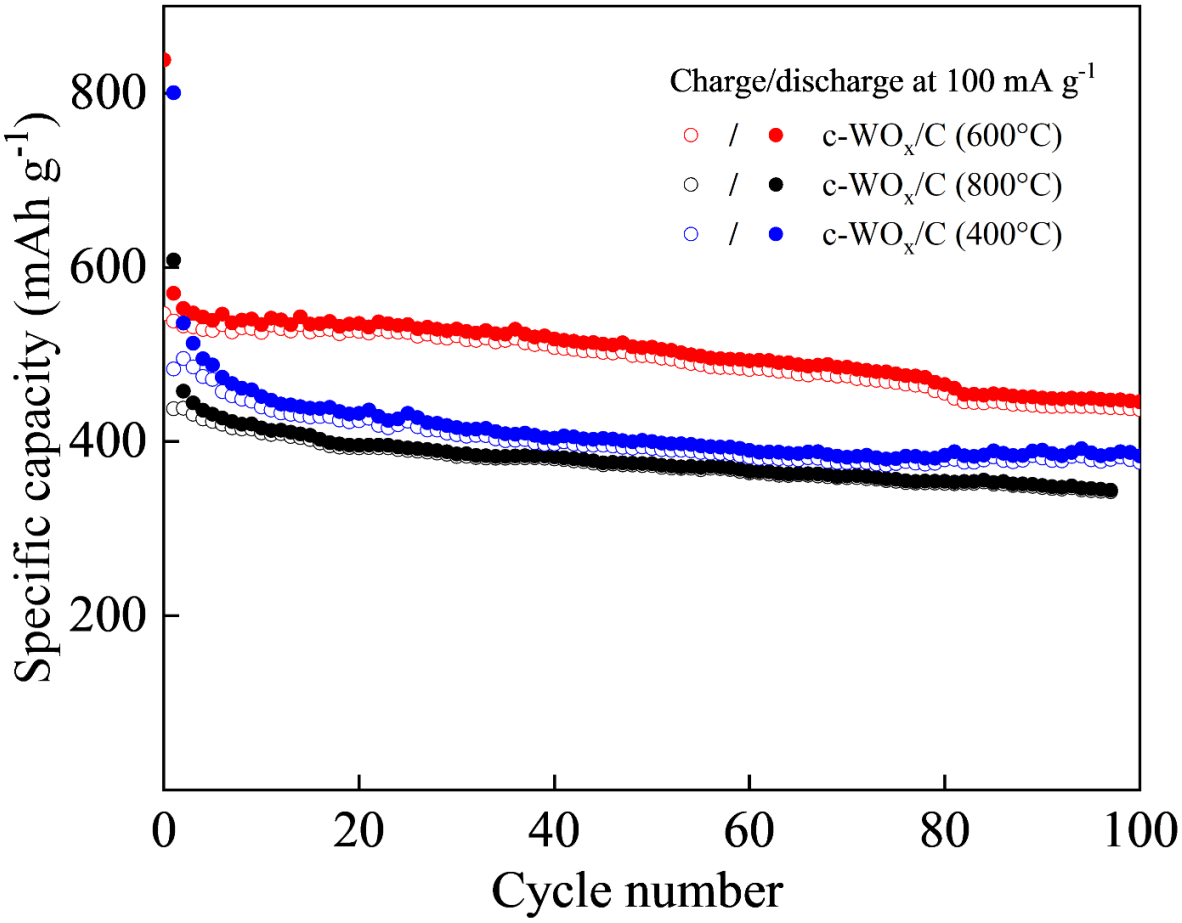

Figure S10. Cycling performance of c-WO_x/C with carbonization temperature 400, 600, 800℃ and fixed CTAB 500 mg.

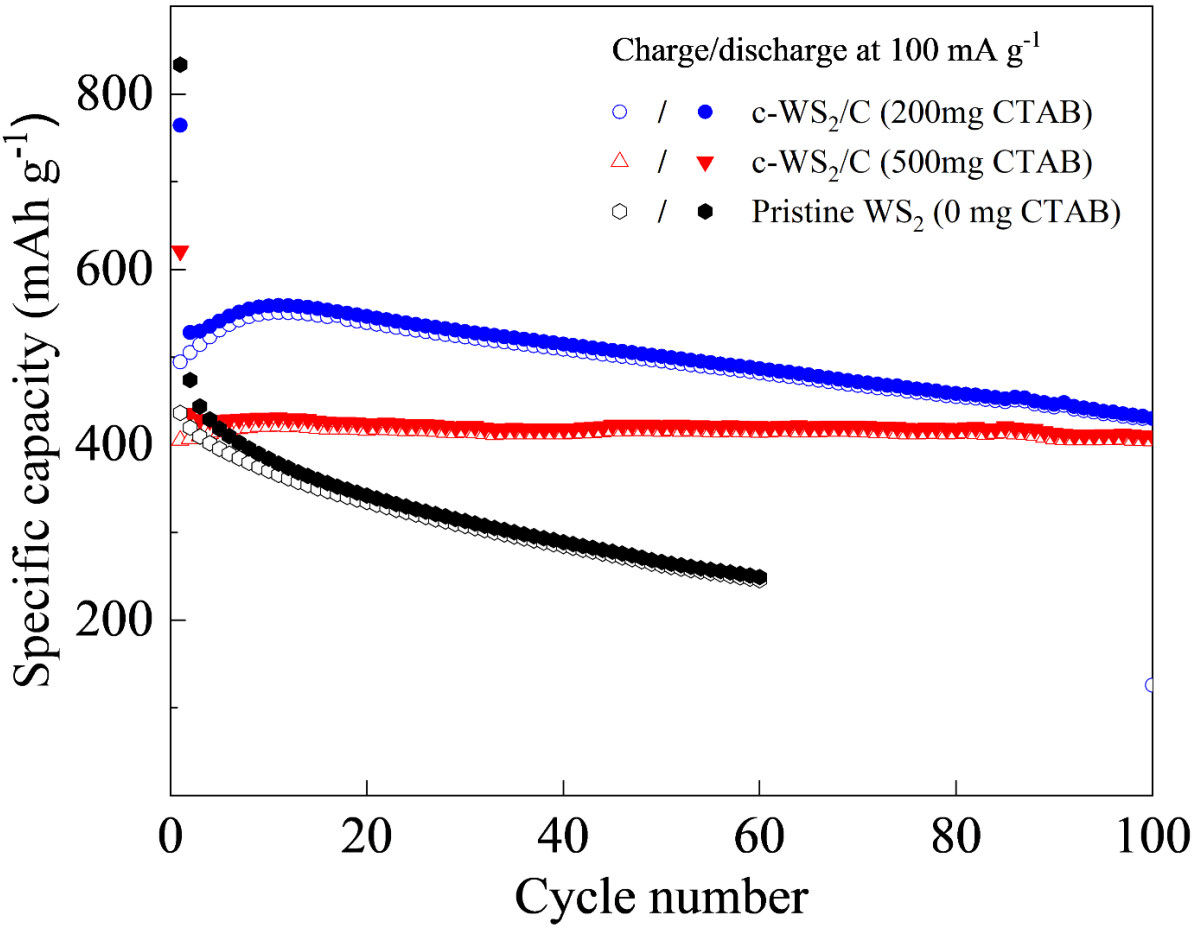

Figure S11. Cycling performance of c-WS_2/C with 0, 200 mg, 500 mg CTAB and fixed sulfurization temperature 800℃.

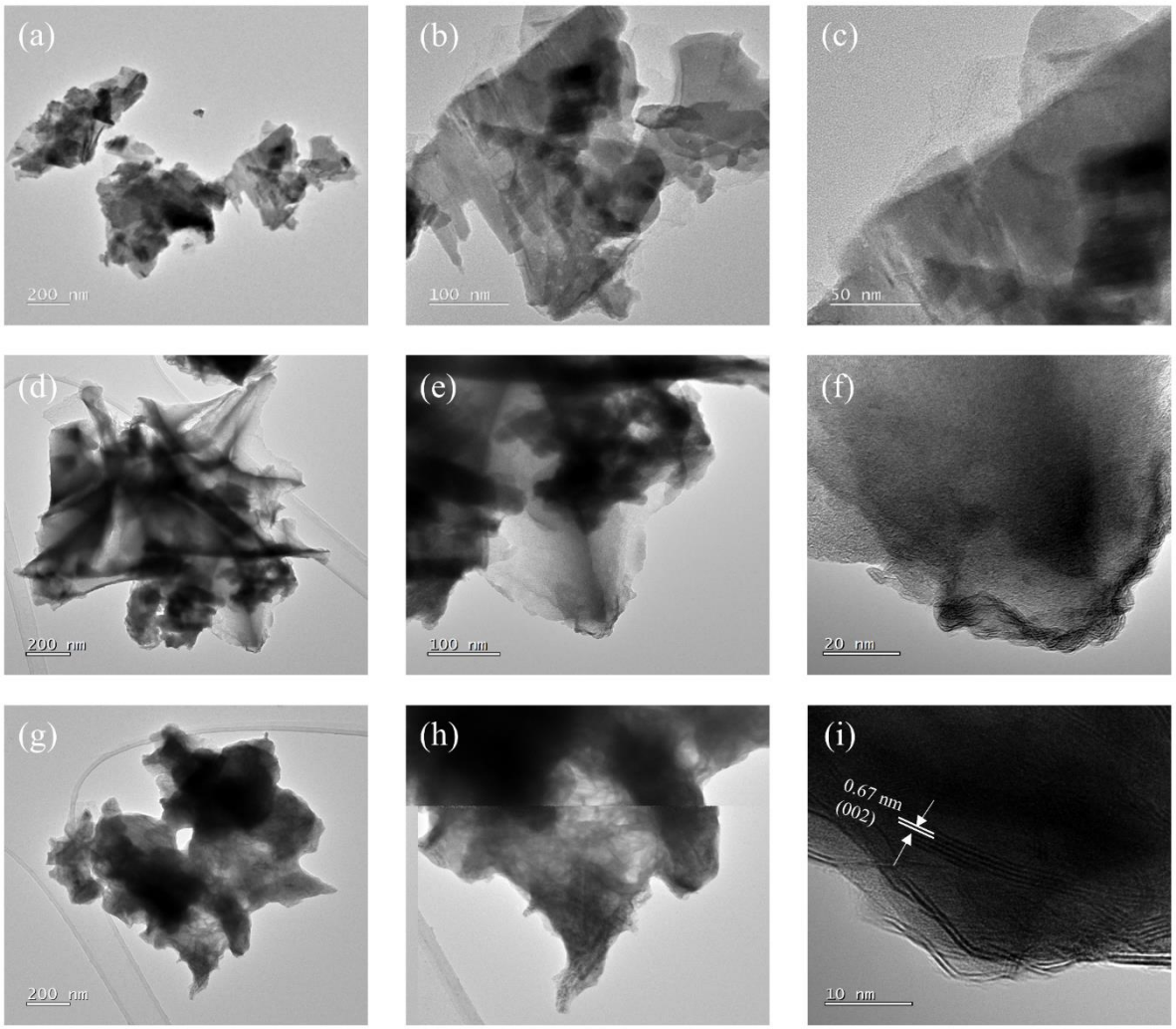

Figure S12. TEM and HR-TEM image of p-WO_x/C (a-c), p-WO_x/C-WS_2/C (d-f) and p-WS_2/C (g-i).

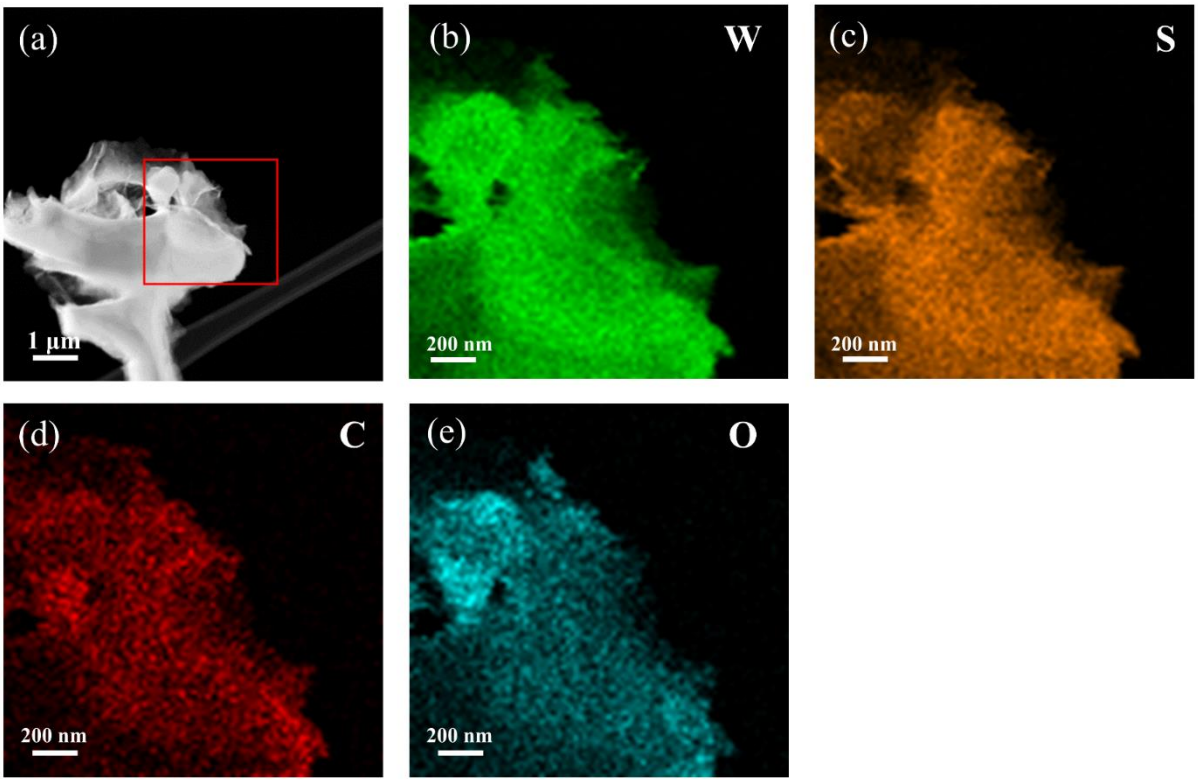

Figure S13. TEM image (a) and EDS elemental mappings (b-e) of p-WO_x/C-WS_2/C.

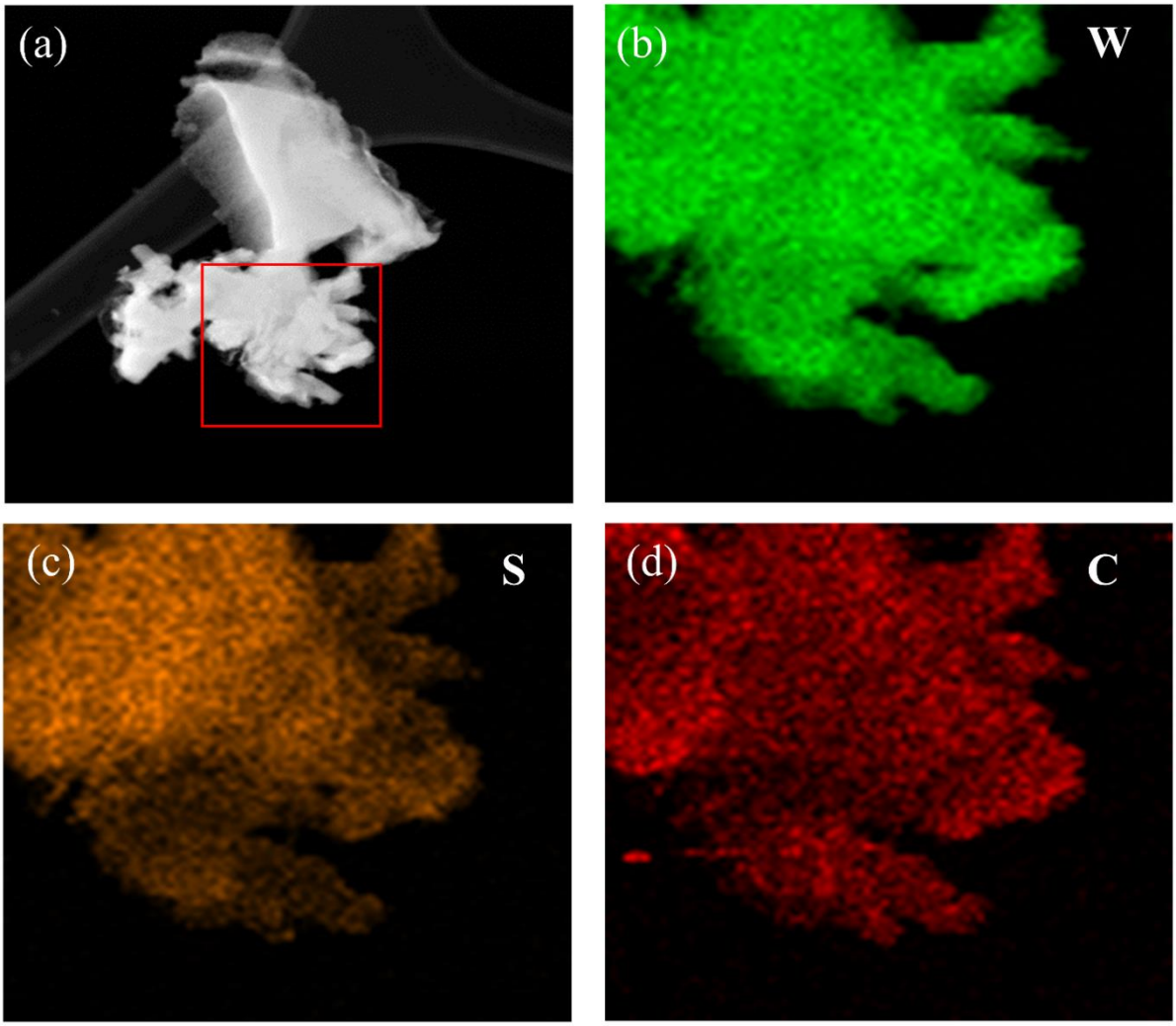

Figure S14. TEM image (a) and EDS elemental mappings (b-d) of p-WS_2/C.

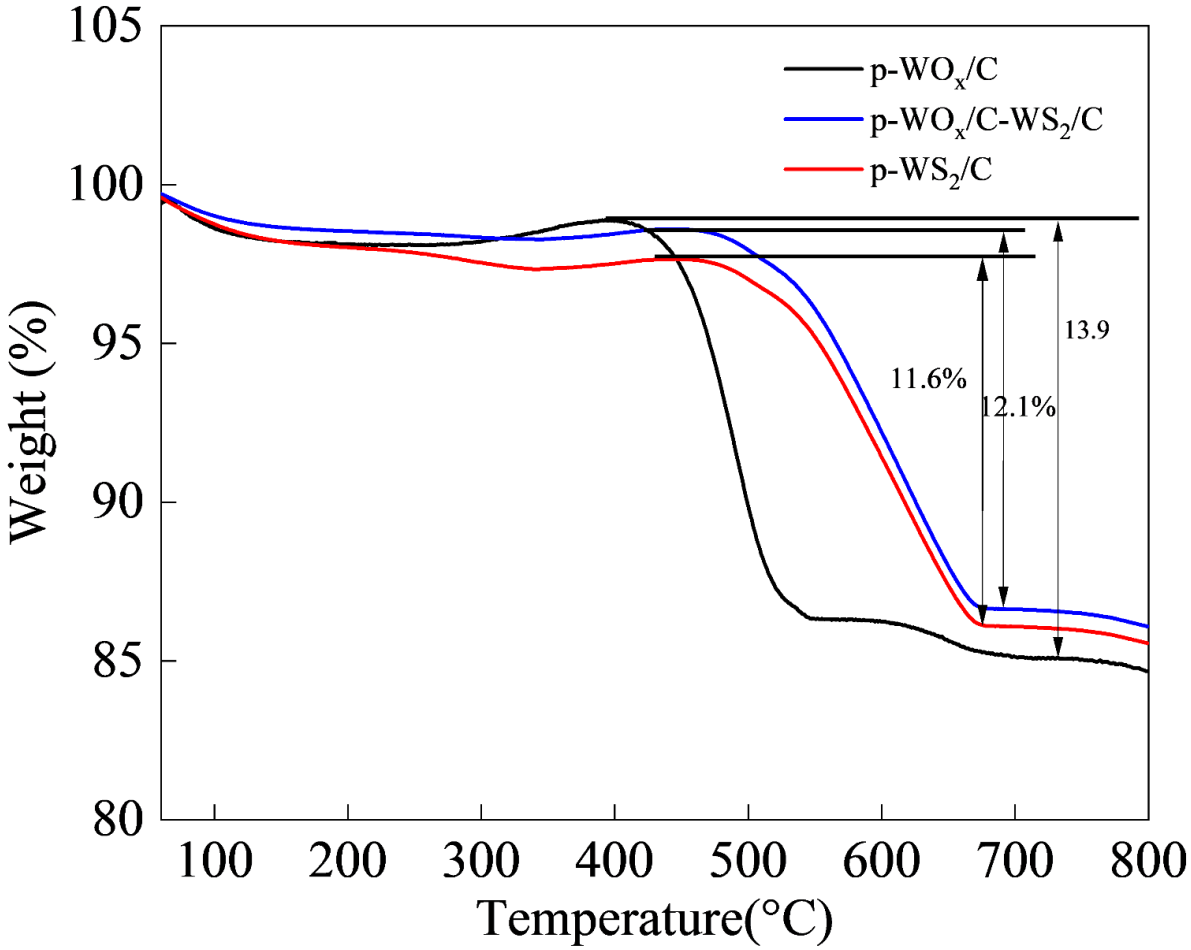

Figure S15. TGA of p-WO_x/C, p-WO_x/C-WS_2/C and p-WS_2/C.

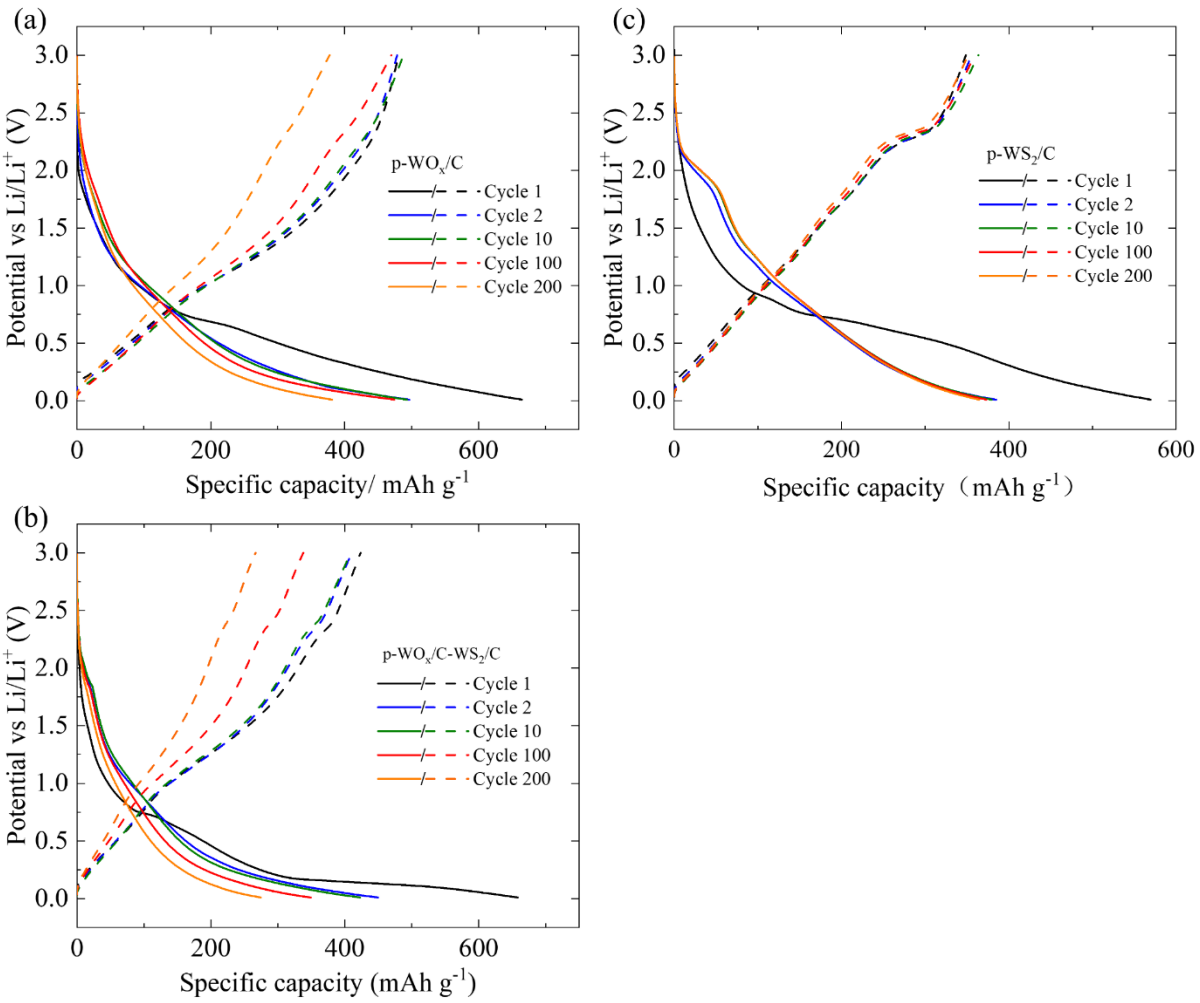

Figure S16. Galvanostatic charge-discharge curves of the p-WO_x (a), p-WO_x-WS_2/C (b), and p-WS_2/C (c) electrodes at a current density of 100 mA g^{-1} for the specific cycles.

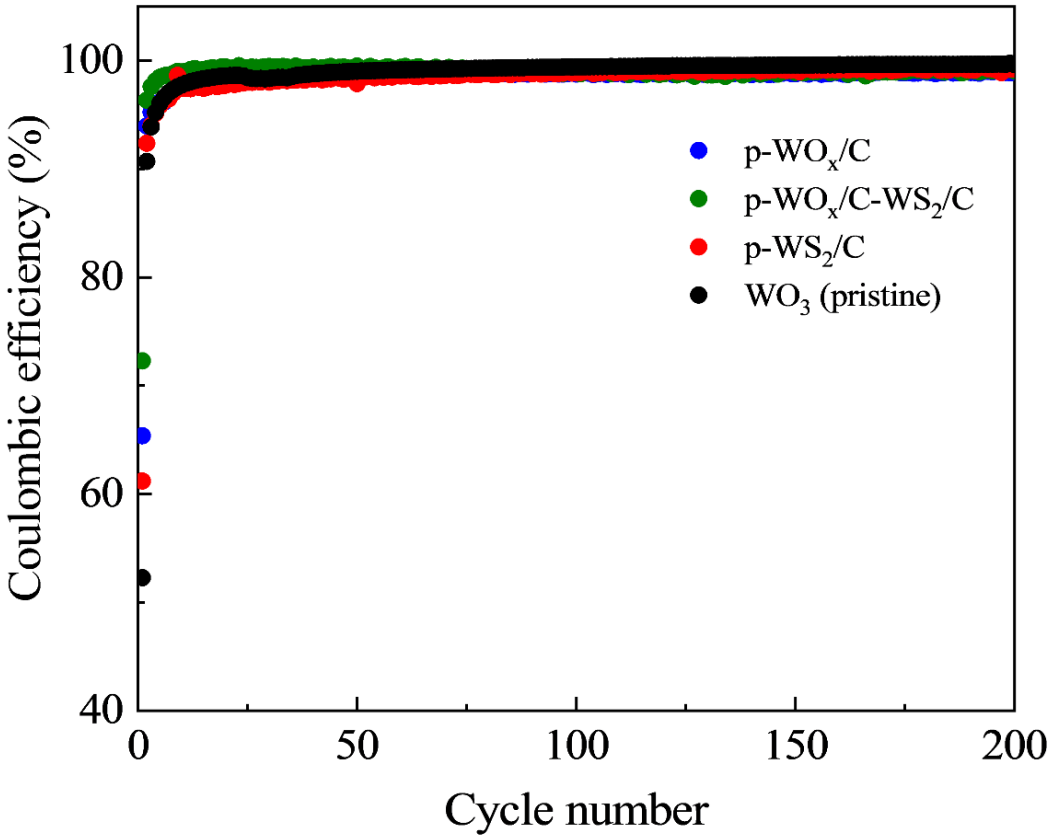

Figure S17. Coulombic efficiency of the p-WO_x, p-WO_x-WS_2/C, p-WS_2/C, and pristine WO_3 electrodes in the first 200 cycles at a current density of 100 mA g^{-1}.

Table S1

The components content in the carbon-coated composites

Active material	WO_x (wt%)	WS_2 (wt%)	Carbon (wt%)
c-WO_x/C	98 (±0.5)	0	2 (±0.5)
c-WO_x/C-WS_2/C	31.3 (±10)	66.6 (±10)	2.1 (±0.5)
c-WS_2/C	0	98 (±0.5)	2 (±0.5)
p-WO_x/C	88.4 (±10)	0	11.6 (±0.5)
p-WO_x/C-WS_2/C	25.9 (±10)	60.2 (±10)	13.9 (±0.5)
p-WS_2/C	0	87.9 (±0.5)	12.1 (±0.5)

Magnetic anisotropy, magnetoelastic coupling and the phase diagram of $Ni_{0.25}Mn_{0.75}TiO_3$

A. Elghandour,[1,*] L. Gries,[1] L. Singer,[1] K. Dey,[1,†] and R. Klingeler[1]

[1] *Kirchhoff Institute for Physics, Heidelberg University, INF 227, D-69120 Heidelberg, Germany*

(Dated: February 22, 2023)

Thermodynamic and magnetic studies on high-quality single crystals are used to investigate the magnetic phase diagram and magneto-structural coupling in the mixed-spin system $Ni_{0.25}Mn_{0.75}TiO_3$. Clear anomalies in the thermal expansion at the spin ordering and spin reorientation temperatures, T_N and T_R, evidence pronounced magneto-elastic effects. Notably, magnetic entropy is released mainly above T_N implying considerable short range magnetic order up to about $4 \times T_N$. This is associated with a large regime of negative thermal expansion of the c axis. Both T_N and T_R exhibit the same sign of uniaxial pressure dependence which is positive (negative) for pressure applied along the b (c) axis. The magnetic phase diagrams are constructed and the uniaxial pressure dependencies of the ordering phenomena are determined. For magnetic fields $B||b$ axis, a sign change and splitting of anomalies implies further magnetic phases. In addition to short-range magnetic order well above T_N, competing anisotropies yield a glass-like behaviour ($T_{SG} \simeq 3.7$ K) as evidenced by AC-χ and quasi-linear of c_p. High-field magnetization up to 50 T clearly demonstrates that in addition to antiferromagnetically ordered spins there are also only weakly coupled moments, at 2 K, with a sizable amount of about 15 % of all Mn^{2+}-spins present in the material. The observed changes in pressure dependence and the magnetostrictive effects shed light on the recently observed flop of electric polarization from $P||c$ to $P||a$ [1], in partcular suggesting that the ME effect is not of direct magnetostrictive origin.

I. INTRODUCTION

Mixed antiferromagnetic (AFM) systems with competing magnetic anisotropies have been extensively studied with regard to their underlying physics and as a platform to realize spin glass states [2–6]. In such mixed AFM systems where, e.g., a magnetic ion (M) is partly substituted by another one (N), i.e., forming $M_{1-x}N_x$, long-range magnetic order appears in the vicinity of the parent compounds while it is suppressed at intermediate concentrations x. The spin arrangement in the AFM long-range ordered state is basically that of the parent compounds, but with two different AFM sublattices resulting from the induced modulation around the magnetic ions [7, 8] and the difference in their ionic radii [9, 10]. A typical example are mixed ilmenite-structured titanates, $A_xMn_{1-x}TiO_3$ (A = Fe, Co, and Ni), where the substituent A is randomly distributed in the structure. While, at intermediate x, spin-glass-like phases are observed, AFM long-range order evolves near the end sides of the phase diagrams and is suppressed in the doped systems [1, 11–18]. The parent compounds $ATiO_3$ (A = Mn, Fe, Co, Ni) crystallize in a hexagonal lattice with space group $R\bar{3}$ [19]. $MnTiO_3$ exhibits G-type AFM order with the crystallographic c direction being the magnetically easy axis [20]. In contrast, in $FeTiO_3$, $NiTiO_3$, and $CoTiO_3$ A-type antiferromagnetism is found with an easy-plane-like anisotropy perpendicular to the c axis [20–23]. This implies not only different exchange interactions but also competing anisotropies in the mixed systems $A_xMn_{1-x}TiO_3$.

Experimental studies on $Ni_xMn_{1-x}TiO_3$ started three decades ago by Ito *et al.* [14] and Yoshizawa *et al.* [15] to address theoretical predictions [2, 7] on the mixed AFM compounds and revived after the discovery of linear magnetoelectric effect (ME) in $MnTiO_3$ [24]. The general trends in $Ni_xMn_{1-x}TiO_3$ upon increasing the Ni-content x are as following [14, 16]: Initially, G-type AFM order is suppressed and a spin-reoriented phase appears around $x \sim 0.2$. Specifically, at $x = 0.33$, G-type AFM order evolves at $T_N = 27.6$ K and spin reorientation at $T_R = 17.5$ K. The latter is accompanied by a flop in the electric polarization [1]. At intermediate concentrations, $0.38 \leq x \leq 0.45$, a spin glass phase emerges [16–18, 25]. Within this glassy phase and particularly at $x = 0.42$, $Ni_xMn_{1-x}TiO_3$ exhibits linear ME [16, 17]. Further increasing the Ni-content to $x \geq 0.48$ results in an A-type AFM long-range ordered phase which does not show ME [1].

Here, we report detailed thermodynamic and magnetic studies on $Ni_{0.25}Mn_{0.75}TiO_3$ single crystals grown by the optical floating-zone technique. Our dilatometric studies provide quantitative information on magnetoelastic coupling in the mixed AFM system. These studies have been motivated by recent studies on the parent compounds $MnTiO_3$ and $NiTiO_3$, which display pronounced thermal expansion and magnetostriction anomalies associated with magnetic ordering and spin-reorientation [26–28]. The present thermodynamic data elucidate magnetoelastic coupling in the G-type AFM ordered phase and in the spin reoriented phase of $Ni_{0.25}Mn_{0.75}TiO_3$. Sharp

* ahmed.elghandour@kip.uni-heidelberg.de

† Current address: Clarendon Laboratory, University of Oxford, Parks Road, Oxford, OX1 3PU, United Kingdom

anomalies in the thermal expansion and magnetostriction coefficients enable us to construct the magnetic phase diagrams and to identify an additional magnetic phase, thereby illustrating the interplay of spin and structure in the mixed anisotropic system under study. We also find that short range correlations persist up to about $4 \times T_{\rm N}$.

II. SINGLE CRYSTAL GROWTH AND EXPERIMENTAL METHODS

Macroscopic single-crystals of $Ni_{0.25}Mn_{0.75}TiO_3$ were grown by the floating-zone technique in a high-pressure optical furnace [29] (HKZ, Scidre) at 5 bar Ar pressure (Fig. S1a in the Supplemental Information (SI)). The employed polycrystalline feedrods were made from stoichiometric amounts of NiO, MnO_2, and TiO_2 precursors similar to the procedure described in Ref. 26. The phase purity of the grown crystals was confirmed by powder XRD studies on ground single crystals using a Bruker D8 Advance ECO diffractometer with Cu K_α radiation. Structural Rietveld refinement (Fig. S1b in the SI) was performed using the FullProf suite 2.0. [30] EDX analysis was done by means of a JEOL JSM-7610F scanning electron microscope with a Thermo Scientific UltraDry silicon drift X-ray detector for EDX analysis. The analysis yields a Ni:Mn ratio of 0.235(5):0.765(5) while the ratio (Ni+Mn):Ti agrees to 1 within the error bars. From the grown boule, mm-sized grains were obtained, oriented and cut to cuboids. Their crystallinity was confirmed by Laue diffraction in back scattering geometry.

The DC magnetization of $Ni_{0.25}Mn_{0.75}TiO_3$, an oriented single crystal, was measured in the temperature range of 2 to 300 K and in magnetic fields up to 7 T using the Magnetic Properties Measurement System (MPMS3, Quantum Design). The data were collected under field-cooled (FC) and zero-field-cooled (ZFC) protocols. The AC magnetization was measured in the temperature range of 2 to 40 K, with a 9 Oe AC excitation field, up to 3 T DC magnetic fields and frequencies ranging from 2 kHz to 10 kHz, using the ACSMII option of the Physical Properties Measurement System (PPMS, Quantum Design). Pulsed-magnetic-field magnetization was measured up to 50 T at Helmholtz Zentrum Dresden Rossendorf by an induction method using a coaxial pick-up coil system [31]. The pulse raising time was 7 ms. The pulsed-field magnetization data were calibrated using static magnetic field measurements. The specific heat capacity was measured in the temperature range of 1.8 to 300 K using the heat capacity option of the Physical Properties Measurement System (PPMS, Quantum Design). High-resolution dilatometry measurements were performed by means of a three-terminal high-resolution capacitance dilatometer in a home-built setup placed inside a Variable Temperature Insert (VTI) of an Oxford magnet system [32, 33]. With this dilatometer, the relative length changes dL_i/L_i along the crystallographic b and c directions, respectively, were measured on an oriented cuboid-shaped single crystal of dimensions $2.400 \times 2.128 \times 0.559$ mm^3. Measurements were performed in the temperature range of 2 to 300 K and in magnetic fields up to 15 T, applied along the direction of the measured length changes. The linear thermal expansion coefficients, $\alpha_i = 1/L_i \times dL_i(T)/dT$, were obtained. In addition, the field-induced length changes, $dL_i(B_i)$, were measured at different fixed temperatures between 2 and 40 K and in magnetic fields up to 15 T. The longitudinal magnetostriction coefficients, $\lambda_i = 1/L_i \times dL_i(B_i)/dB_i$, were derived.

III. EVOLUTION OF MAGNETIC ORDER AT $B = 0$ T

In zero magnetic field, $Ni_{0.25}Mn_{0.75}TiO_3$ exhibits two magnetic phase transitions as evidenced by the static magnetic susceptibility and the specific heat in Fig. 1. Specifically, there is a jump-like feature in the specific heat c_p/T at $T_{\rm N} = 34.8(4)$ K and a rather symmetric hump at $T_{\rm R} \sim 14.8(2)$ K (see Fig. 1c). The jump at $T_{\rm N}$ amounts to $\Delta c_{\rm p} \approx 0.54(11)$ J/(mol K). The magnetic nature of both transitions is evident from associated anomalies in the static magnetic susceptibility (Fig. 1a and b). At high temperatures, the data $\chi_{\rm i}$ along the different crystallographic axes i obey a Curie-Weiss-like behavior and their differences are explained by the ratio of the corresponding g factors (g_i) (see Fig. 2 in the Supplement Information (SI)). At $T_{\rm N}$, $\chi_{\rm c}$ displays a clear kink while only very small anomalies are observed for the other directions, thereby confirming the easy magnetic c axis in the long-range ordered phase below $T_{\rm N}$. This is particularly evident when Fisher's specific heat $\partial(\chi T)/\partial T$ is considered which is proportional to the magnetic specific heat [34]. It displays a λ-shaped behaviour only for $B||c$ axis (Fig. 1). Upon further cooling, the jump-like features in χ_i, at $T_{\rm R}$, suggest rotation of the spins into the ab plane. We note the discontinuous nature of the anomaly at $T_{\rm R}$.

At high temperatures, the static magnetic susceptibility obeys a Curie-Weiss-like behavior. The differences for the different crystallographic axes are attributed to the anisotropy of the g-factor (see Fig. 1a). Fitting χ_c between 120 and 300 K by means of an extended Curie-Weiss law including a temperature-independent term, χ_0, yields the Curie constant $C = 3.6(5)$ erg K mol^{-1} G^2, the Weiss temperature $\Theta = -141(4)$ K, and $\chi_0 = 1.93 \times 10^{-4}$ erg mol^{-1} G^{-2}. The large negative value of the Weiss temperature indicates the presence of dominant antiferromagnetic exchange interactions, aligning with the previously recorded neutron scattering results on $Ni_{0.33}Mn_{0.67}TiO_3$ [1]. The effective moment $\mu_{\rm eff} \approx 5.3(1)\ \mu_{\rm B}$ is derived from the Curie constant. It agrees very well with the expected value calculated using the g-factors $g_{\rm Mn}$ and $g_{\rm Ni}$ of the parent compounds [26, 35].

AC magnetic susceptibility studies confirm the anomalies at $T_{\rm N}$ and $T_{\rm R}$ but do not indicate any frequency dependence in the regime $2.5 \leq f \leq 10$ kHz (see Fig. 5

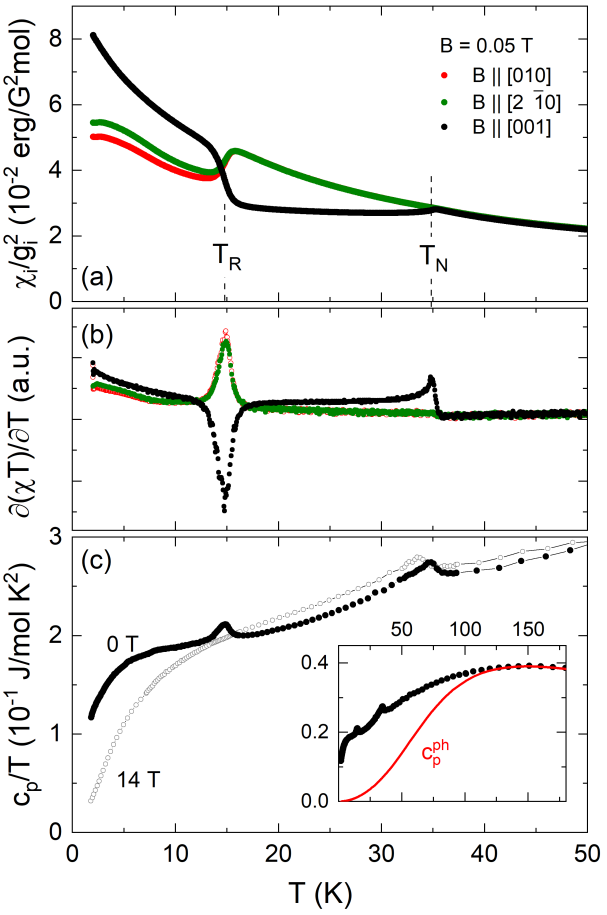

FIG. 1. (a) Static magnetic susceptibility, $\chi = M/B$, of $Ni_{0.25}Mn_{0.75}TiO_3$ as a function of temperature measured along three different crystallographic directions at applied magnetic field $B = 0.05$ T. The data have been normalized by the respective components of the g-factor as fitted to the high-temperature behavior. (b) Corresponding derivatives $\partial(\chi T)/\partial T$, and (c) the specific heat capacity, represented by c_p/T, was measured both at zero magnetic field and at a magnetic field strength of 14 T, with the field applied parallel to the c-axis. The inset shows the zero field specific heat data over an extended temperature range, including an estimated representation of the phononic background (see the text). The vertical dashed lines mark the onset of the long-range magnetic ordering at T_N and the spin reorientation at T_R.

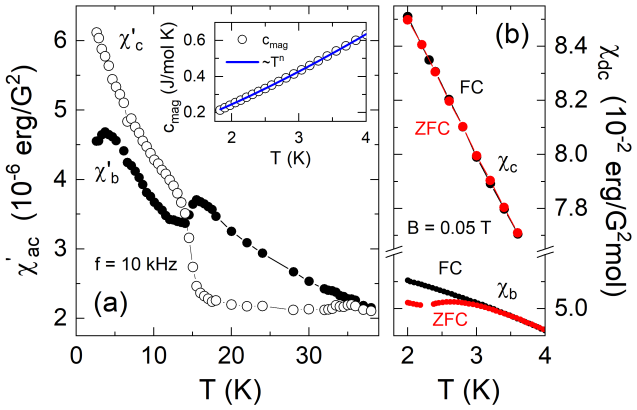

FIG. 2. (a) Real part of AC magnetic susceptibility of $Ni_{0.25}Mn_{0.75}TiO_3$ measured along the crystallographic b and c axes at $f = 10$ kHz. Inset: Magnetic specific heat at low temperatures. The (blue) line represents a fit to the data (see the text). (b) Static magnetic susceptibility measured along the crystallographic b and c axes at $B = 0.05$ T, highlighting the differences between FC and ZFC measurements.

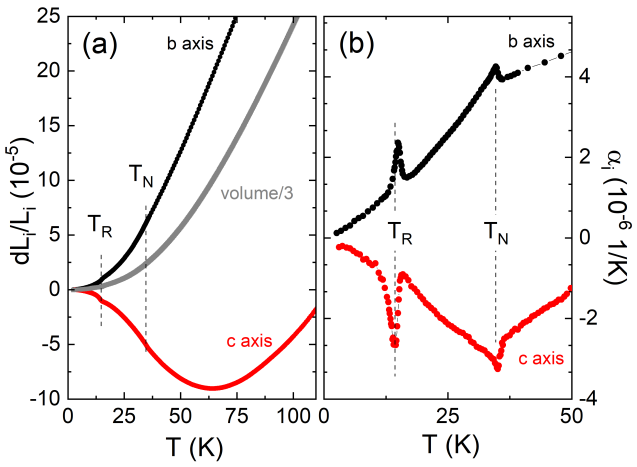

FIG. 3. (a) Relative length changes, dL_i/L_i ($i = b$ and c), of $Ni_{0.25}Mn_{0.75}TiO_3$ measured along the crystallographic i axis in zero applied magnetic field; light grey markers represent the relative volume changes. (b) Corresponding uniaxial thermal expansion coefficients α_i. The dashed lines mark T_N and T_R.

in the SI). We also do not observe any finite dissipative signal χ''. In χ'_b, apart from the anomalies observed at T_N and T_R , we observe an additional broad maximum at $T^* \approx 3.7$ K, as depicted in Fig. 2a. T^* corresponds to the beginning of a thermal hysteresis region seen in χ_b between the zero-field cooled (ZFC) and field cooled (FC) data, as shown in Fig.2b. In contrast, no thermal hysteresis is observed in χ_c and χ'_c.

In the same temperature regime, the magnetic specific heat shows no anomaly but follows a $c_p(T) \propto T^n$ behaviour with $n \approx 1.3(1)$ (see the inset of Fig. 2a). We note that the observed exponent n does not correspond to the expectations $c_p(T) \propto T^3$ describing the low-temperature magnon excitations in a long-range ordered 3D antiferromagnet [36].

The onset of long-range magnetic order at T_N and spin reorientation at T_R are associated with distinct lattice changes as demonstrated by clear anomalies in the thermal expansion in zero field (see Fig. 3). In addition, the thermal expansion exhibits an anisotropic behaviour up to the highest measured temperatures. The evolution of magnetic order is signalled by kinks in the relative length changes dL_i/L_i at T_N, and slightly λ-shaped anomalies in its corresponding thermal expansion α_i. While there is a

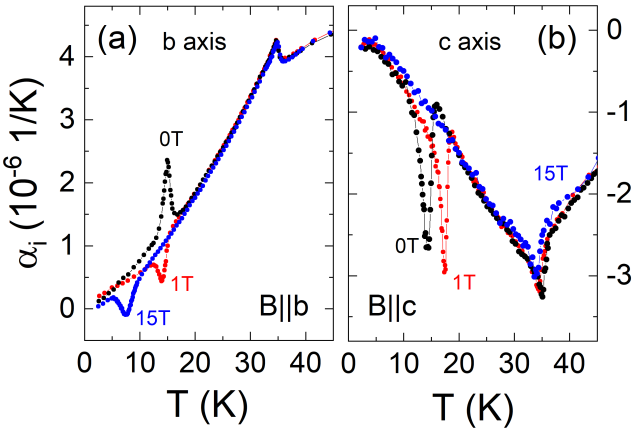

FIG. 4. Temperature dependence of the thermal expansion coefficient α_i ($i = b$ and c), measured at different applied magnetic fields along (a) the b axis, and (b) the c axis.

positive thermal expansion of the b axis in the whole temperature regime under study, the c axis initially shrinks upon heating and expands only above $T = 60$ K. Opposite trends for the different axes are also observed for the actual anomalies in α_i, at T_N, which show opposite signs. Qualitatively, the anomalies in α_i imply a positive uniaxial pressure dependence ($\partial T_{N/R}/\partial p_b > 0$) of T_N and T_R while both are suppressed by uniaxial pressure applied along the c axis.

A. Magnetic phase diagram

Applying magnetic fields up to 15 T significantly affects the spin-reoriented phase and the associated transition temperature T_R, but it hardly affects the long-range ordering temperature T_N. This is clearly visible in the specific heat data shown in Fig. 1c. At $B = 14$ T, while the anomaly at T_R is completely suppressed, the one at T_N is barley shifted to lower temperature. Due to pronounced magnetoelastic coupling evidenced already in Fig. 3, the magnetic field effects on the phase boundaries can be well traced by thermal expansion and magnetostriction measurements. As displayed in Fig. 4, applying a field of $B = 1$ T yields a significant decrease (increase) of T_R when applied along the b axis (c axis). Notably, for $B||b$ axis, the anomaly at T_R changes its sign from positive to negative for $B \geq 1$ T and up to $B = 14$ T (see Fig. 4a). In the static magnetic susceptibility χ_b, at low magnetic fields, there is a noticeable jump-like feature at T_R and a corresponding peak in $\partial(\chi T)/\partial T$. However, these anomalies become weaker as the magnetic field gradually increases and completely vanish at magnetic fields $B||b \geq 0.8$ T (see Fig. 3 in the SI). We conclude that the sign change in α_b at T_R is accompanied by the disappearance of the anomalies observed in χ_b and its corresponding $\partial(\chi T)/\partial T$. The evolution of the anomaly observed at T_R in α_b , $B||b \geq 1$ T, is shown

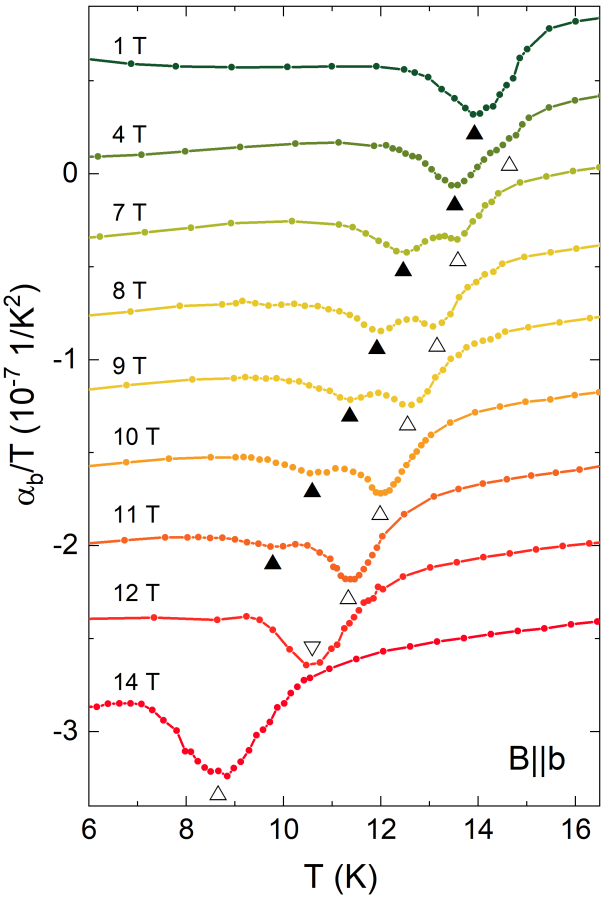

FIG. 5. Thermal expansion coefficient α_b/T at different magnetic fields $B||b$ axis.

in Fig. 5. After the anomaly changed sign as evidenced by the data obtained at $B = 1$ T, an additional feature appears which is only faint at 1 T but increases for larger fields, yielding two clearly separated features split more than 1 K at 7 T. We note that both the emerged (filled triangles) and the initial (open triangles) features shift to lower temperatures with increasing the applied magnetic field which indicates their antiferromagnetic nature. In addition, the emerged feature becomes more pronounced for higher fields while the initial one decreases until it is not detectable anymore above 11 T (see Fig. 5). In contrast, the thermal expansion and magnetisation data signal a significant shift of T_R to higher temperatures when applying $B||c$ axis so that the phase boundary merges into T_N slightly above 2 T (see Fig. 8, and Figs. 4 and 11 in the SI).

The nature of the G-type AFM phase evolving at zero magnetic field at $T_R < T < T_N$ (i.e., AF1 in Fig. 8) is further elucidated by magnetisation and magnetostriction data in Fig. 6. At $T = 16$ K when the spins are predominately parallel to the c axis [1], magnetic fields $||c$ yield a spin-flop-like transition at $B_{SF} = 0.62(8)$ T as demonstrated by the magnetisation data in Fig. 6a.

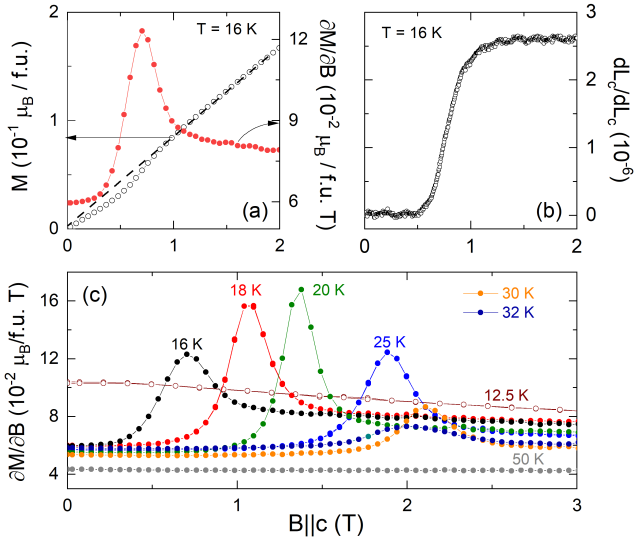

FIG. 6. (a) Isothermal magnetization, measured at 16 K, for $B \parallel c$ axis and corresponding magnetic susceptibility $\partial M/\partial B$. The dashed line linearly extrapolates the high field behaviour to zero field. (b) Magnetostriction dL_c/L_c, at $T = 16$ K as a function of magnetic field $B \parallel c$ axis. (c) Magnetic susceptibility for $B \parallel c$ axis in the temperature regime 16 K $\leq T \leq$ 50 K. Peaks are associated with the spin flip transition at B_{c2}.

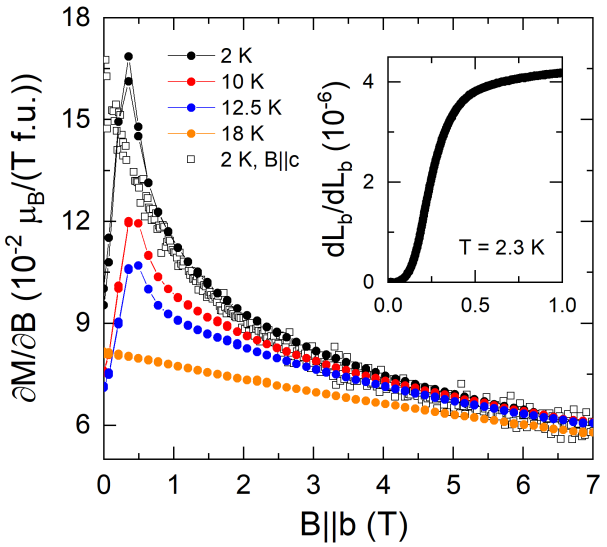

FIG. 7. Magnetic susceptibility $\partial M/\partial B$ in the temperature regime 2 K $\leq T \leq$ 18 K for $B \parallel b$ axis. The peaks signal B_{c1} (see the text). Open squares show $\partial M/\partial B$ at 2 K with $B \parallel c$ axis. Inset: Magnetostriction $dL_b/L_b(B||b)$ at $T = 2.3$ K.

Upon heating, the critical field B_{SF} signalled by the peaks in $\partial M/\partial B$ shifts towards higher fields and disappears above T_N (see Fig. 6c). Concomitantly with the metamagnetic transition there is a sharp increase of the c axis length amounting to $\Delta L_c/L_c = 2.6 \times 10^{-6}$ (Fig. 6b). Below T_R, $B \| c$ does not drive a spin-flop transition (Fig. 6c) which agrees to the suggested spin rotation. In contrast, for $B \| b$ a metamagnetic transition appears only below T_R at a critical field of $B_{C1} \sim 0.4$ T, which barely depends on the temperature (Fig. 7). Again, the metamagnetic transition is associated with anomalous length changes (Fig. 7, inset), amounting to $\Delta L_b/L_b = 3.9 \times 10^{-6}$ at $T = 2.3$ K.

The observed clear features in magnetisation, thermal expansion, magnetostriction, and specific heat enable us to construct the magnetic phase diagrams for both $B \| b$ and $B \| c$ as shown in Fig. 8. For $B \| c$, the G-type antiferromagnetic phase with spins $||c$ evolving in zero field at T_N (AF1 phase) forms a distinct dome bounded by $T_R(B)$ and $B_{SF}(T)$ towards the spin-reoriented AF2-phase (see Fig. 8b). The transition AF1 to AF2 is associated with significant lattice changes. In the field region of the dome, T_N is visibly suppressed by $B||c$ but it increases for higher fields ($B||c > 2$ T) which implies the relevance of critical fluctuations around the tricritical point. A field-driven magneto-structural transition is also observed for $B \| b$ where the low-field AF2 phase is separated by a rather field-independent phase boundary $B_{c1}(T)$ from AF3 (see Fig. 8a). AF2 and AF3 feature uniaxial pressure dependencies of opposite sign. In contrast to T_N which only very weakly depends on $B||b$, AF3 is considerably suppressed and we extrapolate the upper critical field $B_c^{AF3} \simeq 17(2)$ T. Notably, starting from B_{c1}, an intermediate phase AF3' appears. The thermal-expansion anomaly size associated with the phase boundary between AF3 and AF3' continuously decreases when increasing $B||b$ and can not be detected above 11 T in our dilatometric data. This behaviour suggests decrease of the pressure dependence or negligible associated specific heat changes. Since the boundary AF3/AF3' is not associated with a clear anomaly in the magnetisation, we neither can trace it by magnetic measurements in this regime of the phase diagram.

Lastly, our data reveal the presence of weakly coupled magnetic moments at low temperatures. In contrast to $NiTiO_3$ which magnetisation increases linearly up to the saturation field as expected for an long-range ordered AFM [26], magnetisation of $Ni_{0.25}Mn_{0.75}TiO_3$ exhibits pronounced right-bending behaviour (see Fig. 9). Note, that the pulsed-field powder magnetisation data perfectly agree to the single crystal studies up to 14 T. The data can be described by the sum of a modified Brillouin function B_S and a linear term, i.e., $M_{sat}B_S(x) + \chi_0 \times B$; $x = g\mu_B SB/[k_B(T + \Theta*)]$ with M_{sat} the saturation magnetisation of the right-bending term, spin S, field-independent susceptibility χ_0, Boltzmann constant k_B, Bohr magneton μ_B, and the g-factor. $\Theta*$ is a parameter to account for magnetic interactions between the weakly coupled moments. The linear term mainly reflects the response of the long-ranged AF ordered phase. In contrast, the nonlinear term $M_{nl}(B) = M(B) - \chi_0 \times B$ implies the presence of rather weakly coupled spins saturating already at intermediate fields. M_{sat} is the fully satu-

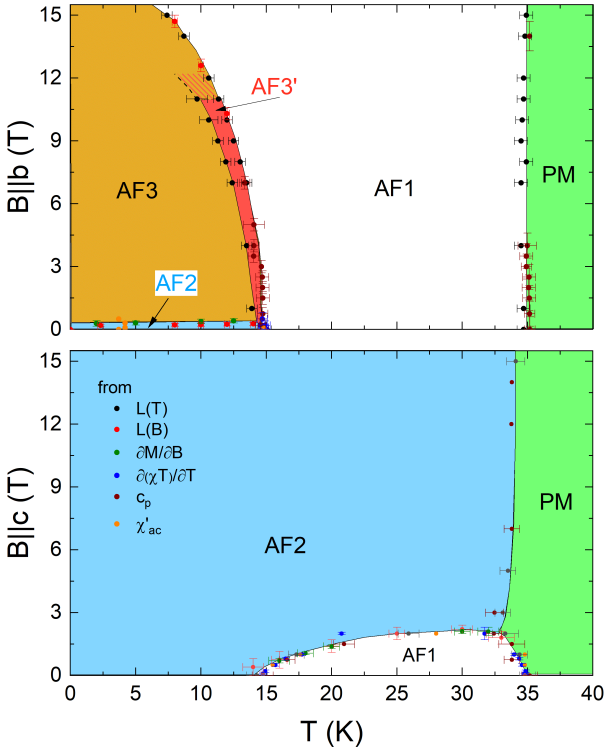

FIG. 8. Magnetic phase diagram of $Ni_{0.25}Mn_{0.75}TiO_3$ derived from magnetization $M(T,B)$, thermal expansion and magnetostriction $L(T,B)$, χ_{ac}, and specific heat data for (a) $B||b$ and (b) $B||c$ axis. PM, AF1, AF2, AF3, and AF3' label the paramagnetic and antiferromagnetic phases while T_N, T_R, B_{SF}, and B_{c1} are associated phase boundaries mentioned in the text.

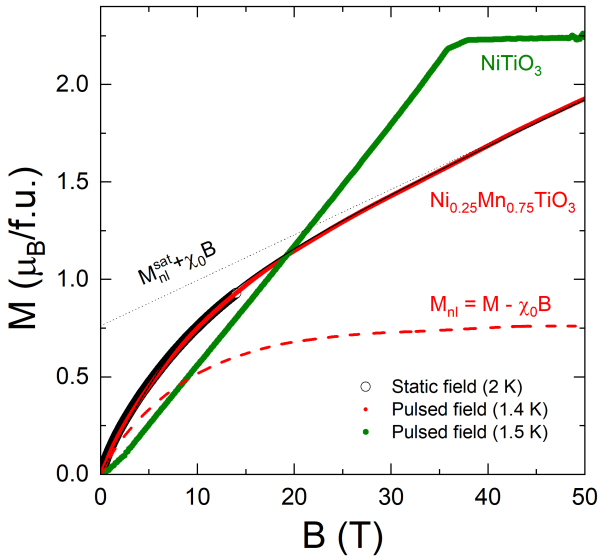

FIG. 9. Magnetisation of $NiTiO_3$ and $Ni_{0.25}Mn_{0.75}TiO_3$ up to 50 T. Open circles show the averaged static field magnetisation of $Ni_{0.25}Mn_{0.75}TiO_3$ single crystals measured up to 14 T. Pulsed-field data are from up-sweeps. The data of $Ni_{0.25}Mn_{0.75}TiO_3$ are well described by the sum of a modified Brillouin function and a linear term $\chi_0 \times B$ (see the text). The dashed line shows the nonlinear magnetisation $M_{nl} = M - \chi_0 \times B$.

rated moment of the weakly coupled spins. It clearly exceeds the fully saturated moment of all Ni^{2+}-spins ($S = 1$, $g = 2.14$, $M_{sat}^{Ni} \simeq 0.53$ μ_B/f.u.) [37] so that $M_{nl}(B)$ can not be attributed only to the Ni^{2+} subsystem. Phenomenologically, using $g = 1.99$ and $S = 5/2$ of the Mn^{2+}-spins, the data are described by $\Theta = 15.5$ K, $M_{sat} = 0.75$ μ_B/f.u., and $\chi_0 = 0.023$ μ_B/T f.u. Hence, attributing $M_{nl}(B)$ to only Mn^{2+}-spins would imply that about 15% of them are weakly coupled.

IV. DISCUSSION

Our data imply the evolution of long-range antiferromagnetic order at $T_N \simeq 35$ K and reorientation of the spin direction at $T_R \simeq 15$ K. This agrees to the sequence of phase transitions reported in the established phase diagram of $Ni_xMn_{1-x}TiO_3$ [14, 16]. As compared to the mother compound $MnTiO_3$ which shows $T_N \simeq 64$ K, the tendency for long-range magnetic order is significantly reduced by Ni-doping. While our results fit the expected phase boundary $T_N(x)$, we find T_R in between the two temperatures proposed as the start and the end temperatures of the spin rotation in [14]. The onset of long-range magnetic order in $Ni_{0.25}Mn_{0.75}TiO_3$ at T_N is signalled by clear anomalies in $\chi_{[001]}$, specific heat and thermal expansion (Figs. 1 and 3) which confirms the easy magnetic c axis and in particular shows significant magneto-elastic coupling. The negative thermal expansion along the c axis as well as strong magnetic field effects on the specific heat well above T_N suggest the presence of short-range ordering phenomena in the paramagnetic phase. The presence of short-range magnetic correlations above T_N results in associated magnetic entropy changes which can be estimated by comparison with the bare lattice contribution. The latter may be obtained by fitting the the specific heat well above T_N by an appropriate phononic model. This results in very similar phonon specific heat as found in $MnTiO_3$. Since in the following we will compare the entropy changes of $Ni_{0.25}Mn_{0.75}TiO_3$ and $MnTiO_3$, for the following entropy analysis we employ the phonon specific heat from Ref. [28] and account for the different atomic masses by multiplying with 1.015 (see Fig. 10a).

Subtracting the lattice contribution from the measured specific heat gives the magnetic specific heat c_p^{mag}. Integrating c_p^{mag}/T yields the magnetic entropy changes $\Delta S_m = 12.3(7)$ J/(mol K) which is close to the full expected magnetic entropy of $0.75R \ln 6 + 0.25R \ln 3 \approx 13.4$ J/(mol K). Notably, our analysis implies magnetic entropy changes up to about 130 K, i.e., persistence of short-range magnetic correlations up to temperatures higher than $4 \times T_N$. The presence of considerable short-

range magnetic order is further confirmed by the fact that the observed anomaly $\Delta c_{\rm p}$, at $T_{\rm N}$, is rather small as it only amounts to a few percent of the value predicated by mean field theory. Quantitatively, the specific heat jump at $T_{\rm N}$ amounts to $\Delta c_{\rm p} = 0.54(11)$ J/(mol K) , which is only a very small fraction ($\approx$ 3 %) of the expected mean field value. This expected value is calculated as $\Delta c_{\rm p} = R \times \frac{5S(S+1)}{S^2+(S+1)^2}$ and is approximately equal to 18.9 J/(mol K) [38]. Note, that the actual jump size associated with the measured anomaly can be even smaller as it may be superimposed by critical fluctuations. Such a small specific heat anomaly either implies significant short-range spin order above $T_{\rm N}$ and/or considerable spin disorder below $T_{\rm N}$.

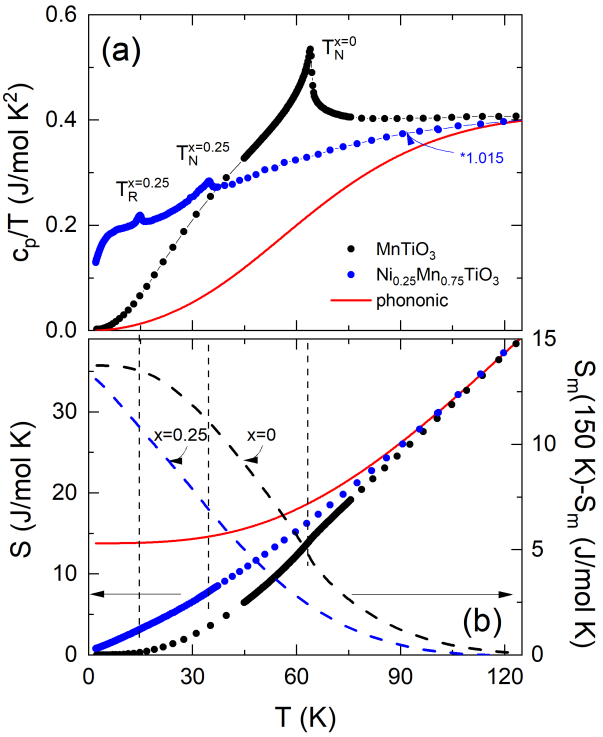

FIG. 10. (a) Temperature dependence of the specific heat, $c_{\rm p}/T$, of $Ni_xMn_{1-x}TiO_3$ with $x = 0$ (from Ref. [28]) and $x = 0.25$ measured at $B = 0$ T. The $Ni_{0.25}Mn_{0.75}TiO_3$ data are multiplied by 1.015 to account for the atomic mass difference. The red line presents the lattice contribution $c_{\rm p}^{\rm ph}$ of $MnTiO_3$. (b) Corresponding entropy changes (left ordinate) derived from integrating $c_{\rm p}/T$. $S_{\rm ph}(T)$ (red line) and $S_{x=0.25}(T)$ (blue circles) are shifted to match $S_{x=0}(T)$ above 120 K (see the text). Right ordinate: Changes of the magnetic entropy for both doping levels with respect to its value at 150 K.

Our experimental data show short-range magnetic order well above $T_{\rm N}$ as well as weakly coupled moments and a glass-like behaviour at low-temperatures. In Fig. 10b we illustrate how magnetic entropy is consumed upon cooling by comparing the specific heat and entropy changes appearing in $Ni_{0.25}Mn_{0.75}TiO_3$ and $MnTiO_3$ (Ref. [28]) with the lattice contributions. In $MnTiO_3$, the specific heat data illustrate a typical example of evolution of 3D long-range magnetic order. In $Ni_{0.25}Mn_{0.75}TiO_3$, at high temperatures, the specific heat data is very similar to that of $MnTiO_3$, which we attribute to the lattice. The main effects of 25 % Ni-doping are as following: (1) Suppression of $T_{\rm N}$ and of the anomaly size as discussed above. (2) Upon cooling below $T_{\rm N}$, in $Ni_{0.25}Mn_{0.75}TiO_3$ the entropy is consumed in a quasi-linear manner which qualitatively differs from from $MnTiO_3$. This is particularly visible in Fig. 10b where in addition to the measured total entropy changes the relative changes of the *magnetic* entropy with respect to the value at high temperature are shown. The figure also illustrates how different magnetic order evolves in $Ni_{0.25}Mn_{0.75}TiO_3$ as compared to $MnTiO_3$. (3) In $Ni_{0.25}Mn_{0.75}TiO_3$, the low temperature behaviour does exhibit a quasi-linear behaviour for $T \lesssim 4$ K where we find $c_{\sim p} \sim T^{1.3}$ as shown in the inset of Fig. 2. This contrasts a T^3-behaviour expected for a 3D AFM which is observed in $MnTiO_3$. Quasi-linear behaviour of $c_{\rm p}$ at low temperatures was previously reported for the spin glass state of $Ni_{0.42}Mn_{0.58}TiO_3$ [16] and also for canonical spin-glass systems such as CuMn [39] ScGd [40].

The presence of considerable magnetic disorder evidenced by our analysis of the entropy changes qualitatively agrees to the observation of weakly coupled paramegnetic moments in $Ni_{0.25}Mn_{0.75}TiO_3$ and the observed glassy-like feature in AC magnetic susceptibility ($T_{\rm SG} \simeq 3.7$ K). For $Ni_{0.4}Mn_{0.6}TiO_3$ Solanki *et al.* observe a similar feature at 9.1 K and report an XY-like spin-glass state with quasi-two-dimensional antiferromagnetic order [18]. By INS studies they conclude the presence of short-range-ordered antiferromagnetic clusters with short-lived spin correlations the XY-like SG state which may be associated with weakly antiferromagnetically-coupled moments observed in the high-field magnetisation data in Fig. 9.

Magneto-elastic coupling is further analysed by quantifying and comparing the thermal expansion and the heat capacity anomalies in $\alpha_{\rm i}$ and $c_{\rm p}$. The ratio of these quantities yields the uniaxial and hydrostatic pressure dependencies of the associated ordering phenomena by exploiting the Clausius Clapeyron relation for discontinuous phase transitions and the Ehrenfest relation for continuous ones [41, 42]. In $Ni_{0.25}Mn_{0.75}TiO_3$, we consider the anomaly at $T_{\rm N}$ a continuous phase transition and its size has been determined by means of a same area construction [43]. At $T_{\rm N}(B = 0$ T) this yields $\Delta\alpha_b = 0.5(1) \times 10^{-6}$ (1/K) and $\Delta\alpha_c = -0.80(15) \times 10^{-6}$ (1/K) (see Figs. 8 and 12 in the SI). Using these values as well as $\Delta c_{\rm p} = 0.54(11)$ J/(mol K) and the molar volume $V_{\rm m} = 3.215 \times 10^{-5}$ m^3/mol, the Ehrenfest relation

$$\left.\frac{\partial T_{\rm N}}{\partial p_i}\right|_B = T_N V_{\rm m} \frac{\Delta\alpha_i}{\Delta c_{\rm p}} \qquad (1)$$

yields $T_{\rm N}/\partial p_{\rm b} = 1.1(3)$ K/GPa and $T_{\rm N}/\partial p_{\rm c} = -1.7(5)$ K/GPa for uniaxial pressure applied along the b

and the c axis, respectively. Further, $T_{\rm N}$ depicts a small positive hydrostatic pressure dependence of $T_{\rm N}/\partial p$ = 0.4(5) K/GPa as qualitatively shown by the anomaly in the volume thermal-expansion coefficient at $T_{\rm N}$.

The uniaxial pressure dependencies of $T_{\rm R}$ are derived from the corresponding jumps $\Delta L_b/L_b = -2.0(2)\times10^{-6}$, $\Delta L_c/L_c$ = 3.1(2) $\times$ 10^{-6}, and ΔS = −0.027(3) J/(mol K) . Using the Clausius-Clapeyron relation for a discontinuous phase transition [41]

$$\left.\frac{\partial T_R}{\partial p_i}\right|_B = V_{\rm m}\frac{\Delta L_i/L_i}{\Delta S} \qquad (2)$$

yields the uniaxial pressure dependencies $T_{\rm R}/\partial p_{\rm b}$ = 2.3(4) K/GPa and $T_{\rm R}/\partial p_{\rm c}$ = −3.7(5) K/GPa. Following the phase boundary $T_{\rm R}(B)$ (AF1 → AF2/AF3' in Fig. 8a), the signs of the thermal expansion anomalies change at $B \simeq 1$ T implying opposite uniaxial pressure dependencies for AF1 → AF2 and AF1 → AF3'. The observed changes in pressure dependence and in particular the magnetostrictive effects shed light on the recently observed flop of electric polarization from $P||c$ to $P||a$ in $Ni_{0.33}Mn_{0.67}TiO_3$ [1]. Chi *et al.* associate linear ME response with rotation of the collinear spins away from the c axis for $T < T_{\rm R}$. Comparison of polarisation and magnetostriction data at the same reduced temperatures $T/T_{\rm R}$ yields the following observations (see Fig. 11): For $B \perp c$, (1) the jump in length at the transition AF2→AF3 indicates the onset of finite ME effect. (2) While magnetostriction is indiscernible in AF3 and AF1, a finite field-induced polarisation appears only in AF3 while it is negligible in AF1. (3) For $B||c$, only AF1 shows no ME effect. While, the peak in P does not correspond to the presence of a peak in $\partial L/\partial B$. Notably, while magneto-elastic coupling is prominent and yields distinct structural anomalies at the phase boundaries as well as differences in the magnetostrictive repsonse of the different magnetic phases and correspondingly the different ME regimes, observation (2) suggests that the ME effect in $Ni_xMn_{1-x}TiO_3$ may not have a direct magnetostrictive origin.

V. CONCLUSIONS

To conclude, we report detailed dilatometric, specific heat, and magnetic studies on macroscopic single crystals of $Ni_{0.25}Mn_{0.75}TiO_3$ grown by means of the optical floating-zone method. Our data imply the evolution of long-range magnetic order at $T_{\rm N} \simeq$ 35K and a spin-reorientation at $T_{\rm R} \simeq$ 15K. The latter is of discontinuous nature and attributed to competing magnetic anisotropies of Mn^{2+} and Ni^{2+} magnetic moments. We find clear anomalies in the length changes at the phase boundaries, indicating pronounced magneto-elastic coupling and sizable pressure dependencies of the associated ordering phenomena respectively energy scales. Quantitatively, our analysis yields $T_{\rm N}/\partial p_{\rm b}$ = 1.1(3) K/GPa, $T_{\rm N}/\partial p_{\rm c}$ = −1.7(5) K/GPa, $T_{\rm R}/\partial p_{\rm b}$ = 2.3(4) K/GPa, and $T_{\rm R}/\partial p_{\rm c}$ = −3.7(5) K/GPa. Applying magnetic fields $B||b$ axis yields a sign change signalling different low-temperature phases. Splitting of the anomalies implies the presence of an intermediate phase AF3'. In addition, our experimental data show short-range magnetic order well above $T_{\rm N}$ as well as, at low-temperatures, weakly coupled moments and a glass-like behaviour ($T_{\rm SG} \simeq$ 3.7 K). The number of weakly coupled moments is sizable and may amount to about 15 % of all Mn^{2+}-spins present in the material. Glass-like behaviour is seen in AC-χ and is further evidenced by quasi-linear T-dependence of $c_{\rm p}$ at low temperatures. The observed changes in pressure dependence and in particular the magnetostrictive effects shed light on the recently observed flop of electric polarization from $P||c$ to $P||a$ [1], suggesting the ME effect in $Ni_xMn_{1-x}TiO_3$ appearing at intermediate doping x does not have a direct magnetostrictive origin.

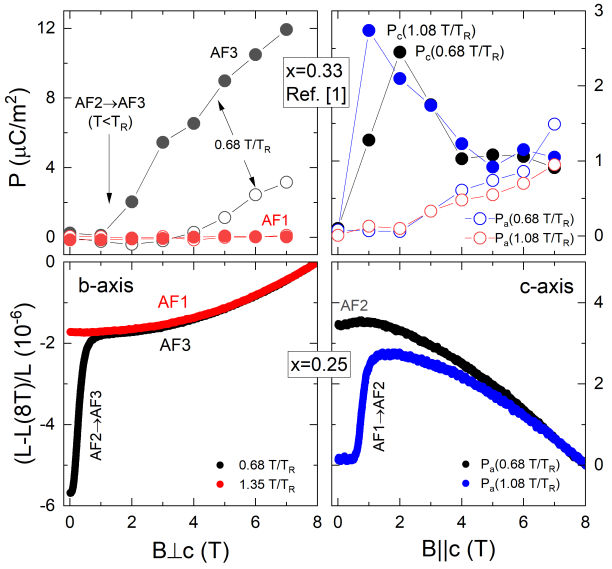

FIG. 11. Magnetic field dependence of electric polarisation (x=0.33, data from Ref. 1; upper panel) and magnetostriction (x=0.25; lower panel) in $Ni_xMn_{1-x}TiO_3$. In order to compare the results, the data are shown for same values of reduced temperature $T/T_{\rm R}$.

VI. ACKNOWLEDGEMENTS

We acknowledge support by BMBF via the project SpinFun (13XP5088) and by Deutsche Forschungsgemeinschaft (DFG) under Germany's Excellence Strategy EXC2181/1-390900948 (the Heidelberg STRUCTURES Excellence Cluster) and project KL 1824/13-1. L.G. and K.D. acknowledge support by IMPRS-QD. A.E. acknowledges support by DAAD through the GSSP program.

[1] S. Chi, F. Ye, H. Zhou, E. Choi, J. Hwang, H. Cao, and J. A. Fernandez-Baca, Physical Review B **90**, 144429 (2014).

[2] D. Sherrington and S. Kirkpatrick, Physical review letters **35**, 1792 (1975).

[3] M. Kobayashi, K. Katsumata, T. Satō, and Y. Miyako, Journal of the Physical Society of Japan **46**, 1467 (1979).

[4] S. Murayama, K. Yokosawa, Y. Miyako, and E. Wassermann, Physical review letters **57**, 1785 (1986).

[5] G. DeFotis, D. Mantus, E. McGhee, K. Echols, and R. Wiese, Physical Review B **38**, 11486 (1988).

[6] T. Ono, T. Kato, H. Tanaka, A. Hoser, N. Stüßer, and U. Schotte, Physical Review B **63**, 224425 (2001).

[7] F. Matsubara and S. Inawashiro, Journal of the Physical Society of Japan **42**, 1529 (1977).

[8] M. Igarashi and K. Nagata, Journal of magnetism and magnetic materials **90**, 363 (1990).

[9] Y. Ishikawa and S.-i. Akimoto, Journal of the Physical Society of Japan **13**, 1110 (1958).

[10] L. Bevaart, E. Frikkee, J. Lebesque, and L. De Jongh, Solid State Communications **25**, 539 (1978).

[11] A. Ito, H. Aruga, E. Torikai, M. Kikuchi, Y. Syono, and H. Takei, Physical review letters **57**, 483 (1986).

[12] A. Ito, H. Aruga, M. Kikuchi, Y. Syono, and H. Takei, Solid state communications **66**, 475 (1988).

[13] T. Kurihara, T. Komai, A. Ito, and T. Goto, Journal of the Physical Society of Japan **60**, 2057 (1991).

[14] A. Ito, H. Kawano, H. Yoshizawa, and K. Motoya, Journal of Magnetism and Magnetic Materials **104**, 1637 (1992).

[15] H. Yoshizawa, H. Kawano, H. Mori, S. Mitsuda, and A. Ito, Physica B: Condensed Matter **180**, 94 (1992).

[16] Y. Yamaguchi, T. Nakano, Y. Nozue, and T. Kimura, Physical review letters **108**, 057203 (2012).

[17] Y. Yamaguchi and T. Kimura, Nature communications **4**, 1 (2013).

[18] R. Solanki, S.-H. Hsieh, C. Du, G. Deng, C. Wang, J. Gardner, H. Tonomoto, T. Kimura, and W. Pong, Physical Review B **95**, 024425 (2017).

[19] J. B. Goodenough and J. J. Stickler, Physical Review **164**, 768 (1967).

[20] G. Shirane, P. SJ, and Y. Ishikawa, Journal of the Physical Society of Japan **14**, 1352 (1959).

[21] R. Newnham, J. Fang, and R. Santoro, Acta Crystallographica **17**, 240 (1964).

[22] H. Kato, Y. Yamaguchi, M. Ohashi, M. Yamada, H. Takei, and S. Funahashi, Solid State Communications **45**, 669 (1983).

[23] M. Hoffmann, K. Dey, J. Werner, R. Bag, J. Kaiser, H. Wadepohl, Y. Skourski, M. Abdel-Hafiez, S. Singh, and R. Klingeler, Physical Review B **104**, 014429 (2021).

[24] N. Mufti, G. Blake, M. Mostovoy, S. Riyadi, A. Nugroho, and T. T. Palstra, Physical Review B **83**, 104416 (2011).

[25] T. Müller, *Order and Disorder in the Charge and Spin Structures of YFe2O4-δ and Ni0. 42Mn0. 58TiO3*, Ph.D. thesis, RWTH Aachen University (2018).

[26] K. Dey, S. Sauerland, J. Werner, Y. Skourski, M. Abdel-Hafiez, R. Bag, S. Singh, and R. Klingeler, Physical Review B **101**, 195122 (2020).

[27] K. Dey, S. Sauerland, B. Ouladdiaf, K. Beauvois, H. Wadepohl, and R. Klingeler, Physical Review B **103**, 134438 (2021).

[28] L. Gries, M. Jonak, A. Elghandour, K. Dey, and R. Klingeler, arXiv preprint arXiv:2207.14750 (2022).

[29] K. Dey, W. Hergett, P. Telang, M. M. Abdel-Hafiez, and R. Klingeler, Journal of Crystal Growth **524**, 125157 (2019).

[30] J. Rodríguez-Carvajal, Physica B: Condensed Matter **192**, 55 (1993).

[31] Y. Skourski, M. Kuz'Min, K. Skokov, A. Andreev, and J. Wosnitza, Physical Review B **83**, 214420 (2011).

[32] R. Küchler, T. Bauer, M. Brando, and F. Steglich, Review of Scientific Instruments **83**, 095102 (2012).

[33] J. Werner, W. Hergett, M. Gertig, J. Park, C. Koo, and R. Klingeler, Physical Review B **95**, 214414 (2017).

[34] M. E. Fisher, Philosophical Magazine **7**, 1731 (1962).

[35] Y. Syono, S.-I. Akimoto, Y. Ishikawa, and Y. Endoh, Journal of Physics and Chemistry of Solids **30**, 1665 (1969).

[36] L. De Jongh, D. Betts, and D. Austen, Solid State Communications **15**, 1711 (1974).

[37] Here, we used the Ni-content as determined by EDX; using the nominal Ni-content does not change the conclusion.

[38] A. Tari, *The specific heat of matter at low temperatures* (World Scientific, 2003).

[39] W. Fogle, J. Ho, and N. Philipps, Le Journal de Physique Colloques **39**, C6 (1978).

[40] R. Caudron, P. Costa, J. Lasjaunias, and B. Levesque, Journal of Physics F: Metal Physics **11**, 451 (1981).

[41] T. Barron and G. White, in *Heat Capacity and Thermal Expansion at Low Temperatures* (Springer, 1999) pp. 153–223.

[42] R. Klingeler, B. Büchner, S.-W. Cheong, and M. Hücker, Physical Review B **72**, 104424 (2005).

[43] R. Küchler, *Thermische Ausdehnung und divergierendes Grüneisenverhältnis in Schwere-Fermionen-Systemen*, Dissertation, Technische Universität Dresden, Dresden (2005).

Literatur

[1] International Renewable Energy Agency, *World Energy Transitions Outlook 1-5 °C Pathway 2022 edition*, 2022. Adresse: https://www.irena.org/publications/2022/Mar/World-Energy-Transitions-Outlook-2022.

[2] G. Assat und J.-M. Tarascon, "Fundamental understanding and practical challenges of anionic redox activity in Li-ion batteries", *Nature Energy*, Jg. 3, Nr. 5, S. 373–386, 2018.

[3] J. M. Tarascon und M. Armand, "Issues and challenges facing rechargeable lithium batteries", *Nature*, Jg. 414, Nr. 6861, S. 359–367, 2001.

[4] N. Nitta, F. Wu, J. T. Lee und G. Yushin, "Li-ion battery materials: present and future", *Materials Today*, Jg. 18, Nr. 5, S. 252–264, 2015.

[5] K. Kubota, M. Dahbi, T. Hosaka, S. Kumakura und S. Komaba, "Towards K-Ion and Na-Ion Batteries as "Beyond Li-Ion"", *Chemical record (New York, N.Y.)*, Jg. 18, Nr. 4, S. 459–479, 2018.

[6] J. B. Goodenough und K.-S. Park, "The Li-ion rechargeable battery: a perspective", *Journal of the American Chemical Society*, Jg. 135, Nr. 4, S. 1167–1176, 2013.

[7] T. Placke, R. Kloepsch, S. Dühnen und M. Winter, "Lithium ion, lithium metal, and alternative rechargeable battery technologies: the odyssey for high energy density", *Journal of Solid State Electrochemistry*, Jg. 21, Nr. 7, S. 1939–1964, 2017.

[8] Tesla Inc, *Battery Day Presentation*. Adresse: https://tesla-share.thron.com/content/?id=96ea71cf-8fda-4648-a62c-753af436c3b6&pkey=S1dbei4.

[9] J. P. Pender, G. Jha, D. H. Youn, J. M. Ziegler, I. Andoni, E. J. Choi, A. Heller, B. S. Dunn, P. S. Weiss, R. M. Penner und C. B. Mullins, "Electrode Degradation in Lithium-Ion Batteries", *ACS nano*, Jg. 14, Nr. 2, S. 1243–1295, 2020.

[10] N. Mahmood, T. Tang und Y. Hou, "Nanostructured Anode Materials for Lithium Ion Batteries: Progress, Challenge and Perspective", *Advanced Energy Materials*, Jg. 6, Nr. 17, S. 1 600 374, 2016.

[11] M. Winter, J. O. Besenhard, M. E. Spahr und P. Novák, "Insertion Electrode Materials for Rechargeable Lithium Batteries", *Advanced Materials*, Jg. 10, Nr. 10, S. 725–763, 1998.

[12] J. Cabana, L. Monconduit, D. Larcher und M. R. Palacín, "Beyond intercalation-based Li-ion batteries: the state of the art and challenges of electrode materials reacting through conversion reactions", *Advanced Materials*, Jg. 22, Nr. 35, E170–92, 2010.

[13] Y. Wang und G. Cao, "Developments in Nanostructured Cathode Materials for High-Performance Lithium-Ion Batteries", *Advanced Materials*, Jg. 20, Nr. 12, S. 2251–2269, 2008.

[14] H. Zhang, Y. Yang, H. Xu, L. Wang, X. Lu und X. He, "$Li_4Ti_5O_{12}$ spinel anode: Fundamentals and advances in rechargeable batteries", *InfoMat*, Jg. 4, Nr. 4, 2022.

[15] J. Lu, Z. Chen, F. Pan, Y. Cui und K. Amine, "High-Performance Anode Materials for Rechargeable Lithium-Ion Batteries", *Electrochemical Energy Reviews*, Jg. 1, Nr. 1, S. 35–53, 2018.

[16] C. Zhang, F. Wang, J. Han, S. Bai, J. Tan, J. Liu und F. Li, "Challenges and Recent Progress on Silicon-Based Anode Materials for Next–Generation Lithium–Ion Batteries", *Small Structures*, Jg. 2, Nr. 6, S. 2 100 009, 2021.

[17] Y. Gao, Z. Pan, J. Sun, Z. Liu und J. Wang, "High-Energy Batteries: Beyond Lithium-Ion and Their Long Road to Commercialisation", *Nano-micro letters*, Jg. 14, Nr. 1, S. 94, 2022.

[18] K. T. Lai, I. Antonyshyn, Y. Prots und M. Valldor, "Anti-Perovskite Li-Battery Cathode Materials", *Journal of the American Chemical Society*, Jg. 139, Nr. 28, S. 9645–9649, 2017.

[19] N. A. Chernova, G. M. Nolis, F. O. Omenya, H. Zhou, Z. Li und M. S. Whittingham, "What can we learn about battery materials from their magnetic properties?", *Journal of Materials Chemistry*, Jg. 21, Nr. 27, S. 9865, 2011.

[20] L. Spieß, G. Teichert, R. Schwarzer, H. Behnken und C. Genzel, *Moderne Röntgenbeugung: Röntgendiffraktometrie für Materialwissenschaftler, Physiker und Chemiker* (Studium), 2., überarb. und erw. Aufl. Wiesbaden: Vieweg + Teubner, 2009, ISBN: 978-3-8351-0166-1.

[21] *Inorganic Crystal Structure Database (ICSD)*. Adresse: `https://icsd.products.fiz-karlsruhe.de/`.

[22] *Crystallography Open Database (COD)*. Adresse: `http://www.crystallography.net/cod/`.

[23] H. Khan, A. S. Yerramilli, A. D'Oliveira, T. L. Alford, D. C. Boffito und G. S. Patience, "Experimental methods in chemical engineering: X–ray diffraction spectroscopy—XRD", *The Canadian Journal of Chemical Engineering*, Jg. 98, Nr. 6, S. 1255–1266, 2020.

[24] K. O'Connell und J. R. Regalbuto, "High Sensitivity Silicon Slit Detectors for 1 nm Powder XRD Size Detection Limit", *Catalysis Letters*, Jg. 145, Nr. 3, S. 777–783, 2015.

[25] A. Weibel, R. Bouchet, F. Boulc' und P. Knauth, "The Big Problem of Small Particles: A Comparison of Methods for Determination of Particle Size in Nanocrystalline Anatase Powders", *Chemistry of Materials*, Jg. 17, Nr. 9, S. 2378–2385, 2005.

[26] A. L. Patterson, "The Scherrer Formula for X-Ray Particle Size Determination", *Physical Review*, Jg. 56, Nr. 10, S. 978–982, 1939.

[27] R. Wang, C. Wang, H. Zhang, J. Tao und X. Bai, Hrsg., *Progress in Nanoscale Characterization and Manipulation* (SpringerLink Bücher). Singapore: Springer Singapore, 2018, Bd. 272, ISBN: 978-981-13-0453-8.

[28] E. J. Mittemeijer, *Fundamentals of Materials Science*. Cham: Springer International Publishing, 2021, ISBN: 978-3-030-60055-6.

[29] "Evaluation of analytical instrumentation. Part XIX CHNS elemental analysers", *Accreditation and Quality Assurance*, Jg. 11, Nr. 11, S. 569–576, 2006.

[30] J. Lefebvre, F. Galli, C. L. Bianchi, G. S. Patience und D. C. Boffito, "Experimental methods in chemical engineering: X–ray photoelectron spectroscopy–XPS", *The Canadian Journal of Chemical Engineering*, Jg. 97, Nr. 10, S. 2588–2593, 2019.

[31] J. F. Moulder, W. F. Stickle, W. M. Sobol und K. D. Bomben, in *Handbook of X-Ray Photoelectron Spectroscopy*, 1992.

[32] S. Blundell, *Magnetism in condensed matter* (Oxford master series in physics Condensed matter physics), 1. Reprinted. Oxford: Oxford Univ. Press, 2003, Bd. 4, ISBN: 9780198505921.

[33] S. Roth und A. Stahl, *Elektrizität und Magnetismus: Experimentalphysik - anschaulich erklärt* (Lehrbuch). Berlin, Germany: Springer, 2018, ISBN: 978-3-662-54445-7.

[34] A. I. Braginski und J. Clarke, Hrsg., *The SQUID handbook: Vol. 1: Fundamentals and technology of SQUIDs and SQUID systems*. Weinheim: Wiley-VCH, 2004, ISBN: 9783527402298. Adresse: https://onlinelibrary.wiley.com/doi/book/10.1002/3527603646.

[35] J. Kieninger, *Electrochemical methods for the micro- and nanoscale: Theoretical essentials, instrumentation and methods for applications in MEMS and nanotechnology*. De Gruyter, 2022, ISBN: 978-3-11-064974-1. Adresse: https://www.degruyter.com/books/9783110649741.

[36] A. J. Bard, L. R. Faulkner und H. S. White, *Electrochemical methods: Fundamentals and applications*, Third edition. Hoboken, NJ: Wiley, 2022, ISBN: 978-1-119-33405-7.

[37] M. Winter und R. J. Brodd, "What are batteries, fuel cells, and supercapacitors?", *Chemical Reviews*, Jg. 104, Nr. 10, S. 4245–4269, 2004.

[38] F. Harnisch und S. Freguia, "A basic tutorial on cyclic voltammetry for the investigation of electroactive microbial biofilms", *Chemistry, an Asian journal*, Jg. 7, Nr. 3, S. 466–475, 2012.

[39] N. Elgrishi, K. J. Rountree, B. D. McCarthy, E. S. Rountree, T. T. Eisenhart und J. L. Dempsey, "A Practical Beginner's Guide to Cyclic Voltammetry", Jg. 95, Nr. 2, S. 197–206, 2018.

[40] Biologic, *Protocols for studying intercalation electrodes materials : Protocols for studying intercalation electrodes materials :Part I: Galvanostatic cycling with potential limitation (GCPL)*, Biologic, Hrsg. Adresse: https://www.biologic.net/documents/gitt-electrochemistry-battery-application-note-1/.

[41] Carsten Jähne, "Synthese und Charakterisierung von nano- und mikroskalierten Elektrodenmaterialien für Lithium-Ionen-Batterien", Doktorarbeit, Universität Heidelberg, 2013.

[42] Jonas Spychala, "Pyrene Tetraone- and Phenothiazine-based Polymers as Cathode Materials for Lithium-Ion Batteries", Masterarbeit, Universität Heidelberg, 2020.

[43] J. Xiao, Q. Li, Y. Bi, M. Cai, B. Dunn, T. Glossmann, J. Liu, T. Osaka, R. Sugiura, B. Wu, J. Yang, J.-G. Zhang und M. S. Whittingham, "Understanding and applying coulombic efficiency in lithium metal batteries", *Nature Energy*, Jg. 5, Nr. 8, S. 561–568, 2020.

[44] N. Meddings, M. Heinrich, F. Overney, J. Lee, V. Ruiz, E. Napolitano, S. Seitz, G. Hinds, R. Raccichini, M. Gaberšček und J. Park, "Application of electrochemical impedance spectroscopy to commercial Li-ion cells: A review", *Journal of Power Sources*, Jg. 480, S. 228 742, 2020.

[45] S. Wang, J. Zhang, O. Gharbi, V. Vivier, M. Gao und M. E. Orazem, "Electrochemical impedance spectroscopy", *Nature Reviews Methods Primers*, Jg. 1, Nr. 1, 2021.

[46] Biologic, *Why use Electrochemical Impedance Spectroscopy (EIS) for battery research?*, Biologic, Hrsg. Adresse: https://www.biologic.net/topics/why-use-electrochemical-impedance-spectroscopy-for-battery-research/.

[47] W. Choi, H.-C. Shin, J. M. Kim, J.-Y. Choi und W.-S. Yoon, "Modeling and Applications of Electrochemical Impedance Spectroscopy (EIS) for Lithium-ion Batteries", *Journal of Electrochemical Science and Technology*, Jg. 11, Nr. 1, S. 1–13, 2020.

[48] E. Barsoukov, Hrsg., *Impedance spectroscopy: Theory, experiment, and applications*, 2. ed. Hoboken, N.J: Wiley-Interscience, 2005, ISBN: 0-471-64749-7.

[49] Biologic, *VMP3*. Adresse: https://www.biologic.net/products/vmp3/.

[50] Biologic, *VSP*. Adresse: https://www.biologic.net/products/vsp/.

[51] Biologic, *Battery Cycler*. Adresse: https://www.biologic.net/products/bcs-800/.

[52] Biologic, *EC-Lab-Software*. Adresse: https://www.biologic.net/support-software/ec-lab-software/.

[53] Elisa Thauer, "Präparation und elektrochemische Charakterisierung von neuartigen Elektrodenmaterialien für Lithium-Ionen-Batterien", Bacherlorarbeit, Universität Heidelberg, 2014.

[54] Abdullah Özkara, "Elektrochemische Charakterisierung des Anti-Perowskits (Li_2Fe)SeO als Kathodenmaterial in Lithium-Ionen-Batterien", Bacherlorarbeit, Universität Heidelberg, 2021.

[55] Denis Djendur, “Characterization and Optimization of Anti-Perovskite Cathodes for Lithium-Ion-Batteries”, Masterarbeit, Universität Heidelberg, 2021.

[56] Henrik Hahn, “Elektrochemische Untersuchung des Anti-Perowskits (Li_2Fe)SeO als Kathodenmaterial in Lithium-Ionen-Batterien”, Bacherlorarbeit, Universität Heidelberg, 2021.

[57] E. Thauer, X. Shi, S. Zhang, X. Chen, L. Deeg, R. Klingeler, K. Wenelska und E. Mijowska, “Mn_3O_4 encapsulated in hollow carbon spheres coated by graphene layer for enhanced magnetization and lithium-ion batteries performance”, *Energy*, Jg. 217, S. 119 399, 2021.

[58] Marte Orderud Skare, “Project thesis - Coated Silicon Nanoparticles as Anode in Lithium Ion Batteries”, Diss., Department of Materials Science and Engineering, Norwegian University of Science and Technology, NTNU, 2016.

[59] V. Murray, D. S. Hall und J. R. Dahn, “A Guide to Full Coin Cell Making for Academic Researchers”, *Journal of The Electrochemical Society*, Jg. 166, Nr. 2, A329–A333, 2019.

[60] El-Cell, *User Manual User Manual PAT-Cell*. Adresse: `https://el-cell.com/wp-content/uploads/downloads/manuals/Manual_PAT-Cell_Release_2.52.pdf`.

[61] El-Cell, *User Manual User Manual PAT-Core*. Adresse: `https://el-cell.com/wp-content/uploads/downloads/manuals/Manual_PAT-Core_Release_1.24.pdf`.

[62] M. Ender, A. Weber und I.-T. Ellen, “Analysis of Three-Electrode Setups for AC-Impedance Measurements on Lithium-Ion Cells by FEM simulations”, *Journal of The Electrochemical Society*, Jg. 159, Nr. 2, A128–A136, 2011.

[63] M. Ender, J. Illig und E. Ivers-Tiffée, “Three-Electrode Setups for Lithium-Ion Batteries”, *Journal of The Electrochemical Society*, Jg. 164, Nr. 2, A71–A79, 2017.

[64] S. Klink, E. Madej, E. Ventosa, A. Lindner, W. Schuhmann und F. La Mantia, “The importance of cell geometry for electrochemical impedance spectroscopy in three-electrode lithium ion battery test cells”, *Electrochemistry Communications*, Jg. 22, S. 120–123, 2012.

[65] S. Fang, D. Bresser und S. Passerini, “Transition Metal Oxide Anodes for Electrochemical Energy Storage in Lithium– and Sodium–Ion Batteries”, *Advanced Energy Materials*, Jg. 10, Nr. 1, S. 1 902 485, 2020.

[66] S.-K. Jung, I. Hwang, D. Chang, K.-Y. Park, S. J. Kim, W. M. Seong, D. Eum, J. Park, B. Kim, J. Kim, J. H. Heo und K. Kang, “Nanoscale Phenomena in Lithium-Ion Batteries”, *Chemical Reviews*, Jg. 120, Nr. 14, S. 6684–6737, 2020.

[67] N. Nitta und G. Yushin, “High-Capacity Anode Materials for Lithium-Ion Batteries: Choice of Elements and Structures for Active Particles”, *Particle & Particle Systems Characterization*, Jg. 31, Nr. 3, S. 317–336, 2014.

[68] H. Li und H. Zhou, “Enhancing the performances of Li-ion batteries by carbon-coating: present and future”, *Chemical communications (Cambridge, England)*, Jg. 48, Nr. 9, S. 1201–1217, 2012.

[69] S.-H. Yu, S. H. Lee, D. J. Lee, Y.-E. Sung und T. Hyeon, "Conversion Reaction-Based Oxide Nanomaterials for Lithium Ion Battery Anodes", *Small (Weinheim an der Bergstrasse, Germany)*, Jg. 12, Nr. 16, S. 2146–2172, 2016.

[70] L. S. Ganapathe, M. A. Mohamed, R. Mohamad Yunus und D. D. Berhanuddin, "Magnetite (Fe_3O_4) Nanoparticles in Biomedical Application: From Synthesis to Surface Functionalisation", *Magnetochemistry*, Jg. 6, Nr. 4, S. 68, 2020.

[71] S. Ni, X. Wang, G. Zhou, F. Yang, J. Wang, Q. Wang und D. He, "Hydrothermal synthesis of Fe_3O_4 nanoparticles and its application in lithium ion battery", *Materials Letters*, Jg. 63, Nr. 30, S. 2701–2703, 2009.

[72] J. Dobson, "Magnetic nanoparticles for drug delivery", *Drug Development Research*, Jg. 67, Nr. 1, S. 55–60, 2006.

[73] G. S. Parkinson, "Iron oxide surfaces", *Surface Science Reports*, Jg. 71, Nr. 1, S. 272–365, 2016.

[74] Q. Li, C. W. Kartikowati, S. Horie, T. Ogi, T. Iwaki und K. Okuyama, "Correlation between particle size/domain structure and magnetic properties of highly crystalline Fe_3O_4 nanoparticles", *Scientific reports*, Jg. 7, Nr. 1, S. 9894, 2017.

[75] M. M. Thackeray, W. David und J. B. Goodenough, "Structural characterization of the lithiated iron oxides $Li_xFe_3O_4$ and $Li_xFe_2O_3$ ($0<x<2$)", *Materials Research Bulletin*, Jg. 17, Nr. 6, S. 785–793, 1982.

[76] D. C. Bock, C. J. Pelliccione, W. Zhang, J. Timoshenko, K. W. Knehr, A. C. West, F. Wang, Y. Li, A. I. Frenkel, E. S. Takeuchi, K. J. Takeuchi und A. C. Marschilok, "Size dependent behavior of Fe_3O_4 crystals during electrochemical (de)lithiation: an in situ X-ray diffraction, ex situ X-ray absorption spectroscopy, transmission electron microscopy and theoretical investigation", *Physical Chemistry Chemical Physics : PCCP*, Jg. 19, Nr. 31, S. 20 867–20 880, 2017.

[77] D. C. Bock, A. C. Marschilok, K. J. Takeuchi und E. S. Takeuchi, "Deliberate modification of the solid electrolyte interphase (SEI) during lithiation of magnetite, Fe_3O_4: impact on electrochemistry", *Chemical communications*, Jg. 53, Nr. 98, S. 13 145–13 148, 2017.

[78] P. Poizot, S. Laruelle, S. Grugeon, L. Dupont und J. M. Tarascon, "Nano-sized transition-metal oxides as negative-electrode materials for lithium-ion batteries", *Nature*, Jg. 407, Nr. 6803, S. 496–499, 2000.

[79] S. Jia, T. Song, B. Zhao, Q. Zhai und Y. Gao, "Dealloyed Fe_3O_4 octahedra as anode material for lithium-ion batteries with stable and high electrochemical performance", *Journal of Alloys and Compounds*, Jg. 617, S. 787–791, 2014.

[80] H. Cao, R. Liang, D. Qian, J. Shao und M. Qu, "l -Serine-Assisted Synthesis of Superparamagnetic Fe 3 O 4 Nanocubes for Lithuium Ion Batteries", *The Journal of Physical Chemistry C*, Jg. 115, Nr. 50, S. 24 688–24 695, 2011.

[81] A. B. Deshmukh, P. K. Dwivedi, A. C. Nalawade, M. S. Qureshi und M. V. Shelke, "Highly durable Li-ion battery anode from Fe_3O_4 nanoparticles embedded in nitrogen-doped porous carbon with improved rate capabilities", *Journal of Materials Science*, Jg. 55, Nr. 33, S. 15 667–15 680, 2020.

[82] Q. Wu, R. Jiang, L. Mu und S. Xu, "Fe_3O_4 anodes for lithium batteries: Production techniques and general applications", *Comptes Rendus Chimie*, Jg. 22, Nr. 1, S. 96–102, 2019.

[83] J. Mao, D. Niu, N. Zheng, G. Jiang, W. Zhao, J. Shi und Y. Li, "Fe_3O_4-Embedded and N-Doped Hierarchically Porous Carbon Nanospheres as High-Performance Lithium Ion Battery Anodes", *ACS Sustainable Chemistry & Engineering*, Jg. 7, Nr. 3, S. 3424–3433, 2019.

[84] S. Hao, B. Zhang, Y. Wang, C. Li, J. Feng, S. Ball, M. Srinivasan, J. Wu und Y. Huang, "Hierarchical three-dimensional Fe_3O_4@porous carbon matrix/graphene anodes for high performance lithium ion batteries", *Electrochimica Acta*, Jg. 260, S. 965–973, 2018.

[85] L. Wang, H. Zheng, X. Jin und Y. Yuan, "Fe_3O_4 Hollow Nanospheres Grown In Situ in Three-Dimensional Honeycomb Macroporous Carbon Boost Long-Life and High-Rate Lithium Ion Storage", *Journal of Electronic Materials*, Jg. 52, Nr. 1, S. 10–22, 2023.

[86] Y.-Y. Hu, Z. Liu, K.-W. Nam, O. J. Borkiewicz, J. Cheng, X. Hua, M. T. Dunstan, X. Yu, K. M. Wiaderek, L.-S. Du, K. W. Chapman, P. J. Chupas, X.-Q. Yang und C. P. Grey, "Origin of additional capacities in metal oxide lithium-ion battery electrodes", *Nature materials*, Jg. 12, Nr. 12, S. 1130–1136, 2013.

[87] J. Jamnik und J. Maier, "Nanocrystallinity effects in lithium battery materials", *Physical Chemistry Chemical Physics*, Jg. 5, Nr. 23, S. 5215, 2003.

[88] Q. Li, H. Li, Q. Xia, Z. Hu, Y. Zhu, S. Yan, C. Ge, Q. Zhang, X. Wang, X. Shang, S. Fan, Y. Long, L. Gu, G.-X. Miao, G. Yu und J. S. Moodera, "Extra storage capacity in transition metal oxide lithium-ion batteries revealed by in situ magnetometry", *Nature materials*, Jg. 20, Nr. 1, S. 76–83, 2021.

[89] W. Cho, J. H. Song, J.-H. Kim, G. Jeong, E. Y. Lee und Y.-J. Kim, "Electrochemical characteristics of nano-sized MoO_2/C composite anode materials for lithium-ion batteries", *Journal of Applied Electrochemistry*, Jg. 42, Nr. 11, S. 909–915, 2012.

[90] J. J. Auborn und Y. L. Barberio, "Lithium Intercalation Cells Without Metallic Lithium: MoO_2/$LiCoO_2$ and WO_2/$LiCoO_2$", *Journal of The Electrochemical Society*, Jg. 134, Nr. 3, S. 638–641, 1987.

[91] J. Dahn und W. Mckinnon, "Structure and electrochemistry of Li_xMoO_2", *Solid State Ionics*, Jg. 23, Nr. 1-2, S. 1–7, 1987.

[92] J. H. Ku, Y. S. Jung, K. T. Lee, C. H. Kim und S. M. Oh, "Thermoelectrochemically Activated MoO_2 Powder Electrode for Lithium Secondary Batteries", *Journal of The Electrochemical Society*, Jg. 156, Nr. 8, A688, 2009.

[93] K. Tang, S. A. Farooqi, X. Wang und C. Yan, "Recent Progress on Molybdenum Oxides for Rechargeable Batteries", *ChemSusChem*, Jg. 12, Nr. 4, S. 755–771, 2019.

[94] D. Koziej, M. D. Rossell, B. Ludi, A. Hintennach, P. Novák, J.-D. Grunwaldt und M. Niederberger, "Interplay between size and crystal structure of molybdenum dioxide nanoparticles–synthesis, growth mechanism, and electrochemical performance", *Small*, Jg. 7, Nr. 3, S. 377–387, 2011.

[95] H.-J. Zhang, J. Shu, K.-X. Wang, X.-T. Chen, Y.-M. Jiang, X. Wei und J.-S. Chen, "Lithiation mechanism of hierarchical porous MoO_2 nanotubes fabricated through one-step carbothermal reduction", *Journal of Materials Chemistry A*, Jg. 2, Nr. 1, S. 80–86, 2014.

[96] X. Zhang, X. Song, S. Gao, Y. Xu, X. Cheng, H. Zhao und L. Huo, "Facile synthesis of yolk–shell MoO_2 microspheres with excellent electrochemical performance as a Li-ion battery anode", *Journal of Materials Chemistry A*, Jg. 1, Nr. 23, S. 6858, 2013.

[97] S. Petnikota, K. W. Teo, L. Chen, A. Sim, S. K. Marka, M. V. Reddy, V. V. S. S. Srikanth, S. Adams und B. V. R. Chowdari, "Exfoliated Graphene Oxide/MoO_2 Composites as Anode Materials in Lithium-Ion Batteries: An Insight into Intercalation of Li and Conversion Mechanism of MoO_2", *ACS applied materials & interfaces*, Jg. 8, Nr. 17, S. 10 884–10 896, 2016.

[98] Z. X. Huang, Y. Wang, Y. G. Zhu, Y. Shi, J. I. Wong und H. Y. Yang, "3D graphene supported MoO2 for high performance binder-free lithium ion battery", *Nanoscale*, Jg. 6, Nr. 16, S. 9839–9845, 2014.

[99] S. Li, K. Wang, G. Zhang, S. Li, Y. Xu, X. Zhang, X. Zhang, S. Zheng, X. Sun und Y. Ma, "Fast Charging Anode Materials for Lithium–Ion Batteries: Current Status and Perspectives", *Advanced Functional Materials*, Jg. 32, Nr. 23, S. 2 200 796, 2022.

[100] J. Bai, B. Zhao, J. Zhou, J. Si, Z. Fang, K. Li, H. Ma, J. Dai, X. Zhu und Y. Sun, "Glucose-Induced Synthesis of 1T-MoS_2/C Hybrid for High-Rate Lithium-Ion Batteries", *Small*, Jg. 15, Nr. 14, e1805420, 2019.

[101] T. Stephenson, Z. Li, B. Olsen und D. Mitlin, "Lithium ion battery applications of molybdenum disulfide (MoS_2) nanocomposites", *Energy Environ. Sci.*, Jg. 7, Nr. 1, S. 209–231, 2014.

[102] R. Zhang, Y. Qin, P. Liu, C. Jia, Y. Tang und H. Wang, "How does Molybdenum Disulfide Store Charge: A Minireview", *ChemSusChem*, Jg. 13, Nr. 6, S. 1354–1365, 2020.

[103] L. Zhang, D. Sun, J. Kang, J. Feng, H. A. Bechtel, L.-W. Wang, E. J. Cairns und J. Guo, "Electrochemical Reaction Mechanism of the MoS_2 Electrode in a Lithium-Ion Cell Revealed by in Situ and Operando X-ray Absorption Spectroscopy", *Nano letters*, Jg. 18, Nr. 2, S. 1466–1475, 2018.

[104] Z. Li, A. Ottmann, Q. Sun, A. K. Kast, K. Wang, T. Zhang, H.-P. Meyer, C. Backes, C. Kübel, R. R. Schröder, J. Xiang, Y. Vaynzof und R. Klingeler, "Hierarchical MoS_2-carbon porous nanorods towards atomic interfacial engineering for high-performance lithium storage", *Journal of Materials Chemistry A*, Jg. 7, Nr. 13, S. 7553–7564, 2019.

[105] X. Zhang, R. Zhao, Q. Wu, W. Li, C. Shen, L. Ni, H. Yan, G. Diao und M. Chen, "Petal-like MoS_2 Nanosheets Space-Confined in Hollow Mesoporous Carbon Spheres for Enhanced Lithium Storage Performance", *ACS nano*, Jg. 11, Nr. 8, S. 8429–8436, 2017.

[106] K. T. Lai, I. Antonyshyn, Y. Prots und M. Valldor, "Extended Chemical Flexibility of Cubic Anti-Perovskite Lithium Battery Cathode Materials", *Inorganic chemistry*, Jg. 57, Nr. 21, S. 13 296–13 299, 2018.

[107] Z. Lu und F. Ciucci, "Anti-perovskite cathodes for lithium batteries", *Journal of Materials Chemistry A*, Jg. 6, Nr. 12, S. 5185–5192, 2018.

[108] D. Mikhailova, L. Giebeler, S. Maletti, S. Oswald, A. Sarapulova, S. Indris, Z. Hu, J. Bednarcik und M. Valldor, "Operando Studies of Antiperovskite Lithium Battery Cathode Material $(Li_2Fe)SO$", *ACS Applied Energy Materials*, Jg. 1, Nr. 11, S. 6593–6599, 2018.

[109] M. V. Gorbunov, S. Carrocci, S. Maletti, M. Valldor, T. Doert, S. Hampel, I. G. Gonzalez Martinez, D. Mikhailova und N. Gräßler, "Synthesis of $(Li_2Fe_{1-y}Mn_y)SO$ Antiperovskites with Comprehensive Investigations of $(Li_2Fe_{0.5}Mn_{0.5})SO$ as Cathode in Li-ion Batteries", *Inorganic chemistry*, Jg. 59, Nr. 21, S. 15 626–15 635, 2020.

[110] M. V. Gorbunov, S. Carocci, I. G. Gonzalez Martinez, V. Baran und D. Mikhailova, "Studies of $Li_2Fe_{0.9}M_{0.1}SO$ Antiperovskite Materials for Lithium–Ion Batteries: The Role of Partial Fe^{2+} to M^{2+} Substitution", *Frontiers in Energy Research*, Jg. 9, 2021.

[111] M. A. A. Mohamed, M. V. Gorbunov, M. Valldor, S. Hampel, N. Gräßler und D. Mikhailova, "Tuning the electrochemical properties by anionic substitution of Li-rich antiperovskite $(Li_2Fe)S_{1-x}Se_xO$ cathodes for Li-ion batteries", *Journal of Materials Chemistry A*, Jg. 9, Nr. 40, S. 23 095–23 105, 2021.

[112] O. E. Barcia und O. R. Mattos, "Reaction model simulating the role of sulphate and chloride in anodic dissolution of iron", *Electrochimica Acta*, Jg. 35, Nr. 10, S. 1601–1608, 1990.

[113] H. Zhang, L. Wang, H. Li und X. He, "Criterion for Identifying Anodes for Practically Accessible High-Energy-Density Lithium-Ion Batteries", *ACS Energy Letters*, Jg. 6, Nr. 10, S. 3719–3724, 2021.

[114] H. Ming, H. Zhou, X. Zhu, S. Zhang, P. Zhao, M. Li, L. Wang und J. Ming, "Advanced Metal Oxide@Carbon Nanotubes for High-Energy Lithium-Ion Full Batteries", *Energy Technology*, Jg. 6, Nr. 4, S. 766–772, 2018.

[115] P. G. Bruce, B. Scrosati und J.-M. Tarascon, “Nanomaterials for rechargeable lithium batteries”, *Angewandte Chemie (International ed. in English)*, Jg. 47, Nr. 16, S. 2930–2946, 2008.

[116] C. Wang, H. Nakamura, H. Komatsu, M. Yoshio und H. Yoshitake, “Electrochemical behaviour of a graphite electrode in propylene carbonate and 1,3-benzodioxol-2-one based electrolyte system”, *Journal of Power Sources*, Jg. 74, Nr. 1, S. 142–145, 1998.

[117] Z. Chen und K. Amine, “Tris(pentafluorophenyl) Borane as an Additive to Improve the Power Capabilities of Lithium-Ion Batteries”, *Journal of The Electrochemical Society*, Jg. 153, Nr. 6, A1221, 2006.

[118] T. Feng, Y. Xu, Z. Zhang, X. Du, X. Sun, L. Xiong, R. Rodriguez und R. Holze, “Low-Cost Al_2O_3 Coating Layer As a Preformed SEI on Natural Graphite Powder To Improve Coulombic Efficiency and High-Rate Cycling Stability of Lithium-Ion Batteries”, *ACS applied materials & interfaces*, Jg. 8, Nr. 10, S. 6512–6519, 2016.

[119] J. Zhao, Z. Lu, N. Liu, H.-W. Lee, M. T. McDowell und Y. Cui, “Dry-air-stable lithium silicide-lithium oxide core-shell nanoparticles as high-capacity prelithiation reagents”, *Nature communications*, Jg. 5, S. 5088, 2014.

[120] M. W. Forney, M. J. Ganter, J. W. Staub, R. D. Ridgley und B. J. Landi, “Prelithiation of silicon-carbon nanotube anodes for lithium ion batteries by stabilized lithium metal powder (SLMP)”, *Nano letters*, Jg. 13, Nr. 9, S. 4158–4163, 2013.

[121] X. Li, X. Sun, X. Hu, F. Fan, S. Cai, C. Zheng und G. D. Stucky, “Review on comprehending and enhancing the initial Coulombic efficiency of anode materials in lithium-ion/sodium-ion batteries”, *Nano Energy*, Jg. 77, S. 105 143, 2020.

[122] P. U. Nzereogu, A. D. Omah, F. I. Ezema, E. I. Iwuoha und A. C. Nwanya, “Anode materials for lithium-ion batteries: A review”, *Applied Surface Science Advances*, Jg. 9, S. 100 233, 2022.

Danksagung

An dieser Stelle möchte ich mich bei allen Menschen bedanken, die zum Gelingen meiner Promotion beigetragen haben.

Allen voran möchte ich Rüdiger Klingeler dafür danken, dass er mir diese Arbeit ermöglicht hat. Seine uneingeschränkte Unterstützung und die unzähligen Gespräche haben mich zu einem besseren Wissenschaftler gemacht.

Des Weiteren möchte ich mich bei Loredana Gastaldo für die Übernahme des Zweitgutachtens bedanken.

Danken möchte ich auch allen Kooperationspartnern innerhalb und außerhalb der Universität Heidelberg, ohne euch wäre diese Arbeit nicht möglich gewesen.

Ich danke allen aktiven und ehemaligen Mitgliedern der F25-Arbeitsgruppe am KIP für die tolle Arbeitsatmosphäre und die produktive Zusammenarbeit. Ich habe die vielen anregenden Gespräche und Diskussionen sowie das freundschaftliche Miteinander immer genossen. Danke für die schöne Zeit!

Ein besonderer Dank geht an meinen Bürokollegen Peng, der mir nicht nur die chinesische Küche näher gebracht hat, sondern mich auch immer wieder mit dem ein oder anderen Snack überrascht hat. Ein weiterer besonderer Dank geht an Tom und Rüdiger für das Korrekturlesen dieser Arbeit.

Nicht zu vergessen sind meine Studenten Viktor, Joshua, Abdullah, Denis und Hendrik, denen ich nicht nur für die vielen Messungen meinen Dank aussprechen möchte, sondern auch für die vielen Diskussionen, die mein Wissen immer wieder erweitert haben.

Meinen Freunden danke ich, dass sie immer für mich da waren! Speziellen Dank geht an dieser Stelle an Sebastian, der seit dem ich denken kann, meinen Weg geteilt hat.

Zu guter Letzt möchte ich mich bei meiner Familie und Luu bedanken. Meine Dankbarkeit für euch kann nicht in Worte gefasst werden.

Eidesstattliche Versicherung gemäß §8 der Promotionsordnung für die Gesamtfakultät für Mathematik, Ingenieur- und Naturwissenschaften der Universität Heidelberg

Ich erkläre hiermit, dass ich diese Arbeit selbstständig verfasst und keine anderen als die angegebenen Quellen und Hilfsmittel benutzt habe.

Heidelberg, den 17. April 2023

Lennart Singer